

Architectural Mimics of [FeFe]-Hydrogenase H-Cluster: Synthesis, Characterization and Electrochemical Studies



seit 1558

Dissertation

(kumulativ)

zur Erlangung des akademischen Grades doctor rerum naturalium

(Dr. rer. nat.)

vorgelegt dem Rat der Chemisch-Geowissenschaftlichen Fakultät

der Friedrich-Schiller-Universität Jena

von M.Sc. Hassan Abul-Futouh

geboren am 07.05.1986 in Zarqa/Jordan

Gutachter (Referees):

1. Prof. Dr. Wolfgang Weigand, Friedrich-Schiller-Universität Jena.
2. Prof. Dr. Kalina Peneva, Friedrich-Schiller-Universität Jena.
3. Prof. Dr. Bernhard Keppler, Universität Wien.

Tag der öffentlichen: 01.11.2017

CONTENTS

ABBREVIATIONS	V
1 LIST OF PUBLICATIONS	1
2 DOCUMENTATION OF AUTHORSHIP	3
2.1 [HAF-1] [FeFe]-HYDROGENASE H-CLUSTER MIMICS WITH UNIQUE PLANAR μ -(SCH ₂)ER ₂ LINKERS (E = GE AND SN)	3
2.2 [HAF-2] SELENIUM MAKES THE DIFFERENCE: PROTONATION OF [FeFe]-HYDROGENASE MIMICS WITH DISELENOLATO LIGANDS	4
2.3 [HAF-3] A NEW MACROCYCLIC [FeFe]-HYDROGENASE H CLUSTER MODEL	5
2.4 [HAF-4] [FeFe]-HYDROGENASE H-CLUSTER MIMICS MEDIATED BY NAPHTHALENE MONOIMIDE DERIVATIVES OF PERI-SUBSTITUTED DICHALCOGENIDES	6
2.5 [HAF-5] A SYSTEMATIC STUDY OF [FeFe]-HYDROGENASE H-CLUSTER MIMICS WITH VARIOUS -S(CH ₂) _N S- LINKER LENGTHS (N = 2-8).....	7
2.6 [HAF-6] ELECTROCHEMICAL INVESTIGATION AND DENSITY FUNCTIONAL CALCULATIONS ON PROTON REDUCTION CYCLE CATALYZED BY [FeFe]-HYDROGENASE MODELS FEATURING [Fe ₂ S ₃] CORE.....	8
2.7 [HAF-7] SYNTHESIS, CHARACTERIZATION AND ELECTROCHEMICAL INVESTIGATIONS OF HETEROCYCLIC-SELENOCARBOXYLATE IRON COMPLEXES.....	9
2.8 DECLARATION	11
3 INTRODUCTION	12
3.1 ENERGY AND HYDROGEN ECONOMY	12
3.2 [FeFe]-HYDROGENASES	15
3.3 SYNTHETIC MODELS FOR THE H-CLUSTER.....	19
3.3.1 <i>First Generation of [FeFe]-Hydrogenase Mimics: An Overview</i>	19
3.3.2 <i>Modification of the Synthetic Models</i>	21
3.4 PROTONATION OF HEXACARBONYL COMPLEXES	41
3.5 MOTIVATION	47
4 PUBLICATIONS	50
4.1 [HAF-1].....	50
4.2 [HAF-2].....	83
4.3 [HAF-3].....	101
4.4 [HAF-4].....	107
4.5 [HAF-5].....	138
4.6 [HAF-6].....	171

4.7	[HAF-7].....	217
5	SUMMARY	227
6	ZUSAMMENFASSUNG	234
7	REFERENCES	242
8	ACKNOWLEDGEMENTS	253
9	CURRICULUM VITAE	254
10	DECLARATION OF AUTHORSHIP	258
11	SELBSTSTÄNDIGKEITSERKLÄRUNG	258

ABBREVIATIONS

Ni	Nickel
H-cluster	Hydrogen activating cluster
DdHase	[FeFe]-hydrogenase from <i>Desulfovibrio desulfuricans</i>
CpI	[FeFe]-hydrogenase from <i>Clostridium pasteurianum</i>
PDB	Protein Databank
3C8Y	Identifier
1HFE	Identifier
Fe _d	distal iron atom
Fe _p	proximal iron atom
pm	picometre
EPR	Electron paramagnetic resonance
FTIR	Fourier transform infrared
IR	Infrared
NMR	Nuclear Magnetic Resonance
EtSH	Ethanethiol
Boc	Tert-butoxycarbonyl
Me	Methyl
Et	Ethyl
Bu	Butyl
DFT	Density functional theory
emp	Empirical
calc	Calculated
cm	Centimeter
Pr	Propyl
ap	apical
ba	basal
pdt	Propanedithiolate
edt	ethanedithiolate

bdt	benzenedithiolate
<i>aa</i>	axial-axial
<i>ae</i>	axial-equatorial
r.t.	Room temperature
ppm	Parts per million
AcOH	Acetic Acid

1 LIST OF PUBLICATIONS

[HAF-1] [FeFe]-Hydrogenase H-Cluster Mimics with Unique Planar μ -(SCH₂)ER₂ Linkers (E = Ge and Sn)

Hassan Abul-Futouh, Laith R. Almazahreh, Takahiro Sakamoto, Nhu Y. T. Stessman, Dennis L. Lichtenberger, Richard S. Glass, Helmar Görls, Mohammad El-Khateeb, Philippe Schollhammer, Grzegorz Mloston, Wolfgang Weigand

Chemistry – A European Journal **2017**, *23*, 346-359.

[HAF-2] Selenium Makes the Difference: Protonation of [FeFe]-Hydrogenase Mimics with Diselenolato Ligands

Hassan Abul-Futouh, Mohammad El-Khateeb, Helmar Görls, Khalil Jamil Asali, Wolfgang Weigand

Dalton Transactions **2017**, *46*, 2937-2947.

[HAF-3] A New Macrocyclic [FeFe]-Hydrogenase H Cluster Model

Hassan Abul-Futouh, Helmar Görls, Wolfgang Weigand

Phosphorus, Sulfur, and Silicon and the Related Elements **2017**, *192*, 634-637.

[HAF-4] [FeFe]-Hydrogenase H-Cluster Mimics Mediated by Naphthalene Monoimide Derivatives of *Peri*-Substituted Dichalcogenides

Hassan Abul-Futouh, Yulian Zaganyarski, Carolin Müller, Martin Schulz, Stephan Kupfer, Helmar Görls, Mohammad El-Khateeb, Stefanie Gräfe, Benjamin Dietzek, Kalina Peneva, Wolfgang Weigand

Dalton Transactions **2017**, *46*, 11180-11191.

[HAF-5] [FeFe]-Hydrogenase H-Cluster Mimics with Various -S(CH₂)_nS- Linker Lengths (n = 2-8): A Systematic Study

Hassan Abul-Futouh, Laith R. Almazahreh, Mohammad Kamal Harb, Helmar Görls, Mohammad El-Khateeb, Wolfgang Weigand

Inorganic Chemistry, **2017**, *56*, 10437-10451.

[HAF-6] Electrochemical Investigation and Density Functional Calculations on Proton Reduction Cycle Catalyzed by [FeFe]-Hydrogenase Models Featuring [Fe₂S₃] Core

Hassan Abul-Futouh, Laith R. Almazahreh, Ahmad Q. Daraosheh, Mohammad El-Khateeb, Luca De Gioia, Giuseppe Zampella, Wolfgang Weigand, Luca Bertini

Ready for Submission.

[HAF-7] Synthesis, Characterization and Electrochemical Investigations of Heterocyclic-Selenocarboxylate Iron Complexes

Mohammad El-Khateeb, **Hassan Abul-Futouh**, Helmar Görls, Wolfgang Weigand, Laith R. Almazahreh

Inorganica Chimica Acta, **2016**, *449*, 14-19.

2 DOCUMENTATION OF AUTHORSHIP

2.1 [HAF-1] [FeFe]-Hydrogenase H-Cluster Mimics with Unique Planar μ -(SCH₂)ER₂ Linkers (E = Ge and Sn)

Hassan Abul-Futouh,¹ Laith R. Almazahreh,² Takahiro Sakamoto,³ Nhu Y. T. Stessman,⁴ Dennis L. Lichtenberger,⁵ Richard S. Glass,⁶ Helmar Görls,⁷ Mohammad El-Khateeb,⁸ Philippe Schollhammer,⁹ Grzegorz Mloston,¹⁰ Wolfgang Weigand¹¹

Chemistry – A European Journal **2017**, *23*, 346-359.

Involved in	Authors										
	1	2	3	4	5	6	7	8	9	10	11
Manuscript preparation	x	x									
Discussion of the manuscript	x	x			x	x			x	x	x
Synthesis of compounds	x	x									
Analytics	x	x									
Cyclic Voltammetry	x	x									
X-Ray structure Determination							x				
Photon electron spectroscopy			x	x	x						
DFT calculations			x	x	x						

Supervision								x			x
Publication equivalents	1.0										

2.2 [HAF-2] Selenium Makes the Difference: Protonation of [FeFe]-Hydrogenase Mimics with Diselenolato Ligands

Hassan Abul-Futouh,¹ Mohammad El-Khateeb,² Helmar Görls,³ Khalil Jamil Asali,⁴ Wolfgang Weigand⁵

Dalton Transactions **2017**, 46, 2937-2947.

Involved in	Authors				
	1	2	3	4	5
Manuscript preparation	x				
Discussion of the manuscript	x			x	x
Synthesis of compounds	x				
Analytcs	x				
Cyclic Voltammetry	x				
X-Ray structure Determination			x		

Supervision		x			x
Publication equivalents	1.0				

2.3 [HAF-3] A New Macrocyclic [FeFe]-Hydrogenase H Cluster Model

Hassan Abul-Futouh,¹ Helmar Görls,² Wolfgang Weigand³

Phosphorus, Sulfur, and Silicon and the Related Elements **2017**, 192, 634-637.

Involved in	Authors		
	1	2	3
Manuscript preparation	x		
Discussion of the manuscript	x		x
Synthesis of compounds	x		
Analytics	x		
X-Ray structure Determination		x	
Supervision			x
Publication equivalents	1.0		

2.4 [HAF-4] [FeFe]-Hydrogenase H-Cluster Mimics Mediated by Naphthalene Monoimide Derivatives of Peri-Substituted Dichalcogenides

Hassan Abul-Futouh,¹ Yulian Zagranyski,² Carolin Müller,³ Martin Schulz,⁴ Stephan Kupfer,⁵ Helmar Görls,⁶ Mohammad El-Khateeb,⁷ Stefanie Gräfe,⁸ Benjamin Dietzek,⁹ Kalina Peneva,¹⁰ Wolfgang Weigand¹¹

Dalton Transactions **2017**, 46, 11180-11191.

Involved in	Authors										
	1	2	3	4	5	6	7	8	9	10	11
Manuscript preparation	x										
Discussion of the manuscript	x			x				x	x	x	x
Synthesis of complexes	x										
Synthesis of naphthalene chromophore		x									
Analytics	x		x		x						
X-Ray structure Determination						x					
Cyclic voltammetry	x										
TDDFT investigations			x		x			x			

Photophysical properties			x	x						x		
Supervision								x			x	x
Publication equivalents	1.0											

2.5 [HAF-5] [FeFe]-Hydrogenase H-Cluster Mimics with Various - S(CH₂)_nS- Linker Lengths (n = 2-8): A Systematic Study

Hassan Abul-Futouh,¹ Laith R. Almazahreh,² Mohammad Kamal Harb,³ Helmar Görls,⁴ Mohammad El-Khateeb,⁵ Wolfgang Weigand⁶

Inorganic Chemistry, **2017**, *56*, 10437-10451.

Involved in	Authors					
	1	2	3	4	5	6
Manuscript preparation	x					
Discussion of the manuscript	x	x	x			x
Synthesis of complexes	x					
Analytics	x					
X-Ray structure Determination				x		

Cyclic voltammetry	x	x					
Supervision						x	x
Publication equivalents	1.0						

2.6 [HAF-6] Electrochemical Investigation and Density Functional Calculations on Proton Reduction Cycle Catalyzed by [FeFe]-Hydrogenase Models Featuring [Fe₂S₃] Core

Hassan Abul-Futouh,¹ Laith R. Almazahreh,² Ahmad Q. Daraosheh,³ Mohammad El-Khateeb,⁴ Luca De Gioia,⁵ Giuseppe Zampella,⁶ Wolfgang Weigand,⁷ Luca Bertini⁸

Ready for Submission.

Involved in	Authors							
	1	2	3	4	5	6	7	8
Manuscript preparation	x							
Discussion of the manuscript	x	x	x				x	x
Synthesis of complexes	x							
Analytics	x	x						x

Cyclic voltammetry	x	x						
DFT calculations					x	x		x
Supervision				x			x	x
Publication equivalents	1.0							

2.7 [HAF-7] Synthesis, Characterization and Electrochemical Investigations of Heterocyclic-Selenocarboxylate Iron Complexes

Mohammad El-Khateeb,¹ Hassan Abul-Futouh,² Helmar Görls,³ Wolfgang Weigand,⁴ Laith R. Almazahreh⁵

Inorganica Chimica Acta, **2016**, *449*, 14-19.

Involved in	Authors				
	1	2	3	4	5
Manuscript preparation	x	x			x
Discussion of the manuscript	x	x		x	x
Synthesis of complexes		x			
Analytics		x			x

X-Ray structure Determination			x		
Cyclic voltammetry		x			x
Supervision	x			x	
Publication equivalents		1.0			

2.8 Declaration

Erklärung zu den Eigenanteilen des Promovenden sowie der weiterer Doktoranden/Doktorandinnen als Koautoren an den Publikationen und Zweitpublikationsrechten bei einer kumulativen Dissertation.

Für alle in dieser kumulativen Dissertation verwendeten Manuskripte liegen die notwendigen Genehmigungen der Verlage für die Zweitpublikation vor.

Die Ko-Autoren der in dieser kumulativen Dissertation verwendeten Manuskripte sind sowohl über die Nutzung, als auch über die oben angegebenen Eigenanteile informiert und stimmen dem zu.

Ich bin mit der Abfassung der Dissertation als publikationsbasiert, d.h. kumulativ, einverstanden und bestätige die vorstehenden Angaben. Eine entsprechend begründete Befürwortung mit Angabe des wissenschaftlichen Anteils des Doktoranden an den verwendeten Publikationen werde ich parallel an den Rat der Fakultät der Chemisch-Geowissenschaftlichen Fakultät richten.

M. Sc. Hassan Abul-Futouh

Jena, _____

Prof. Dr. Wolfgang Weigand

Jena, _____

3 INTRODUCTION

3.1 Energy and Hydrogen Economy

Producing energy from fossil fuels results in massive emission of greenhouse gases which are considered to be the main reason of climate changes.¹ Fossil fuels are non-renewable energy sources and they can be found only in certain part of our planet. Therefore, it is becoming increasingly attractive to replace the current fossil fuels with more environmentally benign alternatives, “Green Alternatives”. Such sources (Figure 1: sun, water, wind, biomass and geothermal) can assist us to reduce the damage that is being done to our earth and protect it for future generations. Besides these primary natural sources, hydrogen is under serious consideration as a clean energy carrier for the future since it is a zero-emission fuel when burned and characterized by high energy density.² Hydrogen can be transformed into electricity by different generation technologies such as hydrogen fuel cell which combines hydrogen and oxygen in the presence of conducting electrolyte to produce electricity, heat and a clean byproduct-pure water (Figure 2).³

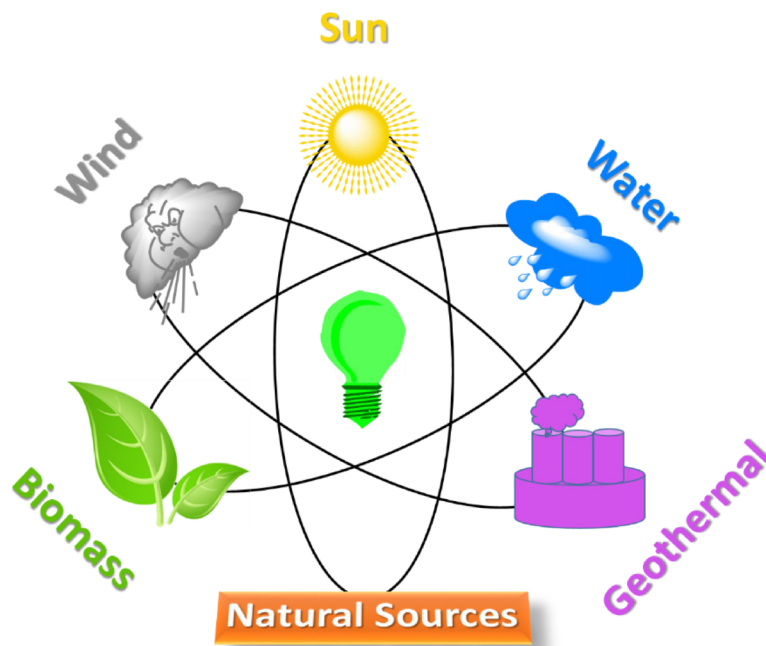


Figure 1. Green energy resources.

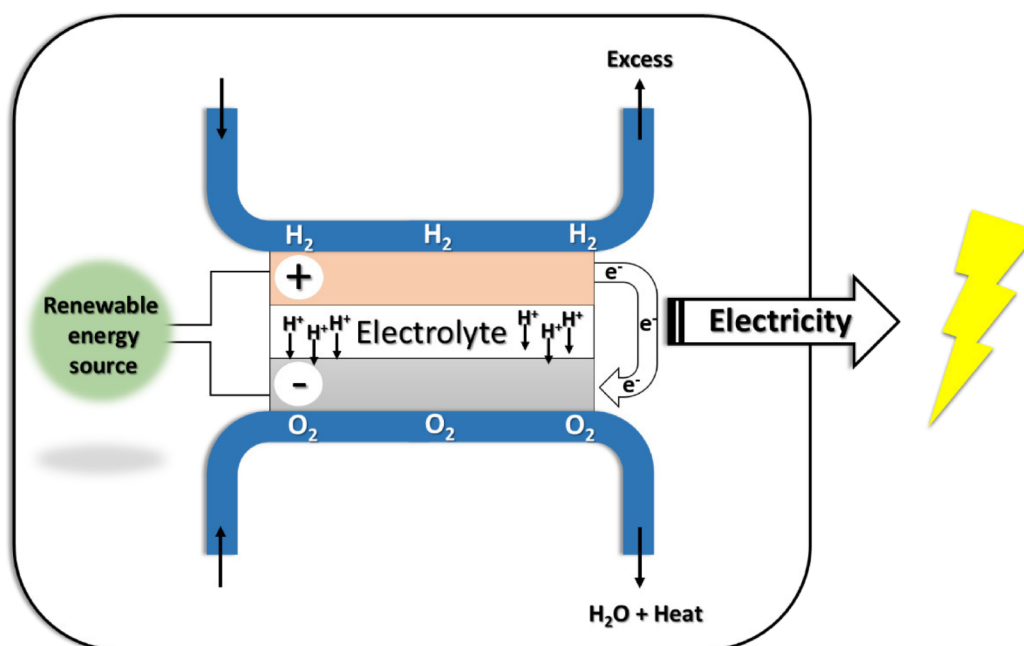


Figure 2. Simplified overview for a hydrogen fuel cell configuration.

In fact, hydrogen gas does not exist naturally on earth and must be produced using a hydrogen-rich source. The main methods of producing hydrogen are: Steam reforming fossil fuels,⁴⁻⁶ gasification of coal,⁷ biomass⁸ and water electrolysis.⁹ The latter has received more attention in virtue of the high abundance of water on earth as well as dioxygen is formed as a side product in the electrolysis cell. However, the efficient but expensive, platinum is still used as a catalyst to split water into hydrogen and dioxygen under mild condition, up to 150 °C.¹⁰ For this reason, researchers aim to design an alternative for platinum which is cheap, efficient (low overpotential and high catalytic activity) and robust catalyst.

In microbes, production and oxidation of hydrogen are catalyzed under ambient conditions with high efficiency and low energy features through enzymes called “hydrogenases”.¹¹⁻¹⁹ These enzymes are classified according to the metal content of their active site into three main classes: [Fe]-hydrogenases, [FeFe]-hydrogenases and [NiFe]-hydrogenases (Table 1).¹¹⁻¹⁹ A subset of the [NiFe]-hydrogenase family, the [NiFeSe]-enzymes, incorporate a selenocysteine coordinated to the Ni in place of one of the terminal cycteine residue of the standard [NiFe]-hydrogenase (Table 1).²⁰

Table 1. Classification of hydrogenase.¹⁹

Classification	Occurrence	Structure	Localization	Function
[Fe]-hydrogenase	Methanogens	Monomeric	Cytoplasmic	Production of hydrogen
[FeFe]-hydrogenase	Photosynthetic bacteria, anaerobic fermentative bacteria, cyanobacteria, green algae, protozoan	Monomeric, Heteromeric	Cytoplasmic, membrane-bound, periplasmic, chloroplast, hydrogenosomes	Production of hydrogen
[NiFe]-hydrogenase	Anaerobic, photosynthetic bacteria, cyanobacteria	Heterodimeric, multimeric	Membrane-bound, cytoplasmic, periplasmic	Uptake of hydrogen
[NiFeSe]-hydrogenase	Sulphate-reducing bacteria, methanogenes	Oligomeric	Membrane-bound, cytoplasmic	Oxidation of hydrogen

Among these, [FeFe]-hydrogenase has the strongest catalytic ability for the hydrogen production. Under optimum condition, this enzyme can produce 9,000 molecules of hydrogen per second at 30 °C (one mole of [FeFe]-hydrogenase could produce enough hydrogen in two hours to fill the main liquid hydrogen tank of the space shuttle).^{13,21} Therefore, much interests are paid to the [FeFe]-hydrogenases as alternative biological catalysts to the commonly used platinum catalyst in the hydrogen fuel cell technology. So, this thesis focuses on the synthesis of model

catalysts mimicking the structure and function of an organometallic cluster, the so-called H-cluster, in the active site of the [FeFe]-hydrogenases.

3.2 [FeFe]-Hydrogenases

[FeFe]-hydrogenases are enzymes that catalyze the reversible interconversion of H₂ to protons and electrons at neutral pH with remarkably high activities and low over potential (-0.1 to -0.5 V vs. NHE).^{22, 23}



Such enzymes are found in anaerobic prokaryotes such as clostridia and sulfate reducers, and in some anaerobic eukaryotes as well as in some green algae.^{14, 24} In fact, most of the reported studies on [FeFe]-hydrogenase are from green algae, *Desulfovibrio desulfuricans* (*DdHase*)¹⁷ and *Clostridium pasteurianum* (*Cpl*).²⁵ Interestingly, the molecular structures of (*DdHase*) and (*Cpl*) revealed that both contain a very similar catalytically active metal center termed as “H-cluster” (Figure 3).²⁶

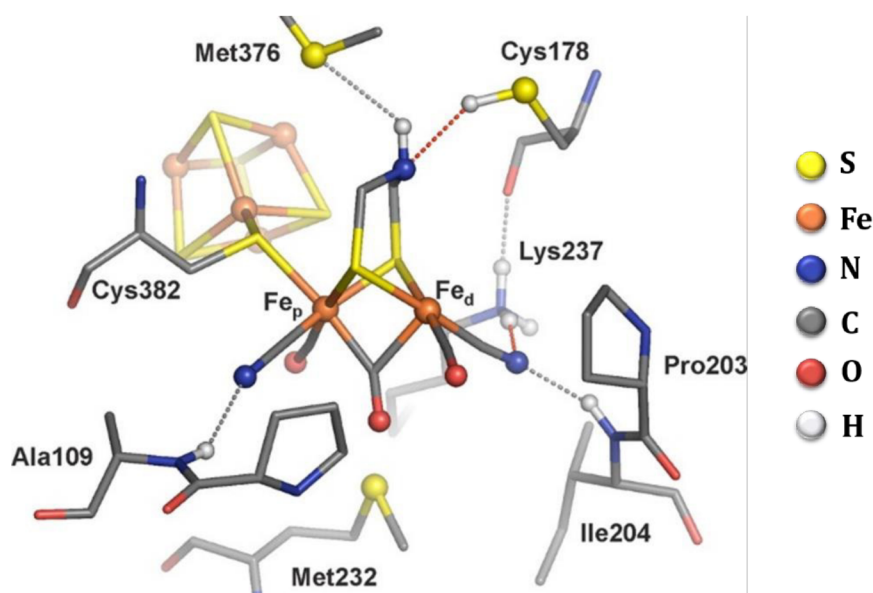


Figure 3. Structural crystallographic model of the active site of [FeFe]-hydrogenase taken from the structure of *Cpl* (PDB 3C8Y).²⁷ The surrounding amino acid residues are taken from the structure of *DdHase* (PDB 1HFE).¹⁷ The hydrogen bonds are depicted by dotted line.²⁶

Crystallographic and spectroscopic studies have shown that this H-cluster consists of a diiron metal center with dithiolato linker that form a butterfly structure of the [2Fe2S] sub-cluster. Furthermore, one of these irons (Fe_p , proximal) is attached to a cubane-like [4Fe4S] cluster through a bridging cysteine sulfur (Figure 3). The nature of the bridgehead atom in the dithiolato ligand was unknown for long time as to whether it is CH_2 , NH or O . Presently, Lubitz and others provided an experimental evidence that the native bridgehead group of the dithiolato ligand is the aza-group.^{28, 29} Both iron atoms (Fe_p and Fe_d , distal) of the [2Fe2S] sub-cluster are coordinated by three CO and two CN^- ligands, where one [Fe(CO)₂CN] unit is rotated with respect to the other unit making one CO ligand to be in bridging position between the two iron atoms and leaving a vacant site in which protons are proposed to bind during the catalytic process (Figure 3).³⁰ The CN^- ligands of the H-cluster interact through hydrogen bonding with the neighboring amino acids as well as the lysine (Lys237) is closely located (440 pm) to the Fe_d and can act as a possible proton distributor during the dihydrogen production (Figure 3).^{17, 26}

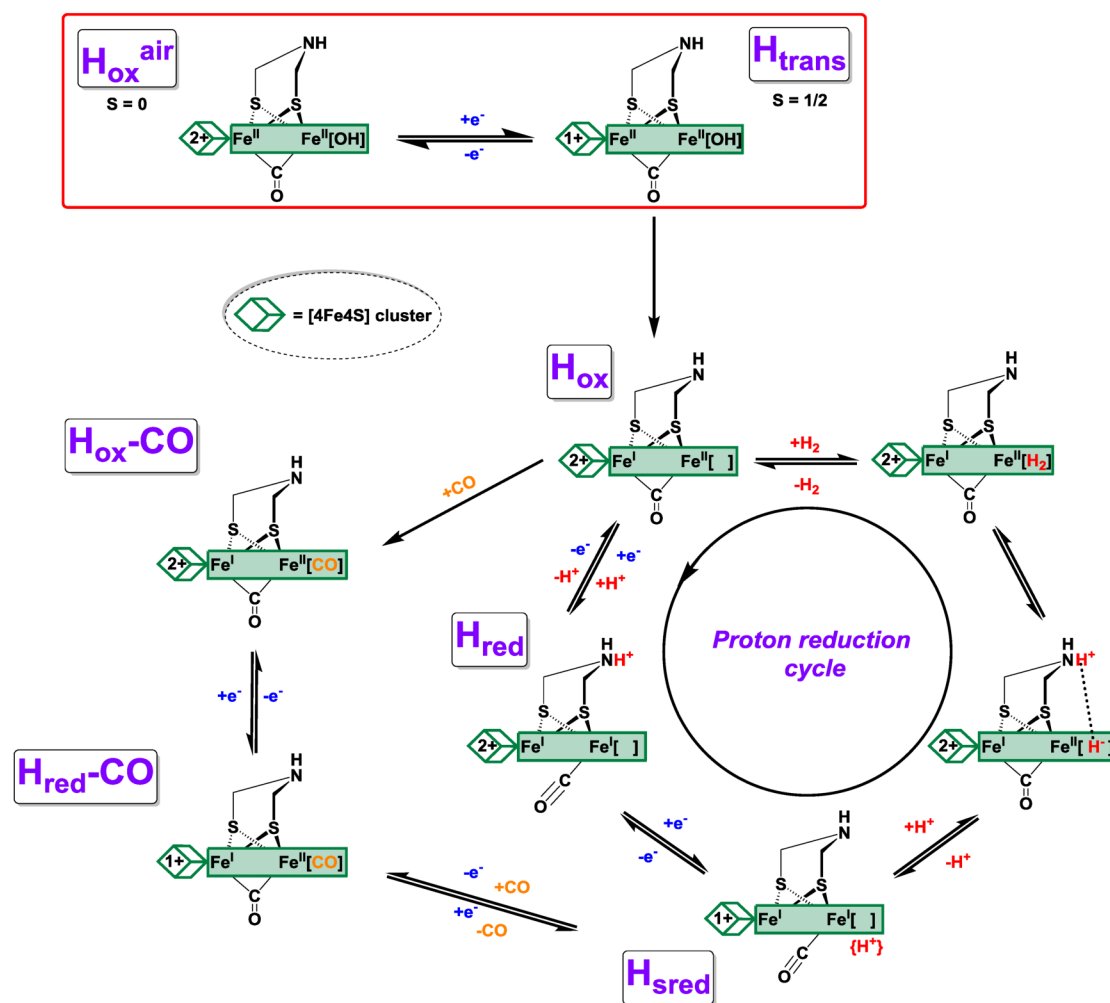
Since [FeFe]-hydrogenases have the strongest catalytic ability for the hydrogen production *in vivo*, a detailed understanding of their catalytic mechanism is of great interest up to the date of this thesis.^{16, 30-34} Until now, the catalytic mechanism for H_2 evolution by the H-cluster remains speculative, nevertheless several feasible mechanisms have been proposed based on EPR, Mössbauer spectroscopy, pH dependent FTIR spectro-electrochemistry and DFT calculations.^{16, 30-39} As a result of these studies, three well characterized redox states of the H-cluster are postulated to play a role in the catalytic cycle under anaerobic conditions:

- (i) The active “oxidized” state \mathbf{H}_{ox} which is paramagnetic and characterized by a mixed-valence ($\text{Fe}^I\text{Fe}^{II}$) diiron part.³⁶⁻³⁹
- (ii) The active “reduced” state \mathbf{H}_{red} which is diamagnetic and adopts the (Fe^IFe^I) configuration.^{30, 32, 34, 39}
- (iii) The “super-reduced” state \mathbf{H}_{sred} which is paramagnetic and adopts the (Fe^IFe^I) configuration together with the reduced cubane [4Fe4S]⁺ cluster.^{30, 32, 34}

Under aerobically conditions, the active site of [FeFe]-hydrogenase exists in a doubly oxidized form termed as $\mathbf{H_{ox}^{air}}$ and reveals no EPR signal ($S = 0$) as shown in Scheme 1 (red rectangle).¹⁶ Accordingly, the latter is reduced by a one-electron step to afford the transient state which termed as $\mathbf{H_{trans}}$ (rhombohedral EPR signals are observed ($S = \frac{1}{2}$) at $g = 2.06, 1.96$ and 1.89) (Scheme 1, red rectangle).^{16, 33} Based on Mössbauer spectroscopy technique and DFT calculations, these two states ($\mathbf{H_{ox}^{air}}$ and $\mathbf{H_{trans}}$) are supposed to adopt ($\text{Fe}^{\text{II}}\text{Fe}^{\text{II}}$) configuration with one CO ligand located at the bridging position between the two iron atoms as well as the vacant site is occupied by an OH-group.^{16, 33, 40-42} By an irreversible redox-dependent process under anaerobic conditions of the $\mathbf{H_{trans}}$ state, the $\mathbf{H_{ox}}$ state is obtained and characterized by a mixed-valence ($\text{Fe}^{\text{I}}\text{Fe}^{\text{II}}$) configuration and the cubane $[\text{4Fe4S}]$ cluster is in the diamagnetic state according to the Mössbauer and ENDOR studies (Scheme 1).³⁶⁻³⁸ Moreover, the $\mathbf{H_{ox}}$ state has one CO bridged between the two iron atoms and a free vacant site.¹⁶ Upon reduction of the $\mathbf{H_{ox}}$ state together with the presence of a proton which bounds at the adt-amine, the bridging CO ligand shifts toward the distal Fe acquiring a semi-bridging coordination *trans* to the vacant site to afford the $\mathbf{H_{red}}$ state which is diamagnetic ($S = 0$) due to the ($\text{Fe}^{\text{I}}\text{Fe}^{\text{I}}$) configuration (Scheme 1).^{32, 39, 43-45} A transfer of another electron at this level affords the paramagnetic super-reduced state, $\mathbf{H_{sred}}$, in which the $[\text{4Fe4S}]$ cluster is considered an essential part since it's singly reduced, while the ($\text{Fe}^{\text{I}}\text{Fe}^{\text{I}}$) configuration does not change (Scheme 1).^{32, 46} In a next step, the former adt-bound proton relays to the vacant site via agostic interaction affording a terminal-hydride species. A second protonation step occurs again to afford an intermediate with hydride and proton in close proximity, ultimately producing molecular hydrogen (Scheme 1).³² DFT calculations suggest that only the second protonation at the adt-bridge triggers the electron transfer from the $[\text{4Fe4S}]$ cluster to the $[\text{2Fe2S}]$ sub-cluster and the formation of the hydride bound to the mixed-valence ($\text{Fe}^{\text{I}}\text{Fe}^{\text{II}}$) core.^{32, 47}

It has been found that the H-cluster of the active protein can be inhibited by CO to afford a species termed as $\mathbf{H_{ox}-CO}$ state which is similar to that of $\mathbf{H_{ox}}$ and is characterized by a mixed-valence ($\text{Fe}^{\text{I}}\text{Fe}^{\text{II}}$) diiron part together with an oxidized $[\text{4Fe4S}]^{2+}$ cluster (Scheme 1).^{26, 48, 49} Such a process is generated at high potentials

by the so called “cannibalization process” in which the CO ligands released from destroyed H-clusters are captured by H-clusters that are still intact.^{31, 46, 50} Lubitz and co-workers have found that the $\mathbf{H}_{\text{ox}}\text{-CO}$ state can generate the \mathbf{H}_{sred} state via two consecutive reduction steps (at $E_p = -470$ mV and at $E_p = -500$ mV, respectively, against NHE) (Scheme 1).³¹ Firstly, the $\mathbf{H}_{\text{ox}}\text{-CO}$ state is reduced to the $\mathbf{H}_{\text{red}}\text{-CO}$ state and is characterized by a mixed-valence ($\text{Fe}^{\text{I}}\text{Fe}^{\text{II}}$) diiron part together with the singly reduced $[4\text{Fe}4\text{S}]^{1+}$ cluster.³¹ Secondly, the $\mathbf{H}_{\text{red}}\text{-CO}$ state is reduced to afford the \mathbf{H}_{sred} state ($\text{Fe}^{\text{I}}\text{Fe}^{\text{I}}$) configuration.³¹



Scheme 1. Schematic representation of the proposed catalytic cycle and the formation of the CO inhibited states.³¹ The red rectangle exhibits the states of the H-cluster under aerobically conditions.¹⁶

3.3 Synthetic Models for the H-Cluster

3.3.1 First Generation of [FeFe]-Hydrogenase Mimics: An Overview

Notably, several groups had described the synthesis of numerous [2Fe2S] complexes which mimic the H-cluster without the knowledge of their biological relevance as models for the [FeFe]-hydrogenases and their ability to produce hydrogen.⁵¹⁻⁵⁷ In 1929, Reihlen *et al.* reported the first type of [2Fe2S] complexes that obtained from the reaction between Fe(CO)₅ with EtSH to afford [Fe₂(CO)₆{μ-(SEt)₂}] (**1**) (Figure 4), but in low yield.⁵¹ After that, in 1937, Hieber *et al.* could enhance the yield of complex **1** via using Fe₃(CO)₁₂ instead of Fe(CO)₅.⁵²⁻⁵⁴ By the early 1960s, King described the synthesis of [Fe₂(CO)₆{μ-(SCH₂)₂}] (**2**) (Figure 4).⁵⁵ In the same period, Dahl and Wei could resolve the molecular structure of complex **1** which emphasized that such a complex has a butterfly structure of the [2Fe2S] core.⁵⁶ In the 1980s, Huttner *et al.* synthesized the complex [Fe₂(CO)₆{μ-(SCH₂)₂CH₂}] (**3**) (Figure 4).⁵⁷

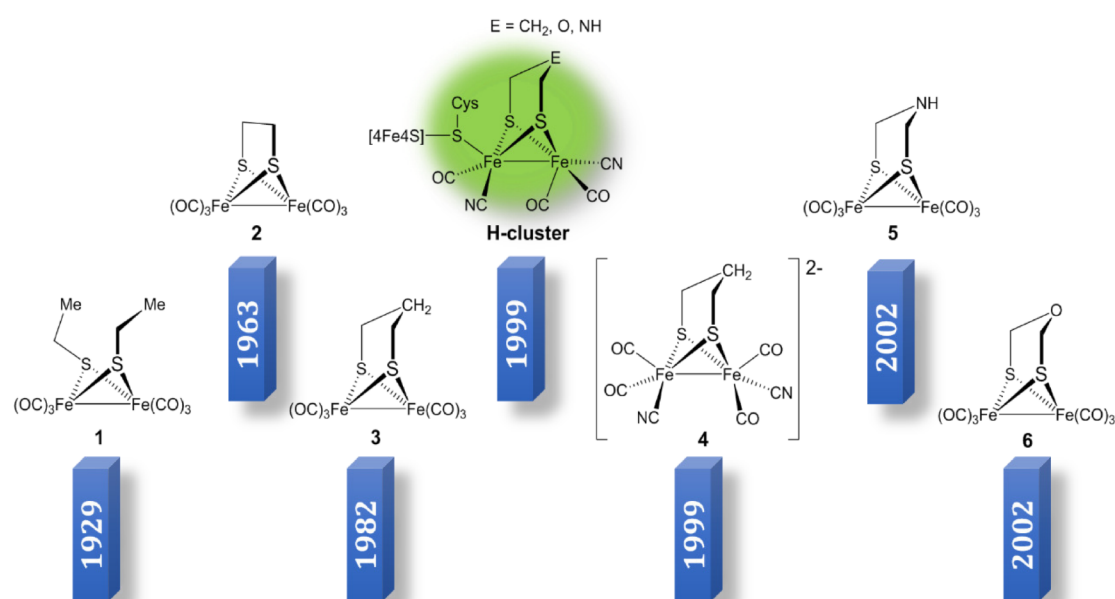


Figure 4. Structural resemblance between the H-cluster and the synthetic complexes **1-6**.

During those years, several attempts have been made to investigate the nature of the H-cluster, but no clear results were observed until Seefeldt *et al.* and

Fontecilla-Camps *et al.* had resolved the molecular structure of the H-cluster for *DdHase* and *CpI* in 1998-1999.^{17, 25} Based on this result, the striking resemblance between the latter and complexes **1-3** (Figure 4) immediately became evident and sparked chemists to develop more models to mimic and to provide a better understanding of the structure and function of the H-cluster. A modification on complex **3** takes place in 1999 that two CO ligands of complex **3** could be replaced by cyanide, to give water-soluble dianions (**4**, Figure 4).⁵⁸⁻⁶⁰ This was followed by the work of Rauchfuss and co-workers in 2002, in which they synthesized a model complex that has an amine functionality (NH) at the bridgehead (**5**, Figure 4) instead of the CH₂ in complex **3** via the condensation of metal sulfides, formaldehyde and primary amine.⁶¹ Within the same year, Rauchfuss, followed by Song and coworkers could also get a complex that contains an oxygen atom at the bridgehead of the dithiolato ligand (**6**, Figure 4).^{61, 62}

Following these earlier investigations, plenty of modifications have been reported within the past 17 years.^{63, 64} Generally, those reported articles have focused on the following aspects:

- The preparation of structural models.
- The development of bio-inspired electro- and photocatalysts for H₂ production.
- The investigation of the mechanism of enzymatic H₂ evolution and uptake.
- Mimicking the active H_{ox} state (Fe^{II}Fe^I) for H₂ oxidation.

Because of the high number of publications regarding these aspects, this thesis will draw out some of salient features of hexacarbonyl models based on altering the nature of the bridging linker in [Fe₂(CO)₆{μ-dithiolate}], replacing the sulfur atoms with heavier chalcogen atoms such as selenium and protonation reactions of the hexacarbonyl model complexes.

3.3.2 Modification of the Synthetic Models

3.3.2.1 Hexacarbonyl Complexes

3.3.2.1.1 The Dinuclear Models

The synthesis of diiron(I) dithiolato carbonyl complexes can be obtained through several pathways. For example, the reaction of $\text{Fe}_2(\text{CO})_9$ or $\text{Fe}_3(\text{CO})_{12}$ with dithiols as well as disulfides afforded complexes of the type $[\text{Fe}_2(\text{CO})_6\{\mu\text{-(SCH}_2)_2\text{E}\}]$.⁶⁴ The mechanism of obtaining such complexes is still an open question and an interest aspect for the researchers. Moreover, it has been found that such model complexes can be also obtained by the reaction of alkyl dihalides with the iron cluster $[\text{Fe}_2\text{S}_2(\text{CO})_6]$ but in low yield in comparison with the first mention methods.⁶⁵

Indeed, the synthetic models related to the structure of the H-cluster may be divided into two categories: i) bioinspired models with azadithiolato linkers (Figure 5a),⁶⁶⁻⁷⁷ and ii) artificial models with non-biological linkers $\mu\text{-(XCH}_2)_2\text{E}$ in which the central atom/group E is CR_2 ,^{64, 78-84} O,^{62, 66} S,^{85, 86} SiR_2 ,⁸⁷⁻⁸⁹ SnMe_2 ^{90, 91} or Ph-P=O ⁹² and X could be S,⁶⁴ Se,^{88, 93-95} Te,^{88, 95} or PR⁹⁶⁻⁹⁸ (Figure 5b). The use of these synthetic models may provide valuable information and answers to basic questions concerning the role of the azadithiolato linker as well as the effect of the unusual E on the structural and functional properties of such artificial H-cluster mimics. For example, previous studies have found that the presence of a pendant nitrogen atom of the dithiolato ligand in $[\text{Fe}_2(\text{CO})_6\{\mu\text{-(SCH}_2)_2\text{NR}\}]$ plays a significant role in the delivery of protons to the catalytically active site, which in turn shifts the potential of hydrogen production to less negative potentials by 230 mV compared to the aliphatic dithiolato ligand in $[\text{Fe}_2(\text{CO})_6\{\mu\text{-(SCH}_2)_2\text{CH}_2\}]$.^{77, 99, 100} Weigand and co-workers have found that the presence of the sulfur/selenium atom at the bridgehead position in the dithiolato linker leads to an ECE reduction mechanism (*i.e.* $E_1^0 - E_2^0 < 0$, potential inversion) (E = Electron transfere, C = Chemical process) due to facile core reorganization accompanying the electron transfer compared to those having an oxygen or carbon atom at bridgehead.⁹³ This chemical process involves rotation of one $\text{Fe}(\text{CO})_3$ unit to locate a CO ligand in a semi-bridging position and cleavage of one Fe-S bonds.¹⁰¹

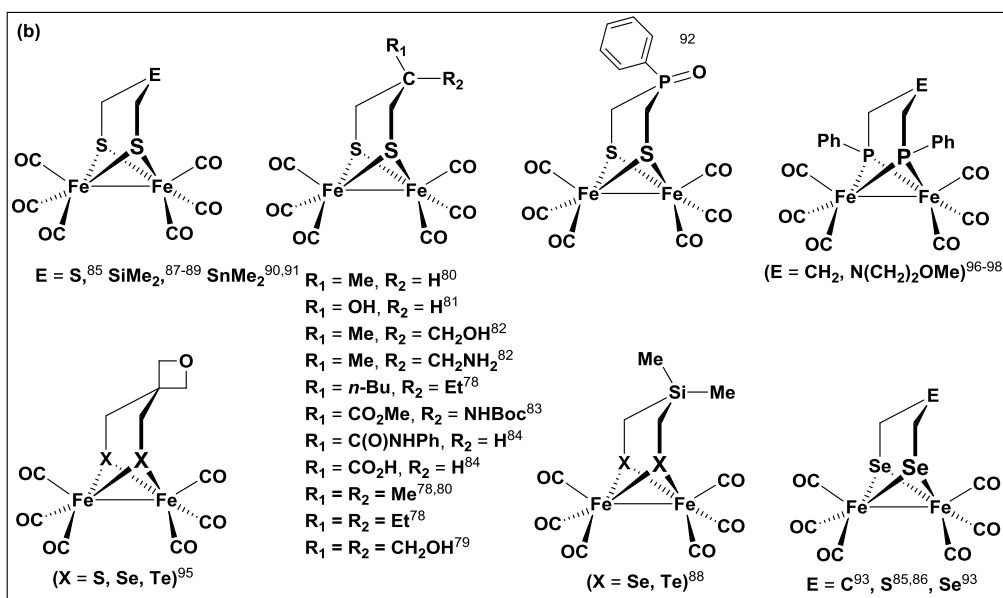
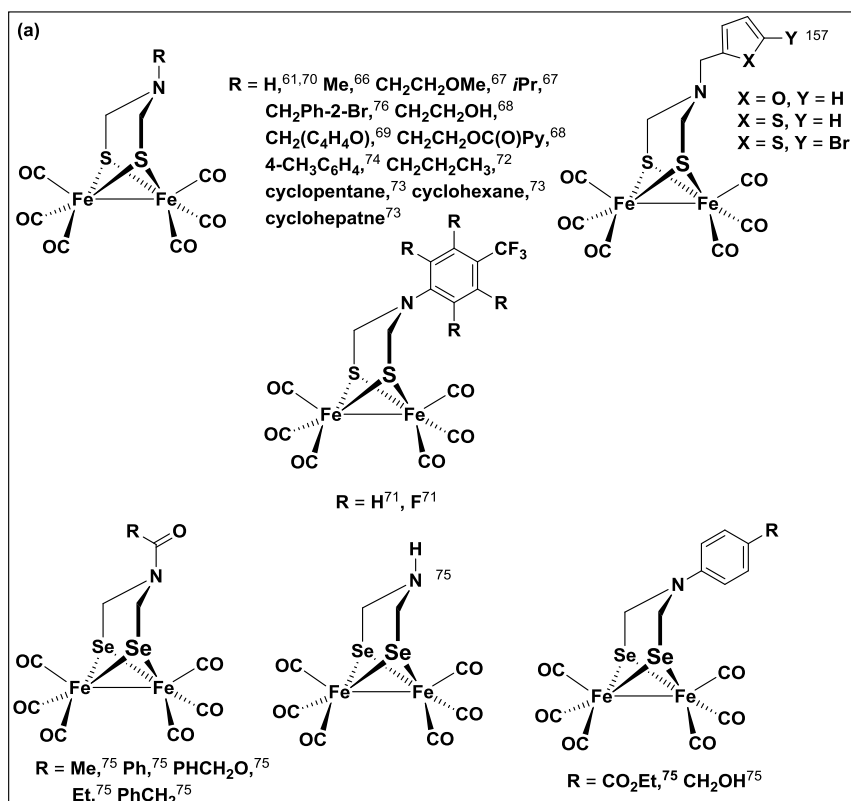
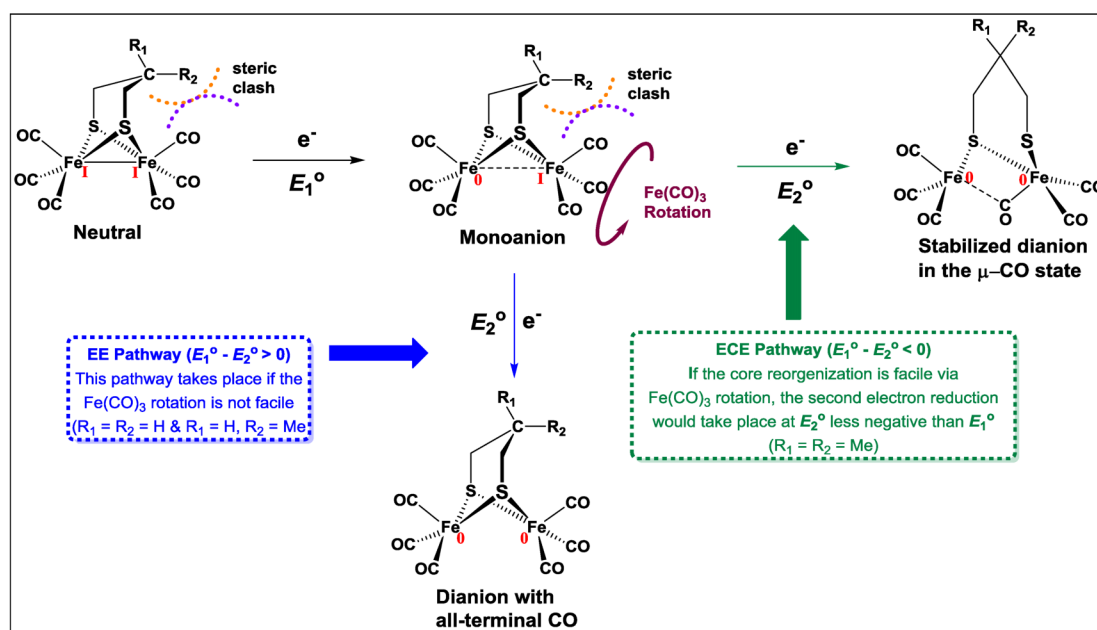


Figure 5. Synthetic Models of the active site of [FeFe]-hydrogenase: (a) bioinspired models with azadithiolato linker and (b) artificial models with non-biological linkers.

Moreover, they also found that increasing the steric bulkiness of E (CH_2 , CHMe , CMe_2) in $[\text{Fe}_2(\text{CO})_6\{\mu\text{-}(\text{SCH}_2)_2\text{E}\}]$ lowers the barrier of $\text{Fe}(\text{CO})_3$ rotation and results

in an ECE reduction mechanism in the case of only $E = \text{CMe}_2$ while in the case of $E = \text{CH}_2$, CHMe proceed via EE reduction mechanism (Scheme 2).⁸⁰



Scheme 2. Comparison between the simple EE and ECE two-electron reduction pathways of the $[\text{FeFe}]$ -hydrogenase models.⁸⁰

Furthermore, it has been found that the replacement of the alkyl substituents in $[\text{Fe}_2(\text{CO})_6\{\mu\text{-(SCH}_2)_2\text{CR}_1\text{R}_2\}]$ ($R_1/R_2 = \text{H}/\text{H}, \text{H}/\text{Me}, \text{Me}/\text{Me}, \text{Et}/\text{Et}$) by CH_2OH substituents results in lowering the reduction potential of the diiron complex. This can be explained in terms of structural change occurs during the cathodic process leading to a *rotated structure*, which involves internal hydrogen bonding ($\text{O-H}\cdots\text{S}$ or $\text{O-H}\cdots\text{Fe}$) in the reduced state as shown in Figure 6.⁷⁹

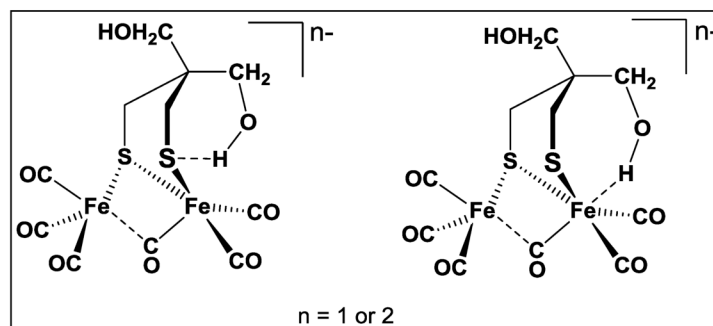
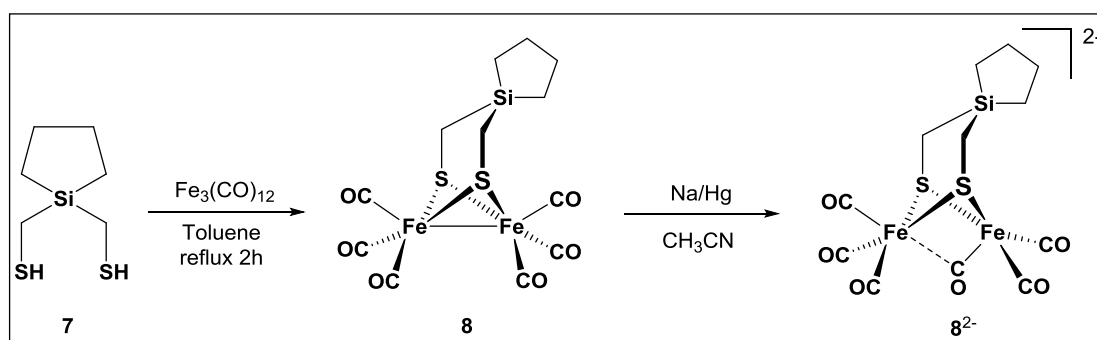


Figure 6. Proposed hydrogen bonding in the reduced diiron complex.⁷⁹

In addition, Apfel *et al.* had investigated the influence of the replacement of the bridgehead carbon atom by silicon in synthetic diiron complexes.⁸⁷⁻⁸⁹ As a result of these studies, the introduction of a silicon atom in the dithiolato linker of [FeFe]-hydrogenase model complexes enhances the electronic and the catalytic properties of these complexes. Based on the DFT calculations, it has been found that the basicity of the sulfur atoms increases by a $\sigma(\text{Si-C}) \rightarrow 3p(\text{S})$ filled-filled interaction.⁸⁹ Such a behavior was previously observed by Glass *et al.* for analogues complex having a tin atom in the bridgehead.⁹⁰ Additionally, it has been also reported that the reaction of silolane-1,1-diylldimethanethiole (**7**) with two molar equivalents of $\text{Fe}_3(\text{CO})_{12}$ in boiling toluene afforded the diiron complex **8** as shown in Scheme 3.⁸⁹

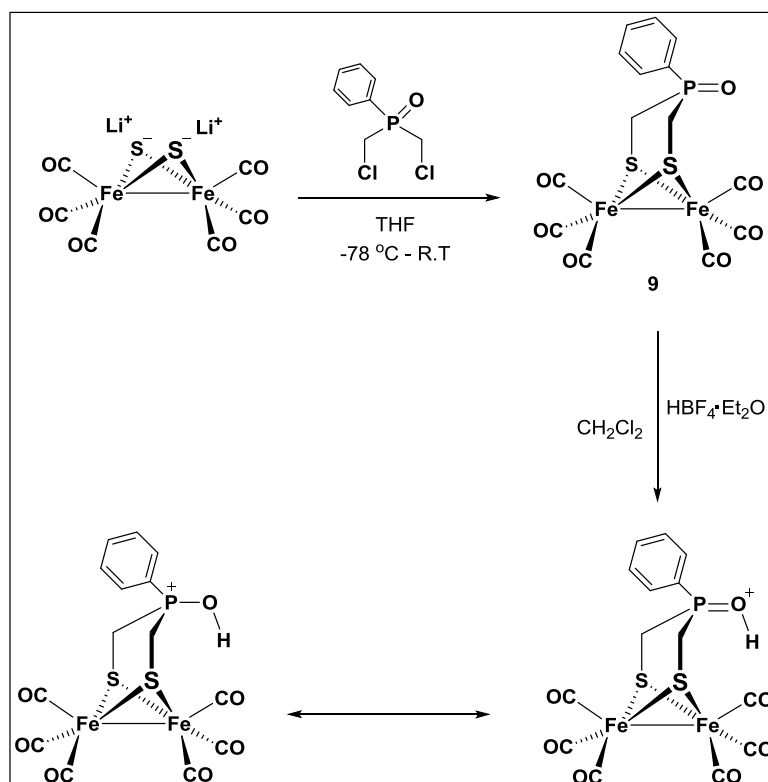


Scheme 3. Synthetic pathways of the formation of complex **8** and its reduced species.⁸⁹

Under reductive conditions, the latter forms a rotated state species (**8**²⁻, Scheme 3) in which one of the CO ligands becomes in a bridging position between the two iron atoms while the Fe-Fe bond and one of the Fe-S bonds are broken as shown in Scheme 3.⁸⁹ This is supported by the appearance of the new absorption band at 1725 cm^{-1} in the IR spectrum of a solution of the reduced complex **8** in acetonitrile together with the DFT calculations.⁸⁹

Almazahreh *et al.* has succeeded in utilizing a phosphine oxide containing compound, $\text{O}=\text{P}(\text{Ph})(\text{CH}_2\text{Cl}_2)$,¹⁰² to serve as a pro-ligand for a complexation with an in situ generated $[\text{Fe}_2(\text{CO})_6\{\mu\text{-(SLi)}_2\}]$ ¹⁰³ to afford a diiron model complex $[\text{Fe}_2(\text{CO})_6\{\mu\text{-(SCH}_2)_2(\text{Ph})\text{P}=\text{O}\}]$ (**9**) (Scheme 4).⁹² The latter features a P=O functionality that is oriented toward one iron atom and provides a potential site

for protonation (*vide infra*) as in the case of the amine functionality as shown in Scheme 4. Moreover, complex **9** undergoes an overall two-electron reduction due to potential inversion of the two individual one-electron processes.



Scheme 4. Synthetic pathway and protonation process of $[\text{Fe}_2(\text{CO})_6\{\mu\text{-}(\text{SCH}_2)_2(\text{Ph})\text{P=O}\}]$ (**9**).⁹²

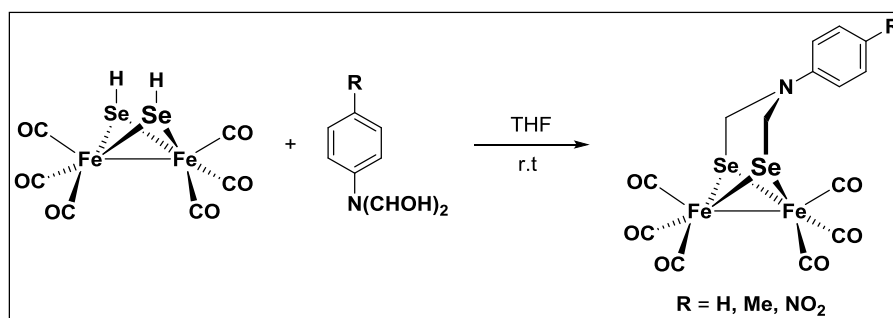
Recently, the tendency to investigate the significant role of selenium in the biological processes becomes more attractive to researchers since the selenium element enhances the chemical reactivity of the enzymatic reactions compared with the sulfur analogues.¹⁰⁴ Hence, the physical and chemical properties of sulfur and selenium are very similar in many respects (Table 2),¹⁰⁵ it would be interesting to investigate the differences between the two chalcogens in the synthetic models that mimic the H-cluster.

Table 2. General properties of selenium and sulfur.¹⁰⁵

Property	Sulfur	Selenium
Electron configuration	[Ne] 3s ² 3p ⁴	[Ar] 3d ¹⁰ 4s ² 4p ⁴
Atomic radius (pm, emp.)	100	115
Atomic radius (pm, calc.)	88	103
Covalent radius (pm, emp.)	102	116
Van der Waals radius (pm)	180	190
Ion radius (Pauling) ox. state (I)	53	66
(VI)	29	42
(-I)	219	232
(-II)	184	198
Bond length (pm) of dichalcogen	205 (S-S)	232 (Se-Se)
Bond length (pm) of carbon-chalcogen	180 (C-S)	196 (C-Se)
Molecular volume (cm³)	15.53	16.42
Diatomic bond energies (kJ mol⁻¹)	425.3 (S-S) 344.3 (S-H)	332.6 (Se-Se) 314.5 (Se-H)

	714.1 (S-C)	590.4 (Se-C)
Ionization energies (kJ mol⁻¹): 1st	999.6	914
2nd	2252	2045
3rd	3357	2973.7
Polarizability (Å³)	2.9	3.8
Pauling electronegativity	2.58	2.55
pK_a	8.3	5.2

The first example of an iron carbonyl cluster bound to selenium, [Fe₃Se₂(CO)₉], was published in 1958 by Hieber *et al.*⁵³ After two years, Beck and Hieber have synthesized a selenium containing complex of the type [Fe(CO)₃SeC₂H₅]₂.⁵⁴ In 2008, Peng and co-workers have investigated diselenolate-bridged [FeFe]-complexes, [Fe₂(CO)₆{μ-(SeCH₂)₂NPhR}] (R = H, Me, NO₂), as synthetic mimics of the H-cluster (Scheme 5).⁹⁴ As a result, these complexes exhibited the same reduction potentials but enhanced reactivity as proton reduction catalysts compared with the corresponding sulfur analogue. Within the same year, Weigand and co-workers have also described the synthesis and characterization study of sugar-based diselenolate diiron complex mimicking the active-site of [FeFe]-hydrogenase (Figure 7).¹⁰⁶ The presence of selenium offers higher activity toward molecular hydrogen production in comparison with the sulfur analogue despite being reduced at more negative potential. Moreover, the selenium containing complex showed higher stability upon deacetylation in approach toward water-soluble catalysts in comparison with sulfur analogue.¹⁰⁶



Scheme 5. Synthetic pathway of $[\text{Fe}_2(\text{CO})_6\{\mu\text{-(SeCH}_2)_2\text{NPhR}\}]$ ($\text{R} = \text{H, Me, NO}_2$) complexes.⁹⁴

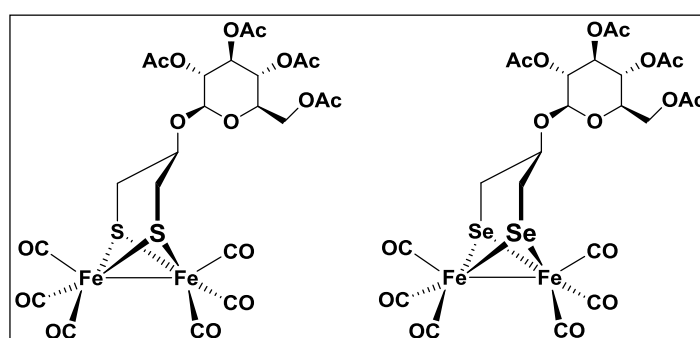


Figure 7. Sugar-Substituted diiron dithiolato (left) and diselenolato analogue (right) mimics the H-cluster.¹⁰⁶

One year later, Song and Weigand groups have described the synthesis of propanediselenolate-based $[\text{FeFe}]$ -complexes, $[\text{Fe}_2(\text{CO})_6\{\mu\text{-(SeCH}_2)_2\text{CH}_2\}]$, which also offers higher activity toward molecular hydrogen production in comparison with the corresponding propanedithiolate-based $[\text{FeFe}]$ -complexes.^{107, 108} Further studies approved the phenomena that the replacement of the sulfur atoms of diiron dithiolato models by selenium atoms are often showed higher activity toward molecular hydrogen production despite being reduced at more negative potential than the corresponding sulfur analogues.^{88, 93, 95, 109} Presently, Happe, and co-workers incorporated the synthetic $[\text{4Fe4Se}]$ -cluster containing the $[\text{2Fe2S}]$ sub-cluster into the enzyme (Figure 8).¹¹⁰

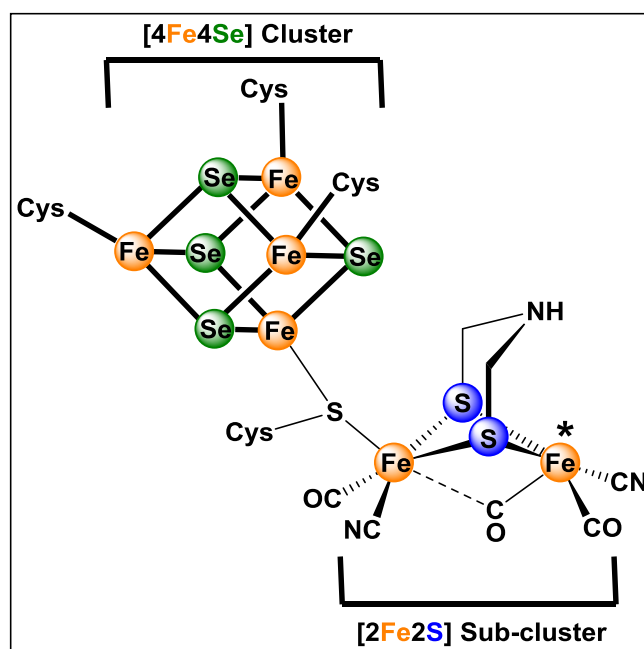


Figure 8. Synthetic model of the selenium-substituted cubane cluster $[4Fe_4Se]$.

*Location of catalytic turnover.¹¹⁰

As a result of this investigation, they found that the $[4Fe_4Se]$ -cluster revealed more positive reduction potentials compared with those of their $[4Fe_4S]$ -counterparts. In the light of the above-mentioned considerations, it can be concluded that the replacement of sulfur atoms by more electropositive selenium atoms of the diiron complexes results in an enhancement of the catalytic activity of them. This could be explained in terms of increasing the electron density at the iron cores and faster electron transfer in such complexes that contain $[2Fe_2Se]$ instead of $[2Fe_2S]$ cores.¹⁰⁹ However, the investigation of the influence of substituting selenium instead of sulfur in the synthetic H-cluster mimics is still an interesting subject for the researchers.

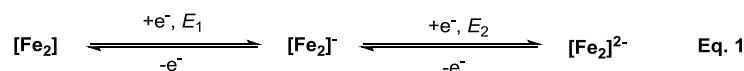
Another strategy for designing the synthetic H-cluster mimics has been developed by inclusion of a suitably substituted aromatic dithiolate ligands in lieu of the aliphatic one regardless that the resulting diiron complexes do not resemble the enzyme active-site in structure (Figure 9).¹¹¹ Indeed, the significant role of these model complexes lies in several points as follows:¹¹²⁻¹²¹

- (i) The rigidity of its backbone enhances the stability of the reduced species.

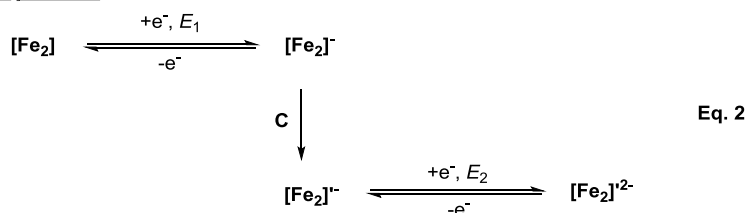
- (ii) Useful for mechanistic investigation of the catalytic cycle since its electrochemistry is generally well behaved with reversible waves in the cyclic voltammograms.
- (iii) The reduction potential of the complex can be adjusted through suitable chemical modification of its backbone, for example the addition of electron-withdrawing substituents can shift the reduction potential of the complex to less negative values.

There is no doubt about the nature of two-electron transfer for diiron mimics.¹²²⁻¹²⁵ For those who have a transfer of two-electrons, the process falls, in theory, into three pathways as illustrated in Equations 1-3:¹¹⁷

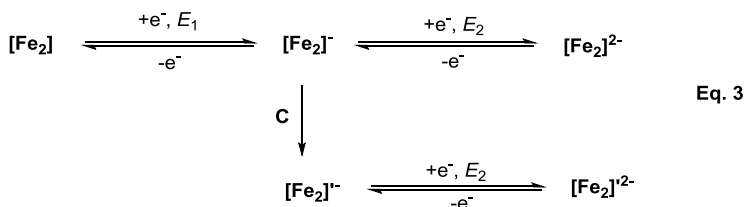
EE process:



ECE process:



EE and ECE processes co-exist



It has been reported that the synthetic models having 1,2-benzenedithioalto bridges and its derivatives (Figure 9, first set) are preferably reduced by two electrons in a single step (**ECE**) unlike the aliphatic dithiolato bridging ligands.^{101, 126-129} On the other hand, the incorporation of a naphthalene-1,8-dithiolato ligand into the synthetic models of [FeFe]-hydrogenase enhanced the stability of the reduced species to proceed via two sequential reversible one-electron steps (**EE**).^{112, 116, 117, 119} Moreover, the introduction of electron-withdrawing groups at the naphthalene skeleton shifts the first reduction peak to less negative potential as well as stabilizes the mono-anionic species in

comparison with the aliphatic analogue, $[\text{Fe}_2(\text{CO})_6\{\mu\text{-(SCH}_2)_2\text{CH}_2\}]$, as evidenced by the $I_{\text{pa}}/I_{\text{pc}}$ ratios in their cyclic voltammograms.^{117, 119, 130} Based on that, the Wasielewski group and others have modified the naphthalene skeleton by introducing an imide group into its backbone.^{118, 130} As a result, they found that the presence of the imide functionality provides additional stability to the monoanionic species due to its strong electron-withdrawing effect and thus serves as a suitable site for the attachment of an additional chromophore (Figure 10).

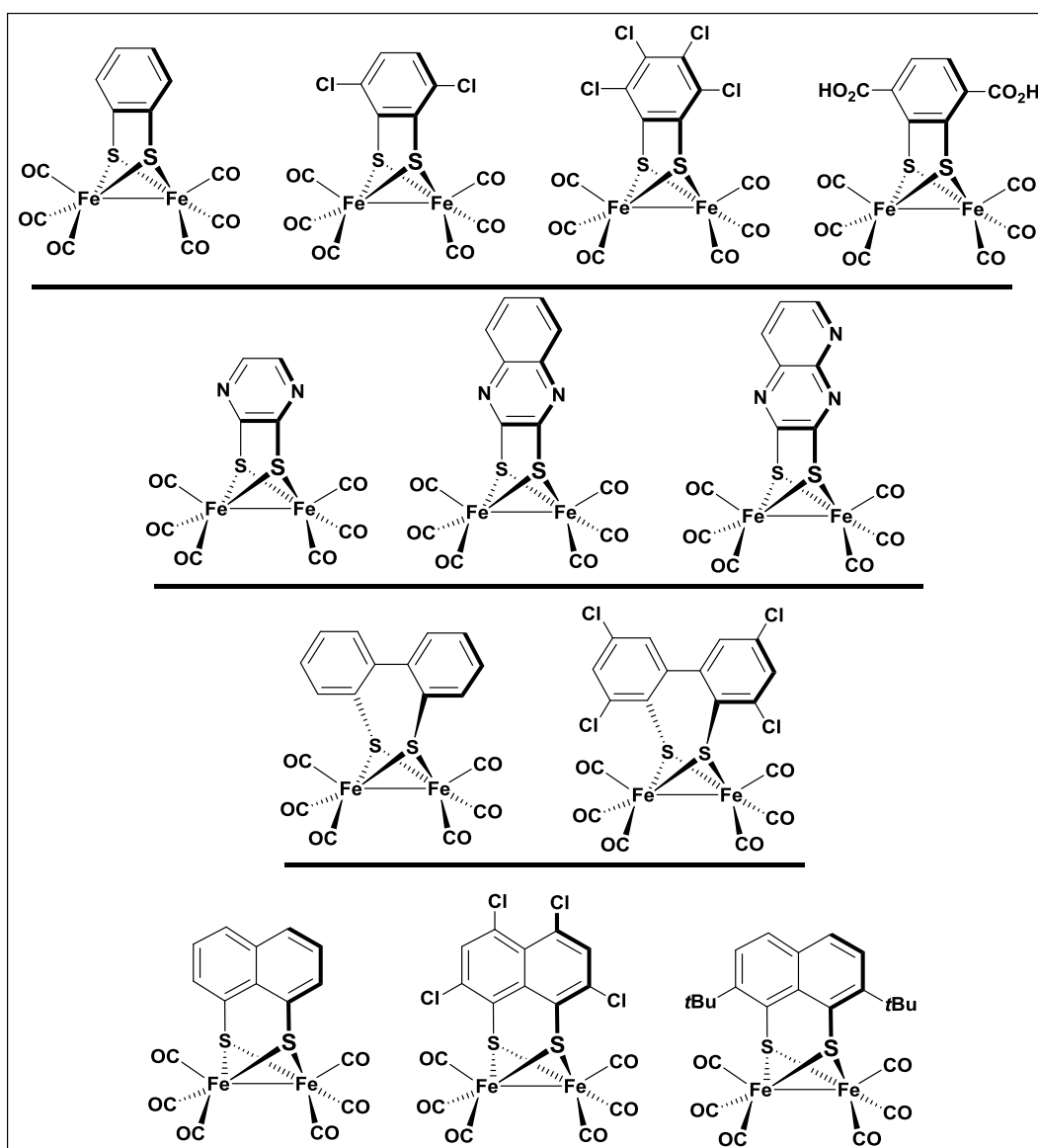


Figure 9. Examples of the reported aromatic dithiolate bridged complexes.¹¹¹

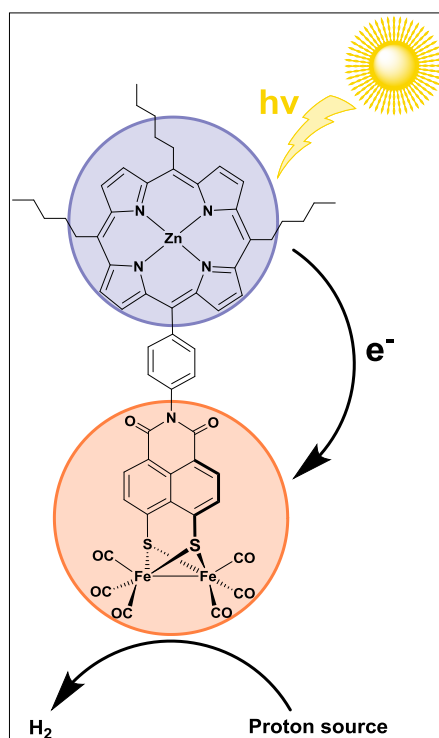


Figure 10. Schematic representation of the light-driven production of hydrogen by diiron complex.¹³⁰

3.3.2.1.2 The Tetranuclear Models (Macrocyclic Complexes)

Recent efforts have been focused on synthesizing macrocyclic complexes that contain two $[\text{Fe}_2\text{X}_2(\text{CO})_6]$ ($\text{X} = \text{S}, \text{Se}$) cores with butterfly structure connected by different linkers leading to systems with two catalytic active centers close to each other. Those macrocyclic complexes might have some applications in numerous field, such as catalysis and molecular recognition.¹³¹⁻¹³⁴

The first example of such complexes that have asymmetrical linkers was reported by Song and co-workers in 2002.¹³⁵ However, such a coordination mode is rare and only few examples have been reported in the literature (Figure 11).^{75, 81, 134, 136-142} Indeed, all these macrocyclic complexes are formed only when the linkers contain more than three atoms between the two sulfur/selenium atoms ($-\text{X}-\text{CH}_2-(\text{E})_n-\text{CH}_2-\text{X}-$, $n > 1$) ($\text{X} = \text{S}, \text{Se}$) and hence the size of these complexes depends on the length of the chain linkers. For example, Chiang and co-workers had reported an 18-membered macrocyclic complex **10** (Figure 11) in which their

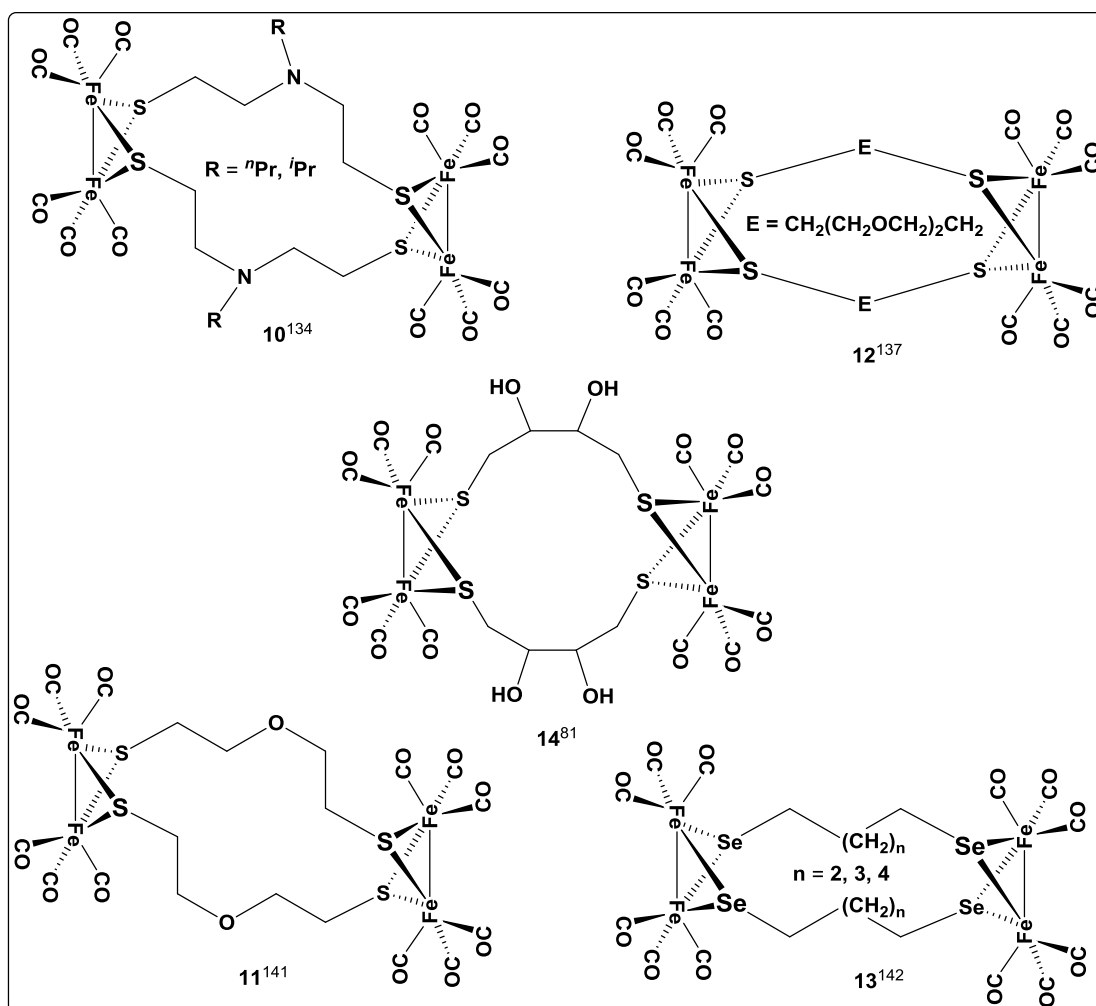


Figure 11. Examples of reported macrocyclic complexes.^{81, 134, 137, 141, 142}

results infer that the lone pairs at the nitrogen atoms are oriented toward the apical CO ligand in each $[\text{Fe}_2\text{S}_2]$ unit. Moreover, they found that the $\text{N}\cdots\text{C}(\text{CO}_{\text{ap}})$ distances arisen from this intramolecular interaction are measured to be 3.497 Å (for $\text{R} = n\text{Pr}$) and 4.011 Å (for $\text{R} = i\text{Pr}$) like the analogue complex **11** (3.182 Å) which contains oxygen atoms instead of nitrogen atoms.¹³⁷ This particular structural feature causes a shift in the frequencies of the CO bands to lower energy.¹³⁴ Therefore, the presence of the nitrogen atom in the linker of complex **10** could consider as a stabilizing factor in the thermodynamic aspect. Song and co-workers could synthesize a 24-membered macrocyclic complex **12**, which is considered as the first crystallographically characterized cyclic double-butterfly $[\text{Fe}_2\text{S}_2]$ units.¹⁴¹ Additionally, Weigand group could also synthesize a 16-membered macrocyclic

complex (**14**) that has a hydroxy group, which may provide the possibility of forming H-bond.⁸¹

Later, Weigand group had succeeded in synthesizing 16-, 18- and 20-membered macrocyclic complexes (**13** as a general structural formula) having two [2Fe2Se] cores with butterfly structures connected by different alkyl chain linkers.¹⁴² Notably, the molecular structures of these macrocyclic complexes show that for each [Fe₂S₂(CO)₆] unit there is an axial (*a*) and equatorial (*e*) CH₂ substituent. Moreover, the ¹H NMR spectra of such complexes show two singlets for the non-equivalent CH₂ groups at room temperature.^{134, 136, 137, 140}

3.3.2.2 [2Fe3S] Model Complexes

As shown in section 3.2, the active center of the enzyme consists of a diiron center with disulfur bridgehead, in which one of these iron atoms (Fe_p, proximal) is additionally sulfur-ligated by a cysteinyl ligand bridged to a [4Fe4S] cluster to possess an unprecedented [2Fe3S] sub-site. Therefore, the synthetic chemists are interested to design model complexes that mimic the [2Fe3S] sub-site of the H-cluster. To the best of my knowledge, such model complexes are rare and only five working groups, Pickett,¹⁴³⁻¹⁴⁶ Rauchfuss,¹⁴⁷ Song,¹⁴⁸ Chen¹⁴⁹ and Weigand^{86, 150} have reported a model complexes that possess the [2Fe3S] sub-site (Figure 12).

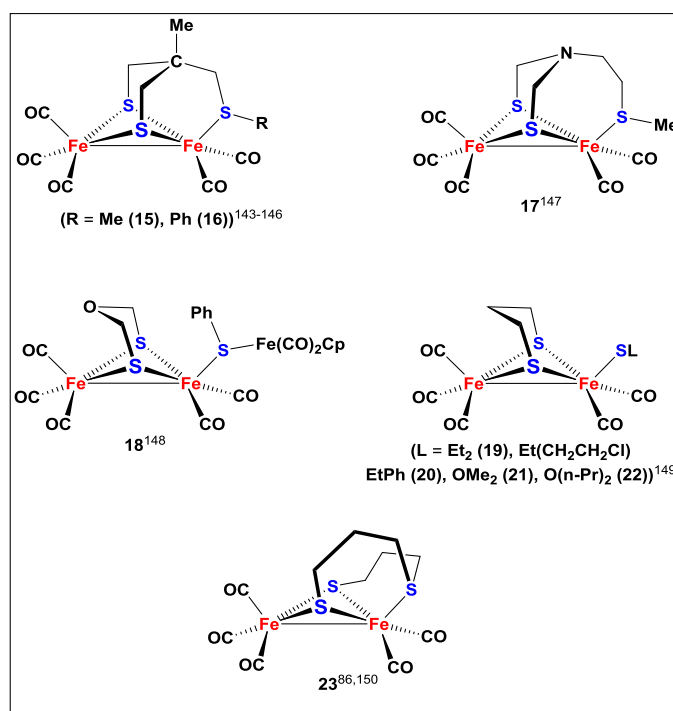
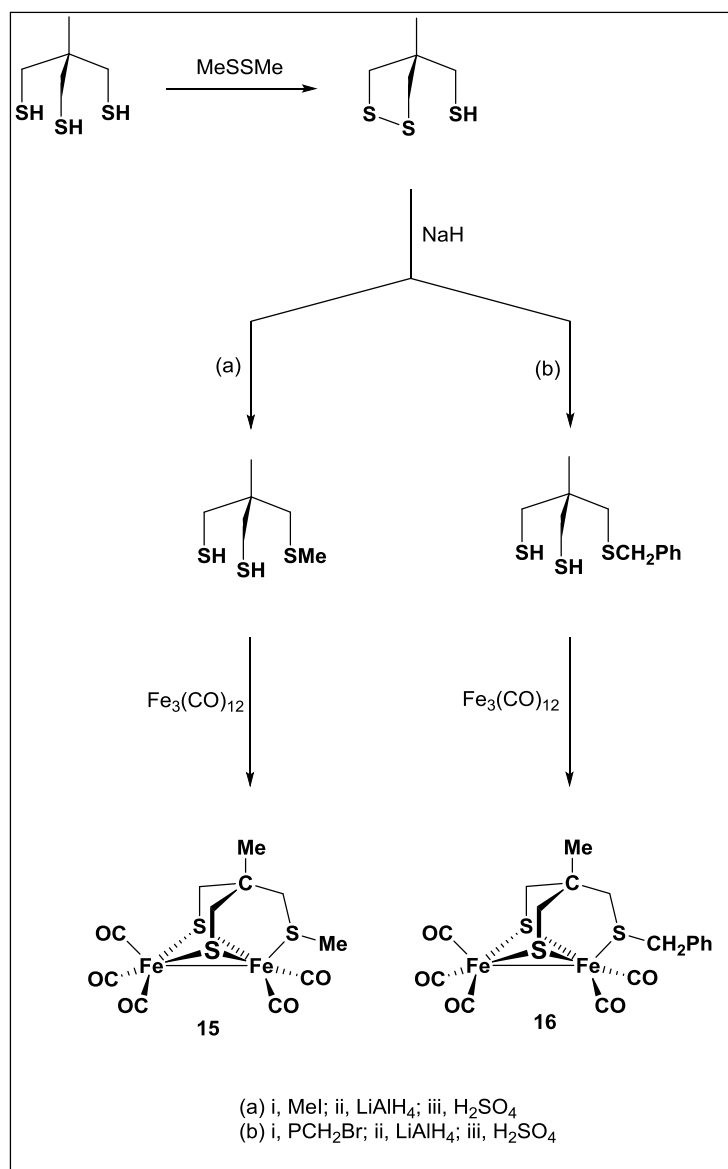


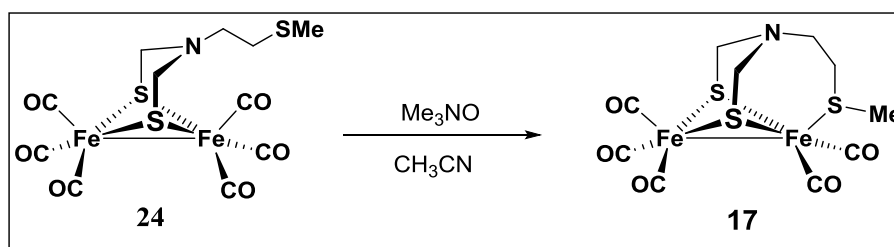
Figure 12. Reported [2Fe₃S] sub-site models of Pickett (**15** and **16**), Rauchfuss (**17**), Song (**18**), Chen (**19-22**) and Weigand (**23**).

In fact, Pickett and co-workers are the first group that reported a synthetic [2Fe₃S] model (Figure 12, **15** and **16**) through the reaction of dithiolate thioether with Fe₃(CO)₁₂ in boiling toluene as shown in Scheme 6.¹⁴³ Firstly, the tripodal thiolate are readily coupled with dimethyl disulfide with the formation of a stable five-membered ring compound. Secondly, the reaction with methyl iodide gives the thioether derivatives, and subsequent reductive cleavage of the disulfide bond gives the backbone functionalized propanedithiol pro-ligands. The latter reacts with Fe₃(CO)₁₂ to afford the [2Fe₃S] models, **15** and **16**, which were characterized by X-ray crystallography.



Scheme 6. Synthetic pathways of complexes **15** and **16**.¹⁴³

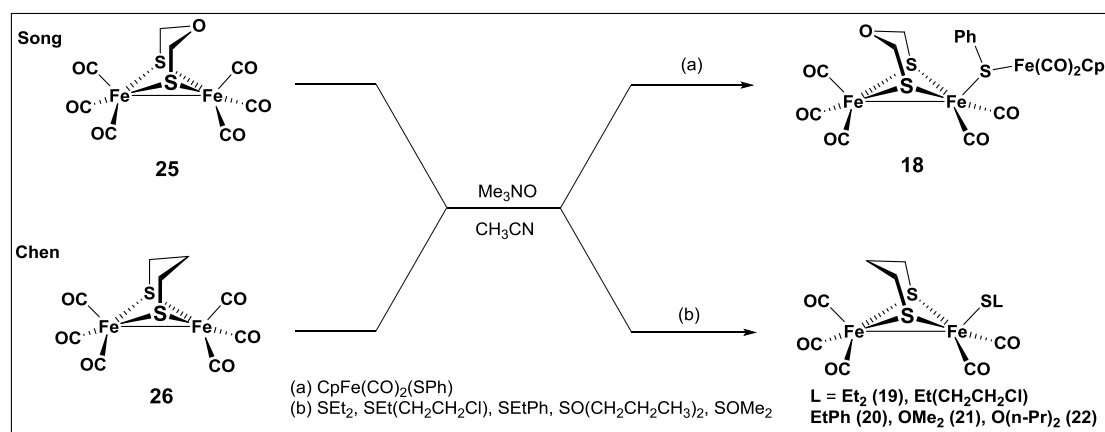
In the same year, Rauchfuss and co-workers also reported another [2Fe₃S] model that is closed to Pickett ones, in which the thioether ligand constitutes the third leg of the sulfur bridge (Figure 12, **17**). As illustrated in Scheme 7, Rauchfuss model was obtained by decarbonylation of complex **24** with Me₃NO and then the thioether coordinates to the iron atom to afford the target [2Fe₃S] model (**17**), in which its molecular structure presents that the thioether is coordinated to one iron atom.¹⁴⁷



Scheme 7. Synthetic pathway of Rauchfuss model (**17**).¹⁴⁷

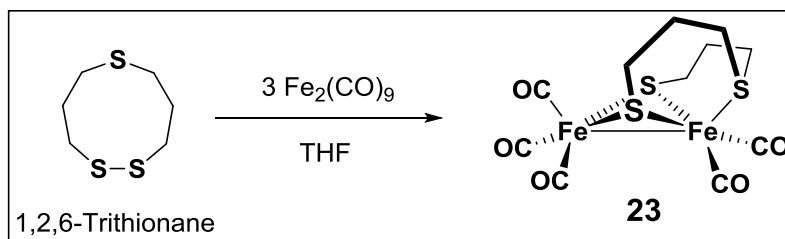
This was followed by the work of Song and Chen, in which they reported another [2Fe3S] models by treatment of an acetonitrile solution of complexes **25** and **26**, respectively, with Me₃NO resulted in oxidative abstraction of CO (decarbonylation) to yield the *in situ* acetonitrile complexes. Subsequent addition of L (L = CpFe(CO)₂(SPh), Song and L = SEt₂, SEt(CH₂CH₂Cl), SEtPh, SO(CH₂CH₂CH₃)₂ and SOMe₂, Chen) afforded the [2Fe3S] models (Scheme 8).¹⁴⁸

149



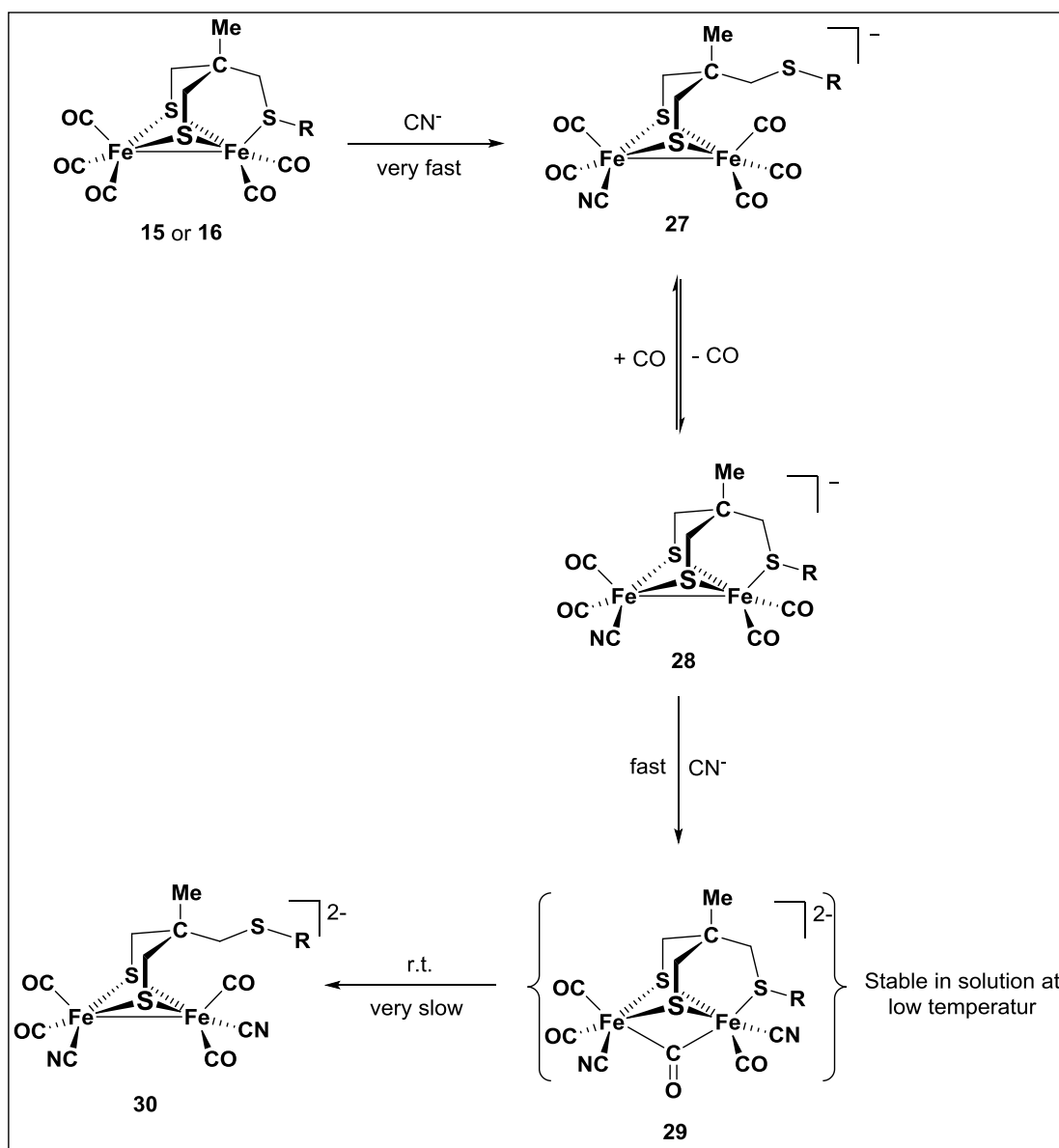
Scheme 8. Synthetic pathways of Song (**18**) and Chen (**19-22**) models.^{148, 149}

On the other hand, Weigand and co-workers could synthesize [2Fe3S] model from the reaction of 1,2,6-trithionane with three equivalent Fe₂(CO)₉ in boiling THF followed by subsequent column chromatography as shown in Scheme 9.⁸⁶ It can be noticed from Scheme 9 that the sulfur atom located in 6-position acts as an additional sulfur donor by intramolecular substitution of one CO ligand.



Scheme 9. Synthetic pathway of Weigand model (**23**).⁸⁶

Among these synthetic [2Fe3S] models (Figure 12), only the reactivity of **15** and **16** have been investigated in detail.¹⁴³⁻¹⁴⁶ The mechanism of cyanation of complexes **15** and **16** to give mono- and dicyanide-substituted products has been proposed as illustrated in Scheme 10.^{145, 146} This mechanism was determined by stopped-flow FTIR mechanistic study, which revealed that the first step is a concerted process involving fast regioselective attack by cyanide and decoordination of the thioether ligand to afford **27** as intermediate. The latter undergoes slower re-binding of the thioether with concerted dissociation of CO ligand to afford **28**, in which its molecular structure was determined by X-ray crystallography. Consequence addition of two or more equivalents of cyanide ligand afforded **29** as moderately stable intermediates, which rearranges slowly at room temperature affording the thermally stable products **30** with all CO ligands in terminal position. In total, Scheme 10 illustrates the role of bridging carbonyls in the assembly of the dicyanide species, how on-off sulfur ligation can have a dramatic effect on cyanation kinetics and how the [2Fe3S] core stabilizes bridging carbonyl species. Moreover, **29** remains up till the date of this thesis the first and only example of sub-site structure that possesses a bridging carbonyl associated with terminal CO and CN ligands, which makes it the closest analogues of the CO-inhibited from the H-cluster as shown in Figure 13.



Scheme 10. Suggested mechanism of cyanation of Pickett models.^{145, 146}

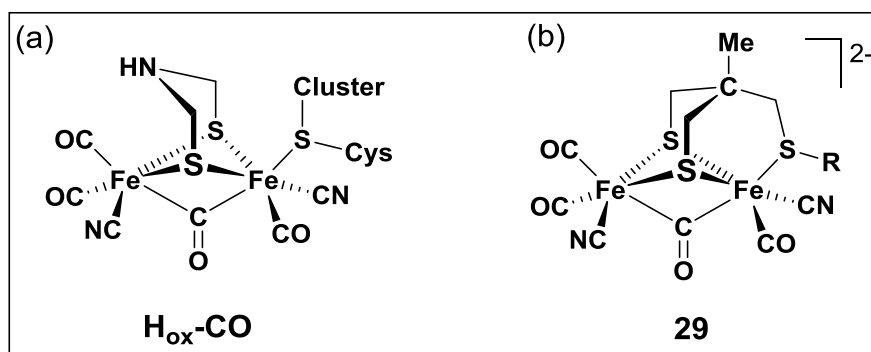
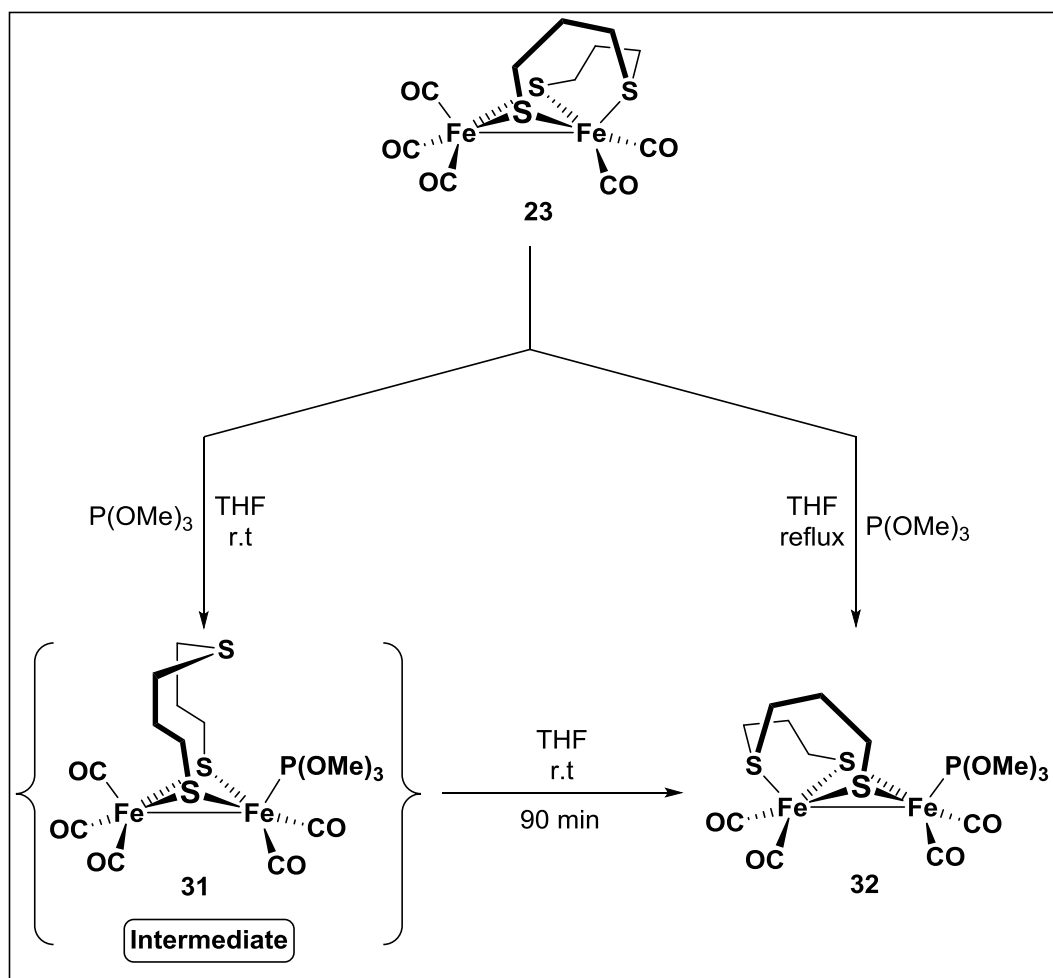


Figure 13. (a) $\text{H}_{\text{ox}}\text{-CO}$ state (CO inhibited) of the H-cluster. (b) **29** intermediate of Pickett model.

It is worth pointing out that Weigand and co-workers have made an experiment to corroborate the mechanism suggested by Pickett for the cyanation reaction of his models, in which they studied the substitution reaction of **23** (Figure 12) using $\text{P}(\text{OMe})_3$ to give complex **32** (Scheme 11) as a result of the on-off coordination of a thioether ligand bound at the iron atom.¹⁵⁰ Additionally, they also could isolate and characterize an intermediate (**31**) analogous to **27** as shown in Scheme 11.



Scheme 11. The pathway of substitution of CO by $\text{P}(\text{OMe})_3$ in Weigand model.¹⁵⁰

Scheme 11 illustrates that complex **W** reacts with one equivalent $\text{P}(\text{OMe})_3$ at room temperature to produce firstly the kinetically controlled product **31**, which then undergoes intramolecular substitution of CO by the pendent thioether to afford complex **32**, the thermodynamically controlled product, upon standing at room temperature for 90 min. On the other hand, performing the reaction under reflux condition produces exclusively complex **32**. The kinetically controlled

product **31** was isolated and characterized by spectroscopic techniques and X-ray crystallography. Such a result elucidates the role of the on-off coordination mode of the pendant thioether group in Weigand model.

3.4 Protonation of Hexacarbonyl Complexes

One of the most important structural features of the synthetic H-cluster mimics is the existence of an internal basic site that could be protonated in the presence of a Brønsted acid which is a crucial step in the catalytic cycle.¹⁵¹⁻¹⁵⁴ Generally, protonation of the bimetallic hexacarbonyl complexes $[\text{Fe}_2(\text{CO})_6\{\mu\text{-(SCH}_2)_2\text{E}}]$ may take place at different sites (Figure 14) based on the strength and amount of the acid added.

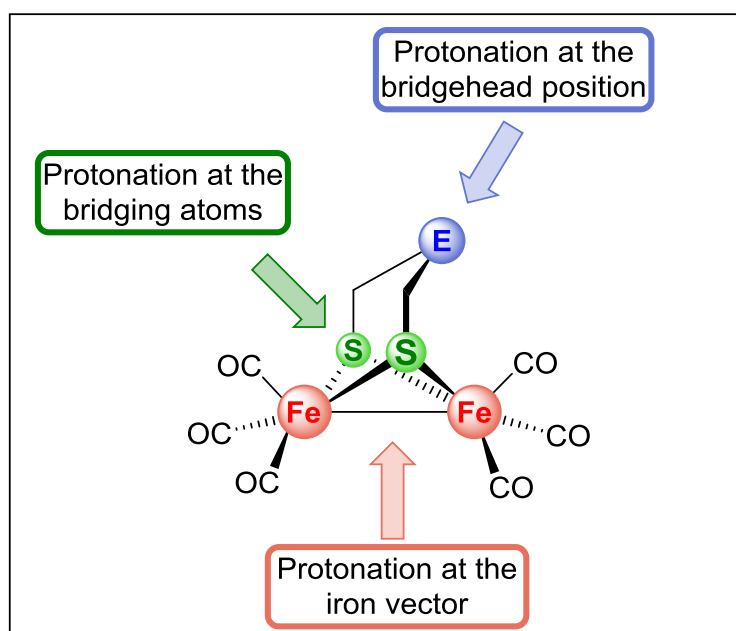
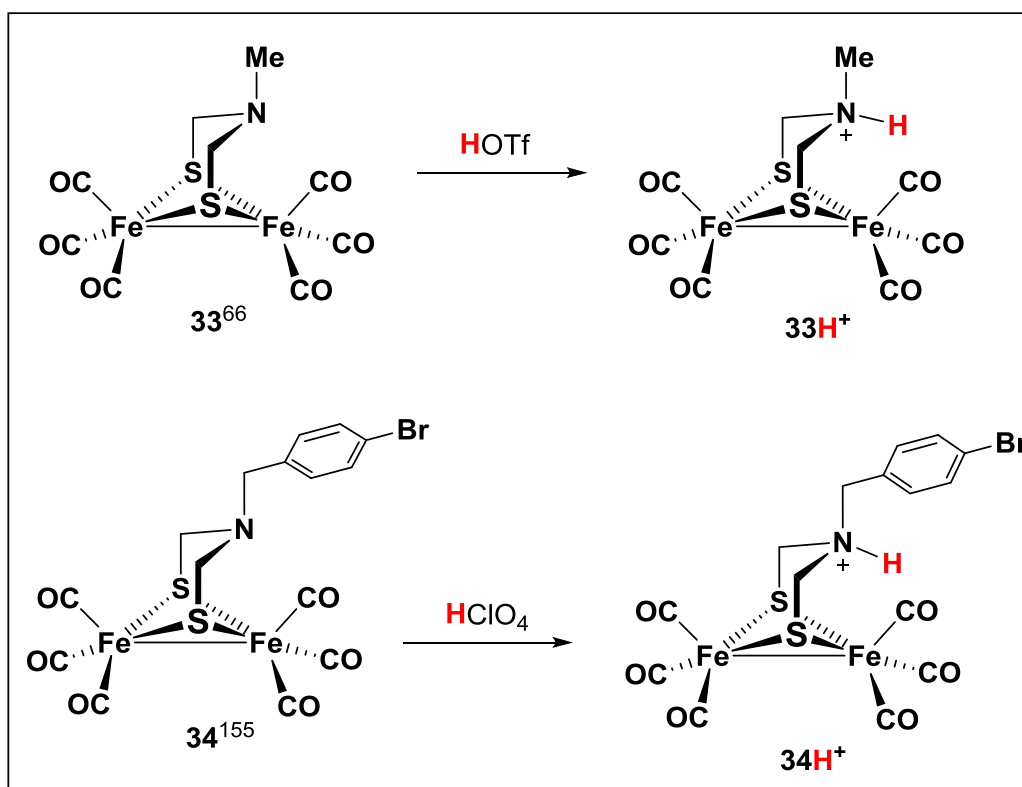


Figure 14. Possible sites for protonation in $[\text{Fe}_2(\text{CO})_6\{\mu\text{-(SCH}_2)_2\text{E}}]$ complexes.

Protonation at the bridgehead position. The reported literatures regarding the protonation at the bridgehead atom/group in the hexacarbonyl complexes, $[\text{Fe}_2(\text{CO})_6\{\mu\text{-(SCH}_2)_2\text{E}}]$, are only observed in the case of $\text{E} = \text{NR}$ or $\text{PhP}=\text{O}$ using strong acids such as $\text{HBF}_4 \cdot \text{Et}_2\text{O}$, HOTf and HClO_4 .^{66, 76, 92, 155-157} Such a behavior displays some typical changes in IR and ^1H NMR spectra as well as in the structure as compared to their original complexes. The groups of Rauchfuss and Lomoth could protonate their complexes **33** and **34**, respectively, (Scheme 12) in the

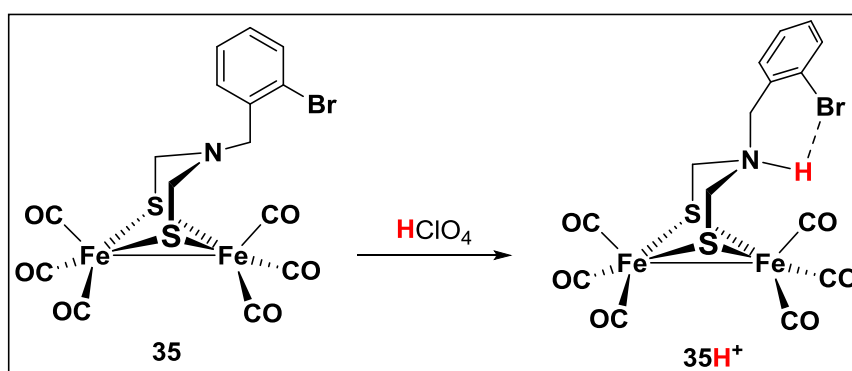
presences of proton acids (HOTf and HClO₄) and the resulting N-protonated complexes **33H⁺** and **34H⁺** were characterized *in situ* by IR and NMR spectroscopy.^{66, 155} As a result, the carbonyl frequencies are shifted ~15 cm⁻¹ to higher energy compared to the parent models. The observed shift indicates that the protonation process occurred at the nitrogen atom and not at other sites, such as, the Fe-Fe bond.¹⁵⁸



Scheme 12. Reaction Scheme for the protonation process involving complexes **33** and **34**.^{66, 155}

Later, Sun had modified complex **34** by introducing an *ortho*-bromobenzyl group to the bridged-N atom (**35**, Scheme 13), and hence enhanced the stabilization of the N-protonated complex (**35H⁺**) due to the intramolecular N-H...Br interaction (3.334(7) Å), which makes it easier to be isolated and determined by X-ray crystallography compared to those of Racuhfuss and Lomoth.⁷⁶ By comparing the molecular structures of both complexes **35** and **35H⁺**, one can notice that the *ortho*-bromobenzyl group in complex **35** is bounded to the nitrogen atom in the axial position while in the N-protonated complex (**35H⁺**) it

takes place in the equatorial position and the proton occupied the axial position toward the iron site.⁷⁶



Scheme 13. Reaction Scheme for the protonation process involving complex **35**.⁷⁶

The same group also reported that the introduction of an electron-rich five-membered heterocycle (furan and thiophene) at the nitrogen atom in the bridgehead enhances the protonation process and gives the N-protonated complexes as shown in Figure 15.¹⁵⁷ Moreover, the presence of the heterocycle make these complexes easier to be reduced at less negative potential in comparison with this of **35**. This can be explained due to the presence of the methylene group near to the heterocycle, which could enhance the electron density in the π system by donating electrons through hyperconjugation and slightly decrease the electron density at the iron cores through the three atoms (N, C, S).

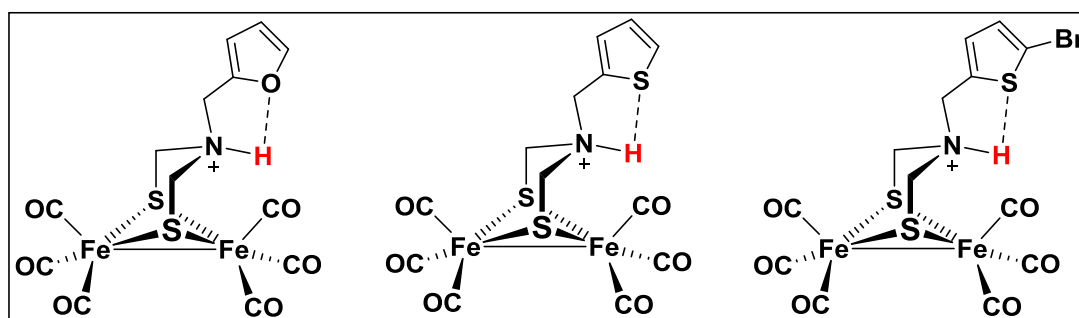
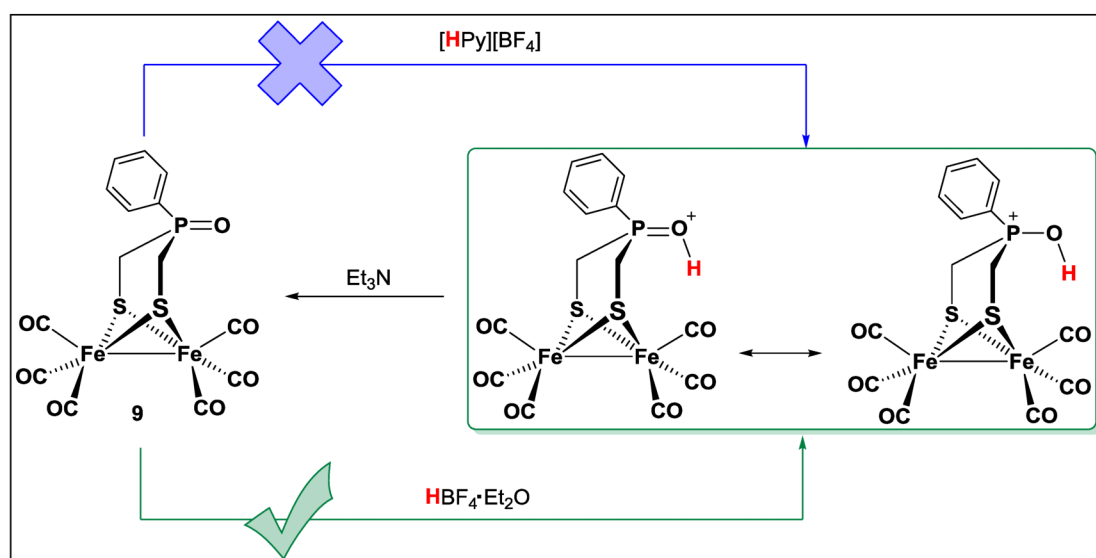


Figure 15. The N-protonated complexes of Sun models after protonation.¹⁵⁷

As mentioned in section 3.3.2, Almazahreh *et. al.* has succeeded in synthesizing a model complex (**9**, Scheme 4) features a P=O functionality, which provides a

potential site for protonation as in the case of the amine functionality.⁹² In this study, he investigated the ability of complex **9** toward protonation in the presence of the moderately strong acid pyridinium tetrafluoroborate [HPy][BF₄] and the very strong acid HBF₄·Et₂O. As a result, complex **9** could be protonated only in the presence of excess HBF₄·Et₂O as illustrated in Scheme 14. The IR spectrum of the solution of complex **9** in the presence of HBF₄·Et₂O shows a shift in the carbonyl region about ~10 cm⁻¹ to higher wavenumber. This shift is consistent with those having an amine functionality in the bridgehead, which implies protonation of the P=O function. Subsequent addition of Et₃N quantitatively restores complex **9**, reflecting the reversibility of the protonation process. Moreover, the ³¹P{H} NMR spectrum of a solution of complex **9** in the presence of HBF₄·Et₂O provides more evidence for the protonation of the P=O function, in which a shift (~36.6 ppm) to lower field was observed in comparison with the parent complex in the absence of the acid. This result is consistent with the protonation of the P=O functionality.



Scheme 14. Reaction Scheme for the protonation process involving complex **9**.⁹²

Protonation at the bridging atoms (μ -S). It has been found that the μ -S atoms in the dithiolato bridge have an important role in the catalytic cycle, which are considered as possible basic sites that could hold the proton that combines with the hydride, or accept the proton during the heterolytic formation and cleavage of dihydrogen.^{153, 159, 160} However, protonation of the μ -S in the hexacarbonyl complexes is very difficult due to its low basicity. In contrast, substitution of the

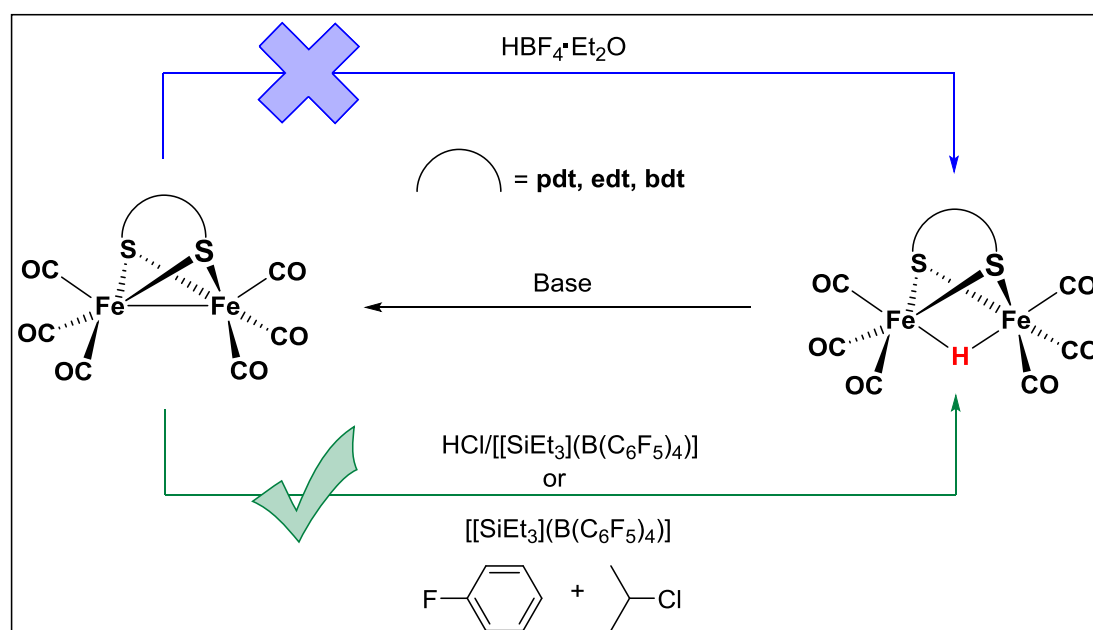
CO ligands in hexacarbonyl complexes with stronger σ -donor ligands, such as PMe_3 and $\text{Ph}_2\text{P}-(\text{CH}_2)_3-\text{PPh}_2$ could enhance the basicity of the μ -S atoms, which makes it more susceptible for protonation.¹⁶⁰⁻¹⁶⁴

Protonation at the iron vector. In general, protonation at the Fe-Fe bond yields either the bridging hydride Fe-H-Fe (μ -H) fashion or the terminal hydride H-Fe-Fe (t -H) fashion based on the applied conditions as well as the environment around the iron cores. The formation of the hydride species (μ -H or t -H) in the diiron dithiolate complexes may display some typical changes in ^1H and IR spectra as well as in the molecular structure in comparison with the parent complexes as follows:¹⁶¹

- Large blue-shifts (*ca.* 50-70 cm^{-1}) of the $\nu(\text{CO})$ bands due to the weaker back-bonding of the iron atoms.
- The appearance of a signal in the region of δ 0 to -20 in the ^1H NMR spectrum.
- The elongation of the Fe-Fe distance in the molecular structure of the protonated complex.

Indeed, protonation of the diiron dithiolato hexacarbonyl complexes at the Fe-Fe vector cannot be accomplished by acids weaker than or similar to $\text{HBF}_4 \cdot \text{Et}_2\text{O}$ with the exception of the methods developed by Heinekey, Chiang and their co-workers to protonate $[\text{Fe}_2(\text{CO})_6\{\mu-(\text{xdt})\}]$ ($\text{xdt} = \text{pdt, edt}$ and bdt) complexes using either HCl gas or arenium ions in the presence of $[[\text{SiEt}_3](\text{B}(\text{C}_6\text{F}_5)_4)]$ to generate super-strong Brønsted acids that are used to activate the Fe-Fe bond (Scheme 15).¹⁶⁵⁻¹⁶⁷ The resulting FTIR spectra showed a shift (*ca.* 60 cm^{-1} for pdt and *ca.* 78 cm^{-1} for edt and bdt) in the carbonyl region to higher energy in comparison to those of the parent complexes suggesting the formation of the μ -H with two Fe^{II} centers (Fe-H-Fe). This is supported by the appearance of signals in the high-field ^1H NMR at δ -15.9, -17.39 and -13.44 for pdt, edt and bdt, respectively, which is assigned to the μ -H. Moreover, the molecular structures of the protonated complexes confirmed the formation of the μ -H and the Fe-Fe bond distances were slightly elongated in comparison with those in the parent complexes as illustrated in Table 3.^{59, 167-169}

In contrast to the hexacarbonyl complexes, the iron atoms of the dithiolato complexes containing stronger σ -donor ligands, such as CN^- , PMe_3 , N-heterocyclic carbenes (NHC) are basic enough to be protonated in the presence of appropriate acids to afford thermodynamically stable ($\text{Fe}^{\text{II}}\text{Fe}^{\text{II}}$) complexes featuring a $\mu\text{-H}$.^{160, 170-172} Moreover, it has been found that the doubly reduced species of the hexacarbonyl model complexes are also basic enough to be protonated even with weak acid, such as carboxylic acids and phenols.^{101, 173-175}



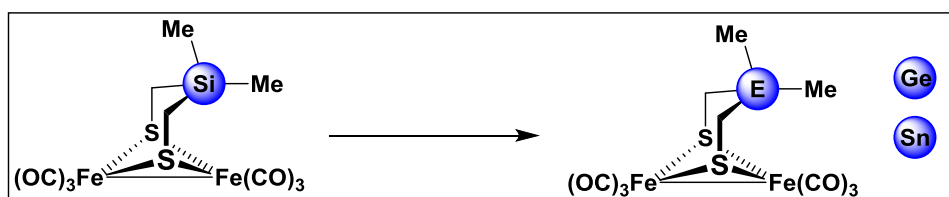
Scheme 15. Reaction Scheme for the protonation process involving $[\text{Fe}_2(\text{CO})_6\{\mu\text{-(xdt)}\}]$ ($\text{xdt} = \text{pdt, edt and bdt}$) model complexes.¹⁶⁷

Table 3. Fe-Fe bond distances of $[\text{Fe}_2(\text{CO})_6\{\mu\text{-(xdt)}\}]$ ($\text{xdt} = \text{pdt, edt and bdt}$) model complexes and their protonated analogues.

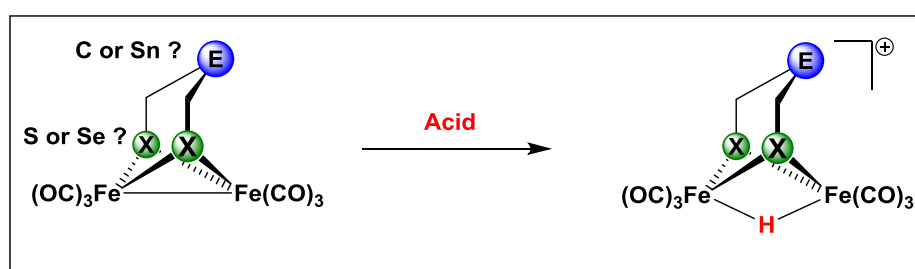
Property	Pdt ^{59,167}	Edt ^{167,169}	Bdt ^{167,168}
Fe—Fe bond (Å)	2.5105(9)	2.505(1)	2.480(2)
$\mu\text{-H—Fe—Fe}$ bond (Å)	2.5641(10)	2.5477(7)	2.5438(7)

3.5 Motivation

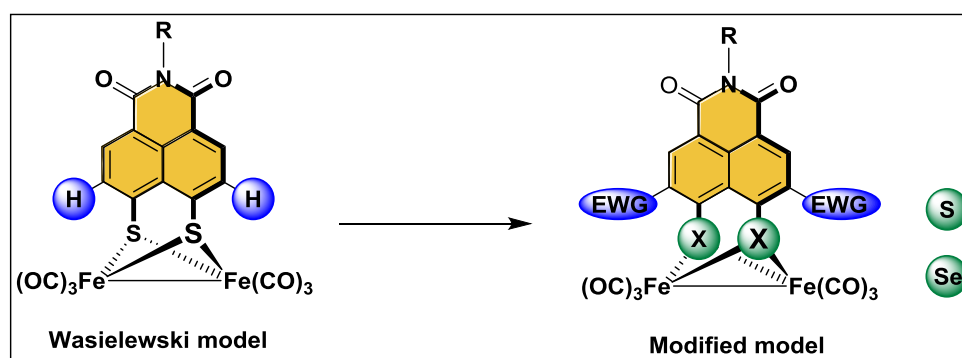
The synthetic diiron(I) dithiolato carbonyl complexes mentioned in the preceding sections were found to be electrocatalytically active for proton reduction to H_2 in the presence of different Brønsted acids.^{122, 129} However, these model complexes are still having large overpotentials, low efficiency and poor stability. Therefore, synthetic chemists are still trying to overcome these weaknesses in synthetic models. As mentioned in in section 3.3.2, the introduction of a silicon atom in the dithiolato linker of [FeFe]-hydrogenase model complexes increased the basicity of the sulfur atoms by a $\sigma(\text{Si-C}) \rightarrow 3p(\text{S})$ filled-filled interaction as well as reduced the overpotentials of proton reduction. Therefore, it is worthy to investigate the molecular structures and electronic structures of complexes that contain the heavier group 14 atoms (Ge and Sn) at the central atom in the dithiolato linker as shown below.



There is no doubt that the existence of an internal basic sites in the synthetic H-cluster mimics that could be protonated in the presence of Brønsted acid, which is a crucial step in the catalytic cycle. Up to date, it was possible to protonate only the bridgehead atom/group in $[\text{Fe}_2(\text{CO})_6\{\mu\text{-(SCH}_2)_2\text{E}\}]$ (E = NR or PhP=O) complexes. Additionally, protonation studies of diiron diselenolato hexacarbonyl complexes in acidic medium have not been previously reported. Thus, it is significant to investigate diiron diselenolato hexacarbonyl complexes toward protonation in the presence of Brønsted acids as shown below.



The Wasielewski group and others have modified the naphthalene skeleton by introducing an imide group into its backbone. They found that the imide functionality provides additional stability to the mono-anionic species due to its strong electron-withdrawing effect and serves as a suitable site for the attachment of an additional chromophore.^{118, 130} It is worthy to modify such model complexes by incorporating electron-withdrawing substituents, such as Br, in the *ortho*-position to the μ -S atoms as well as the replacement of the μ -S atoms by Se atoms to investigate their roles in the redox properties as shown below.



As illustrated in the preceding sections, numerous complexes featuring [2Fe2S] core with the general formula $[\text{Fe}_2(\text{CO})_6\{\mu\text{-(SCH}_2)_2\text{E}}]$ have been synthesized and tested as electrocatalyst to better understand the structure-function relationships of the H-cluster. In contrast, very few models mimicking the [2Fe3S] sub-site of the H-cluster have been studied in the absence and presence of acids. Such a study may provide better information to understand the role of the on-off coordination mode of the pendant thioether group.

This thesis will describe different derivatization strategies of various [FeFe]-hydrogenase model complexes as follows:

- (i) **Project 1.** The synthesis of model complexes with $\mu\text{-(SCH}_2)_2\text{ER}_2$ linkers, where the central atom E is Ge or Sn.
- (ii) **Project 2.** Studying the influence of the presence of $\mu\text{-Se}$ instead of the $\mu\text{-S}$ atoms in $[\text{Fe}_2(\text{CO})_6\{\mu\text{-(SCH}_2)_2\text{E}}]$ ($\text{E} = \text{CH}_2, \text{CMe}_2$ and SnMe_2) towards protonation process using different acids.
- (iii) **Project 3.** The synthesis of a new tetranuclear macrocyclic [FeFe]-hydrogenase H-cluster model.

- (iv) **Project 4.** The synthesis of models containing naphthalene monoimide (NMI) of *peri*-substituted dichalcogenides as bridging linkers.
- (v) **Project 5.** A systematic study of [FeFe]-hydrogenase H-cluster mimics with various -S(CH₂)_nS- linker lengths (n = 2-8).
- (vi) **Project 6.** The electrochemical behaviour of [FeFe]-hydrogenase mimics featuring [2Fe3S] cores, namely [Fe₂(CO)₅{TBPT}] and [Fe₂(CO)₄(P(OMe)₃){TBPT}] was investigated in the absence and presence of acetic acid, AcOH.
- (vii) As a side project of my work, **Project 7** describes the synthesis, characterization and electrochemical investigation of heterocyclic-selenocarboxylate iron complexes.

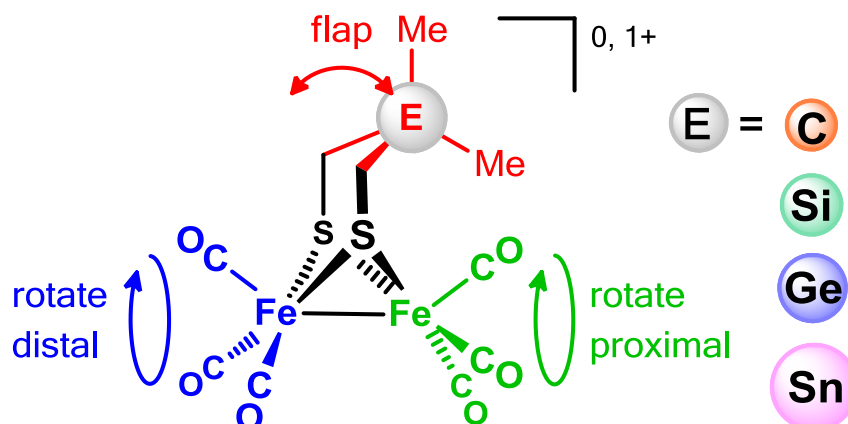
4 PUBLICATIONS

4.1 [HAF-1]

[FeFe]-Hydrogenase H-Cluster Mimics with Unique Planar μ -(SCH₂)ER₂ Linkers (E = Ge and Sn)

Hassan Abul-Futouh, Laith R. Almazahreh, Takahiro Sakamoto, Nhu Y. T. Stessman, Dennis L. Lichtenberger, Richard S. Glass, Helmar Görls, Mohammad El-Khateeb, Philippe Schollhammer, Grzegorz Mloston, Wolfgang Weigand

Chemistry – A European Journal **2017**, *23*, 346-359.



Bioorganometallic Chemistry

[FeFe]-Hydrogenase H-Cluster Mimics with Unique Planar μ -(SCH₂)₂ER₂ Linkers (E = Ge and Sn)Hassan Abul-Futouh,^[a] Laith R. Almazahreh,^{*,[a]} Takahiro Sakamoto,^[b] Nhu Y. T. Stessman,^[b] Dennis L. Lichtenberger,^{*,[b]} Richard S. Glass,^{*,[b]} Helmar Görls,^[a] Mohammad El-Khateeb,^[c] Philippe Schollhammer,^{*,[d]} Grzegorz Mloston,^[e] and Wolfgang Weigand^{*,[a]}

Dedicated to Professor Konstantin Karaghiosoff on the occasion of his 60th birthday

Abstract: Analogues of the [2Fe-2S] subcluster of hydrogenase enzymes in which the central group of the three-atom chain linker between the sulfur atoms is replaced by GeR₂ and SnR₂ groups are studied. The six-membered FeSCECS rings in these complexes (E=Ge or Sn) adopt an unusual conformation with nearly co-planar SCECS atoms perpendicular to the Fe-Fe core. Computational modelling traces this result to the steric interaction of the Me groups with the axial carbonyls of the Fe₂(CO)₆ cluster and low torsional strain for GeMe₂ and SnMe₂ moieties owing to the long C–Ge and C–Sn bonds. Gas-phase photoelectron spectroscopy

of these complexes shows a shift of ionization potentials to lower energies with substantial sulfur orbital character and, as supported by the computations, an increase in sulfur character in the predominantly metal–metal bonding HOMO. Cyclic voltammetry reveals that the complexes follow an ECE-type reduction mechanism (E = electron transfer and C = chemical process) in the absence of acid and catalysis of proton reduction in the presence of acid. Two cyclic tetranuclear complexes featuring the sulfur atoms of two Fe₂S₂(CO)₆ cores bridged by CH₂SnR₂CH₂, R = Me, Ph, linkers were also obtained and characterized.

Introduction

The active H-cluster site of [FeFe]-hydrogenases (Figure 1) contains a [2Fe-2S] subcluster with a semi-bridging carbonyl ligand between the iron centers.^[1] This semi-bridging orientation of the carbonyl ligand is thought to be important because it opens an axial site on the iron atom that is distal to the

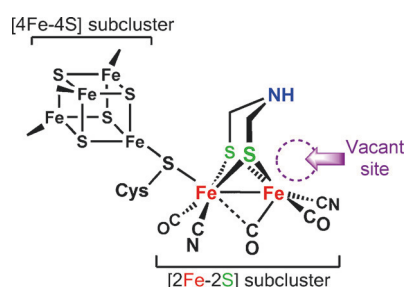


Figure 1. The active H-cluster site of a [FeFe]-hydrogenase.^[1]

[a] M. Sc. H. Abul-Futouh, Dr. L. R. Almazahreh, Dr. H. Görls, Prof. Dr. W. Weigand
Institut für Anorganische und Analytische Chemie
Friedrich-Schiller-Universität Jena, Humboldt Str. 8, 07743 Jena (Germany)
E-mail: laithmazahreh81@gmail.com
wolfgang.weigand@uni-jena.de

[b] Dr. T. Sakamoto, Prof. Dr. N. Y. T. Stessman, Prof. Dr. D. L. Lichtenberger, Prof. Dr. R. S. Glass
Department of Chemistry and Biochemistry
The University of Arizona, Tucson, AZ, 85721 (USA)
E-mail: dlichten@email.arizona.edu
rglass@email.arizona.edu

[c] Prof. Dr. M. El-Khateeb
Chemistry Department
Jordan University of Science and Technology, Irbid 22110 (Jordan)

[d] Prof. Dr. P. Schollhammer
UMR CNRS 6521, Université de Bretagne Occidentale
6 avenue Le Gorgeu, C.S. 93837, 29238 Brest-Cedex (France)
E-mail: philippe.schollhammer@univ-brest.fr

[e] Prof. Dr. G. Mloston
Section of Heteroorganic Compounds, University of Lodz
Tamka 12, 91-403 Łódź (Poland)

Supporting information for this article can be found under:
<http://dx.doi.org/10.1002/chem.201603843>.

[4Fe-4S] cubane subcluster for protonation of the iron center. DFT studies have proposed that protonation of the azadithiolate linker μ -(SCH₂)₂NH at the NH^[1,2] group or protonation of the μ -S atoms^[3] provides low energy kinetic pathways for protonation of the axial site and dihydrogen formation, which occurs with the enzyme at a midpoint potential of –0.42 V (vs. normal hydrogen electrode (NHE))^[4] at pH 8.0, which is close to the thermodynamic potential. Proton relay to the vacant axial iron site through agostic or hydrido-proton interactions from the azadithiolate linker to the iron is thought to be responsible for the high efficiency of catalytic hydrogen release by the H-cluster (ca. 10⁴ turnovers s⁻¹).^[1,2,5]

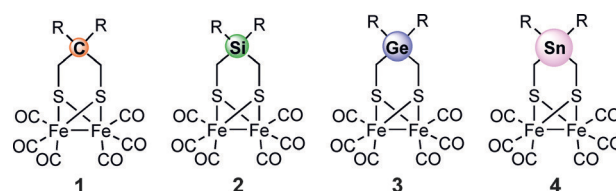
Models for the active site [2Fe-2S] subcluster have been extensively studied.^[6] Although mixed valence analogues with a semi-bridging carbonyl and rotated structure have been reported,^[7] the Fe^IFe^I models typically do not exhibit these essen-

tial features. However, three complexes with these features have been reported.^[8] To adopt these features up to three requirements were necessary: 1) bulkiness of the dithiolato bridge, 2) desymmetrization of the diiron system, and 3) agostic interaction in two cases. Bulkiness in the dithiolato bridge was previously proposed to favor these geometric changes on the basis of computations^[9] and, owing to steric interactions between a methyl group and an apical CO in $\text{Fe}_2(\text{CO})_6\{\mu\text{-S}(\text{CH}_2)_2\text{CMe}_2\}$, the $\text{Fe}(\text{CO})_3$ moiety is twisted.^[10] It should be noted that the $\text{CH}_2\text{CMe}_2\text{CH}_2$ bridge adopts a bent geometry such that the $\text{FeS}_2(\text{CH}_2)_2\text{CMe}_2$ ring may be described as a chair conformation with respect to one Fe and a boat conformation with respect to the other Fe. Furthermore, this chair/boat conformation undergoes ring inversion in analogy with cyclohexane. Even in $[\text{2Fe-2S}]$ models with all terminal CO ligands acting as electrocatalysts for H_2 production from weak acids, the core reorganization may play a critical role. For example, potential inversion, in which the first 1e^- reduction potential is more negative than second 1e^- reduction potential, occurs if there is an intervening reorganization.^[11]

The synthetic models related to the structure of the H-cluster may be divided into two categories: 1) bioinspired models with azadithiolato linkers,^[12] and 2) artificial models with abiological linkers $\mu\text{-(XCH}_2)_2\text{Y}$ in which the central atom/group Y is CR_2 ,^[3d,12o,13] O ,^[13d,14] S ,^[15] Se ,^[16] SiR_2 ,^[3e,17] or Ph-P=O ^[18] and X could be S ,^[12-18] Se ,^[19] Te ,^[19c,d] or PR .^[20] The use of these abiological linkers may provide valuable information and answers to basic questions concerning the role of the dithiolato bridge as well as the effect of the unusual Y on the structural and functional properties of such artificial H-cluster mimics. For example, Goy et al. recently reported a model with an especially bulky Si-containing moiety, namely $\text{Fe}_2(\text{CO})_5(\text{PPh}_3)\{\mu\text{-S}(\text{CH}_2)_2\text{Si}(\text{1-silafluorene})\}$.^[3e] In this case, protonation of the sulfur atoms by triflic acid is favored by the interplay of the presence of the Si atom, the steric bulkiness of the Si-containing moiety, and the presence of one σ -donor PPh_3 ligand at the diiron core. Previous suggestions of the relevance and observation of protonation at sulfur have been made.^[3] In addition, we have previously shown that the electron-richness of thioether moieties, as judged by the ionization energies determined by photoelectron studies on $\text{Fe}_2(\text{CO})_6\{\mu\text{-S}(\text{CH}_2)_2\text{SnR}_2\}$ complexes^[21] and other compounds with SCSn groups,^[22] is dramatically increased by a C-Sn bond owing to a geometry-dependent $\sigma(\text{Sn-C})\leftrightarrow 3\text{p}(\mu\text{-S})$ filled–filled interaction.

We report in the present paper the synthesis of models with $\mu\text{-(SCH}_2)_2\text{ER}_2$ linkers, where the central atom E is Ge or Sn. Here, the steric hindrance can be varied by judicious choice of R. We now study in a systematic manner the molecular structures and electronic structures of the series of complexes depicted in Scheme 1, where complexes **1** ($\text{R}=\text{H}$ or Me)^[10b,13c] and **2** ($\text{R}=\text{Me}$)^[17] have been reported previously.

This series provides insight into the effect of Ge and Sn on the molecular structure of the $\text{Fe}^{\text{I}}\text{Fe}^{\text{I}}$ complexes and their reorganization energies on forming formal $\text{Fe}^{\text{I}}\text{Fe}^{\text{II}}$ ions, as well as the effect of the C-Ge and C-Sn bonds on the electron-richness of the adjacent S atoms. Within the series in Scheme 1, only the models **3** and **4** reveal a unique planarity when $\text{R}=\text{Me}$,



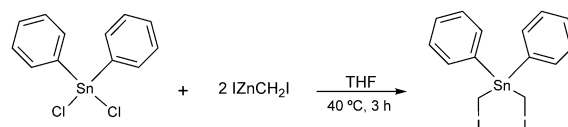
Scheme 1. A series of $[\text{FeFe}]$ -hydrogenase mimics containing group IV elements with increasing size of the bridgehead atoms in the dithiolate linker. The drawings do not depict the variations in the geometries of the linkages and the $\text{Fe}_2(\text{CO})_6$ portions of the structures that are revealed in this study.

Me, which is contrary to all of the previously reported models that show the usual chair/boat conformation of the two fused $\text{FeS}_2\text{C}_2\text{E}$ rings. We herein illuminate the origin of the planarity and its impact on the electron-richness of the S atoms. Furthermore, we report the effect of germanylation and stannylation on the redox properties and describe the electrocatalytic behavior of these complexes toward reduction of protons from moderate and strong acids.

Results and Discussion

Synthesis and characterization of $\text{R}_2\text{Sn}(\text{CH}_2)_2$

The compound $\text{Ph}_2\text{Sn}(\text{CH}_2)_2$ was synthesized by following a similar procedure applied for $\text{Me}_2\text{Sn}(\text{CH}_2)_2$.^[23] The reaction of Ph_2SnCl_2 with two equivalents of in situ generated $[\text{ZnCH}_2]$ afforded $\text{Ph}_2\text{Sn}(\text{CH}_2)_2$ in approximately 48% yield after purification by column chromatography as a colorless liquid (Scheme 2).

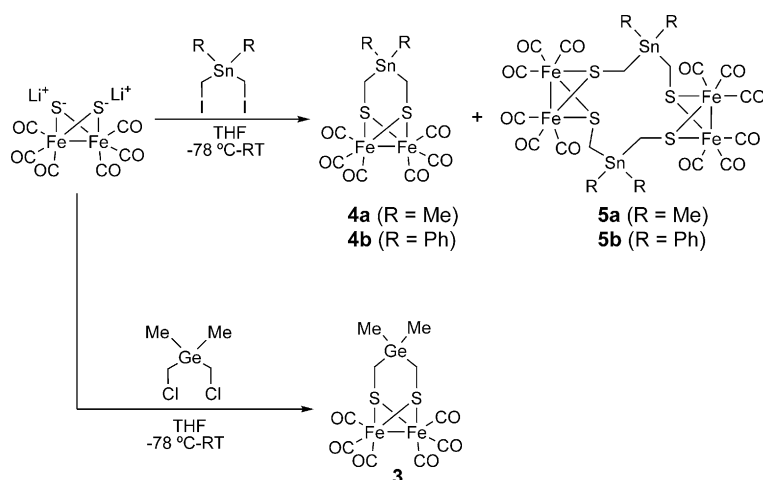


Scheme 2. Synthesis of $\text{Ph}_2\text{Sn}(\text{CH}_2)_2$.

The compound $\text{Ph}_2\text{Sn}(\text{CH}_2)_2$ was characterized by ^1H and $^{13}\text{C}\{^1\text{H}\}$ NMR spectroscopy and mass spectrometry. Its ^1H NMR spectrum (CDCl_3 , 400.08 MHz) exhibits a singlet at 2.41 ppm with Sn satellites ($^2J\{^{117}\text{Sn},^1\text{H}\}=20.9\text{ Hz}$ and $^2J\{^{119}\text{Sn},^1\text{H}\}=41.8\text{ Hz}$) for the CH_2 hydrogen atoms. The hydrogen atoms at the *meta* and *para* positions of the Ph groups show a multiplet in the region of 7.38–7.43 ppm and the hydrogen atoms located at the *ortho* position resonate in the region of 7.55–7.60 ppm. The $^{13}\text{C}\{^1\text{H}\}$ NMR spectrum shows a singlet at -10.53 ppm resulting from the CH_2 carbon atoms. The Ph groups show multiplets at 126.0–128.8 (*meta* and *para* C atoms), 136.85 ppm (*ortho* C atoms), and 139.31 ppm (*ipso* C atoms) in the $^{13}\text{C}\{^1\text{H}\}$ NMR spectrum. In addition, the DEI-MS spectrum shows peaks at m/z 479 $[\text{PhSn}(\text{CH}_2)_2]^+$, 415 $[\text{Ph}_2\text{SnCH}_2]^+$, 351 $[\text{PhSn}(\text{CH}_2)(\text{CH}_2)]^+$, and 273 $[\text{Ph}_2\text{Sn}]^+$.

Synthesis and characterization of the iron complexes

The reaction of in situ generated $(\mu\text{-LiS})_2\text{Fe}_2(\text{CO})_6$ with one equivalent of $\text{R}_2\text{Sn}(\text{CH}_2)_2$ afforded $\text{Fe}_2(\text{CO})_6\{(\mu\text{-SCH}_2)_2\text{SnR}_2\}$ ($\text{R} = \text{Me}$, **4a**, 25% yield and Ph , **4b**, 18%) as air-stable red solids as well as unexpected tetranuclear products $[\text{Fe}_2(\text{CO})_6(\mu\text{-SCH}_2)_2\text{SnR}_2]_2$ ($\text{R} = \text{Me}$, **5a**, 9% yield, and $\text{R} = \text{Ph}$, **5b**, traces) as air-stable orange solids (Scheme 3). On the other hand, we



Scheme 3. Syntheses of complexes 3–5b.

were able to isolate only $\text{Fe}_2(\text{CO})_6\{(\mu\text{-SCH}_2)_2\text{GeMe}_2\}$ (**3**) in 15% yield from the reaction of $(\mu\text{-LiS})_2\text{Fe}_2(\text{CO})_6$ with one equivalent of $\text{Me}_2\text{Ge}(\text{CH}_2\text{Cl})_2$, but not a tetranuclear product. Complexes **3**, **4a**, **4b**, and **5a** were characterized by means of ^1H , $^{13}\text{C}\{^1\text{H}\}$ NMR and IR spectroscopic techniques as well as mass spectrometry, elemental analysis, and X-ray crystallography. Because of the very low yield of **5b**, we were only able to characterize it by X-ray crystallography.

The dinuclear complex 3

The ESI-MS spectrum of **3** shows the parent ion peak at m/z 476 $[M]^+$ as well as the consecutive loss of CO ligands at m/z 448 $[M-\text{CO}]^+$, 420 $[M-2\text{CO}]^+$, 392 $[M-3\text{CO}]^+$, 364 $[M-4\text{CO}]^+$, 334 $[M-5\text{CO}]^+$, and 308 $[M-6\text{CO}]^+$. The IR spectrum (CH_2Cl_2 solution) of **3** displays four absorption bands at $\nu(\text{CO}) = 1990$ (s), 1998 (s), 2032 (vs.), and 2071 cm^{-1} (s) for terminal CO ligands. The $^{13}\text{C}\{^1\text{H}\}$ NMR spectrum of **3** exhibits singlets at 0.13, 6.5, and 207.95 ppm for the CH_3 , CH_2 , and CO carbon atoms, respectively. In the ^1H NMR spectrum, two singlets are observed at 0.26 and 1.66 ppm owing to the CH_3 and CH_2 protons, respectively.

The dinuclear complexes 4a and 4b

The DEI-MS spectra of **4a** and **4b** show parent ion peaks at m/z 520 $[M]^+$ and 646 $[M]^+$, respectively, as well as the consecutive loss of the CO ligands. The IR spectrum (CH_2Cl_2 solution) of **4a** displays four vibration bands at $\nu(\text{CO}) = 1989$ (s), 1997

(s), 2032 (vs.), and 2070 cm^{-1} (s) whereas three $\nu(\text{CO})$ bands are observed at 1989 (vs.), 2033 (vs.) and 2066 cm^{-1} (s) in the case of **4b**. The $\nu(\text{CO})$ wavenumbers (CH_2Cl_2 solution) slightly shift to smaller values on going from **1** ($\text{R} = \text{Me}$; 1990 (s), 2000 (s), 2032 (vs.), 2073 cm^{-1} (s)), **2** ($\text{R} = \text{Me}$; 1990 (s), 1998 (s), 2032 (vs.), 2072 cm^{-1} (s)), and **3** to **4a**. The $^{13}\text{C}\{^1\text{H}\}$ NMR spectrum of **4a** shows singlets at -7.1 , 1.6, and 207.0 ppm for the CH_3 , CH_2 , and CO carbon atoms, respectively, whereas that of **4b** exhibits a singlet at 1.7 ppm for the CH_2 groups as well as peaks from the Ph substituents in the region of 128.7–130.6 ppm (*meta* and *para* C atoms) and 136.7–138.7 ppm (*ipso* and *ortho* C atoms). The CO ligands of **4b** resonate at 208.6 and 209.1 ppm, which is in contrast to the $^{13}\text{C}\{^1\text{H}\}$ NMR spectrum of **4a**, which shows only one signal from the CO ligands. The ^1H NMR spectra of **4a** and **4b** exhibit a singlet at 1.79 ppm (**4a**) and 2.27 ppm (**4b**), respectively, for the CH_2 protons. Complex **4a** shows a singlet at 0.25 ppm resulting from the CH_3 protons in the ^1H NMR spectrum, whereas the spectrum of complex **4b** displays a multiplet in the region of 7.35–7.70 ppm, attributed to the Ph protons.

The tetranuclear complex 5a

The FAB-MS spectrum of **5a** shows a parent ion peak at m/z 1041 $[M]^+$ and the consecutive loss of six CO ligands. The IR spectrum exhibits absorption bands at 1991, 2031, and 2071 cm^{-1} for terminal CO ligands. The $^{13}\text{C}\{^1\text{H}\}$ NMR spectrum displays peaks at -8.1 (CH_3), 1.1 (CH_2), and 209.0 ppm (CO). An apparent singlet at 2.00 ppm was observed at room temperature in the ^1H NMR spectrum for all of the CH_2 hydrogen atoms in the macrocycle and another singlet at 0.36 ppm from the CH_3 groups.

The dinuclear models

Molecular structures

As can be seen from Figure 2, each iron core of **3**, **4a**, and **4b** can be best described as a distorted octahedron in which the central atom is Fe surrounded by three terminal CO ligands in facial fashion as well as two S atoms that bridge both iron atoms. The bicyclic $[\text{2Fe-2S}]$ structure in these complexes reveals a butterfly conformation. The bridgehead E atoms of the linker $\mu\text{-}(\text{SCH}_2)_2\text{ER}_2$ ($\text{ER}_2 = \text{GeMe}_2$, SnMe_2 , SnPh_2) of the complexes is surrounded by atoms in distorted tetrahedral fashion.

The average E–C–S bond angles ($122.42(13)^\circ$ (**3**), $121.96(15)^\circ$ (**4a**), and $119.7(2)^\circ$ (**4b**)) deviate significantly from the ideal tetrahedral angle as was observed in various $\text{Fe}_2(\text{CO})_6\{(\mu\text{-SCH}_2)_2\text{SiR}_2\}$ models, $118.22(12)$ – $122.05(13)^\circ$.^[17] The Fe–Fe bond lengths in **3** (2.5128(4) Å), **4a** (2.5249(5) Å), and **4b** (2.5158(7) Å) are slightly shorter than those of the H-cluster, 2.55–2.62 Å,^[2,24] but are comparable to those in complexes with the $\mu\text{-}(\text{SCH}_2)_2\text{SiR}_2$ linker (ca. 2.518 Å).^[17] The average Fe–CO bond lengths are 1.800(2), 1.802(3), and 1.798(4) Å in **3**, **4a**, and **4b**, respectively. The average Fe–S bond lengths (2.2535(6) Å (**3**), 2.2561(8) Å (**4a**), and 2.2582(10) Å (**4b**))

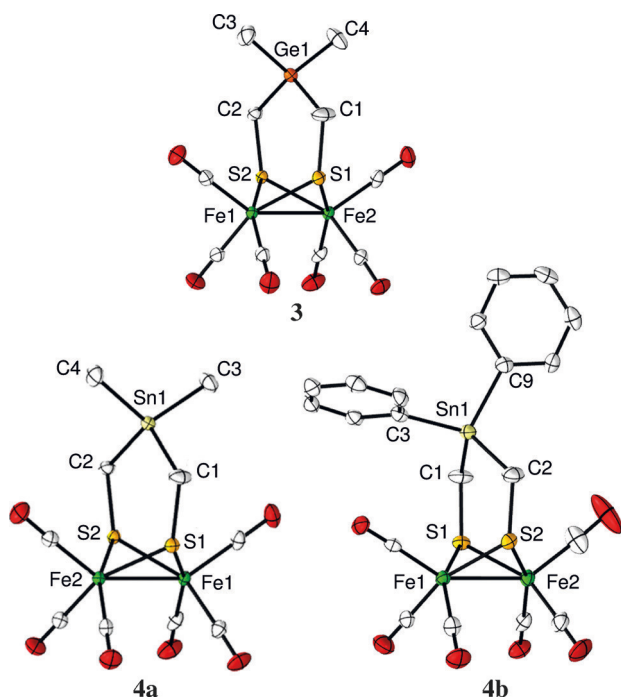


Figure 2. Molecular structures (at the 50% probability level) of **3**, **4a**, and **4b**.

are comparable to those in $\text{Fe}_2(\text{CO})_6\{(\mu\text{-SCH}_2)_2\text{SiMe}_2\}$ (2.2582(6) Å).^[17]

Geometry of the dithiolato linker

All of the previously reported [FeFe]-hydrogenase models adopt a chair/boat conformation (Figure 3) of the two fused six-membered FeSCECS rings in the solid state as well as in solution and many complexes such as **1**, R=H or Me, undergo FeSCECS ring inversion^[10b] with the E atom exchanging places on either side of the molecule. The flap angle (α) formed from the intersection between the C_2E and S_2C_2 planes, as shown in

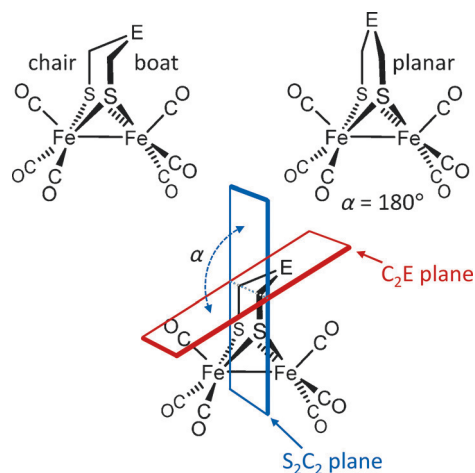


Figure 3. The chair/boat and planar conformations and the definition of the angle α .

Figure 3, lies within the range $118^\circ > \alpha > 160^\circ$ in various [FeFe]-hydrogenase models. Only one complex, namely $\text{Fe}_2(\text{CO})_6\{(\mu\text{-SCH}_2)_2\text{Si}(1\text{-silafluorene})\}$,^[3e] has a large angle $\alpha = 171^\circ$. In the planar conformation, $\alpha = 180^\circ$ and the -SCECS-moiety is planar. Table 1 lists the flap angles α for the homologous series with CMe_2 , SiMe_2 , GeMe_2 , and SnMe_2 in the bridge as well as angles related to the $\text{Fe}(\text{CO})_3$ distortion and twisting. Remarkably, the -SCECS- moiety is nearly planar for E=Ge and Sn. That is, the flap angles α deviate by only 4.8° (E=Ge) and 6.4° (E=Sn) from planarity. In addition, their solution NMR spectra show equivalent Me groups for E=Ge and Sn. This may result from a planar structure or rapid equilibration (ring inversion) of nonplanar isomers (as observed in the room-temperature ^1H NMR spectrum of **1**, R=Me).^[10b] However, the Me groups in **4a** remain equivalent even at -90°C .

To ascertain whether the variations in these structures are solid-state effects or inherent to the molecules, the gas-phase structures were computed and are compared in Table 1 and Table S1 (in the Supporting Information) for the lowest energy conformers. When R is Me, there is a general increase in the flap angle α for E going down the group, with an angle of about 135° when E=C, and it approaches nearly 180° when E=Ge (only in the solid-state structure), E=Sn (in both of the solid- and gas-phase structures). The flap angle in the molecular structure for the molecule with $\text{ER}_2 = \text{GeMe}_2$ seems anomalous, being slightly greater than the angle for $\text{ER}_2 = \text{SnMe}_2$, but examination of the crystal packing suggests that intermolecular interactions are influencing this angle in the solid state. This suggestion is supported by computation of the distortion energies. The gas-phase structures (computational) reproduce the flap angles observed in the solid-state structures within 2° for E=C, Si, and Sn, and place the flap angle for E=Ge intermediate to those for Si and Sn. The computations also account well for the solution carbonyl stretching frequencies (Figure S1 in the Supporting Information). These results indicate that the large flap angles for the heavier elements of group IV are an inherent property of the isolated molecules, but can be influenced by solid-state packing forces especially for E=Ge and Sn.

The change in the R group also has a significant influence on the structure. When E=Sn, the flap angle α for R=Ph is about 20° less than that for R=Me. It is noted in the solid-state structure of **4b** that one phenyl group is oriented approximately edge-on to an apical carbonyl whereas the other is face-on to the other apical carbonyl. The computations reproduce this orientation, but give a larger flap angle than observed in the solid-state structure, and here again the crystal packing indicates intermolecular interactions between the phenyl rings are also at play. When E=C, the comparison for R=H with R=Me is problematic because of disorder in the structure with CH_2 as the central bridge group. The gas-phase structures obtained computationally give a much smaller flap angle of 126.6° for R=H than for R=Me, which is close to the ideal angle of 127° for a perfectly staggered conformation of a cyclohexane ring. Taken together, the above observations indicate that steric factors play a major role in determining the flap angle α . As a computational test for E=Sn, the R groups

Table 1. Influence of ER₂ groups (E=group IV element) on the planarity of the S₂C₂E linker and distortion of the Fe₂(CO)₆ symmetry in Fe₂(CO)₆((μ-SCH₂)₂ER₂) complexes.

ER ₂	CH ₂	CMe ₂	SiMe ₂	GeMe ₂	SnMe ₂	SnPh ₂	SnH ₂
Solid-phase structures							
flap angle α ^[a] [°]	137.1 ^[d]	135.7	150.0	175.2	173.6	152.5	–
Fe-Fe-C(O) ^[b] [°]	148.3/148.3 ^[d]	159.9/148.1	152.8/144.7	147.4/146.4	146.2/145.1	149.5/144.4	–
	Δ = NA ^[d]	Δ = 11.8	Δ = 8.1	Δ = 1.0	Δ = 1.1	Δ = 5.1	
C _a -Fe-Fe-C _a ^[c] [°]	0.0 ^[d]	6.5	0.0	7.9	5.2	7.5	–
Gas-phase structures (computational)							
flap angle α [°]	126.6	137.5	148.0	159.6	172.8	161.6	141.9
Fe-Fe-C _o ^[a] [°]	151.5/146.0	159.2/146.1	154.1/144.0	149.2/144.1	144.8/142.8	148.6/142.9	151.0/144.3
	Δ = 5.5	Δ = 13.1	Δ = 10.1	Δ = 5.1	Δ = 2.0	Δ = 5.7	Δ = 6.7
C _a -Fe-Fe-C _a ^[b] [°]	0.0	0.8	2.2	0.3	0.1	0.1	0.6

[a] See Figure 3 for illustration of the flap angle α. [b] Fe-Fe-C angle for the apical carbonyl proximal to the ER₂ group/Fe-Fe-C angle for the apical carbonyl distal to the ER₂ group (Figure 4), Δ is the difference between these angles. [c] Dihedral twist angle of the apical carbonyl carbon atoms across the Fe-Fe bond. [d] Disorder in the crystal for the case of ER₂=CH₂ averages the structure to C_{2v} symmetry, which masks any symmetry distortion.

were changed to H atoms, and the optimum -SCSnCS- structure bent substantially from planarity (Table 1).

The steric characteristics of the ER₂ groups distort the symmetry of the Fe₂(CO)₆ portion of the molecules. This is reflected in the bending of an apical carbonyl away from the steric interaction with the ER₂ group and a rotation of an Fe(CO)₃ group away from the mirror plane of the molecule. The Fe-Fe-C(O) angles and (O)C-Fe-Fe-C(O) dihedral angles for the apical carbonyls of these molecules are listed in Table 1. The steric effect of the ER₂ group on the metal carbonyl is observed most clearly in the deflection of the apical carbonyl that is proximal to the ER₂ group. As pointed out previously by Darensbourg and co-workers,^[10] there is an appreciable increase in the distortion from ER₂=CH₂ to CMe₂. Unfortunately, the disorder in the solid-state structure for ER₂=CH₂ prevents comparison of the deflection of the carbonyls proximal and distal to the CH₂ group. However, the computations support the increasing deflection of the proximal carbonyl from the CH₂ to the CMe₂ complex. The dimethyl complexes show that the deflection of the apical carbonyl decreases from E=C to Si to Ge to Sn, both in the molecular structures and in the gas-phase structures from the computations.

A deeper insight into the factors that determine this trend is obtained by imagining a split of the molecules into the dithiolato bridges and the Fe₂(CO)₆ fragments and computing the distortion energies of each fragment, as depicted in Figure 4. These distortion energies are thus in the absence of mutual steric and electronic effects between the fragments. The fragments are terminated by hydrogen atoms to satisfy the valence. The flap angle α of the linker is varied from 127°, which is the optimum angle of a fully staggered chair-like conformation, to 180°. Note that at α = 180°, the E-C bonds of the EMe₂ groups are in a fully eclipsed conformation with the C-H bonds of the CH₂ groups. For CMe₂, the planar structure of the linker with the eclipsed bonds is disfavored by 7.7 kcal mol⁻¹, but this value falls by more than half for each substitution down the group (SiMe₂, 2.8 kcal mol⁻¹; GeMe₂, 1.3 kcal mol⁻¹; SnMe₂, 0.5 kcal mol⁻¹). The dramatic decrease in this strain energy for the planar structures is attributed primarily to the

longer E-C bonds that diminish the eclipsed non-bonded repulsions.

The EMe₂ groups are within van der Waals distance interactions with the axial carbonyls of the Fe₂(CO)₆ fragment even at

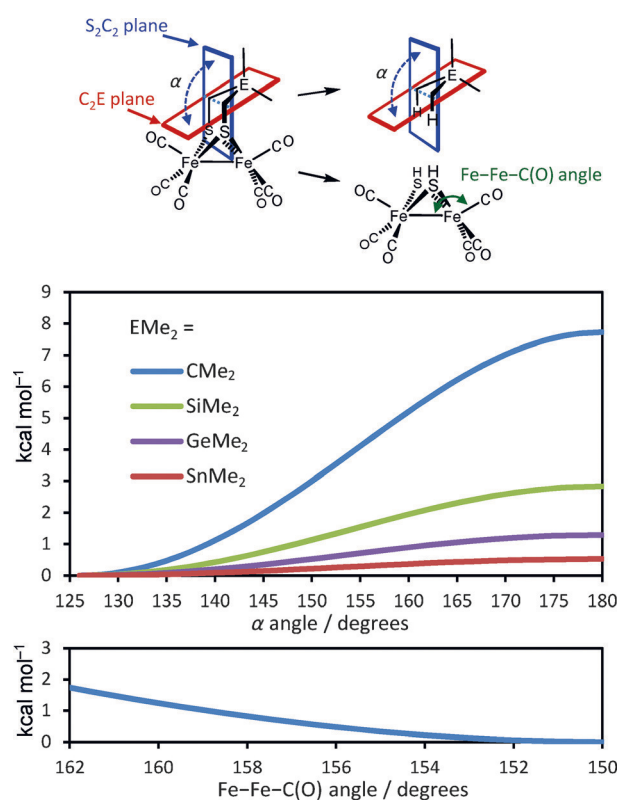


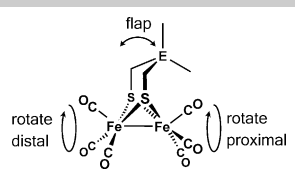
Figure 4. Top: illustration of the conceptual split of the molecule into the linker portion and the [2Fe-2S] portion for separate evaluation of the conformational energies, with definition of the distortion angle α from the fully staggered conformation (α = 127°) to the planar form (α = 180°) where the C-H bonds of the CH₂ groups are eclipsed with the E-C bonds of the EMe₂ group, and definition of the Fe-Fe-C(O) distortion angle. Middle: distortion energies of the linker as a function of the degree of planarity α. Bottom: distortion energy of the metal carbonyl as a function of the deflection of the proximal carbonyl away from the linker methyl group.

the planar geometries. The optimized structures in which the linkers are constrained to be planar give distances from the hydrogen atoms of EMe_2 atom to the axial carbonyl O atom of 2.86 Å for CMe_2 , 2.87 Å for SiMe_2 , 2.88 Å for GeMe_2 , and 2.94 Å for SnMe_2 , whereas the van der Waals distance between these atoms implemented in the MM3 force field^[25] is 3.44 Å and in the UFF force field is 3.19 Å.^[26] This interaction forces a mutual distortion of each fragment.

The bottom of Figure 4 shows the energy cost of distorting the $\text{Fe}_2(\text{CO})_6$ portion of the molecule as a function of the axial Fe-Fe-C(O) angle through the maximum values obtained in the crystal structures and computations. When EMe_2 is CMe_2 , there is a strong driving force toward the staggered linker conformation ($\alpha = 127^\circ$) that pushes a distortion of the $\text{Fe}_2(\text{CO})_6$ portion of the molecule. This driving force toward the staggered conformation of the linker rapidly diminishes down the group of SiMe_2 , GeMe_2 , and SnMe_2 . The potential energies when EMe_2 is GeMe_2 and SnMe_2 are very flat in the region of $\alpha = 180^\circ$, making the structures obtained from the crystal structures susceptible to packing forces as mentioned earlier.

Table 2 shows the calculated activation energies for the flap of the EMe_2 group from one side of the molecule to the other,

Table 2. Calculated activation energies E^\ddagger for fluxional processes [kcal mol⁻¹].



ER_2	CH_2	CMe_2	SiMe_2	GeMe_2	SnMe_2
flap	9.9	5.6	1.0	0.2	0.1
rotate proximal	7.1	4.1	4.8	5.7	6.0
rotate distal	10.4	10.8	10.1	5.6	5.9

in which the geometry where $\alpha = 180^\circ$ is the transition state. For comparison, the case of CMe_2 has a smaller energy than the case of CH_2 in agreement with previous work.^[10] The $\text{E} = \text{Si}$, Ge , and Sn cases have very small energies for the reasons given above, consistent with the low-temperature NMR spectra. Geometries were also optimized by using continuum solvation models for the NMR solvents THF, dichloromethane, and acetone, and these computations gave little difference in the relative conformational energies compared with the gas-phase computations.

The twist of the $\text{Fe}(\text{CO})_3$ group gives a less clear indication of the steric interaction with the linker than the deflection of the axial carbonyl. The gas-phase computations yield very little twist, and both the crystal structures and the computations do not show regular trends with increasing size of the ER_2 group. Nonetheless, the larger ER_2 groups may make the $\text{Fe}(\text{CO})_3$ group more prone to rotation, and the rotations found in the crystal structures may be sensitive to intermolecular interactions. Table 2 includes the calculated activation energies for rotation of the $\text{Fe}(\text{CO})_3$ groups. For the familiar case of **1**, where

ER_2 is CH_2 , the computations indicate the energy barrier for equilibration of the CO groups between axial and basal positions is about 10 kcal mol⁻¹, and this value compares well with the experimental activation energy of 10.4 kcal mol⁻¹ determined from variable-temperature NMR spectroscopy.^[13c,27] Comparison of the energy for rotation of the $\text{Fe}(\text{CO})_3$ group proximal to the ER_2 group of the linker with the rotation of the $\text{Fe}(\text{CO})_3$ group distal to the ER_2 group gives an indication of the effect of the steric interaction of the ER_2 group. The smallest rotation energy for the proximal $\text{Fe}(\text{CO})_3$ group and greatest difference from the rotation energy for the distal $\text{Fe}(\text{CO})_3$ group is found for $\text{ER}_2 = \text{CMe}_2$. The Ge and Sn examples have essentially no difference between the proximal and distal $\text{Fe}(\text{CO})_3$ rotation energies as expected from the near-planar geometries of these linkers.

The near-planar geometries of the -SCECS- bridges in **3** and **4a** are remarkable in comparison to the conformations of cyclohexane. The six-membered FeSCECS moiety is comparable to the cyclohexane conformation with five co-planar atoms **A** (Figure 5). Although initially calculated by molecular mechan-



Figure 5. Cyclohexane conformation with five co-planar atoms **A** and the half-chair conformation **B**.

ics^[28] to be higher in energy than the half-chair^[29] conformation **B**, subsequent calculations suggest that they are comparable in energy^[29] and provide the transition state for conversion of the chair to twist conformation^[30] of cyclohexane with a 10.8 kcal mol⁻¹ barrier.^[31] This is comparable to the 9.9 kcal mol⁻¹ barrier for the similar process to **A** of the [2Fe-2S] complex with $\text{ER}_2 = \text{CH}_2$ shown in Table 2. Nevertheless, it is this conformation that is adopted in **4a** and almost in **3** as well. Previous studies on conformational analysis of cyclohexanes with higher group IV elements in the ring are limited, but there have been studies on silacyclohexanes^[32] as well as a silathia analogue,^[33] germacyclohexanes,^[34] and stannacyclohexanes.^[35] The main conclusion from these studies is that there is a modest flattening of the chair conformation made possible by the greater bond length of C-Si than C-C and consequent decrease in Si-C repulsive torsional interactions as well as decreased ring inversion barriers. This flattening is taken to remarkable extremes in **4a** and **3**. It is interesting to note that $\text{Me} \cdots \text{apical CO}$ repulsion in **1** ($\text{R} = \text{Me}$) is predominantly relieved by $\text{Fe}(\text{CO})_3$ geometry changes, but with **4a** and **3** it induces geometry changes in the -SCECS- flap. As mentioned previously in support of the $\text{Me} \cdots \text{apical CO}$ interaction as the driver in this distortion, calculations on **4** ($\text{R} = \text{H}$) are shown in Table 1 and reveal an α value of only 141.9°. Also note that comparison of the flap angles of **1** ($\text{R} = \text{H}$) and **1** ($\text{R} = \text{Me}$) reflect this interaction as well, although the molecular structures cannot be compared because of disorder in **1** ($\text{R} = \text{H}$).

Photoelectron spectroscopy

Gas-phase ultraviolet photoelectron spectroscopy (UPS) offers a direct experimental probe of the valence electron energies in the absence of intermolecular interactions, and as such can provide information on the electronic structure variations through this series as the central bridgehead atom changes from C to Si to Ge to Sn. The technique is relevant to the study of hydrogenase mimics because the ionization of these molecules give direct access to the formal $[\text{Fe}^{\text{I}}\text{Fe}^{\text{II}}]$ oxidation state in the proposed catalytic cycle of the enzyme.^[2] In addition, the well-defined energy quantities provide experimental validation for the computational methods utilized in this study. The He I spectra of **1–3** ($R = \text{Me}$) in the energy region from 7 to 12 eV were collected and compared with the spectrum of **4a** from a previous study^[21] in Figure 6.

The He I UPS spectra and ionization band assignments of similar compounds have been reported previously.^[19c,36] The broad first ionization band ranging from 7.5 to 8.7 eV represents the Fe–Fe σ bond and six occupied “ t_{2g} -like” 3d orbitals that are oriented for backbonding to the carbonyl ligands on the two distorted octahedral Fe centers, mixed with some S lone pair p orbitals. Ionization in the region from roughly 8.7 to 9.2 eV is primarily sulfur p orbital in character mixed with significant Fe character, and another primarily sulfur p ionization is found around 9.5 eV. The grey lines in Figure 6 trace the shift of these ionizations as a result of the neighboring effects from $E = \text{C}$ to $E = \text{Sn}$.^[21] Additional ionizations ranging from roughly 9.2 to 12.0 eV consist of C, Si, Ge, and Sn character interacting with S character and Fe d orbitals.

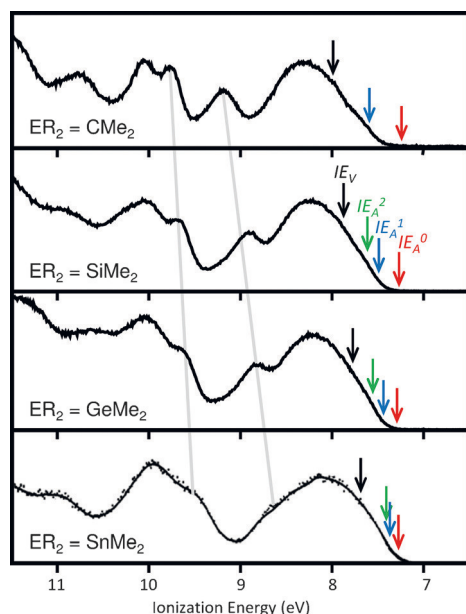


Figure 6. He I photoelectron spectra of **1–4a**. The black arrows point to the calculated vertical ionizations energies (IE_V). The red arrows correspond to the global minimum cation structures (IE_A^0), and blue and green arrows correspond to local minima (IE_A^1 and IE_A^2) of less stable cation structures (see text and Figure 8).

The leading edges of the first ionization bands correspond to ionizations from the HOMO, starting at about 7.5 eV for all molecules. The HOMOs of **1** ($R = \text{CMe}_2$) and **4a** ($ER_2 = \text{SnMe}_2$) are compared in Figure 7 (Figure S2 in the Supporting Informa-

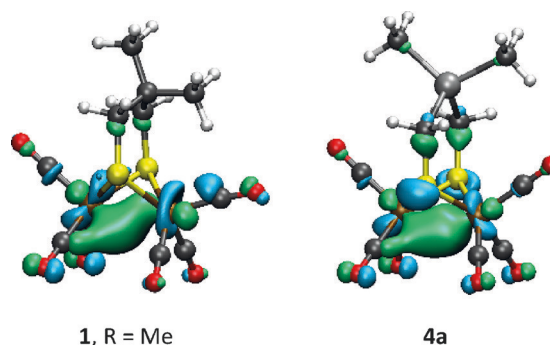


Figure 7. The HOMOs of **1**, $R = \text{Me}$, and **4a** (isosurface value ± 0.05).

tion for the HOMOs of **2**, $R = \text{Me}$, and **3**). In all cases, the HOMO is primarily the Fe–Fe bond. In **1**, the tilt of the CMe_2 group displaces the orbital more toward the distal Fe atom, whereas in **4a** the nearly planar linker between the S atoms (large α angle) creates a more symmetric orbital. Also note the increase in S character in the HOMO of **4a** with some antibonding interaction with the linker atoms, both of which can facilitate protonation of the $[\text{2Fe-2S}]$ cluster. The S character in the HOMO increases in the series $E = \text{C}, \text{Si}, \text{Ge}, \text{Sn}$ (Figure S2 in the Supporting Information) owing to the increasing instability of the E orbitals and E–C sigma bonds, which impart both an inductive and overlap destabilization of the S lone pair that then mixes with the metal–metal bond density in an antibonding fashion in the HOMO.

The calculated ionization energies corresponding to removal of an electron from the HOMO of these molecules are indicated by a series of arrows on the photoelectron spectra shown in Figure 6. The vertical ionization energies (IE_V), calculated by the ΔSCF difference in energy from the neutral molecule to the cation, without change in geometry, are found to decrease from 7.98 eV for **1** to 7.86 eV for **2** to 7.77 eV for **3** and to 7.68 eV for **4a** (Table 3). The adiabatic ionization energies (IE_A^0) of these compounds are calculated by the ΔSCF method with full geometry optimization of the cations as shown in Figure 8 for **4a**.

For all four complexes, the global minimum IE_A^0 conformation of the cation has a rotated $\text{Fe}(\text{CO})_3$ group with a bridging carbonyl and the dimethyl unit bends toward the vacant site. The alternative conformation (corresponding to IE_A^1) with the dimethyl unit in close proximity to the non-rotated apical terminal CO (Figure 8 for **4a** and Figure S3 in the Supporting Information for molecules **1–3**) is a local minimum at higher energy. The difference in ionization energy from IE_A^1 to IE_A^0 for these two conformers is a combination of the stabilization gained from release of the steric interaction of the linker with the apical carbonyl and the stabilization gained from the contribution of the agostic C–H bond to the Fe atom. The energy

ER_2	CMe_2	SiMe_2	GeMe_2	SnMe_2
IE_V	7.98	7.86	7.77	7.68
IE_A^0	7.23	7.26	7.28	7.27
IE_A^1	7.58	7.48	7.43	7.37
IE_A^2	NA ^[b]	7.61	7.52	7.42
λ ^[a]	0.75	0.60	0.49	0.41

[a] Reorganization energy with ionization, $\text{IE}_V - \text{IE}_A^0$. [b] Local minimum for CMe_2 not available. Geometry relaxes automatically to the global minimum.

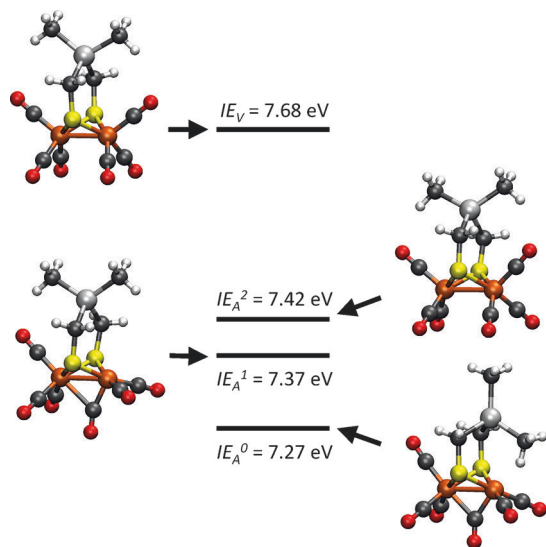


Figure 8. The cation structures and relative energies of **4a**, $\text{Fe}_2(\text{CO})_6\{(\mu\text{-SCH}_2)_2\text{SnMe}_2\}$.

difference decreases down the series from $\text{E}=\text{C}$ (0.35 eV) to Si (0.22 eV) to Ge (0.15 eV) to Sn (0.10 eV).

Another local minimum, IE_A^2 , with an all terminal CO conformation was found for molecules **2**, **3**, and **4a**. However, all attempts to find a local minimum for the cation of molecule **1** ($\text{R}=\text{Me}$) with all terminal carbonyl ligands resulted in collapse to the global minimum conformation with the bridging carbonyl. This is a consequence of the stronger driving force to the rotated $\text{Fe}(\text{CO})_3$ structure when ER_2 is CMe_2 . The energy difference between the cation at the neutral molecule geometry (IE_V) and the optimized structure of the cation (IE_A^0) is the reorganization energy λ . Substantial reduction of the reorganization energy was found; 0.75 eV for **1** ($\text{R}=\text{Me}$), 0.60 eV for **2**, 0.49 eV for **3**, and 0.41 eV for **4a**, which is consistent with the indications of decreasing strain down the series.

The tetranuclear models

The X-ray diffraction analyses confirmed the tetranuclear structures of **5a** and **5b** as macrocycles in which each $\text{Fe}_2\text{S}_2(\text{CO})_6$ unit has nonequivalent axial (*a*) and equatorial (*e*) -CH_2 units (Figure 9). That is, the stereochemistry of the linkers connected

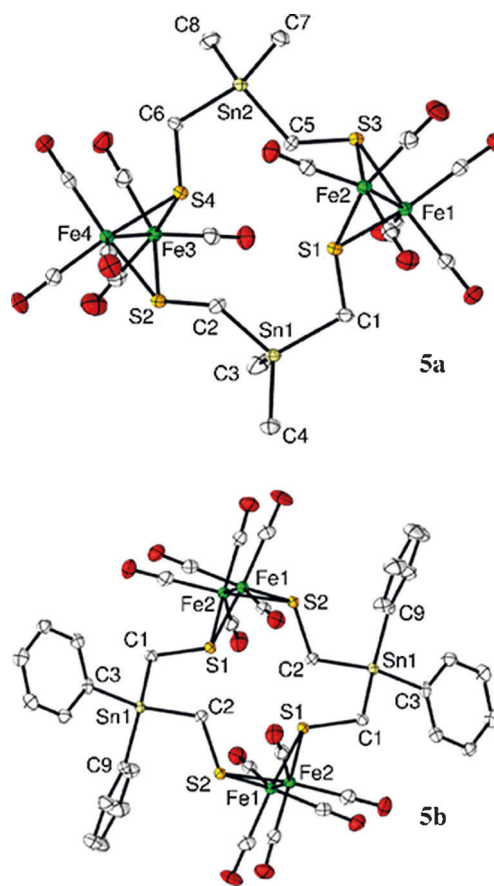


Figure 9. Molecular structures (at the 50% probability level) of complexes **5a** (top) and **5b** (bottom).

to the sulfur atoms in **5a** is *e,a,e',a'* (the unprimed labels correspond to one $[\text{2Fe-2S}]$ cluster and the primed labels to the other $[\text{2Fe-2S}]$ cluster). Although the average Fe-Fe , Fe-CO , and Fe-S bond lengths in **5a** (2.5224(6), 1.797(3), and 2.2638(8) Å, respectively) and **5b** (2.5165(5), 1.803(3), and 2.2616(7) Å, respectively) are comparable to those in **4a** and **4b**, the Sn-C-S bond angles in **5a** (107.32(14)–114.08(14)°) and **5b** (111.19(13)–112.33(13)°) are closer to the ideal tetrahedral angle. Examples of tetranuclear complexes in which two butterfly $[\text{2Fe-2S}]$ clusters are part of a macrocycle are rare in the literature and are reported only when the dithiolato linker contains more than three atoms between the two sulfur atoms ($\text{-S-CH}_2\text{(X)}_n\text{-CH}_2\text{-S-}$, $n > 1$).^[37] In our case, the formation of these macrocycles (**5a** and **5b**) is allowed by the longer dithiolato linker chain $\text{-S-CH}_2\text{-Sn-CH}_2\text{-S-}$ owing to the large size of the Sn atom and hence the relatively long Sn-CH_2 bond (average: 2.155(3) Å for **5a** and 2.156(3) Å for **5b**). Of particular relevance is the tetranuclear macrocycle **C**^[37a] (Figure 10) in which two $\text{Fe}_2\text{S}_2(\text{CO})_6$ moieties are connected by $\text{CH}_2(\text{CH}_2\text{OCH}_2)_2\text{CH}_2$ units forming a 24-membered ring with *e,a,e',a'* stereochemistry similar to **5a**.

The structures of the $\text{Fe}_2\text{S}_2(\text{CO})_6$ units of **5a** and **C** are comparable. However, there is a 14-membered ring in **5a**, which results in the $\text{Fe}_2\text{S}_2(\text{CO})_6$ units being much closer to each other than those in **C**. The intramolecular distances between Fe and

S atoms in one unit and those in the other unit for **5a** are listed in Table S3 (in the Supporting Information). As seen in Table S3, the shortest Fe...S distances are 4.841 and 4.874 Å. All of the Fe...S distances involving the Fe of one Fe₂S₂(CO)₆ and a S of the other cluster in **C** are greater than 7.39 Å.

The molecular structure of **5a** shows that for each Fe₂S₂(CO)₆ unit there is an *a* and *e* CH₂ substituent. Nevertheless, its ¹H NMR spectrum shows a singlet for the CH₂ groups despite their nonequivalence. This observation is surprising because compound **D** (Figure 10),^[21] in which one CH₂SnMe₃ substituent is *a* and the other is *e*, shows two singlets for the non-equivalent CH₂ groups at room temperature.^[38]



Figure 10. Structure of the tetranuclear compound **C** and that of compound **D**, in which one CH₂SnMe₃ substituent is *a* and the other is *e*.

It is possible that the *a* and *e* positions in **5a** interconvert at room temperature. To test this possibility, we performed variable-temperature (VT) ¹H NMR spectroscopic measurements and computational studies and found that the observation of one resonance signal arises from coincidental overlap of the temperature-dependent signals rather than interconversion of *a* and *e* substituents (for more details, see the Supporting information, including Figure S4).

Electrochemical properties

Table 4 summarizes the electrochemical reduction and oxidation potentials from the cyclic voltammetric measurements of the complexes Fe₂(CO)₆{(μ-SCH₂)₂EMe₂} (**1–4a**). Complex **1**, R = Me, shows the occurrence of only one quasi-reversible reduction, whereas complexes **2–4a** exhibit one partially reversible and one irreversible (irr.) reduction event at low scan rates. Increasing the scan rate *v* (see Figure 11 and Figures S5–S7 in the Supporting Information) results in the disappearance of the irreversible reduction event (the more cathodic peak in the cyclic voltammograms of **2–4a**) and an increase of the anodic-to-cathodic peak current ratio (*I*_{pa}/*I*_{pc}) of their first reduction wave. These observations can be readily explained in terms of irreversible follow-up reactions occurring after the first reduction process, forming side products.

The primary oxidation peak of these complexes (*E*_{ox1}) shows an overall cathodic shift of 110 mV on going from complex **1** to **2** to **3** to **4a**. This cathodic shift is a result of an increased electron density at the diiron core and destabilization of the HOMO by the S lone pairs as discussed above, which eases the oxidation process. The potentials *E*_{ox1} correlate linearly with the computed vertical ionization energies from Table 3 with an excellent coefficient of determination *R*² = 0.995 (Figure S11 in the Supporting Information). Correlation of *E*_{ox1} with *I*E_v is con-

Table 4. Summary of the redox features of complexes Fe₂(CO)₆{(μ-SCH₂)₂EMe₂} (**1–4a**) in 0.1 M CH₂Cl₂-[*n*Bu₄N][PF₆] solution measured at *v* = 0.2 V s⁻¹ by using a glassy carbon disk (*A* = 0.072 cm²). Potentials *E* are given in volts (V) and referenced to the ferrocenium/ferrocene couple (Fc⁺/Fc).

Complex	<i>E</i> _{red1} ^[a]	<i>E</i> _{1/2} ^[b]	<i>E</i> _{red2} ^[a]	<i>E</i> _{ox,rot} ^[c]	<i>E</i> _{ox1} ^[d]
1	-1.75 (<i>E</i> _{pc}), -1.61 (<i>E</i> _{pa})	-1.68	-	+0.19	+0.81
2	-1.71 (<i>E</i> _{pc}), -1.61 (<i>E</i> _{pa})	-1.66	-1.84 (<i>E</i> _{pc}) irr.	+0.21	+0.77
3	-1.72 (<i>E</i> _{pc}), -1.62 (<i>E</i> _{pa})	-1.67	-1.85 (<i>E</i> _{pc}) irr.	+0.15	+0.74
4a	-1.68 (<i>E</i> _{pc}), -1.57 (<i>E</i> _{pa})	-1.62	-2.20 (<i>E</i> _{pc}) irr.	+0.13	+0.70

[a] *E*_{red1} and *E*_{red2} are the potentials for the first and the second reductions, where *E*_{pc} and *E*_{pa} are the cathodic and anodic scan peak potentials. [b] *E*_{1/2} is the half-wave potential for the first reduction event. Because the *I*_{pa}/*I*_{pc} value (anodic to cathodic peak currents ratio) at 0.2 V s⁻¹ of the complexes **2–4a** is less than 1, the *E*_{1/2} can be considered as approximated values. [c] *E*_{ox,rot} is the potential of a weak oxidation peak attributed to initial oxidation to the rotated structure as discussed previously for related compounds.^[19a] [d] *E*_{ox1} is the potential of the primary oxidation peak. A second oxidation peak (*E*_{ox2}) is observed for complexes **1**, **2**, and **4a** as a shoulder at the first oxidation peak, where *E*_{ox2} is more positive than *E*_{ox1}.

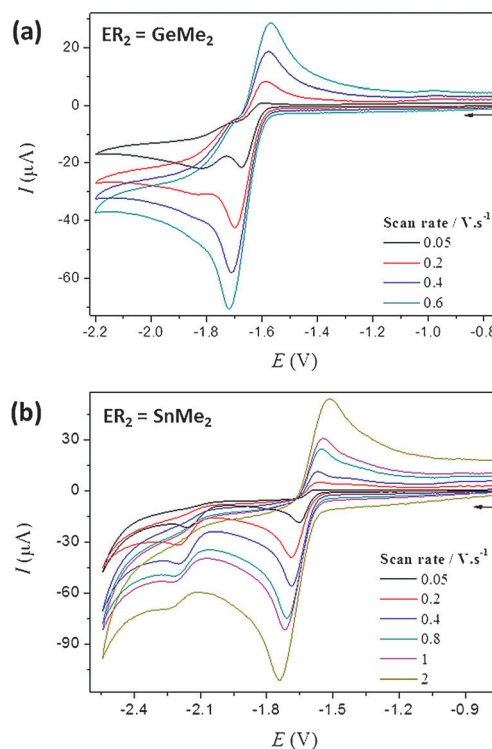


Figure 11. Cyclic voltammetry of: a) 0.84 mM Fe₂(CO)₆{(μ-SCH₂)₂GeMe₂} (**3**), and b) 0.84 mM Fe₂(CO)₆{(μ-SCH₂)₂SnMe₂} (**4a**) in 0.1 M CH₂Cl₂-[*n*Bu₄N][PF₆] solution under Ar at various scan rates. Glassy carbon electrode (*A* = 0.072 cm²). *E* is in V against the Fc⁺/Fc couple. The arrows indicate the scan direction.

sistent with a previous study of related compounds in which this oxidation event was attributed to the initial oxidation to a species with all-terminal carbonyls similar to the structure of the neutral molecule.^[19a] Also similar to the previous study, a very weak oxidation event is observed in the vicinity of 0.1 to -0.2 V, which is consistent with oxidation to the cation with

a rotated $\text{Fe}(\text{CO})_3$ group and a bridging carbonyl ligand (Figure 8). The trend in this potential down the series is less dramatic and is clearly due to the decreasing reorganization energies of the cations.

On going from **1** to **4a**, the reduction potentials are less cathodic. That is, stannylated model **4a** is the easiest to reduce in comparison with the models **1**, **2**, and **3**. This is due to reorganization and stabilization of the reduced species as previously shown in the case of electrochemical reduction of [FeFe]-hydrogenase models with [2Fe-2X] cores, where X=S, Se, or Te.^[6i,19] The reduction of the [2Fe-2X] core in this series of models becomes easier on going from X=S to Se to Te. Thus, these results show how the stannylation can tune the redox features of the [2Fe2S] core of the model complexes.

One important aspect of mechanistic investigation of the a proton reduction cycle catalyzed by a model complex is the determination of the number of electrons involved in the reduction of the model in the absence of a proton source. Studying the current function ($I_{pc}/c \cdot v^{1/2}$, c =complex concentration) of the reduction process at slow and fast scan rates is a useful method to provide mechanistic information.^[39] Figure 12 shows that the $I_{pc}/c \cdot v^{1/2}$ value of the reduction of complexes **1–4a** starts to significantly increase as the scan rate decreases beyond 5 V s^{-1} . This scan rate dependence of the current function suggests that the reduction of complexes **1–4a** follows an ECE-type mechanism at slow scan rates; where E=electron transfer and C=chemical process.^[6i,39,40] Based on theoretical and experimental studies of various [FeFe]-hydrogenase models including **1** and **2**, the intervening chemical process of the ECE reduction mechanism of **3** and **4a** might also involve similar core reorganization such that one Fe–S bond is broken and one $\text{Fe}(\text{CO})_3$ unit rotates and locates one of its CO ligands in a semi-bridging position, leaving an open site at the iron atom.^[6i,11,12b,17] We have recently illustrated how the steric clash between the CMe_2 group and the proximal CO in **1** lowers the

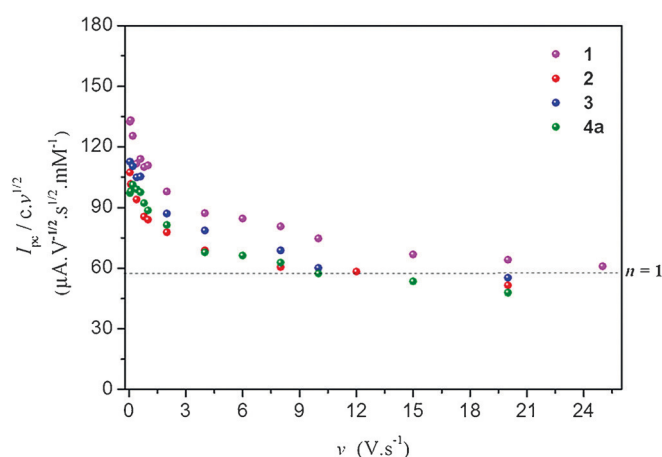


Figure 12. The scan rate dependence of the current function of the primary reduction peaks of complexes **1–4a** in $0.1 \text{ M CH}_2\text{Cl}_2$ -[$n\text{Bu}_4\text{N}$][PF_6] solution under an Ar atmosphere. Glassy carbon electrode ($A=0.072 \text{ cm}^2$). The dashed line represents the current function expected for a one-electron process assuming $D \approx 9 \times 10^{-6} \text{ cm}^2 \text{ s}^{-1}$, a value calculated for various [FeFe]-hydrogenase models.^[6i,18a]

barrier of $\text{Fe}(\text{CO})_3$ rotation during the reduction process and hence leads to an ECE reduction mechanism at slow scan rates. That the intervening core reorganization is a facile process during reduction of complexes **2–4a** can also be explained in terms of the steric bulkiness of their central EMe_2 groups of the dithiolato linkers; notwithstanding the planarity of **3** and **4a** (see Table 2 for the barriers of $\text{Fe}(\text{CO})_3$ rotation of the complexes in the ground Fe^IFe^I states).^[6i]

Electrocatalysis

Furthermore, we have tested the electrochemical behavior of the models **3** and **4a** in the presence of the acids $\text{CF}_3\text{CO}_2\text{H}$ ($\text{p}K_a^{\text{MeCN}} = 12.7$)^[41] and $\text{CF}_3\text{SO}_3\text{H}$ ($\text{p}K_a^{\text{MeCN}} = 0.7$).^[41] The presence of $\text{CF}_3\text{CO}_2\text{H}$ in the solution of **3** (or **4a**) shifts their primary cathodic peak to less negative potentials by approximately 110 mV , which is a typical observation when protonation of a reduced species takes place.^[3e,11a,42] As evident from Figure 13, complexes **3** and **4a** reveal catalytic behavior through two processes: process I at $E_p^{\text{cat}} \approx -1.78 \text{ V}$ for **3** and **4a** and process II at $E_p^{\text{cat}} \approx -1.91 \text{ V}$ or -1.89 V for **3** or **4a**, respectively, where E_p^{cat} is the peak potential of the catalytic waves in Figure 13. The studies of the electrocatalytic properties of **3** and **4a** using the very strong acids $\text{HBF}_4 \cdot \text{Et}_2\text{O}$ ($\text{p}K_a^{\text{DCE}} = -10.3$, DCE=dichloroethane)^[43] or $\text{CF}_3\text{SO}_3\text{H}$ ($\text{p}K_a^{\text{DCE}} = -11.4$)^[43] were possible only at low acid concentrations because of the significant direct reduction of these strong acids

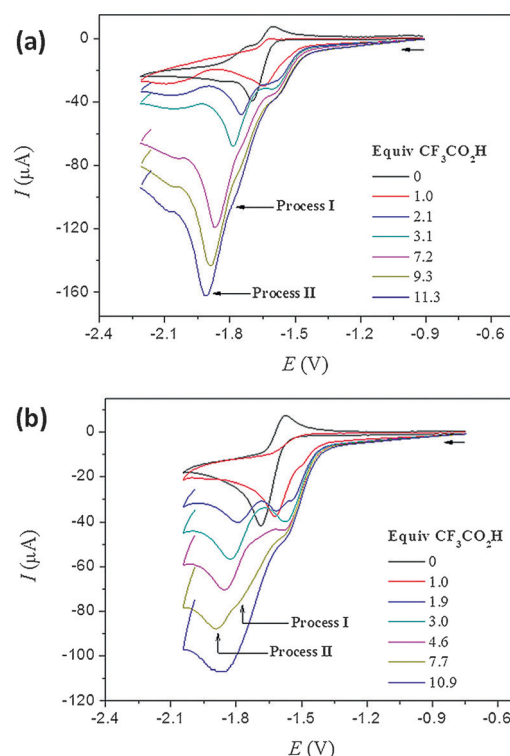


Figure 13. Cyclic voltammetry of complexes: a) $0.632 \text{ mm } \mathbf{3}$, and b) $0.825 \text{ mm } \mathbf{4a}$ in $0.1 \text{ M CH}_2\text{Cl}_2$ -[$n\text{Bu}_4\text{N}$][PF_6] solution in the presence of various equivalents of $\text{CF}_3\text{CO}_2\text{H}$ at 0.2 V s^{-1} . Glassy carbon electrode ($A=0.072 \text{ cm}^2$). E is in V against the Fc^+/Fc couple. The arrows indicate the scan direction.

at the glassy carbon electrode (Figures S8–S10 in the Supporting Information). As shown in Figures S8 to S10, protonation follows reduction of **3** or **4a** at low acid concentration and catalysis occurs at potentials more negative than that of the primary reduction waves of these model complexes.

Conclusions

We report here dinuclear models for the H-cluster featuring unique planarity of their dithiolato linkers $\mu\text{-(SCH}_2)_2\text{ER}_2$ (E = Ge or Sn and R = Me or Ph) and tetranuclear cyclic dimers with a 14-membered ring and unusual temperature-dependent ^1H NMR spectra. As a result of the repulsive steric interaction between the EMe_2 group and the apical carbonyl ligand in $\text{Fe}_2(\text{CO})_6\{\mu\text{-(SCH}_2)_2\text{EMe}_2\}$ complexes, the central six-membered FeSCECS ring preferentially adopts an unusual conformation with five nearly co-planar atoms (-SCECS-) when E = Ge or Sn in dramatic contrast with the chair/boat conformation when E = C or Si. Computations of the complexes in the gas phase support the notion that this near-planarity is the lowest energy conformer. Rings with E = Ge and Sn have less torsional strain and are more deformable than those with E = C. The smaller strain energy also means that the $\text{Fe}(\text{CO})_3$ group proximal to the EMe_2 methyl group is less driven to rotate and exchange the apical and basal carbonyl ligands when E = Ge and Sn.

On ionization, the reorganization energy of the cation to form the rotated structure with a semi-bridging CO substantially decreases in the series C through Sn again because of the decreasing release of strain energy down the series. The sulfur ionization energies are substantially lowered as the central atoms E in $\text{Fe}_2(\text{CO})_6\{\mu\text{-(SCH}_2)_2\text{EMe}_2\}$ complexes change in the series E = C, Si, Ge, Sn owing to increasing orbital interaction between the $\sigma\text{C-E}$ bond and the S lone pair p orbital. Consequently, the sulfur character in the HOMO increases down the series. This denotes greater electron-richness of sulfur in the series going from C to Si to Ge to Sn. This increase in the electron density of the [2Fe-2S] core is also reflected by the electrochemical oxidation potentials, where E_{ox} shifts toward less positive values on going from C to Si to Ge to Sn. Nonetheless, the reduction potential $E_{1/2}$ anodically shifts in this series with the Sn-containing complex the easiest to reduce owing to differences in reorganization energy and anion stabilization. Thus, the Sn-containing complex is the easiest to oxidize and also the easiest to reduce.

In the absence of a proton source, the complexes $\text{Fe}_2(\text{CO})_6\{\mu\text{-(SCH}_2)_2\text{EMe}_2\}$ (E = Ge or Sn) follow an ECE mechanism of reduction similar to the cases of E = C and Si. These complexes catalyze the reduction of protons from moderate and strong acids.

Experimental Section

Materials and techniques

All reactions were performed by using standard Schlenk and vacuum-line techniques under an inert gas (argon or nitrogen). The ^1H and $^{13}\text{C}\{^1\text{H}\}$ spectra were recorded with a Bruker Avance

200 MHz spectrometer. Chemical shifts are given in parts per million with reference to internal SiMe_4 or CHCl_3 . The mass spectrum was recorded with a Finnigan MAT SSQ 710 instrument. The IR spectra were measured with a PerkinElmer System 2000 FTIR spectrometer. Elemental analysis was performed with a Leco CHNS-932 apparatus. Silica gel 60 (0.015–0.040 mm) was used for column chromatography, and TLC was performed by using Merck TLC aluminum sheets (Silica gel 60 F254). Solvents from Fisher Scientific and other chemicals from Acros were used without further purification. All solvents were dried and distilled prior to use according to standard methods. The starting materials $(\mu\text{-S})_2\text{Fe}_2(\text{CO})_6$,^[44] $\text{Me}_2\text{Ge}(\text{CH}_2\text{Cl})_2$,^[45] and $\text{Me}_2\text{Sn}(\text{CH}_2)_2$ ^[23] were prepared according to literature procedures.

Synthesis of $\text{Ph}_2\text{Sn}(\text{CH}_2)_2$

Into a 100 mL three-necked round-bottom flask, $\text{Cu}(\text{OAc})_2\cdot\text{H}_2\text{O}$ (0.026 g, 0.13 mmol) and $\text{CH}_3\text{CO}_2\text{H}$ (6.0 mL) were mixed and heated to 90–100 °C while stirring. To this hot solution, granular zinc (30-mesh, 1.700 g, 26.0 mmol) was added and the mixture was stirred for 2 min while heating. $\text{CH}_3\text{CO}_2\text{H}$ was removed from the settled Cu-Zn couple by using a syringe and fresh $\text{CH}_3\text{CO}_2\text{H}$ (6.0 mL) was added. The mixture was stirred hot for 2 min. $\text{CH}_3\text{CO}_2\text{H}$ was again removed and the couple was cooled, washed with Et_2O (3×7.0 mL) and dried by a stream of N_2 . The deep grey/black colored couple was covered with THF (7.0 mL) and a few drops of CH_2I_2 were added to initiate the reaction. When the color appeared purple, THF (11.0 mL) was added followed by dropwise addition of CH_2I_2 (2.09 mL, 6.96 g, 26.0 mmol) in THF (6.0 mL) by using an addition funnel. The addition should be at a rate that maintains the temperature at 40 °C. The addition took 1 h and mild heating was required during the last 15 min. This THF solution of IZnCH_2I was then cooled to $\approx 0^\circ\text{C}$ and filtered under N_2 into a three-necked round-bottom flask. A solution of diphenyltin dichloride (Ph_2SnCl_2 ; 1.788 g, 5.2 mmol) in THF (6.0 mL) was added dropwise to the in situ generated IZnCH_2I over 1 h at 40 °C. For an additional 2 h, the reaction mixture was stirred at 40 °C. The cloudy, deep-purple reaction mixture was diluted with an equal volume of benzene (30 mL), extracted with 5% HCl (4×60 mL). The organic phase was dried with Na_2SO_4 , concentrated, and purified by column chromatography (SiO_2 , hexane/ CH_2Cl_2 , *n*-hexane 1:1) to afford $\text{Ph}_2\text{Sn}(\text{CH}_2)_2$ (1.393 g, 48% yield) as a colorless oil containing semi-crystalline particles of the same compound.

DEI-MS (m/z): 479 $[\text{PhSn}(\text{CH}_2)_2]^+$, 415 $[\text{Ph}_2\text{SnCH}_2]^+$, 351 $[\text{PhSn}(\text{CH}_2)_2(\text{CH}_2)]^+$, and 273 $[\text{Ph}_2\text{Sn}]^+$; $^{13}\text{C}\{^1\text{H}\}$ NMR (400.08 MHz, CDCl_3): $\delta = -10.53$ (s, CH_2), 126.0–128.78 (m, CCHCHCH), 136.85 (m, CCHCHCH), 139.31 ppm (m, CCHCHCH); ^1H NMR (400.08 MHz, CDCl_3): $\delta = 2.41$ (s with Sn satellites, $^2J\{^{117}\text{Sn}, ^1\text{H}\} = 20.9$ Hz, $^2J\{^{119}\text{Sn}, ^1\text{H}\} = 41.8$ Hz, 4H, CH_2), 7.38–7.43 (m, 4H, CCHCHCH), 7.55–7.60 ppm (m, 2H, CCHCHCH).

Synthesis of $\text{Fe}_2(\text{CO})_6\{\mu\text{-(SCH}_2)_2\text{GeMe}_2\}$ (**3**)

A red solution of $(\mu\text{-S})_2\text{Fe}_2(\text{CO})_6$ (150 mg, 0.436 mmol) in THF (10 mL) was cooled to -78°C and treated dropwise with Et_3BHLI (0.9 mL, 0.872 mmol, 1.0 M in THF) to give a dark-green solution. After stirring the solution for ≈ 20 min at -78°C , $\text{Me}_2\text{Ge}(\text{CH}_2\text{Cl})_2$ (88 mg, 0.436 mmol) in THF (3 mL) was added. The mixture was stirred for 18 h while slowly warming up to room temperature, giving rise to a dark-red solution. Solvent removal was performed under N_2 by using a vacuum transfer line. The residue was extracted several times with pentane and the extracts were collected and dried under N_2 by using a vacuum transfer line. The red residue

was then purified by column chromatography (SiO₂, hexane) to give complex **3** (31 mg, 15% yield).

Elemental analysis calcd (%) for C₁₀H₁₀Fe₂O₆S₂Ge: C 25.30, H 2.12, S 13.51; found: C 25.28, H 2.14, S 13.54; Micro-ESI-MS (*m/z*): 476 [M]⁺, 448 [M-CO]⁺, 420 [M-2CO]⁺, 392 [M-3CO]⁺, 364 [M-4CO]⁺, 334 [M-5CO]⁺, 308 [M-6CO]⁺; IR (CH₂Cl₂): $\tilde{\nu}$ = 1989 (CO), 1996 (CO), 2031 (CO), 2070 cm⁻¹ (CO); ¹³C{¹H} NMR (300 MHz, CD₂Cl₂): δ = 0.13 (CH₃), 6.5 (CH₂), 207.95 ppm (CO); ¹H NMR (300 MHz, CD₂Cl₂): δ = 0.26 (s, 6H, CH₃), 1.66 ppm (s, 4H, CH₂).

Synthesis of Fe₂(CO)₆{ μ -(SCH₂)₂SnMe₂} (4a) and [Fe₂(CO)₆{ μ -(SCH₂)₂SnMe₂}]₂ (5a)

A red solution of (μ -S₂)Fe₂(CO)₆ (185 mg, 0.538 mmol) in THF (15 mL) was cooled to -78 °C and treated dropwise with Et₃BHLi (1.0 mL, 1.08 mmol 1.0 M in THF) to give a dark-green solution. After stirring the solution for \approx 20 min at -78 °C, Me₂Sn(CH₂)₂ (184 mg, 0.427 mmol) in THF (3 mL) was added. The mixture was stirred for 18 h while slowly warming up to room temperature, giving rise to a dark-red solution. Solvent removal was performed under N₂ by using a vacuum transfer line. The residue was extracted several times with pentane and the extracts were collected and dried under N₂ by using a vacuum transfer line. The red residue was then purified by column chromatography (SiO₂, pentane) and two red bands were identified as being **4a** (56 mg, 25% yield) and **5a** (20 mg, 9% yield).

Complex 4a: elemental analysis calcd (%) for C₁₀H₁₀Fe₂O₆S₂Sn: C 23.07, H 1.94, S 12.32; found: C 22.98, H 1.93, S 12.36; Micro-ESI-MS (*m/z*): 520 [M]⁺; IR (CH₂Cl₂): $\tilde{\nu}$ = 2063 (CO), 2031 (CO), 1991 (CO), 1974 cm⁻¹ (CO); ¹³C{¹H} NMR (200 MHz, CD₂Cl₂): δ = -7.1 (CH₃), 1.6 (CH₂), 207.0 ppm (CO); ¹H NMR (200 MHz, CD₂Cl₂): δ = 0.25 (s, 6H, CH₃), 1.79 ppm (s, 4H, CH₂).

Complex 5a: elemental analysis calcd (%) for C₂₀H₂₀Fe₄O₁₂S₄Sn₂: C 23.07, H 1.94, S 12.32; found: C 23.10, H 1.94, S 12.35; Micro-ESI-MS (*m/z*): 1041 [M]⁺; FAB-MS (*m/z*): 1041, 1013, 957, 929, 901, 873; IR (CHCl₃): $\tilde{\nu}$ = 2071 (CO), 2031 (CO), 1991 cm⁻¹ (CO); ¹³C{¹H} NMR (200 MHz, CD₂Cl₂): δ = -8.1 (CH₃), 1.1 (CH₂), 209 ppm (CO); ¹H NMR (200 MHz, CD₂Cl₂): δ = 0.36 (s, 12H, CH₃), 2.00 ppm (s, 8H, CH₂).

Synthesis of Fe₂(CO)₆{ μ -(SCH₂)₂SnPh₂} (4b) and [Fe₂(CO)₆{ μ -(SCH₂)₂SnPh₂}]₂ (5b)

A red solution of (μ -S₂)Fe₂(CO)₆ (95 mg, 0.276 mmol) in THF (15 mL) was cooled to -78 °C and treated dropwise with Et₃BHLi (0.6 mL, 0.553 mmol, 1.0 M in THF) to give a dark-green solution. After stirring the solution for \approx 20 min at -78 °C, Ph₂Sn(CH₂)₂ (307 mg, 0.553 mmol) in THF (3 mL) was added. The mixture was stirred for 18 h while slowly warming up to room temperature, giving rise to a dark-red solution. Solvent removal was performed under N₂ by using a vacuum transfer line. The residue was extracted several times with pentane and the extracts were collected and dried under N₂ by using a vacuum transfer line. The red residue was then purified by column chromatography (SiO₂, pentane) and two red bands were identified as being **4b** (red oil, 32 mg, 18% yield) and **5b** (traces).

Complex 4b: elemental analysis calcd (%) for C₂₀H₁₄Fe₂O₆S₂Sn: C 37.25, H 2.19, S 9.94; found: C 37.23, H 2.20, S 9.96; Micro-ESI-MS (*m/z*): 646 [M]⁺; IR (CH₂Cl₂): $\tilde{\nu}$ = 2066 (CO), 2032 (CO), 1989 cm⁻¹ (CO); ¹³C{¹H} NMR (200 MHz, CD₂Cl₂): δ = 1.70 (CH₂), 128.7–130.6 (c,d-C_{Ph}), 136.7–138.7 (a,b-C_{Ph}), 208.6 (CO), 209.1 ppm (CO); ¹H NMR (200 MHz, CD₂Cl₂): δ = 2.27 (s, 4H, CH₂), 7.35–7.70 ppm (m, 10H, 2C₆H₅).

Photoelectron spectroscopy

Photoelectron spectra were recorded by using an instrument that features a 360 mm radius hemispherical analyzer (McPherson),^[46] with a custom-designed photon source, sample cells, detection, and control electronics. Calibration and data analysis were described previously.^[47] All samples sublimed cleanly, with no visible changes in the spectra during data collection after initial observation of ionizations from the diiron compounds. The sublimation temperatures (at 10⁻⁶ torr) were 52–77, 64–84, and 62–87 °C for compounds **1**, **2**, and **3**, respectively.

Density functional theory (DFT) computations

DFT computations were carried out with the Amsterdam density functional (ADF2014.06) package.^[48,49] The geometries and energies were refined in the gas phase and in solution with the PBE functional^[50] with dispersion corrections according to the method of Grimme by using the BJ damping function (PBE-D3-BJ).^[51] All calculations utilized a triple- ζ Slater type orbital (STO) basis set with one polarization function (TZP) and relativistic effects by the zero-order regular approximation (ZORA).^[52,53] The frozen-core approximation was used for the inner core of all heavy atoms. Diffuse density fitting was employed at the quadruple- ζ level with four polarization functions (QZ4P), and the Becke grid was used with 9402 points.^[54] Geometries were further optimized in the solvents tetrahydrofuran, dichloromethane, and acetone according to the COSMO model with default parameters.^[55] Figures of the optimized geometries and molecular orbital plots were created with the program VMD.^[56]

Structure determinations

The intensity data for the compounds were collected with a Nonius KappaCCD diffractometer using graphite-monochromated MoK α radiation. Data were corrected for Lorentz and polarization effects; absorption was taken into account on a semi-empirical basis by using multiple-scans.^[57–59] The structures were solved by direct methods (SHELXS)^[60] and refined by full-matrix least-squares techniques against F_o² (SHELXL-97).^[60] The hydrogen atoms of **3** and **5b** were located by difference Fourier synthesis and refined isotropically. All other hydrogen atoms were included at calculated positions with fixed thermal parameters. All non-hydrogen atoms were refined anisotropically.^[60] Crystallographic data as well as structure solution and refinement details are summarized in Table S4 in the Supporting Information. MERCURY was used for structure representations.

Cyclic voltammetry

These experiments do not involve corrections for the iR drop. Cyclic voltammetric experiments were performed in a three-electrode cell by using a Radiometer potentiostat (μ -Autolab Type-III or an Autolab PGSTAT 12) driven by the GPES software. The working electrode consisted of a vitreous carbon disk (A = 0.072 cm²) that was polished on a felt tissue with alumina before each CV scan. The Ag/Ag⁺ reference electrode was separated from the analyte by a CH₂Cl₂-[nBu₄N][PF₆] bridge. All the potentials are quoted against the ferrocene/ferrocenium couple (Fc⁺/Fc); ferrocene was added as an internal standard at the end of the experiments.

Acknowledgments

The authors (T.S., D.L.L., and R.S.G.) gratefully acknowledge support of this work by the US National Science Foundation (Grant Nos. 1111718 and 1111570). L.A. and H.A. are grateful to the Deutscher Akademischer Austausch Dienst (DAAD) for scholarships. G.M. and W.W. thank the National Science Center (Cracow, PL) for financial support (Grant Maestro-3; Dec-2012/06/A/ST5/00219). P.S. and W.W. gratefully acknowledge the DAAD for the PROCOPE Project-Related Personal Exchange Program.

Keywords: conformational analysis · density functional calculations · electrocatalysis · photoelectron · sulfur

- [1] a) B. J. Lemon, J. W. Peters, *Biochemistry* **1999**, *38*, 12969–12973; b) A. S. Pandey, T. V. Harris, L. J. Giles, J. W. Peters, R. K. Szilagyi, *J. Am. Chem. Soc.* **2008**, *130*, 4533–4540; c) A. Adamska-Venkatesh, S. Roy, J. F. Siebel, T. R. Simmons, M. Fontecave, V. Artero, E. Reijerse, W. Lubitz, *J. Am. Chem. Soc.* **2015**, *137*, 12744–12747.
- [2] a) J. W. Peters, W. N. Lanzilotta, B. J. Lemon, L. C. Seefeldt, *Science* **1998**, *282*, 1853–1858; b) Y. Nicolet, C. Piras, P. Legrand, E. C. Hatchikian, J. C. Fontecilla-Camps, *Structure* **1999**, *7*, 13–23; c) H.-J. Fan, M. B. Hall, *J. Am. Chem. Soc.* **2001**, *123*, 3828–3829; d) Z.-P. Liu, P. Hu, *J. Am. Chem. Soc.* **2002**, *124*, 5175–5182; e) C. Greco, M. Bruschi, L. D. Gioia, U. Ryde, *Inorg. Chem.* **2007**, *46*, 5911–5921; f) S. Trohalaki, R. Pachter, *Int. J. Hydrogen Energy* **2010**, *35*, 5318–5331.
- [3] a) W. Dong, M. Wang, X. Liu, K. Jin, G. Li, F. Wang, *Chem. Commun.* **2006**, 305–307; b) S. Ezzaher, A. Gogoll, C. Bruhn, S. Ott, *Chem. Commun.* **2010**, *46*, 5775–5777; c) R. J. Wright, W. Zhang, X. Yang, M. Fasulo, T. D. Tilley, *Dalton Trans.* **2012**, *41*, 73–82; d) R. Zaffaroni, T. B. Rauchfuss, D. L. Gray, L. De Gioia, G. Zampella, *J. Am. Chem. Soc.* **2012**, *134*, 19260–19269; e) R. Goy, L. Bertini, H. Görls, L. De Gioia, J. Talarmin, G. Zampella, P. Schollhammer, W. Weigand, *Chem. Eur. J.* **2015**, *21*, 5061–5073.
- [4] M. W. W. Adams, *J. Biol. Chem.* **1987**, *262*, 15054–15061.
- [5] a) M. Frey, *ChemBioChem* **2002**, *3*, 153–160; b) M. Demuez, L. Cournac, O. Guerrini, P. Soucaille, L. Girbal, *FEMS Microbiol. Lett.* **2007**, *275*, 113–121.
- [6] a) G. A. N. Felton, C. A. Mebi, B. J. Petro, A. K. Vannucci, D. H. Evans, R. S. Glass, D. L. Lichtenberger, *J. Organomet. Chem.* **2009**, *694*, 2681–2699; b) C. Tard, C. J. Pickett, *Chem. Rev.* **2009**, *109*, 2245–2274; c) J.-F. Capon, F. Gloaguen, F. Y. Petillon, P. Schollhammer, J. Talarmin, *Coord. Chem. Rev.* **2009**, *253*, 1476–1494; d) F. Gloaguen, T. B. Rauchfuss, *Chem. Soc. Rev.* **2009**, *38*, 100–108; e) S. Tschierlei, S. Ott, R. Lomoth, *Energy Environ. Sci.* **2011**, *4*, 2340–2352; f) N. Wang, M. Wang, L. Chen, L. Sun, *Dalton Trans.* **2013**, *42*, 12059–12071; g) W. Lubitz, H. Ogata, O. Rüdiger, E. Reijerse, *Chem. Rev.* **2014**, *114*, 4081–4148; h) T. R. Simmons, G. Berggren, M. Bacchi, M. Fontecave, V. Artero, *Coord. Chem. Rev.* **2014**, *270–271*, 127–150; i) R. Trautwein, L. R. Almazahreh, H. Görls, W. Weigand, *Dalton Trans.* **2015**, *44*, 18780–18794; j) Y. Li, T. B. Rauchfuss, *Chem. Rev.* **2016**, *116*, 7043–7077.
- [7] a) T. Liu, M. Y. Darensbourg, *J. Am. Chem. Soc.* **2007**, *129*, 7008–7009; b) A. K. Justice, T. B. Rauchfuss, S. R. Wilson, *Angew. Chem. Int. Ed.* **2007**, *46*, 6152–6154; *Angew. Chem.* **2007**, *119*, 6264–6266; c) A. K. Justice, L. De Gioia, M. J. Wilges, T. B. Rauchfuss, S. R. Wilson, G. Zampella, *Inorg. Chem.* **2008**, *47*, 7405–7414; d) C.-H. Hsieh, O. F. Erdem, S. D. Harman, M. L. Singleton, E. Reijerse, W. Lubitz, C. V. Popescu, J. H. Reibenspies, S. M. Brothers, M. B. Hall, M. Y. Darensbourg, *J. Am. Chem. Soc.* **2012**, *134*, 13089–13102.
- [8] a) W. Wang, T. B. Rauchfuss, C. E. Moore, A. L. Rheingold, L. De Gioia, G. Zampella, *Chem. Eur. J.* **2013**, *19*, 15476–15479; b) S. Munery, J.-F. Capon, L. De Gioia, C. Elleouet, C. Greco, F. Y. Petillon, P. Schollhammer, J. Talarmin, G. Zampella, *Chem. Eur. J.* **2013**, *19*, 15458–15461; c) R. Goy, L. Bertini, C. Elleouet, H. Görls, G. Zampella, J. Talarmin, L. Gioia, P. Schollhammer, U.-P. Apfel, W. Weigand, *Dalton Trans.* **2015**, *44*, 1690–1699.
- [9] J. W. Tye, M. Y. Darensbourg, M. B. Hall, *Inorg. Chem.* **2006**, *45*, 1552–1559.
- [10] a) M. L. Singleton, N. Bhuvanesh, J. H. Reibenspies, M. Y. Darensbourg, *Angew. Chem. Int. Ed.* **2008**, *47*, 9492–9495; *Angew. Chem.* **2008**, *120*, 9634–9637; b) D. J. Crouthers, J. A. Denny, R. D. Bethel, D. G. Munoz, M. Y. Darensbourg, *Organometallics* **2014**, *33*, 4747–4755.
- [11] a) G. A. N. Felton, A. K. Vannucci, J. Chen, L. T. Lockett, N. Okumura, B. J. Petro, U. I. Zakai, D. H. Evans, R. S. Glass, D. L. Lichtenberger, *J. Am. Chem. Soc.* **2007**, *129*, 12521–12530; b) G. A. N. Felton, B. J. Petro, R. S. Glass, D. L. Lichtenberger, D. H. Evans, *J. Am. Chem. Soc.* **2009**, *131*, 11290–11291.
- [12] a) J. D. Lawrence, H. X. Li, T. B. Rauchfuss, M. Benard, M. M. Rohmer, *Angew. Chem. Int. Ed.* **2001**, *40*, 1768–1771; *Angew. Chem.* **2001**, *113*, 1818–1821; b) J.-F. Capon, S. Ezzaher, F. Gloaguen, F. Y. Petillon, P. Schollhammer, J. Talarmin, T. J. Davin, J. E. McGrady, L.-C. Sun, *J. Organomet. Chem.* **2007**, *692*, 5501–5507; g) W.-G. Wang, H.-Y. Wang, G. Si, C.-H. Tung, L.-Z. Wu, *Dalton Trans.* **2009**, 2712–2720; h) Y. Na, M. Wang, J. Pan, P. Zhang, B. Åkermark, L. Sun, *Inorg. Chem.* **2008**, *47*, 2805–2810; i) Z. Wang, J. Liu, C. He, S. Jiang, B. Åkermark, L. Sun, *Inorg. Chim. Acta* **2007**, *360*, 2411–2419; j) Y. Si, C. Ma, M. Hu, H. Chen, C. Chen, Q. Liu, *New J. Chem.* **2007**, *31*, 1448–1454; k) L. Schwartz, G. Eilers, L. Eriksson, A. Gogoll, R. Lomoth, S. Ott, *Chem. Commun.* **2006**, 520–526; l) G. Eilers, L. Schwartz, M. Stein, G. Zampella, L. de Gioia, S. Ott, R. Lomoth, *Chem. Eur. J.* **2007**, *13*, 7075–7084; m) J. Hou, X. Peng, J. Liu, Y. Gao, X. Zhao, S. Gao, K. Han, *Eur. J. Inorg. Chem.* **2006**, 4679–4686; n) S. Ezzaher, P.-Y. Orain, J.-F. Capon, F. Gloaguen, F. Y. Petillon, T. Roisnel, P. Schollhammer, J. Talarmin, *Chem. Commun.* **2008**, 2547–2549; o) M. E. Carroll, B. E. Barton, T. B. Rauchfuss, P. J. Carroll, *J. Am. Chem. Soc.* **2012**, *134*, 18843–18852.
- [13] a) A. Winter, L. Zsolnai, G. Huttner, *Chem. Ber.* **1982**, *115*, 1286–1304; b) A. Winter, L. Zsolnai, G. Huttner, *Z. Naturforsch. B* **1982**, *37*, 1430–1436; c) M. L. Singleton, R. M. Jenkins, C. L. Klemashevich, M. Y. Darensbourg, *C. R. Chem.* **2008**, *11*, 861–874; d) B. E. Barton, M. T. Olsen, T. B. Rauchfuss, *J. Am. Chem. Soc.* **2008**, *130*, 16834–16835; e) B. E. Barton, T. B. Rauchfuss, *Inorg. Chem.* **2008**, *47*, 2261–2263; f) R. Trautwein, L. R. Almazahreh, H. Görls, W. Weigand, *Z. Anorg. Allg. Chem.* **2013**, *639*, 1512–1519.
- [14] a) H. X. Li, T. B. Rauchfuss, *J. Am. Chem. Soc.* **2002**, *124*, 726–727; b) L.-C. Song, Z.-Y. Yang, H.-Z. Bian, Y. Liu, H.-T. Wang, X.-F. Liu, Q.-M. Hu, *Organometallics* **2005**, *24*, 6126–6135.
- [15] a) L.-C. Song, Z.-Y. Yang, Y.-J. Hua, H.-T. Wang, Y. Liu, Q.-M. Hu, *Organometallics* **2007**, *26*, 2106–2110; b) J. Windhager, M. Rudolph, S. Brautigam, H. Görls, W. Weigand, *Eur. J. Inorg. Chem.* **2007**, 2748–2760; c) L.-C. Song, A.-G. Zhu, Y.-Q. Guo, *Dalton Trans.* **2016**, *45*, 5021–5029.
- [16] M. Harb, Ph.D. Dissertation, Friedrich-Schiller Universität Jena, Jena, Thüringen, **2009**.
- [17] U.-P. Apfel, D. Troegel, Y. Halpin, S. Tschierlei, U. Uhlemann, H. Görls, M. Schmitt, J. Popp, P. Dunne, M. Venkatesan, M. Coey, M. Rudolph, G. J. Vos, R. Tacke, W. Weigand, *Inorg. Chem.* **2010**, *49*, 10117–10132.
- [18] a) L. R. Almazahreh, U.-P. Apfel, W. Imhof, M. Rudolph, H. Görls, J. Talarmin, P. Schollhammer, M. El-khateeb, W. Weigand, *Organometallics* **2013**, *32*, 4523–4530; b) L. R. Almazahreh, W. Imhof, J. Talarmin, P. Schollhammer, H. Görls, M. Y. El-khateeb, W. Weigand, *Dalton Trans.* **2015**, *44*, 7177–7189.
- [19] a) M. K. Harb, J. Windhager, T. Nicksch, H. Görls, T. Sakamoto, E. R. Smith, R. S. Glass, D. L. Lichtenberger, D. H. Evans, M. El-khateeb, W. Weigand, *Tetrahedron* **2012**, *68*, 10592–10599; b) S. Gao, J. Fan, S. Sun, X. Peng, X. Zhao, J. Hou, *Dalton Trans.* **2008**, 2128–2135; c) M. K. Harb, U.-P. Apfel, J. Kübel, H. Görls, G. A. N. Felton, T. Sakamoto, D. H. Evans, R. S. Glass, D. L. Lichtenberger, M. El-khateeb, W. Weigand, *Organometallics* **2009**, *28*, 6666–6675; d) U.-P. Apfel, H. Görls, G. A. N. Felton, D. H. Evans, R. S. Glass, D. L. Lichtenberger, W. Weigand, *Helv. Chim. Acta* **2012**, *95*, 2168–2175.

- [20] a) P. Das, J.-F. Capon, F. Gloaguen, F. Y. Pétilion, P. Schollhammer, J. Talarmin, K. W. Muir, *Inorg. Chem.* **2004**, *43*, 8203–8205; b) L.-C. Song, Z.-C. Gu, W.-W. Zhang, Q.-L. Li, Y.-X. Wang, H.-F. Wang, *Organometallics* **2015**, *34*, 4147–4157.
- [21] R. S. Glass, N. E. Gruhn, E. Lorance, M. S. Singh, N. Y. T. Stessman, U. I. Zakai, *Inorg. Chem.* **2005**, *44*, 5728–5737.
- [22] a) R. S. Glass, A. M. Radspinner, W. P. Singh, *J. Am. Chem. Soc.* **1992**, *114*, 4921–4923; b) R. S. Glass, Q. Guo, Y. Liu, *Tetrahedron* **1997**, *53*, 12273–12286; c) R. S. Glass, E. Block, N. E. Gruhn, J. Jin, E. Lorance, U. I. Zakai, S.-Z. Zhang, *J. Org. Chem.* **2007**, *72*, 8290–8297.
- [23] D. Seyferth, S. B. Andrews, *J. Organomet. Chem.* **1971**, *30*, 151–166.
- [24] Y. Nicolet, A. L. de Lacey, X. Vernede, V. M. Fernandez, C. E. Hatchikian, J. C. Fontecilla-Camps, *J. Am. Chem. Soc.* **2001**, *123*, 1596–1602.
- [25] N. L. Allinger, X. Zhou, J. Bergsma, *J. Mol. Struct. THEOCHEM* **1994**, *312*, 69–83.
- [26] A. K. Rappé, C. J. Casewit, K. S. Colwell, W. A. Goddard III, W. M. Skiff, *J. Am. Chem. Soc.* **1992**, *114*, 10024–10035.
- [27] E. J. Lyon, I. P. Georgakaki, J. H. Reibenspies, M. Y. Darensbourg, *J. Am. Chem. Soc.* **2001**, *123*, 3268–3278.
- [28] a) J. B. Hendrickson, *J. Am. Chem. Soc.* **1961**, *83*, 4537–4547; b) D. J. Nelson, C. N. Brammer, *J. Chem. Educ.* **2011**, *88*, 292–294.
- [29] a) C. H. Bushweller, in *Conformational Behavior of Six-Membered Rings* (Ed.: E. Juaristi), VCH, Weinheim, **1995**; b) D. A. Dixon, A. Komornicki, *J. Phys. Chem.* **1990**, *94*, 5630–5636; c) C. A. Stortz, *J. Phys. Org. Chem.* **2010**, *23*, 1173–1186.
- [30] K. Kakhiani, U. Lourdera, W. Hu, D. Birney, W. L. Hase, *J. Phys. Chem. A* **2009**, *113*, 4570–4580.
- [31] F. A. L. Anet, A. J. R. Bourn, *J. Am. Chem. Soc.* **1967**, *89*, 760–768.
- [32] R. J. Ouellette, *J. Am. Chem. Soc.* **1974**, *96*, 2421–2425.
- [33] a) M. J. O. Anteunis, R. Dedeyne, *Org. Magn. Reson.* **1977**, *9*, 127–132; b) F. Freeman, C. Cha, C. Fang, A. C. Huang, J. H. Hwang, P. L. Louie, B. A. Shainyan, *J. Phys. Org. Chem.* **2005**, *18*, 35–48; c) S. V. Kirpichenko, E. Kleinpeter, B. A. Shainyan, *J. Phys. Org. Chem.* **2010**, *23*, 859–865.
- [34] a) Y. Takeuchi, Y. Ichikawa, K. Tanaka, N. Kakimoto, *Bull. Chem. Soc. Jpn.* **1988**, *61*, 2875–2880; b) Y. Takeuchi, K. Tanaka, T. Harazono, S. Yoshimura, *Bull. Chem. Soc. Jpn.* **1990**, *63*, 708–715; c) Y. Takeuchi, M. Shimoda, K. Tanaka, S. Tomoda, K. Ogawa, H. Suzuki, *J. Chem. Soc. Perkin 2* **1988**, 7–13; d) K.-H. Chen, N. L. Allinger, *J. Phys. Org. Chem.* **1999**, *12*, 528–540.
- [35] F. Freeman, C. Fang, D. V. Hoang, K. M. Trinh, *Int. J. Quantum Chem.* **2005**, *105*, 416–428.
- [36] a) M. K. Harb, J. Windhager, A. Daraosheh, H. Görls, L. T. Lockett, N. Okumura, D. H. Evans, R. S. Glass, D. L. Lichtenberger, M. El-khateeb, W. Weigand, *Eur. J. Inorg. Chem.* **2009**, 3414–3420; b) M. K. Harb, H. Görls, T. Sakamoto, G. A. N. Felton, D. H. Evans, R. S. Glass, D. L. Lichtenberger, M. El-khateeb, W. Weigand, *Eur. J. Inorg. Chem.* **2010**, 3976–3985; c) M. K. Harb, T. Niksch, J. Windhager, H. Görls, R. Holze, L. T. Lockett, N. Okumura, D. H. Evans, R. S. Glass, D. L. Lichtenberger, M. El-khateeb, W. Weigand, *Organometallics* **2009**, *28*, 1039–1048.
- [37] a) L.-C. Song, F.-H. Gong, T. Meng, J.-H. Ge, L.-N. Cui, Q.-M. Hu, *Organometallics* **2004**, *23*, 823–831; b) L.-C. Song, J.-Y. Wang, F.-H. Gong, J. Cheng, Q.-M. Hu, *J. Organomet. Chem.* **2004**, *689*, 930–935; c) M.-H. Chiang, Y.-C. Liu, S.-T. Yang, G.-H. Lee, *Inorg. Chem.* **2009**, *48*, 7604–7612; d) M. K. Harb, A. Daraosheh, H. Görls, E. R. Smith, G. J. Meyer, M. T. Swenson, T. Sakamoto, R. S. Glass, D. L. Lichtenberger, D. H. Evans, M. El-khateeb, W. Weigand, *Heteroat. Chem.* **2014**, *25*, 592–606.
- [38] The ¹H NMR spectrum of *a,e*-(μ-CH₃HgS)₂Fe₂(CO)₆ shows that the nonequivalent methyl groups have the same chemical shifts: T. C. W. Mak, L. Book, C. Chieh, M. K. Gallagher, L.-C. Song, D. Seyferth, *Inorg. Chim. Acta* **1983**, *73*, 159–164. However, the chemical shifts for the nonequivalent methyl protons in **4** differ by 0.10 ppm and the nonequivalent CH₂ protons by 0.46 ppm.
- [39] R. S. Nicholson, I. Shain, *Anal. Chem.* **1965**, *37*, 178–190.
- [40] D. Chouffai, J.-F. Capon, L. De Gioia, F. Y. Pétilion, P. Schollhammer, J. Talarmin, G. Zampella, *Inorg. Chem.* **2015**, *54*, 299–311.
- [41] K. Izutsu, *Acid-Base Dissociation Constants in Dipolar Aprotic Solvents, Vol. 35*, Blackwell Scientific, Oxford, **1990**.
- [42] S. J. Borg, S. K. Ibrahim, C. J. Pickett, S. P. Best, *C. R. Chim.* **2008**, *11*, 852–860.
- [43] A. Kütt, T. Rodima, J. Saame, E. Raamat, V. Mäemets, I. Kaljurand, I. A. Koppel, R. Y. Garlyauskayte, Y. L. Yagupolskii, L. M. Yagupolskii, E. Bernhardt, H. Willner, I. Leito, *J. Org. Chem.* **2011**, *76*, 391–395.
- [44] P. F. Brandt, D. A. Lesch, P. R. Stafford, T. B. Rauchfuss, *Inorg. Synth.* **1997**, *31*, 112–116.
- [45] a) R. Tacke, S. A. Wagner, J. Sperlich, *Chem. Ber.* **1994**, *127*, 639–642; b) J. Barrau, G. Rima, J. Satgé, *Synth. React. Inorg. Met.-Org. Chem.* **1984**, *14*, 21–37.
- [46] K. Siegbahn, C. Nordling, A. Fahlman, R. Nordberg, *ESCA: Atomic, Molecular and Solid-State Structures Studied by Means of Electron Spectroscopy*, Almqvist & Wiksells, Uppsala, **1967**.
- [47] M. A. Cranswick, A. Dawson, J. J. A. Cooney, N. E. Gruhn, D. L. Lichtenberger, J. H. Enemark, *Inorg. Chem.* **2007**, *46*, 10639–10646.
- [48] G. te Velde, F. M. Bickelhaupt, E. J. Baerends, C. F. Guerra, S. J. A. Van Gisbergen, J. G. Snijders, T. Ziegler, *J. Comput. Chem.* **2001**, *22*, 931–967.
- [49] ADF2014.06, <http://scm.com>.
- [50] J. P. Perdew, K. Burke, M. Ernzerhof, *Phys. Rev. Lett.* **1996**, *77*, 3865–3868.
- [51] S. Grimme, S. Ehrlich, L. Goerigk, *J. Comput. Chem.* **2011**, *32*, 1456–1465.
- [52] E. van Lenthe, E. J. Baerends, J. G. Snijders, *J. Chem. Phys.* **1993**, *99*, 4597–4610.
- [53] E. van Lenthe, A. Ehlers, E. J. Baerends, *J. Chem. Phys.* **1999**, *110*, 8943–8953.
- [54] M. Franchini, P. H. T. Philipsen, L. Visscher, *J. Comput. Chem.* **2013**, *34*, 1819–1827.
- [55] a) C. C. Pye, T. Ziegler, *Theor. Chem. Acc.* **1999**, *101*, 396–408; b) A. Klamt, G. Schüürmann, *J. Chem. Soc. Perkin Trans. 2* **1993**, 799–805.
- [56] W. Humphrey, A. Dalke, K. Schulten, *J. Mol. Graphics* **1996**, *14*, 33–38.
- [57] COLLECT, Data Collection Software, B. V. Nonius, The Netherlands, **1998**.
- [58] “Processing of X-ray Diffraction Data Collected in Oscillation Mode”: Z. Otwinowski, W. Minor, in *Methods in Enzymology, Vol. 276 of Macromolecular Crystallography, Part A* (Eds.: C. W. Carter, R. M. Sweet), Academic Press, **1997**, pp. 307–326.
- [59] SADABS 2.10, Bruker-AXS Inc., **2002**, Madison, WI, USA.
- [60] G. M. Sheldrick, *Acta Crystallogr. Sect. A* **2008**, *64*, 112–122.

Received: August 11, 2016

Published online on November 23, 2016

CHEMISTRY

A **European** Journal

Supporting Information

[FeFe]-Hydrogenase H-Cluster Mimics with Unique Planar μ -(SCH₂)₂ER₂ Linkers (E = Ge and Sn)

Hassan Abul-Futouh,^[a] Laith R. Almazahreh,^{*[a]} Takahiro Sakamoto,^[b] Nhu Y. T. Stessman,^[b] Dennis L. Lichtenberger,^{*[b]} Richard S. Glass,^{*[b]} Helmar Görls,^[a] Mohammad El-Khateeb,^[c] Philippe Schollhammer,^{*[d]} Grzegorz Mloston,^[e] and Wolfgang Weigand^{*[a]}

chem_201603843_sm_miscellaneous_information.pdf

Supporting Information

CONTENTS

- **Figure S-1.** Experimental IR spectra in the region of the carbonyl stretches for $\text{Fe}_2(\text{CO})_6\{(\mu\text{-SCH}_2)_2\text{ER}_2\}$ complexes, and comparison with the frequencies and relative intensities from computations..... S3
- **Table S-1.** Selected structural features from experimental crystallographic data with computational gas-phase values in parentheses for $\text{Fe}_2(\text{CO})_6\{(\mu\text{-SCH}_2)_2\text{ER}_2\}$ complexes..... S3
- **Figure S-2.** Comparison of the HOMO and LUMO orbitals of the $\text{Fe}_2(\text{CO})_6\{(\mu\text{-SCH}_2)_2\text{ER}_2\}$ Complexes S4
- **Figure S-3.** Global and local geometry minima of the cation states of $\text{Fe}_2(\text{CO})_6\{(\mu\text{-SCH}_2)_2\text{ER}_2\}$ complexes..... S5
- **Table S-2.** Sample keywords for computations..... S6
- Synthesis of $\text{Me}_2\text{Ge}(\text{CH}_2\text{Cl})_2$ S7
- **Table S-3.** Selected intramolecular distances [\AA] for complex **5a**..... S9
- **Figure S-4.** Variable temperature ^1H NMR spectra of **5a** in CDCl_3 S9
- **Figure S-5.** Cyclic voltammetry of 0.65 mM complex **2** (CH_2Cl_2 -[n-Bu₄N][PF₆] solution) at $0.2 \text{ V}\cdot\text{s}^{-1}$ S11
- **Figure S-6.** Cyclic voltammetry of complex 0.65 mM complex **2** (CH_2Cl_2 -[n-Bu₄N][PF₆] solution) at 0.05 - $12 \text{ V}\cdot\text{s}^{-1}$ S12
- **Figure S-7.** Cyclic voltammetry of complex 0.84 mM complex **4a** (CH_2Cl_2 -[n-Bu₄N][PF₆] solution) at $0.2 \text{ V}\cdot\text{s}^{-1}$ S12
- **Figure S-8.** Cyclic voltammetry of complex 1.01 mM complex **3** (CH_2Cl_2 -[n-Bu₄N][PF₆] solution) in the presence of 0.5-2 equiv. $\text{CF}_3\text{SO}_3\text{H}$ at $0.2 \text{ V}\cdot\text{s}^{-1}$ S13
- **Figure S-9.** Cyclic voltammetry of complex 0.843 mM complex **3** (CH_2Cl_2 -[n-Bu₄N][PF₆] in the presence of 0-2 equiv. $\text{HBF}_4\cdot\text{Et}_2\text{O}$ at $1 \text{ V}\cdot\text{s}^{-1}$ S14
- **Figure S-10.** Cyclic voltammetry of complex 0.843 mM complex **4a** (CH_2Cl_2 -[n-Bu₄N][PF₆] in the presence of 0-3.7 equiv. $\text{CF}_3\text{SO}_3\text{H}$ at $0.2 \text{ V}\cdot\text{s}^{-1}$ S15
- **Figure S-11.** Correlation of the solution oxidation potentials E_{ox1} (V vs. Fc/Fc+) versus the computed gas-phase vertical ionization energies (eV)..... S15
- **Table S-4.** Crystal data and refinement details for the X-ray structure determinations of the compounds **3-5b**..... S16
- References..... S17

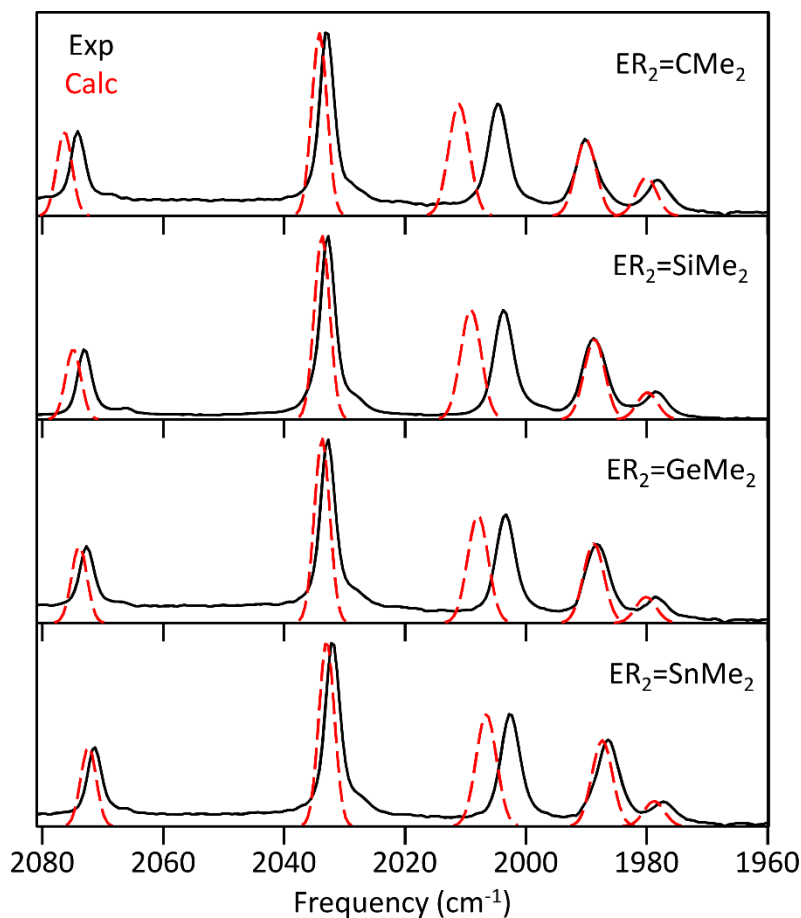


Figure S-1. Experimental IR spectra (Nujol) in the region of the carbonyl stretches for $\text{Fe}_2(\text{CO})_6\{(\mu\text{-SCH}_2)_2\text{ER}_2\}$ complexes, and comparison with the frequencies and relative intensities from computations. The computational model is described in the publication and example keywords are in Table S-2. The calculated frequencies in the gas phase are multiplied by 1.01 for comparison to the experimental values.

Table S-1. Selected structural features from experimental crystallographic data with computational gas-phase values in parentheses for $\text{Fe}_2(\text{CO})_6\{(\mu\text{-SCH}_2)_2\text{ER}_2\}$ complexes. Distances are given in Å and angles in degrees.

	$\text{ER}_2 = \text{CMe}_2^1$	SiMe_2^2	GeMe_2	SnMe_2
Fe–Fe	2.494 (2.539)	2.522 (2.548)	2.513 (2.563)	2.525 (2.576)
Fe–C(O) _{avg}	1.800 (1.798)	1.800 (1.799)	1.800 (1.799)	1.802 (1.800)
Fe–S _{avg}	2.263 (2.300)	2.259 (2.299)	2.254 (2.294)	2.257 (2.293)
S–Fe–S	83.6 (83.7)	87.9 (87.8)	88.8 (89.2)	90.1 (90.7)
E–C _{avg}	1.534 (1.536)	1.868 (1.888)	1.946 (2.020)	2.140 (2.212)

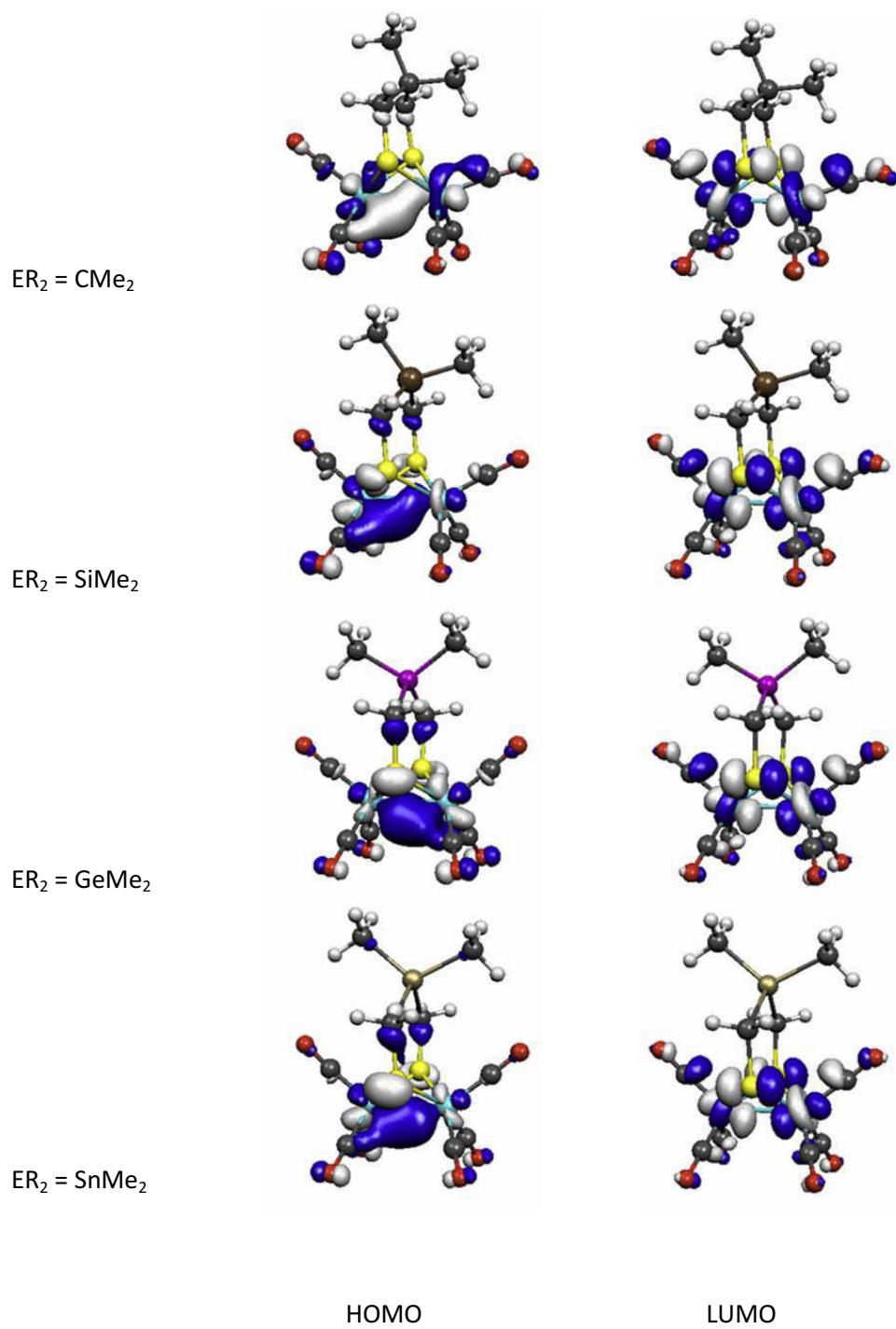
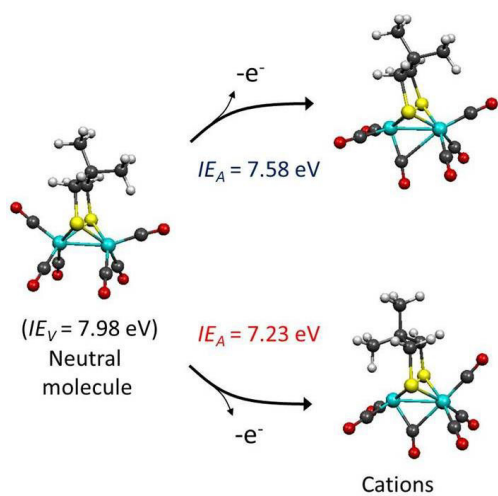
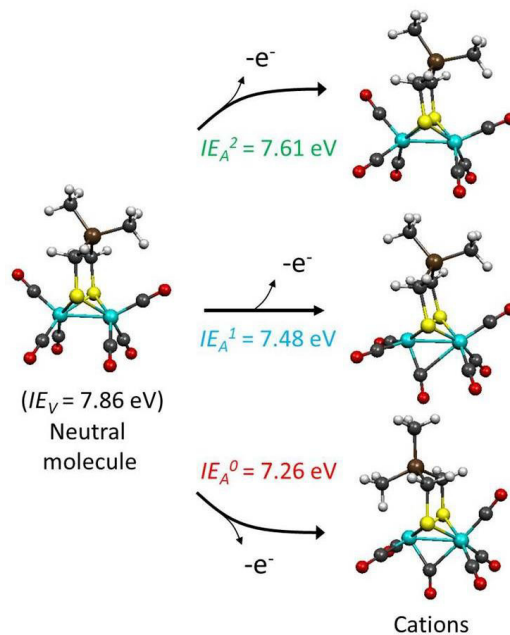


Figure S-2. Comparison of the HOMO and LUMO orbitals of the $Fe_2(CO)_6\{(\mu-SCH_2)_2ER_2\}$ complexes. The isosurface value is ± 0.05 .

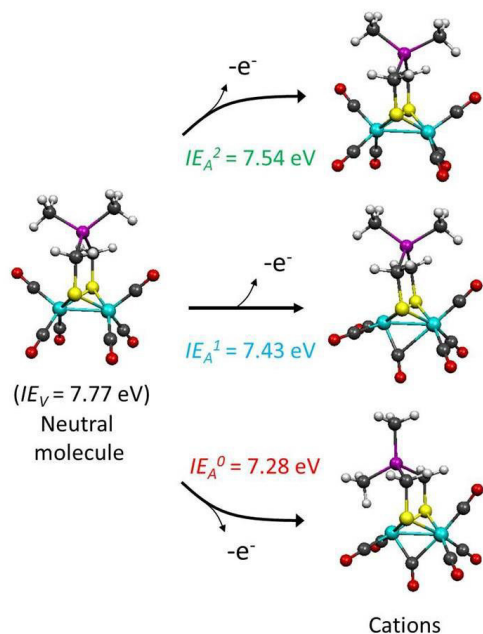
ER₂ = CMe₂



ER₂ = SiMe₂



ER₂ = GeMe₂



ER₂ = SnMe₂

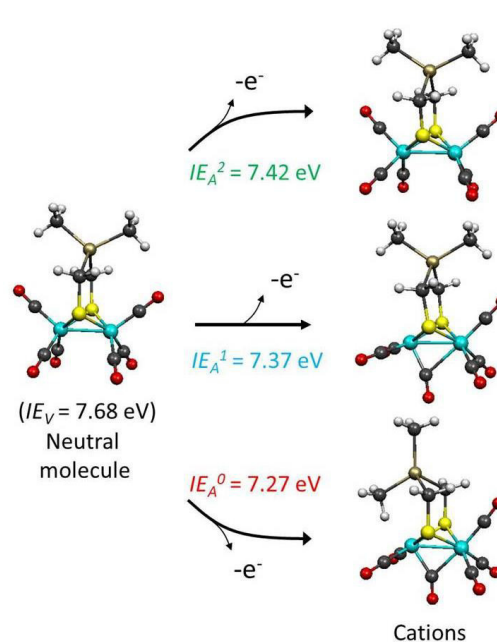


Figure S-3. Global and local geometry minima of the cation states of $Fe_2(CO)_6\{(\mu-SCH_2)_2ER_2\}$ complexes. The ionization energies from the ground states of the neutral molecules indicate the relative energies of the cation states. The cation with $ER_2 = CMe_2$ does not have a local minimum with all terminal carbonyls

Table S-2. Sample keywords for computations. ADF version 2014.06.³

```
basis
  H $ADFRESOURCES/ZORA/TZP/H
  C $ADFRESOURCES/ZORA/TZP/C.1s
  O $ADFRESOURCES/ZORA/TZP/O.1s
  Sn $ADFRESOURCES/ZORA/TZP/Sn.4d
  S $ADFRESOURCES/ZORA/TZP/S.2p
  Fe $ADFRESOURCES/ZORA/TZP/Fe.3p
  FitType $ADFRESOURCES/ZORA/QZ4P/H
  FitType $ADFRESOURCES/ZORA/QZ4P/C
  FitType $ADFRESOURCES/ZORA/QZ4P/O
  FitType $ADFRESOURCES/ZORA/QZ4P/Fe
  FitType $ADFRESOURCES/ZORA/QZ4P/Sn
  FitType $ADFRESOURCES/ZORA/QZ4P/S
end

AddDiffuseFit

relativistic ZORA

BeckeGrid
  Quality Good
end

xc
  gga PBE
  Dispersion GRIMME3 BJDAMP
end

scf
  iterations 200
  converge 1e-6 1e-6
  mix = 0.1
end

geometry
  converge rad=0.001
  iterations 200
end

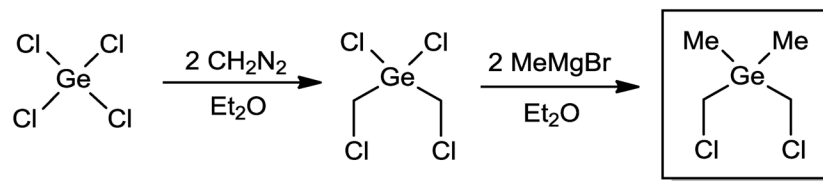
AnalyticalFreq
End

solvation
  SOLV name=dichloromethane
  charged conv=1e-10 iter=1000
  SCF=Var
end

Charge 0 0

atoms cartesian
.
.(atom xyz coordinates)
.
End
```

Synthesis of $\text{Me}_2\text{Ge}(\text{CH}_2\text{Cl})_2$

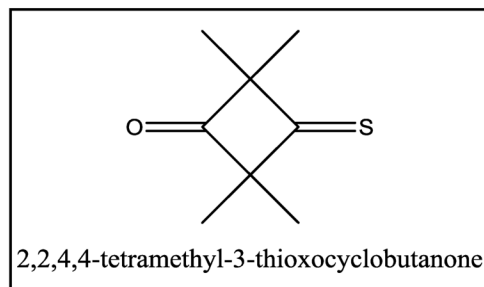


Step 1: Synthesis of 0.5 M CH_2N_2

Caution! Diazomethane (CH_2N_2) is explosive, very toxic and carcinogenic. It is stable only in cold solution ($T \leq 0^\circ\text{C}$) for few days, but it is better to use fresh solutions of diazomethane for the syntheses. The Erlenmeyer flask containing the diazomethane solution should not be tightly closed and plastic caps are used. When using the diazomethane solution, all work must be done in a fume hood.

To a 500 ml Erlenmeyer flask containing KOH (20 g), H_2O (30 mL) and ether (100 mL) at 0°C , 1-methyl-1-nitrosourea (5 g, 0.05 mol) was added in portions (every 1-2 min) with stirring while the temperature is 0°C . The color of the solution turns yellow due to formation of CH_2N_2 . After complete addition, stirring was continued for 15 min. The yellow organic layer was then separated into an Erlenmeyer flask containing KOH and kept at -20°C for 3 h. The purpose of KOH is for drying the ether solution containing the in situ generated CH_2N_2 .

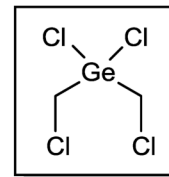
Determination of the concentration of the diazomethane solution. The concentration of the diazomethane solution is determined by titration using 2,2,4,4-tetramethyl-3-thioxocyclobutan-1-one as follows.



A red solution of 2,2,4,4-tetramethyl-3-thioxocyclobutan-1-one (0.156 g, 1 mmol) in ether (4.0 mL) is transferred to a titration buret to titrate the CH_2N_2 solution (1.0 mL). At the end point, the yellow CH_2N_2 solution becomes colorless. The concentration of CH_2N_2 (M_{analyte}) can be determined using the equation: $M_{\text{titrant}} \times V_{\text{titrant}} = M_{\text{analyte}} \times V_{\text{analyte}}$, where M_{titrant} is the concentration of the titrant solution, V_{titrant} volume of titrant required to reach the end point and $V_{\text{analyte}} = 1.0 \text{ mL}$.

Step 2: Synthesis of $\text{Cl}_2\text{Ge}(\text{CH}_2\text{Cl})_2$

GeCl_4 (2.8209 g, 13.16 mmol) was dissolved in a dry ether (20-30 mL) containing Cu (0.2564 g) under N_2 atmosphere and the resulting solution was cooled to $-70\text{ }^\circ\text{C}$. Two equiv. volume of CH_2N_2 solution (61 mL, 0.4343 M) were added dropwise during 1 hour. *Note: Use a small syringe (2 mL volume)*

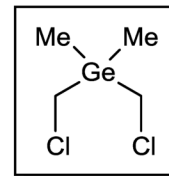


for the addition. During this time the CH_2N_2 solution is kept at low temperature ($T < 0\text{ }^\circ\text{C}$). After complete addition, the solution was stirred for 12 h while the temperature was increasing slowly to r.t. The solution was then decanted from the Cu and the solvent is removed under reduced pressure. The crude product was purified by distillation ($97\text{ }^\circ\text{C} / 35\text{ mmHg}$) to afford $\text{Cl}_2\text{Ge}(\text{CH}_2\text{Cl})_2$ in 70 % yield as a colorless liquid. This compound was stored under N_2 at $5\text{ }^\circ\text{C}$.

$^{13}\text{C}\{^1\text{H}\}$ NMR (600 MHz, CD_2Cl_2): δ 31.6 (s, CH_2). ^1H NMR (600 MHz, CD_2Cl_2): δ 3.68 (s, CH_2).

Step 3: Reaction of $\text{Cl}_2\text{Ge}(\text{CH}_2\text{Cl})_2$ with MeMgBr

$\text{Cl}_2\text{Ge}(\text{CH}_2\text{Cl})_2$ (1.188 g, 4.9 mmol) was added to ether (80 mL) and the resulting solution was cooled to $0\text{ }^\circ\text{C}$. Two equivalents of MeMgBr solution (3.3 mL, 0.3 M) in ether (10 mL) were added dropwise. After complete addition, the solution was stirred for 16 h at r.t. and was then heated at reflux for 4 h. The reaction mixture was filtered and the filtrate was extracted two



times with an ice cold saturated solution of NH_4Cl in water. The combined ethereal solution was dried over anhyd Na_2SO_4 . The solvent was the removed under reduced pressure and the crude product was distilled ($78\text{ }^\circ\text{C} / 20\text{ mmHg}$) to afford $\text{Me}_2\text{Ge}(\text{CH}_2\text{Cl})_2$ in 60 % yield as a colorless liquid.

$^{13}\text{C}\{^1\text{H}\}$ NMR (600 MHz, CD_2Cl_2): δ -5.61 (s, CH_3), 3.098 (s, CH_2) ppm. ^1H NMR (600 MHz, CD_2Cl_2): δ 0.429 (s, 6H, CH_3), 3.098 (s, 4H, CH_2) ppm.

Table S-3. Selected intramolecular distances [\AA] for complex **5a**.

Fe(1)···S(2)	6.923	Fe(3)···S(1)	4.874
Fe(1)···S(4)	6.028	Fe(3)···S(3)	5.860
Fe(2)···S(2)	6.237	Fe(4)···S(1)	6.013
Fe(2)···S(4)	4.841	Fe(4)···S(3)	7.122
S(2)···S(4)	4.317		

The Tetranuclear Complex **5a**-VT ^1H NMR Study

A surprising observation is the presence of only a singlet in the room temperature ^1H NMR spectrum of **5a** for the CH_2 groups despite their nonequivalence. One possibility is that the *a* and *e* positions interconvert at room temperature. To test this possibility the ^1H NMR spectrum of **5a** in CD_2Cl_2 was measured at lowered temperatures. As the temperature is lowered, the singlet splits into two separate singlets of equal areas as expected for nonequivalent CH_2S . If the singlet observed at room temperature represents coalescence then there must be a special mechanism for interconversion of *a* and *e* in **5a**. It is known^[25] that ligand exchange initiated by nucleophiles in analogous systems occurs by an associative mechanism. Consequently, transannular attack by S might initiate isomerization. Alternatively, a coordinated molecular rearrangement (*a* to *e* and *e* to *a*) might affect equilibration. However, no low energy pathway for these processes could be found computationally. An alternative explanation is that there is dramatic dependence of the chemical shifts on temperature. That is, there is not coalescence at room temperature but coincidence of separate signals. To test this hypothesis the variable temperature NMR studies were conducted in CDCl_3 (to facilitate measurements at higher temperatures). The results in Figure S-4 show that in CDCl_3 there is a singlet at $T = 293\text{K}$ that gives rise to two singlets on cooling, similar to the results in CD_2Cl_2 , but on warming two peaks are observed. This unequivocally demonstrates that the observation of one peak is due to coincidental overlap of the temperature-dependent signals not interconversion of *a* and *e* substituents.

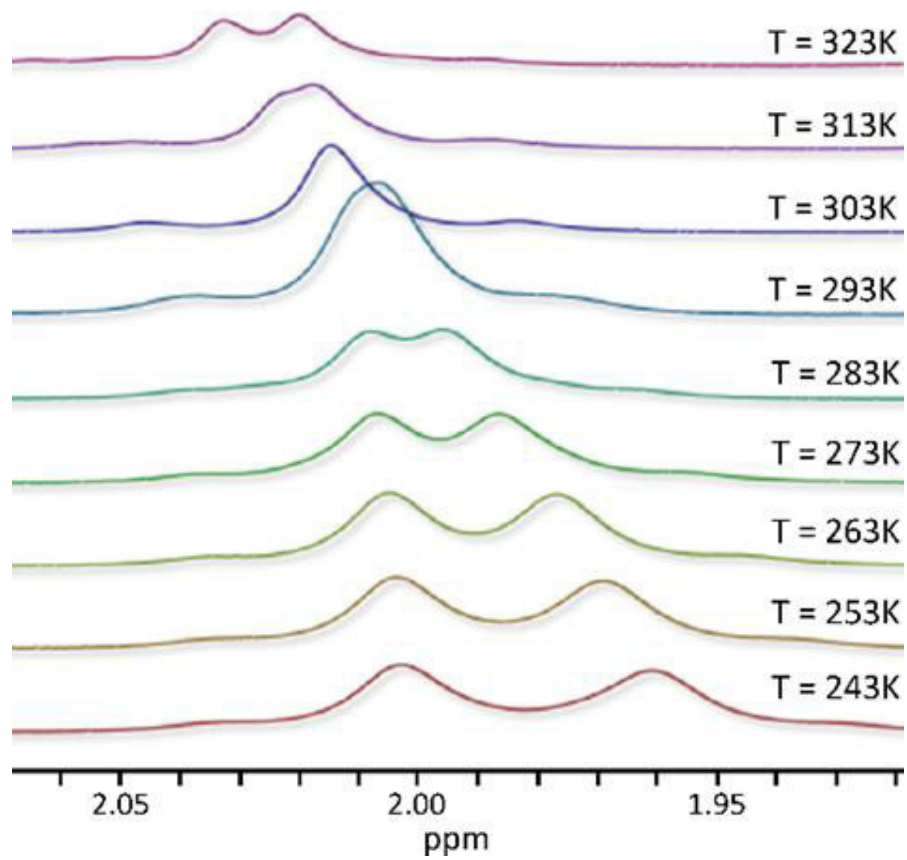


Figure S-4. Variable temperature ^1H NMR spectra of **5a** in CDCl_3 .

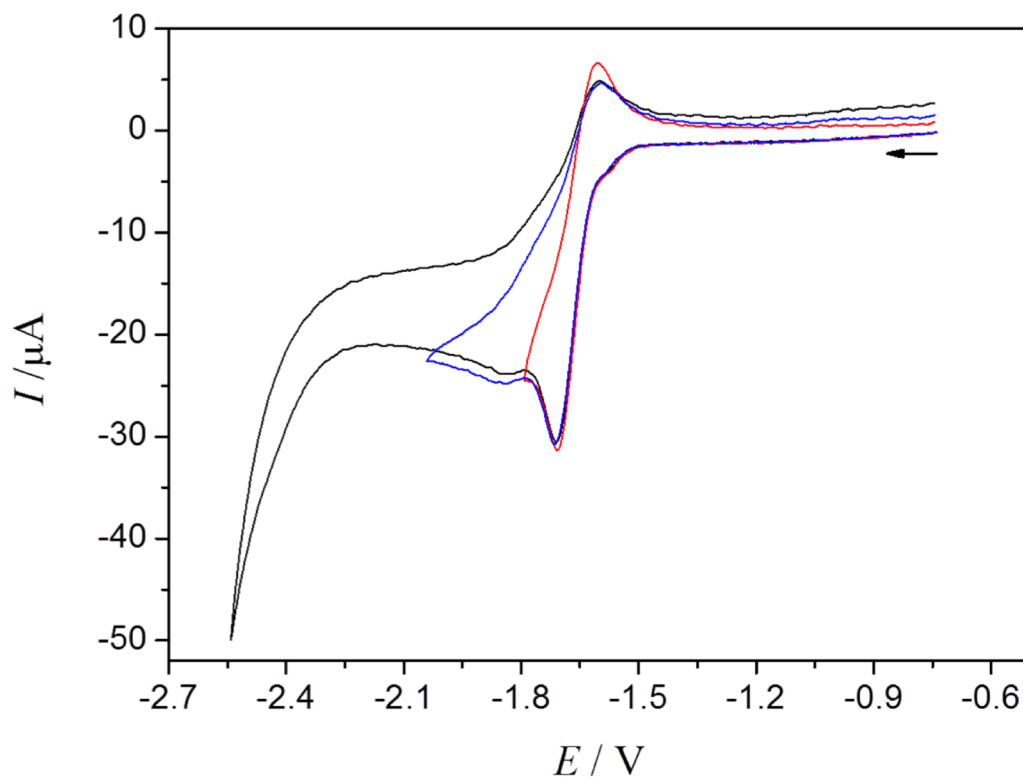


Figure S-5. Cyclic voltammetry of 0.65 mM complex **2** (CH_2Cl_2 -[$n\text{-Bu}_4\text{N}$][PF_6] solution) at $0.2 \text{ V}\cdot\text{s}^{-1}$. Glassy carbon electrode ($A = 0.072 \text{ cm}^2$). E is in V against the Fc^+/Fc couple. The arrow indicates the scan direction.

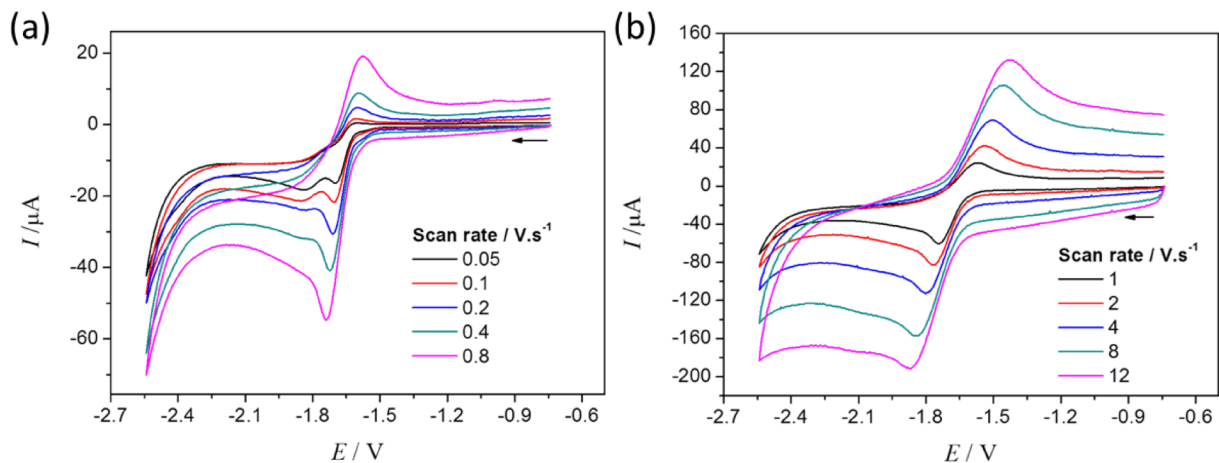


Figure S-6. Cyclic voltammetry of 0.65 mM complex **2** (CH_2Cl_2 -[n-Bu₄N][PF₆] solution) at 0.05-12 $\text{V}\cdot\text{s}^{-1}$. Glassy carbon electrode ($A = 0.072 \text{ cm}^2$). E is in V against the Fc^+/Fc couple. The arrow indicates the scan direction.

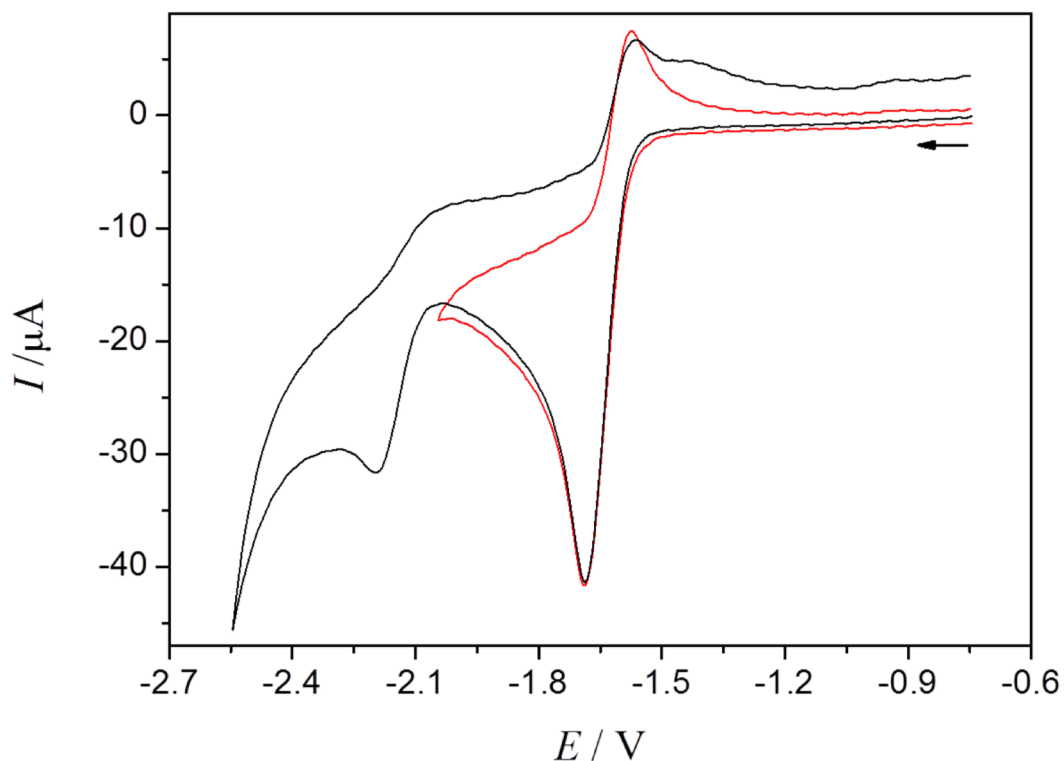


Figure S-7. Cyclic voltammetry of 0.84 mM complex **4a** (CH_2Cl_2 -[n-Bu₄N][PF₆] solution) at 0.2 $\text{V}\cdot\text{s}^{-1}$. Glassy carbon electrode ($A = 0.072 \text{ cm}^2$). E is in V against the Fc^+/Fc couple. The arrow indicates the scan direction.

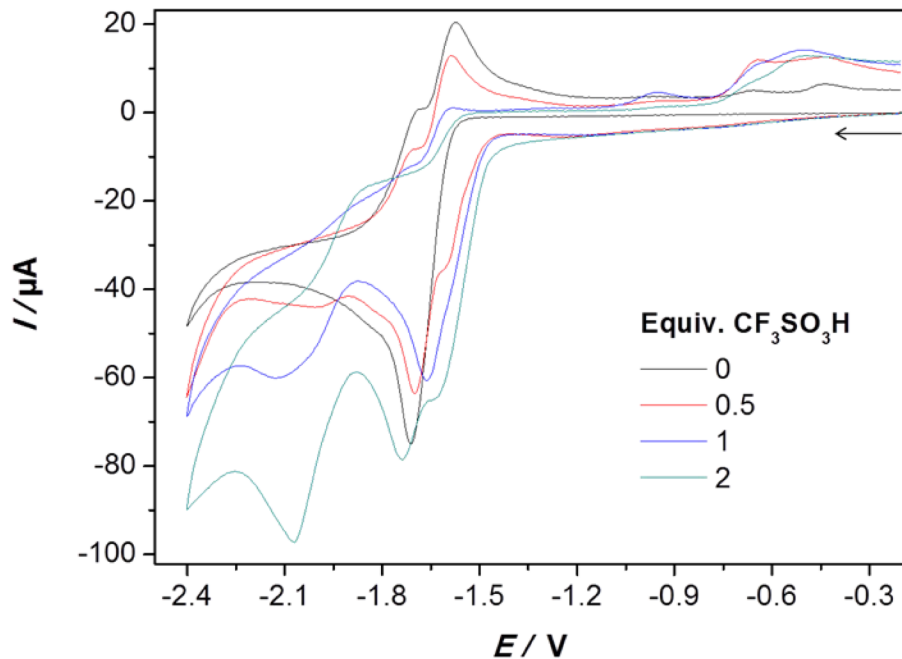


Figure S-8. Cyclic voltammetry of 1.01 mM complex **3** (CH_2Cl_2 -[n-Bu₄N][PF₆] solution) in the presence of 0.5-2 equiv. $\text{CF}_3\text{SO}_3\text{H}$ at $0.2 \text{ V}\cdot\text{s}^{-1}$. Glassy carbon electrode ($A = 0.072 \text{ cm}^2$). E is in V against the Fc^+/Fc couple. The arrow indicates the scan direction.

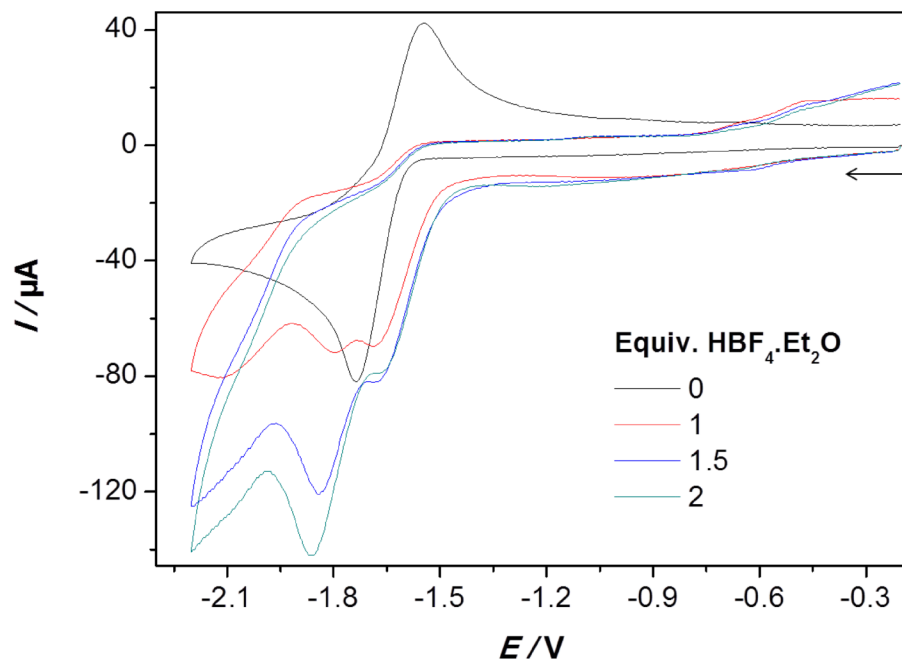


Figure S-9. Cyclic voltammetry of 0.843 mM complex **3** (CH_2Cl_2 -[$n\text{-Bu}_4\text{N}$][PF_6]) in the presence of 0-2 equiv. $\text{HBF}_4 \cdot \text{Et}_2\text{O}$ at $1 \text{ V} \cdot \text{s}^{-1}$. Glassy carbon electrode ($A = 0.072 \text{ cm}^2$). E is in V against the Fc^+/Fc couple. The arrow indicates the scan direction.

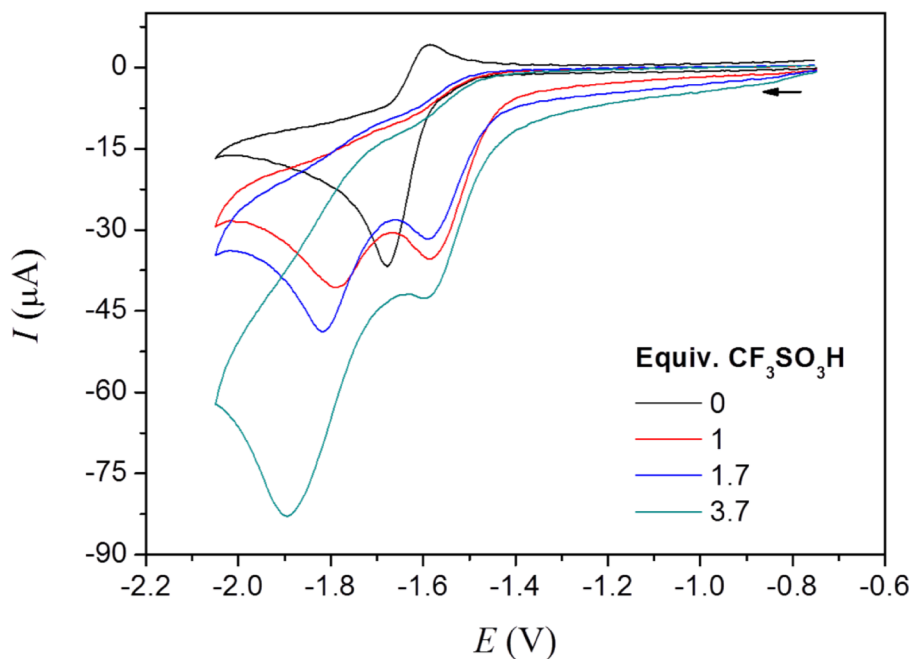


Figure S-10. Cyclic voltammetry of 0.843 mM complex **4a** (CH_2Cl_2 -[*n*-Bu₄N][PF₆]) in the presence of 0-3.7 equiv. $\text{CF}_3\text{SO}_3\text{H}$ at $0.2 \text{ V}\cdot\text{s}^{-1}$. Glassy carbon electrode ($A = 0.072 \text{ cm}^2$). E is in V against the Fc^+/Fc couple. The arrow indicates the scan direction.

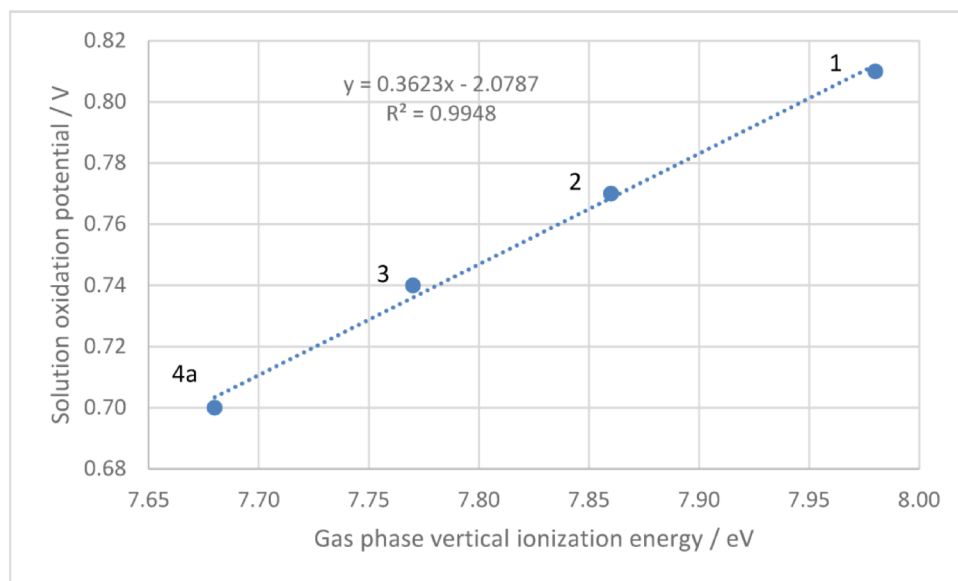


Figure S-11. Correlation of the solution oxidation potentials E_{ox1} (V vs. Fc^+/Fc) versus the computed gas-phase vertical ionization energies (eV).

Table S-4: Crystal data and refinement details for the X-ray structure determinations of the compounds **3** - **5b**.

Compound	3	4a	4b	5a	5b
formula	C ₁₀ H ₁₀ Fe ₂ GeO ₆ S ₂	C ₁₀ H ₁₀ Fe ₂ O ₆ S ₂ Sn	C ₂₀ H ₁₄ Fe ₂ O ₆ S ₂ Sn	C ₂₀ H ₂₀ Fe ₄ O ₁₂ S ₄ Sn ₂	C ₄₀ H ₂₈ Fe ₄ O ₁₂ S ₄ Sn ₂
fw (g·mol ⁻¹)	474.59	520.69	644.82	1041.38	1289.64
T/°C	-140(2)	-140(2)	-140(2)	-140(2)	-140(2)
crystal system	triclinic	triclinic	monoclinic	monoclinic	triclinic
space group	P $\bar{1}$	P $\bar{1}$	P 2 ₁ /n	P 2 ₁ /n	P $\bar{1}$
a/Å	9.0682(2)	9.1219(2)	13.6259(3)	13.1549(2)	8.6642(2)
b/Å	9.7623(3)	9.8783(3)	11.1499(2)	13.4408(2)	11.8378(3)
c/Å	10.3493(3)	10.3369(3)	15.6755(4)	18.6019(4)	13.0867(3)
α /°	62.871(1)	63.175(1)	90	90	116.501(1)
β /°	83.374(2)	83.661(2)	100.473(1)	90.483(1)	104.012(1)
γ /°	88.509(1)	87.631(2)	90	90	95.472(2)
V/Å ³	809.58(4)	826.09(4)	2341.86(9)	3288.93(10)	1133.03(5)
Z	2	2	4	4	1
ρ (g·cm ⁻³)	1.947	2.093	1.829	2.103	1.890
μ (cm ⁻¹)	38.89	35.03	24.92	35.2	25.75
measured data	5247	5188	13574	19757	7028
data with I > 2 σ (I)	3460	3521	4506	6654	4801
unique data (R _{int})	3625/0.0176	3741/0.0159	5351/0.0422	7530/0.0295	5117/0.0175
wR ₂ (all data, on F ²) ^{a)}	0.0556	0.0587	0.0713	0.0561	0.0601
R ₁ (I > 2 σ (I)) ^{a)}	0.0244	0.0260	0.0365	0.0271	0.0262
S ^{b)}	1.068	1.117	1.083	1.121	1.090
Res. dens./e·Å ⁻³	1.206/-0.603	0.468/-0.424	0.531/-0.483	0.737/-0.599	0.601/-0.594
absorpt method	multi-scan	multi-scan	multi-scan	multi-scan	multi-scan
absorpt corr T _{min} /max	0.7069/0.7456	0.6991/0.7456	0.7203/0.7456	0.6909/0.7456	0.6546/0.7456
CCDC No.	1432671	1432672	1432673	1432674	1432675

^{a)} Definition of the R indices: $R_1 = (\sum ||F_o| - |F_c||) / \sum |F_o|$;

$wR_2 = \{ \sum [w(F_o^2 - F_c^2)^2] / \sum [w(F_o^2)^2] \}^{1/2}$ with $w^{-1} = \sigma^2(F_o^2) + (aP)^2 + bP$; $P = [2F_c^2 + \text{Max}(F_o^2)]/3$;

^{b)} $S = \{ \sum [w(F_o^2 - F_c^2)^2] / (N_o - N_p) \}^{1/2}$.

REFERENCES

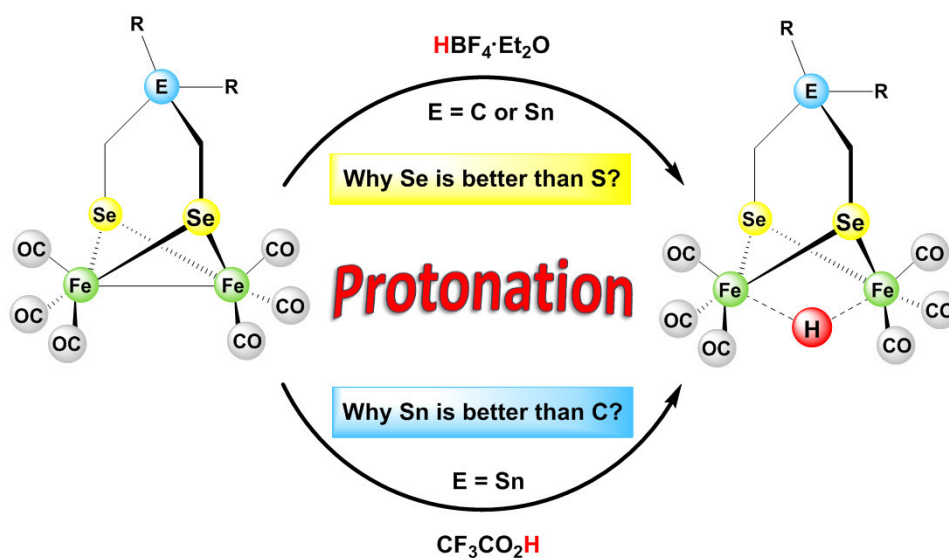
1. M. L. Singleton, R. M. Jenkins, C. L. Klemashevich, M. Y. Darensbourg, *C. R. Chem.* **2008**, *11*, 861-874
2. U.-P. Apfel, D. Troegel, Y. Halpin, S. Tschierli, U. Uhlemann, H. Görls, M. Schmitt, J. Popp, P. Dunne, M. Venkatesan, M. Coey, M. Rudolph, J. G. Vos, R. Tacke, W. Weigand, *Inorg. Chem.* **2010**, *49*, 10117-10132
3. G. Te Velde, F. M. Bickelhaupt, E. J. Baerends, C. Fonseca Guerra, S. J. A. Van Gisbergen, J. G. Snijders, T. Ziegler, *J. Comput. Chem.* **2001**, *22*, 931

4.2 [HAF-2]

Selenium Makes the Difference: Protonation of [FeFe]-Hydrogenase Mimics with Diselenolato Ligands

Hassan Abul-Futouh, Mohammad El-Khateeb, Helmar Görls, Khalil Jamil Asali, Wolfgang Weigand

Dalton Transactions **2017**, 46, 2937-2947.



Reproduced by permission of The Royal Society of Chemistry.

<http://pubs.rsc.org/en/content/articlelanding/2017/dt/c7dt00057j#!divAbstract>



Cite this: *Dalton Trans.*, 2017, **46**, 2937

Selenium makes the difference: protonation of [FeFe]-hydrogenase mimics with diselenolato ligands†‡

Hassan Abul-Futouh,^a Mohammad El-khateeb,^b Helmar Görls,^a Khalil Jamil Asali^b and Wolfgang Weigand*^a

The synthetic models of the active site of an [FeFe]-hydrogenase containing a Sn atom in the bridgehead of the diselenolato ligand, namely [Fe₂(CO)₆{μ-(SeCH₂Se)SnMe₂}], **3** and [Fe₂(CO)₆{μ-(SeCH₂)₂SnMe₂}], **4** have been synthesized and characterized by different spectroscopic methods. The protonation properties of complex **4** have been investigated by monitoring the IR spectra in the carbonyl stretching region, ¹H NMR in the hydride region as well as the ⁷⁷Se{H} NMR upon addition of strong and moderate acids wherein the protonation of the active site of the [FeFe]-hydrogenase at one of its internal basic sites is considered an essential step in the catalytic cycle. Furthermore, we investigated the redox properties and the catalytic behaviour of complexes **3** and **4** in the presence of AcOH as a source of protons suggesting an ECE (E = electrochemical process, C = chemical process) mechanism.

Received 6th January 2017,
Accepted 6th February 2017

DOI: 10.1039/c7dt00057j

rsc.li/dalton

Introduction

Hydrogen is considered one of the best environmentally benign alternatives “Green Alternatives” compared to the presently used fossil fuel due to its high energy density and its clean cold combustion product in fuel cells.^{1–4} In fact, the nature has high ability to catalyse the reversible process of proton reduction with high catalytic efficiency (*ca.* 10⁴ turnover per s)^{5,6} and this occurs through enzymes known as [FeFe]-hydrogenases. The active site of the latter contains an organo-metallic cluster, the so called H cluster, which consists of an [Fe₄S₄] cluster attached through a cysteinyl residue to a butterfly [Fe₂S₂] sub-cluster. This sub-cluster contains a bridging azadithiolato ligand (adt = [SCH₂NHCH₂S]) as well as biologically unusual CO and CN[−] ligands⁷ (Fig. 1a). Over the past few decades, numerous synthetic models which mimic the H cluster with the general formula [Fe₂(CO)₆{μ-(SCH₂)₂E}], in which the central atom/group E is NR,⁸ CR₂,^{8a,9} O,^{9d,10} S,¹¹

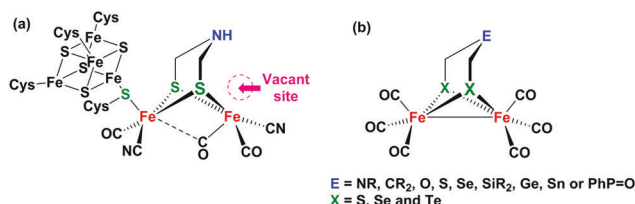


Fig. 1 (a) The active site of the [FeFe]-hydrogenase and (b) synthetic models of the active site of [FeFe]-hydrogenase.

Se,¹² SiR₂,¹³ Ge,^{14a} Sn¹⁴ or Ph-P=O¹⁵ have been reported (Fig. 1b) in order to provide a better understanding of the structure and function of the active site of the enzyme-mimic models. Moreover, these models have been extended to diiron complexes containing diselenolato and ditellurato ligands.¹⁶

One of the most important structural features of the synthetic H cluster mimics is the existence of an internal basic site that could be protonated in the presence of a Brønsted acid which is a crucial step in the catalytic cycle. Generally, protonation of the bimetallic hexacarbonyl complexes [Fe₂(CO)₆{μ-(XCH₂)₂E}] may take place at different sites (Fig. 2) based on the strength and amount of the acid added. In fact, protonation at the bridgehead atom/group in [Fe₂(CO)₆{μ-(SCH₂)₂E}] complexes has been reported only for E = NR or PhP=O using strong acids such as HBF₄·Et₂O, HOTf and HClO₄.^{15a,17} However, protonation at the μ-S is very difficult due to its low basicity. In addition, protonation of diiron dithiolato hexacarbonyl complexes at the Fe–Fe vector cannot be accomplished by acids

^aInstitut für Anorganische und Analytische Chemie, Friedrich-Schiller-Universität Jena, Humboldt Str. 8, 07743 Jena, Germany. E-mail: wolfgang.weigand@uni-jena.de

^bChemistry Department, Jordan University of Science and Technology, Irbid 22110, Jordan. E-mail: kateeb@just.edu.jo

†Dedicated to Professor Wolfgang Beck on the occasion of his 85th birthday, who prepared the first complex of the type [Fe(CO)₃SeR]₂; W. Hieber and W. Beck, *Z. Anorg. Allg. Chem.*, 1960, **305**, 265–273.

‡Electronic supplementary information (ESI) available. CCDC 1519067 and 1519068 for **3** and **4**, respectively. For ESI and crystallographic data in CIF or other electronic format see DOI: 10.1039/c7dt00057j

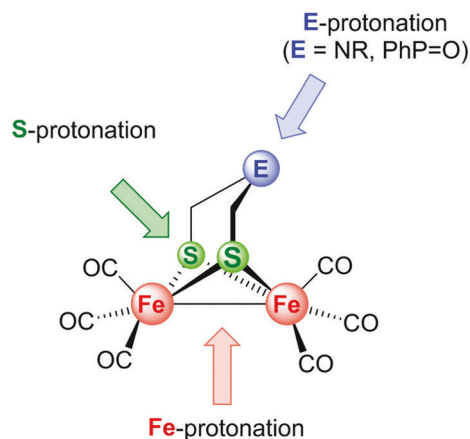


Fig. 2 Possible sites for protonation in $[\text{Fe}_2(\text{CO})_6\{\mu\text{-(SCH}_2)_2\text{E}]\}$ complexes.

weaker than or similar to $\text{HBF}_4\cdot\text{Et}_2\text{O}$ with the exception of the methods developed by Heinekey, Chiang and their co-workers to protonate $[\text{Fe}_2(\text{CO})_6\{\mu\text{-(xdt)}\}][\text{B}(\text{C}_6\text{F}_5)_4]$ (xdt = pdt (propane-dithiolato), edt (ethanedithiolato) and bdt (benzenedithiolato)) model complexes using HCl in the presence of the very strong Lewis acid $[\text{SiEt}_3][\text{B}(\text{C}_6\text{F}_5)_4]$.¹⁸ Moreover, a protonation study of diiron diselenolato hexacarbonyl complexes in acidic medium has not been previously reported. Therefore, it is significant to investigate diiron diselenolato hexacarbonyl complexes toward protonation in the presence of Brønsted acids.

Recently, the tendency to investigate the significant role of the selenium element in the biological processes becomes more attractive to researchers since the selenium element enhances the chemical reactivity of the enzymatic reactions compared with the sulfur analogues.¹⁹ It has also been reported that the incorporation of the selenium atom into the synthetic H cluster revealed more positive reduction potentials compared with those of their sulfur analogues despite increasing the electron density on the iron cores.^{16a,20–22} This could be explained in terms of reorganization and stabilization of the reduced species as has been previously reported by our group.^{16a,22} Presently, we have investigated the effect of the replacement of the central atom of the three-atom chain linker between the sulfur atoms by the series of group 14 atoms going from C to Sn on the electron richness of the $[\text{Fe}_2\text{S}_2]$ core.^{14a} We have illustrated that the electron density of the $[\text{Fe}_2\text{S}_2]$ core increases upon going from C to Sn in $[\text{Fe}_2(\text{CO})_6\{\mu\text{-(SCH}_2)_2\text{EMe}_2\}]\}$ (E = C, Si, Ge and Sn) model complexes. Having this in mind, we tried to investigate the influence of the presence of the Sn atom in the bridgehead linker with the replacement of the $\mu\text{-S}$ of diiron dithiolato models by $\mu\text{-Se}$ atoms. Herein we report the preparation and molecular structures of two novel models, $[\text{Fe}_2(\text{CO})_6\{\mu\text{-(SeCH}_2\text{Se)SnMe}_2\}]\}$, **3** and $[\text{Fe}_2(\text{CO})_6\{\mu\text{-(SeCH}_2)_2\text{SnMe}_2\}]\}$, **4** (Fig. 3). Besides, we have re-synthesized the known complexes **7–9** having the general formula $[\text{Fe}_2(\text{CO})_6\{\mu\text{-(X(CH}_2)_2\text{X}')\text{CR}_2\}]\}$ (X = Se, X' = S or Se and R = H or Me)^{16e,22} (Fig. 3) for comparison purposes. Thus, we

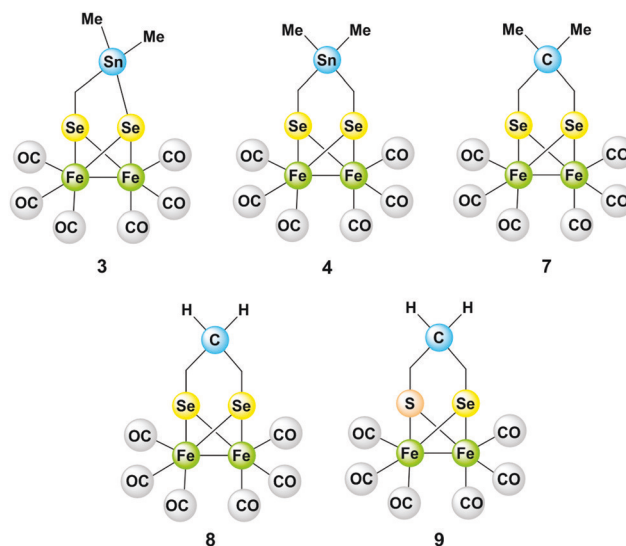


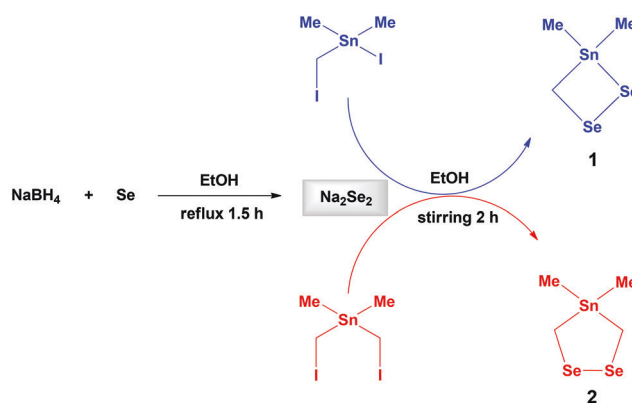
Fig. 3 Synthetic models of the active site of the $[\text{FeFe}]$ -hydrogenase used in this report.

have tested the protonation ability of complex **4** and that of complexes **7–9** in the presence of strong and moderate acids, respectively. In addition, the electrocatalytic behaviour of complexes **3** and **4** toward the reduction of protons exhibited by weak acids is reported.

Results and discussion

Synthesis and characterization of $\text{Me}_2\text{Sn}(\text{CH}_2\text{Se})\text{Se}$

The compound $\text{Me}_2\text{Sn}(\text{CH}_2\text{Se})\text{Se}$, **1**, was synthesized following a similar procedure reported for $\text{Me}_2\text{Sn}(\text{CH}_2\text{Se})_2$, **2** (Scheme 1).²³ The reaction of $\text{Me}_2\text{Sn}(\text{CH}_2\text{I})\text{I}$ ²⁴ with the *in situ* generated Na_2Se_2 afforded **1** as a light red oil (Scheme 1). Compound **1** was characterized by ^1H and $^{13}\text{C}\{\text{H}\}$ NMR spectroscopy and mass spectrometry. The ^1H NMR spectrum of complex **1** exhibits a singlet at 2.37 ppm with Se satellites ($^2J\{\text{Se-H}\} = 19.0$ Hz) for the CH_2 hydrogen atoms and a singlet



Scheme 1 Synthetic pathways of $\text{Me}_2\text{Sn}(\text{CH}_2\text{Se})\text{Se}$, **1** (in blue) and $\text{Me}_2\text{Sn}(\text{CH}_2\text{Se})_2$, **2** (in red).

at 0.68 ppm with Sn satellites ($^2J\{^{117}\text{Sn-H}\} = 54.6$ Hz and $^2J\{^{119}\text{Sn-H}\} = 57.0$ Hz) for the CH_3 hydrogen atoms. The $^{13}\text{C}\{\text{H}\}$ NMR spectrum shows a singlet at 8.95 ppm due to the methylene carbon and a singlet at -3.17 ppm due to the methyl carbons. In addition, the DEI-MS spectrum of **1** shows a molecular ion peak at $m/z = 321$.

Synthesis and characterization of complexes **3** and **4**

The treatment of equimolar amounts of $\text{Fe}_3(\text{CO})_{12}$ and $\text{Me}_2\text{Sn}(\text{CH}_2\text{Se})\text{Se}$, **1**, in THF at 65°C for two hours followed by subsequent column chromatography afforded $[\text{Fe}_2(\text{CO})_6\{\mu\text{-(SeCH}_2\text{Se)SnMe}_2\}]$, **3** and the known complex $[\text{Fe}_3\text{Se}_2(\text{CO})_9]^{25}$ (Scheme 2, in blue). Similarly, the reaction of $\text{Fe}_3(\text{CO})_{12}$ with $\text{Me}_2\text{Sn}(\text{CH}_2\text{Se})_2$, **2**, afforded $[\text{Fe}_2(\text{CO})_6\{\mu\text{-(SeCH}_2)_2\text{SnMe}_2\}]$, **4** and also the known complexes $[\text{Fe}_3\text{Se}_2(\text{CO})_9]^{25}$, **5**²⁶ and **6**²⁶ (Scheme 2, in red). The novel complexes **3** and **4** have been characterized by spectroscopic methods (^1H NMR, $^{13}\text{C}\{\text{H}\}$ NMR, $^{77}\text{Se}\{\text{H}\}$ NMR and IR), mass spectrometry, elemental analysis and X-ray crystallography.

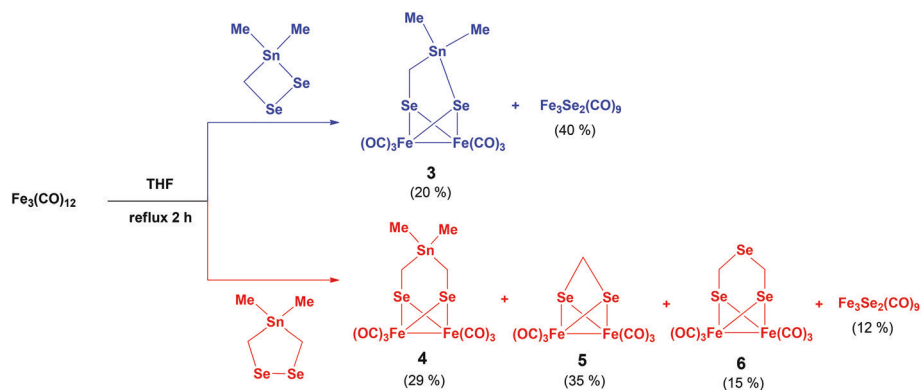
The ^1H NMR (CDCl_3) resonance signals for the SeCH_2 protons of complexes **3** and **4** appear at 2.08 ppm and 1.66 ppm with Sn satellites ($J\{\text{Sn-H}\} = 30.97$ Hz), respectively, while those for the CH_3 protons appear at 0.59 ppm ($J\{\text{Sn-H}\} = 55.8$ Hz) and 0.27 ppm ($J\{\text{Sn-H}\} = 54.4$ Hz) for complexes **3** and **4**, respectively. The $^{13}\text{C}\{\text{H}\}$ NMR spectra (CDCl_3) exhibit two resonances for each complex at 6.83 (CH_2) and -3.15 (CH_3) ppm for **3** and at -7.35 (CH_2) and -12.96 (CH_3) ppm for **4**. In addition, the carbonyl carbon atoms showed resonances at 209.82 ppm and 208.37 ppm for complexes **3** and **4**, respectively. The $^{77}\text{Se}\{\text{H}\}$ NMR (CDCl_3) spectrum of complex **3** displays two signals for the non-equivalent Se atoms at 429.40 ppm for SeCH_2Sn and -182.64 ppm for SeSnCH_2 , while that of **4** shows only one signal for the two chemically equivalent Se atoms at 226.70 ppm. The IR spectra of complexes **3** and **4** in CH_2Cl_2 are almost identical in terms of the number of peaks and frequencies. These complexes exhibit three absorption bands at 1985, 2019 and 2062 cm^{-1} for complex **3** and at 1985, 2025 and 2063 cm^{-1} for complex **4** for the terminal CO ligands. These CO stretching vibrations are generally shifted to slightly lower frequencies compared to those

obtained for the sulfur analogues.¹⁴ This could be explained in terms of increasing back-donation to CO due to the better electron donor ability of Se compared to that of S. Similar trends have previously been observed in comparing sulfur vs. selenium containing $[\text{FeFe}]$ -hydrogenase-mimics.^{21,27} The mass spectra of complexes **3** and **4** show the molecular ion peaks and the peaks resulted from dissociation of the six CO ligands, sequentially.

Molecular structures

Single crystals suitable for X-ray diffraction studies were obtained from a saturated solution of **3** and **4** in pentane at -24°C . The molecular structures of complexes **3** and **4** are shown in Fig. 4.

The geometry around each iron atom in complexes **3** and **4** can be best described as distorted square-pyramidal in which the central iron atom is surrounded by three CO ligands in a facial fashion and two bridging selenium atoms similar to the corresponding sulfur analogues, $[\text{Fe}_2(\text{CO})_6\{\mu\text{-(SCH}_2\text{S)SnMe}_2\}]$ and $[\text{Fe}_2(\text{CO})_6\{\mu\text{-(SCH}_2)_2\text{SnMe}_2\}]$.¹⁴ The bridgehead Sn atoms of the linker $\mu\text{-(SeCH}_2\text{Se)SnMe}_2$ in complex **3** as well as the linker $\mu\text{-(SeCH}_2)_2\text{SnMe}_2$ in complex **4** have a distorted tetrahedral structure. The Sn–C–Se bond angles ($112.67(13)^\circ$ of complex **3** and the average Sn–C–Se bond angles ($122.10(15)^\circ$ of complex **4** deviate from ($112.29(4)^\circ$ in $[\text{Fe}_2(\text{CO})_6\{\mu\text{-(SCH}_2\text{S)SnMe}_2\}]$ and ($121.96(16)^\circ$ in $[\text{Fe}_2(\text{CO})_6\{\mu\text{-(SCH}_2)_2\text{SnMe}_2\}]$ of the sulfur containing systems.¹⁴ The Fe–Fe bond lengths in **3** ($2.5419(6)$ Å) and in **4** ($2.5634(5)$ Å) are slightly longer than those of $[\text{Fe}_2(\text{CO})_6\{\mu\text{-(SCH}_2\text{S)SnMe}_2\}]$ ($2.5242(18)$ Å) and of $[\text{Fe}_2(\text{CO})_6\{\mu\text{-(SCH}_2)_2\text{SnMe}_2\}]$ ($2.5158(7)$ Å).¹⁴ This elongation of the Fe–Fe bond could be attributed to the larger size of Se compared to that of the S atom. The average Fe–CO bond length ($1.793(3)$ Å and $1.796(3)$ Å) for complexes **3** and **4**, respectively, are slightly shorter than the corresponding sulfur analogues, ($1.796(10)$ Å) for $[\text{Fe}_2(\text{CO})_6\{\mu\text{-(SCH}_2\text{S)SnMe}_2\}]$ and ($1.802(3)$ Å) for $[\text{Fe}_2(\text{CO})_6\{\mu\text{-(SCH}_2)_2\text{SnMe}_2\}]$ ¹⁴ due to the more metal to CO back donation ability of Se containing complexes in comparison to the S ones. This observation is supported by the lower carbonyl frequencies in the IR spectra of **3** and **4**. Moreover, the flap angle α formed from the intersection



Scheme 2 Synthetic pathways of $[\text{Fe}_2(\text{CO})_6\{\mu\text{-(SeCH}_2\text{Se)SnMe}_2\}]$, **3** (blue) and $[\text{Fe}_2(\text{CO})_6\{\mu\text{-(SeCH}_2)_2\text{SnMe}_2\}]$, **4** (red).

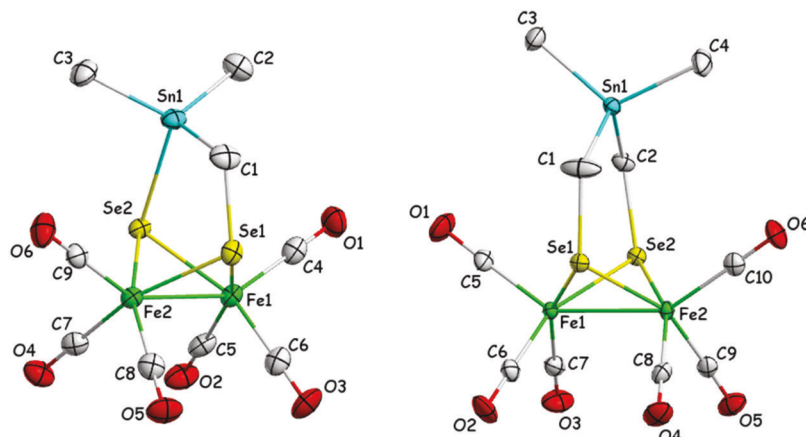


Fig. 4 Molecular structures (50% probability) of complex **3** (left) and complex **4** (right). Hydrogen atoms are omitted for clarity.

between the C_2Sn and Se_2C_2 planes of **4** is 166.24° which reflects the distortion of the diselenolate ligand from planarity compared to the corresponding sulfur analogues ($\alpha = 173.60^\circ$).^{14a} Furthermore, the torsion angle τ formed from the intersection between $CO_{ap}-Fe_1-Fe_2$ and $CO_{ap}-Fe_2-Fe_1$ of **4** is 4.51° which is slightly less distorted from the eclipsed $Fe(CO)_3$ conformation compared to the sulfur analogue ($\tau = 5.15^\circ$).^{14a}

Protonation study

In order to investigate the ability of complex **4** toward protonation, excess protic acid ($HBf_4 \cdot Et_2O$, 100 equiv.) was added to a solution of complex **4** in CH_2Cl_2 at room temperature (Scheme 3). The resulting solution was characterized by spectroscopic methods.

The IR spectrum of complex **4** with $HBf_4 \cdot Et_2O$ (100 equiv.) in CH_2Cl_2 shows a decrease in the intensity of the CO stretching bands concomitantly with the appearance of new bands at higher wavenumbers (2097 and 2119 cm^{-1}). This shift ($\Delta\nu(CO) \sim 84 \text{ cm}^{-1}$) to a higher energy is comparable to those reported in the literature¹⁸ which implies the formation of a bridging hydride, $\{Fe(\mu-H)Fe\}$. This is supported by the high-field 1H NMR (CD_2Cl_2) signal at -14.20 ppm which is assigned to the bridging hydride of $4\mu H^+$ (Fig. 5b) which is similar to those reported in the literature.¹⁸ In addition, the original resonance signals for the methylene and methyl protons are van-

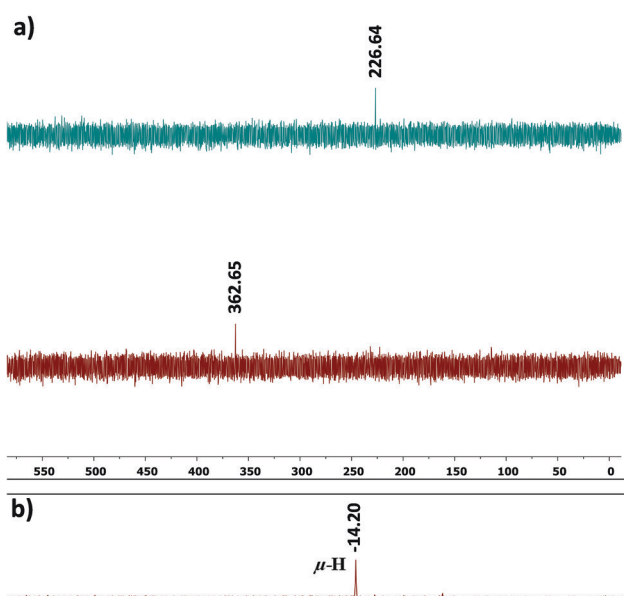
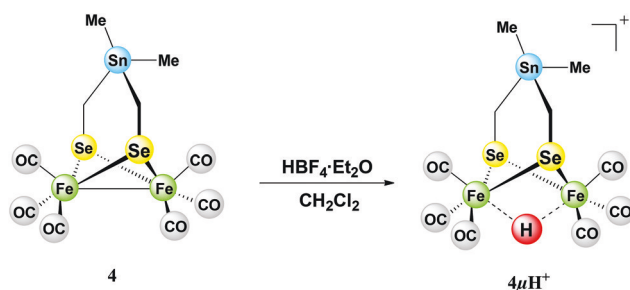


Fig. 5 (a) $^{77}Se\{H\}$ NMR spectra (CD_2Cl_2) of complex **4** before the addition of acid (blue) and after the addition of 100 equiv. of $HBf_4 \cdot Et_2O$ (red). (b) High field 1H NMR spectrum of complex **4** with 100 equiv. of $HBf_4 \cdot Et_2O$.



Scheme 3 Reaction scheme for the protonation process involving complex **4** with $HBf_4 \cdot Et_2O$ (100 equiv.).

ished and new peaks appear at 2.29 ppm with Sn satellites ($J\{Sn-H\} = 30.44$ Hz) and 0.51 ppm with Sn satellites ($J\{Sn-H\} = 59.38$ Hz) which shifted (0.61 ppm and 0.27 ppm, respectively) to a lower field (Fig. S1, ESI ‡). The $^{77}Se\{H\}$ NMR spectrum (CD_2Cl_2) of complex **4** in the presence of $HBf_4 \cdot Et_2O$ shows the disappearance of the original signal at 226.64 ppm and the appearance of a new signal at 362.65 ppm for the corresponding μ -hydride model complex, $4\mu H^+$ (also determined by $^1H\{^{77}Se\}$ HMBC NMR spectroscopy, Fig. S2, ESI ‡) shifted by about 136 ppm to the lower field compared with the parent complex (Fig. 5a). Indeed, these shifts in the $^{77}Se\{H\}$ and 1H NMR along with the appearance of the μ -hydride signal suggest strong evidence for the formation of the

μ -hydride between the two iron cores, an observation which is reported for the first time, using $\text{HBF}_4 \cdot \text{Et}_2\text{O}$ as a source of protons in a hexacarbonyl complex. So, the questions that arise now are: (i) Does the replacement of the diiron bridging S atoms by Se atoms enhance the protonation process? Or (ii) does the presence of the Sn atom in the bridgehead with the bridging Se atoms enrich the electron density on the iron cores?

In order to answer these questions, we firstly re-synthesized the diiron bridging Se model complexes **7** and **8** and the diiron bridging mixed S and Se model complex **9** (Fig. 3) following the same procedures reported in the literature.^{16e,22} These models having the general formula $[\text{Fe}_2(\text{CO})_6\{\mu\text{-}(\text{X}(\text{CH}_2)_2\text{X}')\text{CR}_2\}]$ ($\text{X} = \text{Se}$, $\text{X}' = \text{S}$ or Se and $\text{R} = \text{H}$ or Me); in which a bridgehead Sn atom has been replaced by a C atom to see whether or not these model complexes could be protonated in the presence of $\mu\text{-Se}$ or $\mu\text{-SSe}$ by itself. Surprisingly, we have found that the addition of excess $\text{HBF}_4 \cdot \text{Et}_2\text{O}$ (100 equiv.) to a solution of complexes **7–9** in CH_2Cl_2 at room temperature afforded the corresponding μ -hydride $[\text{Fe}_2(\mu\text{-H})(\text{CO})_6\{\mu\text{-}(\text{X}(\text{CH}_2)_2\text{X}')\text{CR}_2\}]^+$ model complexes, $7\mu\text{H}^+$, $8\mu\text{H}^+$ and $9\mu\text{H}^+$, which are confirmed by spectroscopic methods (see Table 1). The high-field ^1H NMR (CD_2Cl_2) signals at -15.33 , -15.09 and -15.15 ppm were assigned to the bridging hydride in $7\mu\text{H}^+$, $8\mu\text{H}^+$ and $9\mu\text{H}^+$, respectively (Fig. S3, ESI ‡). The $^{77}\text{Se}\{\text{H}\}$ NMR spectra (CD_2Cl_2) of complexes **7–9** in the presence of $\text{HBF}_4 \cdot \text{Et}_2\text{O}$ show the appearance of new signals at 165.01, 197.31 and 190.05 ppm for the corresponding μ -hydride complexes $7\mu\text{H}^+$, $8\mu\text{H}^+$ and $9\mu\text{H}^+$, respectively. These signals for $7\mu\text{H}^+$, $8\mu\text{H}^+$ and $9\mu\text{H}^+$ are shifted by ~ 86 , ~ 52 and ~ 56 ppm, respectively, to the lower field compared to those of the parent models (see Table 1). This result is in contrast to the corresponding sulfur analogues, which are not basic enough to be protonated by using excess $\text{HBF}_4 \cdot \text{Et}_2\text{O}$ as reported in the literature.¹⁸ Thus, replacement of at least one S atom in the diiron dithiolato complexes with the Se atom is enough to make the complexes basic enough to be protonated by a strong acid such as $\text{HBF}_4 \cdot \text{Et}_2\text{O}$. Thus and up to this stage, we only answered the first inquiry regarding the replacement of the chalcogen atoms. To answer the second inquiry regarding the effect of the bridgehead Sn atom, a protonation study on complex **4** and complexes **7–9** employing a moderate strength acid, $\text{CF}_3\text{CO}_2\text{H}$ has been carried out. As a result of this, no

protonation is observed when complexes **7–9** are treated with excess $\text{CF}_3\text{CO}_2\text{H}$ (100 equiv.) in CH_2Cl_2 solution, whereas complex **4** could be protonated when treated with 100 equiv. of $\text{CF}_3\text{CO}_2\text{H}$. The previous observation was deduced from the spectrum of the ^1H NMR which shows a small peak in the area of the μ -hydride at -14.26 ppm and the appearance of new proton resonance peaks of the methylene and methyl moieties at 2.33 and 0.59 ppm, respectively, which is similar to those observed in the case of $\text{HBF}_4 \cdot \text{Et}_2\text{O}$ addition to this complex (Fig. S4, ESI ‡). Moreover, the $^{77}\text{Se}\{\text{H}\}$ NMR spectrum shows the appearance of a new peak at 237.77 ppm (Fig. S4, ESI ‡). In fact, the signals of the parent complex are still present in the ^1H and $^{77}\text{Se}\{\text{H}\}$ NMR spectra which indicate that complex **4** could be only partially protonated by using a moderate acid such as $\text{CF}_3\text{CO}_2\text{H}$ (Fig. S4, ESI ‡). Regarding this, we would suggest that the presence of the Sn atom in the bridgehead together with the $\mu\text{-Se}$ in diiron models enhances the basicity of the iron cores to be protonated across the Fe–Fe vector by using moderate and strong acids. This phenomenon is in contrast to the presence of C atoms at the bridgehead of complexes **7–9**, which are basic enough to react at least with a strong acid due to the absence of the Sn atom in the bridgehead.

Electrochemistry

The electrochemical behaviour of **3** and **4** was investigated by cyclic voltammetry (CVs) as well as that of $[\text{Fe}_2(\text{CO})_6\{\mu\text{-}(\text{SCH}_2)_2\text{SnMe}_2\}]$, for comparison purposes. Fig. 6 shows the cyclic voltammetric reduction of complexes **3** and **4** in CH_2Cl_2 - $[n\text{-Bu}_4\text{N}][\text{BF}_4]$ solutions at a scan rate of 0.2 V s^{-1} .

The cyclic voltammogram of complex **3** at a scan rate of 0.2 V s^{-1} (Fig. 6a) displays a quasi-reversible cathodic peak at $E_{1/2} = -1.64 \text{ V}$ ($E_{\text{pc}} = -1.75 \text{ V}$, $E_{\text{pa}} = -1.53 \text{ V}$), whereas complex **4** displays two reduction waves at $E_{\text{pc}} = -1.63 \text{ V}$ (peak I) and -2.13 V (peak II) under the same conditions (Fig. 6b). Reversing the forward scan of complex **4** at -1.63 V (Fig. 6b: inset red curve) does not enhance the reversibility of the first reduction process, while increasing the scan rates of complexes **3** and **4** up to 6 V s^{-1} results in no wave-splitting for the primary reduction peaks of **3** and **4** (Fig. 7a and b). However, the reversibility of the first reduction wave, (peak I), of **4** was improved along with the disappearance of the second reduction wave, (peak II) (Fig. 7b). This observation can be readily explained in

Table 1 Summary of the ^1H and $^{77}\text{Se}\{\text{H}\}$ NMR data of complexes **4**, **7**, **8** and **9** in the absence and presence of $\text{HBF}_4 \cdot \text{Et}_2\text{O}$

Complex	Without acid		With acid			Δ^a	
	$^{77}\text{Se}\{\text{H}\}$ (ppm)	$^1\text{H}^b$ (ppm)	$^{77}\text{Se}\{\text{H}\}$ (ppm)	$^1\text{H}^b$ (ppm)	^1H ($\mu\text{-H}$) (ppm)	$^{77}\text{Se}\{\text{H}\}$ (ppm)	^1H (ppm)
4	226.64	1.68/0.24	362.65	2.29/0.51	-14.20	~ 136	0.61/0.27
7	79.05	2.15/0.93	165.01	2.84/1.2	-15.33	~ 86	0.69/0.27
8	145.46	2.22/1.62	197.31	2.96/2.04	-15.09	~ 52	0.74/0.42
9^c	133.77	2.14, 2.23 and 1.74	190.05	2.71, 2.95 and 2.16	-15.15	~ 56	0.57, 0.72 and 0.42

^a Δ is the difference in the chemical shift in the ^1H and $^{77}\text{Se}\{\text{H}\}$ NMR data. ^b ^1H NMR for the CH_2/CH_3 moieties respectively. ^c Complex **9** has only CH_2 moieties.

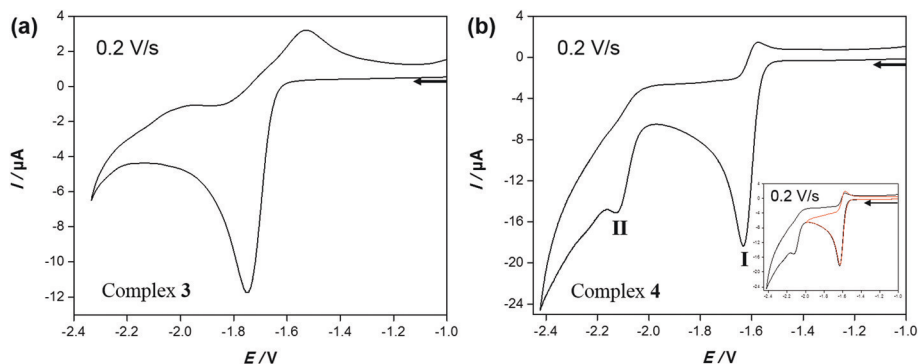


Fig. 6 Cyclic voltammetry of (a) 0.87 mM complex **3** and (b) 1.0 mM complex **4** in CH_2Cl_2 - $[\text{n-Bu}_4\text{N}][\text{BF}_4]$ (0.1 M) solutions at 0.2 V s^{-1} scan rate. The inset in (b) shows the reverse scan of peak (I). The arrows indicate the scan direction. The potentials E are given in V and referenced to the Fc^+/Fc couple.

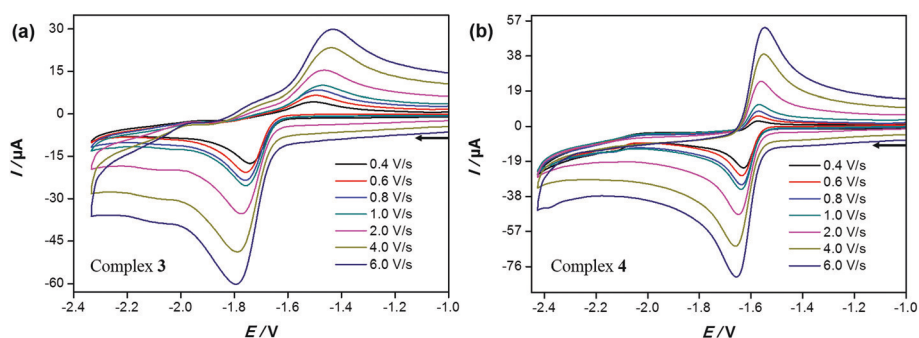


Fig. 7 Cyclic voltammetry of (a) 0.87 mM complex **3** and (b) 1.0 mM complex **4** in CH_2Cl_2 - $[\text{n-Bu}_4\text{N}][\text{BF}_4]$ (0.1 M) solutions at various scan rates. The arrows indicate the scan direction. The potentials E are given in V and referenced to the Fc^+/Fc couple.

terms of the irreversible follow-up reaction which occurs after the first reduction process that forms side products as previously found for hexacarbonyl complexes reported in the literature.²⁸ The reduction peaks of **3** ($E_{\text{pc}} = -1.75 \text{ V}$) and **4** ($E_{\text{pc}} = -1.63 \text{ V}$) are due to two-electron reduction in a single step based on the study of the current function, ($I_{\text{pc}}/c \cdot \nu^{1/2}$, c = concentration) of these complexes as seen from the height of the peaks compared to that of $[\text{Fe}_2(\text{CO})_6\{\mu\text{-(SCH}_2)_2\text{SnMe}_2\}]$ which is known to undergo an overall two-electron reduction with potential inversion.^{14a} In fact, such a study (current function) is known to provide mechanistic information regarding the number of electrons involved in the reduction process.²⁹

Fig. S5 in the ESI† shows that the current functions of complexes **3** and **4** decrease significantly as the scan rates increase suggesting the presence of an intervening chemical process during the electron transfer processes; *i.e.* ECE mechanism (E = electrochemical process, C = chemical process) assuming $D \approx 9 \times 10^{-6} \text{ cm}^2 \text{ s}^{-1}$.^{15a,16e} This behaviour is similar to that observed for hexacarbonyl model complexes reported in the literature.^{14a,16e,30} It can be noted that the reduction of complex **4** occurs at a less negative potential ($\sim 50 \text{ mV}$) compared to the corresponding sulfur analogue, $[\text{Fe}_2(\text{CO})_6\{\mu\text{-(SCH}_2)_2\text{SnMe}_2\}]$ (Fig. S6, ESI†). Generally, the higher the electron density of the iron cores, the more the negative reduction potential is

observed. This is in contrast to our results found for the selenium containing complex **4**. This could be explained in terms of reorganization and stabilization of the reduced species as previously reported.^{14a,22,16a-d}

Electrocatalysis

The electrochemical behaviour of **3** and **4** was investigated in the presence of various concentrations of acetic acid (AcOH). Upon initiating the electrochemical scan in the cathodic direction concomitantly with the addition of different equivalents of AcOH to a solution of complexes **3** and **4**, the primary cathodic peaks of complexes **3** and **4** show small shifts ($\sim 40 \text{ mV}$) to less negative potentials (Fig. 8), which is a typical observation when protonation of a reduced species takes place.^{16e,31} Moreover, it is evident from Fig. 8a that complex **3** shows catalytic behaviour through two processes: process I at $E_{\text{p}}^{\text{cat}} \approx -2.05 \text{ V}$ which levels off at $[\text{AcOH}] \approx 6 \text{ equiv.}$ and process II at $E_{\text{p}}^{\text{cat}} \approx -2.24 \text{ V}$, while complex **4** reveal a catalytic process at $E_{\text{p}}^{\text{cat}} \approx -2.20 \text{ V}$ (Fig. 8b). However, such catalytic behaviours are similar to those reported in the literature for other hexacarbonyl complexes.^{16e,31}

The reduction of 10 mM AcOH in CH_2Cl_2 - $[\text{n-Bu}_4\text{N}][\text{BF}_4]$ in the absence of models **3** and **4** starts near -2.55 V (Fig. S7, ESI†) which indicates that the increase in the current with the

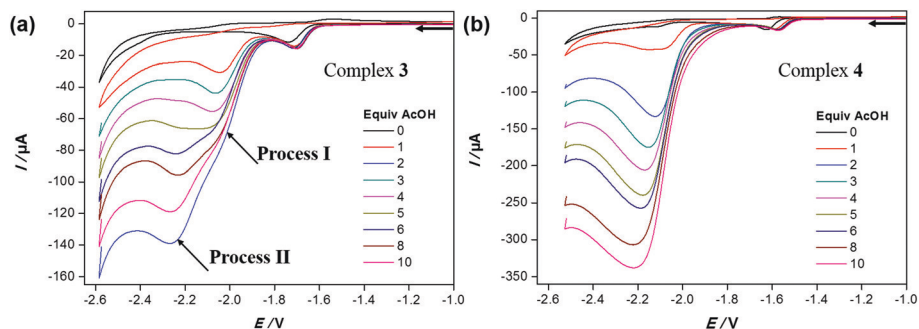
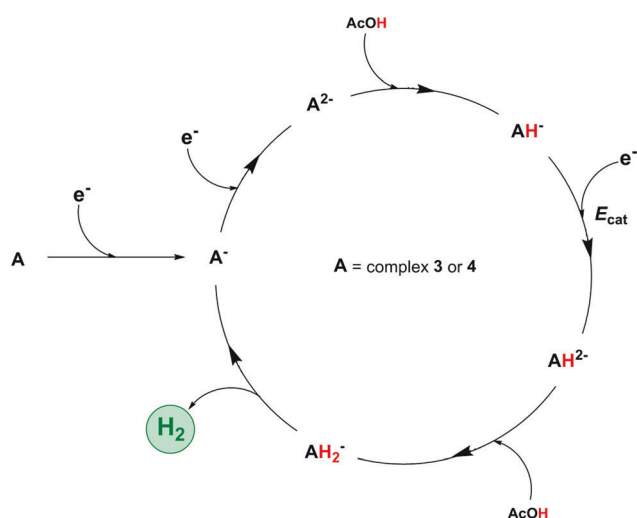


Fig. 8 Cyclic voltammetry of (a) 0.87 mM complex 3 and (b) 1.0 mM complex 4 in CH_2Cl_2 -[*n*-Bu₄N][BF₄] (0.1 M) solutions at 0.2 V s^{-1} in the presence of different concentrations of AcOH. The arrows indicate the scan direction. The potentials E are given in V and referenced to the Fc^+/Fc couple.



Scheme 4 Possible mechanism for the proton reduction cycle catalysed by complexes 3 and 4 in the presence of AcOH.

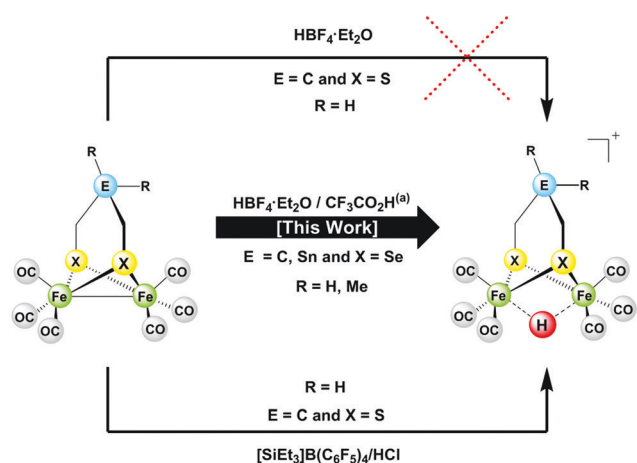


Fig. 9 Summary scheme for the protonation process involved in this report as well as the reported process in the literature.¹⁸ (a) In the case of $\text{CF}_3\text{CO}_2\text{H}$, it shows only partial protonation.

increasing AcOH concentration is due to catalytic processes as presented in Scheme 4 which summarizes the catalytic processes of complex 3 and complex 4.

Conclusions

In this report, two novel models $[\text{Fe}_2(\text{CO})_6\{\mu-(\text{SeCH}_2\text{Se})\text{SnMe}_2\}]$, 3 and $[\text{Fe}_2(\text{CO})_6\{\mu-(\text{SeCH}_2)_2\text{SnMe}_2\}]$, 4 have been synthesized and characterized by spectroscopic methods. Also we have investigated the influence of both the bridgehead atom and the bridging chalcogen atoms in determining the basicity properties of [FeFe]-complexes. We have found that the replacement of the μ -S atoms in the dithiolato linker by Se atoms enhances the electron density of the iron cores, which makes it more susceptible to be protonated across the Fe–Fe vector by using a strong acid such as $\text{HBF}_4 \cdot \text{Et}_2\text{O}$. Moreover, the replacement of the bridgehead carbon atom by the Sn atom in combination with the μ -Se moieties makes it possible for these complexes to be partially protonated employing a moderate acid such as $\text{CF}_3\text{CO}_2\text{H}$ (Fig. 9). In addition, the electrochemical behaviour of complexes 3 and 4 was investigated. Thus, it was concluded that both complexes 3 and 4 follow an ECE reduction mechanism. The proton reduction catalysed by complexes 3 and 4 was also investigated by cyclic voltammetry using acetic acid as a proton source.

Experimental part

Materials and techniques

All reactions were performed using standard Schlenk and vacuum-line techniques under an inert gas (nitrogen). The ^1H , $^{13}\text{C}\{^1\text{H}\}$, $^{77}\text{Se}\{^1\text{H}\}$ and $^1\text{H} \ ^{77}\text{Se}$ HMBC NMR spectra were recorded with a Bruker Avance 400 or 600 MHz spectrometer. Chemical shifts are given in parts per million with references to internal SiMe_4 (^1H , ^{13}C) or to Me_2Se (^{77}Se , $^1\text{H} \ ^{77}\text{Se}$ HMBC). The mass spectrum was recorded with Finnigan MAT SSQ 710 instrument. The IR spectra were recorded with a Bruker Equinox 55 spectrometer equipped with an ATR unit.

Elemental analysis was performed with a Leco CHNS-932 apparatus. TLC was performed by using Merck TLC aluminum sheets (silica gel 60 F254). Solvents from Fisher Scientific and other chemicals from Acros and Aldrich were used without further purification. All solvents were dried and distilled prior to use according to standard methods. $\text{Me}_2\text{Sn}(\text{CH}_2\text{I})\text{I}$,²⁴ $\text{Me}_2\text{Sn}(\text{CH}_2\text{I})_2$,²³ compound **2**²³ as well as complexes **7**,^{16e} **8**,^{16e} **9**²² and $[\text{Fe}_2(\text{CO})_6\{\mu\text{-(SCH}_2)_2\text{SnMe}_2\}]^{14a}$ were synthesized according to the known literature methods.

Electrochemistry

Corrections for the *iR* drop were performed for all experiments. Cyclic voltammetric measurements were conducted in a three-electrode system [glassy carbon disk (diameter *d* = 1.6 mm) as a working electrode, Ag/Ag⁺ in MeCN as a reference electrode, and Pt wire as a counter electrode] using a Reference 600 Potentiostat (Gamry Instruments). All experiments were performed in CH_2Cl_2 solutions (concentration of the complexes: 1.0 mM except complex **3**, 0.87 mM) containing 0.1 M [*n*-Bu₄N][BF₄] at room temperature. The solutions were purged with N₂ and a stream of it was maintained over the solutions during the measurements. The vitreous carbon disk was polished on a felt tissue with alumina before each measurement. All potential values reported in this paper are referenced to the potential of the ferrocenium/ferrocene (Fc⁺/Fc) couple.

Crystal structure determination

The intensity data were collected on a Nonius KappaCCD diffractometer, using graphite-monochromated Mo-K_α radiation. Data were corrected for Lorentz and polarization effects; absorption was taken into account on a semi-empirical basis using multiple-scans.^{32–34} The structure was solved by direct methods (SHELXS³⁵) and refined by full-matrix least squares techniques against *F*_o.³³ (SHELXL-97³⁵). The hydrogen atoms bonded to the methylene carbon atom C1 of **3** and all hydrogen atoms of **4** were located by difference Fourier synthesis and refined isotropically. All other hydrogen atom positions were included at the calculated positions with fixed thermal parameters. MERCURY³⁶ was used for structure representations.

Crystal data for 3: C₉H₈Fe₂O₆Se₂Sn, *M*_r = 600.46 g mol⁻¹, red-brown prism, size 0.042 × 0.038 × 0.022 mm³, monoclinic, space group *P*2₁/*c*, *a* = 7.5890(2), *b* = 11.1312(2), *c* = 19.3376(4) Å, β = 100.731(1)°, *V* = 1604.97(6) Å³, *T* = -140 °C, *Z* = 4, ρ_{calcd} = 2.485 g cm⁻³, μ (Mo-K_α) = 78.79 cm⁻¹, multi-scan, *trans*_{min}: 0.5246, *trans*_{max}: 0.7456, *F*(000) = 1120, 12 633 reflections in *h*(-9/9), *k*(-14/13), *l*(-25/25), measured in the range 2.12° ≤ θ ≤ 27.55°, completeness θ_{max} = 99.5%, 3690 independent reflections, *R*_{int} = 0.0363, 3458 reflections with *F*_o > 4σ(*F*_o), 191 parameters, 0 restraints, *R*_{1 obs} = 0.0211, *wR*_{2 obs} = 0.0462, *R*_{1 all} = 0.0240, *wR*_{2 all} = 0.0480, GOOF = 1.110, largest difference peak and hole: 0.482/-0.675 e Å⁻³.

Crystal data for 4: C₁₀H₁₀Fe₂O₆Se₂Sn, *M*_r = 614.49 g mol⁻¹, red-brown prism, size 0.098 × 0.090 × 0.078 mm³, triclinic, space group *P*1̄, *a* = 9.1082(2), *b* = 9.9385(2), *c* = 10.4292(2) Å, α = 64.181(1), β = 84.863(1), γ = 88.364(2)°, *V* = 846.36(3) Å³, *T* =

-140 °C, *Z* = 2, ρ_{calcd} = 2.411 g cm⁻³, μ (Mo-K_α) = 74.73 cm⁻¹, multi-scan, *trans*_{min}: 0.5626, *trans*_{max}: 0.7456, *F*(000) = 576, 5909 reflections in *h*(-11/10), *k*(-12/12), *l*(-13/13), measured in the range 2.18° ≤ θ ≤ 27.10°, completeness θ_{max} = 99.4%, 3711 independent reflections, *R*_{int} = 0.0199, 3589 reflections with *F*_o > 4σ(*F*_o), 230 parameters, 0 restraints, *R*_{1 obs} = 0.0186, *wR*_{2 obs} = 0.0427, *R*_{1 all} = 0.0196, *wR*_{2 all} = 0.0433, GOOF = 1.096, largest difference peak and hole: 0.475/-0.758 e Å⁻³.

Synthesis of Me₂Sn(CH₂Se)Se (1)

A mixture of NaBH₄ (91 mg, 2.39 mmol) and Se (284 mg, 3.59 mmol) was cooled down to 0 °C before the addition of 13 mL of ethanol. After the initial reaction had subsided, the mixture was stirred and heated at reflux for 1.5 h with N₂ passing into the liquid in order to dissolve the Se and eject H₂Se. The resulting deep-red ethanolic solution of Na₂Se₂ was cooled down again to 0 °C before the addition of Me₂Sn(CH₂I)I (500 mg, 1.20 mmol) dissolved in 3 mL ethanol. The ice-bath was removed and the mixture was stirred for 1 h at room temperature. The solution was poured into water (20 mL) and extracted with CH₂Cl₂ (2 × 20 mL). The extract was washed with water (4 × 20 mL), dried (Na₂SO₄) and concentrated *in vacuo*. The residue was introduced to column chromatography using 1 : 12 ethyl acetate : hexane to give compound **1** as a red oil (78% yield); ¹H NMR (400 MHz, CDCl₃): 0.68 (s, with Sn satellites, ²*J*{¹¹⁷Sn-H} = 54.6 Hz and ²*J*{¹¹⁹Sn-H} = 57.0 Hz, 6H, CH₃) δ = 2.37 (s, with ⁷⁷Se satellites, ²*J*{H-Se} = 19.0 Hz, 2H, SeCH₂). ¹³C{H} NMR (400 MHz, CDCl₃): δ = -3.17 (s, CH₃), 8.95 (s, CH₂). DEI-MS: *m/z* = 321, [Me₂Sn(CH₂Se)Se]⁺.

General procedure for the synthesis of [Fe₂(CO)₆{μ-(SeCH₂Se)SnMe₂}] (3) and [Fe₂(CO)₆{μ-(SeCH₂)₂SnMe₂}] (4)

A solution of Fe₃(CO)₁₂ (200 mg, 0.40 mmol) and compound **1** (127 mg, 0.40 mmol) or compound **2** (133 mg, 0.40 mmol) in THF (25 mL) was heated at reflux for 1 hour under N₂. The green solution turned deep-red and the solvent was removed under reduced pressure. The residue was purified by column chromatography using 100% pentane. A violet fraction representing the side product [Fe₃Se₂(CO)₉], the second light orange fraction containing complex **5**, the third red main fraction containing complexes **3** and **4** and the fourth orange fraction containing complex **6** were collected and the solvent was removed *in vacuo*. The products were obtained as red solids for complexes **3** and **4**. The spectroscopic data for complexes [Fe₃Se₂(CO)₉], **5** and **6** match those of the previously reported data in the literature.^{25,26}

[Fe₂(CO)₆{μ-(SeCH₂Se)SnMe₂}], **3**. Yield: 20% (50 mg, 0.08 mmol). Elemental analysis for C₉H₈Fe₂O₆Se₂Sn: calculated C 18.00, H 1.34; found C 18.19, H 1.24 IR (CH₂Cl₂): 1985, 2019, 2062 cm⁻¹. ¹H NMR (400 MHz, CDCl₃): δ = 0.59 ppm (s, with Sn satellites, ²*J*{H-Sn} = 55.80 Hz, 6H, CH₃), 2.08 ppm (s, with Sn satellites, ²*J*{H-Sn} = 30.97 Hz, 2H, SeCH₂). ¹³C{H} NMR (400 MHz, CDCl₃): δ = -3.15 ppm (s, CH₃), 6.83 ppm (s, CH₂), 209.82 (s, CO). ⁷⁷Se{H} NMR (400 MHz, CDCl₃): δ = -182.64 ppm (s, SeSnCH₂), 429.40 ppm (s, SeCH₂Sn). DEI-MS:

$m/z = 600 [M]^+$, $572 [M - CO]^+$, $544 [M - 2CO]^+$, $516 [M - 3CO]^+$, $488 [M - 4CO]^+$, $460 [M - 5CO]^+$, $432 [M - 6CO]^+$.

$[Fe_2(CO)_6\{\mu-(SeCH_2)_2SnMe_2\}]$, **4**. Yield: 29% (70 mg, 0.11 mmol). Elemental analysis for $C_{10}H_{10}Fe_2O_6Se_2Sn$: calculated C 19.55, H 1.64; found C 19.69, H 1.1.49. IR (CH_2Cl_2): 1985, 2025, 2063 cm^{-1} . 1H NMR (400 MHz, $CDCl_3$): $\delta = 0.27$ ppm (s, with Sn satellites, $^2J\{H-Sn\} = 54.40$ Hz, 6H, CH_3), 1.66 ppm (s, with Sn satellites, $^2J\{H-Sn\} = 30.97$ Hz, 4H, $SeCH_2$). $^{13}C\{H\}$ NMR (400 MHz, $CDCl_3$): $\delta = -12.96$ ppm (s, CH_3), -7.35 ppm (s, CH_2), 208.37 (s, CO). $^{77}Se\{H\}$ NMR (400 MHz, $CDCl_3$): $\delta = 226.70$ (s, $SeSnCH_2$). DEI-MS: $m/z = 614 [M]^+$, $586 [M - CO]^+$, $558 [M - 2CO]^+$, $530 [M - 3CO]^+$, $502 [M - 4CO]^+$, $474 [M - 5CO]^+$, $446 [M - 6CO]^+$.

Acknowledgements

H. Abul-Futouh thanks the Deutscher Akademischer Austausch Dienst (DAAD) for scholarship. K. J. Asali thanks the Jordan University of Science and Technology for a sabbatical leave.

Notes and references

- 1 Y. Nicolet, C. Cavazza and J. C. J. Fontecilla-Camps, *Inorg. Biochem.*, 2002, **91**, 1–8.
- 2 S. Shima, O. Pilak, S. Vogt, M. Schick, M. S. Stagni, W. M. Klauke, E. Warkentin, R. K. Thauer and U. Ermler, *Science*, 2008, **321**, 572–575.
- 3 T. Happe, A. Hemschemeier, M. Winkler and A. Kaminski, *Trends Plant Sci.*, 2002, **7**, 246–250.
- 4 M. Frey, *ChemBioChem*, 2002, **3**, 153–160.
- 5 M. W. Adams, *Biochim. Biophys. Acta*, 1990, **1020**, 115–145.
- 6 M. Frey, *ChemBioChem*, 2002, **3**, 153–160.
- 7 (a) A. Adamska, S. Roy, J. F. Siebel, T. R. Simmons, M. Fontecave, V. Artero, E. Reijerse and W. Lubitz, *J. Am. Chem. Soc.*, 2015, **137**, 12744–12747; (b) A. Adamska, A. Silakov, C. Lambert, O. Rüdiger, T. Happe, E. Reijerse and W. Lubitz, *Angew. Chem., Int. Ed.*, 2012, **124**, 11624–11629; (c) H.-J. Fan and M. B. Hall, *J. Am. Chem. Soc.*, 2001, **123**, 3828–3829; (d) J. W. Peters, W. N. Lanzilotta, B. J. Lemon and L. C. Seefeldt, *Science*, 1998, **282**, 1853–1858; (e) Y. Nicolet, A. L. de Lacey, X. Verne, V. M. Fernandez, E. C. Hatchikian and J. C. Fontecilla-Camps, *J. Am. Chem. Soc.*, 2001, **123**, 1596–1601.
- 8 (a) J. D. Lawrence, H. X. Li, T. B. Rauchfuss, M. Benard and M. M. Rohmer, *Angew. Chem., Int. Ed.*, 2001, **40**, 1768–1771; (b) J.-F. Capon, S. Ezzaher, F. Gloaguen, F. Y. Pétillon, P. Schollhammer, J. Talarmin, T. J. Davin, J. E. McGrady and K. W. Muir, *New J. Chem.*, 2007, **31**, 2052–2064; (c) F. Wang, M. Wang, X. Liu, K. Jin, W. Dong and L. Sun, *Dalton Trans.*, 2007, 3812–3819; (d) H.-G. Cui, M. Wang, W.-B. Dong, L.-L. Duan, P. Li and L.-C. Sun, *Polyhedron*, 2007, **26**, 904–910; (e) S. Jiang, J. Liu and L. Sun, *Inorg. Chem. Commun.*, 2006, **9**, 290–292; (f) Z. Wang, J.-H. Liu, C.-J. He, S. Jiang, B. Åkermark and L.-C. Sun, *J. Organomet. Chem.*, 2007, **692**, 5501–5507; (g) W.-G. Wang, H.-Y. Wang, G. Si, C.-H. Tung and L.-Z. Wu, *Dalton Trans.*, 2009, 2712–2720; (h) Y. Na, M. Wang, J. Pan, P. Zhang, B. Åkermark and L. Sun, *Inorg. Chem.*, 2008, **47**, 2805–2810; (i) Z. Wang, J. Liu, C. He, S. Jiang, B. Åkermark and L. Sun, *Inorg. Chim. Acta*, 2007, **360**, 2411–2419; (j) Y. Si, C. Ma, M. Hu, H. Chen, C. Chen and Q. Liu, *New J. Chem.*, 2007, **31**, 1448–1454; (k) L. Schwartz, G. Eilers, L. Eriksson, A. Gogoll, R. Lomoth and S. Ott, *Chem. Commun.*, 2006, 520–526; (l) G. Eilers, L. Schwartz, M. Stein, G. Zampella, L. de Gioia, S. Ott and R. Lomoth, *Chem. – Eur. J.*, 2007, **13**, 7075–7084; (m) J. Hou, X. Peng, J. Liu, Y. Gao, X. Zhao, S. Gao and K. Han, *Eur. J. Inorg. Chem.*, 2006, 4679–4686; (n) S. Ezzaher, P.-Y. Orain, J.-F. Capon, F. Gloaguen, F. Y. Pétillon, T. Roisnel, P. Schollhammer and J. Talarmin, *Chem. Commun.*, 2008, 2547–2549; (o) M. E. Carroll, B. E. Barton, T. B. Rauchfuss and P. J. Carroll, *J. Am. Chem. Soc.*, 2012, **134**, 18843–18852.
- 9 (a) R. Zaffaroni, T. B. Rauchfuss, D. L. Gray, L. De Gioia and G. Zampella, *J. Am. Chem. Soc.*, 2012, **134**, 19260–19269; (b) A. Winter, L. Zsolnai and G. Huttner, *Chem. Ber.*, 1982, **115**, 1286–1304; (c) A. Winter, L. Zsolnai and G. Huttner, *Z. Naturforsch., B: Anorg. Chem. Org. Chem.*, 1982, **37**, 1430–1436; (d) M. L. Singleton, R. M. Jenkins, C. L. Klemashevich and M. Y. Darensbourg, *C. R. Chim.*, 2008, **11**, 861–874; (e) B. E. Barton, M. T. Olsen and T. B. Rauchfuss, *J. Am. Chem. Soc.*, 2008, **130**, 16834–16835; (f) B. E. Barton and T. B. Rauchfuss, *Inorg. Chem.*, 2008, **47**, 2261–2263; (g) R. Trautwein, L. R. Almazahreh, H. Görls and W. Weigand, *Z. Anorg. Allg. Chem.*, 2013, **639**, 1512–1519.
- 10 (a) H. X. Li and T. B. Rauchfuss, *J. Am. Chem. Soc.*, 2002, **124**, 726–727; (b) L.-C. Song, Z.-Y. Yang, H.-Z. Bian, Y. Liu, H.-T. Wang, X.-F. Liu and Q.-M. Hu, *Organometallics*, 2005, **24**, 6126–6135.
- 11 (a) L.-C. Song, Z.-Y. Yang, Y.-J. Hua, H.-T. Wang, Y. Liu and Q.-M. Hu, *Organometallics*, 2007, **26**, 2106–2110; (b) J. Windhager, M. Rudolph, S. Brautigam, H. Görls and W. Weigand, *Eur. J. Inorg. Chem.*, 2007, 2748–2760; (c) L.-C. Song, A.-G. Zhu and Y.-Q. Guo, *Dalton Trans.*, 2016, 45, 5021–5029.
- 12 M. Harb, Ph.D. Dissertation, Friedrich-Schiller Universität Jena, Jena, Thüringen, 2009.
- 13 (a) R. Goy, L. Bertini, H. Görls, L. De Gioia, J. Talarmin, G. Zampella, P. Schollhammer and W. Weigand, *Chem. – Eur. J.*, 2015, **21**, 5061–5073; (b) U.-P. Apfel, D. Troegel, Y. Halpin, S. Tschierlei, U. Uhlemann, H. Görls, M. Schmitt, J. Popp, P. Dunne, M. Venkatesan, M. Coey, M. Rudolph, G. J. Vos, R. Tacke and W. Weigand, *Inorg. Chem.*, 2010, **49**, 10117–10132.
- 14 (a) H. Abul-Futouh, L. R. Almazahreh, T. Sakamoto, N. Y. T. Stessman, D. L. Lichtenberger, R. S. Glass, H. Görls, M. El-khateeb, P. Schollhammer, G. Mloston and W. Weigand, *Chem. – Eur. J.*, 2017, **23**, 346–359; (b) R. S. Glass, N. E. Gruhn, E. Lorange, M. S. Singh,

- N. Y. T. Stessman and U. I. Zakai, *Inorg. Chem.*, 2005, **44**, 5728–5737.
- 15 (a) L. R. Almazahreh, U.-P. Apfel, W. Imhof, M. Rudolph, H. Görls, J. Talarmin, P. Schollhammer, M. El-khateeb and W. Weigand, *Organometallics*, 2013, **32**, 4523–4530; (b) L. R. Almazahreh, W. Imhof, J. Talarmin, P. Schollhammer, H. Görls, M. El-khateeb and W. Weigand, *Dalton Trans.*, 2015, **44**, 7177–7189.
- 16 (a) M. K. Harb, J. Windhager, T. Niksch, H. Görls, T. Sakamoto, E. R. Smith, R. S. Glass, D. L. Lichtenberger, D. H. Evans, M. El-khateeb and W. Weigand, *Tetrahedron*, 2012, **68**, 10592–10599; (b) S. Gao, J. Fan, S. Sun, X. Peng, X. Zhao and J. Hou, *Dalton Trans.*, 2008, 2128–2135; (c) M. K. Harb, U.-P. Apfel, J. Kübel, H. Görls, G. A. N. Felton, T. Sakamoto, D. H. Evans, R. S. Glass, D. L. Lichtenberger, M. El-khateeb and W. Weigand, *Organometallics*, 2009, **28**, 6666–6675; (d) U.-P. Apfel, H. Görls, G. A. N. Felton, D. H. Evans, R. S. Glass, D. L. Lichtenberger and W. Weigand, *Helv. Chim. Acta*, 2012, **95**, 2168–2175; (e) R. Trautwein, L. R. Almazahreh, H. Görls and W. Weigand, *Dalton Trans.*, 2015, **44**, 18780–18794; (f) W. Gao, L.-C. Song, B.-S. Yin, H.-N. Zan, D.-F. Wang and H.-B. Song, *Organometallics*, 2011, **30**, 4097–4107; (g) L.-C. Song, W. Gao, C.-P. Feng, D.-F. Wang and Q.-M. Hu, *Organometallics*, 2009, **28**, 6121–6130; L.-C. Song, S.-Z. Mei, C.-P. Feng, F.-H. Gong, J.-H. Ge and Q.-M. Hu, *Organometallics*, 2010, **29**, 5050–5060.
- 17 (a) W. Gao, J. Sun, T. Åkermark, M. Li, L. Eriksson, L. Sun and B. Åkermark, *Chem. – Eur. J.*, 2010, **16**, 2537–2546; (b) S. Ott, M. Kritikos, B. Åkermark, L. Sun and R. L. Lomoth, *Angew. Chem., Int. Ed.*, 2004, **116**, 1024–1024; (c) F. Wang, M. Wang, X. Liu, K. Jin, W. Dong and L. Sun, *Dalton Trans.*, 2007, 3812–3819; (d) J. D. Lawrence, H. Li, T. B. Rauchfuss, M. Bénard and M.-M. Rohmer, *Angew. Chem., Int. Ed.*, 2001, **40**, 1768–1771; (e) S. Jiang, J. Liu, Y. Shi, Z. Wang, B. Åkermark and L. Sun, *Dalton Trans.*, 2007, 896–902.
- 18 (a) S. L. Matthews and D. M. Heinekey, *Inorg. Chem.*, 2010, **49**, 9746–9748; (b) Y.-C. Liu, K.-T. Chu, Y.-L. Huang, C.-H. Hsu, G.-H. Lee, M.-C. Tseng and M.-H. Chiang, *ACS Catal.*, 2016, **6**, 2559–2576; (c) D. Schilter, J. M. Camara, M. T. Huynh, S. Hammes-Schiffer and T. B. Rauchfuss, *Chem. Rev.*, 2016, **116**, 8693–8749.
- 19 H. J. Reich and R. J. Handal, *ACS Chem. Biol.*, 2016, **11**, 821–841.
- 20 (a) J. Noth, J. Esselborn, J. Gülenhaupt, A. Brünje, A. Sawyer, U.-P. Apfel, K. Gerwert, E. Hofmann, M. Winkler and T. Happe, *Angew. Chem., Int. Ed.*, 2016, **55**, 8396–8400; (b) L.-C. Song, B. Gai, H.-T. Wang and Q.-M. Hu, *J. Inorg. Biochem.*, 2009, **103**, 805–812; (c) L.-C. Song, B. Gai, Z.-H. Feng, Z.-Q. Du, Z.-J. Xie, X.-J. Sun and H.-B. Song, *Organometallics*, 2013, **32**, 3673–3684.
- 21 M. K. Harb, U.-P. Apfel, T. Sakamoto, M. El-khateeb and W. Weigand, *Eur. J. Inorg. Chem.*, 2011, 986–993 and the references cited there.
- 22 M. K. Harb, H. Görls, T. Sakamoto, G. A. N. Felton, D. H. Evans, R. S. Glass, D. L. Lichtenberger, M. El-khateeb and W. Weigand, *Eur. J. Inorg. Chem.*, 2010, 3976–3985.
- 23 E. Block, E. V. Dikarev, R. S. Glass, J. Jin, B. Li, X. Li and S.-Z. Zhang, *J. Am. Chem. Soc.*, 2006, **128**, 14949–11496.
- 24 D. Seyferth and S. C. Vic, *Synth. React. Inorg. Met.-Org. Chem.*, 1974, **4**, 515–521.
- 25 W. Hieber and J. Gruber, *Z. Anorg. Allg. Chem.*, 1958, **296**, 91–103.
- 26 M. K. Harb, T. Niksch, J. Windhager, H. Görls, R. Holze, L. T. Lockett, N. Okumura, D. H. Evans, R. S. Glass, D. L. Lichtenberger, M. El-khateeb and W. Weigand, *Organometallics*, 2009, **28**, 1039–1048.
- 27 (a) M. K. Harb, U.-P. Apfel, T. Sakamoto, M. El-khateeb and W. Weigand, *Eur. J. Inorg. Chem.*, 2011, 986–993; (b) C. Figliola, L. Male, P. N. Horton, M. B. Pitak, S. J. Coles, S. L. Horswell and R. S. Grainger, *Organometallics*, 2014, **33**, 4449–4460.
- 28 (a) E. J. Lyon, I. P. Georgakaki, J. H. Reibenspies and M. Y. Darensbourg, *Angew. Chem., Int. Ed.*, 1999, **38**, 3178–3180; (b) S. J. Borg, T. Behrsing, S. P. Best, M. Razavet, X. M. Liu and C. J. Pickett, *J. Am. Chem. Soc.*, 2004, **126**, 16988–16999; (c) J. W. Tye, J. Lee, H.-W. Wang, R. Mejia-Rodriguez, J. H. Reibenspies, M. B. Hall and M. Y. Darensbourg, *Inorg. Chem.*, 2005, **44**, 5550–5552; (d) E. J. Lyon, I. P. Georgakaki, J. H. Reibenspies and M. Y. Darensbourg, *J. Am. Chem. Soc.*, 2001, **123**, 3268–3278; (e) F. Robin, R. Rumin, J. Talarmin, F. Y. Pétillon and K. W. Muir, *Organometallics*, 1993, **12**, 365–380.
- 29 R. S. Nicholson and I. Shain, *Anal. Chem.*, 1965, **37**, 178–190.
- 30 (a) F. Gloaguen, D. Morvan, J.-F. Capon, P. Schollhammer and J. Talarmin, *J. Electroanal. Chem.*, 2007, **603**, 15–20; (b) L. Schwartz, P. S. Singh, L. Eriksson, R. Lomoth and S. Ott, *C. R. Chim.*, 2008, **11**, 875–889; (c) J.-F. Capon, F. Gloaguen, P. Schollhammer and J. Talarmin, *J. Electroanal. Chem.*, 2004, **566**, 241–247; (d) J. Chen, A. K. Vannucci, C. A. Mebi, N. Okumura, S. C. Borowski, M. Swenson, L. T. Lockett, D. H. Evans, R. S. Glass and D. L. Lichtenberger, *Organometallics*, 2010, **29**, 5330–5340; (e) J. Zhao, Z. Wei, X. Zeng and X. Liu, *Dalton Trans.*, 2012, **41**, 11125–11133; (f) G. A. N. Felton, C. A. Mebi, B. J. Petro, A. K. Vannucci, D. H. Evans, R. S. Glass and D. L. Lichtenberger, *J. Organomet. Chem.*, 2009, **694**, 2681–2699; (g) S. P. Best, S. J. Borg, J. M. White, M. Razavet and C. J. Pickett, *Chem. Commun.*, 2007, 4348–4350; (h) S. J. Borg, T. Behrsing, S. P. Best, M. Razavet, X. Liu and C. J. Pickett, *J. Am. Chem. Soc.*, 2004, **126**, 16988–16999; (i) L. Schwartz, J. Ekstrom, R. Lomoth and S. Ott, *Chem. Commun.*, 2006, 4206–4208; (j) D. Streich, M. Karnahl, Y. Astuti, C. W. Cady, L. Hammarstrom, R. Lomoth and S. Ott, *Eur. J. Inorg. Chem.*, 2011, 1106–1111; (k) G. Qian, H. Wang, W. Zhong and X. Liu, *Electrochim. Acta*, 2015, **163**, 190–195; (l) F. Gloaguen and T. B. Rauchfuss, *Chem. Soc. Rev.*, 2009, **38**, 100–108; (m) G. Qian, W. Zhong, Z. Wei, H. Wang, Z. Xiao, L. Long and X. Liu, *New J. Chem.*, 2015, **39**, 9752–9760.

- 31 (a) G. A. N. Felton, A. K. Vannucci, J. Chen, L. T. Lockett, N. Okumura, B. J. Petro, U. I. Zakai, D. H. Evans, R. S. Glass and D. L. Lichtenberger, *J. Am. Chem. Soc.*, 2007, **129**, 12521–12530; (b) S. J. Borg, S. K. Ibrahim, C. J. Pickett and S. P. Best, *C. R. Chim.*, 2008, **11**, 852–860.
- 32 *COLLECT, Data Collection Software*, Nonius B.V., Netherlands, 1998.
- 33 Z. Otwinowski and W. Minor, Processing of X-Ray Diffraction Data Collected in Oscillation Mode, in *Methods in Enzymology, Vol. 276, Macromolecular Crystallography, Part A*, ed. C. W. Carter and R. M. Sweet, Academic Press, San Diego, USA, 1997, pp. 307–326.
- 34 *SADABS 2.10*, Bruker-AXS inc., Madison, WI, USA, 2002.
- 35 G. M. Sheldrick, *Acta Crystallogr., Sect. A: Fundam. Crystallogr.*, 2008, **64**, 112–122.
- 36 C. F. Macrae, P. R. Edgington, P. McCabe, E. Pidcock, G. P. Shields, R. Taylor, M. Towler and J. van de Streek, *J. Appl. Crystallogr.*, 2006, **39**, 453–457.

Supplementary Material

Selenium makes the difference: Protonation of [FeFe]-hydrogenase mimics with diselenolato ligands

Hassan Abul-Futouh,^a Mohammad El-khateeb,^b Helmar Görls,^a Khalil J. Asali^b and Wolfgang Weigand^{a*}

^a *Institut für Anorganische und Analytische Chemie, Friedrich-Schiller-Universität Jena, Humboldt Str. 8, 07743 Jena, Germany Email: wolfgang.weigand@uni-jena.de*

^b *Chemistry Department, Jordan University of Science and Technology, Irbid 22110, Jordan. Email: kateeb@just.edu.jo*

Figure S1. A) ^1H NMR spectrum (CD_2Cl_2) of complex **4** without $\text{HBF}_4\cdot\text{Et}_2\text{O}$. **B)** ^1H NMR spectrum (CD_2Cl_2) of complex **4** with (100 equiv.) $\text{HBF}_4\cdot\text{Et}_2\text{O}$. (●) peaks of Et_2O in the acid.

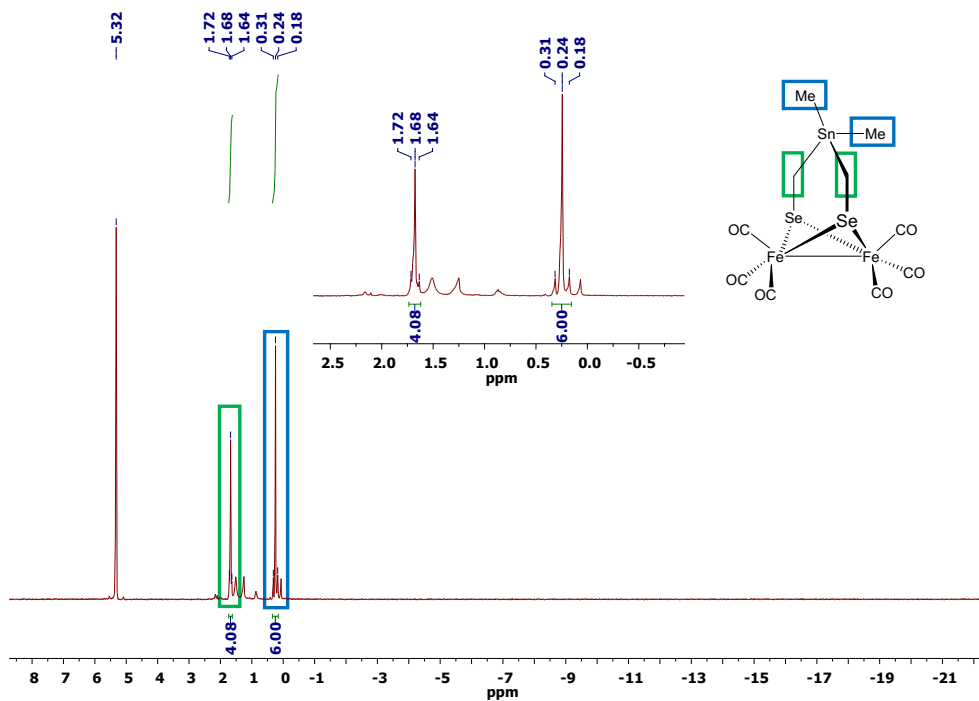


Figure S2. The ^1H , $^{77}\text{Se}\{\text{H}\}$ HMBC NMR spectrum of $4\mu\text{H}^+$ in CD_2Cl_2 .

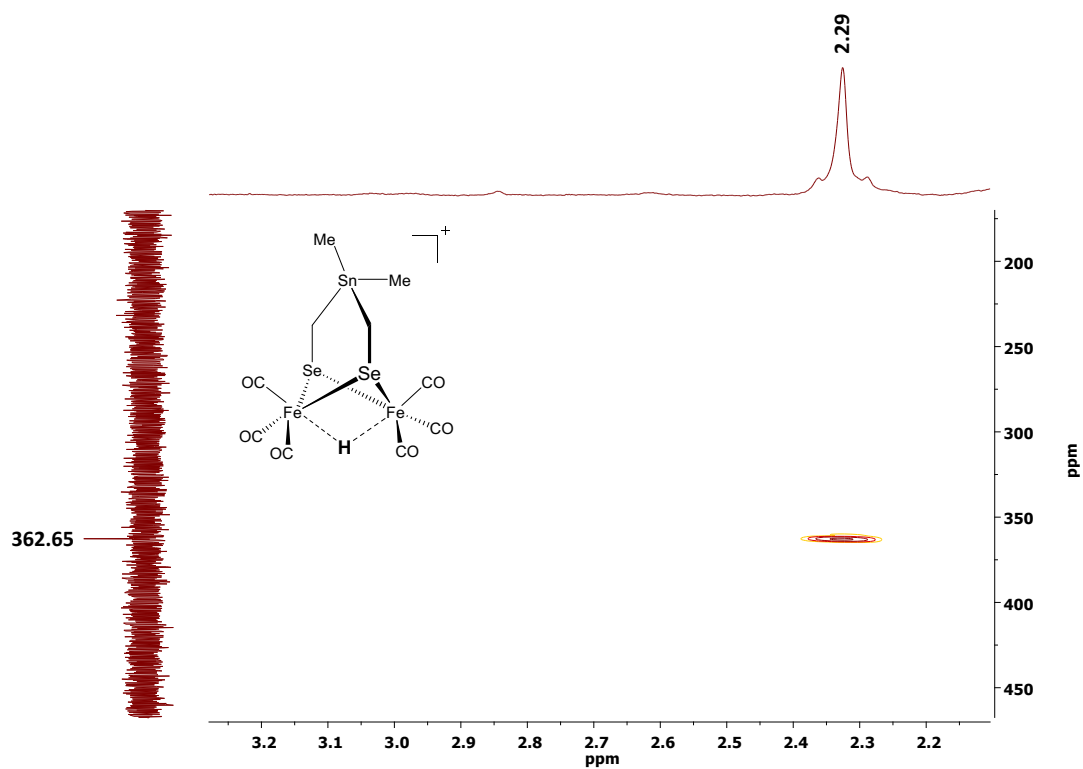


Figure S3. The high field ^1H NMR spectrum (CD_2Cl_2) of complexes **7** (blue), **8** (green) and **9** (red) with 100 equiv. $\text{HBF}_4 \cdot \text{Et}_2\text{O}$.

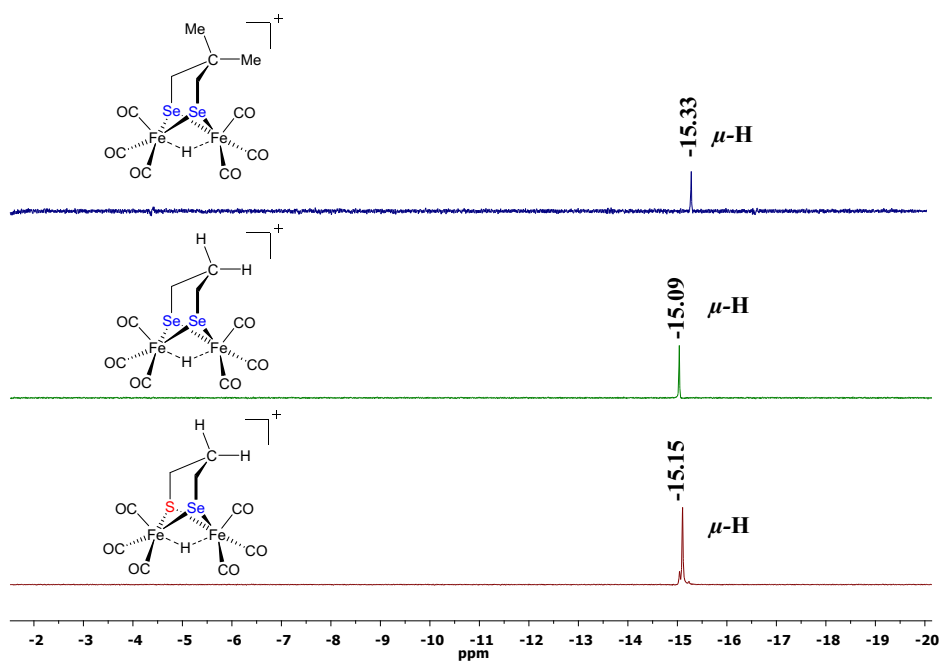


Figure S4. ^1H NMR spectrum (CD_2Cl_2) of complex **4** with 100 equiv. $\text{CF}_3\text{CO}_2\text{H}$ (top) and $^{77}\text{Se}\{\text{H}\}$ NMR spectrum (CD_2Cl_2) of complex **4** with 100 equiv. $\text{CF}_3\text{CO}_2\text{H}$ (bottom). (\blacktriangledown) Signals for the new CH_2 (2.33 ppm) and CH_3 (0.59 ppm) moieties. (\bullet) Signals for the CH_2 and CH_3 in the parent complex.

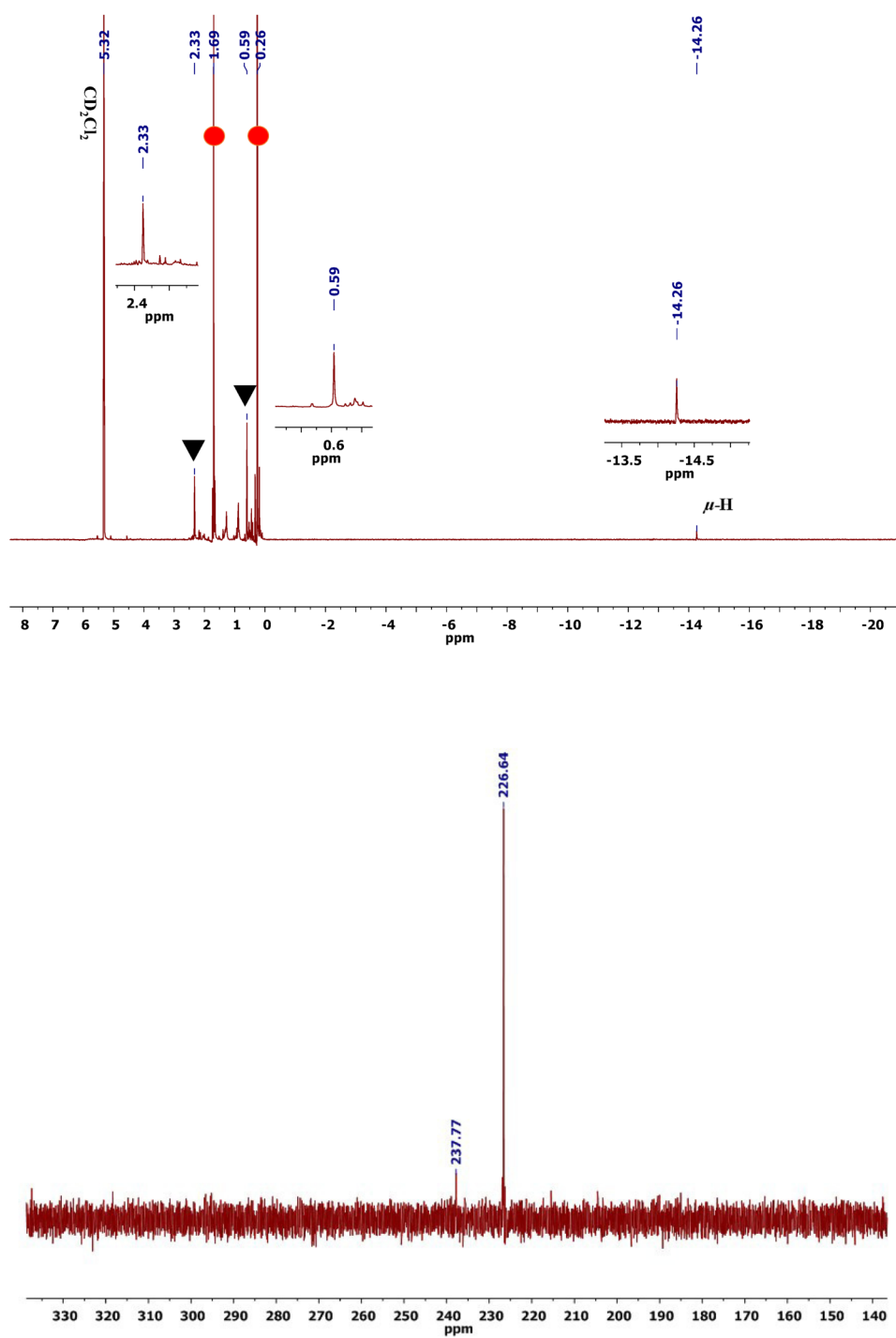
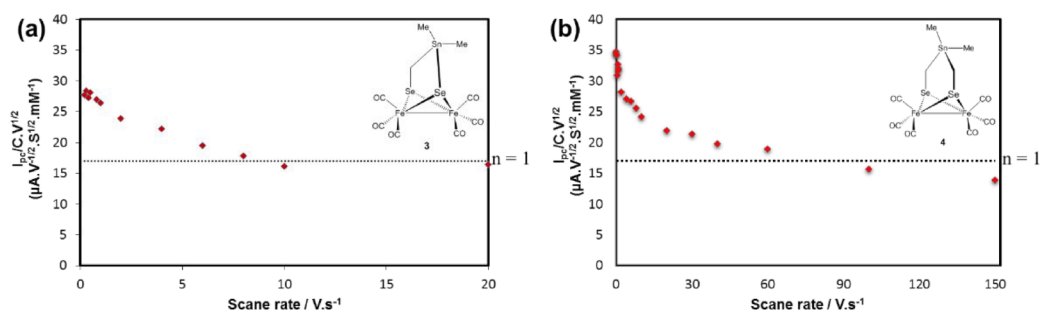


Figure S5. The scan rates dependence of the current function of the primary reduction peaks of (a) 0.87 mM complex **3** and (b) 1.0 mM complex **4** in CH₂Cl₂-[*n*-Bu₄N][PF₄] (0.1 M) solutions. Glassy carbon electrode ($A = 0.0206 \text{ cm}^2$). The dashed line represents the current function expected for a one electron process assuming $D \approx 9 \times 10^{-6} \text{ cm}^2 \text{ S}^{-1}$, a value calculated for various [FeFe]-Hydrogenase models.



The current function ($I_{pc}/C.v^{1/2}$) is given by the equation $I_{pc}/C.v^{1/2} = (2.69 \times 10^5) \cdot A \cdot D^{1/2} \cdot n^{3/2}$, where I_{pc} is the cathodic peak current in μA , C is the bulk concentration of the complex in mM, A is the surface area of the electrode in cm^2 , $D \approx 9 \times 10^{-6} \text{ cm}^2 \text{ s}^{-1}$ and n is the number of electrons responsible for the reduction event. In general, when the reduction process does not have any chemical route (simple E mechanism, $n = 1$), the current function of this reduction process should remain constant at all scan rates since $2.69 \times 10^5) \cdot A \cdot D^{1/2} \cdot n^{3/2}$ is constant. In contrast, when an ECE mechanism ($n = 2$) in which a chemical process takes place, the current function of this reduction process decreases significantly toward that expected for a one electron as the scan rates increase. This means, at higher scan rates there is not enough time for such a chemical process to occur and thus the second electron transfer will not take place (i.e. conversion of the mechanism from ECE to simple E process).

Figure S6. Cyclic voltammogram of 1 mM complexes $[\text{Fe}_2(\text{CO})_6\{\mu-(\text{SCH}_2)_2\text{SnMe}_2\}]$, **4S**, (black line) and **4** (red line) in CH_2Cl_2 - $[n\text{-Bu}_4\text{N}][\text{PF}_4]$ (0.1 M) solution at 0.2 V s^{-1} scan rate. The arrows indicate the scan direction. The potentials E are given in V and referenced to the Fc^+/Fc couple.

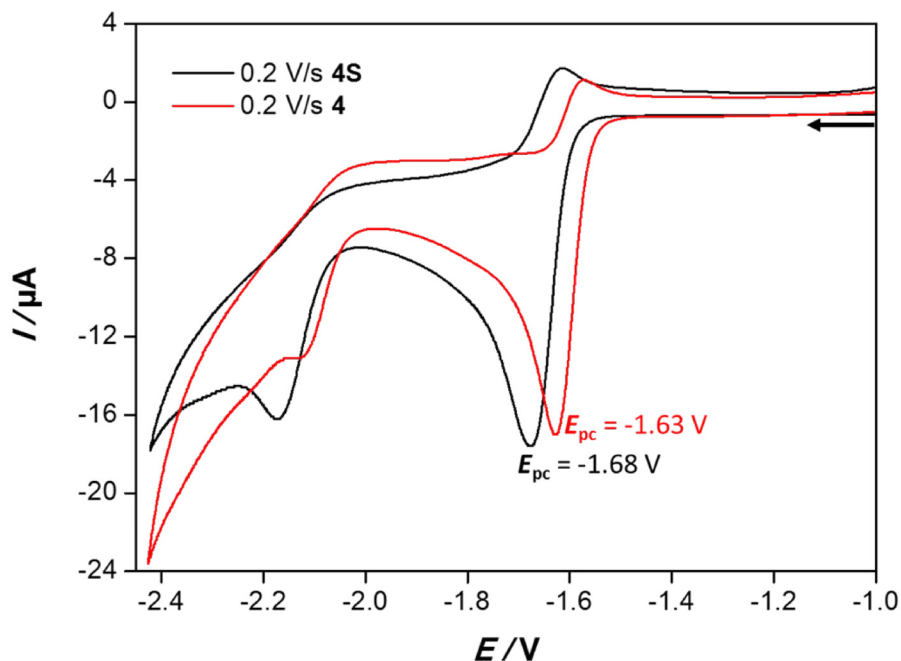
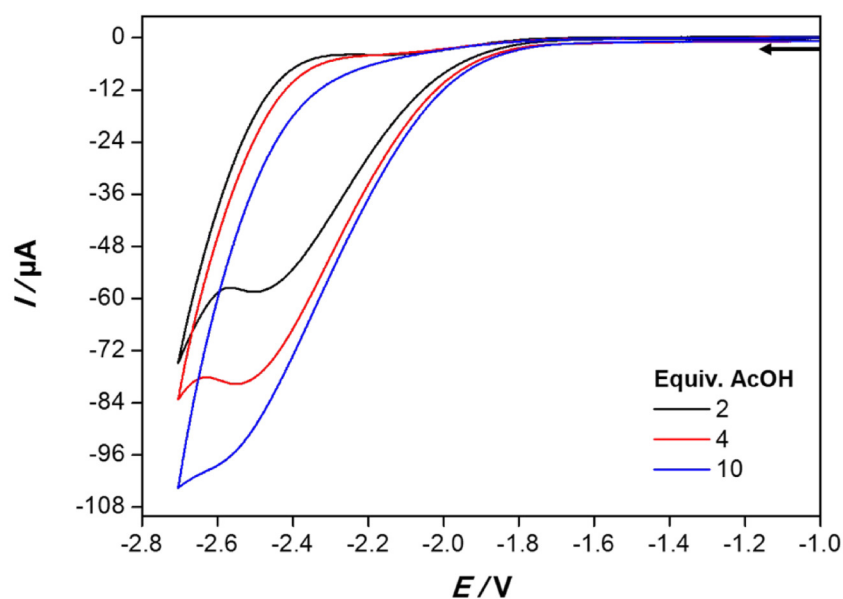


Figure S7. Cyclic voltammogram of various concentration of AcOH in CH_2Cl_2 - $[n\text{-Bu}_4\text{N}][\text{PF}_4]$ (0.1 M) solution at 0.2 V s^{-1} scan rate in the absence of catalyst (model complexes). The arrows indicate the scan direction. The potentials E are given in V and referenced to the Fc^+/Fc couple.

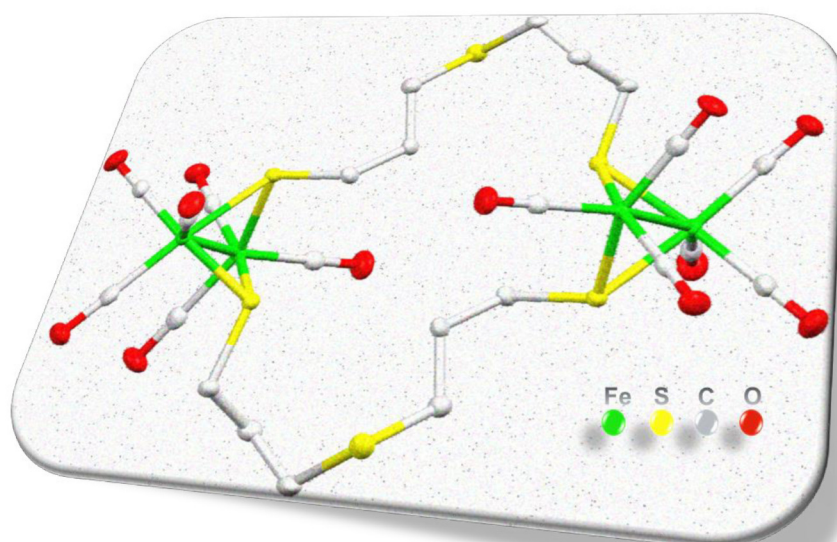


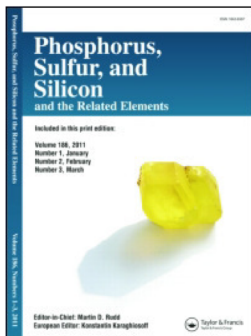
4.3 [HAF-3]

A New Macrocyclic [FeFe]-Hydrogenase H Cluster Model

Hassan Abul-Futouh, Helmar Görls, Wolfgang Weigand

Phosphorus, Sulfur, and Silicon and the Related Elements **2017**, 192, 634-637.





A new macrocyclic [FeFe]-hydrogenase H cluster model

Hassan Abul-Futouh, Helmar Görls & Wolfgang Weigand

To cite this article: Hassan Abul-Futouh, Helmar Görls & Wolfgang Weigand (2017) A new macrocyclic [FeFe]-hydrogenase H cluster model, Phosphorus, Sulfur, and Silicon and the Related Elements, 192:6, 634-637, DOI: [10.1080/10426507.2017.1284840](https://doi.org/10.1080/10426507.2017.1284840)

To link to this article: <http://dx.doi.org/10.1080/10426507.2017.1284840>



Accepted author version posted online: 24 Jan 2017.
Published online: 24 Jan 2017.



Submit your article to this journal [↗](#)



Article views: 13



View related articles [↗](#)



View Crossmark data [↗](#)

A new macrocyclic [FeFe]-hydrogenase H cluster model

Hassan Abul-Futouh, Helmar Görls, and Wolfgang Weigand

Institut für Anorganische und Analytische Chemie, Friedrich-Schiller-Universität Jena, Jena, Germany

ABSTRACT

A novel macrocyclic complex $[\text{Fe}_2(\text{CO})_6\{\mu\text{-(S(CH}_2)_3)_2\text{S}}\}_2$ (**2**) has been synthesized by the reaction of $\text{Fe}_3(\text{CO})_{12}$ with 1,2,6,10,11,15-hexathiacyclooctadecane (**1**). This tetranuclear macrocyclic complex has been isolated and characterized by IR spectroscopy, ^1H NMR spectroscopy, mass spectrometry as well as elemental analysis. The solid state structures of 1,2,6,10,11,15-hexathiacyclooctadecane (**1**) and $[\text{Fe}_2(\text{CO})_6\{\mu\text{-(S(CH}_2)_3)_2\text{S}}\}_2$ (**2**) were determined by X-ray crystal structure analysis.

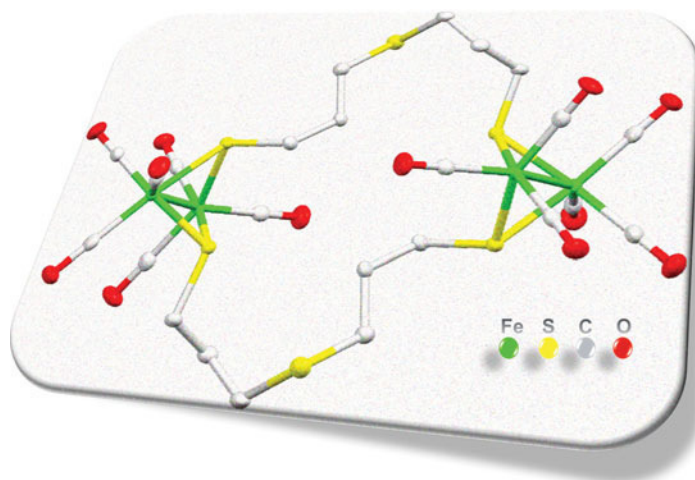
ARTICLE HISTORY

Received 12 December 2016
Accepted 17 January 2017

KEYWORDS

H cluster; hydrogenase;
macrocyclic; thioether; active
site



GRAPHICAL ABSTRACT



Introduction

The natural energy resources are dearth and were found to be more harmful for the environment. Therefore, the search for new energy sources, like hydrogen, is of great interest to scientists nowadays.^{1–3} In fact, the nature has high ability to catalyze the reversible process of proton reduction with high catalytic efficiency (ca. 10^4 turnover s^{-1}) and this occurs through enzymes known as [FeFe]-hydrogenases.^{4,5} The so-called H cluster, which is the active site of the [FeFe]-hydrogenases enzyme consisting of a $[\text{Fe}_4\text{S}_4]$ cluster attached through a cysteinyl residue to a butterfly $[\text{Fe}_2\text{S}_2]$ subcluster. This subcluster features a bridging azadithiolato ligand ($\text{adt} = [\text{SCH}_2\text{NHCH}_2\text{S}]$) as well as biologically unusual CO and CN^- ligands^{6–10} (Figure 1).

Recent efforts have been paid to the synthetic models that mimic the H cluster of the [FeFe]-hydrogenase in order to provide a better understanding of the structure and function of the active site of the enzyme.¹¹ One of these efforts focused on synthesizing macrocyclic complexes that contain two $\text{Fe}_2\text{S}_2(\text{CO})_6$ subcluster cores with butterfly structure connected by different linkers leading to systems with two catalytic active centers close to each other. Such macrocyclic complexes, however, are rare and only few examples were reported in the literature.^{12–19} Indeed, the size of these macrocyclic complexes depends on the nature of the chain linkers, where Song et al. reported an 18-membered macrocyclic complex, $[\text{Fe}_2(\text{CO})_6\{\mu\text{-(S(CH}_2)_2)_2\text{E}}\}_2$ ($\text{E}=\text{O}$ or N^iPr),^{13,14} while Zhang et al. prepared a 16-membered macrocyclic complex,

CONTACT Wolfgang Weigand  wolfgang.weigand@uni-jena.de  Institut für Anorganische und Analytische Chemie, Friedrich-Schiller-Universität Jena, Humboldt Str. 8, 07743 Jena, Germany.

Color versions of one or more of the figures in the article can be found online at www.tandfonline.com/gpss.

Supporting Information Available: Crystallographic data deposited at the Cambridge Crystallographic Data Centre under CCDC-1519992 for 1, and CCDC-1519993 for 2 contain the supplementary crystallographic data excluding structure factors; this data can be obtained free of charge via www.ccdc.cam.ac.uk/conts/retrieving.html (or from the Cambridge Crystallographic Data Centre, 12, Union Road, Cambridge CB2 1EZ, UK; fax: (+44) 1223-336-033; or deposit@ccdc.cam.ac.uk).

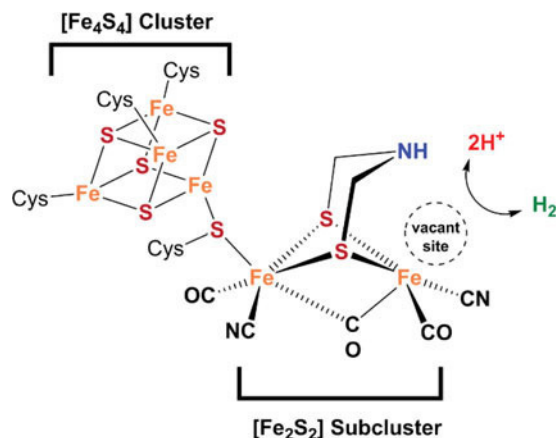


Figure 1. The structure of the H cluster.

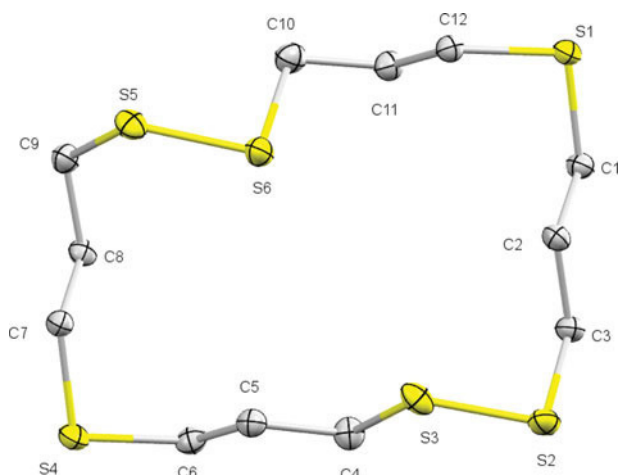


Figure 2. The molecular structure of compound 1. Hydrogen atoms are omitted for clarity.

$[\text{Fe}_2(\text{CO})_6\{\mu-(\text{S}(\text{CH}_2)_4)_2\}]_2$.¹⁵ In this context, we herein report the preparation and the molecular structure of the novel 22-membered macrocyclic complex $[\text{Fe}_2(\text{CO})_6\{\mu-(\text{S}(\text{CH}_2)_2)_2\text{S}\}]_2$ (**2**).

Results and discussion

The starting compound 1,2,6,10,11,15-hexathiacyclooctadecane (**1**) was synthesized by following a procedure described in the literature.²⁰ Colourless needles suitable for X-ray diffraction analysis were obtained by recrystallization of compound **1** from pentane at -20°C . The molecular structure of compound **1** is shown in Figure 2. The two disulfide bonds length, (S_2-S_3 , 2.0375(10) Å and S_5-S_6 , 2.0325(10) Å), are slightly shorter than the corresponding bond in the elemental sulfur $\alpha\text{-S}_8$ (2.05 Å). Moreover, the average dihedral angle for $\text{C}_{4(9)}-\text{S}_{3(5)}-\text{S}_{2(6)}-\text{C}_{3(10)}$ is 78.79° and the average S–C bond is 1.816(3) Å.

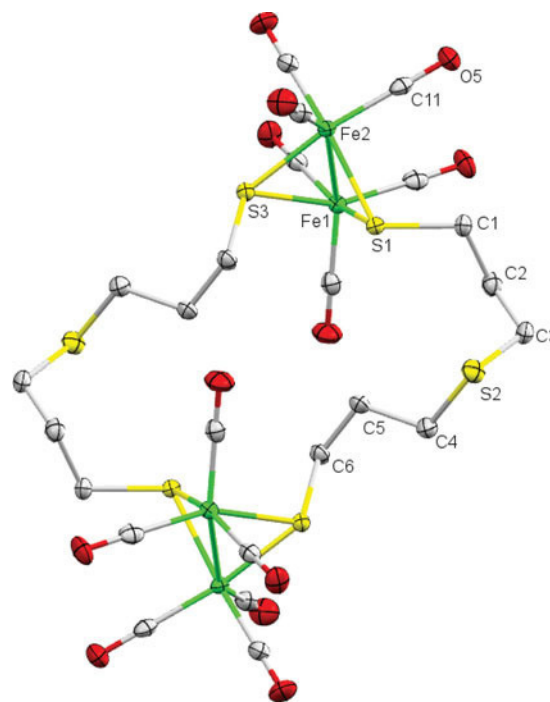
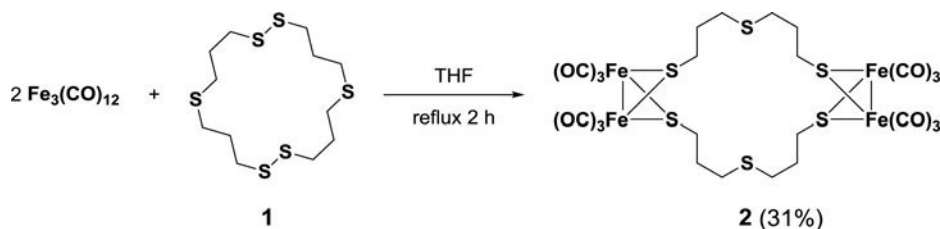


Figure 3. The molecular structure of complex **2**. Hydrogen atoms are omitted for clarity.

Treatment of two equiv. of $\text{Fe}_3(\text{CO})_{12}$ with one equiv. of **1** in boiling THF for two hours followed by subsequent column chromatography afforded $[\text{Fe}_2(\text{CO})_6\{\mu-(\text{S}(\text{CH}_2)_2)_2\text{S}\}]_2$, **2**, as a red solid (Scheme 1). The novel complex **2** is air stable as solid but decomposes slowly in solution with time. It is soluble in common organic solvents such as THF and CH_2Cl_2 but it is insoluble in hydrocarbon solvents such as hexane. Complex **2** has been characterized by ^1H NMR spectroscopy, IR spectroscopy, mass spectrometry, elemental analysis, and X-ray crystallography.

The IR spectrum of complex **2** exhibited four absorption bands at 1957, 1981, 2019, and 2065 cm^{-1} for the terminal CO ligands. These stretching vibrations are shifted to slightly lower wavenumbers compared to those of analogues system reported in the literature.^{13,14} This might be due to the presence of the sulfur atom in the chain linker. The ^1H NMR spectrum of complex **2** showed a broad singlet at 1.68 ppm for the SCH_2 moieties located at the axial position, multiplet in the region 1.94–2.23 ppm for the SCH_2CH_2 moieties, broad singlet in the region 2.52 ppm that could be assigned to the SCH_2 moieties in equatorial position as well as a multiplet in the region 2.69–2.80 ppm for the CH_2SCH_2 moieties. Single crystals suitable for X-ray diffraction studies were obtained by diffusion of hexane into a CH_2Cl_2 solution of complex **2** at -20°C . The molecular structure of complex **2** is shown in Figure 3. Complex **2** is



Scheme 1. Synthesis of complex **2**.

composed of two butterfly cluster cores which are linked together by two identical thioether chains to form a 22-membered macrocycle complex. The geometry around each iron atom in complex **2** can be best described as a distorted octahedron with three CO ligands in a facial fashion, two bridging sulfur atoms and one iron atom. The Fe–Fe bond length (2.5221(5) Å) in complex **2** are comparable to those in the corresponding analogues reported in the literature.^{12–16} Furthermore, the average Fe–S bond (2.2596(7) Å) and the average S–C bond (1.820(3) Å) are similar to those in the reported analogues system.^{12–16}

Conclusion

In this report we have synthesized and characterized a novel 22-membered macrocyclic complex, $[\text{Fe}_2(\text{CO})_6\{\mu\text{-}(\text{S}(\text{CH}_2)_3)_2\text{S}\}]_2$ (**2**) by thermal reaction of 1,2,6,10,11,15-hexathiacyclooctadecane (**1**) with $\text{Fe}_3(\text{CO})_{12}$. The molecular structure of complex **2** displays two $\text{Fe}_2\text{S}_2(\text{CO})_6$ subcluster cores with butterfly structure connected via two identical thioether chain linkers.

Experimental

All reactions were performed using standard Schlenk and vacuum-line techniques under an inert gas (nitrogen). The ^1H NMR spectra were recorded with a Bruker Avance 400 MHz spectrometer. Chemical shifts are given in parts per million with references to internal SiMe_4 . The mass spectrum was recorded with Finnigan MAT SSQ 710 instrument. The IR spectra were recorded with a Bruker Equinox 55 spectrometer equipped with an ATR unit. Elemental analysis was performed with a Leco CHNS-932 apparatus. TLC was performed by using Merck TLC aluminum sheets (Silica gel 60 F254). Solvents from Fisher Scientific and other chemicals from Acros and Aldrich were used without further purification. All solvents were dried and distilled prior to use according to standard methods. The compound 1,2,6,10,11,15-hexathiacyclooctadecane (**1**) was synthesized according to the known literature method.²⁰

Crystal structure determination

The intensity data were collected on a Nonius KappaCCD diffractometer using graphite-monochromated Mo- K_α radiation. Data were corrected for Lorentz and polarization effects, absorption was taken into account on a semi-empirical basis using multiple-scans.^{21–23} The structure was solved by direct methods (SHELXS)²⁴ and refined by full-matrix least squares techniques against F_o^2 (SHELXL-97).²⁴ The hydrogen atoms of **2** were located by difference Fourier synthesis and refined isotropically. All hydrogen atom positions of **1** were included at calculated positions with fixed thermal parameters. MERCURY²⁵ was used for structure representations.

Crystal Data for 1: $\text{C}_{12}\text{H}_{24}\text{S}_6$, Mr = 360.67 g mol^{-1} , colourless prism, size 0.134 × 0.098 × 0.056 mm^3 , orthorhombic, space group Pca_21 , a = 20.9147(4), b = 5.33730(10), c = 15.3094(3) Å, V = 1708.96(6) Å³, T = –140°C, Z = 4, $\rho_{\text{calcd.}}$ =

1.402 g cm^{-3} , μ (Mo- K_α) = 7.83 cm^{-1} , multi-scan, transmin: 0.6942, transmax: 0.7456, F(000) = 768, 11378 reflections in $h(-27/27)$, $k(-6/6)$, $l(-16/19)$, measured in the range $1.95^\circ \leq \Theta \leq 27.51^\circ$, completeness $\Theta_{\text{max}} = 99.8\%$, 3659 independent reflections, $R_{\text{int}} = 0.0394$, 3364 reflections with $F_o > 4\sigma(F_o)$, 163 parameters, 1 restraints, $R1_{\text{obs}} = 0.0298$, $wR2_{\text{obs}} = 0.0615$, $R1_{\text{all}} = 0.0343$, $wR2_{\text{all}} = 0.0639$, GOOF = 1.040, Flack-parameter 0.41(11), largest difference peak and hole: 0.264/–0.179 $e \text{ \AA}^{-3}$.

Crystal Data for 2: $\text{C}_{24}\text{H}_{24}\text{Fe}_4\text{O}_{12}\text{S}_6$, Mr = 920.19 g mol^{-1} , red-brown prism, size 0.110 × 0.098 × 0.090 mm^3 , monoclinic, space group $P2_1/n$, a = 14.5539(8), b = 7.7643(3), c = 16.4300(8) Å, $\beta = 114.011(2)^\circ$, V = 1695.95(14) Å³, T = –140°C, Z = 2, $\rho_{\text{calcd.}}$ = 1.802 g cm^{-3} , μ (Mo- K_α) = 21.03 cm^{-1} , multi-scan, trans. min: 0.6617, trans. max: 0.7456, F(000) = 928, 10801 reflections in $h(-18/18)$, $k(-9/9)$, $l(-21/21)$, measured in the range $2.42^\circ \leq \Theta \leq 27.10^\circ$, completeness $\Theta_{\text{max}} = 99.6\%$, 3714 independent reflections, $R_{\text{int}} = 0.0367$, 3340 reflections with $F_o > 4\sigma(F_o)$, 256 parameters, 0 restraints, $R1_{\text{obs}} = 0.0346$, $wR2_{\text{obs}} = 0.0650$, $R1_{\text{all}} = 0.0415$, $wR2_{\text{all}} = 0.0674$, GOOF = 1.148, largest difference peak and hole: 0.453/–0.300 $e \text{ \AA}^{-3}$.

General procedure for the synthesis of $[\text{Fe}_2(\text{CO})_6\{\mu\text{-}(\text{S}(\text{CH}_2)_3)_2\text{S}\}]_2$ (**2**)

A mixture of $\text{Fe}_3(\text{CO})_{12}$ (280 mg, 0.56 mmol) and compound **1** (100 mg, 0.28 mmol) in THF was heating at reflux for two hours. The resulting deep-red solution was cooled down to room temperature and the solvent removed under reduced pressure. The residue was purified by column chromatography with $\text{CH}_2\text{Cl}_2/\text{Hexane}$ (v/v 1:2) as eluent. The complex was collected from the second, red colored fraction. Yield: 31%. Elemental analysis for $\text{C}_{24}\text{H}_{24}\text{Fe}_4\text{O}_{12}\text{S}_6$: calculated C 31.33, H 2.63, S 20.90; found C 31.61, H 2.68, S 20.95. IR $\nu(\text{CO}) = 1957, 1981, 2019, 2065 \text{ cm}^{-1}$. ^1H NMR (400 MHz, CDCl_3): $\delta = 1.68 \text{ ppm}$ (bs, 4H, a-SCH₂), 1.94–2.23 ppm (m, 8H, SCH₂CH₂), 2.52 ppm (bs, 4H, e-SCH₂), 2.69–2.80 ppm (m, 8H, CH₂SCH₂). DEI-MS: m/z = 920 [M]⁺.

Funding

H. Abul-Futouh thanks the Deutscher Akademischer Austausch Dienst (DAAD) for scholarship.

References

- Woodward, J.; Orr, M.; Cordray, K.; Greenbaum, E. *Nature* **2000**, 405, 1014–1015.
- Nicolet, Y.; Cavazza, C.; Fontecilla-Camps, J. C. J. *Inorg. Biochem.* **2002**, 91, 1–8.
- Ball, M.; Wietschel, M. *Int. J. Hydrogen Energy* **2009**, 34, 615–627.
- Adams, M. W. *Biochim. Biophys. Acta.* **1990**, 1020, 115–145.
- (a) Frey, M. *ChemBioChem.* **2002**, 3, 153–160. (b) Tard, C.; Pickett, C. J., *Chem Rev.*, **2009**, 109, 2245–2274. (c) Lubitz, W.; Ogata, H.; Rüdiger, O.; Reijerse, E., *Chem. Rev.* **2014**, 114, 4081–4148.
- Adamska, A.; Roy, S.; Siebel, J. F.; Simmons, T. R.; Fontecave, M.; Artero, V.; Reijerse, E.; Lubitz, W. *J. Am. Chem. Soc.* **2015**, 137, 12744–12747.

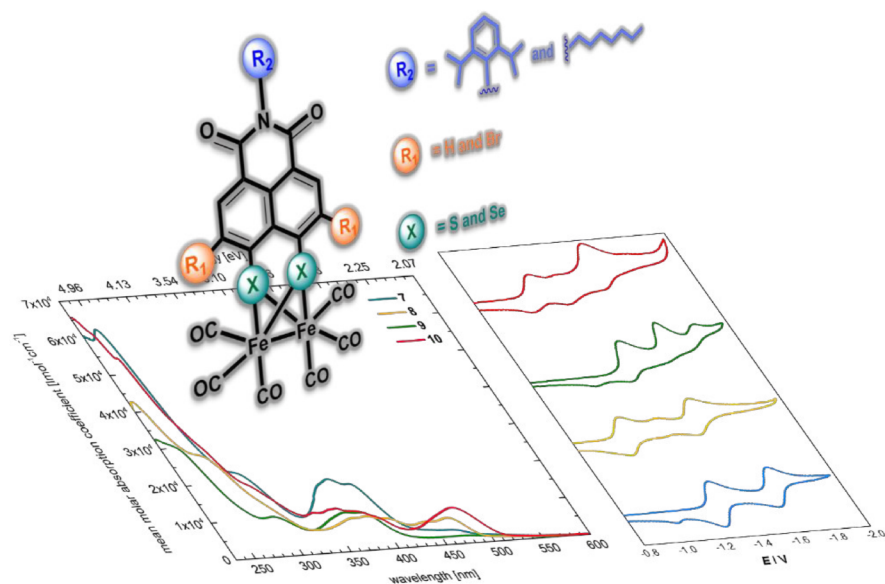
7. Adamska, A.; Silakov, A.; Lambertz, C.; Rüdiger, O.; Happe, T.; Reijerse, E.; Lubitz, W. *Angew. Chem., Int. Ed.* **2012**, 124, 11624-11629.
8. Fan, H.-J.; Hall, M. B. *J. Am. Chem. Soc.* **2001**, 123, 3828-3829.
9. Peters, J. W.; Lanzilotta, W. N.; Lemon, B. J.; Seefeldt, L. C. *Science* **1998**, 282, 1853-1858.
10. Nicolet, Y.; de Lacey, A. L.; Vernede, X.; Fernandez, V. M.; Hatchikian, E. C.; Fontecilla-Camps, J. C. *J. Am. Chem. Soc.* **2001**, 123, 1596-1601.
11. (a) Li, Y.; Rauchfuss, T. B. *Chem. Rev.* **2016**, 116, 7043-7077. (b) Abul-Futouh, H.; Almazahreh, L. R.; Sakamoto, T.; Stessman, N. Y. T.; Licht- enberger, D. L.; Glass, R. S.; Görls, H.; El-khateeb, M.; Schollhammer, P.; Mloston, G.; Weigand, W. *Chem. Eur. J.* **2017**, 23, 346-359. (c) Abul-Futouh, H.; El-khateeb, M.; Görls, H.; Asali, K. J.; Weigand, W. *Dalton Trans.* **2017**, DOI: [10.1039/C7DT00057J](https://doi.org/10.1039/C7DT00057J).
12. Chiang, M.-H.; Liu, Y.-C.; Yang, S.-T.; Lee, G.-H. *Inorg. Chem.* **2009**, 48, 7604-7612.
13. Song, L.-C.; Gao, J.; Wang, H.-T.; Hua, Y.-J.; Fan, H.-T.; Zhang, X.-G.; Hu, Q.-M. *Organometallics* **2006**, 25, 5724-5729.
14. Liu, Y.-C.; Tu, L.-K.; Yen, T.-H.; Lee, G.-H.; Yang, S.-T.; Chiang, M.-H. *Inorg. Chem.* **2010**, 49, 6409-6420.
15. Zhang, Y.; Si, Y.-T.; Hu, M.-Q.; Chen, C.-N.; Liu, Q.-T. *Acta. Cryst.* **2007**, C63, m499-m500.
16. Apfel, U.-P.; Halpin, Y.; Görls, H.; Vos, J.-G.; Schweizer, B.; Linti, G.; Weigand, W. *Chemistry & Biodiversity* **2007**, 4, 2138-2148.
17. Liu, Y.-C.; Tu, L.-K.; Yen, T.-H.; Lee, G.-H.; Chiang, M.-H. *Dalton Trans.* **2011**, 40, 2528-2541.
18. Gao, W.; Liu, J.; Åkermark, B.; Sun, L. *Inorg. Chem.* **2006**, 45, 9169-9171.
19. Song, L.-C.; Gong, F.-H.; Meng, T.; Ge, J.-H.; Cui, L.-N.; Hu, Q.-M. *Organometallics* **2004**, 23, 823-831.
20. Goodrow, M. H.; Musker, W. K. *Synthesis* **1981**, 457-459.
21. *COLLECT, Data Collection Software*. Nonius, B.V., Netherlands, **1998**.
22. Otwinowski, Z.; Minor, W. Processing of X-ray diffraction data collected in oscillation mode. In: C. W. Carter and R.M. Sweet (Eds.), *Methods in Enzymology, Vol. 276, Macromolecular Crystallography, Part A*. Academic Press: San Diego, USA, **1997**, 307-326.
23. *SADABS 2.10*. Bruker-AXS inc.: Madison, WI, USA, **2002**.
24. Sheldrick, G. M. *Acta Crystallogr., Sect. A: Fundam. Crystallogr.* **2008**, 64, 112-122.
25. Macrae, C. F.; Edgington, P. R.; McCabe, P.; Pidcock, E.; Shields, G. P.; Taylor, R.; Towler, M.; Streek, J. van de. *J. Appl. Crystallogr.* **2006**, 39, 453-457.

4.4 [HAF-4]

[FeFe]-Hydrogenase H-Cluster Mimics Mediated by Naphthalene Monoimide Derivatives of *Peri*-Substituted Dichalcogenides

Hassan Abul-Futouh, Yulian Zagranyski, Carolin Müller, Martin Schulz, Stephan Kupfer, Helmar Görls, Mohammad El-Khateeb, Stefanie Gräfe, Benjamin Dietzek, Kalina Peneva, Wolfgang Weigand

Dalton Transactions **2017**, 46, 11180-11190.



Reproduced by permission of The Royal Society of Chemistry.

<http://pubs.rsc.org/en/content/articlelanding/2017/dt/c7dt02079a#!divAbstract>

PAPER

Cite this: *Dalton Trans.*, 2017, **46**, 11180**[FeFe]-Hydrogenase H-cluster mimics mediated by naphthalene monoimide derivatives of *peri*-substituted dichalcogenides†**Hassan Abul-Futouh,^{†a} Yulian Zagranyski,^{†b} Carolin Müller,^c Martin Schulz,^{†c} Stephan Kupfer,^c Helmar Görls,^a Mohammad El-khateeb,^d Stefanie Gräfe,^{†c} Benjamin Dietzek,^{c,e} Kalina Peneva,^{†f,g} and Wolfgang Weigand^{†*a}

Synthetic models of the active site of [FeFe]-hydrogenase containing naphthalene monoimide (NMI) of *peri*-substituted dichalcogenides as bridging linkers have been prepared and characterized using different spectroscopic methods. The influence of the imide functionality and the chalcogen atoms on the redox properties and the catalytic behaviour of complexes **7–10** was studied using cyclic voltammetry. The results revealed that the imide functionality has improved the chemical stability of the reduced species and the replacement of the S atoms by Se caused a cathodic shift in the oxidation peaks. Moreover, the optical properties of compounds **1**, **2**, **4**, and **5** and the respective diiron complexes **7–10** were investigated by UV-Vis absorption and fluorescence spectroscopy assisted by quantum chemical simulations. The structures of complexes **6–9** were confirmed by X-ray diffraction analysis.

Received 7th June 2017,
Accepted 24th June 2017

DOI: 10.1039/c7dt02079a

rsc.li/dalton

Introduction

The conversion of industry from fossil fuels driven to hydrogen is considered an ideal solution to overcome the rapid exhaustion of fossil fuels and the anthropogenic green-house effect.^{1–3} Hydrogen exhibits a high energy density and the combustion of hydrogen in fuel cells results in the formation of water as the only by-product. In nature, the reversible reduction of protons to molecular hydrogen occurs through enzymes, such as [FeFe]-hydrogenases.^{4,5} The active site, the so

called H-cluster, of this enzyme consists of a [Fe₄S₄] cluster attached through a S atom of a cysteinyl residue to a butterfly [Fe₂S₂] sub-cluster as had been shown by X-ray crystallographic studies and theoretical calculations of [FeFe]-hydrogenase isolated from *Desulfovibrio desulfuricans*⁶ and *Clostridium pasteurianum*.⁷ Moreover, the [Fe₂S₂] sub-cluster contains a bridging azadithiolato ligand (adt = [SCH₂NHCH₂S]) and biologically unusual CO and CN⁻ ligands⁸ (Fig. 1). In the past few decades, there have been remarkable attempts to understand the relationship between the structure and function of the active site in [FeFe]-hydrogenases, which sparked the development of numerous synthetic routes based on dithiolato ligands bridging diiron complexes.⁹ The nature of the bridging dithiolate

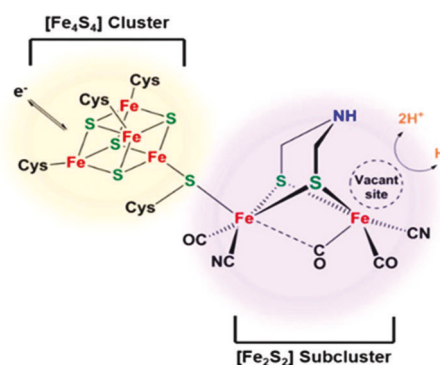


Fig. 1 Schematic structure of the H-cluster of [FeFe]-hydrogenase in naturally occurring enzymes.

^aInstitut für Anorganische und Analytische Chemie, Friedrich-Schiller-Universität Jena, Humboldt Str. 8, 07743 Jena, Germany. E-mail: wolfgang.weigand@uni-jena.de

^bFaculty of Chemistry and Pharmacy, Sofia University 'St. Kliment Ohridski', 1 James Bourchier Ave., Sofia 1164, Bulgaria

^cInstitut für Physikalische Chemie and Abbe Center of Photonics, Friedrich-Schiller-Universität Jena, Helmholtzweg 4, 07743 Jena, Germany

^dChemistry Department, Jordan University of Science and Technology, Irbid 22110, Jordan

^eLeibniz-Institut für Photonische Technologien e.V., Department of Functional Interfaces, Albert-Einstein-Str. 9, 07745 Jena, Germany

^fInstitute of Organic Chemistry and Macromolecular Chemistry, Friedrich-Schiller-Universität Jena, Lessingstrasse 8, 07743 Jena, Germany. E-mail: kalina.peneva@uni-jena.de

^gCenter for Energy and Environmental Chemistry Jena (CEEC Jena), Friedrich-Schiller-Universität Jena, Philosophenweg 7a, 07743 Jena, Germany

†Electronic supplementary information (ESI) available. CCDC 1530273 for **6**, 1530274 for **8**, and 1530275 for **9**. For ESI and crystallographic data in CIF or other electronic format see DOI: 10.1039/c7dt02079a

‡These authors contributed equally.

linkers plays a crucial role in the chemical reversibility and in the number of electrons involved in the reduction process.^{9c,10g} It has been reported that the synthetic models having 1,2-benzenedithiolato bridges are preferably reduced by two electrons in a single step unlike the aliphatic dithiolato bridging ligands.¹⁰ On the other hand, incorporation of a naphthalene-1,8-dithiolato ligand^{11a,b} into the synthetic models of [FeFe]-hydrogenase enhanced the stability of the reduced species to proceed *via* two sequential reversible one-electron steps.^{11c-f} Moreover, it has been found that the reduction potential of the latter model can be adjusted through chemical modification of the naphthalene backbone. For example, the introduction of electron-withdrawing substituents at the 2- and 7-positions of the naphthalene skeleton shifts the first reduction peak to a less negative potential as well as stabilizes the mono-anionic species compared with the aliphatic dithiolate bridging linker.^{11c,d} In light of the above-mentioned considerations, the Wasielewski group and others have modified the naphthalene skeleton by introducing an imide group into its backbone.¹² As a result, they found that the presence of the imide functionality provides additional stability to the monoanionic species due to its strong electron-withdrawing effect and thus serves as a suitable site for the attachment of an additional chromophore. Furthermore, it has been reported that the replacement of the S atoms of diiron dithiolato models by Se atoms increases the electron density on the iron cores.^{11e,13} On the basis of these findings, we have synthesized different naphthalene monoimide (NMI) dithiolato and diselenolato ligands (Fig. 2) in an attempt to investigate their electrochemical and fluorescence properties in the synthetic [FeFe]-hydrogenase subunit mimics. Herein, we describe the first NMI-diselenolate derivatives as well as the preparation of novel NMI-dithiolate and diselenate containing two additional halogen atoms in the *ortho* position to the two chalcogens allowing further fine-tuning of the reduction potential of the respected complexes. The resulting compounds are fully characterized employing a variety of analytical techniques (NMR spectroscopy, elemental analysis, and mass spectrometry and X-ray structure determination of compound 6). Furthermore, we introduce the synthesis and characterization study of four new models (7–10) mimicking the active site of [FeFe]-hydrogenase. The structures of complexes 7–9 are determined using X-ray single crystal diffraction analysis. In addition, we present an investigation of the redox properties and the catalytic behaviour of the diiron

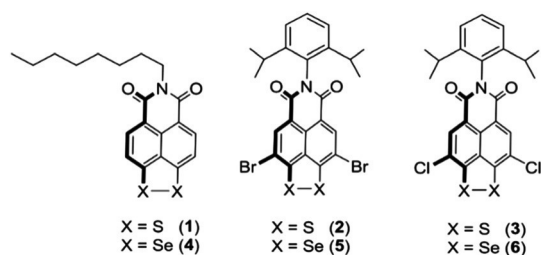


Fig. 2 Chemical structures of naphthalene monoimide (NMI) dithiol and diselenol compounds 1–6.

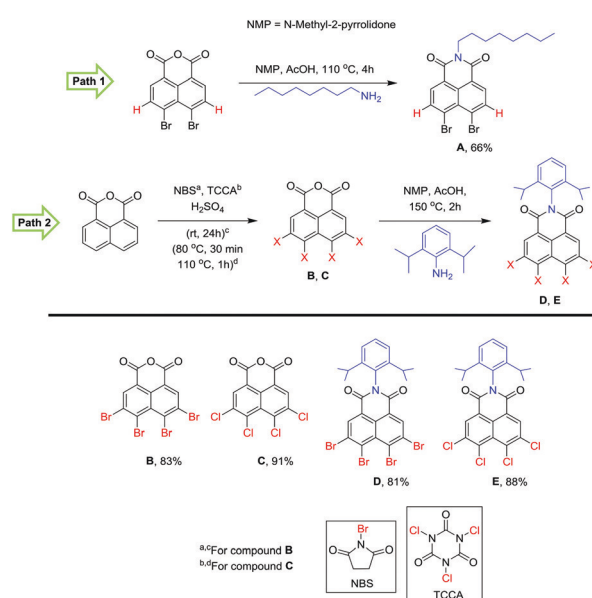
complexes 7–10 as well as the fluorescence properties of compounds 1, 2, 4, and 5 and complexes 7–10. Furthermore, the fundamental transitions underlying the bright excitation of complexes 7 and 9 within the Franck–Condon region are unravelled by virtue of time-dependent density functional theory (TDDFT).

Results and discussion

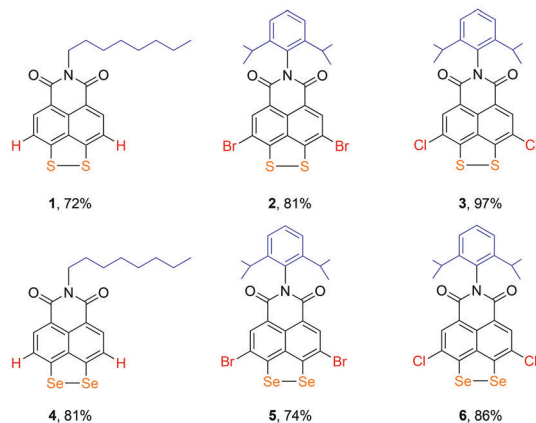
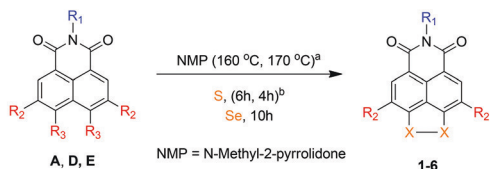
Synthesis and characterization of compounds 1–6

The synthetic procedures and characterization of precursors A–E (Scheme 1) required for the preparation of compounds 1–6 are described in detail in the ESI.†

Compound A was prepared from the imidization of 4,5-dibromo-1,8-naphthalic anhydride with 1-amino-octane (Scheme 1, path 1) as previously described in the literature.^{14a} In parallel, we have prepared a novel tetrabromonaphthalene monoanhydride derivate B as well as the tetrachloro naphthalene monoanhydride derivate C^{14b} (Scheme 1, path 2), which we could modify selectively at the *peri*-positions of the aromatic core (compounds 2–6). As illustrated in Scheme 2, compounds 1 and 4 were obtained in 72% and 81% yield, respectively, by treatment of *N*-octyl-4,5-dibromonaphthalene monoimide (A) with S (or Se) in NMP at 160 °C for 6 hours (10 hours for Se). Similarly, the reaction of precursor D (or E) with S (or Se) in NMP at 170 °C for 4 hours (10 hours for Se) afforded the NMI-disulfide bridges 2 and 3 as well as the NMI-diselenide bridges 5 and 6 in 81%, 97%, 74% and 86% yield, respectively, as shown in Scheme 2. Compounds 1–6 have been characterized by means of ¹H, ¹³C{¹H}, ⁷⁷Se{¹H} NMR spectroscopic techniques as well as elemental analysis, mass spectrometry (see the Experimental section) and X-ray structure determination of compound 6 (Fig. S1, ESI†).



Scheme 1 Synthetic pathways of precursors A–D.

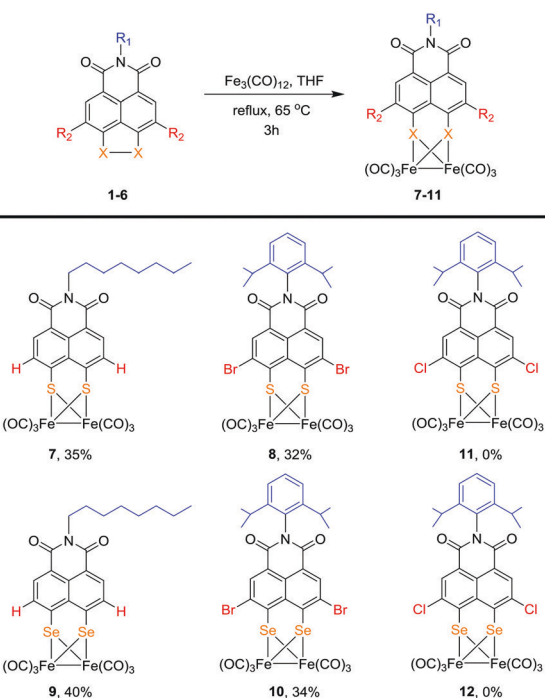


^a160 °C for the precursors **A** and 170 °C for the precursors **D** and **E**
^b6h for the precursor **A** and 4h for the precursors **D** and **E** in the case of **S**

Scheme 2 Synthetic pathway of compounds 1–6.

Synthesis and characterization of the diiron complexes

Treatment of equimolar amounts of $\text{Fe}_3(\text{CO})_{12}$ and compounds **1**, **2**, **4**, and **5**, respectively, in THF at 65 °C for three hours followed by subsequent column chromatography afforded complexes **7–10** in 32–40% yield as shown in Scheme 3.



Scheme 3 Synthetic pathway of complexes 7–12.

Table 1 Carbonyl stretching vibrations for complexes 7–10

Complex	$\nu(\text{CO})$ (cm^{-1})
7	2074(s), 2040(m), 1989(m)
8	2077(s), 2036(m), 1981(m)
9	2065(s), 2028(m), 1981(m)
10	2070(s), 2032(m), 1978(m)

Unfortunately, refluxing of compound **3** or **6** with $\text{Fe}_3(\text{CO})_{12}$ in THF did not afford complex **11** or **12** as shown in Scheme 3. However, such behaviour has been previously reported in the literature.^{11e}

The novel complexes **7–10** have been characterized by spectroscopic methods (^1H NMR, $^{13}\text{C}\{^1\text{H}\}$ NMR, $^{77}\text{Se}\{^1\text{H}\}$ NMR and IR), mass spectrometry, elemental analysis and X-ray crystallography for **7–9**. The IR spectra of complexes **7–10** exhibit three absorption bands for the terminal CO ligands of each complex as illustrated in Table 1. It is evident that the CO stretching vibrations appear at lower frequencies when the S atoms are substituted by Se atoms (Table 1). This finding can be rationalized in terms of increasing back-donation to CO due to the enhanced electron donor ability of Se with respect to S.^{11e,13,15}

The ^1H NMR spectra of complexes **7** and **9** exhibit a broad signal in the range 8.40–8.45 ppm for the protons of the naphthalene backbone similar to that observed in the literature.¹⁶ Additionally, four signals at 4.11, 1.68, 1.27 and 0.86 ppm were also detected in each spectrum for the remaining protons in the alkyl chain. Furthermore, the $^{13}\text{C}\{^1\text{H}\}$ NMR spectra of these complexes show only one signal (**7**: 207.2 ppm and **9**: 207.8 ppm) for the carbonyl ligands at room temperature as previously reported for similar diiron complexes.^{12,16}

The signals for the remaining carbon atoms in complexes **7** and **9** were also detected in the spectra (see the Experimental section). Moreover, the $^{77}\text{Se}\{^1\text{H}\}$ NMR spectrum of complex **9** displays one signal for the two chemically equivalent Se atoms at 209.82 ppm. The ^1H NMR spectra of complexes **8** and **10** exhibit a broad signal peak at 8.72 ppm for the protons of the naphthalene ring and a multiplet in the region of 7.34–7.49 ppm for the aromatic protons. Thus, the isopropyl group protons are shown as two peaks at 2.63 ppm and at 1.14 ppm which are assigned to the $-\text{CH}$ and $-\text{CH}_3$ moieties, respectively. The $^{13}\text{C}\{^1\text{H}\}$ NMR spectra of **8** and **10** display one signal for the carbonyl ligands (**8**: 206.1 ppm, **10**: 207.3 ppm) in addition to the peaks for the naphthalene monoimide skeleton (see the Experimental section). A signal at 270.26 ppm was detected in the $^{77}\text{Se}\{^1\text{H}\}$ NMR spectrum of complex **10** which is assigned to the two chemically equivalent Se atoms. The mass spectra of complexes **7–10** show the molecular ion peaks and the peaks resulting from the dissociation of the six CO ligands, sequentially.

Molecular structures

The diffusion of hexane into a dichloromethane solution of complexes **8** and **9** at 20 °C afforded a suitable single crystal for X-ray diffraction studies. Unfortunately, no single crystal of

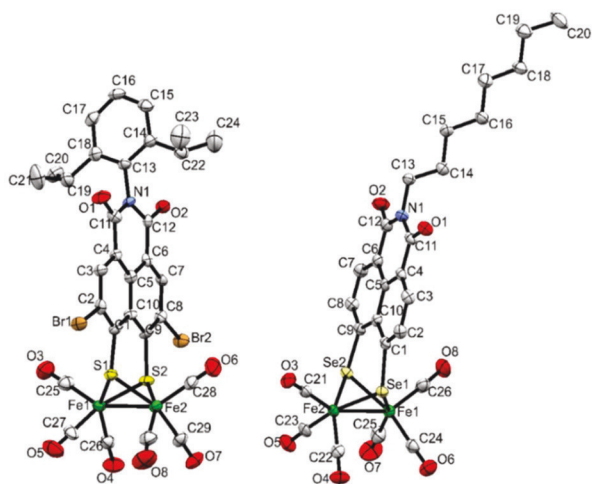


Fig. 3 Molecular structures (60% probability) of complex **8** (left) and complex **9** (right). Hydrogen atoms are omitted for clarity.

complex **10** could be obtained and the crystallization of **7** gave low quality crystals that resulted only in a structural motif of complex **7** due to the presence of a long alkyl chain in the imide structure, which can disturb the dense packing of the molecules (Fig. S2, ESI†). Fig. 3 depicts the molecular structures of complexes **8** and **9** with ellipsoids drawn at the 60% probability level. In the case of complex **8**, the structure includes two molecules of dichloromethane solvent which are omitted from Fig. 3 for clarity. Both **8** and **9** revealed the typical butterfly conformation of $[\text{Fe}_2\text{X}_2]$ ($\text{X} = \text{S}$ or Se). The geometry around each iron atom can be best described as a distorted octahedron in which the central atom is Fe surrounded by three terminal CO ligands in a facial fashion as well as two chalcogen atoms that bridge both iron centres. The Fe–Fe bond length of **8** (2.5139(12) Å) is slightly shorter than that of **9** (2.5607(7) Å), which is comparable to those observed in the literature.^{11e,15a} This is attributed to the enhanced van der Waals radii of Se compared to S. The average Fe–CO bond length in **8** (1.804(7) Å) is slightly longer than that of **9** (1.797(4) Å) due to less metal to CO back donation in the case of the dithiolato complexes relative to the diselenolato analogues, which is in agreement with the IR data (Table 1). It is notable that the average Fe–S (2.2419(17) Å) and Fe–Se (2.3599(7) Å) bond lengths are comparable to those of naphthalene containing complexes observed in the literature,^{11c,e} indicating that the imide functionality has no influence on the bond length. Additionally, the torsion angle τ formed from the intersection between $\text{OC}_{\text{ap}}\text{--Fe}_1\text{--Fe}_2$ and $\text{OC}_{\text{ap}}\text{--Fe}_2\text{--Fe}_1$ of **8** is 14.71° which is less distorted from the eclipsed $\text{Fe}(\text{CO})_3$ conformation compared to that of **9** ($\tau = 26.83^\circ$).

Electrochemistry

The electrochemical properties of complexes **7–10** were investigated with respect to the influence of both the imide functionality and the chalcogen atoms on the reduction potentials. Table 2 summarizes the electrochemical reduction and ox-

Table 2 Summary of the redox features of complexes **7–10** in 0.1 M $\text{CH}_2\text{Cl}_2\text{--}[\text{n-Bu}_4\text{N}][\text{BF}_4]$ solution measured at $\nu = 0.2 \text{ V s}^{-1}$ using a glassy carbon disk ($d = 1.6 \text{ mm}$). Potentials E are given in volts (V) and referenced to the Fc^+/Fc couple

Complex	E_{red1}^a	$E_{1/2}^b$	E_{red2}^a	$E_{1/2}^b$	E_{ox}
7	−1.34 (E_{pc}) −1.27 (E_{pa})	−1.31	−1.68 (E_{pc}) −1.62 (E_{pa})	−1.65	0.93
8	−1.12 (E_{pc}) −1.06 (E_{pa})	−1.09	−1.54 (E_{pc}) −1.46 (E_{pa})	−1.50	1.11
9	−1.39 (E_{pc}) −1.31 (E_{pa})	−1.35	−1.63 (E_{pc})	—	0.89
10	−1.17 (E_{pc}) −1.07 (E_{pa})	−1.12	−1.55 (E_{pc})	—	0.98

^a E_{red1} and E_{red2} are the potentials for the first and the second reductions, where E_{pc} and E_{pa} are the cathodic and anodic scan peak potentials. ^b $E_{1/2}$ is the half-wave potential for the first and the second reduction events. Because the $I_{\text{pa}}/I_{\text{pc}}$ value (anodic to cathodic peak current ratio) at 0.2 V s^{-1} of complexes **7–10** is less than 1, the $E_{1/2}$ can be considered as approximated values.

idation potentials from the cyclic voltammetric measurements of **7–10**. The voltammetric profiles presented in Fig. 4 indicate that complexes **7** and **8** are reduced *via* two sequential quasi-reversible one-electron steps ($E_{1/2} = -1.31$ and -1.65 V for complex **7**, $E_{1/2} = -1.09$ and -1.50 V for complex **8**) which are assigned to $\text{Fe}^{\text{I}}\text{Fe}^{\text{I}} \rightarrow \text{Fe}^{\text{I}}\text{Fe}^0$ and $\text{Fe}^{\text{I}}\text{Fe}^0 \rightarrow \text{Fe}^0\text{Fe}^0$ similar to their reported analogue complexes.^{11c-f,12,16} The small oxidation peak observed at $E_{\text{pa}} = -1.05 \text{ V}$ in the return sweep of complex **7** might arise from the oxidation of a species formed in a slow reaction following the reduction of the dianionic species, while the reduction event observed at $E_{\text{pc}} = -1.31 \text{ V}$ for complex **8** might be correlated due to the reduction of a species formed upon reduction of the initial complex. However, these oxidation and reduction events are vanishing at higher scan rates up to 1.0 V s^{-1} (Fig. S3, ESI†). Reversing the scan at -1.53 V and -1.39 V for complexes **7** and **8**, respectively, does not enhance the reversibility of the first reduction events (Fig. S3, ESI†). A plot of the current function ($I_{\text{pc}}/C \cdot \nu^{1/2}$) vs. the scan rates (ν) for the first and the second reduction events of complexes **7** and **8** (Fig. S4, ESI†) shows the expected invariance for a process involving the transfer of one electron without any chemical complications which suggest an EE process ($E = \text{electrochemical process}$).^{9c,17} It is noteworthy that the electron-withdrawing bromide substituents in complex **8** cause a shift ($\sim 220 \text{ mV}$ and $\sim 150 \text{ mV}$) of the reduction peaks to less negative potentials compared to that of complex **7**. This can be seen by comparing $E_{1/2}$ values for the first and the second reduction waves of complex **8** and of complex **7** (see $E_{1/2}$ values in Table 2). Such a behaviour has been reported for various diiron carbonyl complexes.^{11c-f} The replacement of the $\mu\text{-S}$ atoms with Se in the bridging linker of complexes **9** and **10** leads to variations in the cathodic processes compared to the corresponding S analogues **7** and **8** as shown in Fig. 5. The cyclic voltammograms of complexes **9** and **10** (Fig. 5) display two main reduction events for each complex as a quasi-reversible one electron reduction step at $E_{1/2} = -1.39$ and -1.17 V , respectively, as well as an irreversible one electron reduction

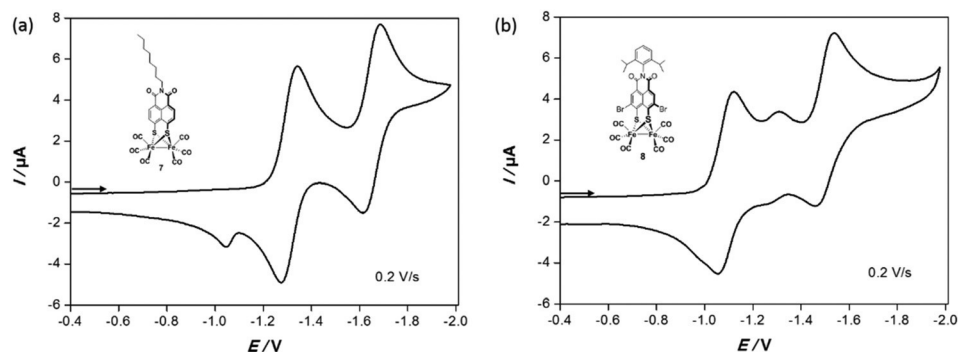


Fig. 4 Cyclic voltammetry of (a) 1.0 mM complex **7** and (b) 1.0 mM complex **8** in CH_2Cl_2 -[*n*-Bu₄N][BF₄] (0.1 M) solutions at 0.2 V s⁻¹ scan rate. The arrows indicate the scan direction. The potentials *E* are given in V and referenced to the Fc⁺/Fc couple.

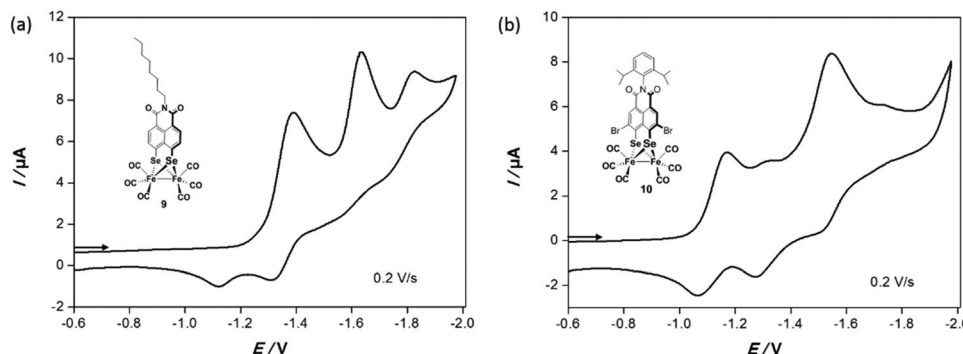


Fig. 5 Cyclic voltammetry of (a) 1.0 mM complex **9** and (b) 1.0 mM complex **10** in CH_2Cl_2 -[*n*-Bu₄N][BF₄] (0.1 M) solutions at 0.2 V s⁻¹ scan rate. The arrows indicate the scan direction. The potentials *E* are given in V and referenced to the Fc⁺/Fc couple.

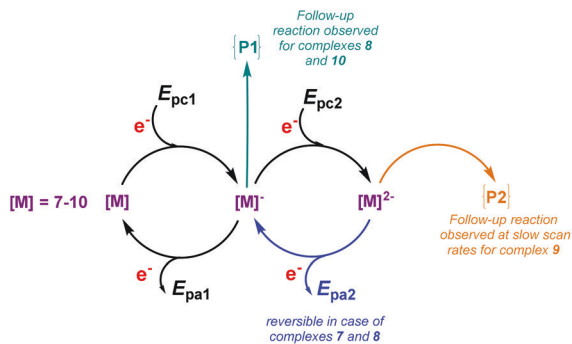
step at -1.63 V for complex **9** and at -1.55 V for complex **10**. These reduction events are assigned to $\text{Fe}^{\text{I}}\text{Fe}^{\text{I}} \rightarrow \text{Fe}^{\text{I}}\text{Fe}^{\text{0}}$ and $\text{Fe}^{\text{I}}\text{Fe}^{\text{0}} \rightarrow \text{Fe}^{\text{0}}\text{Fe}^{\text{0}}$ similar to the corresponding S analogues. The current functions of the first and the second reduction waves for complexes **9** and **10** show a similar behaviour to those observed for the S containing complexes **7** and **8** (Fig. S5, ESI[†]). The reversibility of the first reduction peak of complex **9** is enhanced by reversing the forward scan at -1.53 V, while the second reduction peak remains irreversible by switching the forward scan at -1.75 V (Fig. S6, ESI[†]). Moreover, the existence of a small irreversible reduction event at -1.83 V for complex **9** (Fig. 5a) could be assigned to reduction of daughter products of the follow-up reaction from the second reduced species as reported for various diiron carbonyl complexes.^{9c,18} In contrast, the reversibility of the first reduction peak of complex **10** is not affected by reversing the forward scan at -1.25 V (Fig. S7, ESI[†]).

Furthermore, a reduction event at -1.32 V appears again similar to that of complex **8**. Additionally, the stability of complexes **7–10** is slightly reduced under electrochemical conditions when the scan was repeated up to 5 times at 0.2 V s⁻¹ (Fig. S8, ESI[†]). Upon initiating the electrochemical scan in the positive direction of complexes **7–10**, an irreversible oxidation peak is observed for each complex (Table 2) which

could be assigned to the one-electron oxidation process of $\text{Fe}^{\text{I}}\text{Fe}^{\text{I}} \rightarrow \text{Fe}^{\text{I}}\text{Fe}^{\text{II}}$ as previously reported for various diiron complexes.^{11e,13b,19a-c} Moreover, it is remarkable that complexes **9** and **10** are readily oxidized which emphasized that the electron density at their iron cores is slightly higher than those of the S analogue complexes. Overall, the voltammetric profiles of complexes **7–10** demonstrate that the presence of the imide functionality enhances the chemical stability of the mono- and direduced species resulting in a normal ordering of potential (EE mechanism) with peak potential separation of about ~ 350 mV. Unfortunately, the replacement of μ -S with Se diminished the stability of complexes **8** and **10** under reductive conditions as reported previously.^{11e,f} Scheme 4 depicts the proposed mechanism for the cathodic processes of complexes **7–10** at slow (0.2 V s⁻¹) and fast scan rates (1.0 V s⁻¹).

Electrocatalysis

Furthermore, we have tested the electrocatalytic behavior of complexes **7–10** in the presence of various concentrations of acetic acid (AcOH) and the CVs are illustrated in Fig. 6. The presence of one equiv. of AcOH in the solutions of complexes **7–10** revealed that none of the complexes showed any response toward the acid at the first reduction events of complexes **7–10**



Scheme 4 Proposed cathodic processes of complexes 7–10 at slow (0.2 V s^{-1}) and fast (1.0 V s^{-1}) scan rates.

(Fig. 6a–d), while the second reduction events of complexes 7–10 show small shifts (~ 63 , ~ 46 , ~ 16 and ~ 33 mV, respectively) to less negative potentials (Fig. 6a–d) which is a typical observation when protonation of a dianionic species takes place.^{9c,i,19d} However, when the acid concentration was increased, the current of this process remained constant. At more reducing potentials in the vicinity of -1.80 V to -2.4 V for complexes 7–10, the voltammetric profile of each complex shows catalytic behavior through two processes: process I at $E_p^{\text{cat}} \approx -1.98$, -1.84 , -2.06 and -2.04 V , respectively, which levels off at $[\text{AcOH}] \approx 6$ equiv. and process II at $E_p^{\text{cat}} \approx -2.34$, -2.32 , -2.30 and -2.29 V , respectively (Fig. 6). The reduction of AcOH in CH_2Cl_2 - $[n\text{-Bu}_4\text{N}][\text{BF}_4]$ in the absence of complexes 7–10 starts near -2.55 V (Fig. S9, ESI[†]) which indicates that the increase in the current with increasing AcOH concentration is due to catalytic processes.

Ground-state absorption and steady state emission properties

The photophysical properties of compounds 1, 2, 4 and 5 as well as those of complexes 7–10 were studied by steady state absorption and emission spectroscopy. Compounds 1, 2, 4 and 5 exhibit broad absorption bands in the visible range between 380 and 520 nm with absorption coefficients of up to $4 \times 10^4 \text{ M}^{-1} \text{ cm}^{-1}$ as well as strong absorption in the UV between 230 and 320 nm (cf. Table 3 and Fig. 7). The UV absorption features are composed of several bands, which appear as shoulders to one main band at around 270 nm. For the diisopropylphenyl-substituted naphthalene monoimides 2 and 5, the UV absorption features appear red-shifted with respect to their octyl-substituted counterparts 1 and 4. Moreover, the substitution of S atoms in compounds 1 and 2 by Se (4 and 5) leads to decreased absorption coefficients (about 50%) of the 270 nm band. The influence of the chalcogen atoms is also apparent in the Vis-absorption band. The S substituted compounds (1 and 2) show a pronounced shoulder at the short-wavelength flank of the Vis-absorption band, while in the case of the Se substituted compounds (4 and 5), this band remains structureless. The N-bound substituent has only a minor influence on the Vis-absorption band, i.e. shifting the maximum by about 0.04 eV to the red for the diisopropylphenyl-substituted compounds 2 and 5 with respect to the octyl-substituted 1 and 4. It is important to note that several very weak bands are observed between the major UV- and Vis-absorption bands (ca. 320–400 nm) with absorption coefficients between 2×10^2 and $2 \times 10^3 \text{ M}^{-1} \text{ cm}^{-1}$. Upon complexation, the bands between 320 and 400 nm gain significant oscillator strength (about one order of magnitude; cf. Fig. 7) for the corresponding diiron complexes 7–10, while the absorption coefficient of the Vis-

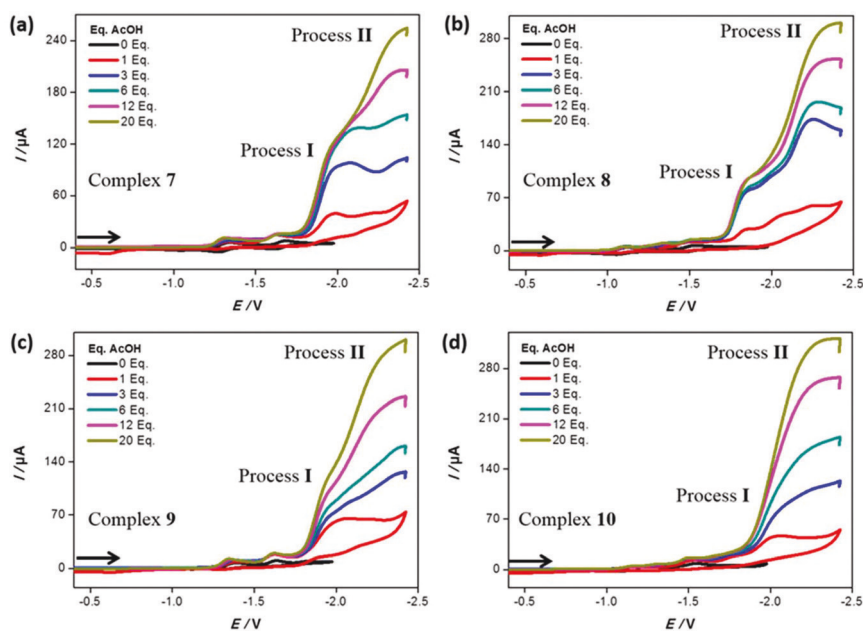


Fig. 6 Cyclic voltammetry of 1.0 mM complexes 7–10 in CH_2Cl_2 - $[n\text{-Bu}_4\text{N}][\text{BF}_4]$ (0.1 M) solutions at 0.2 V s^{-1} in the presence of various concentrations of AcOH. The arrows indicate the scan directions. The potentials E are given in V and referenced to the Fc^+/Fc couple.

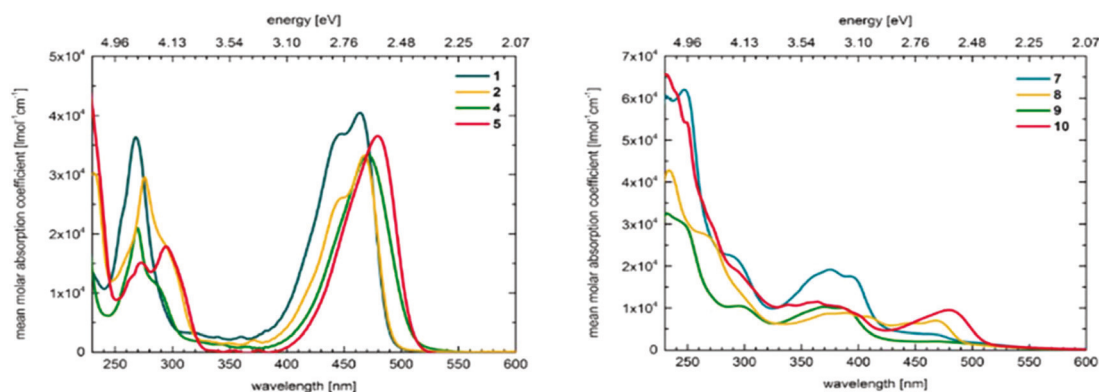
Table 3 Summary of the photophysical properties of compounds **1**, **2**, **4** and **5** as well as complexes **7–10** in CH₂Cl₂

Compound	$\lambda_{\text{max, abs}}$ [nm]	ϵ^a [10^4 L mol ⁻¹ cm ⁻¹]	$\lambda_{\text{max, em}}$ [nm]	Φ^b [%]
1	269	3.6	489 (432)	0.18
	447	3.7		
	464	4.0		
2	232	3.0	489 (432)	1.67
	276	3.0		
4	468	3.3	414 (530)	0.59
	269	2.1		
5	471	3.3	504 (430)	0.07
	272	1.5		
	294	1.8		
7	478	3.6	442	0.02
	247	6.2		
	375	1.9		
8	464	0.4	432	0.02
	233	4.3		
	388	0.9		
9	467	0.7	419	n.a. ^c
	232	3.3		
	370	1.0		
10	471	0.2	417	0.02
	230	6.6		
	363	1.1		
	479	0.9		

^a Molar absorption coefficients are an average of six samples with varying concentrations. ^b Determination of quantum yields using perylene as a standard ($\Phi = 94\%$) with excitation at 390 nm. ^c The quantum yield could not reliably be determined to overlap of the very weak emission band with the solvent Raman signal.

absorption band around 480 nm decreases significantly. Contrarily, the bands located below 320 nm for the diiron complexes **7–10** gain oscillator strength by about a factor of two and thus appear broadened compared to their corresponding ligand precursors. To gain insight into the electronic transitions underlying the absorption spectra of this class of compounds, quantum chemical simulations have been performed exemplary for **7** and **9**. The TDDFT simulations performed within the fully optimized equilibrium geometries of **7** and **9** allowed an unambiguous assignment of the bright absorption features in the range of 320–400 nm. For complex **7**, TD-B3LYP

predicts a very bright $\pi\pi^*$ intra-ligand excitation (IL, S₇) localized on the NMI moiety at 398 nm (3.11 eV), while a medium bright metal centred (MC, S₉) excitation associated with the opening of the Fe–Fe bond is obtained at 383 nm (3.24 eV). Analogously, a bright IL excitation as well as a medium bright MC excitation were observed for **9** at 397 (3.13 eV) and 391 nm (3.17 eV), respectively. The weakly absorbing red-sided absorption feature in **7** and **9** at approximately 464 (2.67 eV) and at 471 nm (2.63 eV), respectively, can be assigned to excitation into the weakly absorbing states S₂–S₄ of mixed electronic character in the range of 413–428 nm (3.00–2.89 eV) for **7** and 423–434 nm (2.92–2.86 eV) for **9**. Interestingly, these states are partially of direct charge transfer nature from the S/Se p-orbitals as well as from the NMI moiety towards the [FeFe]-fragment. Detailed information with respect to the quantum chemical calculations and computational setup can be found in the ESI (see Tables S1–S4†). The emission properties of **1**, **2**, **4** and **5** as well as **7–10** were investigated by steady state emission spectroscopy in dichloromethane. Quantum yields were determined (as specified in the Experimental section) and the results are summarised in Table 3 and Fig. S10–S13 in the ESI.† The S substituted compounds **1** and **2** exhibit emission with the maximum at 489 nm as well as a weak emission around 432 and 451 nm, respectively. The 489 nm emission band overlaps with the Vis-absorption band but its seemingly negligible Stokes-shift can be rationalized by the corresponding excitation spectrum, which shows two maxima at about 380 and 269 nm. Apparently, excitation of the complex in the UV-absorption bands as well as at the weak absorption bands between 320 and 400 nm lead to the population of emissive states. Additionally, for the *N*-octyl substituted **1** a weak structured emission band is observed at 530 nm. A similar structured emission band is observed for the *N*-octyl and selenium substituted compound **4** together with a weaker emission at 414 nm. The *N*-diisopropylphenyl substituted compound **5** shows a broad emission band around 504 nm as well as a weaker band at 430 nm. The diiron complexes are barely emissive. For **7** and **8**, a negligible structureless emission is observed around 442 and 432 nm, respectively (*cf.* Table 3). For both complexes, excitation at the absorption bands around

**Fig. 7** UV-Vis absorption spectra of **1**, **2**, **4** and **5** (left) and **7–10** (right) in dichloromethane.

390 nm furnishes the highest emission (albeit still drastically lower than those of the respective ligand precursors). For the diiron complexes **9** and **10** similar emission characteristics to **7** and **8** are observed, however, with a band centred around 419 and 417 nm, respectively. Excitation at the 370 nm absorption band furnishes the highest quantum yields (again they are much lower than in the respective ligand precursors). The drastically quenched emission of the diiron complexes with respect to the ligand precursors points to the transfer of the photo-excited electron to the diiron center. Nonetheless, a detailed mechanistic photophysical study of **7–10** is pending.

Conclusions

Herein we report the synthesis of naphthalene monoimides of *peri*-substituted dithiol and diselenole compounds. Additionally, we modified the naphthalene scaffold by incorporating electron withdrawing substituents in the *ortho*-position to the two chalcogens. The latter compounds were tested as a ligand to react with $\text{Fe}_3(\text{CO})_{12}$ in boiling THF in which we could obtain the [FeFe]-hydrogenase synthetic mimics **7–10** and characterize them by different spectroscopic techniques and TDDFT. The presence of the imide functionality in the naphthalene skeleton enhanced the chemical stability of the reduced species to proceed *via* normal two sequential one-electron processes (EE mechanism). Thus, the introduction of bromine substituents at the 2- and 7-positions of the naphthalene skeleton caused a fine-tuning of the reduction potential of **8** and **10** while the replacement of the S atoms with Se in the bridging linker caused a cathodic shift in the oxidation peaks compared with the S analogues. The proton reduction catalyzed by complexes **7–10** was also investigated by cyclic voltammetry using AcOH as a proton source. Furthermore, the photophysical properties of compounds **1**, **2**, **4**, and **5** and complexes **7–10** were determined by means of steady state absorption and emission spectroscopy. The quantum chemical simulations performed for complexes **7** and **9** indicate their potential to directly transfer a photo-excited electron from the chromophore towards the [FeFe] moiety.

Experimental part

Materials and techniques

The reactions of complexes **7–10** were performed using standard Schlenk and vacuum-line techniques under an inert gas (nitrogen) atmosphere. The ^1H , $^{13}\text{C}\{^1\text{H}\}$, $^{77}\text{Se}\{^1\text{H}\}$ NMR spectra were recorded with a Bruker Avance 300, 500 and 400 MHz spectrometer. Chemical shifts are given in parts per million with references to internal SiMe_4 (^1H , ^{13}C) or Me_2Se . The (^{77}Se) mass spectrum was recorded with a Finnigan MAT SSQ 710 instrument. The IR spectra were recorded with a Bruker Equinox 55 spectrometer equipped with an ATR unit. Elemental analysis was performed with a Leco CHNS-932 apparatus. Melting points were recorded on a polarization

microscope (Axiolab) connected to a heating unit (THS-600) using the software Linkam LNP and CI 93. TLC was performed by using Merck TLC aluminum sheets (Silica gel 60 F254). Solvents from Fisher Scientific and other chemicals from Acros and Aldrich were used without further purification. All solvents were dried and distilled prior to use according to standard methods.

Electrochemistry

Cyclic voltammetric measurements were conducted in the three-electrode technique [glassy carbon disk (diameter $d = 1.6$ mm) as the working electrode, Ag/Ag^+ in MeCN as the reference electrode, and Pt wire as the counter electrode] using a Reference 600 Potentiostat (Gamry Instruments). All experiments were performed in dichloromethane solutions (concentration of the complexes was 1.0 mM) containing 0.1 M $[\text{n-Bu}_4\text{N}][\text{BF}_4]$ at room temperature. The solutions were purged with N_2 and a stream of it was maintained over the solutions during the measurements. The vitreous carbon disk was polished on a felt tissue with alumina before each measurement. All potential values reported in this paper are referenced to the potential of the ferrocenium/ferrocene (Fc^+/Fc) couple. Corrections for the iR drop were performed for all experiments.

UV-Vis absorption and emission

UV-Vis absorption spectra were recorded on a Varian Cary5000 spectrophotometer in dichloromethane using 1 cm quartz cuvettes. Molar absorption coefficients were determined as an average of six samples with six different concentrations ranging from 10^{-4} to 10^{-2} mol L^{-1} (each sample was measured twice). Emission spectra were recorded from dichloromethane solutions (*ca.* 0.04 mmol L^{-1}) on a Jasco FP-6500 using a xenon lamp as the light source and are corrected for the instrumental response function. Quantum yields Φ were determined against perylene as the standard in cyclohexane ($\Phi_{\text{Standard}} = 0.94$) and were calculated with the following equation with the refractive indices n of the ($n_{\text{cyclohexane}} = 1.4266$; $n_{\text{dichloromethane}} = 1.4242$), the integrated emission I and the absorbance at the excitation wavelength A :

$$\Phi_{\text{Sample}} = \Phi_{\text{Standard}} \frac{I_{\text{Sample}} A_{\text{Standard}} n_{\text{dichloromethane}}^2}{I_{\text{Standard}} A_{\text{Sample}} n_{\text{cyclohexane}}^2}$$

Crystal structure determination

The intensity data for the compounds were collected on a Nonius KappaCCD diffractometer using graphite-monochromated $\text{Mo-K}\alpha$ radiation. Data were corrected for Lorentz and polarization effects; absorption was taken into account on a semi-empirical basis using multiple-scans.^{20–22} The structures were solved by direct methods (SHELXS)²³ and refined by full-matrix least squares techniques against F_o^2 (SHELXL-97).²³ The hydrogen atoms of **9** (with the exception of the methyl group of C20 and the methene group of C13) were located by difference Fourier synthesis and refined isotropically. All other hydrogen atoms were included at calculated positions with

fixed thermal parameters. The crystal of **8** contains large voids, filled with disordered solvent molecules. The size of the voids is 106 \AA^3 per unit cell. Their contribution to the structure factors was secured by back-Fourier transformation using the SQUEEZE routine of the program PLATON²⁴ resulting in 42 electrons per unit cell. The crystals of **7** were extremely thin and of low quality, resulting in a substandard data set; however, the structure is sufficient to show connectivity and geometry despite the high final *R* value. We will only publish the conformation of the molecule and the crystallographic data. We will not deposit the data in the Cambridge Crystallographic Data Centre. All non-disordered, non-hydrogen atoms were refined anisotropically.²³ Crystallographic data as well as structure solution and refinement details are summarized in Table S5 in the ESI.† MERCURY²⁵ was used for structure representations.

Computational details

All quantum chemical calculations were performed using the Gaussian 09²⁶ program. The fully optimized ground state equilibrium structures of complexes **7** and **9** were obtained at the density functional level of theory (DFT) by means of the GGA functional BP86²⁷ in cooperation with the triple- ζ -valence-polarization (TZVP) basis set;²⁸ for the iron atoms the MDF10²⁹ core potential was utilized. The experimental X-ray structure of **9** was used as initial geometry in all geometry optimizations. A subsequent vibrational analysis confirmed that the optimization structures (for **7** and **9**) correspond to the minima of the 3*N*-6 dimensional potential energy hypersurface. The analysis of the electronic ground state properties was followed by an investigation of the excited state properties of **7** and **9** at the TFDFT level of theory within the Franck-Condon region by means of the 50 lowest singlet excited states. All TDDFT calculations were performed with the B3LYP³⁰ functional in association with the same basis set and pseudo potential as the respective ground state calculations. The effects of solvation on ground and excited state properties (dichloromethane: $\epsilon = 8.93$; $n = 1.4242$) were considered based on the integral equation formalism of the polarizable continuum model.³¹

General procedure for the preparation of compounds 1–6

A mixture of compound A (C or E) (2 mmol) and S (or Se) (10 mmol) in 25 mL NMP was stirred at 160–170 °C for 4–10 hours. The mixture was cooled to room temperature and poured into ice. The precipitate was filtered, washed with water and dried. The crude product was purified by column chromatography using hexane/dichloromethane as the eluent on silica to afford the desired compounds as a yellow solid for 1–3 and as an orange solid for 4–6.

6-Octyl-5*H*-[1,2]dithiolo[3',4',5':4,5]naphtho[1,8-*cd*]pyridine-5,7(6*H*)-dione (1). Yield: 72%. Mp 146–147 °C. Elemental analysis for C₂₀H₂₁NO₂S₂: calculated C 64.66, H 5.70, N 3.77, S 17.26; found C 65.10, H 5.69, N 3.91, S 16.80. IR (cm⁻¹): 2951w, 2923w, 2851w, 1695s, 1646s, 1585s, 1539w, 1496w, 1458s, 1380w, 1351s, 1089w, 796s, 743s. ¹H NMR (300 MHz,

CDCl₃, ppm): $\delta = 8.36$ (d, *J* = 8.0 Hz, 2H), 7.49 (d, *J* = 8.0 Hz, 2H), 4.11 (t, *J* = 7.4 Hz, 2H), 1.73–1.63 (m, 2H), 1.36–1.27 (m, 10H), 0.90–0.86 (m, 3H). ¹³C{¹H} NMR (75 MHz, CDCl₃, ppm): $\delta = 162.1, 152.9, 133.6, 132.6, 129.9, 116.7, 40.4, 31.7, 29.2, 27.9, 27.1, 22.6, 14.1$. DEI-MS: *m/z* = 371 [M]⁺.

3,9-Dibromo-6-(2,6-diisopropylphenyl)-5*H*-[1,2]dithiolo[3',4',5':4,5]naphtho[1,8-*cd*]pyridine-5,7(6*H*)-dione (2). Yield: 81%. Mp > 300 °C. Elemental analysis for C₂₄H₁₉Br₂NO₂S₂: calculated C 49.93, H 3.32, N 2.43, S 11.11; found C 49.50, H 3.26, N 2.25, S 11.04. IR (cm⁻¹): 3081w, 3055w, 3044w, 2958w, 2926w, 2866w, 1707s, 1663s, 1576w, 1534s, 1465s, 1379s, 1355w, 1030w, 846s, 811s, 733s. ¹H NMR (500 MHz, CDCl₃, ppm): $\delta = 8.59$ (s, 2H), 7.48 (t, *J* = 7.8 Hz, 1H), 7.33 (d, *J* = 7.8 Hz, 2H), 2.64 (hept, *J* = 6.9 Hz, 2H), 1.15 (d, *J* = 6.9 Hz, 12H). ¹³C{¹H} NMR (125 MHz, CDCl₃, ppm): $\delta = 162.3, 154.2, 145.6, 135.1, 133.9, 130.8, 129.8, 128.2, 124.3, 119.5, 110.7, 29.3, 24.1$. DEI-MS: *m/z* = 577 [M]⁺.

3,9-Dichloro-6-(2,6-diisopropylphenyl)-5*H*-[1,2]dithiolo[3',4',5':4,5]naphtho[1,8-*cd*]pyridine-5,7(6*H*)-dione (3). Yield: 97%. Mp > 300 °C. Elemental analysis for C₂₄H₁₉Cl₂NO₂S₂: calculated C 59.02, H 3.92, N 2.87, S 13.13; found C 59.16, H 3.86, N 2.84, S 13.36. IR (cm⁻¹): 3084w, 3057w, 3045w, 2959w, 2926w, 2867w, 1712s, 1668s, 1581w, 1542s, 1468s, 1386w, 1357w, 1034w, 849s, 801s, 742s. ¹H NMR (500 MHz, CDCl₃, ppm): $\delta = 8.47$ (s, 2H), 7.48 (t, *J* = 7.8 Hz, 1H), 7.33 (d, *J* = 7.8 Hz, 2H), 2.64 (hept, *J* = 6.9 Hz, 2H), 1.15 (d, *J* = 6.9 Hz, 12H). ¹³C{¹H} NMR (125 MHz, CDCl₃, ppm): $\delta = 162.4, 151.1, 145.6, 135.1, 132.6, 130.8, 129.8, 127.5, 124.3, 123.5, 119.7, 29.3, 24.1$. DEI-MS: *m/z* = 488 [M]⁺.

6-Octyl-5*H*-[1,2]diselenolo[3',4',5':4,5]naphtho[1,8-*cd*]pyridine-5,7(6*H*)-dione (4). Yield: 81%. Mp 209–210 °C. Elemental analysis for C₂₀H₂₁NO₂Se₂: calculated C 51.63, H 4.55, N 3.01; found C 51.91, H 4.45, N 3.04. IR (cm⁻¹): 2950w, 2924w, 2852w, 1692s, 1630s, 1570s, 1540w, 1491w, 1458s, 1375w, 1338s, 1088w, 793s, 741s. ¹H NMR (500 MHz, CDCl₃, ppm): $\delta = 8.29$ (d, *J* = 8.0 Hz, 2H), 7.6 (d, *J* = 8.0 Hz, 2H), 4.10 (t, *J* = 7.4 Hz, 2H), 1.71–1.65 (m, 2H), 1.42–1.27 (m, 10H), 0.89–0.87 (m, 3H). ¹³C{¹H} NMR (125 MHz, CDCl₃, ppm): $\delta = 163.3, 152.5, 136.7, 132.2, 121.8, 118.7, 40.6, 31.9, 29.4, 28.2, 27.3, 22.8, 14.3$. ⁷⁷Se{¹H} NMR (95 MHz, CDCl₃, ppm): $\delta = 512.55$. DEI-MS: *m/z* = 465 [M]⁺.

3,9-Dibromo-6-(2,6-diisopropylphenyl)-5*H*-[1,2]diselenolo[3',4',5':4,5]naphtho[1,8-*cd*]pyridine-5,7(6*H*)-dione (5). Yield: 74%. Mp > 300 °C. Elemental analysis for C₂₄H₁₉Br₂NO₂Se₂: calculated C 42.95, H 2.85, N 2.09; found C 42.54, H 2.89, N 2.08. IR (cm⁻¹): 3078w, 3064w, 3032w, 2958w, 2917w, 2865w, 1700s, 1640s, 1560s, 1525w, 1457w, 1359w, 1279s, 1236s, 845s, 801s, 726s. ¹H NMR (500 MHz, CDCl₃, ppm): $\delta = 8.56$ (s, 2H), 7.48 (t, *J* = 7.8 Hz, 1H), 7.33 (d, *J* = 7.8 Hz, 2H), 2.64 (hept, *J* = 6.8 Hz, 2H), 1.15 (d, *J* = 6.9 Hz, 12H). ¹³C{¹H} NMR (125 MHz, CDCl₃, ppm): $\delta = 162.8, 155.0, 145.9, 136.6, 134.6, 130.1, 130.3, 130.1, 124.5, 121.3, 116.9, 29.6, 24.4$. ⁷⁷Se{¹H} NMR (95 MHz, CDCl₃, ppm): $\delta = 545.78$. DEI-MS: *m/z* = 671 [M]⁺.

3,9-Dichloro-6-(2,6-diisopropylphenyl)-5*H*-[1,2]diselenolo[3',4',5':4,5]naphtho[1,8-*cd*]pyridine-5,7(6*H*)-dione (6). Yield: 86%. Mp > 300 °C. Elemental analysis for C₂₄H₁₉Cl₂NO₂Se₂:

calculated C 49.51, H 3.29, N 2.41; found C 49.42, H 3.24, N 2.35. IR (cm⁻¹): 3082w, 3057w, 3036w, 2958w, 2927w, 2907w, 1707s, 1653s, 1572w, 1534s, 1372w, 1316s, 1242w, 1022w, 846s, 801s, 728s. ¹H NMR (500 MHz, CDCl₃, ppm): δ = 8.45 (s, 2H), 7.48 (t, *J* = 7.8 Hz, 1H), 7.33 (d, *J* = 7.8 Hz, 2H), 2.65 (hept, *J* = 6.8 Hz, 2H), 1.15 (d, *J* = 6.9 Hz, 12H). ¹³C{¹H} NMR (125 MHz, CDCl₃, ppm): δ = 162.7, 151.3, 145.7, 137.6, 131.8, 130.7, 129.9, 129.3, 128.1, 124.3, 121.3, 29.3, 24.1. ⁷⁷Se{¹H} NMR (95 MHz, CDCl₃, ppm): δ = 538.67. DEI-MS: *m/z* = 582 [M]⁺.

General procedure for the preparation of complexes 7–10

A solution of Fe₃(CO)₁₂ (200 mg, 0.40 mmol) and compounds 1–6, respectively, (0.40 mmol) in THF (30 mL) was heated at reflux for 3 hours under N₂. The green solution turned deep red and the solvent was removed under reduced pressure. The residue was purified by column chromatography using hexane/dichloromethane (2 : 1) as the eluent. The complexes were collected always from the second fraction and then the solvent was removed *in vacuo*. The products were obtained as a red-orange solid for complexes 7–10.

NMI-Fe₂S₂ (7). Yield: 35%. Mp 151–152 °C. Elemental analysis for C₂₆H₂₁Fe₂NO₈S₂: calculated C 47.95, H 3.25, N 2.15, S 9.85; found C 47.50, H 3.45, N 2.10, S 9.52. IR (νCO, cm⁻¹): 2074s, 2040 m, 1989 m. ¹H NMR (400 MHz, CDCl₃, ppm): δ = 8.40 (bs, 4H), 4.11 (bs, 2H), 1.68 (bs, 2H), 1.28 (bs, 10H), 0.86 (s, 3H). ¹³C{¹H} NMR (100 MHz, CDCl₃, ppm): δ = 207.2, 163.2, 153.1, 134.7, 132.9, 129.6, 125.0, 40.7, 31.8, 29.2, 28.1, 27.1, 22.63, 14.1. DEI-MS: *m/z* = 651 [M]⁺, 623 [M - CO]⁺, 595 [M - 2CO]⁺, 567 [M - 3CO]⁺, 539 [M - 4CO]⁺, 511 [M - 5CO]⁺, 483 [M - 6CO]⁺.

DiBr-NMI-Fe₂S₂ (8). Yield: 32%. Mp > 300 °C. Elemental analysis for C₃₀H₁₉Br₂Fe₂NO₈S₂: calculated C 42.04, H 2.23, N 1.63, S 7.48; found C 42.52, H 2.30, N 1.67, S 7.73. IR (νCO, cm⁻¹): 2077, 2036 m, 1981 m. ¹H NMR (400 MHz, CDCl₃, ppm): δ = 8.72 (bs, 2H), 7.49–7.34 (m, 3H), 2.63 (bs, 2H), 1.14 (bs, 12H). ¹³C{¹H} NMR (100 MHz, CDCl₃, ppm): δ = 206.1, 163.3, 154.2, 146.4, 135.4, 133.9, 130.3, 129.8, 128.2, 124.3, 119.5, 115.7, 29.7, 24.2. DEI-MS: *m/z* = 857 [M]⁺, 829 [M - CO]⁺, 801 [M - 2CO]⁺, 773 [M - 3CO]⁺, 745 [M - 4CO]⁺, 717 [M - 5CO]⁺, 689 [M - 6CO]⁺.

NMI-Fe₂Se₂ (9). Yield: 40%. Mp 159–160 °C. Elemental analysis for C₂₆H₂₁Fe₂NO₈Se₂: calculated C 41.91, H 2.84, N 1.88; found C 42.13, H 2.88, N 1.88. IR (νCO, cm⁻¹): 2065s, 2028 m, 1981 m. ¹H NMR (400 MHz, CDCl₃, ppm): δ = 8.45 (bs, 4H), 4.11 (bs, 2H), 1.68 (bs, 2H), 1.27 (bs, 10H), 0.86 (s, 3H). ¹³C{¹H} NMR (100 MHz, CDCl₃, ppm): δ = 207.8, 163.3, 152.6, 136.7, 132.2, 121.8, 118.7, 40.6, 31.9, 29.4, 28.2, 27.3, 22.8, 14.3. ⁷⁷Se{¹H} NMR (76 MHz, CDCl₃, ppm): δ = 209.82. DEI-MS: *m/z* = 745 [M]⁺, 717 [M - CO]⁺, 689 [M - 2CO]⁺, 661 [M - 3CO]⁺, 633 [M - 4CO]⁺, 605 [M - 5CO]⁺, 577 [M - 6CO]⁺.

DiBr-NMI-Fe₂Se₂ (10). Yield: 34%. Mp > 300 °C. Elemental analysis for C₃₀H₁₉Br₂Fe₂NO₈Se₂: calculated C 37.89, H 2.01, N 1.47; found C 37.46, H 2.15, N 1.56. IR (νCO, cm⁻¹): 2070s, 2032 m, 1978 m. ¹H NMR (400 MHz, CDCl₃, ppm): δ = 8.72 (s, 2H), 7.49–7.34 (m, 3H), 2.63 (bs, 2H), 1.14 (bs, 12H). ¹³C{¹H} NMR (100 MHz, CDCl₃, ppm): δ = 207.3, 163.2, 155.2,

146.4, 136.6, 134.4, 130.1, 130.3, 130.1, 124.5, 121.3, 116.9, 29.7, 24.2. ⁷⁷Se{¹H} NMR (76 MHz, CDCl₃, ppm): δ = 270.26. DEI-MS: *m/z* = 950 [M]⁺, 922 [M - CO]⁺, 894 [M - 2CO]⁺, 866 [M - 3CO]⁺, 838 [M - 4CO]⁺, 810 [M - 5CO]⁺, 782 [M - 6CO]⁺.

Acknowledgements

H. Abul-Futouh thanks the Deutscher Akademischer Austausch Dienst (DAAD) for scholarship. Y. Zagranyski is grateful to the Sofia University Scientific Fund (grant 136/2016) and the Horizon 2020 program of the European Commission (project Materials Networking) for the financial support. The authors thank Philipp Schüler for his contributions to the emission measurements. All calculations have been performed at the Universitätsrechenzentrum of the Friedrich Schiller University Jena and at the HP computers of the Theoretical Chemistry group in Jena.

Notes and references

- 1 D. J. Wuebbles and A. K. Jain, *Fuel Process. Technol.*, 2001, **71**, 99–119.
- 2 S. Dunn, *Int. J. Hydrogen Energy*, 2002, **27**, 235–264.
- 3 M. Momirlan and T. N. Veziroglu, *Int. J. Hydrogen Energy*, 2005, **30**, 795–802.
- 4 M. W. Adams, *Biochim. Biophys. Acta*, 1990, **1020**, 115–145.
- 5 M. Frey, *ChemBioChem*, 2002, **3**, 153–160.
- 6 Y. Nicolet, C. Piras, P. Legrand, C. E. Hatchikian and J. C. Fontecilla-Camps, *Structure*, 1999, **7**, 13–23.
- 7 J. W. Peters, W. N. Lanzilotta, B. J. Lemon and L. C. Seefeldt, *Science*, 1998, **282**, 1853–1858.
- 8 (a) A. Adamska, S. Roy, J. F. Siebel, T. R. Simmons, M. Fontecave, V. Artero, E. Reijerse and W. Lubitz, *J. Am. Chem. Soc.*, 2015, **137**, 12744–12747; (b) A. Adamska, A. Silakov, C. Lambertz, O. Rüdiger, T. Happe, E. Reijerse and W. Lubitz, *Angew. Chem., Int. Ed.*, 2012, **124**, 11624–11629; (c) H.-J. Fan and M. B. Hall, *J. Am. Chem. Soc.*, 2001, **123**, 3828–3829; (d) J. W. Peters, W. N. Lanzilotta, B. J. Lemon and L. C. Seefeldt, *Science*, 1998, **282**, 1853–1858; (e) Y. Nicolet, A. L. de Lacey, X. Vernede, V. M. Fernandez, E. C. Hatchikian and J. C. Fontecilla-Camps, *J. Am. Chem. Soc.*, 2001, **123**, 1596–1601; (f) A. Silakov, B. Wenk, E. Reijerse and W. Lubitz, *Phys. Chem. Chem. Phys.*, 2009, **11**, 6592–6599; (g) G. Berggren, A. Adamska, C. Lambertz, T. R. Simmons, J. Esselborn, M. Atta, S. Gambarelli, J. M. Mouesca, E. Reijerse, W. Lubitz, T. Happe, V. Artero and M. Fontecave, *Nature*, 2013, **499**, 66–69.
- 9 (a) For a review see: Y. Li and T. B. Rauchfuss, *Chem. Rev.*, 2016, **116**, 7043–7077; (b) H. Abul-Futouh, L. R. Almazahreh, T. Sakamoto, N. Y. T. Stessman, D. L. Lichtenberger, R. S. Glass, H. Görls, M. El-khateeb, P. Schollhammer, G. Mloston and W. Weigand, *Chem. – Eur. J.*, 2017, **23**, 346–359; (c) R. Trautwein,

- L. R. Almazahreh, H. Görls and W. Weigand, *Dalton Trans.*, 2015, **44**, 18780–18794; (d) T. B. Rauchfuss, *Acc. Chem. Res.*, 2015, **48**, 2107–2116; (e) L.-C. Song, Z.-Y. Yang, H.-Z. Bian, Y. Liu, H.-T. Wang, X.-F. Liu and Q.-M. Hu, *Organometallics*, 2005, **24**, 6126–6135; (f) J. Windhager, M. Rudolph, S. Bräutigam, H. Görls and W. Weigand, *Eur. J. Inorg. Chem.*, 2007, 2748–2760; (g) Z. Wang, J.-H. Liu, C.-J. He, S. Jiang, B. Åkermark and L.-C. Sun, *J. Organomet. Chem.*, 2007, **692**, 5501–5507; (h) G. Si, W.-G. Wang, H.-Y. Wang, C.-H. Tung and L.-Z. Wu, *Inorg. Chem.*, 2008, **47**, 8101–8111; (i) H. Abul-Futouh, M. El-khateeb, H. Görls, K. J. Asali and W. Weigand, *Dalton Trans.*, 2017, **46**, 2937–2947; (j) H. Abul-Futouh, H. Görls and W. Weigand, *Phosphorus, Sulfur Silicon Relat. Elem.*, 2017, **192**, 634–637.
- 10 (a) F. Gloaguen, D. Morvan, J.-F. Capon, P. Schollhammer and J. Talarmin, *J. Electroanal. Chem.*, 2007, **603**, 15–20; (b) G. A. N. Felton, A. K. Vannucci, J. Chen, L. T. Lockett, N. Okumura, B. J. Petro, U. I. Zakai, D. H. Evans, R. S. Glass and D. L. Lichtenberger, *J. Am. Chem. Soc.*, 2007, **129**, 12521–12530; (c) L. Schwartz, P. S. Singh, L. Eriksson, R. Lomoth and S. Ott, *C. R. Chim.*, 2008, **11**, 875–889; (d) J.-F. Capon, F. Gloaguen, P. Schollhammer and J. Talarmin, *J. Electroanal. Chem.*, 2004, **566**, 241–247; (e) J. Chen, A. K. Vannucci, C. A. Mebi, N. Okumura, S. C. Borowski, M. Swenson, L. T. Lockett, D. H. Evans, R. S. Glass and D. L. Lichtenberger, *Organometallics*, 2010, **29**, 5330–5340; (f) E. S. Donovan, J. J. McCormick, G. S. Nichol and G. A. N. Felton, *Organometallics*, 2012, **31**, 8067–8070; (g) G. A. N. Felton, C. A. Mebi, B. J. Petro, A. K. Vannucci, D. H. Evans, R. S. Glass and D. L. Lichtenberger, *J. Organomet. Chem.*, 2009, **694**, 2681–2699.
- 11 (a) P. Kilian, F. R. Knight and J. D. Woollins, *Coord. Chem. Rev.*, 2011, **255**, 1387–1413; (b) P. Kilian, F. R. Knight and J. D. Woollins, *Chem. – Eur. J.*, 2011, **17**, 2302–2328; (c) R. J. Wright, C. Lim and T. D. Tilley, *Chem. – Eur. J.*, 2009, **15**, 8518–8525; (d) G. Qian, W. Zhong, Z. Wei, H. Wang, Z. Xiao, L. Long and X. Liu, *New J. Chem.*, 2015, **39**, 9752–9760; (e) C. Figliola, L. Male, P. N. Horton, M. B. Pitak, S. J. Coles, S. L. Horswell and R. S. Grainger, *Organometallics*, 2014, **33**, 4449–4460; (f) C. Figliola, L. Male, S. L. Horswell and R. S. Grainger, *Eur. J. Inorg. Chem.*, 2015, 3146–3156.
- 12 (a) A. P. S. Samuel, D. T. Co, C. L. Stern and M. R. Wasielewski, *J. Am. Chem. Soc.*, 2010, **132**, 8813–8815; (b) P. Li, S. Amirjalayer, F. Hartl, M. Lutz, B. Bruin, R. Becker, S. Woutersen and J. N. H. Reek, *Inorg. Chem.*, 2014, **53**, 5373–5383; (c) P. Poddutoori, D. T. Co, A. P. S. Samuel, C. H. Kim, M. T. Vagnini and M. R. Wasielewski, *Energy Environ. Sci.*, 2011, **4**, 2441–2450.
- 13 (a) For a review, see: M. K. Harb, U.-P. Apfel, T. Sakamoto, M. El-khateeb and W. Weigand, *Eur. J. Inorg. Chem.*, 2011, 986–993; (b) M. K. Harb, J. Windhager, T. Niksch, H. Görls, T. Sakamoto, E. R. Smith, R. S. Glass, D. L. Lichtenberger, D. H. Evans, M. El-khateeb and W. Weigand, *Tetrahedron*, 2012, **68**, 10592–10599.
- 14 (a) S. Kaloyanova, Y. Zagranyski, S. Ritz, M. Hanulová, K. Koynov, A. Vonderheit, K. Müllen and K. Peneva, *J. Am. Chem. Soc.*, 2016, **138**, 2881–2884; (b) Compound C was previously reported as a patent: S. Tsutomu and K. Mitsuru, Tetrachloronaphthalic Acid Derivatives, *Jpn. Kokai Tokkyo Koho*, JP52130820A19771102, 1977.
- 15 (a) M. K. Harb, U.-P. Apfel, J. Kübel, H. Görls, G. A. N. Felton, T. Sakamoto, D. H. Evans, R. S. Glass, D. L. Lichtenberger, M. El-khateeb and W. Weigand, *Organometallics*, 2009, **28**, 6666–6675; (b) J. Windhager, R. A. Seidel, U.-P. Apfel, H. Görls, G. Linti and W. Weigand, *Chem. Biodiversity*, 2008, **5**, 2023–2041; (c) L.-C. Song, B. Gai, H. T. Wang and Q. M. Hu, *J. Inorg. Biochem.*, 2009, **103**, 805–812; (d) S. Gao, J. Fan, S. Sun, X. Peng, X. Zhao and J. Hou, *Dalton Trans.*, 2008, 2128–2135.
- 16 Y. Na, P. Wei and L. Zhou, *Chem. – Eur. J.*, 2016, **22**, 10365–10368.
- 17 (a) J. Courtot-Coupez, M. Gubguen, J. E. Guerchais, F. Y. Pétillon and J. Talarmin, *J. Chem. Soc., Dalton Trans.*, 1986, 1923–1929; (b) K. Charreteur, M. Kdider, J.-F. Capon, F. Gloaguen, F. Y. Pétillon, P. Schollhammer and J. Talarmin, *Inorg. Chem.*, 2010, **49**, 2496–2501.
- 18 (a) J.-F. Capon, S. Ezzaher, F. Gloaguen, F. Y. Pétillon, P. Schollhammer, J. Talarmin, T. J. Davin, J. E. McGrady and K. W. Muir, *New J. Chem.*, 2007, **31**, 2052–2064; (b) S. J. Borg, T. Behrsing, S. P. Best, M. Razavet, X. Liu and C. J. Pickett, *J. Am. Chem. Soc.*, 2004, **126**, 16988–16999.
- 19 (a) M. K. Harb, T. Niksch, J. Windhager, H. Görls, R. Holze, L. T. Lockett, N. Okumura, D. H. Evans, R. S. Glass, D. L. Lichtenberger, M. El-khateeb and W. Weigand, *Organometallics*, 2009, **28**, 1039–1048; (b) S. Gao, J. Fan, S. Sun, X. Peng, X. Zhao and J. Hou, *Dalton Trans.*, 2008, 2128–2135; (c) U. P. Apfel, Y. Halpin, H. Görls, J. G. Vos, B. Schweizer, G. Linti and W. Weigand, *Chem. Biodiversity*, 2007, **4**, 2138–2148; (d) P. Surawatanawong, J. W. Tye, M. Y. Darensbourg and M. B. Hall, *Dalton Trans.*, 2010, **39**, 3093–3104.
- 20 COLLECT, *Data Collection Software*, Nonius B.V., Netherlands, 1998.
- 21 Z. Otwinowski and W. Minor, Processing of X-Ray Diffraction Data Collected in Oscillation Mode, in *Methods in Enzymology*, Vol. 276, *Macromolecular Crystallography, Part A*, ed. C. W. Carter and R. M. Sweet, Academic Press, San Diego, USA, 1997, pp. 307–326.
- 22 SADABS 2.10, Bruker-AXS inc., Madison, WI, USA, 2002.
- 23 G. M. Sheldrick, *Acta Crystallogr., Sect. A: Fundam. Crystallogr.*, 2008, **64**, 112–122.
- 24 A. L. Spek, *Acta Crystallogr., Sect. D: Biol. Crystallogr.*, 2009, **65**, 148–155.
- 25 C. F. Macrae, P. R. Edgington, P. McCabe, E. Pidcock, G. P. Shields, R. Taylor, M. Towler and J. van de Streek, *J. Appl. Crystallogr.*, 2006, **39**, 453–457.
- 26 M. J. Frisch, G. W. Trucks, H. B. Schlegel, G. E. Scuseria, M. A. Robb, J. R. Cheeseman, G. Scalmani, V. Barone, B. Mennucci, G. A. Petersson, H. Nakatsuji, M. Caricato,

- X. Li, H. P. Hratchian, A. F. Izmaylov, J. Bloino, G. Zheng, J. L. Sonnenberg, M. Hada, M. Ehara, K. Toyota, R. Fukuda, J. Hasegawa, M. Ishida, T. Nakajima, Y. Honda, O. Kitao, H. Nakai, T. Vreven, J. A. Montgomery Jr., J. E. Peralta, F. Ogliaro, M. Bearpark, J. J. Heyd, E. Brothers, K. N. Kudin, V. N. Staroverov, R. Kobayashi, J. Normand, K. Raghavachari, A. Rendell, J. C. Burant, S. S. Iyengar, J. Tomasi, M. Cossi, N. Rega, J. M. Millam, M. Klene, J. E. Knox, J. B. Cross, V. Bakken, C. Adamo, J. Jaramillo, R. Gomperts, R. E. Stratmann, O. Yazyev, A. J. Austin, R. Cammi, C. Pomelli, J. W. Ochterski, R. L. Martin, K. Morokuma, V. G. Zakrzewski, G. A. Voth, P. Salvador, J. J. Dannenberg, S. Dapprich, A. D. Daniels, Ö. Farkas, J. B. Foresman, J. V. Ortiz, J. Cioslowski and D. J. Fox, Gaussian, Inc., Wallingford CT, 2009.
- 27 (a) A. D. Becke, *Phys. Rev. A*, 1988, **38**, 3098–3100; (b) J. P. Perdew, *Phys. Rev. B: Condens. Matter*, 1986, **33**, 8822–8824.
- 28 T. H. Dunning, *J. Chem. Phys.*, 1971, **55**, 716–723.
- 29 M. Dolg, U. Wedig, H. Stoll and H. Preuss, *J. Chem. Phys.*, 1987, **86**, 2123–2131.
- 30 (a) C. Lee, W. Yang and R. G. Parr, *Phys. Rev. B: Condens. Matter*, 1988, **37**, 785–789; (b) A. D. Becke, *J. Chem. Phys.*, 1993, **98**, 5648–5652.
- 31 B. Mennucci, C. Cappelli, C. A. Guido, R. Cammi and J. Tomasi, *J. Phys. Chem. A*, 2009, **113**, 3009–3020.

Supporting Information

[FeFe]-Hydrogenase H-Cluster Mimics Mediated by Naphthalene Monoimide Derivatives of *Peri*-Substituted Dichalcogenides

Hassan Abul-Futouh,^{a†} Yulian Zagranyski,^{b†} Carolin Müller,^c Martin Schulz,^c
Stephan Kupfer,^c Helmar Görls,^a Mohammad El-khateeb,^d Stefanie Gräfe,^c Benjamin
Dietzek,^{c,e} Kalina Peneva,^{f,g*} and Wolfgang Weigand^{a*}

^a *Institut für Anorganische und Analytische Chemie, Friedrich-Schiller-Universität Jena, Humboldt Str. 8, 07743 Jena, Germany. Email: wolfgang.weigand@uni-jena.de.*

^b *Faculty of Chemistry and Pharmacy, Sofia University 'St. Kliment Ohridski', 1 James Bourchier Ave., Sofia 1164, Bulgaria.*

^c *Institut für Physikalische Chemie and Abbe Center of Photonics, Friedrich-Schiller-Universität Jena, Helmholtzweg 4, 07743 Jena, Germany.*

^d *Chemistry Department, Jordan University of Science and Technology, Irbid 22110, Jordan.*

^e *Leibniz-Institut für Photonische Technologien e.V., Department of Functional Interfaces, Albert-Einstein-Str. 9, 07745 Jena, Germany.*

^f *Institute of Organic Chemistry and Macromolecular Chemistry, Friedrich-Schiller-University Jena, Lessingstrasse 8, 07743 Jena, Germany, Email: kalina.peneva@uni-jena.de.*

^g *Center for Energy and Environmental Chemistry Jena (CEEC Jena), Friedrich-Schiller-University, Philosophenweg 7a, 07743 Jena, Germany.*

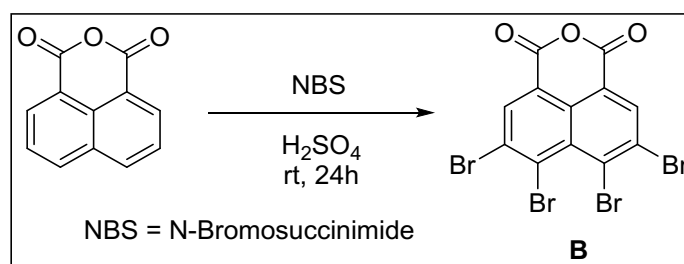
[†] These authors contributed equally

General experimental details

All solvents and starting materials that have not been synthesized by us were commercial products (Acros Organics, Fisher Scientific, Fluka, Merck and Sigma Aldrich,) and were used without further purification. The progress of all reactions was monitored by thin layer chromatography (Macherey- Nagel F 254 silica gel sheet) with appropriate solvents described for each compound in the synthetic procedures. Column chromatography purifications were carried out on silica gel from Macherey Nagel (0.063 mm – 0.200 mm). NMR spectra were recorded on Bruker Avance 500MHz instruments. Spectra (^1H , $^{13}\text{C}\{^1\text{H}\}$) were referenced to appropriate residual solvent signals (CDCl_3 , $\text{DMSO-}d^6$) and $^77\text{Se}\{^1\text{H}\}$ -NMR to Me_2Se . Elemental analysis was performed with a Leco CHNS-932 apparatus.

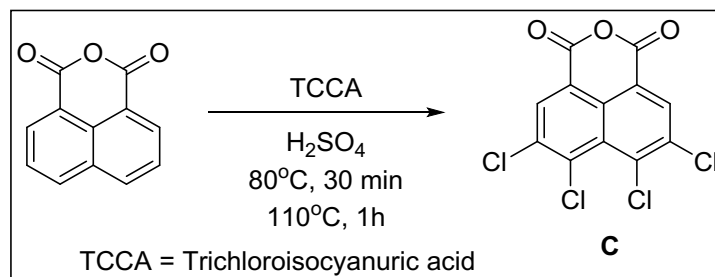
Procedures for the preparation of the precursors B-E.

Synthesis of 5,6,7,8-tetrabromo-1H,3H-benzo[de]isochromene-1,3-dione (B).



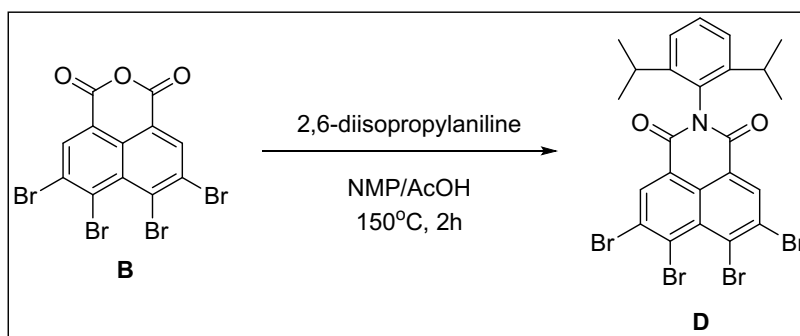
To a solution of 1,8-naphthalic anhydride (50 mmol, 9.92 g) in 500 ml sulfuric acid (95-97%) at room temperature, NBS (300 mmol, 53.40 g) was added. The reaction mixture was stirred at room temperature for 24 h and the mixture was poured into 500 g ice. The precipitate was filtered and washed several times with water and dried. Yield of crude product 24.0 g (93%). The crude product was recrystallized from chlorobenzene to give compound **B** as a white solid. Yield 21.30 g (83%). Elemental analysis for $\text{C}_{12}\text{H}_2\text{Br}_4\text{O}_3$: calculated C 28.05, H 0.39; found C 27.91, H 0.28. ^1H NMR (500 MHz, $\text{DMSO-}d^6$, ppm): $\delta = 8.69$, (s, 2H). $^{13}\text{C}\{^1\text{H}\}$ NMR (125 MHz, $\text{DMSO-}d^6$, ppm): $\delta = 158.8$, 135.5, 132.0, 130.7, 129.6, 129.5, 120.7.

Synthesis of 5,6,7,8-tetrachloro-1*H*,3*H*-benzo[*de*]isochromene-1,3-dione (**C**).



To a solution of 1,8-naphthalic anhydride (40 mmol, 7.93 g) in sulfuric acid (95-97%, 150 ml) at room temperature, TCCA (60 mmol, 13.95 g) was added. The reaction mixture was heated at 90°C for 30 min and then slowly increases to 110°C and stirred for 1 h. The mixture was cooled to room temperature and poured into 300 g ice. The precipitate was filtered and washed several times with water and dried. The crude product was recrystallized from chlorobenzene to give compound **C** as a white solid. Yield 12.20 g (91%). Elemental analysis for C₁₂H₂Cl₄O₃: calculated C 42.90, H 0.60; found C 43.11, H 0.55. ¹H NMR (500 MHz, DMSO-*d*⁶, ppm): δ = 8.67, (s, 2H). ¹³C {¹H} NMR (125 MHz, DMSO-*d*⁶, ppm): δ = 158.6, 136.1, 134.4, 133.0, 129.7, 128.0, 120.3.

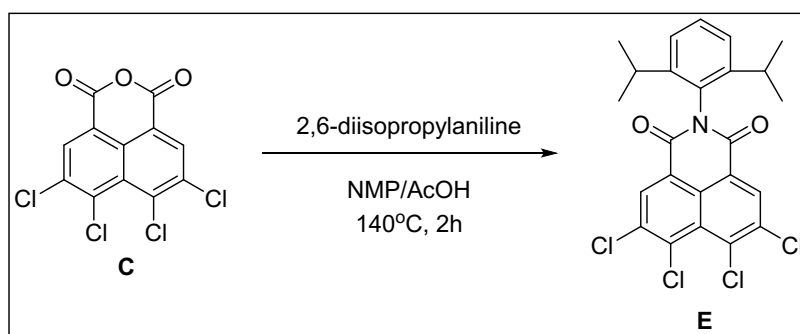
Synthesis of 5,6,7,8-tetrabromo-2-(2,6-diisopropylphenyl)-1*H*-benzo[*de*]isoquinoline-1,3(2*H*)-dione (**D**).



A mixture of 3,4,5,6-tetrabromonaphthalene monoanhydride (**B**) (10.0 mmol, 5.14 g), 2,6-diisopropylaniline (20.0 mmol, 3.54 g) in NMP (30 ml) and acetic acid (30 ml) was stirred at 150°C for 2 h. The reaction mixture was poured into ice (100 g) and the precipitate was filtered and dried. The crude product was purified by column chromatography (SiO₂, hexane-dichloromethane, 3:2) to give the diimide **D** as a white solid. Yield 5.45 g (81%). Elemental analysis for C₂₄H₁₉Br₄NO₂: calculated C 42.83, H 2.85, N 2.08; found C 42.60, H 2.71, N 1.87. ¹H NMR (500 MHz, CDCl₃, ppm): δ =

8.86 (s, 2H), 7.50 (t, $J = 7.8$ Hz, 1H), 7.33 (d, $J = 7.8$ Hz, 2H), 2.62 (hept, $J = 6.7$ Hz, 2H), 1.15 (d, $J = 6.9$ Hz, 12H). $^{13}\text{C}\{\text{H}\}$ NMR (125 MHz, CDCl_3 , ppm): $\delta = 162.2$, 145.6, 136.2, 133.1, 131.6, 130.2, 130.2, 129.8, 128.5, 124.4, 122.9, 29.4, 24.1.

Synthesis of 5,6,7,8-tetrachloro-2-(2,6-diisopropylphenyl)-1*H*-benzo[*de*]isoquinoline-1,3(2*H*)-dione (E).



A mixture of 3,4,5,6-tetrachloronaphthalene monoanhydride (**C**) (20.0 mmol, 6.72 g), 2,6-diisopropylaniline (40.0 mmol, 7.08 g) in NMP (30 ml) and acetic acid (30 ml) was stirred at 140°C for 2 h. The reaction mixture was poured into ice (100 g) and the precipitate was filtered and dried. The crude product was purified by column chromatography (SiO_2 , hexane-dichloromethane, 3:2) to give the diimide **E** as a white solid. Yield 8.69 g (88%). Elemental analysis for $\text{C}_{24}\text{H}_{19}\text{Cl}_4\text{NO}_2$: calculated C 58.21, H 3.87, N 2.83; found C 57.99, H 3.73, N 2.93. ^1H NMR (500 MHz, CDCl_3 , ppm): $\delta = 8.74$ (s, 2H), 7.50 (t, $J = 7.8$ Hz, 1H), 7.33 (d, $J = 7.8$ Hz, 2H), 2.63 (hept, $J = 6.8$ Hz, 2H), 1.15 (d, $J = 6.9$ Hz, 12H). $^{13}\text{C}\{\text{H}\}$ NMR (125 MHz, CDCl_3 , ppm): $\delta = 162.1$, 145.6, 137.3, 135.9, 133.4, 130.2, 129.8, 129.3, 128.4, 124.4, 122.4, 29.4, 24.1.

Figure S1. Molecular structure (60% probability) of compound **6**. Two crystallographically independent molecules and one molecules of dichloromethane were determined in the unit cell of compound **6**, only one of them is shown here. The hydrogen atoms are omitted for clarity reasons.

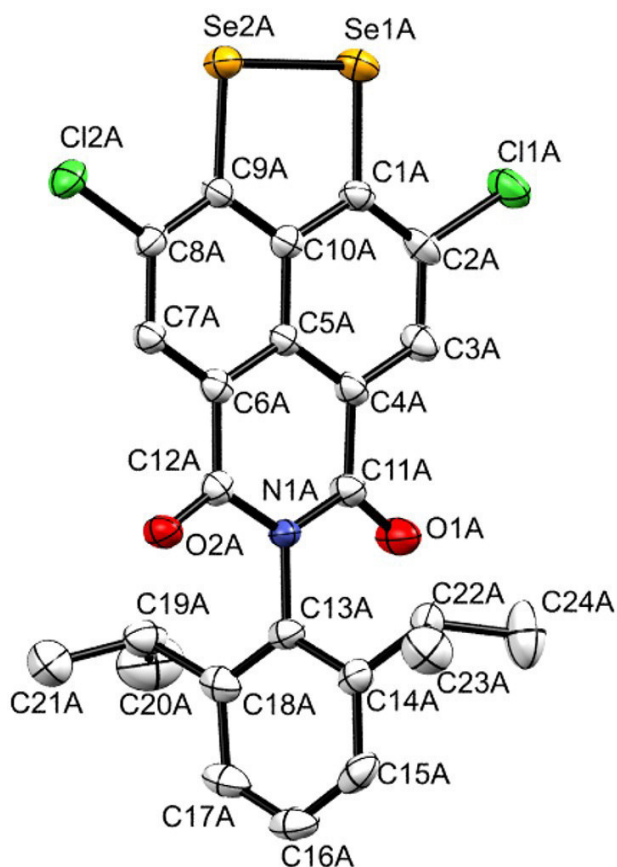


Figure S2. Motif structure of complex 7. Due to the poor quality of the crystal we could not deposit this complex in the Cambridge data base.

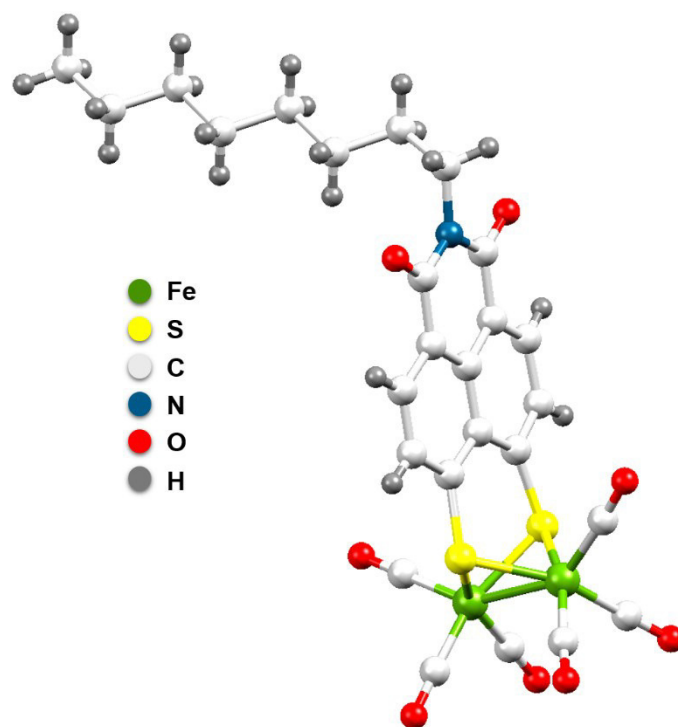


Figure S3. (Top): Cyclic voltammetry of **(a)** 1.0 mM complex **7** and **(b)** 1.0 mM complex **8** in CH_2Cl_2 - $[\text{n-Bu}_4\text{N}][\text{BF}_4]$ (0.1 M) solutions at various scan rates. (Bottom): The reverse scan at 0.2 V s^{-1} of the first reduction peaks of **(a)** complex **7** and **(b)** complex **8**. The arrows indicate the scan direction. The potentials E are given in V and referenced to the Fc^+/Fc couple.

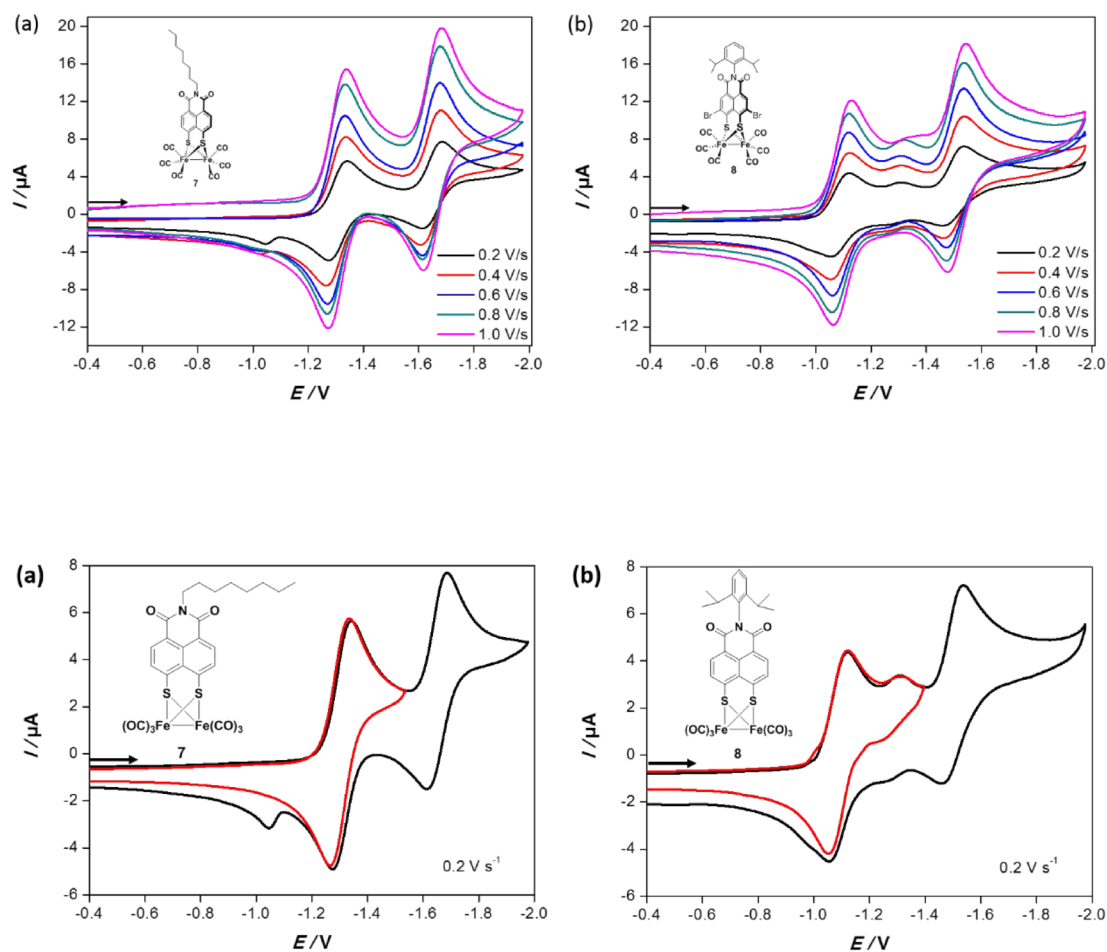


Figure S4. Plot of the cathodic current function *vs* scan rates for the first and second reduction waves of complexes **7** and **8**.

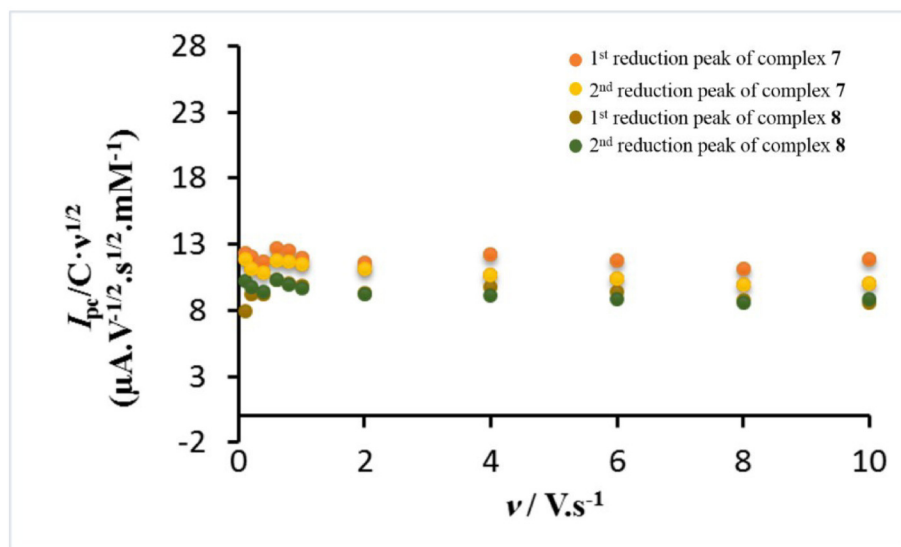


Figure S5. Plot of the cathodic current function *vs* scan rates for the first and second reduction waves of complexes **9** and **10**.

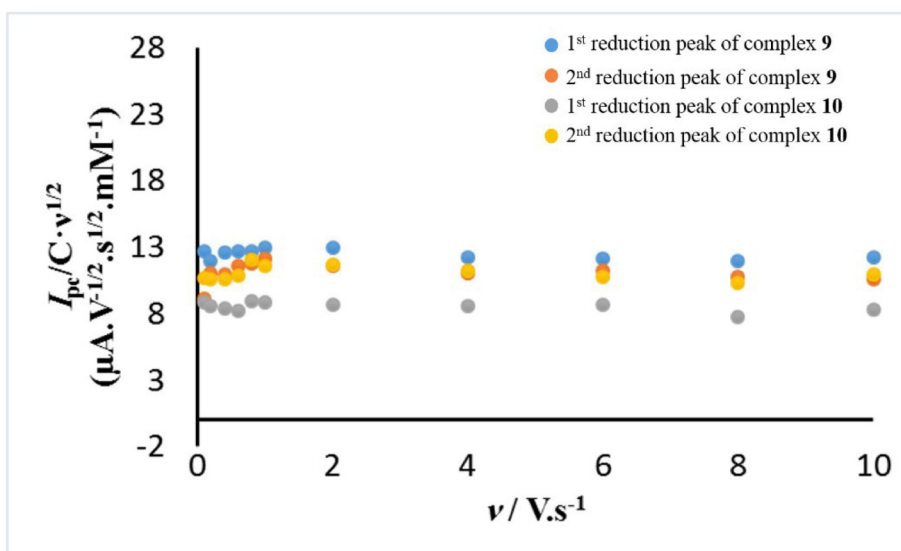


Figure S6. Cyclic voltammetry of 1.0 mM complex **9** in CH_2Cl_2 -[*n*-Bu₄N][BF₄] (0.1 M) solutions at (a) 0.2 V s⁻¹ scan rate, the red and the blue profiles show the reverse scan of the first and the second reduction peaks of complex **9**. (b) Various scan rates of complexes **9**. The arrows indicate the scan direction. The potentials *E* are given in V and referenced to the Fc⁺/Fc couple.

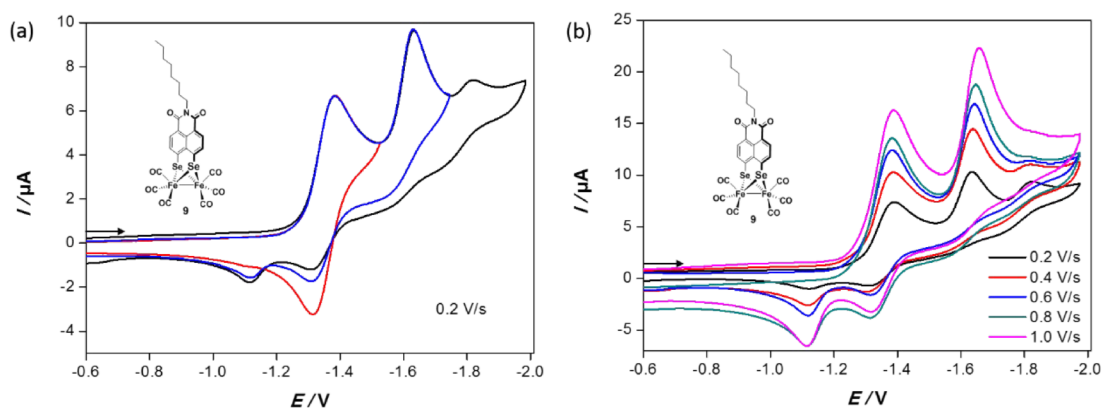


Figure S7. Cyclic voltammetry of 1.0 mM complex **10** in CH_2Cl_2 -[*n*-Bu₄N][BF₄] (0.1 M) solutions at (a) 0.2 V s⁻¹ scan rate, the red profile shows the reverse scan of the first reduction peak of complex **10**. (b) Various scan rates of complexes **10**. The arrows indicate the scan direction. The potentials *E* are given in V and referenced to the Fc⁺/Fc couple.

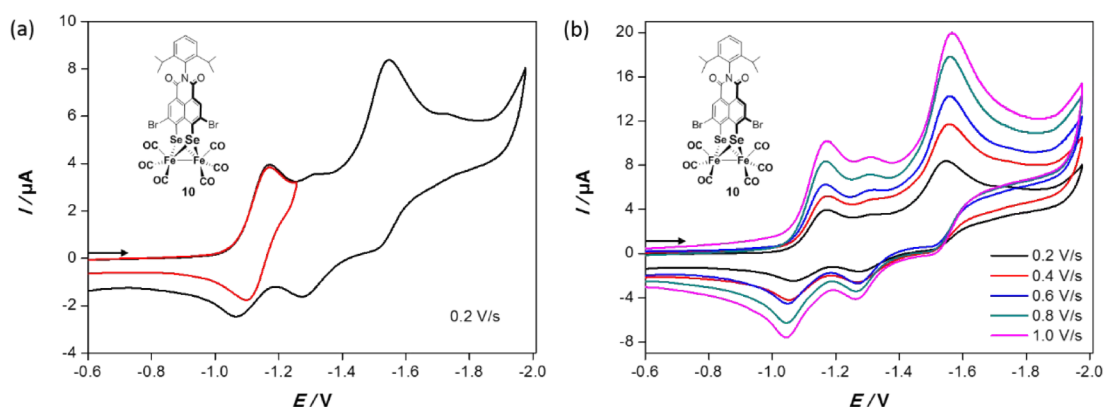


Figure S8. Repeated scan of complexes **7-10** in CH_2Cl_2 - $[n\text{-Bu}_4\text{N}][\text{BF}_4]$ (0.1 M) solutions at 0.2 V s^{-1} scan rate. The arrows indicate the scan direction. The potentials E are given in V and referenced to the Fc^+/Fc couple.

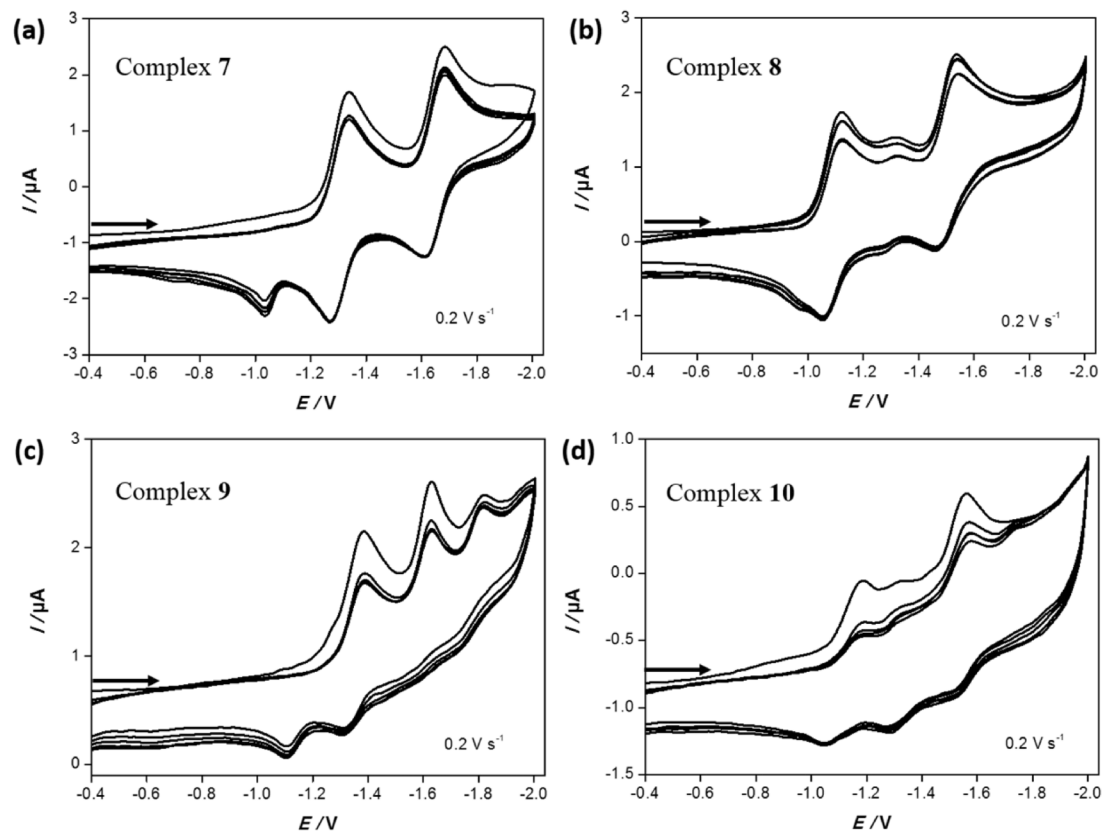


Figure S9. Cyclic voltammogram of various concentration of AcOH in CH_2Cl_2 -[*n*- Bu_4N][BF_4] (0.1 M) solution at 0.2 V s^{-1} scan rate in the absence of complexes **7-10**. The arrows indicate the scan direction. The potentials E are given in V and referenced to the Fc^+/Fc couple.

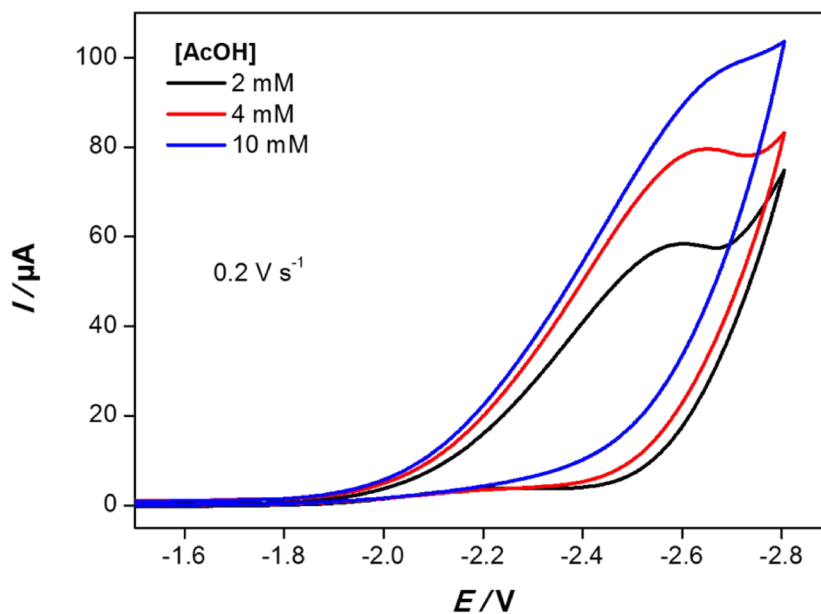


Figure S10. Contour plot of the emission characteristics of compound **1** (left) and compound **2** (right) obtained in dichloromethane. Horizontal reading gives the emission spectra at the respective excitation wavelength. Vertical reading gives the excitation spectra at the respective emission wavelength. Diagonal signals are due to residues of the excitation light and second order stray light as well as the solvent Raman band.

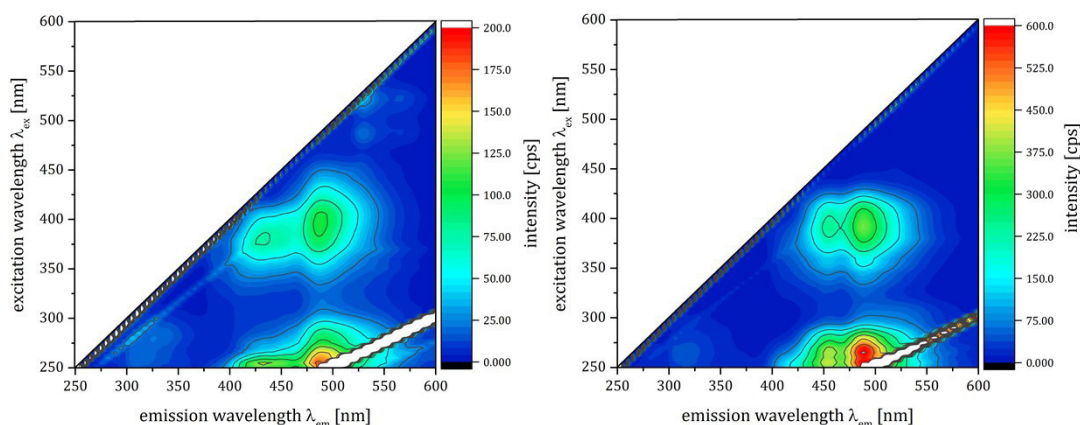


Figure S11. Contour plot of the emission characteristics of compound **4** (left) and compound **5** (right) obtained in dichloromethane. Horizontal reading gives the emission spectra at the respective excitation wavelength. Vertical reading gives the excitation spectra at the respective emission wavelength. Diagonal signals are due to residues of the excitation light and second order stray light as well as the solvent Raman band.

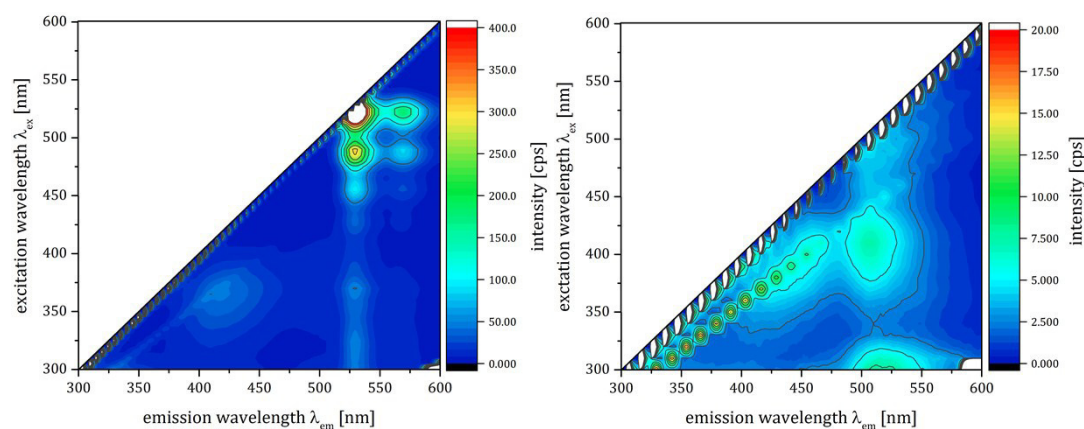


Figure S12. Contour plot of the emission characteristics of compound **7** (left) and compound **8** (right) obtained in dichloromethane. Horizontal reading gives the emission spectra at the respective excitation wavelength. Vertical reading gives the excitation spectra at the respective emission wavelength. Diagonal signals are due to residues of the excitation light and second order stray light as well as the solvent Raman band.

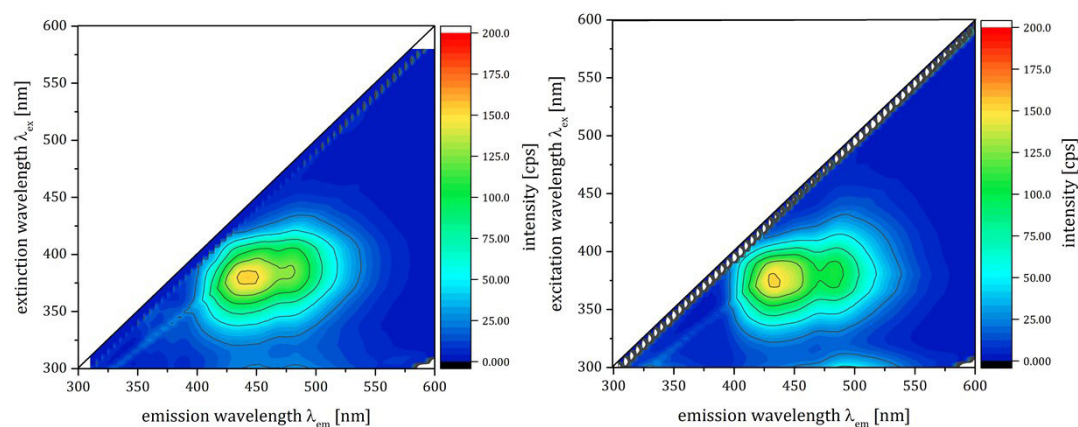


Figure S13. Contour plot of the emission characteristics of compound **9** (left) and compound **10** (right) obtained in dichloromethane. Horizontal reading gives the emission spectra at the respective excitation wavelength. Vertical reading gives the excitation spectra at the respective emission wavelength. Diagonal signals are due to residues of the excitation light and second order stray light as well as the solvent Raman band.

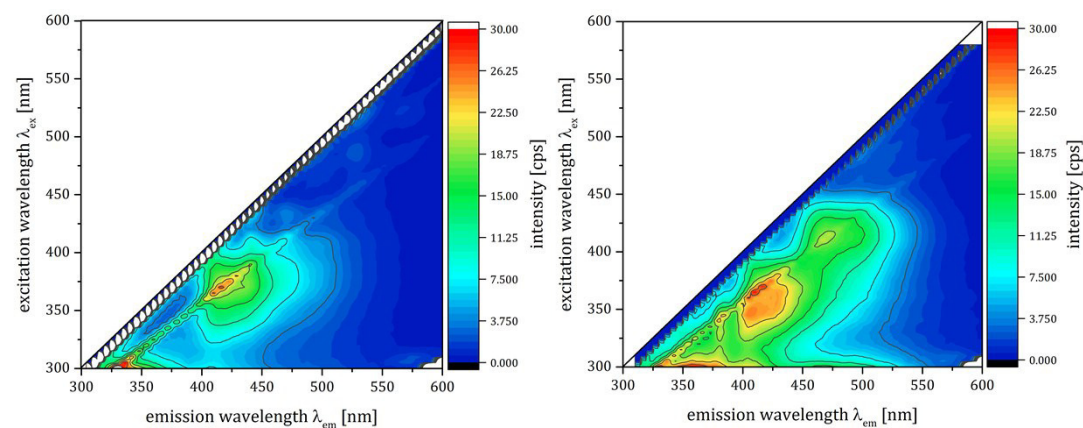


Table S1: Structural parameters such as selected bond lengths (d / pm), bond angles (α / °) and dihedral angles (δ / °) for the equilibrium geometries of complexes **7** and **9** at the BP86/TZVP level of theory (in dichloromethane) and the X-ray structure of complex **9**.

	7 ($X_1 = X_2 = S$)		9 ($X_1 = X_2 = Se$)	
	BP86	X-ray	BP86	BP86
$d(Fe_1, X_1)$ / pm	229.0	235.6(7)	239.8	
$d(Fe_1, X_2)$ / pm	229.0	236.5(7)	239.8	
$d(Fe_2, X_1)$ / pm	229.0	236.2(7)	239.7	
$d(Fe_2, X_2)$ / pm	229.0	235.7(6)	239.7	
$\alpha(X_1, C_1, X_2)$ / °	64.50	64.56	64.56	
$\alpha(O_1, Fe_1, O_2)$ / °	98.32	98.64	98.66	
$\alpha(O_1, Fe_1, O_3)$ / °	98.32	103.79	98.66	
$\alpha(O_2, Fe_1, O_3)$ / °	90.51	91.88	90.42	
$\alpha(O_4, Fe_2, O_5)$ / °	98.28	101.82	98.62	
$\alpha(O_4, Fe_2, O_6)$ / °	98.28	97.67	98.62	
$\alpha(O_5, Fe_2, O_6)$ / °	90.49	86.68	90.46	
$\delta(O_1, Fe_1, C_1, C_2)$ / °	0.03	4.20	0.03	
$\delta(O_4, Fe_2, C_1, C_2)$ / °	0.03	12.19	0.03	

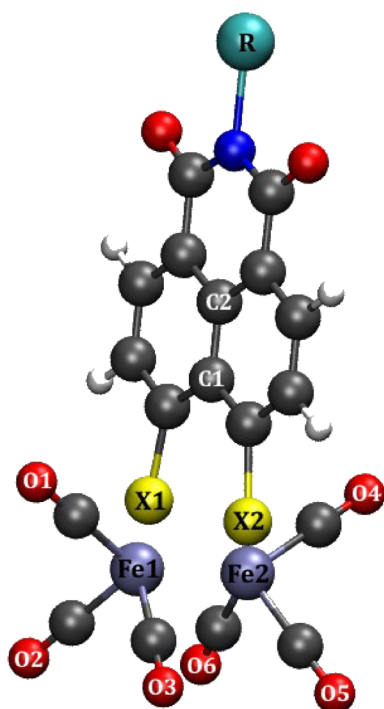


Table S2: Excited state properties, obtained at the TD-B3LYP/TZVP level of theory within dichloromethane using a PCM, of complexes **7** and **9** associated to the main absorption features within the UV/Vis region, namely, leading transitions with weights (%), excitation energies E^e (eV), wave lengths λ (nm), oscillator strengths f and assigned experimental absorption bands λ_{exp} .

7						
State	Transition	weight	$E^e /$	$\lambda /$	f	$\lambda_{\text{exp}} /$
		%	eV	nm		nm
S ₂	p _S (153) → σ _{FeFe} * (158) (LMCT)	50	2.89	428	0.012	464
	π+d _{Fe} (149) → σ _{FeFe} * (158) (LMCT)	21				
	π+d _{Fe} (147) → σ _{FeFe} * (158) (LMCT)	11				
S ₃	d _{Fe} (148) → σ _{FeFe} * (158) (MC)	54	2.96	419	0.002	464
	p _S (153) → π* (157) (ILCT)	15				
	π(155) → σ _{FeFe} * (158) (LMCT)	10				
S ₄	σ _{FeFe} (156) → σ _{FeFe} * (158) (MC)	55	3.00	413	0.082	464
	p _S (154) → π* (157) (ILCT)	34				
S ₇	π(155) → π* (157) (IL)	96	3.11	398	0.544	375
S ₉	p _S (154) → π* (157) (ILCT)	44	3.24	383	0.138	375
	σ _{FeFe} (156) → σ _{FeFe} * (158) (MC)	25				
9						
State	Transition	weight	$E^e /$	$\lambda /$	f	$\lambda_{\text{exp}} /$
		%	eV	nm		nm
S ₂	p _{Se} (171) → σ _{FeFe} * (176) (LMCT)	55	2.86	434	0.014	471
	π+d _{Fe} (166) → σ _{FeFe} * (176) (LMCT)	20				
S ₃	σ _{FeFe} (174) → σ _{FeFe} * (176) (MC)	51	2.91	426	0.059	471
	p _{Se} (172) → π* (175) (ILCT)	39				
S ₄	n _O +d _{Fe} (168) → σ _{FeFe} * (176) (LMCT)	42	2.92	423	0.002	471
	π(173) → σ _{FeFe} * (176) (LMCT)	15				
	n _O +d _{Fe} (167) → σ _{FeFe} * (176) (LMCT)	12				
		10				
S ₇	p _{Se} (171) → π* (175) (ILCT)	93	3.13	397	0.519	370
	π(173) → π* (175) (IL)	93				
S ₉	p _{Se} (172) → π* (175) (ILCT)	47	3.17	391	0.126	370
	σ _{FeFe} (174) → σ _{FeFe} * (176) (MC)	29				

Table S3: Molecular orbitals involved in the leading transitions of the excited states listed in Table S2 for complex 7.

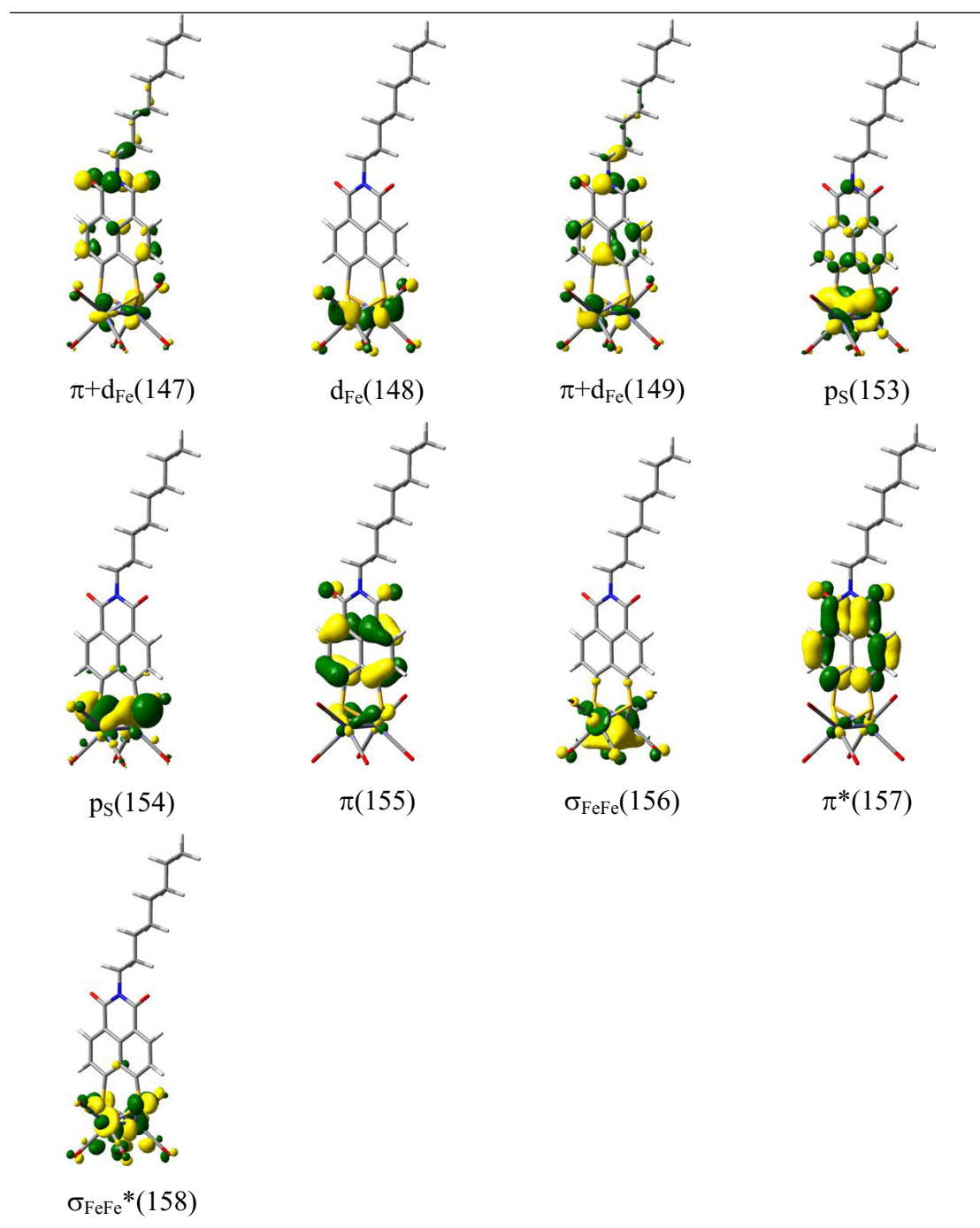


Table S4: Molecular orbitals involved in the leading transitions of the excited states listed in Table S2 for complex **9**.

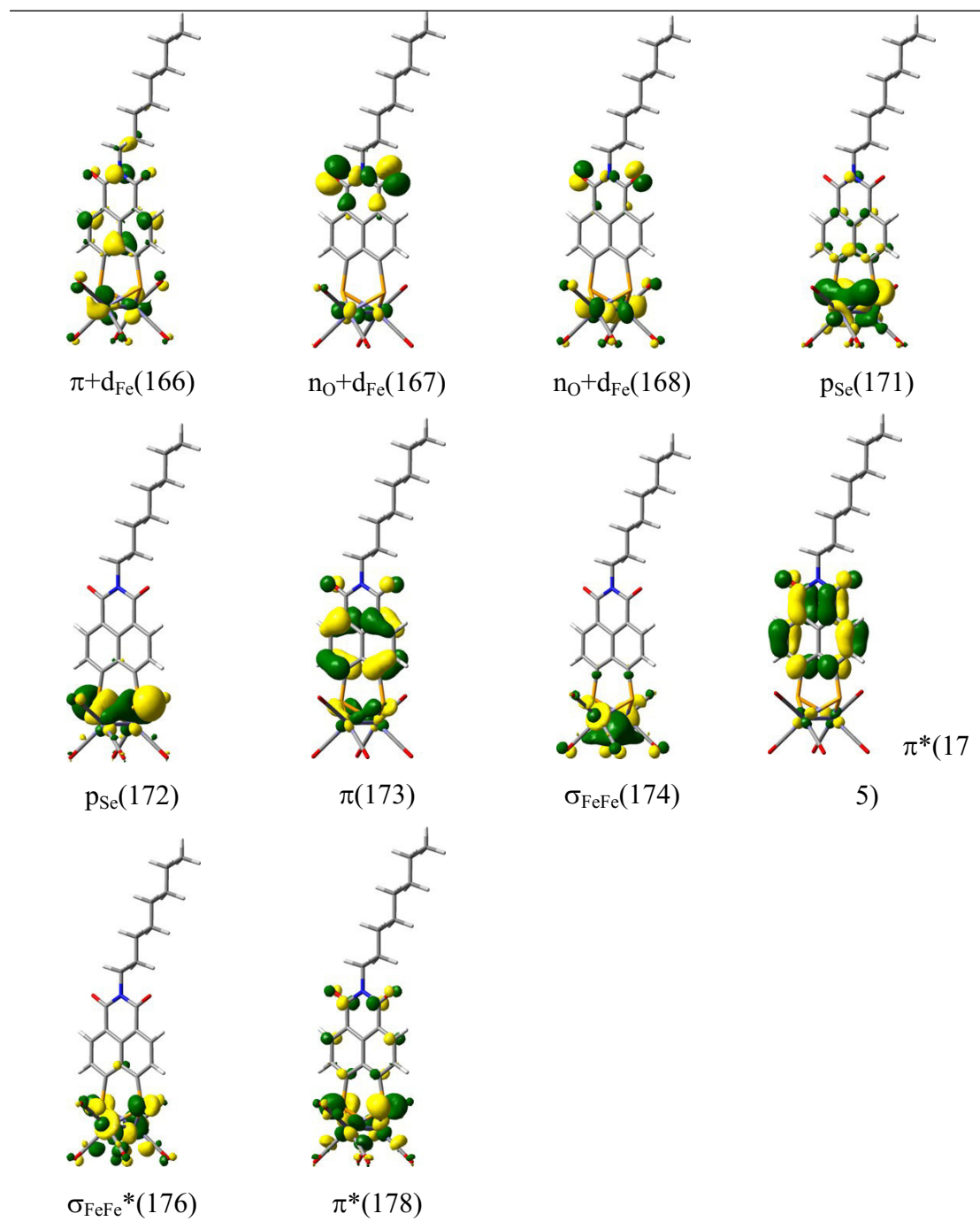


Table S5. Crystal data and refinement details for the X-ray structure determination of the compounds **6-9**.

Compound	6	7	8	9
formula	C ₂₄ H ₂₀ Cl ₃ NO ₂ Se ₂	C ₂₇ H ₂₄ Fe ₂ NO ₈ S ₂	C ₃₂ H ₂₃ Br ₂ Cl ₄ Fe ₂ NO ₈ S ₂ [*]	C ₂₆ H ₂₁ Fe ₂ NO ₈ Se ₂
fw (g·mol ⁻¹)	624.68	672.80	1026.95[*]	745.06
T/°C	-140(2)	-140(2)	-140(2)	-140(2)
crystal system	monoclinic	triclinic	orthorhombic	monoclinic
space group	P 2 ₁ /n	P $\bar{1}$	P 2 ₁ 2 ₁ 2 ₁	P 2 ₁ /c
a/ Å	8.2929(2)	9.3219(3)	13.9262(3)	15.9293(5)
b/ Å	27.6030(6)	18.0889(5)	14.1295(3)	10.8047(3)
c/ Å	21.7671(4)	18.3328(6)	19.6116(3)	16.2295(5)
α /°	90	100.726(2)	90	90
β /°	98.931(1)	93.001(2)	90	95.760(1)
γ /°	90	91.652(2)	90	90
V/Å ³	4922.27(18)	3030.81(16)	3858.98(13)	2779.18(14)
Z	8	4	4	4
ρ (g·cm ⁻³)	1.686	1.474	1.768[*]	1.781
μ (cm ⁻¹)	33.53	11.42	32.57[*]	37.12
measured data	33596	13452	23620	17737
data with I > 2 σ (I)	8798	9972	7849	5292
unique data (R _{int})	11117/0.0567	13452/0.0718	8839/0.0599	6275/0.0510
wR ₂ (all data, on F ²) ^{a)}	0.1017	0.3845	0.1156	0.0879
R ₁ (I > 2 σ (I)) ^{a)}	0.0481	0.1475	0.0523	0.0408
S ^{b)}	1.067	1.112	1.092	1.065
Res. dens./e·Å ⁻³	1.129/-0.515	1.788/-1.455	1.422/-0.943	0.580/-0.603
Flack-parameter	-	-	0.473(10)	-
absorpt method	multi-scan	multi-scan	multi-scan	multi-scan
absorpt corr T _{min} /max	0.6426/0.7456	0.5200/0.7456	0.5025/0.7456	0.5809/0.7456
CCDC No.	1530273	motif	1530274	1530275

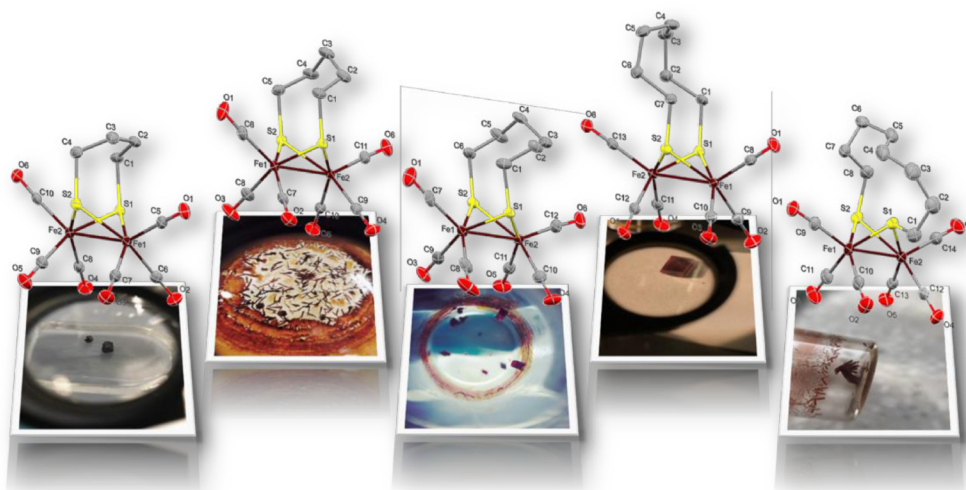
[*] derived parameters do not contain the contribution of the disordered solvent.^{a)} Definition of the R indices: $R_1 = (\sum ||F_o| - |F_c||) / \sum |F_o|$; $wR_2 = \{\sum [w(F_o^2 - F_c^2)^2] / \sum [w(F_o^2)^2]\}^{1/2}$ with $w^{-1} = \sigma^2(F_o^2) + (aP)^2 + bP$; $P = [2F_c^2 + \text{Max}(F_o^2)]/3$;^{b)} $S = \{\sum [w(F_o^2 - F_c^2)^2] / (N_o - N_p)\}^{1/2}$

4.5 [HAF-5]

[FeFe]-Hydrogenase H-Cluster Mimics with Various $-S(CH_2)_nS-$ Linker Lengths ($n = 2-8$): A Systematic Study

Hassan Abul-Futouh, Laith R. Almazahreh, Mohammad Kamal Harb, Helmar Görls, Mohammad El-Khateeb, Wolfgang Weigand

Inorganic Chemistry, **2017**, *56*, 10437-10451.



Reprinted with permission from *Inorg. Chem.* 2017, 56, 10437-10451. Copyright (2017) American Chemical Society.

[FeFe]-Hydrogenase H-Cluster Mimics with Various $-\text{S}(\text{CH}_2)_n\text{S}-$ Linker Lengths ($n = 2-8$): A Systematic Study

Hassan Abul-Futouh,[†] Laith R. Almazahreh,^{†,‡} Mohammad Kamal Harb,[§] Helmar Görls,[†] Mohammad El-khateeb,^{||} and Wolfgang Weigand^{*,†}

[†]Institut für Anorganische und Analytische Chemie, Friedrich-Schiller-Universität Jena, Humboldt Str. 8, 07743 Jena, Germany

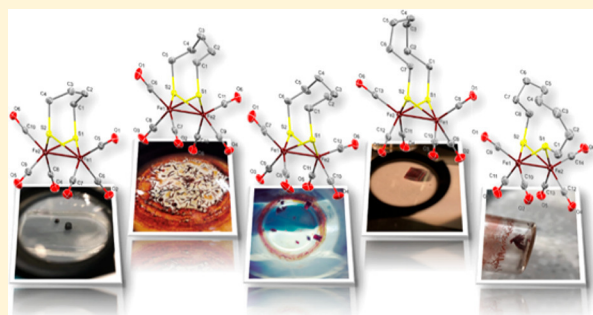
[‡]ERCOSPLAN Ingenieurbüro Anlagentechnik GmbH, Arnstädter Straße 28, 99096 Erfurt, Germany

[§]Department of Pharmacy, Al-Zytoonah University of Jordan, P.O. Box 130, Amman 11733, Jordan

^{||}Chemistry Department, Jordan University of Science and Technology, Irbid 22110, Jordan

Supporting Information

ABSTRACT: The effect of the nature of the dithiolato ligand on the physical and electrochemical properties of synthetic H-cluster mimics of the [FeFe]-hydrogenase is still of significant concern. In this report we describe the cyclization of various alkanedithiols to afford cyclic disulfide, tetrasulfide, and hexasulfide compounds. The latter compounds were used as proligands for the synthesis of a series of [FeFe]-hydrogenase H-cluster mimics having the general formulas $[\text{Fe}_2(\text{CO})_6\{\mu\text{-S}(\text{CH}_2)_n\text{S}\}]$ ($n = 4-8$), $[\text{Fe}_2(\text{CO})_6\{\mu\text{-S}(\text{CH}_2)_n\text{S}\}_2]$ ($n = 6-8$), and $[\text{Fe}_2(\text{CO})_6\{\mu\text{-S}(\text{CH}_2)_n\text{S}\}_2]$ ($n = 6-8$). The resulting complexes were characterized by ^1H and $^{13}\text{C}\{^1\text{H}\}$ NMR and IR spectroscopic techniques, mass spectrometry, and elemental analysis as well as X-ray analysis. The purpose of this research was to study the influence of the systematic increase of n from 2 to 7 on the redox potentials of the models and the catalytic ability in the presence of acetic acid (AcOH) by applying cyclic voltammetry.



INTRODUCTION

In step with population growth, the increased consumption of fossil fuels has led to the greenhouse effect and global warming.¹ Therefore, finding alternative energy sources is essential to meet the inexorable rise of the energy demand. Hydrogen is a zero-emission fuel when burned, and it is characterized by high energy density.^{2a} In addition, hydrogen is essential for the fertilizer economy (e.g., nitrate of potash (NOP) production), where ammonia is produced via the Haber–Bosch process.^{2b,c} The cleanest way to produce hydrogen is via water electrolysis using platinum catalysts,³ which limits the wide spread of the hydrogen economy. Accordingly, the challenge is to develop a cheap, efficient, and robust electrocatalyst as an alternative to platinum. In biological processes, hydrogen production or consumption are catalyzed by enzymes known as [FeFe]-hydrogenases.⁴⁻⁶ The active site of these enzymes contains an organometallic Fe/S cluster, the so-called H-cluster (Figure 1a), that is responsible for the catalytic process.⁷

Over the past few decades, several diiron dithiolato complexes that mimic the butterfly $[\text{Fe}_2\text{S}_2]$ subcluster of the H-cluster have been synthesized by altering the bridge in $[\text{Fe}_2(\text{CO})_6\{\mu\text{-S}(\text{bridge})\text{S}\}]$ (Figure 1b) and tested as electrocatalysts.⁸⁻¹⁶ Moreover, these complexes have been modified to contain heavier chalcogen atoms such as selenium or tellurium instead of sulfur.¹⁷ In addition, substitution of the CO ligands

in $[\text{Fe}_2(\text{CO})_6\{\mu\text{-S}(\text{CH}_2\text{YCH}_2)\text{S}\}]$ ($\text{Y} = \text{CH}_2, \text{NR}, \text{O}, \text{SiR}_2, \text{PhP}=\text{O}$) by cyanide,¹⁸ phosphanes,^{12f,13a,19} phosphites,^{12f,13a,19b-1} carbenes,^{12m,13d,19b,20} nitrosyl,²¹ or sulfides^{18b,22} to produce mono-, di-, tri-, and tetrasubstituted complexes has been extensively studied.^{12m,18-22} Furthermore, other efforts have focused on synthesizing macrocyclic complexes that contain two $[\text{Fe}_2\text{S}_2]$ clusters connected by different linkers, which provide two catalytic active centers. The first example of such macrocycles that have nonsymmetric linkers was reported by Song and co-workers in 2002.^{23a} Later, Song also described the synthesis of a complex containing two $[\text{Fe}_2\text{S}_2]$ clusters connected by two equivalent butyl chains, forming a 16-membered macrocycle.^{23d} However, such unique architectures are rare, and only few examples are known.^{15a,23} It is worth pointing out that diiron complexes with the general formula $[\text{Fe}_2(\text{CO})_6\{\mu\text{-}(\text{SR})_2\}]$ may adopt three possible stereoisomers based on the orientation of the R substituents: axial–axial (*aa*), axial–equatorial (*ae*), and equatorial–equatorial (*ee*), as illustrated in Figure 1c.⁸ Whereas chelating dithiolate organic substituents, such as 1,2-ethanedithiolate (edt) and 1,2-propanedithiolate (pdt), always form the *aa* isomer, non-chelating ones like methyl (Me) and ethyl (Et) groups give

Received: June 1, 2017

Published: August 15, 2017

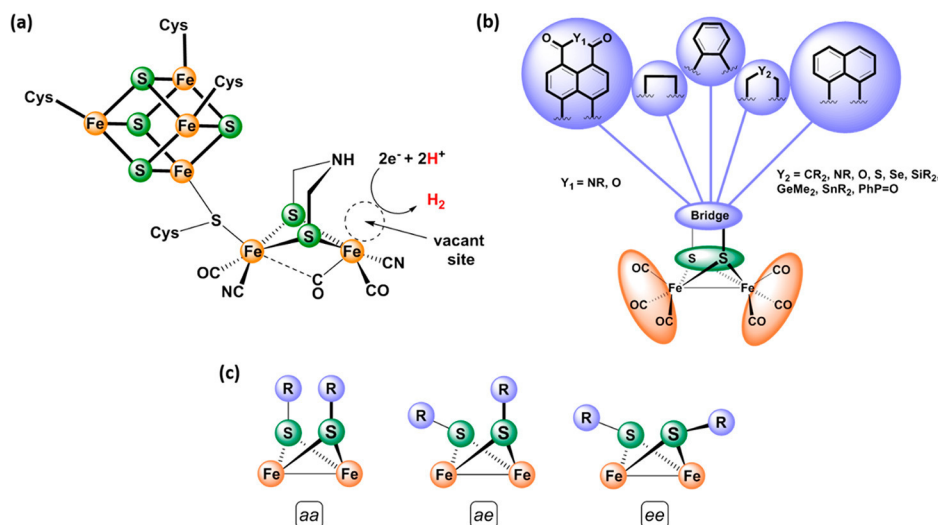


Figure 1. (a) Structure of the H-cluster. (b) Synthetic models of the active site of [FeFe]-hydrogenase. (c) Three isomers of diiron dithiolato carbonyls (CO ligands have been omitted for clarity).

only a mixture of the *ae* and *ee* isomers in different ratios based on the nature of the R substituents.⁸

In the total picture, a basic aim of the synthetic chemistry is to mimic the electronic and structural characteristics of the [Fe₂S₂] core of the H-cluster and to provide a good understanding of the factors stabilizing its rotated state. In fact, within the numerous complexes for the reduced state of the H-cluster (H_{red}), in which the two iron units are in a fully or distorted eclipsed conformation, only two [Fe^IFe^I] complexes featuring the rotated structure have been reported,^{24a,b} and one complex exhibits a semirotated state.^{24c} Remarkably, the steric bulk of the dithiolato linker and asymmetrical coordination at the two Fe atoms play a crucial role in stabilizing the rotated/semirotated states of these complexes. On the other hand, the reduction of [Fe^IFe^I] hexacarbonyl complexes, e.g., [Fe₂(CO)₆{μ-S(C₆H₄)S}],^{11b} may trigger inversion of one of the Fe(CO)₃ units to locate one CO ligand in a semibringing position for stabilization of the negative charge.^{9b,11a,c–e,g,17e,25}

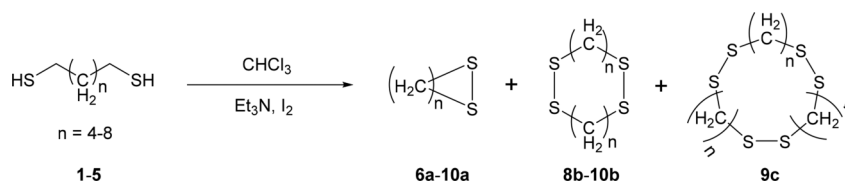
One focus of our group is to investigate the effect of the nature of the dithiolato ligand on the physical and electrochemical properties of the diiron dithiolato complexes. In this respect, we have published several studies in which we systematically altered the structure of the ligand [–XCH₂YCH₂X–] as follows: (1) X = S is replaced by X = Se or Te, which results in an increase in the electron-richness at the diiron core in going from S to Se to Te, accompanied by a decrease in the reduction potential of the model system.^{17c} (2) The presence of Y = S or Se instead of O leads to an ECE reduction mechanism (E = electron transfer, C = chemical process) due to a facile core reorganization accompanying the electron transfer.^{17a} (3) Increasing the steric bulkiness of Y (CH₂, CHMe, CMe₂) lowers the barrier for Fe(CO)₃ rotation and results in an ECE reduction mechanism only in the case of Y = CMe₂.^{17c} (4) The introduction of heavier group 14 atoms at the bridgehead position (Y) stabilizes the –SCYCS– moiety in a nearly planar state for Y = GeMe₂ or SnMe₂.^{15a} We have also confirmed that the electron density of the μ-S atoms (and hence that of Fe–Fe bond)^{15a} increase in going from CMe₂ to SiMe₂ to GeMe₂ to SnMe₂ and that protonation of the Fe–Fe bond using the moderately strong acid CF₃CO₂H can be accomplished in the case of Y = SnMe₂ and X = Se.^{17d}

Herein we report the cyclization of different alkanedithiols by means of the high-dilution technique to afford cyclic disulfides, tetrasulfides, and hexasulfides (**6a–10a**, **8b–10b**, and **9c**, respectively; Table 1). The resulting compounds were fully characterized by a variety of analytical techniques (NMR spectroscopy, elemental analysis, mass spectrometry, and X-ray structure determination of compounds **8b–10b** and **9c**). Subsequently, these compounds were used as proligands to synthesize a series of complexes of the type [Fe₂(CO)₆{μ-S(CH₂)_nS}] (n = 4–8) (**13–17**), [Fe₂(CO)₆{μ-S(CH₂)_nS}]₂ (n = 6–8) (**18–20**), and [Fe₂(CO)₆{(μ-S(CH₂)_nS)₂}] (n = 6–8) (**21–23**). The molecular structures of complexes **13–20** and **22** were determined using single-crystal X-ray diffraction analysis. In addition, we also resynthesized the known complexes [Fe₂(CO)₆{μ-S(CH₂)₂S}] (**11**)^{26a} and [Fe₂(CO)₆{μ-S(CH₂)₃S}] (**12**)^{26b} to study how the physical, electrochemical, and electrocatalytic features are influenced by the systematic increase of n from 2 to 8 in complexes **11–17**.

RESULTS AND DISCUSSION

Synthesis and Characterization of Cyclic Di-, Tetra-, and Hexasulfides. The synthetic procedures and characterizations of the precursors **1–5** required for the preparation of compounds **6a–10a**, **8b–10b**, and **9c** are described in detail in the Supporting Information. The syntheses of the cyclic disulfides (**6a–10a**), tetrasulfides (**8b–10b**), and hexasulfide (**9c**) were carried out by following the high-dilution technique previously described in the literature (Table 1).²⁷ Simultaneous addition of solutions of the dithiols and excess I₂ in CHCl₃ to a vigorously stirred solution of Et₃N in CHCl₃ followed by column chromatography afforded the disulfides with n = 4 and 5 (**6a** and **7a**), while for n = 6–9 the same mixture had two products, the disulfides (**8a–10a**) and the tetrasulfides (**8b–10b**) (Table 1). In the case of n = 7, trace amounts of the hexasulfide (**9c**) were obtained. To the best of our knowledge, compounds **9b** and **9c** are reported for the first time in this paper, and the yields of compounds **6a–10a**, **8b**, and **10b** obtained by this method are higher than those reported in the literature.²⁸ Single crystals of compounds **8b–10b** and **9c** were obtained from saturated solutions of hexane at –20 °C for X-ray diffraction studies. The molecular structures of these

Table 1. Synthetic Pathway for Compounds 6a–10a, 8b–10b, and 9c



Entry	Product					
	Cyclic disulfide	Isolated yield (%)	Dimeric disulfide	Isolated yield (%)	Trimeric disulfide	Isolated yield (%)
HS(CH ₂) ₄ SH (1) 6a		95%	-	-	-	-
HS(CH ₂) ₅ SH (2) 7a		90%	-	-	-	-
HS(CH ₂) ₆ SH (3) 8a		65%		25%	-	-
HS(CH ₂) ₇ SH (4) 9a		65%		15%		15%
HS(CH ₂) ₈ SH (5) 10a		75%		20%	-	-

compounds (Figure 2) show cyclic molecules consisting of methylene chains in a zigzag conformation linked by disulfide bonds. The average C–C–C bond angles of **8b–10b** and **9c** are around 113.4° indicating an sp³ hybridized C atoms, while the average C–C bond distance of these compounds is ~1.524 Å, a typical value for cyclic hydrocarbons.^{29a,b} In addition, the average S–S bond distance is 2.0394 Å which is in agreement with the corresponding bond in α-S₈ (2.05 Å)^{29c} and the average dihedral angles between the planes through the two sets of C–S–S and S–S–C atoms are 82.02° for the compounds **8b–10b** and **9c**.

Synthesis and Characterization of Dinuclear and Tetranuclear Complexes 13–23. The dinuclear complexes **13–17** were synthesized as shown in Scheme 1. Unexpectedly, neither the reaction of in situ-generated (μ-LiS)₂Fe₂(CO)₆ with 1 equiv of alkyl dibromide [Br(CH₂)_nBr] (n = 4–8) (Scheme 1A) nor the reaction of alkyldithiol [SH(CH₂)_nSH] (n = 4–8) with Fe₃(CO)₁₂ in boiling THF (Scheme 1B) afforded the

dinuclear complexes **13**³¹–**17**. In contrast, the reactions of compounds **6a–10a** with equimolar amounts of Fe₃(CO)₁₂ in boiling THF for 1 h followed by column chromatography afforded the dinuclear complexes **13–17**, as illustrated in Scheme 1C. Complexes **13–17** could be formed by the general route proposed by Nametkin and co-workers,³⁰ in which thermal decomposition of Fe₃(CO)₁₂ takes place initially to afford the unsaturated 16-electron species Fe(CO)₄, which subsequently reacts with the disulfide sulfur atoms to generate [(OC)₄FeSRSFe(CO)₄] as an intermediate. The latter then releases two CO ligands to afford complexes **13–17**.

Otherwise, the reaction of 2 equiv of Fe₃(CO)₁₂ with 1 equiv of **8b–10b** in boiling THF for 2 h afforded the tetranuclear complexes **18–20**, whereas the reaction of Fe₃(CO)₁₂ with compounds **8b–10b** in a 1:1 molar ratio under the same conditions with the same separation procedure afforded complexes **21–23** containing one [Fe₂S₂] subcluster as well as traces of the tetranuclear complexes **18–20** (Scheme 2). The

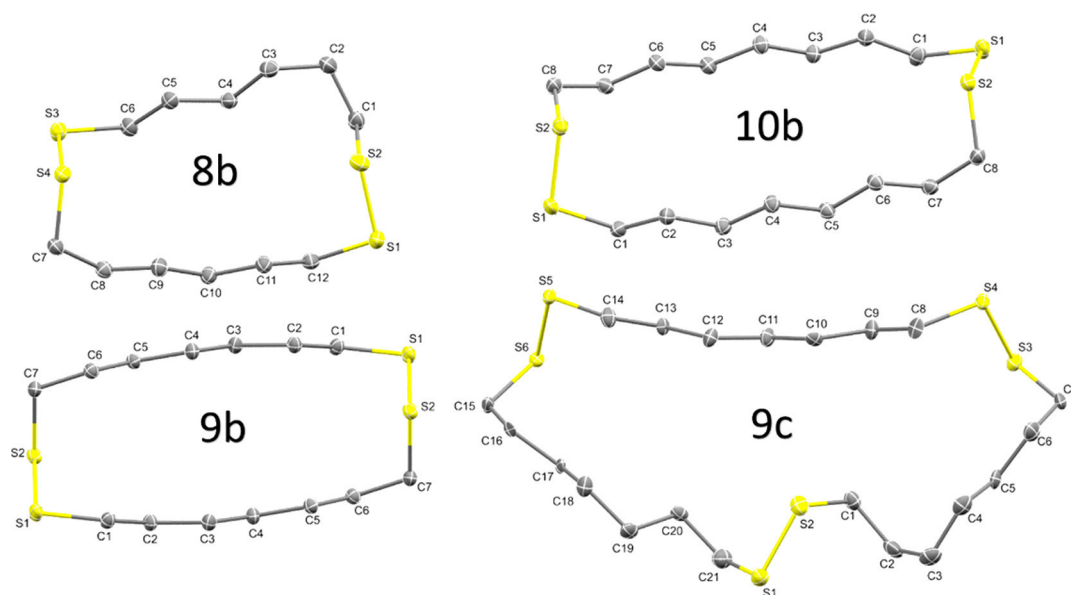
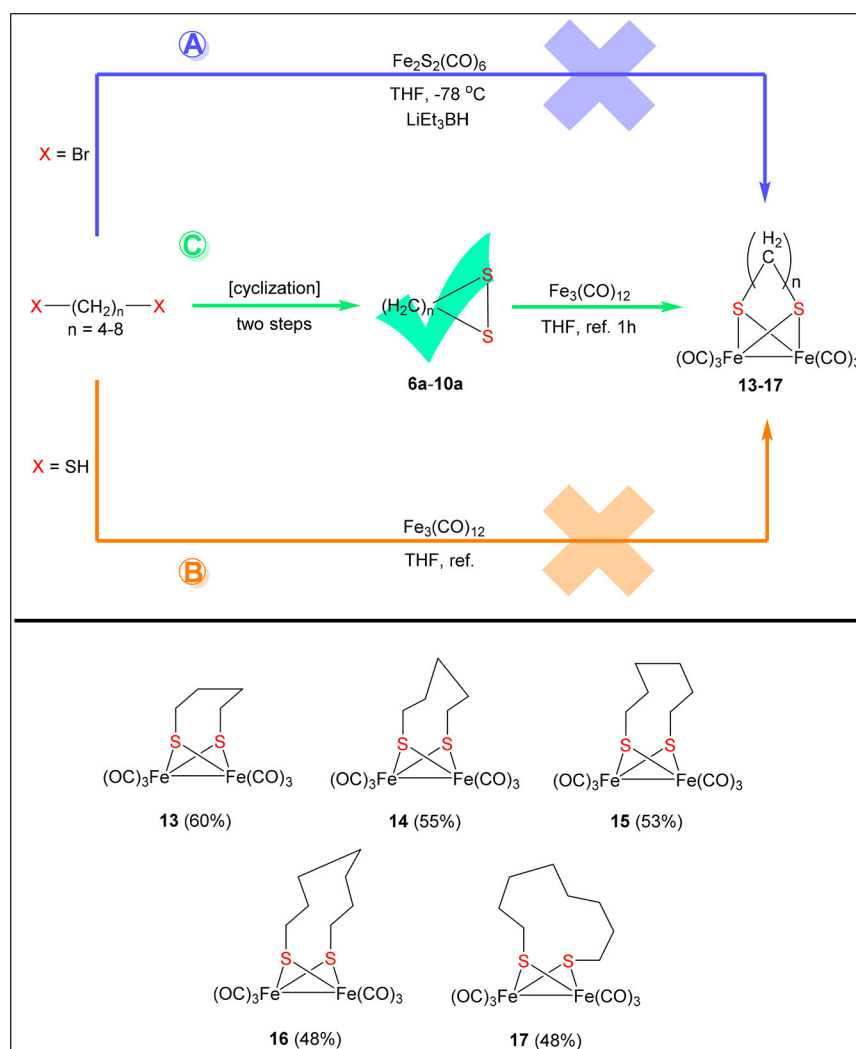


Figure 2. Molecular structures (50% probability) of compounds **8b–10b** and **9c**. Hydrogen atoms have been omitted for clarity.

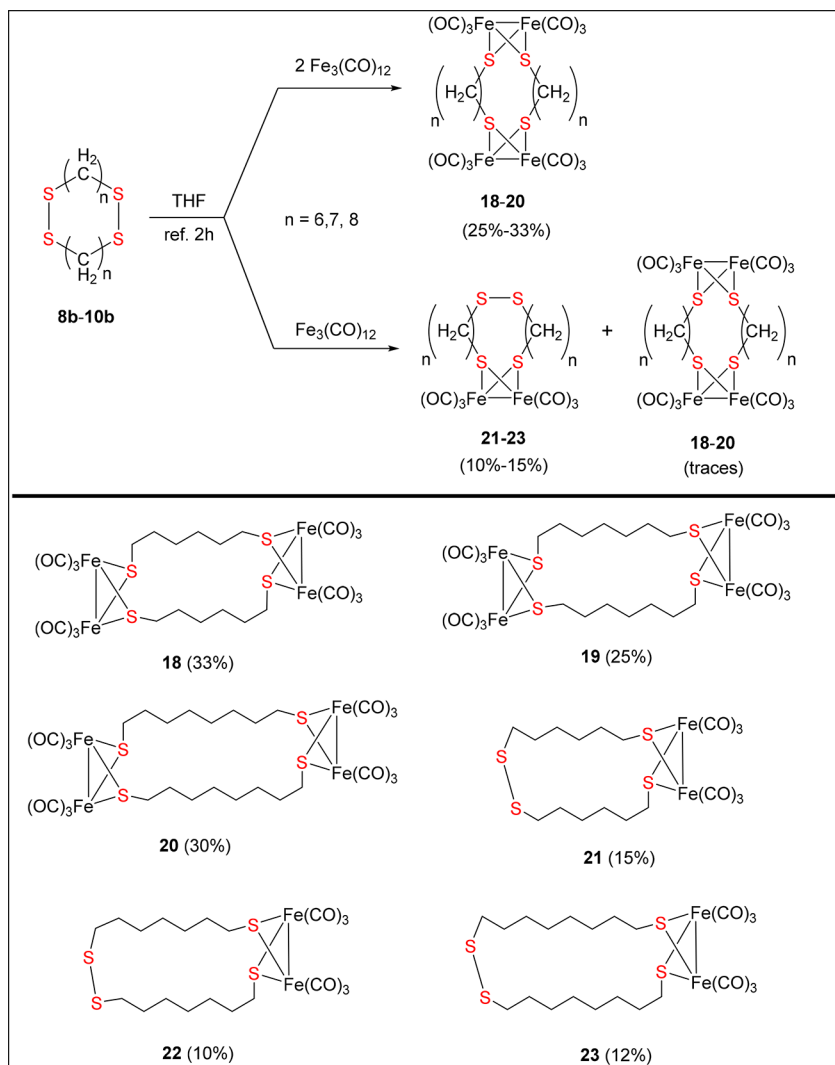
Scheme 1. Attempts To Prepare the Dinuclear Complexes **13–17**



resulting complexes **13–23** were characterized by spectroscopic techniques (^1H NMR, $^{13}\text{C}\{^1\text{H}\}$ NMR (except for complexes

21–23), and IR), mass spectrometry, and elemental analysis as well as X-ray crystallography for complexes **13–20** and **22**.

Scheme 2. Synthetic Pathways for Complexes 18–23



The IR spectra of complexes 13–17 and those of complexes 18–23 in CH_2Cl_2 are nearly identical to each other in terms of the number of peaks and frequencies (Table S1 in the Supporting Information). It is evident from Table S1 that the average $\nu(\text{CO})$ wavenumbers shift to slightly smaller values in going from 11 to 17, which indicates that increasing the length of the dithiolato bridge does not harshly change the electron-donating ability of the dithiolato bridge. The ^1H NMR spectra of the dinuclear complexes 13–16 show signals at 2.59, 2.61, 2.49, and 2.30 ppm for protons in the methylene groups attached directly to $\mu\text{-S}$ and another set of signals at 1.66, 1.75, 1.64, and 1.60 ppm for the SCH_2CH_2 moieties. Furthermore, the signals of the protons in the rest of the methylene groups of the chain linkers appear at 1.56 ppm for complex 14 and 1.53 ppm for complex 15, while those of complex 16 appear at 1.48 and 1.38 ppm.

On the other hand, the ^1H – ^1H COSY analysis of 17 allowed the assignment of the ^1H NMR resonances of the two singlets with an equal intensity at 2.45 and 2.18 ppm to the protons in the SCH_2 moieties located at the equatorial (e) and axial (a) positions, respectively. Thus, the two signals at 1.87 and 1.54 ppm were assigned to the protons of the e and a CH_2 groups in SCH_2CH_2 moieties, while the three signals at 1.63, 1.44, and 1.34 ppm were assigned to the remaining protons in the chain

linker. The $^{13}\text{C}\{^1\text{H}\}$ NMR spectra display one signal for the carbonyl carbon atoms at 207.9 ppm for complex 13 and at 207.7 ppm for complexes 14–16, whereas for complex 17 the signal appears at 209.4 ppm. The signals for the methylene carbons in the chain linkers were also detected in the range of 23.4–37.4 ppm for complexes 13–17 (see the Experimental Section). In the case of the tetranuclear complexes 18–20, the ^1H NMR spectra exhibit two signals in the range of 2.08–2.47 ppm for the methylene protons connected to the $\mu\text{-S}$ atoms and located at the e and a positions. Another set of signals was detected in the range of 1.59–1.75 ppm for the protons in the SCH_2CH_2 moieties, as was a multiplet in the range of 1.26–1.52 ppm for protons in the remaining CH_2 groups. Similar to the dinuclear complexes, the $^{13}\text{C}\{^1\text{H}\}$ NMR spectra of complexes 18–20 showed one singlet for the carbonyl carbon atoms, at 208.9 ppm for complexes 18 and 19 and at 209.1 ppm for complex 20. Besides, the signals of the methylene carbon atoms of the chain linker were detected in the range of 23.84–39.37 ppm (see the Experimental Section). Moreover, the ^1H NMR spectra of complexes 21–23 show broad signals at 2.71, 2.75, and 2.72 ppm, respectively, for the methylene protons connected to the S–S bond. Another two singlets with the same intensity for complexes 21 (2.51 and 2.14 ppm), 22 (2.50 and 2.11 ppm), and 23 (2.52 and 2.15 ppm) were assigned to

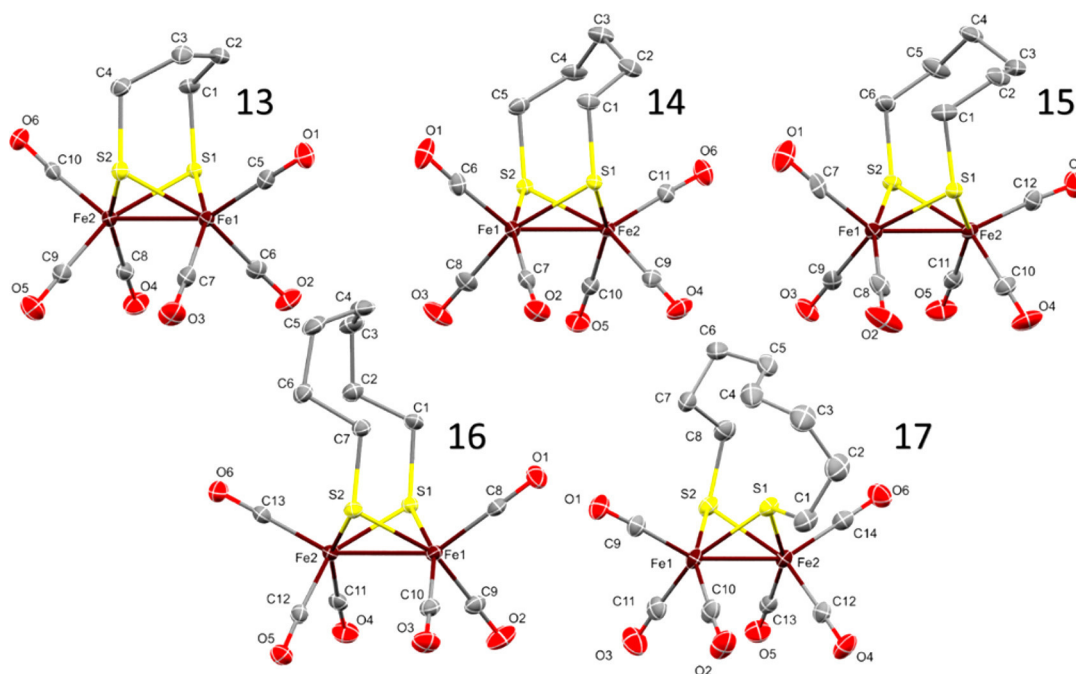


Figure 3. Molecular structures (50% probability) of complexes 13–17. Hydrogen atoms have been omitted for clarity.

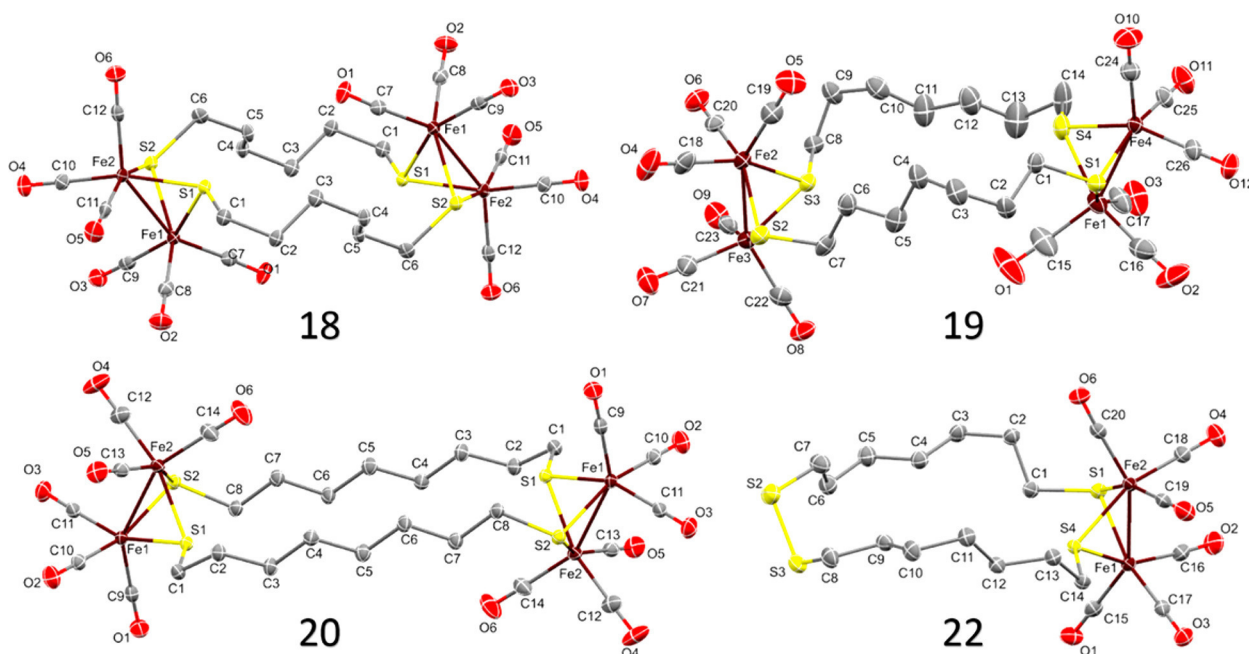


Figure 4. Molecular structures (50% probability) of complexes 18–20 and 22. Hydrogen atoms have been omitted for clarity.

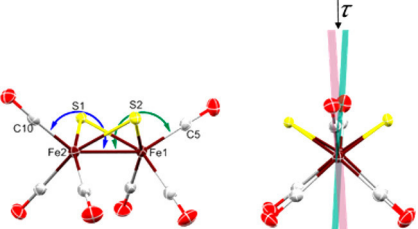
the methylene protons attached to the single $[\text{Fe}_2\text{S}_2]$ subcluster. This implies that these CH_2 moieties are oriented in the a and e positions. The mass spectra of complexes 13–23 showed the molecular ion peaks and the peaks resulting from dissociation of the CO ligands sequentially.

Molecular Structures. Single crystals suitable for X-ray diffraction studies were obtained from pentane-saturated solutions of complexes 13–17 at -20°C , while those for 18–20 and 22 were obtained by diffusion of hexane into CH_2Cl_2 solutions also at -20°C . The molecular structures of complexes 13–20 and 22 are shown in Figures 3 and 4, and selected bond lengths and angles for complexes 13–17 are given in Table 2. Three crystallographically independent

molecules in the unit cell of complex 15 were determined; only one of them is shown in Figure 3.

It is evident from Figure 3 that each complex has a butterfly $[\text{Fe}_2\text{S}_2]$ -cluster core that contains a bridging alkyldithiolato linker $[\mu\text{-S}(\text{CH}_2)_n\text{S}\text{-}\mu]$ ($n = 4\text{--}8$) and that each iron atom is bonded to three carbonyl ligands, similar to the corresponding complexes 11 and 12 reported in the literature.²⁶ The two S–C bonds are in axial positions with exception of complex 17, in which one S–C is axial and the other one is equatorial. Such orientation was also observed by Song and co-workers for $[\text{Fe}_2(\text{CO})_6\{\mu\text{-SCH}_2(\text{CH}_2\text{OCH}_2)_n\text{CH}_2\text{S}\text{-}\mu\}]$ ($n = 3, 4$).^{23b} The Fe–Fe bond lengths of complexes 13–17 are very close to those in the corresponding complexes 11 and 12 (Table 2), as

Table 2. Structural Comparison of Complexes 13–17



Complex	Fe2-Fe1 (Å)	S1...S2 (Å)	C10-Fe2-Fe1-C5, (τ) ($^\circ$) ^b	Fe-Fe-C10, C5 ($^\circ$)
11 ^{26a}	2.505(1)	2.892(2)	6.3(6)	149.7(2), 149.0(2)
12 ^{26b}	2.5105(9)	3.050	0.0(3)	148.32(9), 148.32(9)
13	2.5179(3)	3.0930(4)	6.6(1)	144.93(5), 151.25(5)
14	2.5178(3)	3.1403(5)	8.2(2)	152.82(6), 144.92(6)
15 ^a	2.5188(14)	3.1737(4)	6.83(7)	155.07(2), 144.84(3)
16	2.5074(2)	3.2135(4)	12.6(1)	151.79(4), 145.26(4)
17	2.4997(4)	2.8434(6)	2.0(2)	149.40(6), 154.48(6)

^aAverage of three independent molecules. ^bTorsion angle formed from the intersection between the apical carbonyl carbon atoms across the Fe–Fe bond.

is the average Fe–CO bond length (1.801 Å). Furthermore, the distance between the two sulfur atoms is slightly increased in going from 13 to 16 compared with complexes 11 and 12, while in the case of complex 17 it becomes shorter than those of 11 and 12 (see Table 2). In addition, it is clear from the torsion angle (τ), formed from the intersection between (O)C–Fe–Fe–C(O), together with the Fe–Fe–C(O) angles (Table 2) that the steric characteristics of the chain linkers distort the symmetry of the Fe(CO)₃ portion of the molecule. In the case of the tetranuclear complexes 18–20 and complex 22, Figure 4 confirms that complexes 18–20 are composed of two butterfly [Fe₂S₂]-cluster cores that are linked together by alkyl chains [–(CH₂)_n–] ($n = 6–8$) to form 20-, 22-, and 24-membered macrocyclic complexes, respectively. Complex 22 contains only one butterfly [Fe₂S₂]-cluster core bridged by the linker [–(CH₂)₇SS(CH₂)₇–] to form a 20-membered macrocyclic complex. All of the S–C bonds are in *e* and *a* positions, and their average bond lengths (*e*, 1.826 Å; *a*, 1.836 Å) are in agreement with those in the corresponding reported complexes.²³ Moreover, the average Fe–Fe bond length (2.513 Å) is in agreement with that in complex 12, which emphasizes that the formation of the macrocycle has no influence on the Fe–Fe distance.

Electrochemical Investigation. Table 3 summarizes the redox potentials of complexes 11–16 in CH₂Cl₂/[*n*-Bu₄N][BF₄] obtained by cyclic voltammetry. The cyclic voltammograms of the complexes, measured at 0.2 V s^{–1}, are shown in Figure 5. In the series from 11 to 15 (Table 3), the reduction potential of the diiron core becomes less negative with an overall anodic shift ($\Delta E_{1/2}$) of 330 mV. While increasing the number of carbon atoms in this series makes the reduction easier, the oxidation also becomes easier, with an overall cathodic shift (ΔE_{ox}) of 170 mV. The cathodic shift of the oxidation potential would suggest that the electron density at the diiron core has increased, but if this were the case, the reduction would become more difficult in this series. Therefore,

Table 3. Summary of the Redox Features of Complexes 11–16 in 0.1 M CH₂Cl₂/[*n*-Bu₄N][BF₄] Solution Measured at 0.2 V s^{–1} Using a Glassy Carbon Disk ($d = 1.6$ mm); Potentials *E* Are Given in Volts and Referenced to the Ferrocenium/Ferrocene (Fc⁺/Fc) Couple

complex	E_{pc} (V)	E_{pa} (V)	$E_{1/2}$ (V) ^b	E_{ox} (V)
11	–1.85	–1.62 ^a	–1.80	0.86
12	–1.85	–1.71	–1.78	0.78
13	–1.66	–1.61	–1.62	0.76
14	–1.57, –1.83	–1.50	–1.52	0.70
15	–1.54, –1.85	–	–1.47	0.69
16	–1.56, –1.87	–	–1.51	0.74

^aThis anodic event is not attributed to the oxidation of 11^{2–}. Further description of the cyclic voltammetry of 11 is given in the Supporting Information (Figure S1). ^bBecause the reduction of the complexes was irreversible or partially reversible, the $E_{1/2}$ values were estimated at the half-height of the reduction wave.

these redox reactions may be affected by reorganization processes that lead to stabilization of the electron-transfer products.^{15a} Interestingly, in going from 15 to 16, cathodic and anodic shifts in the reduction and oxidation, respectively, are observed, where $\Delta E_{1/2} = 40$ mV and $\Delta E_{\text{ox}} = 50$ mV. Thus, the complex containing six carbon atoms in the dithiolato ligand, 15, is the easiest to reduce and to oxidize in this series of complexes. One aspect of special importance for mechanistic investigation of catalytic proton reduction is the determination of the number of electrons involved in the reduction of the complex in the absence of a proton source. The reduction of diiron dithiolato complexes at the [Fe^IFe^I] redox state might occur in a stepwise two-electron-transfer fashion at E_1° and E_2° for the first and second reduction steps, respectively, where $E_1^\circ - E_2^\circ > 0$, or via transfer of two electrons at the same applied potential due to potential inversion of the two reduction steps, i.e., $E_1^\circ - E_2^\circ < 0$. It is well-established that the dependence of

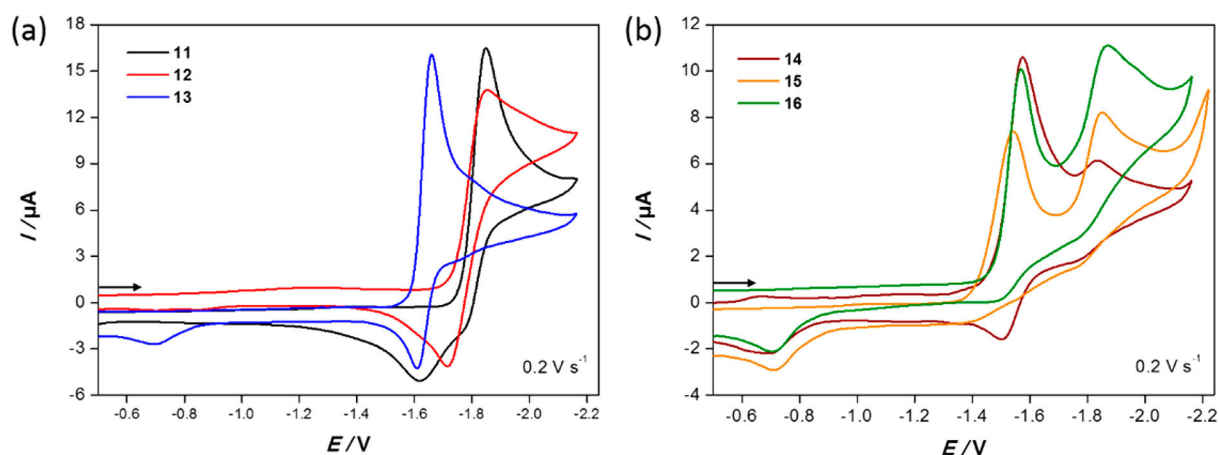


Figure 5. Cyclic voltammetry of 1.0 mM solutions of (a) complexes **11–13** and (b) complexes **14–16** in $\text{CH}_2\text{Cl}_2/[n\text{-Bu}_4\text{N}][\text{BF}_4]$ (0.1 M) at a scan rate of 0.2 V s^{-1} using a glassy carbon disk ($d = 1.6 \text{ mm}$). The potentials E are given in volts and referenced to the Fc^+/Fc couple. The arrows indicate the scan direction.

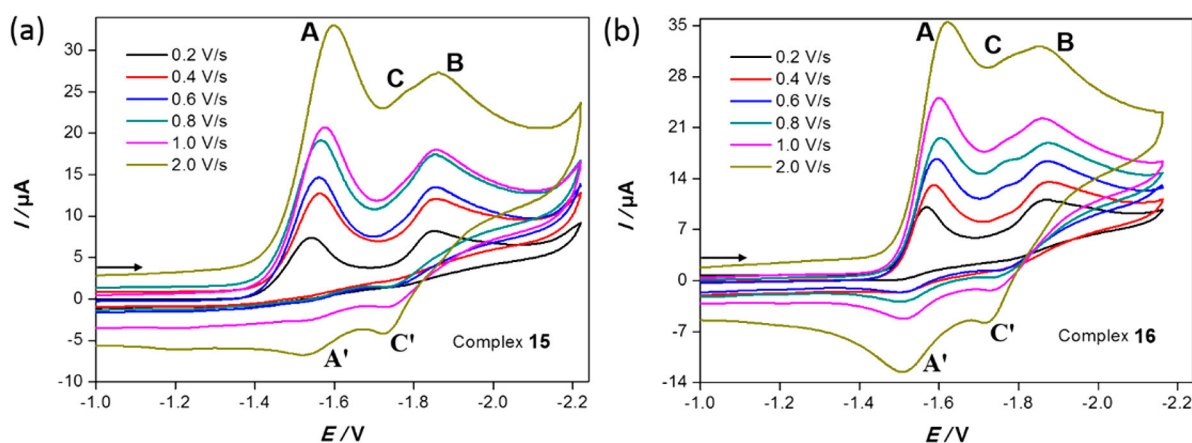


Figure 6. Cyclic voltammetry of 1.0 mM solutions of (a) complex **15** and (b) complex **16** in $\text{CH}_2\text{Cl}_2/[n\text{-Bu}_4\text{N}][\text{BF}_4]$ (0.1 M) at various scan rates using a glassy carbon disk ($d = 1.6 \text{ mm}$). The potentials E are given in volts and referenced to the Fc^+/Fc couple. The arrows indicate the scan direction.

the current function ($I_p/c \cdot \nu^{1/2} = (2.69 \times 10^5) \cdot A \cdot D^{1/2} \cdot n^{3/2}$, where I_p is the peak current, ν is the scan rate, c is the complex concentration, A is the electrode area, D is the diffusion coefficient, and n is the number of transferred electrons) on the scan rate provides mechanistic information on the electron-transfer chemistry and the number of electrons n at a given potential.^{9b,11a,c–e,g,17e,25} The scan-rate dependence of $I_p/c \cdot \nu^{1/2}$ for the first reduction of complexes **11–16** is shown in Figure S2. The value of $I_p/c \cdot \nu^{1/2}$ for the reduction peaks of complexes **11** and **13** is almost twice the magnitude of that for the other complexes, but it decreases with increasing ν toward a value predicted for a one-electron reduction, suggesting an intervening chemical process in an ECE reduction mechanism.^{9b,11a,c–e,g,17e,25} In other words, the structural change accompanying the electron transfer leads to the formation of dianionic species of **11** and **13** at a potential less negative than that required for the first electron transfer. These results are consistent with the study by Lichtenberger and co-workers,^{32a} confirming that the two-electron reduction of **11** is a consequence of a potential inversion ($E_1^0 - E_2^0 < 0$) that arises from structural changes in an ECE process. In our previous report, we discussed in detail why the value of $I_p/c \cdot \nu^{1/2}$ for the reduction of complex **12** is slightly higher than that expected for $n = 1$ and attributed that to an EC_{irr} ($E = \text{electron transfer,}$

C_{irr} = irreversible chemical reaction) process, where a product of the follow-up reaction is reduced at a potential closely spaced with that required to form the monoanion **12**.^{17e} In comparison, the current function of complexes **14–16** is independent of the scan rate and close to the value for $n = 1$. The cyclic voltammetry of complexes **11–13** (Figure 4a) was previously reported by us or others.^{12b,17e,32} The reduction of complex **14** (Figure 4b) is a partially reversible process at 0.2 V s^{-1} with the ratio of anodic peak current to cathodic peak current ($I_{\text{pa}}/I_{\text{pc}}$ ratio) approaching unity at higher scan rates (Figures S3 and S4a). An $I_{\text{pa}}/I_{\text{pc}}$ ratio less than 1 is a consequence of a follow-up chemical process that is prevented at high scan rates. The second reduction event of complex **14** at $E_{\text{pc}2} = -1.83 \text{ V}$ arises from species of follow-up reactions. Increasing the scan rate lowers the current of the second reduction event, which is accompanied by an increase in the $I_{\text{pa}}/I_{\text{pc}}$ ratio.^{20a,25c,33} The one-electron reduction of complexes **15** ($E_{\text{pc}1} = -1.54 \text{ V}$) and **16** ($E_{\text{pc}1} = -1.56 \text{ V}$) is an irreversible process at 0.2 V s^{-1} , as judged from reversal of the forward scans at -1.69 V (for **15**) and -1.70 V (for **16**) (see Figure S4b,c). The second irreversible reduction peaks of complexes **15** ($E_{\text{pc}2} = -1.85 \text{ V}$) and **16** ($E_{\text{pc}2} = -1.87 \text{ V}$) do not vanish when the scan rate is increased to 2.0 V s^{-1} , in contrast to the case of complex **14**. Moreover, a new reduction peak (C) starts

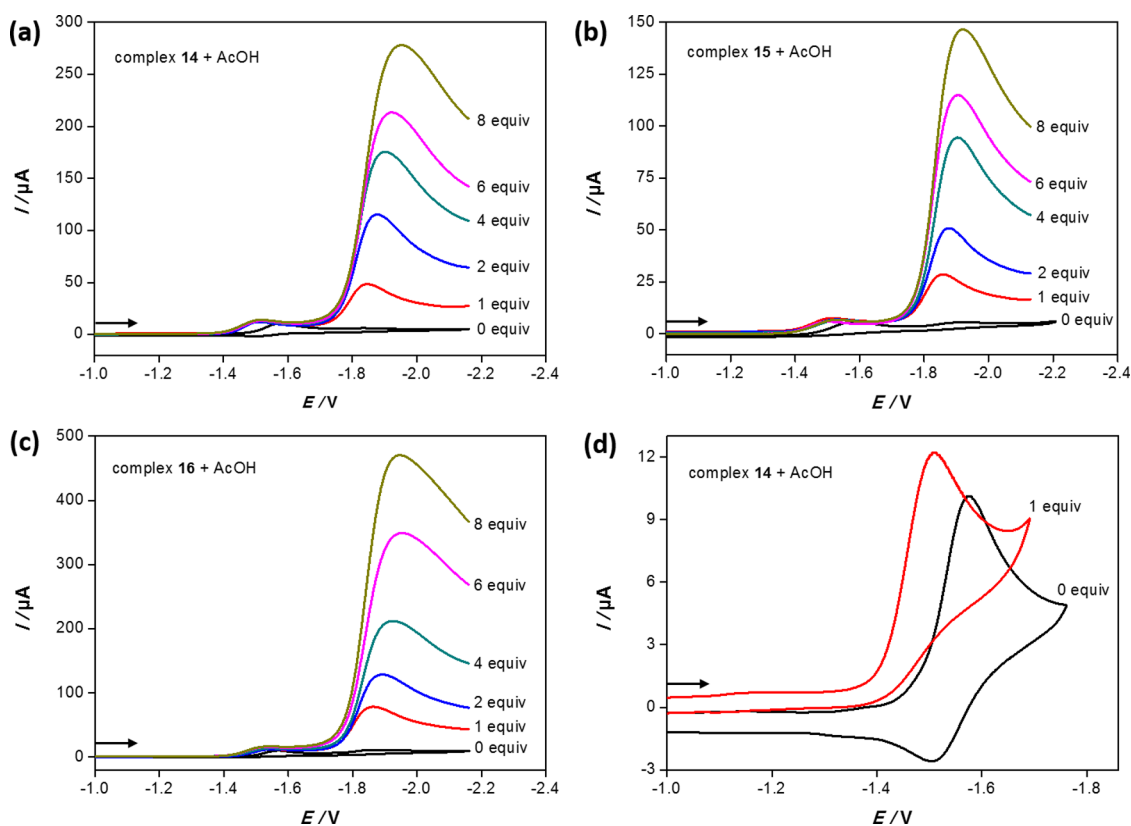


Figure 7. Cyclic voltammetry of 1.0 mM solutions of (a) complex **14**, (b) complex **15**, and (c) complex **16** in $\text{CH}_2\text{Cl}_2/[n\text{-Bu}_4\text{N}][\text{PF}_6]$ (0.1 M) at 0.2 V s^{-1} in the presence of different concentrations of AcOH using a glassy carbon disk ($d = 1.6 \text{ mm}$) and of (d) complex **15** with 1 equiv of AcOH. The arrows indicate the scan direction. The potentials E are given in V and referenced to the Fc^+/Fc couple.

to appear at $\nu \geq 2 \text{ V s}^{-1}$ ($E_{\text{pc}3} = -1.78 \text{ V}$) and $\nu \geq 0.6 \text{ V s}^{-1}$ ($E_{\text{pc}3} = -1.76 \text{ V}$) for complexes **15** and **16**, respectively (Figure 6).

The relative height of peak B with respect to A in the voltammograms of complexes **15** (Figure S5) and **16** (Figure S6) decreases as the scan rate increases. This observation is accompanied by the growth of peak C as well as the appearance of two anodic events in the return sweep, indicating enhanced reversibility of the one-electron reduction of complexes **15** and **16**. The oxidation of the monoanionic species occurs at peak A' (Figures 6, S5, and S6). These observations suggest that peak B is due to an irreversible reduction of a species formed from chemical reactions following the one-electron reduction of **15** or **16**. At high scan rates, where the follow-up reactions start to be prevented, the $\text{Fe}^{\text{I}}\text{Fe}^0/\text{Fe}^0\text{Fe}^0$ redox couple of complexes **15** and **16** is detected and indicated by C and C'.

Catalytic Reduction of Protons. The catalytic behavior of complexes **14–16** was investigated by cyclic voltammetry in the presence of various amounts of AcOH, as illustrated in Figure 7a–c. The presence of 1 equiv of AcOH in the solutions of complexes **14–16** shifts their primary reduction peaks to less negative potentials by approximately 70, 50, and 40 mV, respectively (to $E_{\text{pc}} = -1.50, -1.49, \text{ and } -1.52 \text{ V}$, respectively). This anodic shift suggests that there is an interaction between the acid and the reduced species of these complexes in CH_2Cl_2 .^{32b} As is evident from the dependence of $I_p/c\nu^{1/2}$ on the scan rate (Figure S2), these reduced species result from one-electron reduction of complexes **14–16**. Further experimental confirmation of the interaction of the acid with the monoanionic species (using complex **14** as a representative example) is shown in Figure 7d. The disappearance of the

anodic peak in the reverse scan upon addition of 1 equiv of AcOH suggests the occurrence of a chemical reaction (protonation) following the one-electron reduction of **14** in CH_2Cl_2 .^{17c} At more reducing potentials in the vicinity of -1.80 to -1.90 V for complexes **14–16**, the voltammetric profile of each complex (Figure 7a–c) shows a reduction peak with a current that increases in response to the systematic increase in the acid concentration, indicating a catalytic proton reduction. These observations suggest that the products of the EC process ($E = \text{reduction}$, $C = \text{protonation}$) for **14–16**, which occurs at ca. -1.5 V , do not lead to H_2 production unless further reduction and protonation take place at more negative potentials. For systematic comparison of the effect of the linker length on the catalytic features, we reinvestigated the behavior of complexes **11–13** in the presence of various concentrations of AcOH (data not shown in this report). Similar to complexes **14–16**, complexes **11–13** do not exhibit catalysis at their primary reduction wave but only upon application of a more negative potential. Because complexes **11** and **13** exhibit an ECE mechanism of reduction at 0.2 V s^{-1} (Figure S2), the presence of acid will lead to protonation of their dianionic species. Once the applied potential becomes sufficiently negative for subsequent reduction–protonation processes, H_2 is produced.

One property of a catalyst that describes its performance is the catalytic overpotential, which is defined in our case as the difference between the potential at half the catalytic peak current ($E_{\text{cat}/2}$) and the standard reduction potential of the acid.^{11g} A low overpotential points to an effective catalyst, which means that the catalyst operates at a potential that is close to the standard reduction potential of the acid. Because

the standard reduction potentials of acids in CH_2Cl_2 are unknown, we use the values of $E_{\text{cat}/2}$ for comparison. The catalytic potential of complex **11** ($E_{\text{cat}/2} = -2.07$ V) is ca. 300 mV more negative than those of complexes **12–16**, which in turn accomplish catalysis with comparable overpotentials reflected by $E_{\text{cat}/2} = -1.81$ V (**12**), -1.79 V (**13**), -1.77 V (**14**), -1.78 V (**15**), and -1.79 V (**16**). Another feature of the catalytic performance is the amount of current developed in response to a systematic increase in the acid concentration. The higher the current, the higher the apparent catalytic activity is. The currents for the catalytic processes of complexes **11–16** were plotted against the amount of AcOH, and the slopes were taken as a criterion of comparative catalytic activity (Figure 8).³⁴ Accordingly, complex **16** containing seven carbon atoms

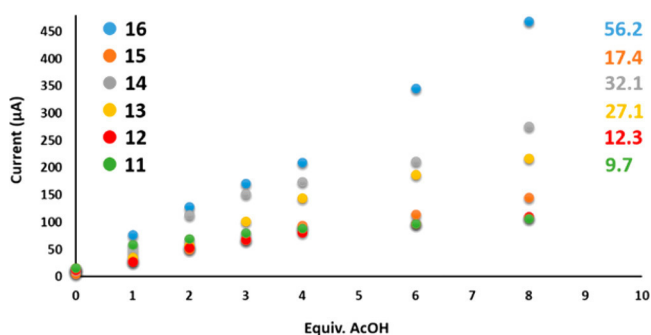


Figure 8. Dependence of the catalytic current of 1.0 mM complexes **11–16** on the amount of AcOH. The slope of each plot is given in the inset.

in the dithiolate moiety shows the greatest catalytic ability and about 6-fold higher performance compared with complex **11** containing two carbon atoms in the dithiolato ligand.

CONCLUSION

In this paper we have reported the cyclization of a series of alkyldithiols having the general formula $[\text{SH}(\text{CH}_2)_n\text{SH}]$ ($n = 4–8$) by the high-dilution technique. As a result, the monomeric, dimeric, and trimeric disulfides (**6a–10a**, **8b–10b**, and **9c**, respectively) were obtained and characterized by spectroscopic techniques as well as by X-ray structure determination in the case of **8b–10b** and **9c**. The latter compounds, with the exception of **9c**, were tested as proligands to react with $\text{Fe}_3(\text{CO})_{12}$ under different conditions in boiling THF in order to obtain complexes with the general formulas $[\text{Fe}_2(\text{CO})_6\{\mu\text{-S}(\text{CH}_2)_n\text{S}\}]$ ($n = 4–8$) (**13–17**), $[\text{Fe}_2(\text{CO})_6\{\mu\text{-S}(\text{CH}_2)_n\text{S}\}]_2$ ($n = 6–8$) (**18–20**) and $[\text{Fe}_2(\text{CO})_6\{\mu\text{-S}(\text{CH}_2)_n\text{S}\}_2]$ ($n = 6–8$) (**21–23**). Moreover, we have also reported how the physical, electrochemical, and electrocatalytic features are influenced by the systematic increase in n from 2 to 8 in complexes **11–17**. Overall, increasing the length of the linker chain of the dithiolato ligand in the all-CO complexes does not harshly change the electronic properties of the $\text{Fe}(\text{CO})_3$ units. Otherwise, the molecular structures of complexes **13–16** showed that the organic substituents are constrained to the *aa* conformation, similar to their analogous complexes **11** and **12**.^{26a,b} In contrast, the molecular structure of complex **17** exhibits an *ae* conformation, and its ^1H NMR spectrum does not show the presence of the *aa* isomer at room temperature. Therefore, to determine whether there is a dynamic interconversion between the *aa* and *ae* isomers of complex **17**, a temperature-dependent ^1H NMR experiment

was applied to a solution of complex **17** in toluene- d_8 , and we could not observe the *aa* isomer by increasing the temperature of the solution to 85 °C. The absence of the *aa* isomer in complex **17** could be explained by the short distance between the *a*- CH_2 and the sulfur atom bound to the *e*- CH_2 (3.003(2) Å) in comparison with those in complexes **13–16** (average ~ 3.694 Å). In the light of the above-mentioned considerations as well as Song's results,^{23b} we suggest that $[\text{Fe}_2(\text{CO})_6\{\mu\text{-S}(\text{CH}_2)_n\text{S}\}]$ gives only the *ae* isomer for $n \geq 8$ as a result of steric encumbrance, which is overcome for $n \leq 7$. Interestingly, the reduction and oxidation potentials of the diiron core in the systematic series from **11** to **15** are lowered with overall anodic $\Delta E_{1/2}$ and cathodic ΔE_{ox} shifts of 330 and 170 mV, respectively. Furthermore, proton reduction catalyzed by complexes **11–16** was also investigated by cyclic voltammetry in the presence of the weak acid AcOH as a proton source. It was concluded that complexes **12–16** catalyze the reduction of protons with comparable overpotentials (gauged from $E_{\text{cat}/2}$) and less negative potentials than complex **11** (ca. 300 mV). Additionally, the catalytic ability of complexes **11–16** varies in the following order: **16** > **14** > **13** > **15** > **12** > **11**.

EXPERIMENTAL SECTION

Materials and Techniques. All of the reactions were performed using standard Schlenk and vacuum-line techniques under an inert gas (nitrogen). The ^1H and $^{13}\text{C}\{^1\text{H}\}$ NMR spectra were recorded with a Bruker Avance 400 MHz spectrometer. Chemical shifts are given in parts per million with reference to internal SiMe_4 or CHCl_3 . The mass spectra were recorded with a Finnigan MAT SSQ 710 instrument. The IR spectra were recorded with a Bruker Equinox 55 spectrometer equipped with an attenuated total reflectance unit. Elemental analysis was performed with a Leco CHNS-932 apparatus. Thin-layer chromatography (TLC) was performed using Merck TLC aluminum sheets (silica gel 60 F₂₅₄). Solvents from Fisher Scientific and other chemicals from Acros and Aldrich were used without further purification. Melting points were recorded on a polarization microscope (Axiolab) connected to a heating unit (THS-600) using the software Linkam LNP and CI 93. All of the solvents were dried and distilled prior to use according to standard methods. Complexes **11** and **12** were synthesized according to the known literature methods.^{17e,32} The preparations of compounds **1–5**, **6a–10a**, **8b–10b**, and **9c** are described in detail in the Supporting Information.

Electrochemistry. Corrections for the *iR* drop were performed for all experiments. Cyclic voltammetry measurements were conducted using the three-electrode technique (glassy carbon disk (diameter $d = 1.6$ mm) as the working electrode, Ag/Ag^+ in MeCN as the reference electrode, and Pt wire as the counter electrode) with a Reference 600 potentiostat (Gamry Instruments). All of the experiments were performed in CH_2Cl_2 solution containing 0.1 M $[n\text{-Bu}_4\text{N}][\text{BF}_4]$ at room temperature; the concentration of the complexes was 1.0 mM. Solutions were deaerated by purging with N_2 for 5–10 min, and a blanket of N_2 was maintained over the solutions during the measurements. The vitreous carbon disk was polished on a felt tissue with alumina before each measurement. All of the potential values reported in this paper are referenced to the potential of the ferrocenium/ferrocene (Fc^+/Fc) couple.

Crystal Structure Determination. The intensity data for the compounds were collected on a Nonius KappaCCD diffractometer using graphite-monochromatized Mo $K\alpha$ radiation. Data were corrected for Lorentz and polarization effects; absorption was taken into account on a semiempirical basis using multiple scans.^{35–37} The structures were solved by direct methods (SHELXS³⁸) and refined by full-matrix least-squares techniques against F_o^2 (SHELXL-97³⁸). The hydrogen atoms of compounds **9c**, **15**, and **19** were included at calculated positions with fixed thermal parameters. All of the other hydrogen atoms were located by difference Fourier synthesis and refined isotropically. All non-hydrogen atoms were refined anisotropically.

cally.³⁸ The crystal of **9c** was a partial merohedral twin. The twin law was determined by PLATON³⁹ to (1.001 0.000 0.003/0.000 -1.000 0.000/-0.333 0.000 -1.001). The contribution of the main component was refined to 0.819(3). Crystallographic data as well as structure solution and refinement details are summarized in Tables S2–S4. XP (SIEMENS Analytical X-ray Instruments, Inc.) was used for structure representations.

General Procedure for the Synthesis of $[\text{Fe}_2(\text{CO})_6\{\mu\text{-S}(\text{CH}_2)_n\text{S}\}]$ ($n = 4\text{--}8$) (13–17). A solution of $\text{Fe}_3(\text{CO})_{12}$ (200 mg, 0.40 mmol) and cyclic disulfide (**6a–10a**, 0.40 mmol) in THF (30 mL) was heated at reflux for 1 h under N_2 . The green solution turned deep red, and the solvent was removed under reduced pressure. The residue was purified by column chromatography using 100% hexane. A red-orange fraction representing the complex (13–17, respectively) was collected, and the solvent was removed in vacuo. The product was obtained as a red-orange solid.

$[\text{Fe}_2(\text{CO})_6\{\mu\text{-S}(\text{CH}_2)_4\text{S}\}]$ (**13**). Yield: 60% (0.24 mmol). Mp = 113–115 °C. Anal. Calcd for $\text{C}_{10}\text{H}_8\text{Fe}_2\text{O}_6\text{S}_2$: C, 30.03; H, 2.02; S, 16.03. Found: C, 30.40; H, 2.27; S, 16.20. ^1H NMR (400 MHz, CDCl_3 , ppm): δ 2.59 (bs, 4H, SCH_2), 1.66 (bs, 4H, SCH_2CH_2). $^{13}\text{C}\{^1\text{H}\}$ NMR (100 MHz, CDCl_3 , ppm): δ 207.90 (s, CO), 33.80 (s, SCH_2), 26.09 (s, SCH_2CH_2). IR (ν_{CO} , cm^{-1}): 2072(m), 2033(vs), 1997(s). DEI-MS (m/z): 400 $[\text{M}]^+$.

$[\text{Fe}_2(\text{CO})_6\{\mu\text{-S}(\text{CH}_2)_5\text{S}\}]$ (**14**). Yield: 55% (0.22 mmol). Mp = 116–118 °C. Anal. Calcd for $\text{C}_{11}\text{H}_{10}\text{Fe}_2\text{O}_6\text{S}_2$: C, 31.91; H, 2.43; S, 15.49. Found: C, 32.31; H, 2.61; S, 15.79. ^1H NMR (400 MHz, CDCl_3 , ppm): δ 2.61 (t, 4H, SCH_2), 1.75 (p, 4H, SCH_2CH_2), 1.56 (p, 2H, $\text{SCH}_2\text{CH}_2\text{CH}_2$). $^{13}\text{C}\{^1\text{H}\}$ NMR (100 MHz, CDCl_3 , ppm): δ 207.72 (s, CO), 30.21 (s, SCH_2), 29.37 (s, SCH_2CH_2), 28.64 (s, $\text{SCH}_2\text{CH}_2\text{CH}_2$). IR (ν_{CO} , cm^{-1}): 2072(m), 2033(vs), 1999(s). DEI-MS (m/z): 414 $[\text{M}]^+$.

$[\text{Fe}_2(\text{CO})_6\{\mu\text{-S}(\text{CH}_2)_6\text{S}\}]$ (**15**). Yield: 53% (0.21 mmol). Mp = 119–121 °C. Anal. Calcd for $\text{C}_{12}\text{H}_{12}\text{Fe}_2\text{O}_6\text{S}_2$: C, 33.67; H, 2.83; S, 14.98. Found: C, 33.96; H, 3.14; S, 15.12. ^1H NMR (400 MHz, CDCl_3 , ppm): δ 2.49 (t, 4H, SCH_2), 1.64 (bs, 4H, SCH_2CH_2), 1.53 (bs, 4H, $\text{SCH}_2\text{CH}_2\text{CH}_2$). $^{13}\text{C}\{^1\text{H}\}$ NMR (100 MHz, CDCl_3 , ppm): δ 207.68 (s, CO), 32.08 (s, SCH_2), 30.52 (s, SCH_2CH_2), 26.01 (s, $\text{SCH}_2\text{CH}_2\text{CH}_2$). IR (ν_{CO} , cm^{-1}): 2072(m), 2033(vs), 1998(s). DEI-MS (m/z): 428 $[\text{M}]^+$.

$[\text{Fe}_2(\text{CO})_6\{\mu\text{-S}(\text{CH}_2)_7\text{S}\}]$ (**16**). Yield: 48% (0.19 mmol). Mp = 94–96 °C. Anal. Calcd for $\text{C}_{13}\text{H}_{14}\text{Fe}_2\text{O}_6\text{S}_2$: C, 35.32; H, 3.19; S, 14.50. Found: C, 35.72; H, 3.30; S, 14.70. ^1H NMR (400 MHz, CDCl_3 , ppm): δ 2.30 (bs, 4H, SCH_2), 1.60 (bs, 4H, SCH_2CH_2), 1.48 (bs, 4H, $\text{SCH}_2\text{CH}_2\text{CH}_2$), 1.38 (bs, 2H, $\text{SCH}_2\text{CH}_2\text{CH}_2\text{CH}_2$). $^{13}\text{C}\{^1\text{H}\}$ NMR (100 MHz, CDCl_3 , ppm): δ 207.70 (s, CO), 31.83 (s, SCH_2), 29.40 (s, SCH_2CH_2), 27.54 (s, $\text{SCH}_2\text{CH}_2\text{CH}_2$), 25.81 (s, $\text{SCH}_2\text{CH}_2\text{CH}_2\text{CH}_2$). IR (ν_{CO} , cm^{-1}): 2072(m), 2033(vs), 1994(s). DEI-MS (m/z): 442 $[\text{M}]^+$.

$[\text{Fe}_2(\text{CO})_6\{\mu\text{-S}(\text{CH}_2)_8\text{S}\}]$ (**17**). Yield: 48% (0.19 mmol). Mp = 83–85 °C. Anal. Calcd for $\text{C}_{14}\text{H}_{16}\text{Fe}_2\text{O}_6\text{S}_2$: C, 36.87; H, 3.54; S, 14.06. Found: C, 37.13; H, 3.49; S, 14.33. ^1H NMR (400 MHz, CDCl_3 , ppm): δ 2.45 (bs, 2H, $e\text{-SCH}_2$), 2.18 (bs, 2H, $a\text{-SCH}_2$), 1.87 (bs, 2H, $e\text{-SCH}_2\text{CH}_2$), 1.63 (bs, 2H, $\text{SCH}_2\text{CH}_2\text{CH}_2$), 1.54 (bs, 2H, $a\text{-SCH}_2\text{CH}_2$), 1.44 (bs, 2H, $\text{SCH}_2\text{CH}_2\text{CH}_2\text{CH}_2$), 1.34 (bs, 2H, $\text{S}(\text{CH}_2)_4\text{CH}_2$). $^{13}\text{C}\{^1\text{H}\}$ NMR (100 MHz, CDCl_3 , ppm): δ 209.17 (s, CO), 37.36 (s, $e\text{-SCH}_2$), 30.46 (s, $e\text{-SCH}_2\text{CH}_2$), 29.84 (s, $\text{SCH}_2\text{CH}_2\text{CH}_2$), 28.28 (s, $\text{SCH}_2\text{CH}_2\text{CH}_2\text{CH}_2$), 27.26 (s, $\text{S}(\text{CH}_2)_3\text{CH}_2$), 26.82 (s, $\text{S}(\text{CH}_2)_4\text{CH}_2$), 24.77 (s, $a\text{-SCH}_2\text{CH}_2$), 23.42 (s, $a\text{-SCH}_2$). IR (ν_{CO} , cm^{-1}): 2069(m), 2030(vs), 1992(s). DEI-MS (m/z): 456 $[\text{M}]^+$.

General Procedure for the Synthesis of Complexes 18–20 via Reaction of Compounds 8b–10b with $\text{Fe}_3(\text{CO})_{12}$ in a 1:2 Molar Ratio. A solution of $\text{Fe}_3(\text{CO})_{12}$ (400 mg, 0.80 mmol) and cyclic tetrasulfide (**8b–10b**, 0.40 mmol) in THF (40 mL) was heated at reflux for 2 h under N_2 . The green solution turned deep red, and the solvent was removed under reduced pressure. The residue was purified by column chromatography using 100% hexane. A red-orange fraction representing the complex (18–20, respectively) was collected, and the solvent was removed in vacuo. The product was obtained as a red-orange solid.

$[\text{Fe}_2(\text{CO})_6\{\mu\text{-S}(\text{CH}_2)_6\text{S}\}]_2$ (**18**). Yield: 33% (0.13 mmol). Mp = 210–211 °C. Anal. Calcd for $\text{C}_{24}\text{H}_{24}\text{Fe}_4\text{O}_{12}\text{S}_4$: C, 33.67; H, 2.83; S, 14.98. Found: C, 33.99; H, 3.10; S, 15.20. ^1H NMR (400 MHz, CDCl_3 , ppm): δ 2.46 (bs, 4H, $e\text{-SCH}_2$), 2.13 (bs, 4H, $a\text{-SCH}_2$), 1.62 (bs, 8H, SCH_2CH_2), 1.48 (bs, 8H, $\text{SCH}_2\text{CH}_2\text{CH}_2$). $^{13}\text{C}\{^1\text{H}\}$ NMR (100 MHz, CDCl_3 , ppm): δ 208.97 (s, CO), 39.05 (s, $e\text{-SCH}_2$), 32.68, 31.41, 28.76, 26.42, 23.84 (s, $a\text{-SCH}_2$). IR (ν_{CO} , cm^{-1}): 2068(m), 2033(vs), 1991(s). DEI-MS (m/z): 856 $[\text{M}]^+$.

$[\text{Fe}_2(\text{CO})_6\{\mu\text{-S}(\text{CH}_2)_7\text{S}\}]_2$ (**19**). Yield: 25% (0.10 mmol). Mp = 102–103 °C. Anal. Calcd for $\text{C}_{26}\text{H}_{28}\text{Fe}_4\text{O}_{12}\text{S}_4$: C, 35.32; H, 3.19; S, 14.50. Found: C, 35.62; H, 3.38; S, 14.67. ^1H NMR (400 MHz, CDCl_3 , ppm): δ 2.47 (bs, 4H, $e\text{-SCH}_2$), 2.08 (bs, 4H, $a\text{-SCH}_2$), 1.75–1.59 (m, 8H, SCH_2CH_2), 1.46–1.26 (m, 12H, $\text{SCH}_2\text{CH}_2(\text{CH}_2)_2$). $^{13}\text{C}\{^1\text{H}\}$ NMR (100 MHz, CDCl_3 , ppm): δ 208.97 (s, CO), 39.04 (s, $e\text{-SCH}_2$), 32.68, 31.41, 28.76, 26.42, 23.84 (s, $a\text{-SCH}_2$). IR (ν_{CO} , cm^{-1}): 2068(m), 2033(vs), 1990(s). DEI-MS (m/z): 884 $[\text{M}]^+$.

$[\text{Fe}_2(\text{CO})_6\{\mu\text{-S}(\text{CH}_2)_8\text{S}\}]_2$ (**20**). Yield: 30% (0.12 mmol). Mp = 165–166 °C. Anal. Calcd for $\text{C}_{28}\text{H}_{32}\text{Fe}_4\text{O}_{12}\text{S}_4$: C, 36.87; H, 3.54; S, 14.06. Found: C, 37.20; H, 3.65; S, 14.31. ^1H NMR (400 MHz, CDCl_3 , ppm): δ 2.44 (bs, 4H, $e\text{-SCH}_2$), 2.11 (bs, 4H, $a\text{-SCH}_2$), 1.67 (bs, 8H, SCH_2CH_2), 1.52 (bs, 8H, $\text{SCH}_2\text{CH}_2\text{CH}_2$), 1.44 (bs, 4H, $\text{S}(\text{CH}_2)_3\text{CH}_2$), 1.31 (bs, 4H, $\text{S}(\text{CH}_2)_4\text{CH}_2$). $^{13}\text{C}\{^1\text{H}\}$ NMR (100 MHz, CDCl_3 , ppm): δ 209.04 (s, CO), 39.37 (s, $e\text{-SCH}_2$), 32.96, 31.93, 29.12, 28.95, 28.42, 28.01, 24.64 (s, $a\text{-SCH}_2$). IR (ν_{CO} , cm^{-1}): 2068(m), 2032(vs), 1991(s). DEI-MS (m/z): 912 $[\text{M}]^+$, 884 $[\text{M} - \text{CO}]^+$, 856 $[\text{M} - 2\text{CO}]^+$, 828 $[\text{M} - 3\text{CO}]^+$, 800 $[\text{M} - 4\text{CO}]^+$, 772 $[\text{M} - 5\text{CO}]^+$, 744 $[\text{M} - 6\text{CO}]^+$, 716 $[\text{M} - 7\text{CO}]^+$, 688 $[\text{M} - 8\text{CO}]^+$, 660 $[\text{M} - 9\text{CO}]^+$, 632 $[\text{M} - 10\text{CO}]^+$, 604 $[\text{M} - 11\text{CO}]^+$, 576 $[\text{M} - 12\text{CO}]^+$.

General Procedure for the Synthesis of Complexes 21–23 via Reaction of Compounds 8b–10b with $\text{Fe}_3(\text{CO})_{12}$ in a 1:1 Molar Ratio. A solution of $\text{Fe}_3(\text{CO})_{12}$ (100 mg, 0.20 mmol) and cyclic tetrasulfide (**8b–10b**, 0.20 mmol) in THF (40 mL) was heated at reflux for 2 h under N_2 . The green solution turned deep red, and the solvent was removed under reduced pressure. The residue was purified by column chromatography using 100% hexane. A yellow-orange fraction representing the complex (21–23, respectively) was collected, and the solvent was removed in vacuo. The product was obtained as a red-orange solid.

$[\text{Fe}_2(\text{CO})_6\{\mu\text{-S}(\text{CH}_2)_6\text{S}\}]$ (**21**). Yield: 15% (0.030 mmol). Mp = 170–171 °C. Anal. Calcd for $\text{C}_{18}\text{H}_{24}\text{Fe}_2\text{O}_6\text{S}_4$: C, 37.51; H, 4.20; S, 22.25. Found: C, 37.26; H, 4.03; S, 21.96. ^1H NMR (400 MHz, CDCl_3 , ppm): δ 2.71 (bs, 4H, SSCH_2), 2.51 (bs, 2H, $e\text{-SCH}_2$), 2.14 (bs, 2H, $a\text{-SCH}_2$), 1.72 (bs, 4H, SSCH_2CH_2), 1.43 (bs, 4H, SCH_2CH_2), 1.27 (bs, 8H, $\text{S}(\text{CH}_2)_2(\text{CH}_2)_2$). IR (ν_{CO} , cm^{-1}): 2069(m), 2031(vs), 1992(s). DEI-MS (m/z): 576 $[\text{M}]^+$.

$[\text{Fe}_2(\text{CO})_6\{\mu\text{-S}(\text{CH}_2)_7\text{S}\}]$ (**22**). Yield: 10% (0.020 mmol). Mp = 73–75 °C. Anal. Calcd for $\text{C}_{20}\text{H}_{28}\text{Fe}_2\text{O}_6\text{S}_4$: C, 39.75; H, 4.67; S, 21.22. Found: C, 39.95; H, 4.48; S, 21.46. ^1H NMR (400 MHz, CDCl_3 , ppm): δ 2.75 (bs, 4H, SSCH_2), 2.50 (bs, 2H, $e\text{-SCH}_2$), 2.11 (bs, 2H, $a\text{-SCH}_2$), 1.73 (bs, 4H, SSCH_2CH_2), 1.46 (bs, 4H, SCH_2CH_2), 1.33–1.29 (m, 12H, $\text{S}(\text{CH}_2)_2(\text{CH}_2)_2$). IR (ν_{CO} , cm^{-1}): 2069(m), 2032(vs), 1991(s). DEI-MS (m/z): 604 $[\text{M}]^+$.

$[\text{Fe}_2(\text{CO})_6\{\mu\text{-S}(\text{CH}_2)_8\text{S}\}]$ (**23**). Yield: 12% (0.024 mmol). Mp = 122–123 °C. Anal. Calcd for $\text{C}_{22}\text{H}_{32}\text{Fe}_2\text{O}_6\text{S}_4$: C, 41.78; H, 5.10; S, 20.28. Found: C, 41.48; H, 5.32; S, 19.99. ^1H NMR (400 MHz, CDCl_3 , ppm): δ 2.72 (bs, 4H, SSCH_2), 2.52 (bs, 2H, $e\text{-SCH}_2$), 2.15 (bs, 2H, $a\text{-SCH}_2$), 1.70 (bs, 4H, SSCH_2CH_2), 1.45 (bs, 4H, SCH_2CH_2), 1.40 (bs, 8H, $\text{SCH}_2\text{CH}_2\text{CH}_2$), 1.39 (bs, 4H, $\text{S}(\text{CH}_2)_3\text{CH}_2$), 1.30 (bs, 4H, $\text{S}(\text{CH}_2)_4\text{CH}_2$). IR (ν_{CO} , cm^{-1}): 2069(m), 2030(vs), 1991(s). DEI-MS (m/z): 632 $[\text{M}]^+$.

■ ASSOCIATED CONTENT

Supporting Information

The Supporting Information is available free of charge on the ACS Publications website at DOI: 10.1021/acs.inorgchem.7b01398.

General experimental details, cyclic voltammetry of complex **11** in CH₂Cl₂, Figures S1–S6, and Tables S1–S4 (PDF)

Accession Codes

CCDC 1546654–1546666 contain the supplementary crystallographic data for this paper. These data can be obtained free of charge via www.ccdc.cam.ac.uk/data_request/cif, or by emailing data_request@ccdc.cam.ac.uk, or by contacting The Cambridge Crystallographic Data Centre, 12 Union Road, Cambridge CB2 1EZ, U.K.; fax: +44 1223 336033.

AUTHOR INFORMATION

Corresponding Author

*E-mail: wolfgang.weigand@uni-jena.de.

ORCID

Hassan Abul-Futouh: 0000-0003-2419-9782

Wolfgang Weigand: 0000-0001-5177-1006

Notes

The authors declare no competing financial interest.

ACKNOWLEDGMENTS

H.A.-F. thanks the Deutscher Akademischer Austausch Dienst (DAAD) for a scholarship. We are grateful to Dr. Manfred Rudolph for valuable discussions.

DEDICATION

Dedicated to Prof. Marian Mikolajczyk on the occasion of his 80th birthday.

REFERENCES

- (1) Wuebbles, D. J.; Jain, A. K. Concerns About Climate Change and the Role of Fossil Fuel Use. *Fuel Process. Technol.* **2001**, *71*, 99–119.
- (2) (a) Koroneos, C.; Dompros, A.; Roumbas, G.; Moussiopoulos, N. Life Cycle Assessment of Hydrogen Fuel Production Processes. *Int. J. Hydrogen Energy* **2004**, *29*, 1443–1450. (b) Hignett, T. P. *Fertilizers Manual*; Springer: Dordrecht, The Netherlands, 1985. (c) Rauche, H. *Die Kaliindustrie im 21 Jahrhundert*; Springer: Berlin, 2015.
- (3) Borup, R.; Meyers, J.; Pivovar, B.; Kim, Y. S.; Mukundan, R.; Garland, N.; Myers, D.; Wilson, M.; Garzon, F.; Wood, D.; Zelenay, P.; More, K.; Stroh, K.; Zawodzinski, T.; Boncella, J.; McGrath, J. E.; Inaba, M.; Miyatake, K.; Hori, M.; Ota, K.; Ogumi, Z.; Miyata, S.; Nishikata, A.; Siroma, Z.; Uchimoto, Y.; Yasuda, K.; Kimijima, K. I.; Iwashita, N. Scientific Aspects of Polymer Electrolyte Fuel Cell Durability and Degradation. *Chem. Rev.* **2007**, *107*, 3904–3951.
- (4) (a) Adams, M. W. The Structure and Mechanism of Iron-Hydrogenases. *Biochim. Biophys. Acta, Bioenerg.* **1990**, *1020*, 115–145. (b) Frey, M. Hydrogenases: Hydrogen-Activating Enzyme. *Chem-BioChem* **2002**, *3*, 153–160. (c) Evans, D. J.; Pickett, C. J. Chemistry and the Hydrogenases. *Chem. Soc. Rev.* **2003**, *32*, 268–275. (d) Volbeda, A.; Fontecilla-Camps, J. C. Structure-Function Relationships of Nickel-Iron Sites in Hydrogenase and a Comparison with the Active Sites of Other Nickel-Iron Enzymes. *Coord. Chem. Rev.* **2005**, *249*, 1609–1619.
- (5) Fontecilla-Camps, J. C.; Volbeda, A.; Cavazza, C.; Nicolet, Y. Structure/Function Relationships of [NiFe]- and [FeFe]-Hydrogenases. *Chem. Rev.* **2007**, *107*, 4273–4303.
- (6) Lubitz, W.; Ogata, H.; Rüdiger, O.; Reijerse, E. Hydrogenases. *Chem. Rev.* **2014**, *114*, 4081–4148.
- (7) (a) Adamska-Venkatesh, A.; Roy, S.; Siebel, J. F.; Simmons, T. R.; Fontecave, M.; Artero, V.; Reijerse, E.; Lubitz, W. Spectroscopic Characterization of the Bridging Amine in the Active Site of [FeFe] Hydrogenase Using Isotopologues of the H-Cluster. *J. Am. Chem. Soc.* **2015**, *137*, 12744–12747. (b) Adamska, A.; Silakov, A.; Lambert, C.; Rüdiger, O.; Happe, T.; Reijerse, E.; Lubitz, W. Identification

and Characterization of the “Super-Reduced” State of the H-Cluster in [FeFe] Hydrogenase: A New Building Block for the Catalytic Cycle? *Angew. Chem., Int. Ed.* **2012**, *51*, 11458–11462. (c) Fan, H.-J.; Hall, M. B. A Capable Bridging Ligand for Fe-Only Hydrogenase: Density Functional Calculations of a Low-Energy Route for Heterolytic Cleavage and Formation of Dihydrogen. *J. Am. Chem. Soc.* **2001**, *123*, 3828–3829. (d) Peters, J. W.; Lanzilotta, W. N.; Lemon, B. J.; Seefeldt, L. C. X-ray Crystal Structure of the Fe-Only Hydrogenase (CpI) from *Clostridium pasteurianum* to 1.8 Å Resolution. *Science* **1998**, *282*, 1853–1858. (e) Nicolet, Y.; de Lacey, A. L.; Vernede, X.; Fernandez, V. M.; Hatchikian, E. C.; Fontecilla-Camps, J. C. Crystallographic and FTIR Spectroscopic Evidence of Changes in Fe Coordination Upon Reduction of the Active Site of the Fe-Only Hydrogenase from *Desulfovibrio desulfuricans*. *J. Am. Chem. Soc.* **2001**, *123*, 1596–1601. (f) Reijerse, E. J.; Pham, C. C.; Pelmenschikov, V.; Gilbert-Wilson, R.; Adamska-Venkatesh, A.; Siebel, J. F.; Gee, L. B.; Yoda, Y.; Tamasaku, K.; Lubitz, W.; Rauchfuss, T. B.; Cramer, S. P. Direct Observation of an Iron-Bound Terminal Hydride in [FeFe]-Hydrogenase by Nuclear Resonance Vibrational Spectroscopy. *J. Am. Chem. Soc.* **2017**, *139*, 4306–4309.

(8) Li, Y.; Rauchfuss, T. B. Synthesis of Diiron(I) Dithiolate Carbonyl Complexes. *Chem. Rev.* **2016**, *116*, 7043–7077 and references cited therein.

(9) (a) Wright, R. J.; Lim, C.; Tilley, T. D. Diiron Proton Reduction Catalysts Possessing Electron-Rich and Electron-Poor Naphthalene-1,8-dithiolate Ligands. *Chem. - Eur. J.* **2009**, *15*, 8518–8525. (b) Qian, G.; Zhong, W.; Wei, Z.; Wang, H.; Xiao, Z.; Long, L.; Liu, X. Diiron Hexacarbonyl Complexes Bearing Naphthalene-1,8-Dithiolate Bridge Moiety as Mimics of the Sub-Unit of [FeFe]-Hydrogenase: Synthesis, Characterisation and Electrochemical Investigations. *New J. Chem.* **2015**, *39*, 9752–9760. (c) Figliola, C.; Male, L.; Horton, P. N.; Pitak, M. B.; Coles, S. J.; Horswell, S. L.; Grainger, R. S. [FeFe]-Hydrogenase Synthetic Mimics Based on Peri-Substituted Dichalcogenides. *Organometallics* **2014**, *33*, 4449–4460. (d) Figliola, C.; Male, L.; Horswell, S. L.; Grainger, R. S. N-Derivatives of Peri-Substituted Dichalcogenide [FeFe]-Hydrogenase Mimics: Towards Photocatalytic Dyads for Hydrogen Production. *Eur. J. Inorg. Chem.* **2015**, *2015*, 3146–3156. (e) Topf, C.; Monkowius, U.; Knör, G. Design, Synthesis and Characterization of a Modular Bridging Ligand Platform for Bio-Inspired Hydrogen Production. *Inorg. Chem. Commun.* **2012**, *21*, 147–150. (f) Mebi, C. A.; Noll, B. C.; Gao, R.; Karr, D. Binuclear Iron(I) Complex Containing Bridging Phenanthrene-4,5-dithiolate Ligand: Preparation, Spectroscopy, Crystal Structure, and Electrochemistry. *Z. Anorg. Allg. Chem.* **2010**, *636*, 2550–2554. (g) Abul-Futouh, H.; Zagranjarski, Y.; Müller, C.; Schulz, M.; Kupfer, S.; Görls, H.; El-khateeb, M.; Gräfe, S.; Dietzek, B.; Peneva, K.; Weigand, W. [FeFe]-Hydrogenase H-cluster Mimics Mediated by Naphthalene Monoimide Derivatives of Peri-Substituted Dichalcogenides. *Dalton Trans.* **2017**, DOI: 10.1039/C7DT02079A.

(10) (a) Samuel, A. P. S.; Co, D. T.; Stern, C. L.; Wasielewski, M. R. Ultrafast Photodriven Intramolecular Electron Transfer from a Zinc Porphyrin to a Readily Reduced Diiron Hydrogenase Model Complex. *J. Am. Chem. Soc.* **2010**, *132*, 8813–8815. (b) Li, P.; Amirjalayer, S.; Hartl, F.; Lutz, M.; Bruin, B.; Becker, R.; Woutersen, S.; Reek, J. N. H. Direct Probing of Photoinduced Electron Transfer in a Self-Assembled Biomimetic [2Fe2S]-Hydrogenase Complex Using Ultrafast Vibrational Spectroscopy. *Inorg. Chem.* **2014**, *53*, 5373–5383.

(11) (a) Gloaguen, F.; Morvan, D.; Capon, J.-F.; Schollhammer, P.; Talarmin, J. Electrochemical Proton Reduction at Mild Potentials by Monosubstituted Diiron Organometallic Complexes Bearing a Benzenedithiolate Bridge. *J. Electroanal. Chem.* **2007**, *603*, 15–20. (b) Felton, G. A. N.; Vannucci, A. K.; Chen, J.; Lockett, L. T.; Okumura, N.; Petro, B. J.; Zakai, U. I.; Evans, D. H.; Glass, R. S.; Lichtenberger, D. L. Hydrogen Generation from Weak Acids: Electrochemical and Computational Studies of a Diiron Hydrogenase Mimic. *J. Am. Chem. Soc.* **2007**, *129*, 12521–12530. (c) Schwartz, L.; Singh, P. S.; Eriksson, L.; Lomoth, R.; Ott, S. Tuning the Electronic Properties of Fe₂(μ-Arenedithiolate)(CO)_{6-n}(PMe₃)_n (n = 0, 2) Complexes Related to the [Fe–Fe]-Hydrogenase Active Site. *C. R.*

Chim. **2008**, *11*, 875–889. (d) Capon, J.-F.; Gloaguen, F.; Schollhammer, P.; Talarmin, J. Electrochemical Proton Reduction by Thiolate-Bridged Hexacarbonyl Diiron Clusters. *J. Electroanal. Chem.* **2004**, *566*, 241–247. (e) Chen, J.; Vannucci, A. K.; Mebi, C. A.; Okumura, N.; Borowski, S. C.; Swenson, M.; Lockett, L. T.; Evans, D. H.; Glass, R. S.; Lichtenberger, D. L. Synthesis of Diiron Hydrogenase Mimics Bearing Hydroquinone and Related Ligands. Electrochemical and Computational Studies of the Mechanism of Hydrogen Production and the Role of O–H...S Hydrogen Bonding. *Organometallics* **2010**, *29*, 5330–5340. (f) Donovan, E. S.; McCormick, J. J.; Nichol, G. S.; Felton, G. A. N. Cyclic Voltammetric Studies of Chlorine-Substituted Diiron Benzenedithiolato Hexacarbonyl Electrocatalysts Inspired by the [FeFe]-Hydrogenase Active Site. *Organometallics* **2012**, *31*, 8067–8070. (g) Felton, G. A. N.; Mebi, C. A.; Petro, B. J.; Vannucci, A. K.; Evans, D. H.; Glass, R. S.; Lichtenberger, D. L. Review of Electrochemical Studies of Complexes Containing the [Fe₂S₂] Core Characteristic of [FeFe]-Hydrogenases Including Catalysis by These Complexes of the Reduction of Acids to Form Dihydrogen. *J. Organomet. Chem.* **2009**, *694*, 2681–2699.

(12) (a) Lawrence, J. D.; Li, H. X.; Rauchfuss, T. B.; Benard, M.; Rohmer, M. M. Diiron Azadithiolates as Models for the Iron-Only Hydrogenase Active Site: Synthesis, Structure, and Stereoelectronics. *Angew. Chem., Int. Ed.* **2001**, *40*, 1768–1771. (b) Capon, J.-F.; Ezzaher, S.; Gloaguen, F.; Pétilion, F. Y.; Schollhammer, P.; Talarmin, J.; Davin, T. J.; McGrady, J. E.; Muir, K. W. Electrochemical and Theoretical Investigations of the Reduction of [Fe₂(CO)₃L{μ-SCH₂XCH₂S}] Complexes Related to [FeFe] Hydrogenase. *New J. Chem.* **2007**, *31*, 2052–2064. (c) Wang, F.; Wang, M.; Liu, X.; Jin, K.; Dong, W.; Sun, L. Protonation, Electrochemical Properties and Molecular Structures of Halogen-Functionalized Diiron Azadithiolate Complexes Related to the Active Site of Iron-Only Hydrogenases. *Dalton Trans.* **2007**, 3812–3819. (d) Cui, H.-G.; Wang, M.; Dong, W.-B.; Duan, L.-L.; Li, P.; Sun, L.-C. Synthesis, Structures and Electrochemical Properties of Hydroxyl- and Pyridyl-Functionalized Diiron Azadithiolate Complexes. *Polyhedron* **2007**, *26*, 904–910. (e) Jiang, S.; Liu, J.; Sun, A. Furan-Containing Diiron Azadithiolate Hexacarbonyl Complex with Unusual Lower Catalytic Proton Reduction Potential. *Inorg. Chem. Commun.* **2006**, *9*, 290–292. (f) Wang, Z.; Liu, J.-H.; He, C.-J.; Jiang, S.; Åkermark, B.; Sun, L.-C. Azadithiolates Cofactor of the Iron-Only Hydrogenase and its PR₃-Monosubstituted Derivatives: Synthesis, Structure, Electrochemistry and Protonation. *J. Organomet. Chem.* **2007**, *692*, 5501–5507. (g) Wang, W.-G.; Wang, H.-Y.; Si, G.; Tung, C.-H.; Wu, L.-Z. Fluorophenyl-Substituted Fe-Only Hydrogenases Active Site ADT Models: Different Electrocatalytic Process for Proton Reduction in HOAc and HBF₄/Et₂O. *Dalton Trans.* **2009**, 2712–2720. (h) Na, Y.; Wang, M.; Pan, J.; Zhang, P.; Åkermark, B.; Sun, L. Visible Light-Driven Electron Transfer and Hydrogen Generation Catalyzed by Bioinspired [2Fe₂S] Complexes. *Inorg. Chem.* **2008**, *47*, 2805–2810. (i) Wang, Z.; Liu, J.; He, C.; Jiang, S.; Åkermark, B.; Sun, L. Diiron Azadithiolates with Hydrophilic Phosphatridiazadamantane Ligand as Iron-Only Hydrogenase Active Site Models: Synthesis, Structure, and Electrochemical Study. *Inorg. Chim. Acta* **2007**, *360*, 2411–2419. (j) Si, Y.; Ma, C.; Hu, M.; Chen, H.; Chen, C.; Liu, Q. (N-C_nH_{2n-1})-1,3-Azapropandithiolate (n = 5, 6, 7)-Bridged Diiron Complexes as Mimics for the Active Site of [FeFe]-Hydrogenases: The Influence of the Bridge on the Diiron Complex. *New J. Chem.* **2007**, *31*, 1448–1454. (k) Schwartz, L.; Eilers, G.; Eriksson, L.; Gogoll, A.; Lomoth, R.; Ott, S. Iron Hydrogenase Active Site Mimic Holding a Proton and a Hydride. *Chem. Commun.* **2006**, 520–526. (l) Eilers, G.; Schwartz, L.; Stein, M.; Zampella, G.; De Gioia, L.; Ott, S.; Lomoth, R. Ligand versus Metal Protonation of an Iron Hydrogenase Active Site Mimic. *Chem. - Eur. J.* **2007**, *13*, 7075–7084. (m) Hou, J.; Peng, X.; Liu, J.; Gao, Y.; Zhao, X.; Gao, S.; Han, K. A Binuclear Isocyanide Azadithiolatoiron Complex Relevant to the Active Site of Fe-Only Hydrogenases: Synthesis, Structure and Electrochemical Properties. *Eur. J. Inorg. Chem.* **2006**, *2006*, 4679–4686. (n) Ezzaher, S.; Orain, P.-Y.; Capon, J.-F.; Gloaguen, F.; Pétilion, F. Y.; Roisnel, T.; Schollhammer, P.; Talarmin, J. First Insights Into the Protonation of Dissymmetrically Disubstituted Di-Iron

Azadithiolate Models of the [FeFe]H₂ases Active Site. *Chem. Commun.* **2008**, 2547–2549. (o) Carroll, M. E.; Barton, B. E.; Rauchfuss, T. B.; Carroll, J. P. Synthetic Models for the Active Site of the [FeFe]-Hydrogenase: Catalytic Proton Reduction and the Structure of the Doubly Protonated Intermediate. *J. Am. Chem. Soc.* **2012**, *134*, 18843–18852.

(13) (a) Zaffaroni, R.; Rauchfuss, T. B.; Gray, D. L.; De Gioia, L.; Zampella, G. Terminal vs Bridging Hydrides of Diiron Dithiolates: Protonation of Fe₂(dithiolate)(CO)₂(PMe₃)₄. *J. Am. Chem. Soc.* **2012**, *134*, 19260–19269. (b) Winter, A.; Zsolnai, L.; Huttner, G. Deprotonierung und Substitutionsreaktionen Dreikerniger Eisencluster Fe₃(CO)₉(H)(SR). *Chem. Ber.* **1982**, *115*, 1286–1304. (c) Winter, A.; Zsolnai, L.; Huttner, G. Dinuclear and Trinuclear Carbonyliron Complexes Containing 1,2- and 1,3-Dithiolato Bridging Ligands. *Z. Naturforsch., B: J. Chem. Sci.* **1982**, *37*, 1430–1436. (d) Singleton, M. L.; Jenkins, R. M.; Klemashevich, C. L.; Darensbourg, M. Y. The Effect of Bridgehead Steric Bulk on the Ground State and Intramolecular Exchange Processes of (μ-SCH₂CR₂CH₂S)[Fe(CO)₃][Fe(CO)₂L] Complexes. *C. R. Chim.* **2008**, *11*, 861–874. (e) Barton, B. E.; Olsen, M. T.; Rauchfuss, T. B. Aza- and Oxadithiolates Are Probable Proton Relays in Functional Models for the [FeFe]-Hydrogenases. *J. Am. Chem. Soc.* **2008**, *130*, 16834–16835. (f) Barton, B. E.; Rauchfuss, T. B. Terminal Hydride in [FeFe]-Hydrogenase Model Has Lower Potential for H₂ Production Than the Isomeric Bridging Hydride. *Inorg. Chem.* **2008**, *47*, 2261–2263. (g) Trautwein, R.; Almazahreh, L. R.; Görls, H.; Weigand, W. The Influence of OH Groups in [Fe(CO)₃]₂(μ-ECH₂)₂C(CH₂OH)₂ (E = S, Se) Complexes Toward the Cathodic Process. *Z. Anorg. Allg. Chem.* **2013**, *639*, 1512–1519.

(14) (a) Goy, R.; Bertini, L.; Görls, H.; De Gioia, L.; Talarmin, J.; Zampella, G.; Schollhammer, P.; Weigand, W. Silicon-Heteroaromatic [FeFe] Hydrogenase Model Complexes: Insight into Protonation, Electrochemical Properties, and Molecular Structures. *Chem. - Eur. J.* **2015**, *21*, 5061–5073. (b) Apfel, U.-P.; Troegel, D.; Halpin, Y.; Tschierlei, S.; Uhlemann, U.; Görls, H.; Schmitt, M.; Popp, J.; Dunne, P.; Venkatesan, M.; Coey, M.; Rudolph, M.; Vos, G. J.; Tacke, R.; Weigand, W. Models for the Active Site in [FeFe] Hydrogenase with Iron-Bound Ligands Derived from Bis-, Tris-, and Tetrakis(mercaptomethyl)silanes. *Inorg. Chem.* **2010**, *49*, 10117–10132.

(15) (a) Abul-Futouh, H.; Almazahreh, L. R.; Sakamoto, T.; Stessman, N. Y. T.; Lichtenberger, D. L.; Glass, R. S.; Görls, H.; El-khateeb, M.; Schollhammer, P.; Mloston, G.; Weigand, W. [FeFe]-Hydrogenase H-Cluster Mimics with Unique Planar μ-(SCH₂)₂ER₂ Linkers (E = Ge and Sn). *Chem. - Eur. J.* **2017**, *23*, 346–359. (b) Glass, R. S.; Gruhn, N. E.; Lorange, E.; Singh, M. S.; Stessman, N. Y. T.; Zakai, U. I. Synthesis, Gas-Phase Photoelectron Spectroscopic, and Theoretical Studies of Stannylated Dinuclear Iron Dithiolates. *Inorg. Chem.* **2005**, *44*, 5728–5737.

(16) Almazahreh, L. R.; Apfel, U.-P.; Imhof, W.; Rudolph, M.; Görls, H.; Talarmin, J.; Schollhammer, P.; El-khateeb, M.; Weigand, W. A Novel [FeFe] Hydrogenase Model with a (SCH₂)₂P=O Moiety. *Organometallics* **2013**, *32*, 4523–4530.

(17) (a) Harb, M. K.; Windhager, J.; Niksch, T.; Görls, H.; Sakamoto, T.; Smith, E. R.; Glass, R. S.; Lichtenberger, D. L.; Evans, D. H.; El-khateeb, M.; Weigand, W. Comparison of S and Se Dichalcogenolato [FeFe]-Hydrogenase Models with Central S and Se Atoms in the Bridgehead Chain. *Tetrahedron* **2012**, *68*, 10592–10599. (b) Gao, S.; Fan, J.; Sun, S.; Peng, X.; Zhao, X.; Hou, J. Selenium-Bridged Diiron Hexacarbonyl Complexes as Biomimetic Models for the Active site of Fe–Fe Hydrogenases. *Dalton Trans.* **2008**, 2128–2135. (c) Harb, M. K.; Apfel, U.-P.; Kübel, J.; Görls, H.; Felton, G. A. N.; Sakamoto, T.; Evans, D. H.; Glass, R. S.; Lichtenberger, D. L.; El-khateeb, M.; Weigand, W. Preparation and Characterization of Homologous Diiron Dithiolato, Diselenato, and Ditetellurato Complexes: [FeFe]-Hydrogenase Models. *Organometallics* **2009**, *28*, 6666–6675. (d) Abul-Futouh, H.; El-khateeb, M.; Görls, H.; Asali, K. J.; Weigand, W. Selenium Makes the Difference: Protonation of [FeFe]-Hydrogenase Mimics with Diselenolato Ligands. *Dalton Trans.* **2017**, *46*, 2937–2947. (e) Trautwein, R.; Almazahreh, L. R.; Görls, H.;

Weigand, W. Steric Effect of the Dithiolato Linker on the Reduction Mechanism of $[\text{Fe}_2(\text{CO})_6\{\mu-(\text{XCH}_2)_2\text{CRR}'\}]$ Hydrogenase Models (X = S, Se). *Dalton Trans.* **2015**, *44*, 18780–18794. (f) Gao, W.; Song, L.-C.; Yin, B.-S.; Zan, H.-N.; Wang, D.-F.; Song, H.-B. Synthesis and Characterization of Single, Double, and Triple Butterfly $[2\text{Fe}_2\text{E}]$ (E = Se, S) Cluster Complexes Related to the Active Site of $[\text{FeFe}]$ -Hydrogenases. *Organometallics* **2011**, *30*, 4097–4107. (g) Song, L.-C.; Gao, W.; Feng, C.-P.; Wang, D.-F.; Hu, Q.-M. Investigations on Synthesis, Structure, and Properties of New Butterfly $[2\text{Fe}_2\text{Se}]$ Cluster Complexes Relevant to Active Sites of Some Hydrogenases. *Organometallics* **2009**, *28*, 6121–6130. (h) Song, L.-C.; Mei, S.-Z.; Feng, C.-P.; Gong, F.-H.; Ge, J.-H.; Hu, Q.-M. Reactions of Monoanions $[(\mu\text{-RE})(\mu\text{-E})\text{Fe}_2(\text{CO})_6]^-$ and Dianions $[(\mu\text{-E})_2\text{Fe}_2(\text{CO})_6]^{2-}$ (E = Se, S) with N-Substituted Benzimidazolyl Chlorides, Leading to Novel Butterfly Fe/E Cluster Complexes. *Organometallics* **2010**, *29*, 5050–5060.

(18) (a) Apfel, U.-P.; Halpin, Y.; Görls, H.; Vos, G. J.; Weigand, W. Influence of the Introduction of Cyanido and Phosphane Ligands in Multifunctionalized (Mercaptomethyl)silane $[\text{FeFe}]$ Hydrogenase Model Systems. *Eur. J. Inorg. Chem.* **2011**, *2011*, 581–588. (b) Razavet, M.; Davies, S. C.; Hughes, D. L.; Barclay, J. E.; Evans, D. J.; Fairhurst, S. A.; Liu, X.; Pickett, C. J. All-Iron Hydrogenase: Synthesis, Structure and Properties of $\{2\text{Fe}_3\text{S}\}$ -Assemblies Related to the Di-Iron Sub-Site of the H-Cluster. *Dalton Trans.* **2003**, 586–595. (c) Gloaguen, F.; Lawrence, J. D.; Schmidt, M.; Wilson, S. R.; Rauchfuss, T. B. Synthetic and Structural Studies on $[\text{Fe}_2(\text{SR})_2(\text{CN})_x(\text{CO})_{6-x}]^x$ as Active Site Models for Fe-Only Hydrogenases. *J. Am. Chem. Soc.* **2001**, *123*, 12518–12527. (d) Le Cloirec, A.; Best, S. P.; Borg, S.; Davies, S. C.; Evans, D. J.; Hughes, D. L.; Pickett, C. J. A Di-iron Dithiolate Possessing Structural Elements of the Carbonyl/Cyanide Sub-Site of the H-Centre of Fe-Only Hydrogenase. *Chem. Commun.* **1999**, 2285–2286.

(19) (a) Song, L.-C.; Yang, Z.-Y.; Bian, H.-Z.; Liu, Y.; Wang, H.-T.; Liu, X.-F.; Hu, Q.-M. Diiron Oxadithiolate Type Models for the Active Site of Iron-Only Hydrogenases and Biomimetic Hydrogen Evolution Catalyzed by $\text{Fe}_2(\mu\text{-SCH}_2\text{OCH}_2\text{S}\mu)(\text{CO})_6$. *Organometallics* **2005**, *24*, 6126–6135. (b) Song, L.-C.; Li, Q.-L.; Feng, Z.-H.; Sun, X.-J.; Xie, Z.-J.; Song, H.-B. Synthesis, Characterization, and Electrochemical Properties of Diiron Propanedithiolate (PDTe) Complexes as Active Site Models of $[\text{FeFe}]$ -Hydrogenases. *Dalton Trans.* **2013**, *42*, 1612–1626. (c) Thomas, C. M.; Rudiger, O.; Liu, T.; Carson, C. E.; Hall, M. B.; Darensbourg, M. Y. Synthesis of Carboxylic Acid-Modified $[\text{FeFe}]$ -Hydrogenase Model Complexes Amenable to Surface Immobilization. *Organometallics* **2007**, *26*, 3976–3984. (d) Ezzaher, S.; Capon, J.-F.; Gloaguen, F.; Petillon, F. Y.; Schollhammer, P.; Talarmin, J.; Kervarec, N. Influence of a Pendant Amine in the Second Coordination Sphere on Proton Transfer at a Dissymmetrically Disubstituted Diiron System Related to the $[2\text{Fe}]_2\text{H}$ Subsite of $[\text{FeFe}]_2\text{H}_2$ ase. *Inorg. Chem.* **2009**, *48*, 2–4. (e) Li, P.; Wang, M.; He, C.; Liu, X.; Jin, K.; Sun, L. Phosphane and Phosphite Unsymmetrically Disubstituted Diiron Complexes Related to the Fe-Only Hydrogenase Active Site. *Eur. J. Inorg. Chem.* **2007**, *2007*, 3718–3727. (f) Morvan, D.; Capon, J.-F.; Gloaguen, F.; Schollhammer, P.; Talarmin, J. Electrochemical Synthesis of Mono- and Disubstituted Diiron Dithiolate Complexes as Models for the Active Site of Iron-Only Hydrogenases. *Eur. J. Inorg. Chem.* **2007**, *2007*, 5062–5068. (g) Gao, Ekstrom, W. J.; Liu, J.; Chen, C.; Eriksson, L.; Weng, L.; Åkermark, B.; Sun, L. Binuclear Iron–Sulfur Complexes with Bidentate Phosphine Ligands as Active Site Models of Fe-Hydrogenase and Their Catalytic Proton Reduction. *Inorg. Chem.* **2007**, *46*, 1981–1991. (h) Song, L.-C.; Li, C.-G.; Ge, J.-H.; Yang, Z.-Y.; Wang, H.-T.; Zhang, J.; Hu, Q.-M. Synthesis and Structural Characterization of the Mono- and Diphosphine-Containing Diiron Propanedithiolate Complexes Related to $[\text{FeFe}]$ -Hydrogenases. Biomimetic H_2 Evolution Catalyzed by $(\mu\text{-PDT})\text{Fe}_2(\text{CO})_4[(\text{Ph}_2\text{P})_2\text{N}(\text{n-Pr})]$. *J. Inorg. Biochem.* **2008**, *102*, 1973–1979. (i) Ezzaher, S.; Capon, J.-F.; Gloaguen, F.; Petillon, F. Y.; Schollhammer, P.; Talarmin, J. Electron-Transfer-Catalyzed Rearrangement of Unsymmetrically Substituted Diiron Dithiolate Complexes Related to the Active Site of the $[\text{FeFe}]$ -Hydrogenases. *Inorg.*

Chem. **2007**, *46*, 9863–9872. (j) Jablonskytė, A.; Wright, J. A.; Pickett, C. J. $[\text{FeFe}]$ -Hydrogenase Models: Unexpected Variation in Protonation Rate between Dithiolate Bridge Analogues. *Eur. J. Inorg. Chem.* **2011**, *2011*, 1033–1037. (k) Liu, Y.-C.; Lee, C.-H.; Lee, G.-H.; Chiang, M.-H. Influence of a Redox-Active Phosphane Ligand on the Oxidations of a Diiron Core Related to the Active Site of Fe-Only Hydrogenase. *Eur. J. Inorg. Chem.* **2011**, *2011*, 1155–1162. (l) Almazahreh, L. R.; Imhof, W.; Talarmin, J.; Schollhammer, P.; Görls, H.; El-khateeb, M.; Weigand, W. Ligand Effects on the Electrochemical Behavior of $[\text{Fe}_2(\text{CO})_5(\text{L})\{\mu-(\text{SCH}_2)_2(\text{Ph})\text{P}=\text{O}\}]$ (L = PPh_3 , $\text{P}(\text{OEt})_3$) Hydrogenase Model Complexes. *Dalton Trans.* **2015**, *44*, 7177–7189.

(20) (a) Tye, J. W.; Lee, J.; Wang, H.-W.; Mejia-Rodriguez, R.; Reibenspies, J. H.; Hall, M. B.; Darensbourg, M. Y. Dual Electron Uptake by Simultaneous Iron and Ligand Reduction in an N-Heterocyclic Carbene Substituted $[\text{FeFe}]$ Hydrogenase Model Compound. *Inorg. Chem.* **2005**, *44*, 5550–5552. (b) Thomas, C. M.; Liu, T.; Hall, M. B.; Darensbourg, M. Y. Series of Mixed Valent Fe(II)Fe(I) Complexes That Model the H_{ox} State of $[\text{FeFe}]$ -Hydrogenase: Redox Properties, Density-Functional Theory Investigation, and Reactivities with Extrinsic CO. *Inorg. Chem.* **2008**, *47*, 7009–7024. (c) Liu, T.; Darensbourg, M. Y. A Mixed-Valent, Fe(II)Fe(I), Diiron Complex Reproduces the Unique Rotated State of the $[\text{FeFe}]$ Hydrogenase Active Site. *J. Am. Chem. Soc.* **2007**, *129*, 7008–7009.

(21) (a) Hsieh, C.-H.; Erdem, Ö.-F.; Harman, S. D.; Singleton, M. L.; Reijerse, E.; Lubitz, W.; Popescu, C. V.; Reibenspies, J. H.; Brothers, S. M.; Hall, M. B.; Darensbourg, M. Y. Structural and Spectroscopic Features of Mixed Valent $\text{Fe}^{\text{II}}\text{Fe}^{\text{I}}$ Complexes and Factors Related to the Rotated Configuration of Diiron Hydrogenase. *J. Am. Chem. Soc.* **2012**, *134*, 13089–13102. (b) Justice, A. K.; Rauchfuss, T. B.; Wilson, S. R. Unsaturated, Mixed-Valence Diiron Dithiolate Model for the H_{ox} State of the $[\text{FeFe}]$ Hydrogenase. *Angew. Chem., Int. Ed.* **2007**, *46*, 6152–6154. (c) Olsen, M. T.; Bruschi, M.; De Gioia, L.; Rauchfuss, T. B.; Wilson, S. R. Nitrosyl Derivatives of Diiron(I) Dithiolates Mimic the Structure and Lewis Acidity of the $[\text{FeFe}]$ -Hydrogenase Active Site. *J. Am. Chem. Soc.* **2008**, *130*, 12021–12030.

(22) (a) Hu, M.-Q.; Ma, C.-B.; Si, Y.-T.; Chen, C.-N.; Liu, Q.-T. Diiron Models for the Active Site of Fe-Only Hydrogenase with Terminal Organosulfur Ligation: Synthesis, Structures and Electrochemistry. *J. Inorg. Biochem.* **2007**, *101*, 1370–1375. (b) Razavet, M.; Davies, S. C.; Hughes, D. L.; Pickett, C. J. $\{2\text{Fe}_3\text{S}\}$ Clusters Related to the Di-Iron Sub-Site of the H-Centre of All-Iron Hydrogenases. *Chem. Commun.* **2001**, 847–848. (c) Lawrence, J. D.; Li, H.; Rauchfuss, T. B. Beyond Fe-Only Hydrogenases: N-Functionalized 2-Aza-1,3-Dithiolates $\text{Fe}_2[(\text{SCH}_2)_2\text{NR}](\text{CO})_x$ (x = 5, 6). *Chem. Commun.* **2001**, 1482–1483. (d) Song, L.-C.; Yang, Z.-Y.; Bian, H.-Z.; Hu, Q.-M. Novel Single and Double Diiron Oxadithiolates as Models for the Active Site of $[\text{Fe}]$ -Only Hydrogenases. *Organometallics* **2004**, *23*, 3082–3084. (e) Daraosheh, A. Q.; Harb, M. K.; Windhager, J.; Görls, H.; El-khateeb, M.; Weigand, W. Substitution Reactions at $[\text{FeFe}]$ Hydrogenase Models Containing $[2\text{Fe}_3\text{S}]$ Assembly by Phosphine or Phosphite Ligands. *Organometallics* **2009**, *28*, 6275–6280.

(23) (a) Song, C.-L.; Fan, H.-T.; Hu, Q.-M. The First Example of Macrocycles Containing Butterfly Transition Metal Cluster Cores via Novel Tandem Reactions. *J. Am. Chem. Soc.* **2002**, *124*, 4566–4567. (b) Song, L.-C.; Gao, J.; Wang, H.-T.; Hua, Y.-J.; Fan, H.-T.; Zhang, X.-G.; Hu, Q.-M. Synthesis and Structural Characterization of Metallocrown Ethers Containing Butterfly Fe_2S_2 Cluster Cores. Biomimetic Hydrogen Evolution Catalyzed by $\text{Fe}_2(\mu\text{-SCH}_2\text{CH}_2\text{OCH}_2\text{CH}_2\text{S}\mu)(\text{CO})_6$. *Organometallics* **2006**, *25*, 5724–5729. (c) Liu, Y.-C.; Tu, L.-K.; Yen, T.-H.; Lee, G.-H.; Yang, S.-T.; Chiang, M.-H. Secondary Coordination Sphere Interactions within the Biomimetic Iron Azadithiolate Complexes Related to Fe-Only Hydrogenase: Dynamic Measure of Electron Density about the Fe Sites. *Inorg. Chem.* **2010**, *49*, 6409–6420. (d) Zhang, Y.; Si, Y.-T.; Hu, M.-Q.; Chen, C.-N.; Liu, Q.-T. Bis(μ^4 -Butane-1,4-dithiolato)bis-[hexacarbonyldiiron(II)(Fe–Fe)]. *Acta Crystallogr., Sect. C: Cryst. Struct. Commun.* **2007**, *63*, m499–m500. (e) Apfel, U.-P.; Halpin, Y.;

- Görls, H.; Vos, J.-G.; Schweizer, B.; Linti, G.; Weigand, W. Synthesis and Characterization of Hydroxy-Functionalized Models for the Active Site in Fe-Only-Hydrogenases. *Chem. Biodiversity* **2007**, *4*, 2138–2148.
- (f) Liu, Y.-C.; Tu, L.-K.; Yen, T.-H.; Lee, G.-H.; Chiang, M.-H. Influences on the Rotated Structure of Diiron Dithiolate Complexes: Electronic Asymmetry vs. Secondary Coordination Sphere Interaction. *Dalton Trans.* **2011**, *40*, 2528–2541.
- (g) Gao, W.; Liu, J.; Åkermærk, B.; Sun, L. Bidentate Phosphine Ligand Based Fe₂S₂-Containing Macromolecules: Synthesis, Characterization, and Catalytic Electrochemical Hydrogen Production. *Inorg. Chem.* **2006**, *45*, 9169–9171.
- (h) Song, L.-C.; Gong, F.-H.; Meng, T.; Ge, J.-H.; Cui, L.-N.; Hu, Q.-M. General Synthetic Route to Double-Butterfly Fe/S Cluster Complexes via Reactions of the Dianions $\{[(\mu\text{-CO})\text{Fe}_2(\text{CO})_6]_2(\mu\text{-SZS}\text{-}\mu)\}^{2-}$ with Electrophiles. *Organometallics* **2004**, *23*, 823–831.
- (i) Abul-Futouh, H.; Görls, H.; Weigand, W. A New Macrocyclic [FeFe]-Hydrogenase H Cluster model. *Phosphorus, Sulfur Silicon Relat. Elem.* **2017**, *192*, 634–637.
- (j) Chiang, M.-H.; Liu, Y.-C.; Yang, S.-T.; Lee, G.-H. Biomimetic Model Featuring the NH Proton and Bridging Hydride Related to a Proposed Intermediate in Enzymatic H₂ Production by Fe-Only Hydrogenase. *Inorg. Chem.* **2009**, *48*, 7604–7612.
- (24) (a) Munery, S.; Capon, J.-F.; De Gioia, L.; Elleouet, C.; Greco, C.; Pétilion, F. Y.; Schollhammer, P.; Talarmin, J.; Zampella, G. New Fe^I–Fe^I Complex Featuring a Rotated Conformation Related to the [2Fe]_H Subsite of [Fe–Fe] Hydrogenase. *Chem. - Eur. J.* **2013**, *19*, 15458–15461. (b) Wang, W.; Rauchfuss, T. B.; Moore, C. E.; Rheingold, A. L.; De Gioia, L.; Zampella, G. Crystallographic Characterization of a Fully Rotated, Basic Diiron Dithiolate: Model for the H_{red} State? *Chem. - Eur. J.* **2013**, *19*, 15476–15479. (c) Goy, R.; Bertini, L.; Elleouet, C.; Görls, H.; Zampella, G.; Talarmin, J.; De Gioia, L.; Schollhammer, P.; Apfel, U.-P.; Weigand, W. A Sterically Stabilized Fe^I–Fe^I Semi-Rotated Conformation of [FeFe] Hydrogenase Subsite Model. *Dalton Trans.* **2015**, *44*, 1690–1699.
- (25) (a) Zhao, J.; Wei, Z.; Zeng, X.; Liu, X. Three Diiron Complexes Bearing an Aromatic Ring as Mimics of the Diiron Subunit of [FeFe]-Hydrogenase: Synthesis, Electron Transfer and Coupled Chemical Reactions. *Dalton Trans.* **2012**, *41*, 11125–11133. (b) Best, S. P.; Borg, S. J.; White, J. M.; Razavet, M.; Pickett, C. J. On the Structure of a Proposed Mixed-Valent Analogue of the Diiron Subsite of [FeFe]-Hydrogenase. *Chem. Commun.* **2007**, 4348–4350. (c) Borg, S. J.; Behrsing, T.; Best, S. P.; Razavet, M.; Liu, X.; Pickett, C. J. Electron Transfer at a Dithiolate-Bridged Diiron Assembly: Electrocatalytic Hydrogen Evolution. *J. Am. Chem. Soc.* **2004**, *126*, 16988–16999. (d) Schwartz, L.; Ekstrom, J.; Lomoth, R.; Ott, S. Dynamic Ligation at the First Amine-Coordinated Iron Hydrogenase Active Site Mimic. *Chem. Commun.* **2006**, 4206–4208. (e) Streich, D.; Karnahl, M.; Astuti, Y.; Cady, C. W.; Hammarstrom, L.; Lomoth, R.; Ott, S. Comparing the Reactivity of Benzenedithiolate- versus Alkyldithiolate-Bridged Fe₂(CO)₆ Complexes with Competing Ligands. *Eur. J. Inorg. Chem.* **2011**, *2011*, 1106–1111. (f) Qian, G.; Wang, H.; Zhong, W.; Liu, X. Electrochemical Investigation into the Electron Transfer Mechanism of a Diiron Hexacarbonyl Complex Bearing a Bridging Naphthalene Moiety. *Electrochim. Acta* **2015**, *163*, 190–195. (g) Gloaguen, F.; Rauchfuss, T. B. Small Molecule Mimics of Hydrogenases: Hydrides and Redox. *Chem. Soc. Rev.* **2009**, *38*, 100–108.
- (26) (a) Ortega-Alfaro, M. C.; Hernández, N.; Cerna, I.; López-Cortés, J. G.; Gómez, E.; Toscano, R. A.; Alvarez-Toledano, C. Novel Dinuclear Iron(0) Complexes from α,β -Unsaturated Ketones β -Positioned with Sulfide and Sulfoxide Groups. *J. Organomet. Chem.* **2004**, *689*, 885–893. (b) Lyon, E. J.; Georgakaki, I. P.; Reibenspies, J. H.; Darensbourg, M. Y. Carbon Monoxide and Cyanide Ligands in a Classical Organometallic Complex Model for Fe-Only Hydrogenase. *Angew. Chem., Int. Ed.* **1999**, *38*, 3178–3180.
- (27) Goodrow, M. H.; Musker, W. K. Synthesis of Medium Ring Disulfides by Titrimetry; An Improvement on High Dilution Techniques. *Synthesis* **1981**, *1981*, 457–459.
- (28) (a) Noureldin, N. A.; Caldwell, M.; Hendry, J.; Lee, D. G. Heterogeneous Permanganate Oxidation of Thiols. *Synthesis* **1998**, 1587–1589. (b) Kato, E.; Oya, M.; Iso, T.; Iwao, J.-I. Conversion of Thiols into Disulfides with Diethyl Bromomalonate. *Chem. Pharm. Bull.* **1986**, *34*, 486–495. (c) Harpp, D. N.; Bodzay, S. J.; Aida, T.; Chan, T. H. High Yield Preparation of Cyclic Disulfides Using Alkyltin Thiolates. *Tetrahedron Lett.* **1986**, *27*, 441–444. (d) Affleck, J. G.; Dougherty, G. The Preparation and Relative Reactivities of Many-Membered Cyclic Disulfides. *J. Org. Chem.* **1950**, *15*, 865–868. (e) Ma, M.; Zhang, X.; Peng, L.; Wang, J. Electrophilic Reaction of Nitric Oxide with Wittig Reagents. *Tetrahedron Lett.* **2007**, *48*, 1095–1097.
- (29) (a) Groth, P. The Crystal Conformations of Cyclotetraeicosane and Cyclohexaeicosane at –160 °C. *Acta Chem. Scand.* **1979**, *33a*, 199–201. (b) Newman, B. A.; Kay, H. F. Chain Folding in Polyethylene and Cyclic Paraffins. *J. Appl. Phys.* **1967**, *38*, 4105–4109. (c) Holleman, A. F.; Wiberg, N. *Lehrbuch der Anorganischen Chemie*; Walter de Gruyter Verlag: Berlin, 1995.
- (30) Nametkin, N. S.; Tyurin, V. D.; Kukina, M. A. Synthesis and Some Properties of Sulfur-Containing Iron Tricarbonyl Complexes. *J. Organomet. Chem.* **1978**, *149*, 355–370.
- (31) Compound **13** was previously reported by Seyferth et al. using the synthetic pathway shown in Scheme 1A. See: Seyferth, D.; Henderson, R. S.; Song, L.-C. The Dithiobis(tricarbonyliron) Dianion: Improved Preparation and New Chemistry. *J. Organomet. Chem.* **1980**, *192*, C1–C5. Indeed, several attempts were carried out to obtain complex **13** by following their method, but unfortunately, without success.
- (32) (a) Felton, G. A. N.; Petro, B. J.; Glass, R. S.; Lichtenberger, D. L.; Evans, D. H. One- to Two-Electron Reduction of an [FeFe]-Hydrogenase Active Site Mimic: The Critical Role of Fluxionality of the [2Fe₂S] Core. *J. Am. Chem. Soc.* **2009**, *131*, 11290–11291. (b) Harb, M. K.; Daraosheh, A.; Görls, H.; Smith, E. R.; Meyer, G. J.; Swenson, M. T.; Sakamoto, T.; Glass, R. S.; Lichtenberger, D. L.; Evans, D. H.; El-khateeb, M.; Weigand, W. Effects of Alkane Linker Length and Chalcogen Character in [FeFe]-Hydrogenase Inspired Compounds. *Heteroat. Chem.* **2014**, *25*, 592–606.
- (33) (a) Lyon, E. J.; Georgakaki, I. P.; Reibenspies, J. H.; Darensbourg, M. Y. *J. Am. Chem. Soc.* **2001**, *123*, 3268–3278. (b) Robin, F.; Rumin, R.; Talarmin, J.; Pétilion, F. Y.; Muir, K. W. *Organometallics* **1993**, *12*, 365–380.
- (34) Crouthers, D. J.; Denny, J. A.; Bethel, R. D.; Munoz, D. G.; Darensbourg, M. Y. Conformational Mobility and Pendent Base Effects on Electrochemistry of Synthetic Analogues of the [FeFe]-Hydrogenase Active Site. *Organometallics* **2014**, *33*, 4747–4755.
- (35) COLLECT Data Collection Software; Nonius B.V.: Delft, The Netherlands, 1998.
- (36) Otwinowski, Z.; Minor, W. Processing of X-Ray Diffraction Data Collected in Oscillation Mode. *Methods Enzymol.* **1997**, *276*, 307–326.
- (37) SADABS, version 2.10; Bruker AXS: Madison, WI, 2002.
- (38) Sheldrick, G. M. A Short History of SHELX. *Acta Crystallogr., Sect. A: Found. Crystallogr.* **2008**, *64*, 112–122.
- (39) Spek, A. L. PLATON SQUEEZE: A Tool for the Calculation of the Disordered Solvent Contribution to the Calculated Structure Factors. *Acta Crystallogr., Sect. C: Struct. Chem.* **2015**, *71*, 9–18.

[FeFe]-Hydrogenase H-Cluster Mimics with Various $-\text{S}(\text{CH}_2)_n\text{S}-$ Linker Lengths ($n = 2-8$): A Systematic Study

*Hassan Abul-Futouh,^a Laith R. Almazahreh,^{a,b} Mohammad Kamal Harb,^c Helmar Görls,^a
Mohammad El-khateeb,^d and Wolfgang Weigand^{a*}*

^a Institut für Anorganische und Analytische Chemie, Friedrich-Schiller-Universität Jena,
Humboldt Str. 8, 07743 Jena, Germany Email: wolfgang.weigand@uni-jena.de.

^b ERCOSPLAN Ingenieurbüro Anlagentechnik GmbH Arnstädter Straße 28, 99096
Erfurt, Germany.

^c Department of Pharmacy, Al-Zytoonah University of Jordan, P.O.Box 130 Amman
11733 Jordan

^d Chemistry Department, Jordan University of Science and Technology, Irbid 22110,
Jordan.

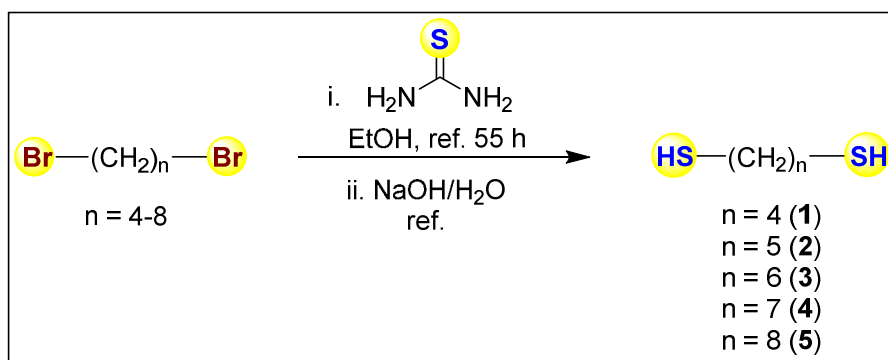
Table of Contents

<i>General Experimental Details</i>	3
<i>General Procedure for the Preparation of the Precursors 1-5.</i>	3
<i>Butane-1,4-dithiol (1)</i>	4
<i>Pentane-1,5-dithiol (2)</i>	4
<i>Hexane-1,6-dithiol (3)</i>	4
<i>Heptane-1,7-dithiol (4)</i>	4
<i>Octane-1,8-dithiol (5)</i>	4
<i>General Procedure for the Synthesis of Compounds 6a-10a, 8b-10b and 9c.</i>	5
<i>1,2-Dithiane (6a)</i>	5
<i>1,2-Dithiepane (7a)</i>	5
<i>1,2-Dithiocane (8a)</i>	6
<i>1,2-Dithionane (9a)</i>	6
<i>1,2-Dithiecene (10a)</i>	6
<i>1,2,9,10-Tetrathiacyclohexadecane (8b)</i>	7
<i>1,2,10,11-Tetrathiacyclooctadecane (9b)</i>	7
<i>1,2,11,12-Tetrathiacycloicosane (10b)</i>	7
<i>1,2,10,11,19,20-Hexathiacycloheptacosane (9c)</i>	8
<i>Cyclic Voltammetry of Complex 11 in CH₂Cl₂</i>	8
Figure S1	9
Figure S2	10
Figure S3	10
Figure S4	11
Figure S5.	12
Figure S6	13
Table S1. A list of CO stretching frequencies for complexes 11-21 in CH ₂ Cl ₂	14
Table S2. Crystal data and refinement details for the X-ray structure determinations of the compounds 8b-10b	15
Table S3. Crystal data and refinement details for the X-ray structure determinations of the compounds 13-17	16
Table S4. Crystal data and refinement details for the X-ray structure determinations of the compounds 18-21	17

General Experimental Details

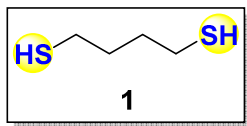
All solvents and starting materials that have not been synthesized by us were commercial products (Acros Organics, Fisher Scientific, Fluka, Merck and Sigma Aldrich,) and were used without further purification. The progress of all reactions was monitored by thin layer chromatography using Merck TLC aluminum sheets (Silica gel 60 F254) with appropriate solvents. NMR spectra were recorded on Bruker Avance 400MHz instruments. ^1H and $^{13}\text{C}\{^1\text{H}\}$ Spectra were referenced to appropriate residual solvent signals (CDCl_3).

General Procedure for the Preparation of the Precursors 1-5.²⁷



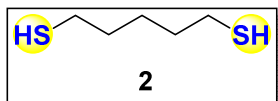
The known dithiol compounds **1-5** used in this report were prepared by refluxing a solution of alkyl dibromide $[\text{Br}(\text{CH}_2)_n\text{Br}]$ ($n = 4-8$) (0.041 mmol) and thiourea $[\text{SC}(\text{NH}_2)_2]$ (0.082 mmol) in 95% ethanol (120 mL) for 55 h under inert condition (N_2). The resulting colorless solution was cooled down and then the solvent removed by rotary evaporator to give the thiuronium salt as a white solid. This resulting salt was mixed with solution of sodium hydroxide (0.082 mmol) in water (120 mL) and heated under reflux. The resulting unclear solution was cooled down and acidified to $\text{pH} \approx 1-2$ which was then extracted with CH_2Cl_2 (5 x 50 mL) and dried over sodium sulfate. The solvent then was removed to give the crude product as yellow oil. The crude product was then purified by bulb-to-bulb distillation (70-90 $^\circ\text{C}/0.40$ mbar) to give a colorless oil. The resulting compounds **1-5** were characterized by ^1H NMR and $^{13}\text{C}\{^1\text{H}\}$ NMR. Their $^1\text{H}, ^1\text{H}$ COSY and $^1\text{H}, ^{13}\text{C}$ HSQC analysis verified the assignments of their signals.

Butane-1,4-dithiol (1).



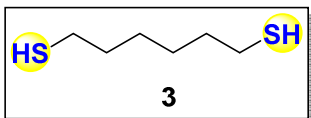
Yield: 90% (4.5 g, 0.037 mol). **^1H NMR** (400 MHz, CDCl_3 , ppm): δ 2.57-2.50 (m, 4H, HSCH_2), 1.76-1.67 (m, 4H, HSCH_2CH_2), 1.34 (t, $J = 7.8$ Hz, 2H, *HS*). **$^{13}\text{C}\{^1\text{H}\}$** (100 MHz, CDCl_3 , ppm): δ 32.66 (s, HSCH_2CH_2), 24.20 (s, HSCH_2).

Pentane-1,5-dithiol (2).



Yield: 86% (4.8 g, 0.035 mol). **^1H NMR** (400 MHz, CDCl_3 , ppm): δ 2.48 (dd, $J = 14.6, 7.3$ Hz, 4H, HSCH_2), 1.62-1.52 (m, 4H, HSCH_2CH_2), 1.49-1.40 (m, 2H, $\text{HSCH}_2\text{CH}_2\text{CH}_2$), 1.31 (t, $J = 7.8$ Hz, 2H, *HS*). **$^{13}\text{C}\{^1\text{H}\}$** (100 MHz, CDCl_3 , ppm): δ 33.39 (s, HSCH_2CH_2), 27.02 (s, $\text{HSCH}_2\text{CH}_2\text{CH}_2$), 24.46 (s, HSCH_2).

Hexane-1,6-dithiol (3).



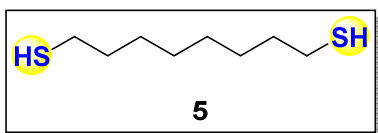
Yield: 95% (5.8 g, 0.039 mol). **^1H NMR** (400 MHz, CDCl_3 , ppm): δ 2.52 (dd, $J = 14.6, 7.4$ Hz, 4H, HSCH_2), 1.67-1.56 (m, 4H, HSCH_2CH_2), 1.46-1.36 (m, 4H, $\text{HSCH}_2\text{CH}_2\text{CH}_2$), 1.31 (t, $J = 7.7$ Hz, 2H, *HS*). **$^{13}\text{C}\{^1\text{H}\}$** (100 MHz, CDCl_3 , ppm): δ 33.74 (s, HSCH_2CH_2), 27.70 (s, $\text{HSCH}_2\text{CH}_2\text{CH}_2$), 24.39 (s, HSCH_2).

Heptane-1,7-dithiol (4).



Yield: 85% (5.7 g, 0.035 mol). **^1H NMR** (400 MHz, CDCl_3 , ppm): δ 2.49 (dd, $J = 14.7, 7.4$ Hz, 4H, HSCH_2), 1.62-1.53 (m, 4H, HSCH_2CH_2), 1.40-1.34 (m, 6H, $\text{HSCH}_2\text{CH}_2(\text{CH}_2)_3$), 1.30 (t, $J = 7.7$ Hz, 2H, *HS*). **$^{13}\text{C}\{^1\text{H}\}$** (100 MHz, CDCl_3 , ppm): δ 33.86 (s, HSCH_2CH_2), 28.46 (s, $\text{HS}(\text{CH}_2)_3\text{CH}_2$), 28.16 (s, $\text{HSCH}_2\text{CH}_2\text{CH}_2$), 24.53 (s, HSCH_2).

Octane-1,8-dithiol (5).



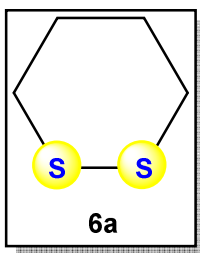
Yield: 81% (5.9 g, 0.033 mol). **^1H NMR** (400 MHz, CDCl_3 , ppm): δ 2.49-2.42 (m, 4H, HSCH_2), 1.59-1.49 (m, 4H, HSCH_2CH_2), 1.36-1.21 (m, 8H, $\text{HSCH}_2\text{CH}_2(\text{CH}_2)_4$),

1.26 (t, $J = 7.7$ Hz, 2H, HS). $^{13}\text{C}\{^1\text{H}\}$ (100 MHz, CDCl_3 , ppm): δ 33.96 (s, HSCH_2CH_2), 28.92 (s, $\text{HS}(\text{CH}_2)_3\text{CH}_2$), 28.26 (s, $\text{HSCH}_2\text{CH}_2\text{CH}_2$), 24.61 (s, HSCH_2).

General Procedure for the Synthesis of Compounds 6a-10a, 8b-10b and 9c.¹

The solutions of compounds **1-5**, respectively, (20 mmol) were dissolved in CHCl_3 (125 mL) and placed in a dropping funnel on a 500 mL three-necked flask equipped with magnetic stirring bar. Another dropping funnel was filled with iodine (20 mmol) dissolved in CHCl_3 (150 mL). The two solutions were added dropwise and simultaneously to Et_3N (41 mmol) in CHCl_3 (100 mL) over a period of three hours. After the addition was completed, the resulting light orange solution was stirred for two hours at room temperature and then washed with dilute sodium thiosulphate solution (60 mL), 0.1 M HCl (2 x 25 mL) and water (2 x 50 mL). The solvent was removed under reduced pressure after drying over Na_2SO_4 . The resulting pale yellow oil was introduced into column chromatography using first 100% hexane as eluent to give the compounds **6a-10a**, respectively, as colourless oil and then using hexane/ CH_2Cl_2 (3:1) to give the compounds **6b-10b**, respectively, as a white solid and compound **9c** as colourless oil.

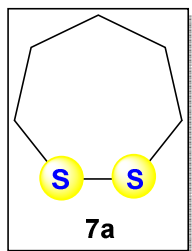
1,2-Dithiane (6a).



Yield: 95% (19 mmol). Anal. Calcd. for $\text{C}_4\text{H}_8\text{S}_2$: C, 39.96; H, 6.71; S, 53.33. Found: C, 40.26; H, 7.11; S, 53.68. ^1H NMR (400 MHz, CDCl_3 , ppm): δ 2.84 (s, 4H, SCH_2), 1.97 (s, 4H, SCH_2CH_2). $^{13}\text{C}\{^1\text{H}\}$ (100 MHz, CDCl_3 , ppm): δ 33.35 (s, SCH_2), 27.79 (s, SCH_2CH_2). DEI-MS

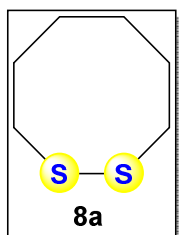
(m/z): 120 $[\text{M}]^+$.

1,2-Dithiepane (7a).



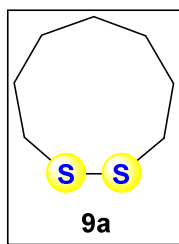
Yield: 90% (18 mmol). Anal. Calcd. for $C_5H_{10}S_2$: C, 44.73; H, 7.13; S, 50.39. Found: C, 45.02; H, 7.43; S, 50.79. 1H NMR (400 MHz, $CDCl_3$, ppm): δ 2.83 (t, 4H, SCH_2), 2.04-2.00 (m, 4H, SCH_2CH_2), 1.79-1.75 (m, 2H, $SCH_2CH_2CH_2$). $^{13}C\{^1H\}$ (100 MHz, $CDCl_3$, ppm): δ 39.68 (s, SCH_2), 30.45 (s, SCH_2CH_2), 26.46 (s, $SCH_2CH_2CH_2$). DEI-MS (m/z): 134 $[M]^+$.

1,2-Dithiocane (8a).



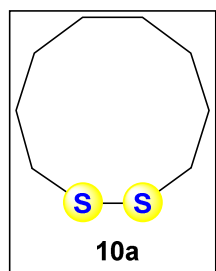
Yield: 65% (13 mmol). Anal. Calcd. for $C_6H_{12}S_2$: C, 48.60; H, 8.16; S, 43.24. Found: C, 48.80; H, 8.31; S, 43.46. 1H NMR (400 MHz, $CDCl_3$, ppm): δ 2.73 (t, 4H, SCH_2), 1.95-1.89 (m, 4H, SCH_2CH_2), 1.47-1.40 (m, 4H, $SCH_2CH_2CH_2$). $^{13}C\{^1H\}$ (100 MHz, $CDCl_3$, ppm): δ 37.97 (s, SCH_2), 25.52 (s, SCH_2CH_2), 24.51 (s, $SCH_2CH_2CH_2$). DEI-MS (m/z): 148 $[M]^+$.

1,2-Dithionane (9a).



Yield: 65% (13 mmol). Anal. Calcd. for $C_7H_{14}S_2$: C, 51.80; H, 8.69; S, 39.50. Found: C, 52.06; H, 8.94; S, 39.89. 1H NMR (400 MHz, $CDCl_3$, ppm): δ 2.84 (t, 4H, SCH_2), 1.88-1.80 (m, 4H, SCH_2CH_2), 1.73-1.60 (m, 6H, $SCH_2CH_2CH_2$). $^{13}C\{^1H\}$ (100 MHz, $CDCl_3$, ppm): δ 40.17 (s, SCH_2), 26.10 (s, SCH_2CH_2), 25.41 (s, $SCH_2CH_2CH_2$), 24.28 (s, $SCH_2CH_2CH_2CH_2$). DEI-MS (m/z): 162 $[M]^+$.

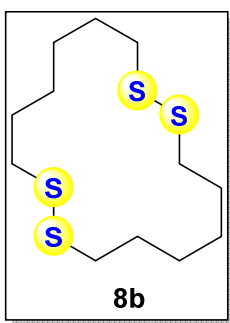
1,2-Dithiepane (10a).



Yield: 75% (15 mmol). Anal. Calcd. for $C_8H_{16}S_2$: C, 54.49; H, 9.15; S, 36.36. Found: C, 54.86; H, 9.55; S, 36.66. 1H NMR (400 MHz, $CDCl_3$, ppm): δ 2.82 (t, 4H, SCH_2), 1.86-1.80 (m, 4H, SCH_2CH_2),

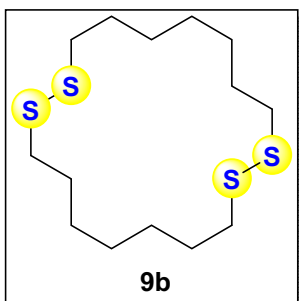
1.72-1.65 (m, 4H, SCH₂CH₂CH₂), 1.55-1.51 (m, 4H, SCH₂CH₂CH₂CH₂). ¹³C{¹H} (100 MHz, CDCl₃, ppm): δ 39.20 (s, SCH₂), 26.50 (s, SCH₂CH₂), 25.53 (s, SCH₂CH₂CH₂), 25.25 (s, SCH₂CH₂CH₂CH₂). DEI-MS (*m/z*): 176 [M]⁺.

1,2,9,10-Tetrathiacyclohexadecane (8b).



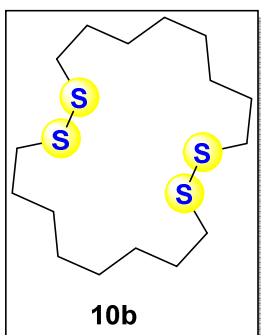
Yield: 25% (5.0 mmol). M.p = 35 °C. Anal. Calcd. for C₁₂H₂₄S₄: C, 48.60; H, 8.16; S, 43.24. Found: C, 48.91; H, 8.38; S, 43.54. ¹H NMR (400 MHz, CDCl₃, ppm): δ 2.73 (t, 8H, SCH₂), 1.77-1.70 (m, 8H, SCH₂CH₂), 1.51-1.47 (m, 8H, SCH₂CH₂CH₂). ¹³C{¹H} (100 MHz, CDCl₃, ppm): δ 39.45 (s, SCH₂), 28.62 (s, SCH₂CH₂), 27.53 (s, SCH₂CH₂CH₂). DEI-MS (*m/z*): 296 [M]⁺.

1,2,10,11-Tetrathiacyclooctadecane (9b).



Yield: 15% (3.0 mmol). M.p = 51 °C. Anal. Calcd. for C₁₄H₂₈S₄: C, 51.80; H, 8.69; S, 39.50. Found: C, 52.10; H, 8.90; S, 39.82. ¹H NMR (400 MHz, CDCl₃, ppm): δ 2.72 (t, 8H, SCH₂), 1.76-1.69 (m, 8H, SCH₂CH₂), 1.49-1.42 (m, 8H, SCH₂CH₂CH₂), 1.41-1.35 (m, 4H, SCH₂CH₂CH₂CH₂). ¹³C{¹H} (100 MHz, CDCl₃, ppm): δ 40.26 (s, SCH₂), 29.45 (s, SCH₂CH₂), 28.77 (s, SCH₂CH₂CH₂), 28.36 (s, SCH₂CH₂CH₂CH₂). DEI-MS (*m/z*): 324 [M]⁺.

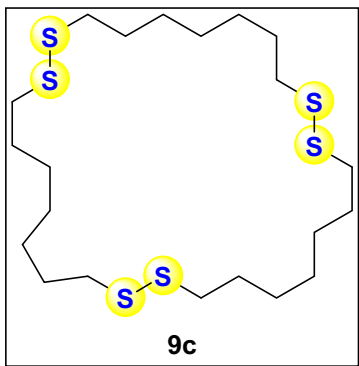
1,2,11,12-Tetrathiacycloicosane (10b).



Yield: 20% (4.0 mmol). M.p = 62 °C. Anal. Calcd. for C₁₆H₃₂S₄: C, 54.49; H, 9.15; S, 36.36. Found: C, 54.83; H, 9.30; S, 36.75. ¹H NMR (400 MHz, CDCl₃, ppm): δ 2.71 (t, 8H, SCH₂), 1.74-1.67

(m, 8H, SCH₂CH₂), 1.47-1.40 (m, 8H, SCH₂CH₂CH₂), 1.38-1.33 (m, 8H, SCH₂CH₂CH₂CH₂). ¹³C{¹H} (100 MHz, CDCl₃, ppm): δ 39.90 (s, SCH₂), 29.16 (s, SCH₂CH₂), 28.89 (s, SCH₂CH₂CH₂), 28.33 (s, SCH₂CH₂CH₂CH₂). DEI-MS (*m/z*): 352 [M]⁺.

1,2,10,11,19,20-Hexathiacycloheptacosane (9c).



Yield: 15% (3.0 mmol). Anal. Calcd. for C₂₁H₄₂S₆: C, 51.80; H, 8.69; S, 39.50. Found: C, 52.08; H, 8.70; S, 39.80. ¹H NMR (400 MHz, CDCl₃, ppm): δ 2.70 (t, 12H, SCH₂), 1.73-1.65 (m, 12H, SCH₂CH₂), 1.46-1.35 (m, 18H, SCH₂CH₂(CH₂)₃). ¹³C{¹H} (100 MHz, CDCl₃, ppm): δ 39.87 (s, SCH₂), 29.54 (s, SCH₂CH₂), 28.91, 28.43 (s,

SCH₂CH₂(CH₂)₃). DEI-MS (*m/z*): 486 [M]⁺.

Cyclic Voltammetry of Complex 11 in CH₂Cl₂.

Lichtenberger and coworkers have reported a detailed electrochemical study of complex **11** in MeCN (Felton, G. A. N.; Petro, B. J.; Glass, R. S.; Lichtenberger, D. L.; Evans, D. H. *J. Am. Chem. Soc.* **2009**, *131*, 11290-11291). Figure S1 displays the cyclic voltammetry of **11** in CH₂Cl₂ at 0.2 V s⁻¹ ≤ *v* ≤ 20 V s⁻¹ and shows that the two electron

remains irreversible process. However, a small anodic event at ca. -1.8 V is detected in the return sweep at faster scan rates and attributed to the oxidation of $\mathbf{11}^{2-}$. The anodic event near -1.6 V arises from oxidation of products of reactions following the reduction of $\mathbf{11}$. That the reduction of $\mathbf{11}$ remains irreversible up to 20 V s^{-1} indicates fast follow-up reactions.

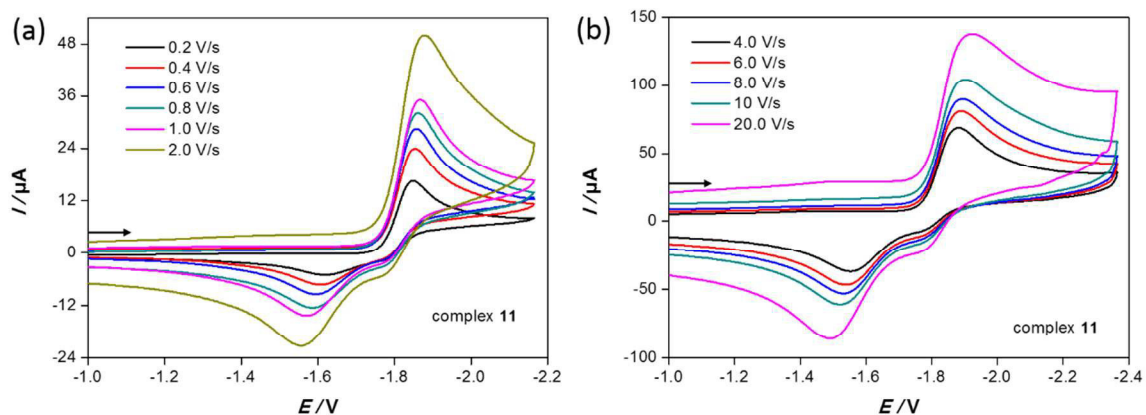


Figure S1. Cyclic voltammetry of 1.0 mM complex $\mathbf{11}$ in CH_2Cl_2 -[n -Bu $_4$ N][BF $_4$] (0.1 M) solutions at various scan rates: (a) $0.2 \text{ V s}^{-1} \leq \nu \leq 2.0 \text{ V s}^{-1}$ and (b) $4.0 \text{ V s}^{-1} \leq \nu \leq 20.0 \text{ V s}^{-1}$. The arrows indicate the scan direction. The potentials E are given in V and referenced to the Fc^+/Fc couple.

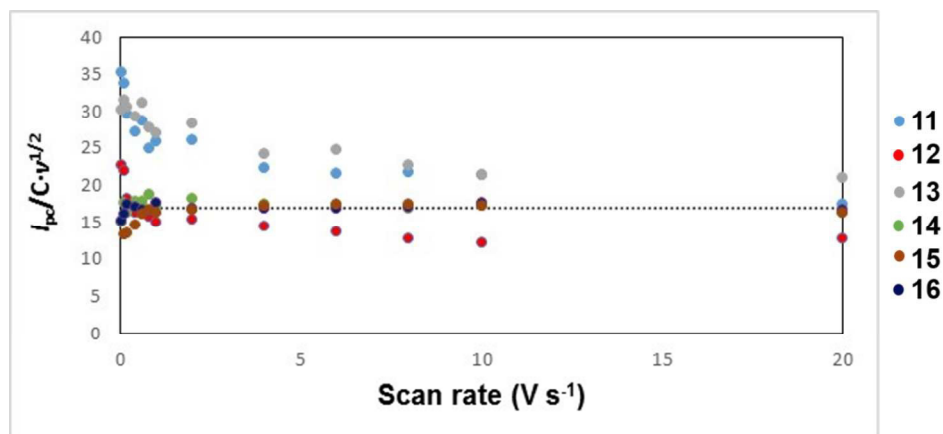


Figure S2. The scan rates dependence of the current function of the primary reduction peaks of 1.0 mM complexes **11-16** in CH_2Cl_2 -[*n*-Bu₄N][PF₄] (0.1 M) solutions. Glassy carbon electrode ($A = 0.0206 \text{ cm}^2$). The dashed line represents the current function expected for a one electron process assuming $D \approx 9 \times 10^{-6} \text{ cm}^2 \text{ S}^{-1}$, a value calculated for various [FeFe]-Hydrogenase models.

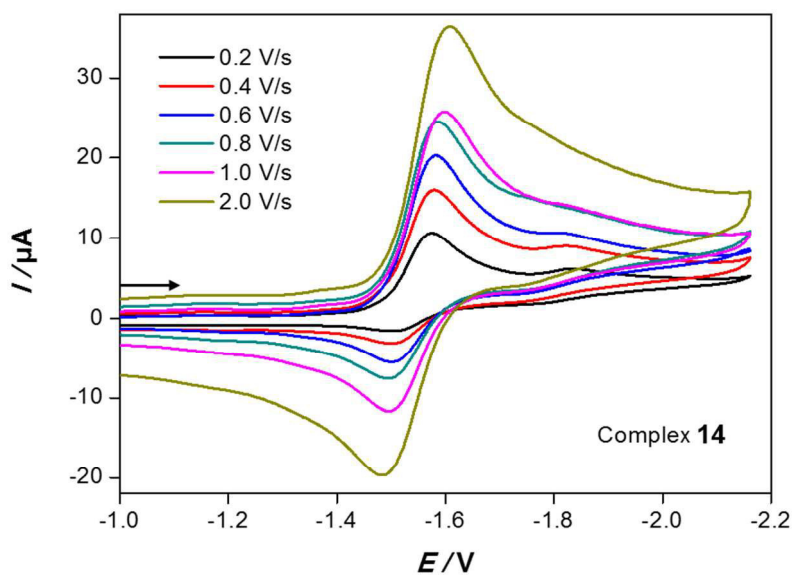


Figure S3. Cyclic voltammetry of 1.0 mM complex **14** in CH_2Cl_2 -[*n*-Bu₄N][BF₄] (0.1 M) solutions at various scan rates. The arrows indicate the scan direction. The potentials E are given in V and referenced to the Fc^+/Fc couple.

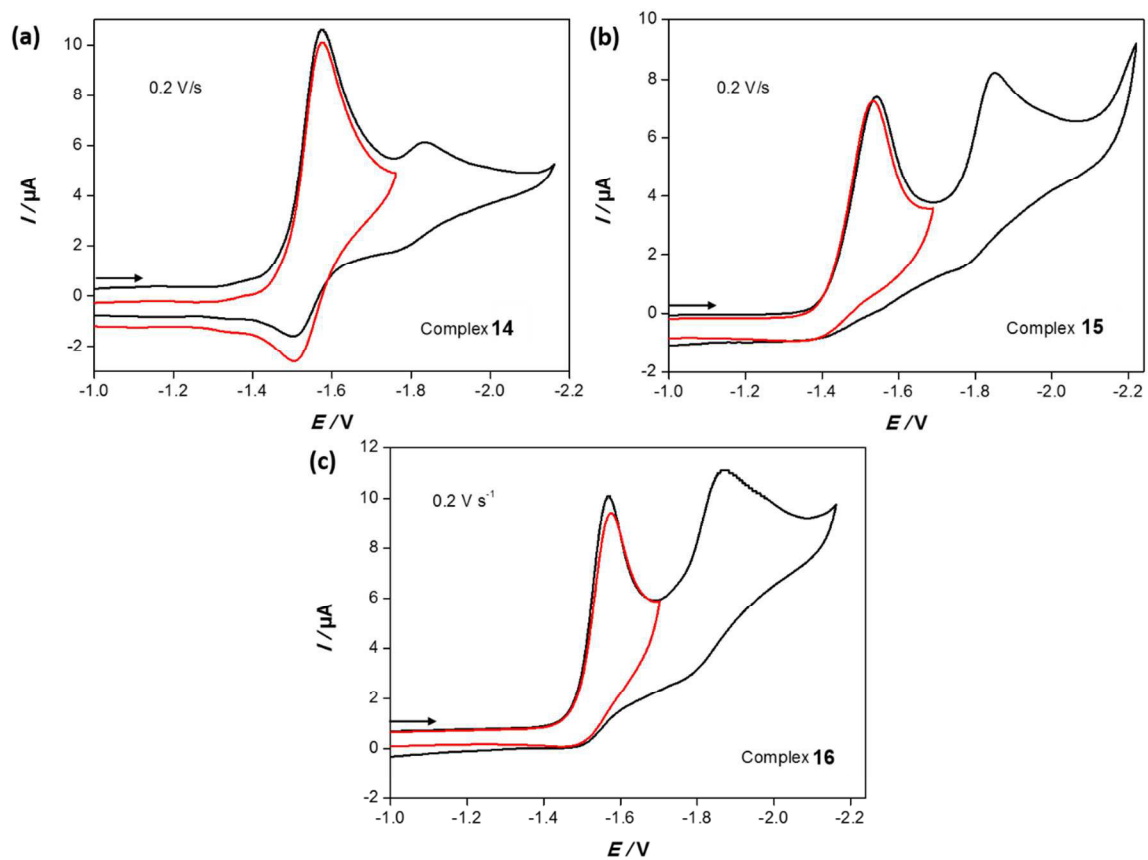


Figure S4. Cyclic voltammetry of 1.0 mM (a) complex **14**, (b) complex **15** and (c) complex **16** in CH_2Cl_2 - $[n\text{-Bu}_4\text{N}][\text{BF}_4]$ (0.1 M) solutions at 0.2 V s^{-1} scan rate, the red profiles show the reverse scan of the first reduction peaks of each complex. The arrows indicate the scan direction. The potentials E are given in V and referenced to the Fc^+/Fc couple.

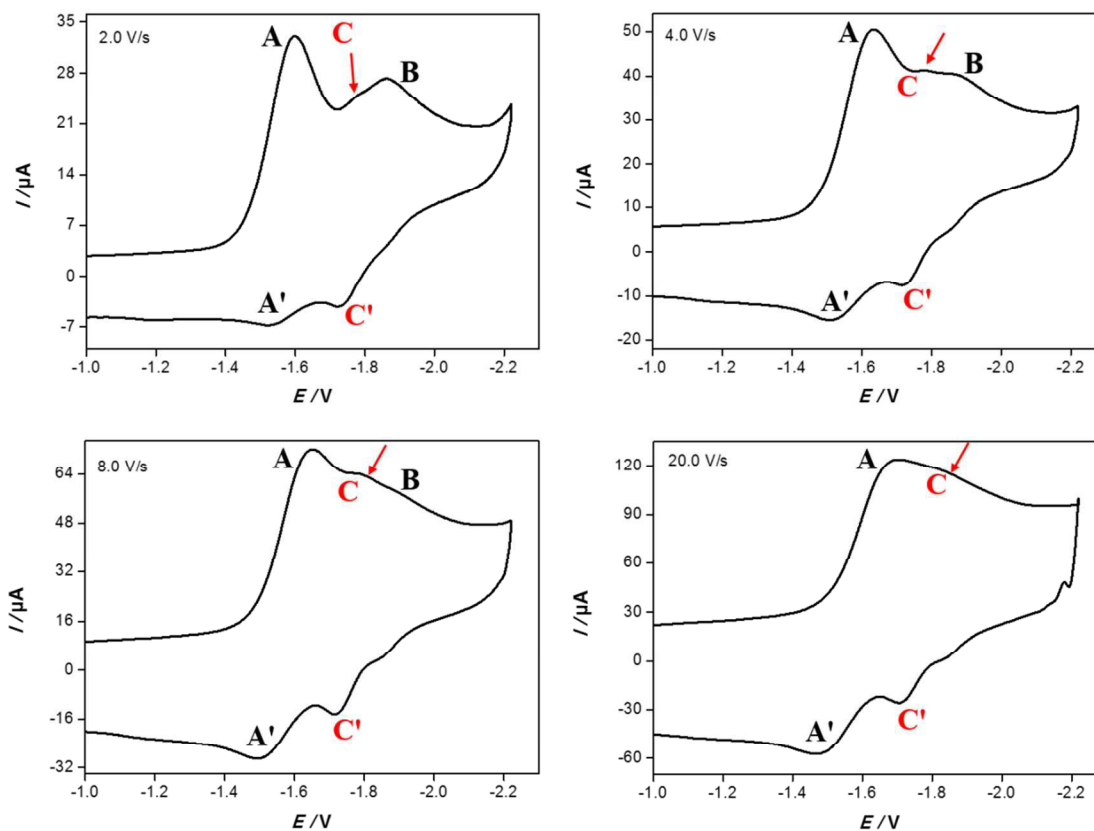


Figure S5. Cyclic voltammetry of 1.0 mM complex **15** in CH_2Cl_2 - $[\text{n-Bu}_4\text{N}][\text{BF}_4]$ (0.1 M) solutions at scan rate 2.0, 4.0, 8.0 and 20.0 V s^{-1} . The arrows indicate the scan direction. The potentials E are given in V and referenced to the Fc^+/Fc couple.

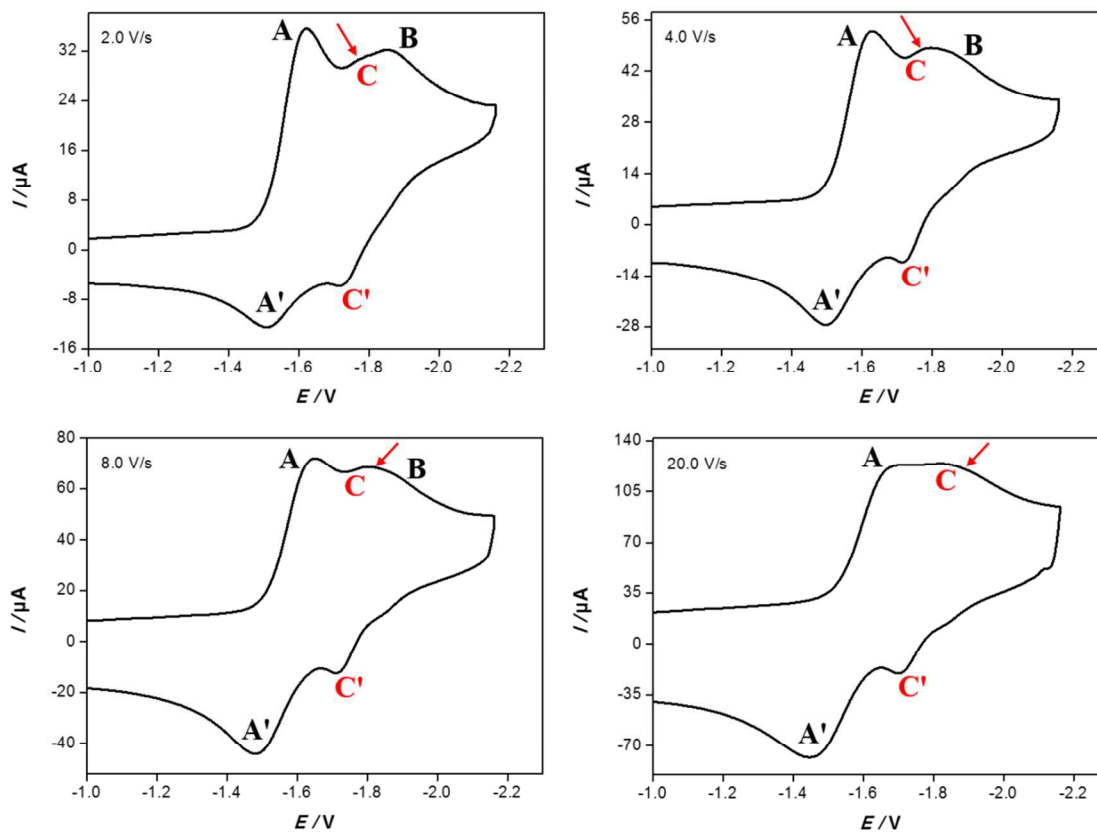


Figure S6. Cyclic voltammetry of 1.0 mM complex **15** in CH_2Cl_2 - $[\text{n-Bu}_4\text{N}][\text{BF}_4]$ (0.1 M) solutions at scan rate 2.0, 4.0, 8.0 and 20.0 V s^{-1} . The arrows indicate the scan direction. The potentials E are given in V and referenced to the Fc^+/Fc couple.

Table S1. A list of CO stretching frequencies for complexes **11-21** in CH₂Cl₂.

Complex	ν (CO) cm ⁻¹
[Fe ₂ (CO) ₆ { μ -S(CH ₂) ₂ S}], 11	2075(m), 2035(vs), 1999(s)
[Fe ₂ (CO) ₆ { μ -S(CH ₂) ₃ S}], 12	2073(m), 2033(vs), 1997(s)
[Fe ₂ (CO) ₆ { μ -S(CH ₂) ₄ S}], 13	2072(m), 2033(vs), 1997(s)
[Fe ₂ (CO) ₆ { μ -S(CH ₂) ₅ S}], 14	2072(m), 2033(vs), 1999(s)
[Fe ₂ (CO) ₆ { μ -S(CH ₂) ₆ S}], 15	2072(m), 2033(vs), 1998(s)
[Fe ₂ (CO) ₆ { μ -S(CH ₂) ₇ S}], 16	2072(m), 2033(vs), 1994(s)
[Fe ₂ (CO) ₆ { μ -S(CH ₂) ₈ S}], 17	2069(m), 2030(vs), 1992(s)
[Fe ₂ (CO) ₆ { μ -S(CH ₂) ₆ S}] ₂ , 18	2068(m), 2033(vs), 1991(s)
[Fe ₂ (CO) ₆ { μ -S(CH ₂) ₇ S}] ₂ , 19	2068(m), 2033(vs), 1990(s)
[Fe ₂ (CO) ₆ { μ -S(CH ₂) ₈ S}] ₂ , 20	2068(m), 2032(vs), 1991(s)
[Fe ₂ (CO) ₆ {(μ -S(CH ₂) ₆ S) ₂ }], 21	2069(m), 2031(vs), 1992(s)
[Fe ₂ (CO) ₆ {(μ -S(CH ₂) ₇ S) ₂ }], 22	2069(m), 2032(vs), 1991(s)
[Fe ₂ (CO) ₆ {(μ -S(CH ₂) ₆ S) ₂ }], 23	2069(m), 2030(vs), 1991(s)

Table S2. Crystal data and refinement details for the X-ray structure determinations of the compounds **8b-10b**.

Compound	8b	9b	9c	10b
formula	C ₁₂ H ₂₄ S ₄	C ₁₄ H ₂₈ S ₄	C ₂₁ H ₄₂ S ₆	C ₁₆ H ₃₂ S ₄
fw (g·mol ⁻¹)	296.55	324.60	486.91	352.66
°C	-140(2)	-140(2)	-140(2)	-140(2)
crystal system	monoclinic	triclinic	monoclinic	orthorhombic
space group	P 2 ₁ /c	P $\bar{1}$	P 2 ₁	P c c n
<i>a</i> / Å	10.6252(3)	5.4762(2)	5.2890(5)	10.5759(2)
<i>b</i> / Å	15.9987(4)	7.1162(3)	8.2109(7)	19.6736(4)
<i>c</i> / Å	9.7926(2)	10.7625(5)	29.907(2)	9.1061(2)
α /°	90	97.912(2)	90	90
β /°	112.722(1)	95.626(3)	92.235(5)	90
γ /°	90	91.727(3)	90	90
<i>V</i> /Å ³	1535.44(7)	413.01(3)	1297.81(19)	1894.67(7)
<i>Z</i>	4	1	2	4
ρ (g·cm ⁻³)	1.283	1.305	1.246	1.236
μ (cm ⁻¹)	5.94	5.58	5.33	4.92
measured data	11064	2212	4847	12276
data with <i>I</i> > 2 σ (<i>I</i>)	3198	1717	4495	2035
unique data (<i>R</i> _{int})	3485/0.0306	1750/0.0111	4847/0.0673	2157/0.0294
w <i>R</i> ₂ (all data, on F ²) ^{a)}	0.0585	0.0529	0.1476	0.0568
<i>R</i> ₁ (<i>I</i> > 2 σ (<i>I</i>)) ^{a)}	0.0266	0.0196	0.0653	0.0225
<i>S</i> ^{b)}	1.067	1.065	1.158	1.104
Res. dens./e·Å ⁻³	0.301/-0.190	0.298/-0.195	0.787/-0.546	0.329/-0.170
Flack-parameter	-	-	0.24(17)	-
absorpt method	multi-scan	multi-scan	multi-scan	multi-scan
absorpt corr T _{min} /max	0.7030/0.7456	0.7026/0.7456	0.5614/0.7456	0.7225/0.7456
CCDC No.	1546654	1546655	1546656	1546657

Table S3. Crystal data and refinement details for the X-ray structure determinations of the compounds **13-17**.

Compound	13	14	15	16	17
formula	C ₁₀ H ₈ Fe ₂ O ₆ S ₂	C ₁₁ H ₁₀ Fe ₂ O ₆ S ₂	C ₁₂ H ₁₂ Fe ₂ O ₆ S ₂	C ₁₃ H ₁₄ Fe ₂ O ₆ S ₂	C ₁₄ H ₁₆ Fe ₂ O ₆ S ₂
fw (g·mol ⁻¹)	399.98	414.01	428.04	442.06	456.09
°C	-140(2)	-140(2)	-140(2)	-140(2)	-140(2)
crystal system	monoclinic	triclinic	triclinic	monoclinic	monoclinic
space group	P 2 ₁ /n	P $\bar{1}$	P $\bar{1}$	P 2 ₁ /n	P 2 ₁ /n
a/ Å	7.5465(2)	7.6039(2)	11.0848(4)	9.5009(2)	8.7472(2)
b/ Å	16.4265(3)	10.0260(3)	12.0436(4)	12.4179(2)	14.0359(3)
c/ Å	11.7807(2)	10.9003(3)	18.8998(7)	15.1226(3)	15.2643(3)
α /°	90	70.566(2)	84.340(2)	90	90
β /°	104.362(1)	78.663(2)	74.725(2)	108.308(2)	104.374(1)
γ /°	90	83.670(1)	82.401(2)	90	90
V/Å ³	1414.73(5)	767.46(4)	2407.25(15)	1693.87(6)	1815.41(7)
Z	4	2	6	4	4
ρ (g·cm ⁻³)	1.878	1.792	1.772	1.733	1.669
μ (cm ⁻¹)	23.63	21.82	20.9	19.83	18.53
measured data	11051	11078	26281	12397	14033
data with I > 2 σ (I)	3067	3243	6484	3687	3839
unique data (R _{int})	3220/0.0247	3499/0.0244	10147/0.0614	3845/0.0183	4142/0.0261
wR ₂ (all data, on F ²) ^{a)}	0.0415	0.0473	0.1577	0.0423	0.0629
R ₁ (I > 2 σ (I)) ^{a)}	0.0188	0.0218	0.0826	0.0175	0.0277
S ^{b)}	1.071	1.052	1.119	1.072	1.046
Res. dens./e·Å ⁻³	0.310/-0.251	0.316/-0.275	0.778/-0.622	0.295/-0.243	1.129/-0.411
absorpt method	multi-scan	multi-scan	multi-scan	multi-scan	multi-scan
absorpt corr T _{min} /max	0.6828/0.7456	0.6722/0.7456	0.6492/0.7456	0.6750/0.7456	0.6822/0.7456
CCDC No.	1546658	1546659	1546660	1546661	1546662

Table S4. Crystal data and refinement details for the X-ray structure determinations of the compounds **18-20** and **22**.

Compound	18	19	20	22
formula	C ₂₄ H ₂₄ Fe ₄ O ₁₂ S ₄	C ₂₆ H ₂₈ Fe ₄ O ₁₂ S ₄	C ₂₈ H ₃₂ Fe ₄ O ₁₂ S ₄	C ₂₀ H ₂₈ Fe ₂ O ₆ S ₄
fw (g·mol ⁻¹)	856.07	884.12	912.18	604.36
°C	-140(2)	-140(2)	-140(2)	-140(2)
crystal system	triclinic	triclinic	triclinic	triclinic
space group	P $\bar{1}$	P $\bar{1}$	P $\bar{1}$	P $\bar{1}$
<i>a</i> / Å	7.8503(4)	11.7725(5)	7.9159(3)	11.2698(3)
<i>b</i> / Å	7.9765(4)	12.9993(5)	7.9691(3)	11.4819(3)
<i>c</i> / Å	13.0296(5)	14.1932(6)	15.3911(5)	11.8770(3)
α /°	84.592(3)	108.625(2)	97.536(2)	62.537(1)
β /°	84.439(3)	104.780(2)	94.769(2)	82.514(2)
γ /°	74.403(2)	107.353(2)	106.319(2)	72.148(2)
<i>V</i> /Å ³	780.16(6)	1811.23(13)	916.37(6)	1297.91(6)
<i>Z</i>	1	2	1	2
ρ (g·cm ⁻³)	1.822	1.621	1.653	1.546
μ (cm ⁻¹)	21.49	18.54	18.35	14.72
measured data	7245	18135	5607	10096
data with <i>I</i> > 2 σ (<i>I</i>)	2837	5863	3864	5384
unique data (<i>R</i> _{int})	3402/0.0401	7894/0.0479	4131/0.0179	5820/0.0190
<i>wR</i> ₂ (all data, on <i>F</i> ²) ^{a)}	0.0886	0.1378	0.0688	0.0656
<i>R</i> ₁ (<i>I</i> > 2 σ (<i>I</i>)) ^{a)}	0.0409	0.0693	0.0296	0.0286
<i>S</i> ^{b)}	1.089	1.103	1.117	1.097
Res. dens./e·Å ⁻³	0.552/-0.460	1.175/-0.763	0.521/-0.303	0.386/-0.283
absorpt method	multi-scan	multi-scan	multi-scan	multi-scan
absorpt corr T _{min} /max	0.5492/0.7456	0.6194/0.7456	0.6644/0.7456	0.6733/0.7456
CCDC No.	1546663	1546664	1546665	1546666

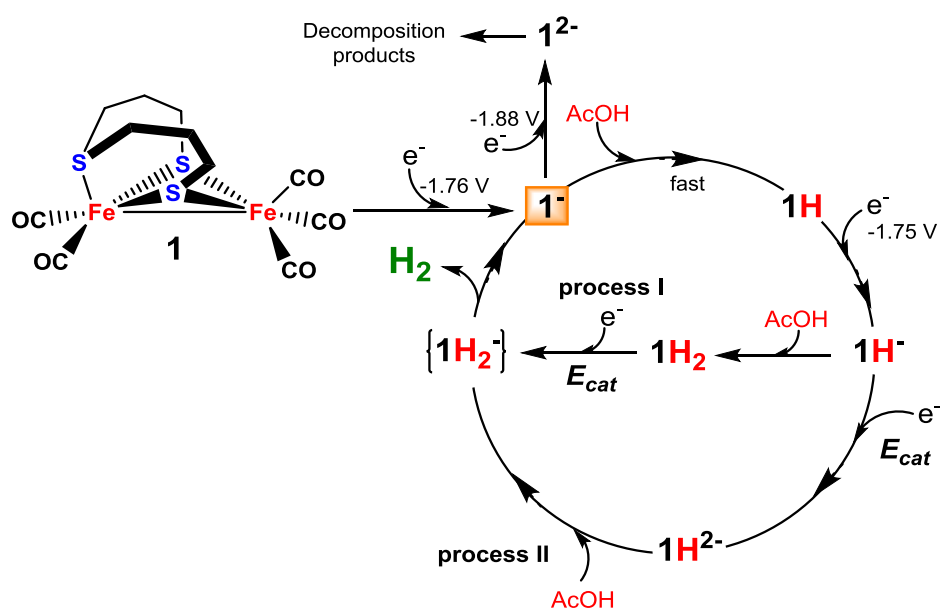
a) Definition of the R indices: $R_1 = (\sum ||F_o| - |F_c||) / \sum |F_o|$; $wR^2 = \{\sum [w(F_o^2 - F_c^2)^2] / \sum [w(F_o^2)^2]\}^{1/2}$ with $w^{-1} = \sigma^2(F_o^2) + (aP)^2 + bP$; $P = [2F_c^2 + \text{Max}(F_o^2)]/3$; b) $s = \{\sum [w(F_o^2 - F_c^2)^2] / (N_o - N_p)\}^{1/2}$

4.6 [HAF-6]

Electrochemical Investigation and Density Functional Calculations on Proton Reduction Cycle Catalyzed by [FeFe]-Hydrogenase Models Featuring [Fe₂S₃] Core

Hassan Abul-Futouh, Laith R. Almazahreh, Ahmad Q. Daraosheh, Mohammad El-Khateeb, Luca De Gioia, Giuseppe Zampella, Wolfgang Weigand, Luca Bertini

Ready for Submission.



Electrochemical Investigations and Density Functional Calculations on Proton Reduction Cycle Catalyzed by [FeFe]-Hydrogenase Models Featuring [Fe₂S₃] Core

Hassan Abul-futouh,[†] , Laith R. Almazahreh,[†] Ahmad Q. Daraosheh,[‡] Mohammad El-khateeb,[⊥] Luca De Gioia,[§] Giuseppe Zampella^{*§} Wolfgang Weigand^{*†} and Luca Bertini^{*§}

[†]*Institut für Anorganische und Analytische Chemie, Friedrich-Schiller-Universität Jena,
Humboldtstrasse 8, D-07743 Jena, Germany,*

[‡]*Faculty of pharmacy, Isra University, P.O. Box 22, 11622 Amman, Jordan.*

[§]*Department of Biotechnology and Biosciences, University of Milano-Bicocca, 20126 Milan, Italy,*

[⊥]*Chemistry Department, Jordan University of Science and Technology, 22110 Irbid, Jordan.*

AUTHOR EMAIL ADDRESS (luca.bertini@unimib.it)

* To whom correspondence should be addressed. E-mail: luca.bertini@unimib.it Tel: +390264483438

Abstract: The electrochemical behaviour of [FeFe]-hydrogenase models featuring [Fe₂S₃] cores, namely [Fe₂(CO)₅{TBPT}] (**1**) (TBPT = μ -(SC₃H₆)₂S- μ) and [Fe₂(CO)₄(P(OMe)₃){TBPT}] (**2**), was investigated in the absence and presence of acetic acid, AcOH. In the absence of acid, complex **1** undergoes two successive irreversible one-electron reductions with closely spaced cathodic peak potentials ($\Delta E_{pc} = 130$ mV (CH₂Cl₂) or 165 mV (CH₃CN) vs. ferrocenium/ferrocene couple) whereas only one irreversible one-electron reduction process ($E_{pc} = -2.11$ V) is observed for complex **2** in CH₂Cl₂. In the presence of AcOH, complex **1** catalyzes the reduction of protons via one process ($E_{cat} \sim -2.1$ V) with high efficiency while two catalytic processes, at -2.05 V and -2.19 V, were observed in the case of complex **2**. Based on the electrochemical studies, two mechanisms for the catalytic proton reduction by complexes **1** and **2** have been proposed. The structure of the reduced species of the complex **1** as well as the mechanism of the H₂ production was elucidated in detail by Density Functional Theory calculations.

Keywords: [FeFe]-hydrogenase, [Fe₂S₃] core, electrochemistry, proton reduction, DFT calculations

Introduction

Rapid depletion of fossil fuels and anthropogenic global warming have been making mandatory the overcoming of fossil energy systems. Along such line, hydrogen economy appears as an ideal solution to both issues. Indeed, fossil fuels have several disadvantages: they are non-renewable sources, can be found only in certain part of our planet and, as aforementioned, produce several pollutants among which are found carbon dioxide and other greenhouse gases that are considered to be the main reason of climate changes.¹ In contrast, hydrogen is the most abundant element in the universe²⁻³, characterized by a high energy density and produce zero pollutants. These facts make hydrogen the promising energy source for future. In biological process, hydrogen production or consumption ($2H^+ + 2e^- \leftrightarrow H_2$) are catalyzed by metalloenzymes called hydrogenases (H₂ase)⁴, which are commonly classified into three classes based on their metal content, [NiFe] H₂ase, [FeFe] H₂ase and [Fe] H₂ase. X-ray crystallographic and IR spectroscopic studies of [FeFe] H₂ase isolated from *Desulfovibrio desulfuricans*⁵ and *Clostridium pasteurianum*⁶ show that the H cluster (the active site at which protons are reduced to hydrogen or

hydrogen oxidized to protons) can be viewed as $[\text{Fe}_2\text{S}_3]$ sub-site at which CO and CN ligands are bound. The two Fe atoms (proximal, Fe_p and distal, Fe_d) of the sub-site share two bridging sulfur ligands of a dithiolate, the Fe_p is connected to a $[\text{Fe}_4\text{S}_4]$ cluster by the sulfur atom of cysteine ligand (Figure 1a). Numerous complexes featuring $[\text{Fe}_2\text{S}_2]$ core with the general formula $[\text{Fe}_2(\text{CO})_6\text{L}_n\{\mu-(\text{SCH}_2)_2\text{X}\}]^{7-31}$ (Figure 1b) have been synthesized and tested as electrocatalysts to better understand the structure-function relationships of the H cluster. In contrast, very few models mimicking the $[\text{Fe}_2\text{S}_3]$ sub-site of the H cluster are reported, notably by Rauchfuss³², Song³³, Pickett³⁴⁻³⁷, Chen³⁸ and our group^{17,39} (Figure 2).

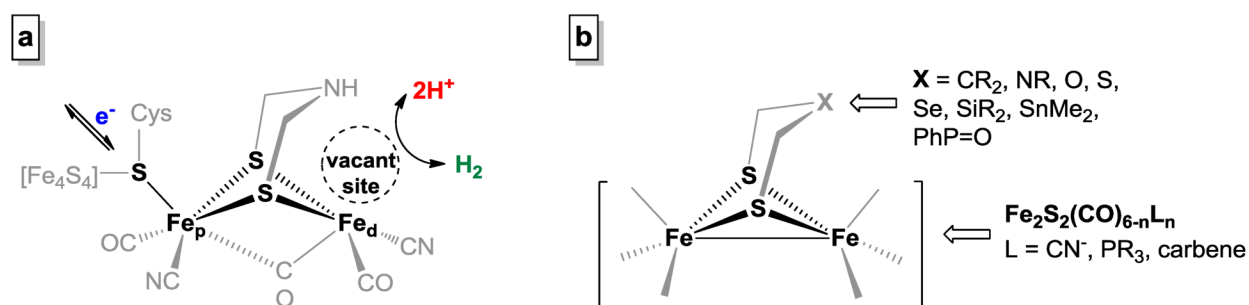


Figure 1. Representation of (a) the structure of the H cluster and of (b) synthetic models featuring $[\text{Fe}_2\text{S}_2]$ core.

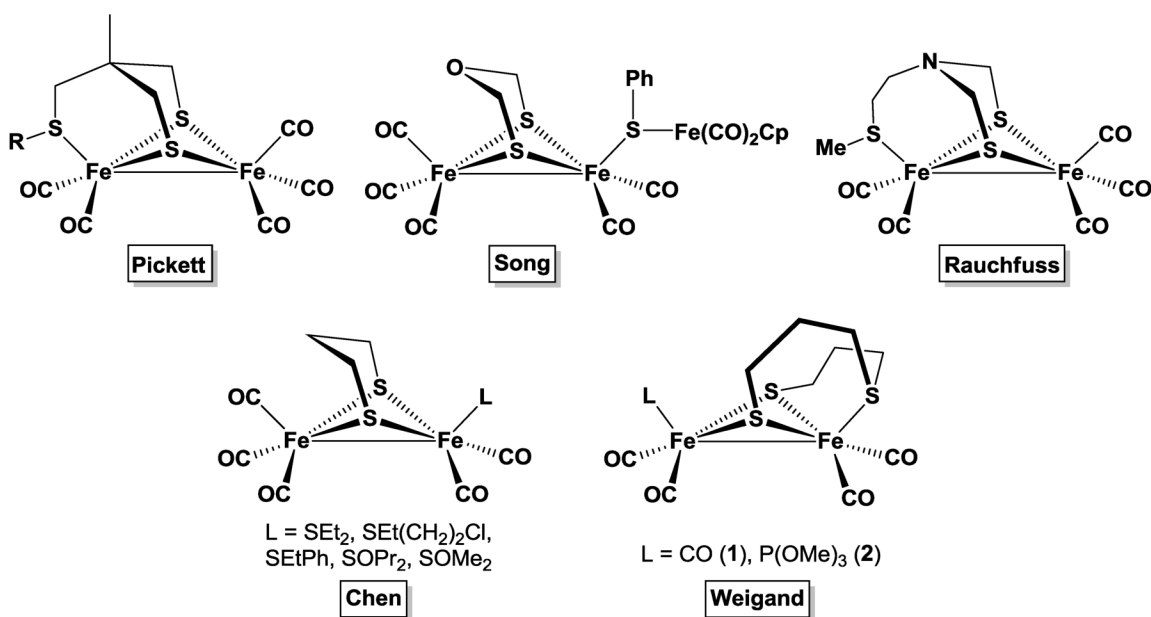
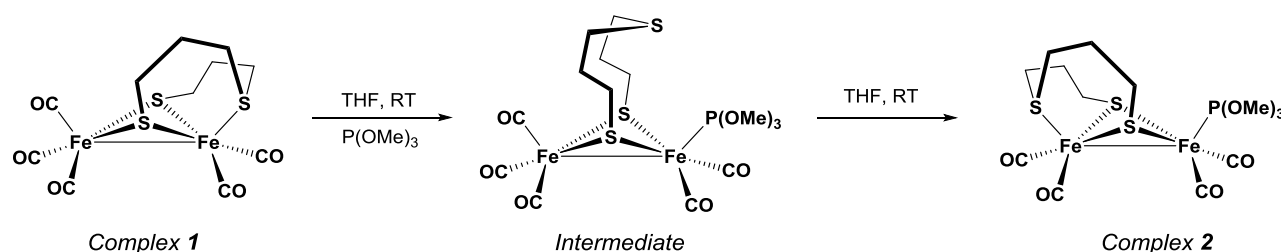


Figure 2. Synthetic models with a $[\text{Fe}_2\text{S}_3]$ core.

As reported by Chen and coworkers,³⁸ the reduction of the model systems $[\text{Fe}_2(\text{CO})_5(\text{L})\{\mu\text{-(SCH}_2)_2\text{CH}_2\}]$ ($\text{L} = \text{SEt}_2, \text{S}(\text{CH}_2\text{CH}_3)(\text{CH}_2\text{CH}_2\text{Cl}), \text{S}(\text{CH}_2\text{CH}_3)(\text{C}_6\text{H}_5), \text{SO}(\text{CH}_2\text{CH}_2\text{CH}_3)_2, \text{SO}(\text{CH}_3)_2$) (Figure 2) in CH_3CN is assigned to be an irreversible one-electron process. Moreover, these complexes showed catalytic response toward reduction of protons from AcOH , but without describing mechanistic details. Recently, Pickett and coworkers have reported the protonation of $[\text{Fe}_2(\text{CO})_4(\text{PMe}_3)\{\mu\text{-(SCH}_2)_2\text{CH}_2\text{S-}\mu\text{Me}\}]$ by HCl to afford a bridging hydride species $[\text{Fe}_2(\text{CO})_4(\text{PMe}_3)(\mu\text{-H})\{\mu\text{-(SCH}_2)_2\text{CH}_2\text{S-}\mu\text{Me}\}][\text{PF}_6]$, which undergoes dissociation of the pendant thioether after reduction as confirmed by spectroelectrochemistry.⁴⁰ The reductive behavior and the electrocatalytic properties of the complexes $[\text{Fe}_2(\text{CO})_5\{\mu\text{-(SCH}_2)_2\text{NCH}_2\text{CH}_2\text{S}(\text{Me})\text{-}\mu\}]$ ³² and $[\text{Fe}_2(\text{CO})_5\{\mu\text{-(SCH}_2\text{OCH}_2\text{S}(\text{CpFe}(\text{CO})_2\text{SPh})\text{-}\mu)\}]$ ³³ (Figure 2) that were reported by Rauchfuss and Song, respectively, have not been investigated.

In continuation of our studies on the model system $[\text{Fe}_2(\text{CO})_5\{\text{TBPT}\}]$ (**1**) and a substitution of CO by $\text{P}(\text{OMe})_3$ in complex (**1**) to give $[\text{Fe}_2(\text{CO})_4(\text{P}(\text{OMe})_3)\{\text{TBPT}\}]$ (**2**) as a result of the on-off coordination of a thioether ligand bound at the iron atom³⁹. In addition we isolated and characterized the structure of $[\text{Fe}_2(\text{CO})_5(\text{P}(\text{OMe})_3)\{\text{TBPT}\}]$, which is believed to be the intermediate of the reaction pathway (Scheme 1)³⁹. This result could be seen as an important contribution to corroborate the mechanism for the cyanation reaction of $[\text{Fe}_2\text{S}_3]$ cluster³⁷.

Scheme 1. The pathway of substitution of CO by $\text{P}(\text{OMe})_3$ in complex **1**.



We introduce herein detailed investigations of the electrochemical and electrocatalytic features of these complexes in the absence and presence of AcOH . Moreover, we apply DFT calculations in order to

gain insights on the structure of the intermediates involved in the proposed catalytic cycles as well as the possible mechanisms of H₂ release.

Results and Discussion

Electrochemical Investigations in the Absence of Acid. The cyclic voltammograms of complex **1** in CH₂Cl₂-NBu₄PF₆ at scan rates of $0.05 \text{ V}\cdot\text{s}^{-1} \leq \nu \leq 10 \text{ V}\cdot\text{s}^{-1}$ are shown in Figures 3a-c.

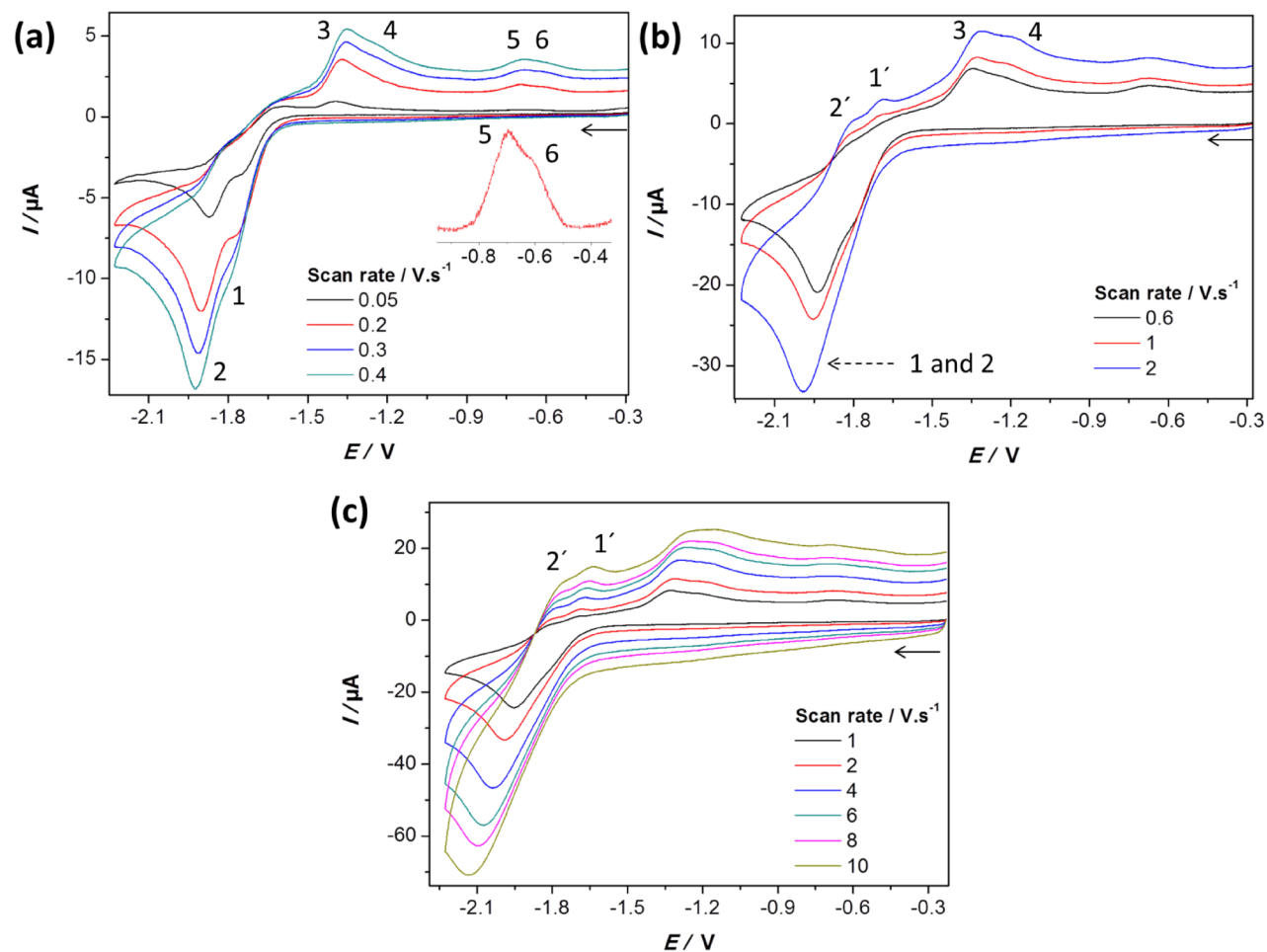


Figure 3. Cyclic voltammetry of 1.0 mM complex **1** in CH₂Cl₂-NBu₄PF₆ solution: (a) $0.05 \text{ V}\cdot\text{s}^{-1} \leq \nu \leq 0.4 \text{ V}\cdot\text{s}^{-1}$, (b) $0.6 \text{ V}\cdot\text{s}^{-1} \leq \nu \leq 2 \text{ V}\cdot\text{s}^{-1}$ and (c) $1 \text{ V}\cdot\text{s}^{-1} \leq \nu \leq 10 \text{ V}\cdot\text{s}^{-1}$. E is in V against the ferrocenium/ferrocene couple. The arrows indicate the scan direction.

The two irreversible peaks 1 and 2 (Figure 3a) are assigned to two sequential reduction steps *RS1* and *RS2*, respectively:



Where k_{s1} and k_{s2} are the heterogenous rate constants for the first and the second reduction steps, respectively, and the E_{pc} values are the cathodic peak potentials when $\nu = 0.2 \text{ V}\cdot\text{s}^{-1}$. We can see from Figures 3a-c that increasing the scan rate results in (i) an overlapping of the two reduction peaks (1 and 2) and (ii) an appearance of new small peaks 1' and 2' for the oxidation of the monoanion $\mathbf{1}^-$ (see Figure S1) and the dianion $\mathbf{1}^{2-}$, respectively. The detection of peaks 1' and 2' at higher scan rates states that small population of the reduced species of complex **1** rides out the follow-up reactions, which are responsible for the irreversibility of the reduction of complex **1** and the oxidation events 3-6 in Figure 3. The overlapping of peaks 1 and 2 at higher scan rates reflects the relative rates of the first and the second reduction steps such that $k_{s1} < k_{s2}$.^{11,12,17,41-43} Reversing the forward scan at -1.79 V (Figure S1) results in the appearance of the small peak 1' for the oxidation of $\mathbf{1}^-$ as well as the disappearance of the oxidation events 3-6. Thus, most of the follow-up reactions (decomposition) take place after the second electron transfer. In MeCN-NBu₄PF₆ solution, complex **1** is also reduced in two steps with E_{pc1} and E_{pc2} equal to -1.62 V and -1.78 V, respectively (Figure 4a). The less negative reduction potentials with larger separation ($\Delta E_{pc} = 165 \text{ mV}$) in the case of MeCN-NBu₄PF₆ solution compared to that of CH₂Cl₂-NBu₄PF₆ solution ($\Delta E_{pc} = 130 \text{ mV}$) might be related to the higher resistance of CH₂Cl₂ compared to that of MeCN.⁴⁴ In contrast to the study in CH₂Cl₂-NBu₄PF₆ solution, increasing the scan rate up to $1.0 \text{ V}\cdot\text{s}^{-1}$ does not affect neither the peak potentials, E_{pc1} and E_{pc2} , nor their separation (ΔE_{pc}), which is also related to the lower resistance of MeCN compared to CH₂Cl₂.⁴⁴ We have observed that complex **1** is less stable in MeCN than in CH₂Cl₂ and for this reason we investigated the electrocatalytic behavior of the complex in CH₂Cl₂ solution (see later).

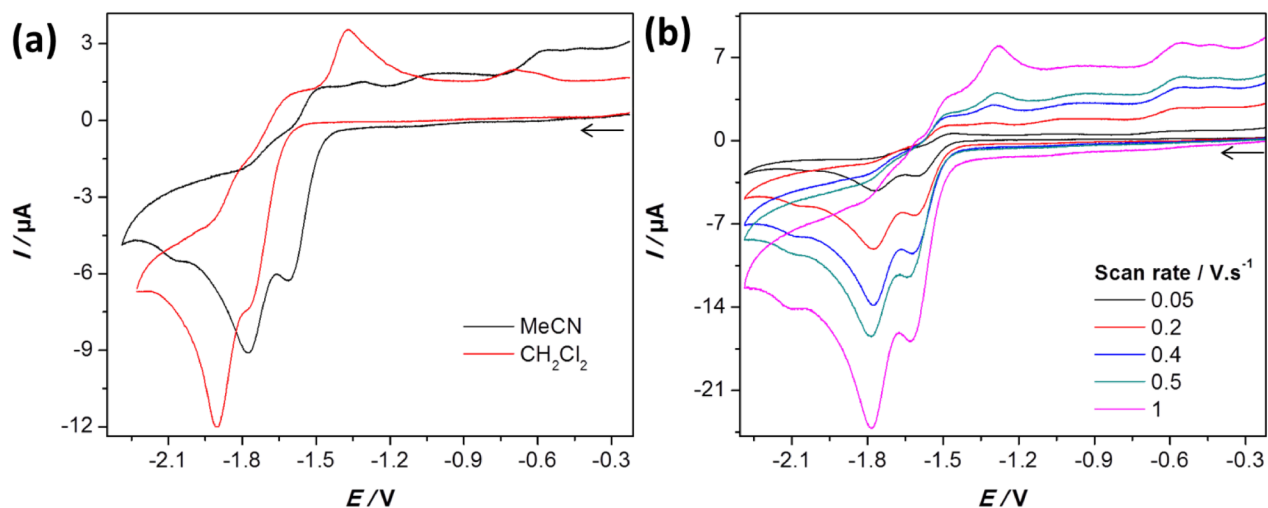


Figure 4. (a) Comparison between the cyclic voltammetry of 1.0 mM complex **1** in MeCN-NBu₄PF₆ and CH₂Cl₂-NBu₄PF₆ solutions. (b) Cyclic voltammetry of 1.0 mM complex **1** in MeCN-NBu₄PF₆ at various scan rates: $0.05 \text{ V}\cdot\text{s}^{-1} \leq \nu \leq 1 \text{ V}\cdot\text{s}^{-1}$. E is in V against the ferrocenium/ferrocene couple. The arrows indicate the scan direction.

Cyclic voltammetry of complex **2** in CH₂Cl₂-NBu₄PF₆ demonstrates only an irreversible one-electron reduction wave at -2.11 V at $0.2 \text{ V}\cdot\text{s}^{-1}$. The one-electron assignment is based on comparing the maximum current of the reduction wave of complex **2** with that of a known two-electron reduction of [Fe₂(CO)₆{ μ -bdt}] (bdt = benzenedithiolate) (Figure S2).⁴⁵ The more negative reduction potential of complex **2** compared to those of complex **1** is a result of the stronger electron donating ligand set at the [FeFe] core of **2** than that of **1**. The expected second one-electron reduction of complex **2** cannot be observed within the solvent window, which is also a consequence of the high electron density at the [FeFe] core. Even by increasing the scan rate to $10 \text{ V}\cdot\text{s}^{-1}$, the reduction of **2** remains chemically irreversible and only anodic waves due to products of follow-up reactions are observed in the return scan at -1.57 V, -0.97 V and -0.42 V (Figure 5).

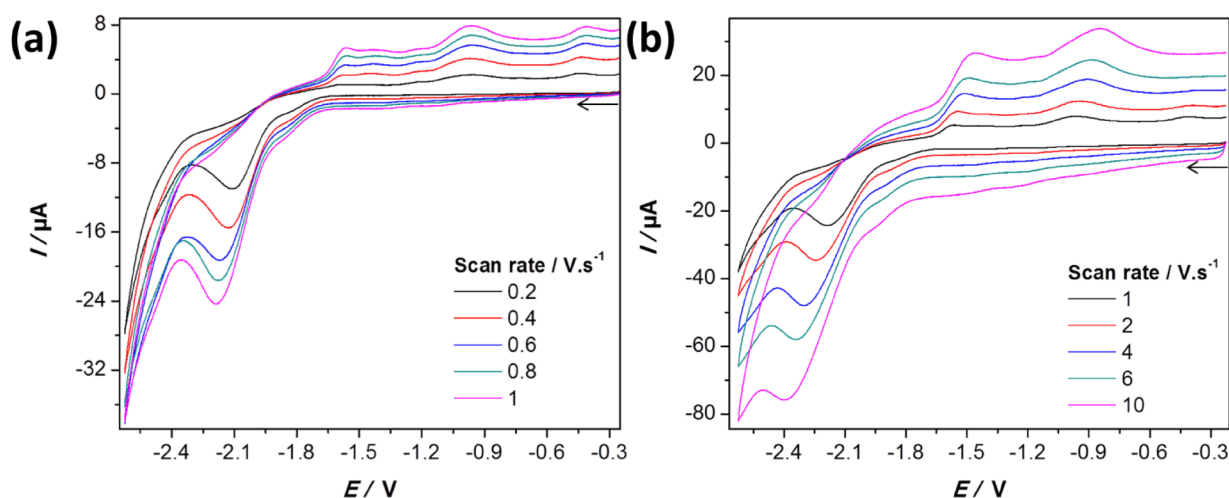


Figure 5. Cyclic voltammetry of 1.0 mM complex **2** in $\text{CH}_2\text{Cl}_2\text{-NBu}_4\text{PF}_6$ solution at (a) $0.2 \text{ V}\cdot\text{s}^{-1} \leq \nu \leq 1 \text{ V}\cdot\text{s}^{-1}$ and (b) $1 \text{ V}\cdot\text{s}^{-1} \leq \nu \leq 10 \text{ V}\cdot\text{s}^{-1}$. E is in V against the ferrocenium/ferrocene couple. The arrows indicate the scan direction.

Catalytic Reduction of AcOH by Complex 1. The addition of 1 equiv. AcOH to the $\text{CH}_2\text{Cl}_2\text{-NBu}_4\text{PF}_6$ solution of complex **1** (Figure 6) results in a reduction peak at $E_{\text{pc}3} = -1.75 \text{ V}$ with a current ~ 1.7 times higher than that of peak 1 ($E_{\text{pc}1} = -1.76 \text{ V}$) and the disappearance of peak 2 ($E_{\text{pc}2} = -1.89 \text{ V}$).

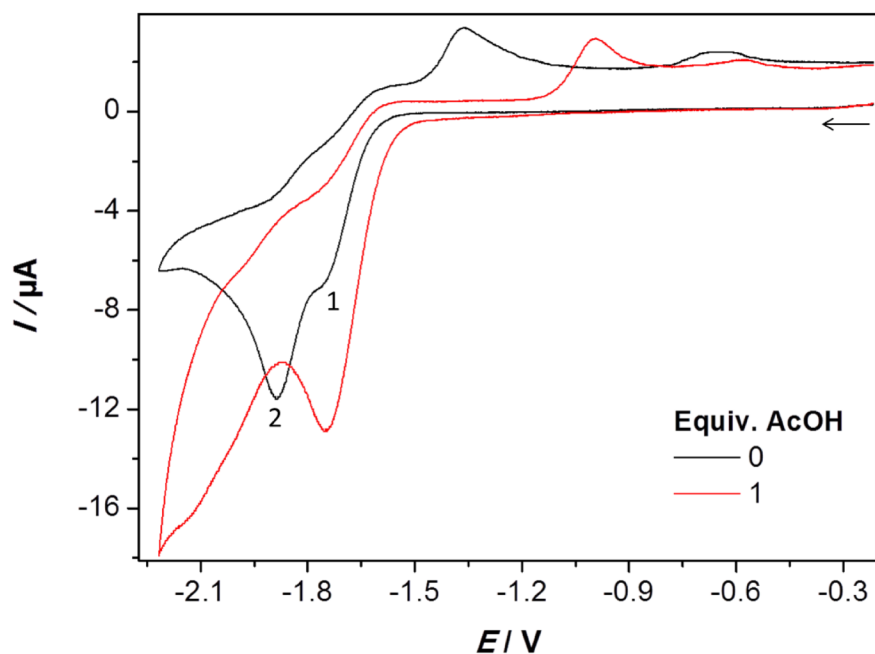
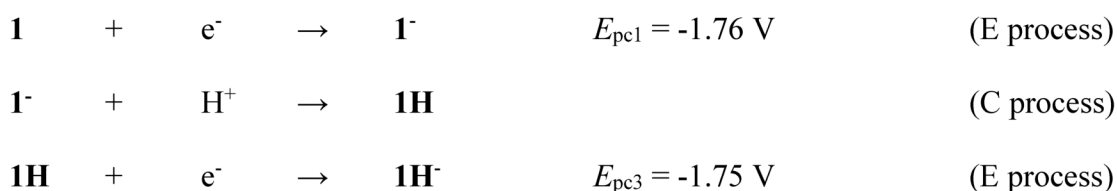


Figure 6. Cyclic voltammetry of 1.0 mM complex **1** in $\text{CH}_2\text{Cl}_2\text{-NBu}_4\text{PF}_6$ solution at $0.2 \text{ V}\cdot\text{s}^{-1}$ in the absence and presence of 1 equiv. AcOH. E is in V against the ferrocenium/ferrocene couple. The arrow indicates the scan direction.

The disappearance of peak 2 and the oxidation events associated with it suggest that $\mathbf{1}^{2-}$ is not formed anymore owing to a fast protonation of $\mathbf{1}^-$ to give a new species $\mathbf{1H}$, which undergoes reduction at a less negative potential than that of $\mathbf{1}$ by 10 mV. Previous digital simulations as well as DFT calculations revealed that the protonated monoanion of [FeFe]-hydrogenase synthetic models is reduced at potential equal to or less negative than that of the neutral species.^{46,47} Accordingly, an ECE mechanism (E = electron transfer process and C = chemical reaction) takes place in the presence of 1 equiv. AcOH at -1.75 V:



The occurrence of the ECE mechanism explains the higher current of the wave at -1.75 V in the presence of 1 equiv. AcOH compared to that of peak 1 in the absence of acid. Assuming an ECE mechanism, semi-integration of the curves shows that the charge consumed in the forward scan between -1.6 V and -2.1 V

in the absence of acid equals that consumed during the cathodic scan (-1.5 V to -1.9 V) if 1 equiv. AcOH is added. With increasing the concentration of AcOH, a catalytic process occurs near -2.1 V as shown in Figure 7.

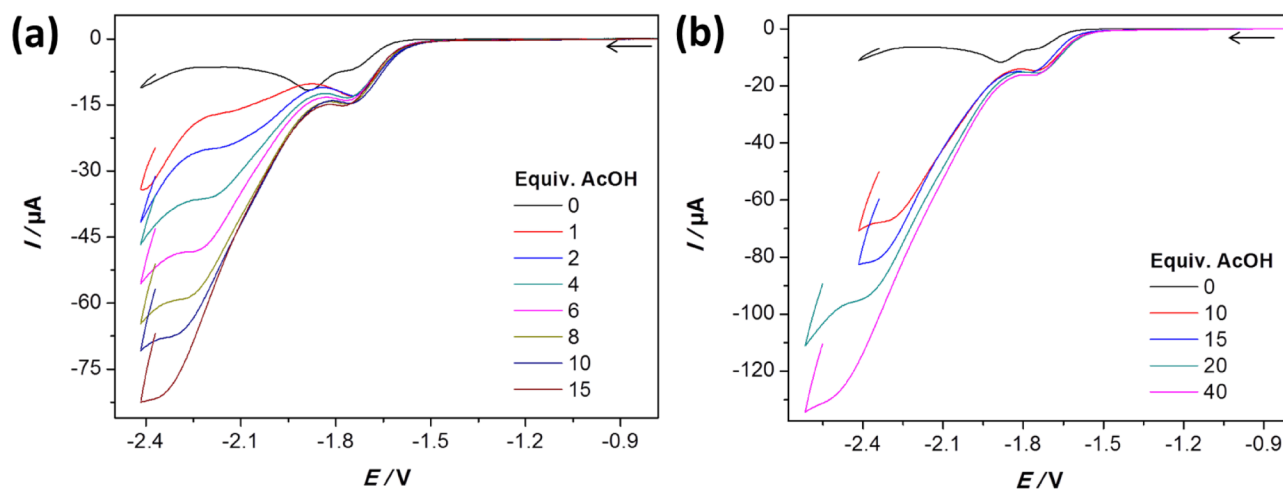


Figure 7. Cyclic voltammetry of 1.0 mM complex **1** in $\text{CH}_2\text{Cl}_2/\text{NBu}_4\text{PF}_6$ solution at $0.2 \text{ V}\cdot\text{s}^{-1}$ in the presence of various equivalents of AcOH: (a) 0-15 equiv. AcOH and (b) 0-40 equiv. AcOH. E is in V against the ferrocenium/ferrocene couple. The arrows indicate the scan direction.

Scheme 2 summarizes our proposed mechanism for the catalytic reduction of AcOH. According to this scheme, two pathways for H_2 evolution are possible:

- (i) Once $\mathbf{1H}^\cdot$ is formed at -1.75 V, it undergoes protonation to $\mathbf{1H}_2$, which does not release H_2 until it is reduced into $\mathbf{1H}_2^\cdot$. We propose that $\mathbf{1H}_2$ is not a H_2 -releasing species as no catalysis is observed at -1.75 V.
- (ii) Alternatively, $\mathbf{1H}^\cdot$ is reduced to $\mathbf{1H}^{2\cdot}$, which is then protonated affording $\mathbf{1H}_2^\cdot$ that releases H_2 .

The two pathways lead to the same H_2 -releasing intermediate $\mathbf{1H}_2^\cdot$, but the difference is only at which potential the intermediate $\mathbf{1H}_2^\cdot$ is formed. DFT calculations based on Scheme 2 will be discussed later.

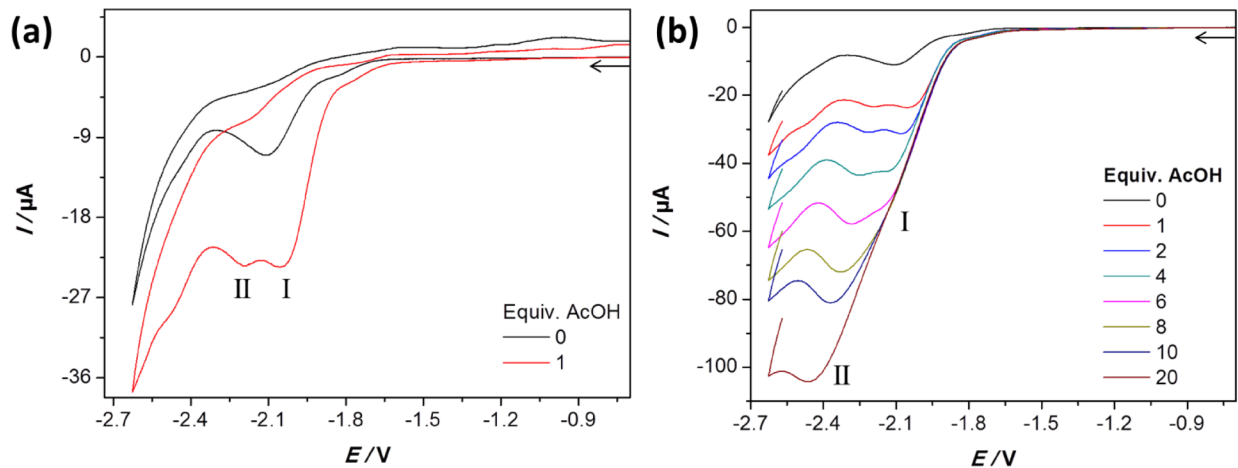
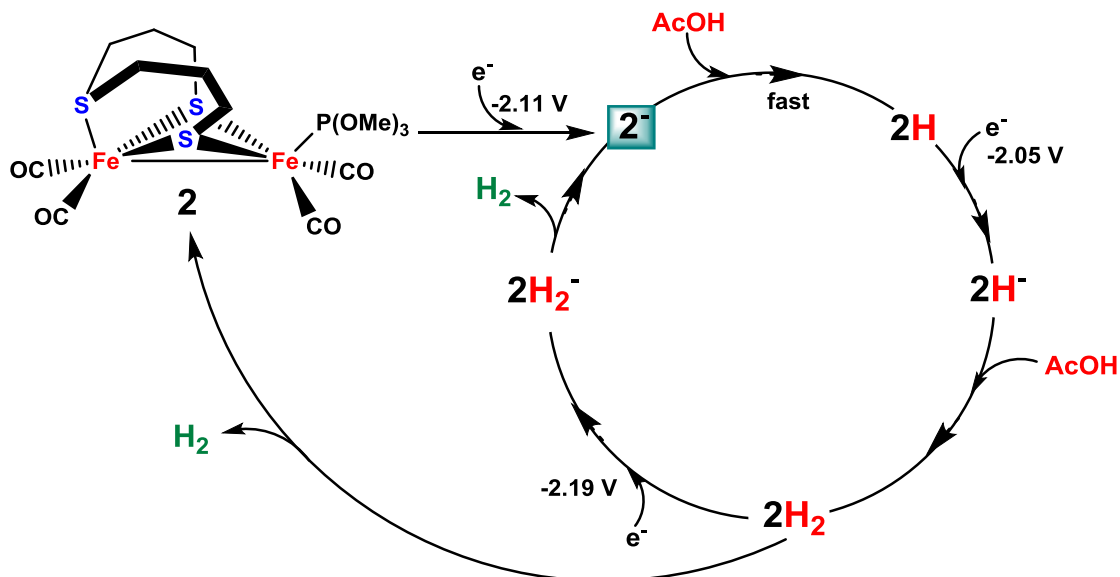


Figure 8. Cyclic voltammetry of 1.0 mM complex **2** in $\text{CH}_2\text{Cl}_2\text{-NBu}_4\text{PF}_6$ solution at $0.2 \text{ V}\cdot\text{s}^{-1}$ in the presence of (a) 0 and 1 equiv. AcOH and (b) 0-20 equiv. AcOH. E is in V against the ferrocenium/ferrocene couple. The arrows indicate the scan direction.

A fast protonation of $\mathbf{2}^-$ affording $\mathbf{2H}$ should explain the 60 mV anodic shift and the subsequent reduction of $\mathbf{2H}$ to $\mathbf{2H}^-$, a process that requires less negative potential to occur than the formation of $\mathbf{2}^-$ from **2**, elucidates the observed overall two-electron assignment of peak I. We assign the reduction event observed at -2.48 V in Figure 8a (red curve) to the direct reduction of AcOH at the glassy carbon electrode (see Figure S3) while the reduction wave at -2.19 V (peak II) could be due to the reduction of $\mathbf{2H}^-$ or the diprotonated $\mathbf{2H}_2$ species. The increase in the current of the reduction waves I and II as a function of acid concentration (Figure 8b) reveals the catalytic behaviour of model **2**. However, the current of the first process levels off at $[\text{HOAc}] \approx 6 \text{ mM}$, which is an indication of a slow H_2 release. The catalytic response of wave I suggests that once $\mathbf{2H}^-$ is formed at -2.05 V, it undergoes protonation into $\mathbf{2H}_2$, which subsequently releases H_2 and regenerates the starting neutral complex **2**.

Reduction of $\mathbf{2H}_2$ followed by H_2 release from $\mathbf{2H}_2^-$ is a reasonable mechanism for the second catalytic process (wave II). Scheme 3 summarizes the proposed pathways for the catalytic proton reduction processes by complex **2**.

Scheme 3. Possible pathways for the reduction of AcOH catalyzed by complex **2**.



The main difference between the catalytic behaviour of complexes **1** and **2** is the ability of the latter to catalyze the proton reduction via two processes in which the **2H**₂ and **2H**₂^{-•} are the H₂-releasing intermediates (Scheme 3) whereas only **1H**₂^{-•} can release H₂ according to the proposed mechanism in Scheme 2. The higher electron richness of the diiron core of complex **2** compared to that of complex **1** may argue the H₂-releasing ability of **2H**₂, but not **1H**₂. To evaluate the electrocatalytic activity of complexes **1** and **2** toward proton reduction in the presence of AcOH, the plots of I_c/I_p (I_c = the reduction current of the catalytic processes, I_p = the reduction current in the absence of acid) of both complexes vs. the equiv. AcOH (i.e. [AcOH]/[complex]) are drawn in Figure 9.

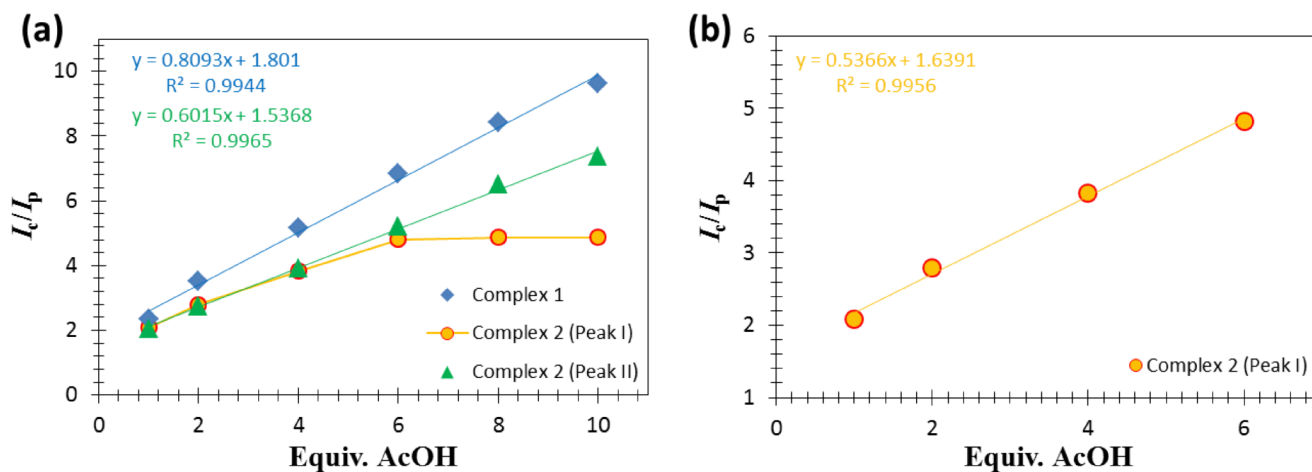


Figure 9. Dependence of I_c/I_p of electrocatalytic events for complexes **1** (1.0 mM) and **2** (1.0 mM) on the equiv. AcOH: (a) 1–10 equiv. AcOH and (b) the acid-dependent region of the catalytic current of peak I for complex **2**.

The plot for the catalytic process of complex **1** (Figure 9a), which occurs at -2.10 V in the presence of 1 equiv. AcOH, is steeper than that for the catalytic process of complex **2** at peak I (Figure 9b, $E_{\text{cat}} = -2.05$ V for 1 equiv. AcOH) or peak II (Figure 9a, $E_{\text{cat}} = -2.19$ V for 1 equiv. AcOH). Thus, the catalytic activity of complex **1** is better than that of complex **2** and takes place with less overpotential. It is shown by Figure 9a that I_c/I_p of first catalytic process of complex **2** ($E_{\text{cat}} = -2.05$ V for 1 equiv. AcOH) reaches a plateau near 5 for $[\text{AcOH}] \sim 6$ mM, which indicates saturation with acid and a rate-determining step that could be release of H_2 as has been described previously.⁴³ From the acid-independent region, the rate constant, k , for the H_2 evolution by complex **1** at peak I can be estimated to be 10 mol of H_2 per 1 mol of catalyst per second using the following relation⁴⁸:

$$\frac{I_c}{I_p} = \frac{n}{0.4463} \sqrt{\frac{R \cdot T \cdot k}{F \cdot \nu}}$$

Where $n = 2$ (number of electrons involved in the catalytic process), $R = 8.314 \text{ J} \cdot \text{mol}^{-1} \cdot \text{K}^{-1}$, $F = 96485 \text{ C} \cdot \text{mol}^{-1}$ and ν is the scan rate in $\text{V} \cdot \text{s}^{-1}$.

DFT calculations

Analysis of the neutral, mono di bi-anionic forms. In this section, we discuss the structure and the electronic properties of complex **1** and its mono- and di-anionic forms. In Figure 10 the main geometry parameters are reported for the neutral form (**1**), the monoanionic (**1⁻**) and dianionic (**1²⁻**) forms (numerical values are reported in Table S1). Gas-phase BP86/TZVP level of theory well reproduces **1** XRD geometry parameters. In general, bond distances are slightly overestimated, in particular Fe-S bonds (on average 0.033 Å). The **1_{rot}** isomer, a rotated form of the complex, results 5.3 kcal·mol⁻¹ higher in energy compared to the minimum energy form. As preliminary step in the investigation of the **1⁻** anionic forms, we can discuss their structure on the basis of the shape of the LUMO of the neutral complex (reported in Figure S4 along with the HOMO). The LUMO is characterized by a Fe-Fe σ^* orbital contribution and a significant *p*-orbital contribution of the three sulfur atoms with a clear antibonding character along the Fe-S bond of the TBPT ligand. Moreover, Mulliken LUMO populations indicate that the extra electron will be essentially localized on the Fe atoms and on the sulfur atoms, although by a lesser extent. These observations implied that we have focused the structure investigation toward three sets of isomers which differ essentially in the bonding network of the TBPT ligand: i) weakening/dissociation of a Fe-S bond that involves the thiolate or ii) dissociation of the Fe-S bond that involves the sulfide or iii) the Fe-Fe bond weakening (Figure S6). Moreover, to identify the possible TBPT conformation upon Fe-S sulfide bond dissociation, we carried out a preliminary minimum search at molecular mechanics level finding eight possible starting point structures.

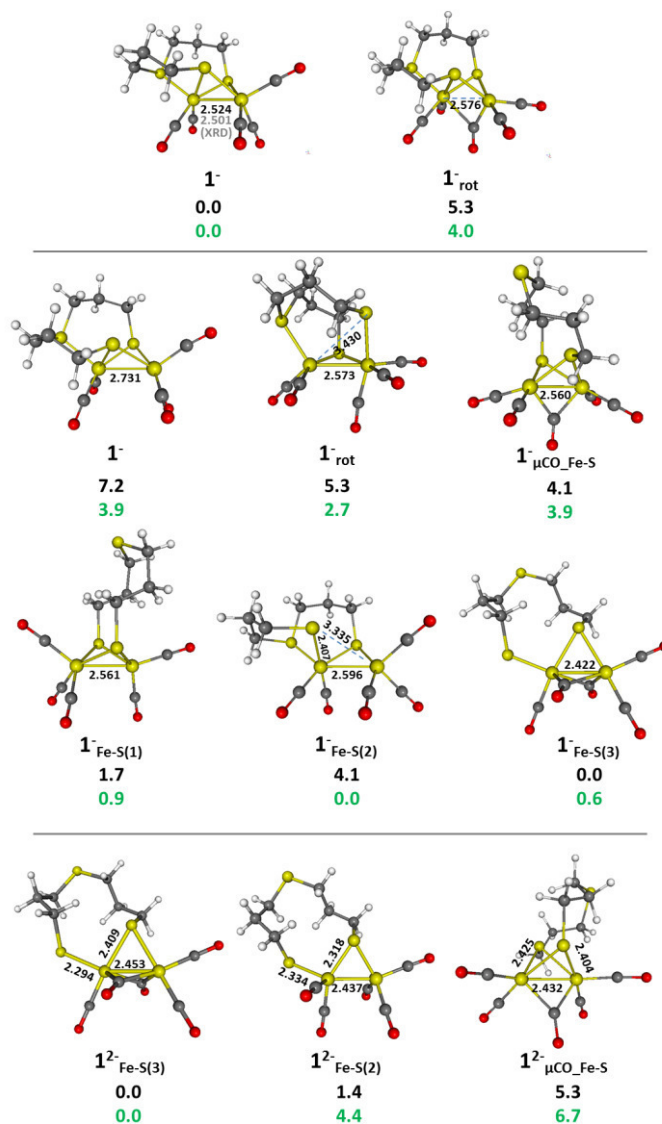


Figure 10. Structure of the low energy isomers of the neutral, anionic and bis-anionic form. Energy differences are computed in kcal·mol⁻¹ with respect to the lowest energy isomer in gas phase (black) or in implicit CH₂Cl₂ (grey). Bond distances in Å.

Anions **1⁻** and **1^{-rot}** were obtained using the structures of **1** and **1_{rot}** as starting points, respectively. In **1⁻** the five Fe-S bonds are slightly elongated and the effect of the reduction is a significant Fe-Fe bond elongation (+0.207Å compared with **1**). The remaining isomers are lower in energy compared to **1⁻** and are characterized by the dissociation of at least one Fe-S bond. In gas-phase, the lowest energy anionic form (**1⁻Fe-S(3)**) features the dissociation of two Fe-S bond and the shortening of the Fe-Fe bond due to the shift of two CO ligands in bridging position. We found that **1⁻Fe-S(1)** in which the Fe-S bond of the sulfide

that belong to the TBPP is dissociated is slightly higher in energy than $\mathbf{1}_{\text{Fe-S}(3)}$ by $1.7 \text{ kcal}\cdot\text{mol}^{-1}$. The form $\mathbf{1}_{\text{Fe-S}(2)}$ is $4.1 \text{ kcal}\cdot\text{mol}^{-1}$ higher in energy and it is characterized by the dissociation of one Fe-S thiolate bond. Solvent corrected (CH_2Cl_2) energy differences among the various structures decrease and the first three most stable forms become essentially isoenergetic, where $\mathbf{1}_{\text{Fe-S}(2)}$ is the most stable form.

The computation of the NBO atomic spin densities evidences that the unpaired electron is almost completely localized at the unsaturated Fe atom while atomic charges evidence a significant increase of the negative charge on the sulfur atoms that belong to the dissociated Fe-S bond (Figure S7). On the basis of these results, we conclude that the reduced form of $\mathbf{1}$ is likely characterized at least by the dissociation of one Fe-S bond.

Using the monoanionic structures as starting point, we have optimized the geometry of the most stable bisanionic isomers. These are characterized by shorter Fe-Fe bonds compared to those of the starting monoanions as well as by the dissociation of the thioether Fe-S bonds. According to the NBO atomic charges, the second electron is only partially localized on the sulfur atoms, while most of the negative charge is delocalized on the CO ligands (see Figure S8). The Fe-Fe bond shortening is the result of the Fe-Fe bond order increasing as already observed in the $\text{Fe}_2(\text{CO})_x$ ($x < 9$) unsaturated complex.⁵⁰ This observation can be rationalized by the tendency of unsaturated dinuclear carbonyl models to partially fulfill the 18-electron rule by increasing the metal-metal bond order.

In Table 1 reduction potentials of $\mathbf{1}$ and $\mathbf{1}^-$ are reported. To better evaluate the reduction potential in the case of the $\mathbf{1}^-/\mathbf{1}^{2-}$ couple, we included explicit K^+ counterion for all the systems considered. At the employed level of theory, theoretical values are in nice agreement with the experimental ones, resulting the former more negative on average only by 57 mV.

Table 1. Computed and experimental reduction potentials (in V) referred to the Fc/Fc^+ couple.

	Theor. E°	Exp E°
$\mathbf{1} \rightarrow \mathbf{1}^-$	-1.83	-1.76
$\mathbf{1}^- \rightarrow \mathbf{1}^{2-}$	-1.93	-1.88

Investigation of the mechanism of H₂ formation.

Herein we have considered all possible structures of the intermediates shown in Scheme 2, i.e. the monoprotonated (**1H**, **1H⁻**, **1H²⁻**) and the diprotonated (**1H₂**, **1H₂⁻**) species. All the structures are reported in the supplementary materials (Figure S9). In addition, we provide as supporting information the possible protonation products of the neutral complex **1** (i.e. the isomers of the monoprotonated species **1H⁺**, Figures S10 and S11), where the most stable one is the μ -hydride species. In Figure 11 are reported the structures of the most relevant isomers in the discussion of the H₂ production cycle.

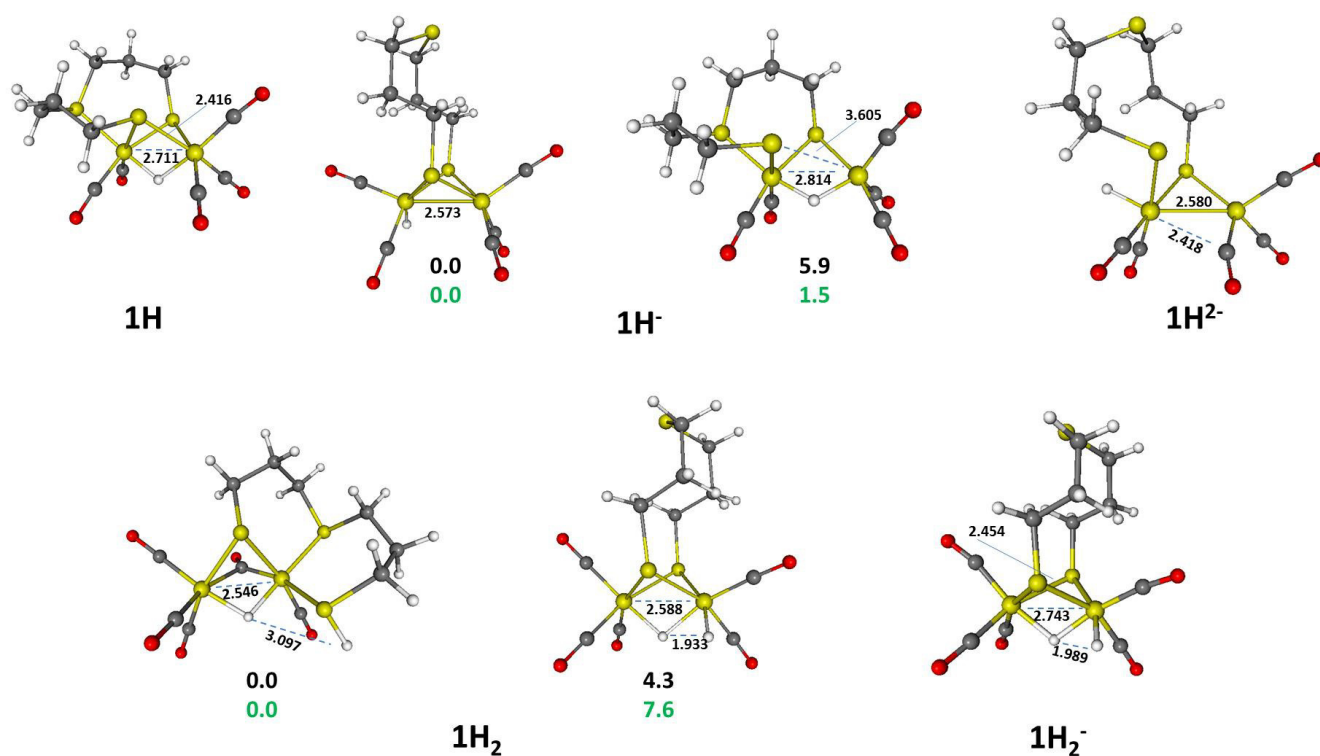


Figure 11. Structure and energetic of the most relevant isomers of **1H**, **1H⁻**, **1H²⁻**, **1H₂** and **1H₂⁻**. Distances are in Å. Energy differences are computed in kcal·mol⁻¹ with respect to the lowest energy isomers either in gas phase (black) or in CH₂Cl₂ (grey).

The monoprotonated intermediate 1H. According to the proposed mechanism depicted in Scheme 2, the one-electron reduction of **1** is followed by protonation of **1⁻** to give **1H**. In the exploration of the potential energy surface of **1H** species, two criteria have been adopted: **1H** species can be considered

either as the reduced form of $\mathbf{1H}^+$ or as the protonated form of $\mathbf{1}^-$. In the first case we used $\mathbf{1H}^+$ isomer as starting point for geometry optimization and in the second case we have proposed a number of possible protonated forms starting from the two most stable monoanionic structures associated with $\mathbf{1}$: ($\mathbf{1}^-_{\text{Fe-S}(1)}$ and $\mathbf{1}^-_{\text{Fe-S}(3)}$, see Figure 10).

The most stable isomer of $\mathbf{1H}$ is derived from the $\mathbf{1H}^+$ lowest energy isomer. It exhibits a bridging hydride and shows an elongation of both the Fe-Fe bond and of one of the Fe-S bonds, by 0.128 Å and 0.126 Å, respectively. This observation is easily explained on the basis of the non-bonding/antibonding character with respect to both Fe-Fe and Fe-S bond interactions of the LUMO of $\mathbf{1H}^+$ which becomes singly occupied upon reduction. According to NBO charge differences between $\mathbf{1H}^+$ (Figure S11) and $\mathbf{1H}$, the negative charge accumulation is mainly localized on the three sulfur atoms and on the apical CO ligand. The $\mathbf{1H}$ isomer, protonated at the thiolate sulfur atom, is much lower in energy with respect to $\mathbf{1H}^+$ (+6.7 kcal·mol⁻¹ instead of +20.8 kcal·mol⁻¹). The most stable terminal hydride form is 8.7 kcal·mol⁻¹ higher in energy than the lowest energy bridging hydride. In CH₂Cl₂, the bridging hydride is still the lowest energy form but the isomer protonated at the thiolate sulfur atom is only 1.9 kcal·mol⁻¹ higher in energy.

One-electron reduction of $\mathbf{1H}$. As for $\mathbf{1H}$, we used the 12 optimized $\mathbf{1H}$ isomers as starting points for $\mathbf{1H}^-$ minimum search. At variance with $\mathbf{1H}$, the most stable isomers in this case are obtained from protonation of the minimum structure of $\mathbf{1}^-$ and feature the hydride in terminal coordination on the unsaturated Fe atom. The most stable isomer with the hydride in bridging coordination is 5.9 kcal·mol⁻¹ higher in energy. Moreover, the formyl species, which was found as the most stable form in the $\mathbf{1H}^-$ analogue of Fe₂(pdt)(CO)₆⁵¹ is 13.5 kcal·mol⁻¹ higher in energy with respect to the lowest energy form. Due to the negative charge of $\mathbf{1H}^-$, the effect of the implicit CH₂Cl₂ presence becomes more relevant in determining the relative stability of the different isomers. Both gas phase and solvent simulations predict bridging hydride to be higher in energy than terminal hydride. In particular CH₂Cl₂ stabilizes the terminal hydride in apical position, while in gas-phase the equatorial position is favored. Regarding the electronic structure of $\mathbf{1H}^-$, NBO charges again indicate a negative charge accumulation on the sulfur atoms and on the five CO ligands. The negative charge of the hydride is only slightly affected by the reduction.

Reduction of the **1H** lowest energy isomer yields a **1H⁻** form, which is 5.9 kcal·mol⁻¹ higher in energy with respect to the lowest energy form.

The dianionic 1H²⁻ species. Further reduction of **1H⁻** yields **1H²⁻** species. Herein we considered only the energy differences computed in implicit CH₂Cl₂ since at the gas-phase level, the further electron added to **1H⁻** results not bound (the energy of any **1H⁻** isomer is always lower than those of **1H²⁻** isomers). All of the isomers of **1H²⁻** exhibit at least one completely dissociated Fe-S bond. In the most stable isomer, the hydride is terminally coordinated while the bridging hydride isomer is only 2.4 kcal·mol⁻¹ higher in energy. Another bridging hydride isomer with one bridging CO ligand is also close in energy (+2.9 kcal·mol⁻¹).

1H₂ species and its reduced form 1H₂⁻.

In this section we discuss the closely related structures of the diprotonated **1H₂** species and its reduced form **1H₂⁻**. We explored all of the possible structures obtained by protonation of the two **1H⁻** forms identified as the most representative (the bridging hydride form and the equatorial terminal hydride form reported in Figure 11).

The first two more stable isomers feature one bridging hydride. The most stable one has been obtained by protonation of the **1H⁻** isomer derived from **1⁻_{Fe-S(2)}**, while in the second isomer the second hydride is terminally coordinated to the Fe atom. NBO atomic charge differences (see Figure S13) between **1H⁻** and the most stable form of **1H₂** species evidence a significant CT toward the second proton (the second hydride carried a charge of 0.15 units with respect to the initial +1 charge of the incoming proton). We have found a further isomer of **1H₂** with a peculiar structure in which the Fe-Fe bond is completely dissociated and the two hydrides occupy the bridging region of the molecule (Figure S14). This isomer has already been identified in the H₂ production catalytic cycle of the simpler model Fe₂(pdt)(CO)₆ and is the analogues of the Fe-Fe butterfly form of Fe₂S₂(CO)₆⁴⁶. In these types of butterfly forms, it is always observed a planarization of the pseudo-tetrahedral Fe₂S₂ unit. In this particular case, in order to stabilize the electronic structure, the Fe-S bond with sulfide group is restored. This isomer is only 3.6 kcal·mol⁻¹ higher in energy, but in the case of Fe₂(pdt)(CO)₆, it was found that the computed pathway for H₂

formation starting from this structure is accompanied by a conformational rearrangement of the bridging bidentate ligand giving a quite large energy barrier for the H₂ evolution. For this reason, this structure will not be considered in the following.

Starting from the identified **1H₂** isomer structures, it has been explored the conformational space of **1H₂⁻**. Lower energy isomer of **1H₂⁻** features one Fe-S dissociated bond. The most stable **1H₂⁻** form features one bridging hydride close to a terminal hydride at 1.989 Å. We found two local minima in which both hydrides are bound to the unsaturated Fe with a H-H bond distance close to that of free molecular H₂. The structure obtained reducing lowest energy **1H₂** isomer results higher in energy.

As a final comment regarding the protonated forms, we found that protonation at the sulfide of the TBPT ligand yields structure much higher in energy with respect to the corresponding minimum energy isomers (Figure S15).

The computed potentials discussed above suggest that the second reduction process is the **1H₂→1H₂⁻** reduction, and therefore H₂ should be released from the **1H₂⁻** species. However, we also considered the H₂ formation from **1H₂** specie for sake of completeness.

In Figure 12 are reported the computed mechanisms for the H₂ formation starting from **1H₂** and **1H₂⁻** isomers in which the two hydrides are bound the Fe in bridging and terminal coordination, respectively.

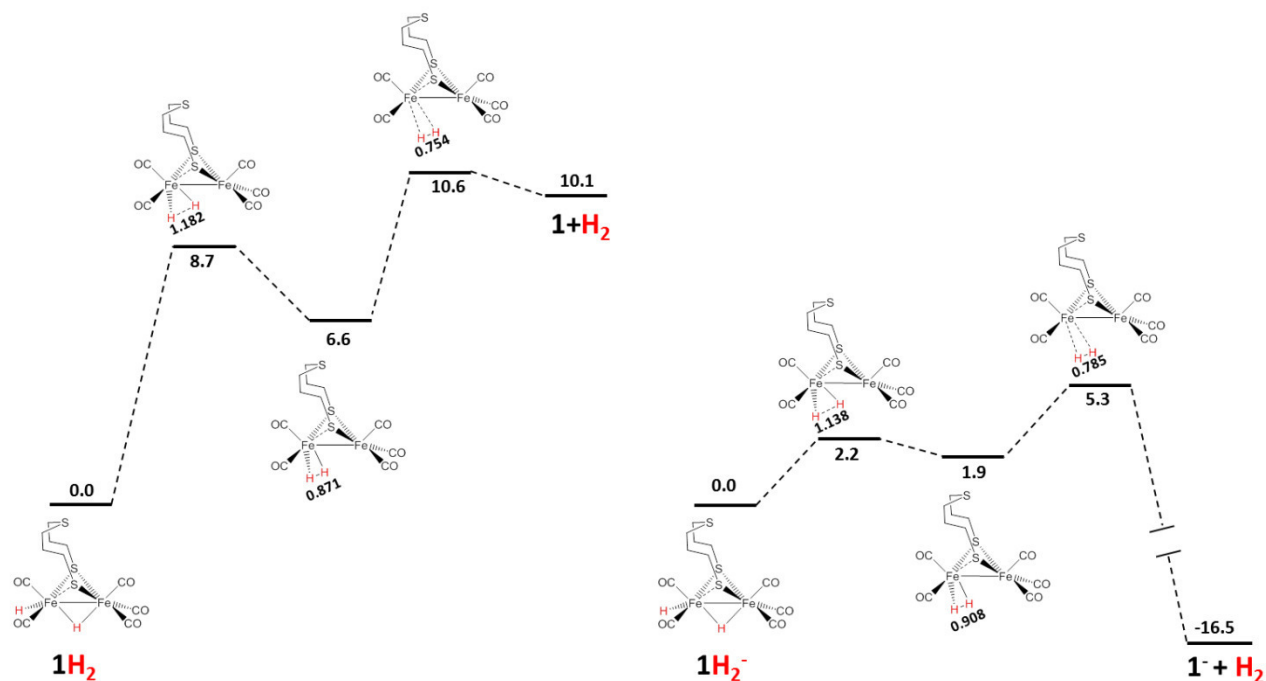


Figure 12. H₂ formation pathways starting from the bridging hydride/terminal hydride **1H₂** and **1H₂⁻** isomers. H-H interatomic distance in Å. Energy differences are computed in kcal·mol⁻¹ with respect to starting point.

As showed above, in the case of **1H₂**, this isomer is not the lowest in energy, at variance with **1H₂⁻**. Starting from **1H₂**, the final product is an H₂ molecule and the model in Fe^IFe^I redox state in a conformation that is 22.9 kcal·mol⁻¹ higher in energy with respect to the **1** lowest energy isomer. The highest free energy barrier (8.7 kcal·mol⁻¹) in this pathway involves an isomerization process in which the terminal hydride moves toward the bridging hydride with the formation of a η²-H₂ complex. The same pathway on the **1H₂⁻** PES goes through similar transition states and intermediates but the final product is the **1⁻** in its lowest energy form. In this case the highest free energy barrier is only 3.4 kcal·mol⁻¹.

In Figure 13 below is reported the H₂ production pathway starting from the **1H₂⁻** structure with one bridging hydride and one protonated sulfur atom that belong to the TBPT. This isomer is 5.4 kcal·mol⁻¹ higher in energy compared with the lowest energy isomer but the reduction potential suggest that this is actually the specie formed during the catalytic cycle.

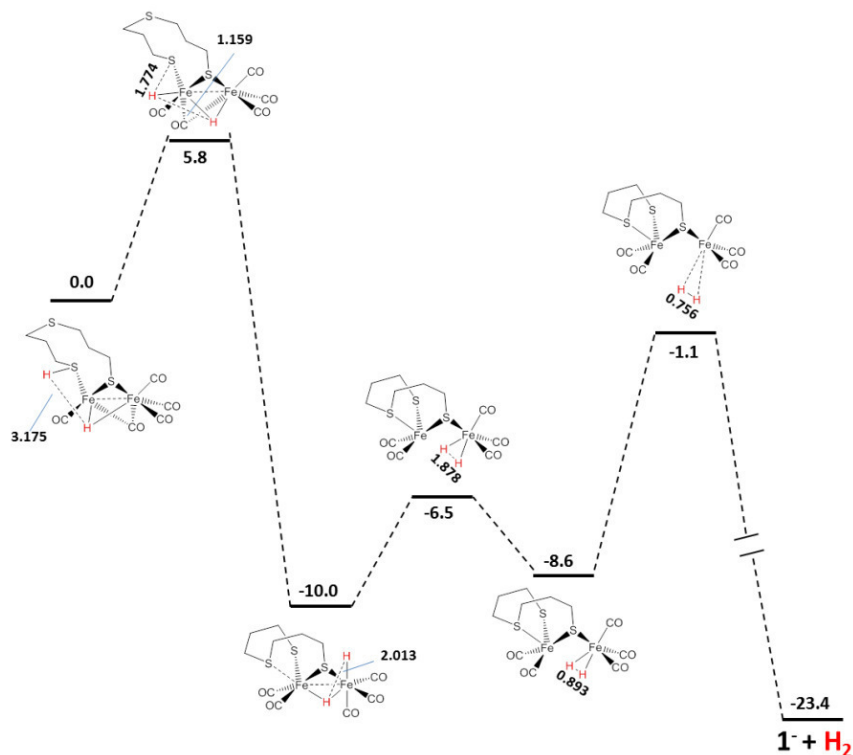
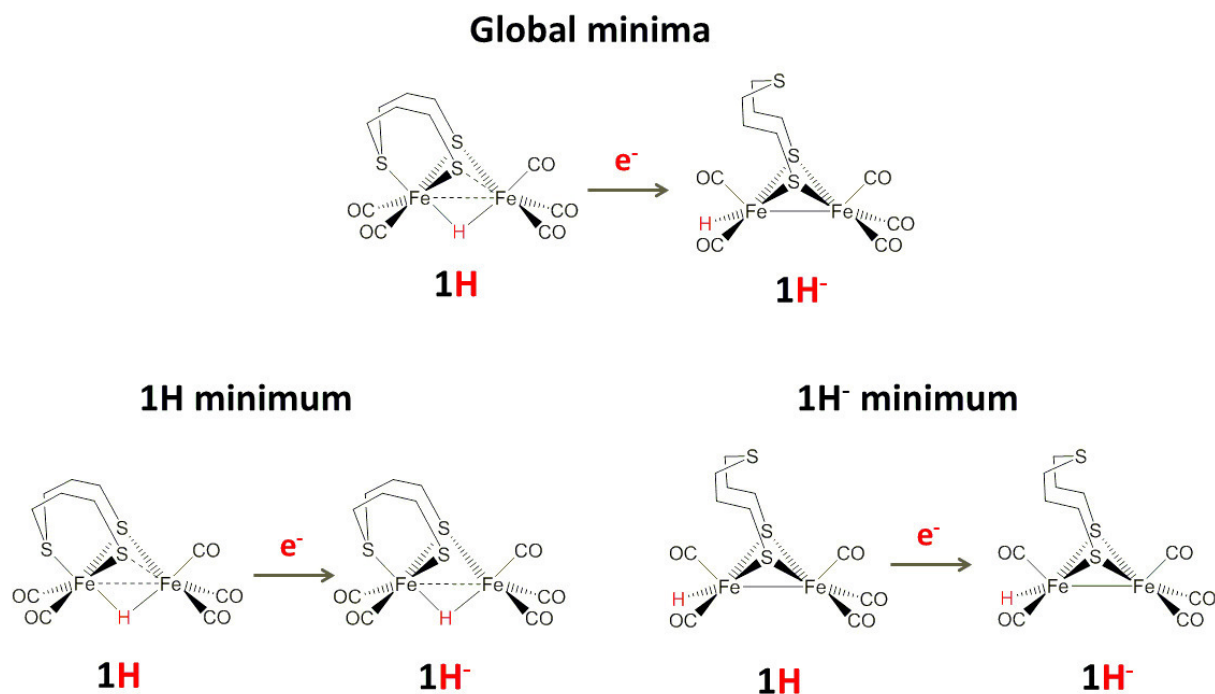


Figure 13. H₂ formation pathway starting from the bridging hydride/protonated TBPT **1H₂⁻** isomer. H-H interatomic distance in Å. Energy differences are computed in kcal·mol⁻¹ with respect to starting point.

This pathway is characterized by the isomerization to a lower energy isomer in which both hydride are bound to the same Fe atom and then by a 7.5 kcal·mol⁻¹ barrier toward the H₂ evolution. The same pathway on the **1H₂** PES has not been considered because the **1** isomer obtained after H₂ evolution would be too high in energy, therefore excluding the feasibility of this process.

Reduction potentials. In this section we have computed the reduction potential of three reductions likely involved in the H₂ formation mechanism. Resuming the experimental evidences, the cyclic voltammetry experiment in presence of 1 equivalent of acetic acid shows a peak at -1.75 V which is assigned to the **1H** → **1H⁻** reduction. Then, two not well separated peaks are found at -2.0 and -2.1 V which becomes a single peak when the acid concentration increases. Considering these two reduction processes as a single process, there are two possible assignments i.e the **1H⁻** → **1H²⁻** reduction or the **1H₂** → **1H₂⁻** reduction. In the following we try to elucidate the mechanism underlying this latter reduction peak. First we investigated the **1H** → **1H⁻** reduction, finding which are the most likely isomers involved according to the corresponding computed reduction potential, and successively, on the basis of these results we compute the either the **1H⁻** → **1H²⁻** or the **1H₂** → **1H₂⁻** reduction potential observing which process better fit with the -2.0/-2.1 V reduction potential.

We then considered the reduction of the **1H** and **1H⁻** species. As already pointed out above, to better reproduce the potentials, one negative charge was compensated by a K⁺ counter ion. The structures thus obtained were been fully optimized anew. The speciation presented above essentially suggests three possible couple of **1H** and **1H⁻** isomers. The first is the one formed by the lowest energy minimum of the two species, which are structurally different while the other two couples are formed by the **1H** and **1H⁻** isomers structurally similar as showed in Scheme 4.



Scheme 4. **1H** possible reduction pathways considered for the modelling of the -1.75 V reduction potential observed experimentally.

In Table 2 below are reported the reduction potential values for three reduction processes.

Table 2. Computed reduction potential (in V) referred to the Fc/Fc⁺ couple. δ is the difference (in mV) between computed and experimental value of -1.75 V.

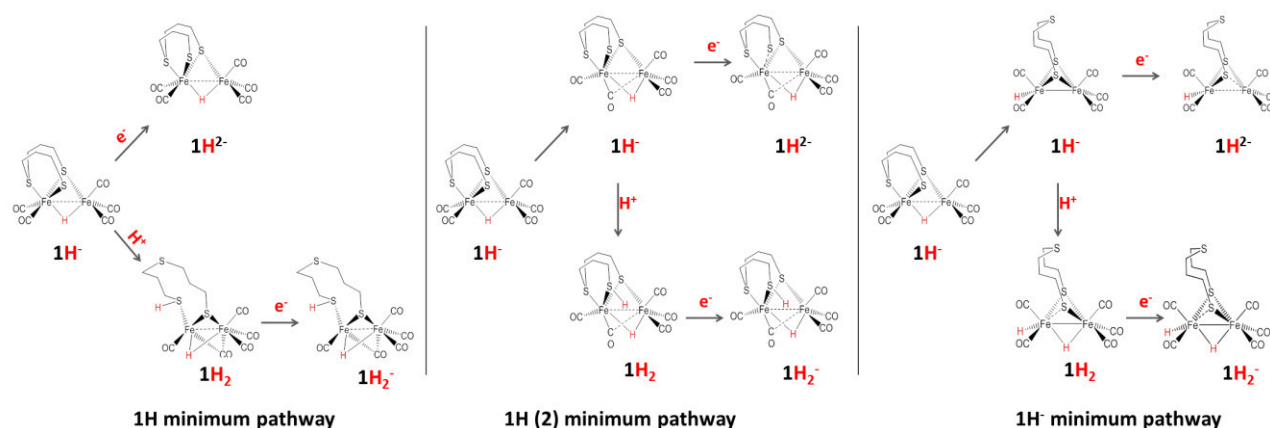
	Geometries	Computed Reduction potential (V)	δ (mV)
1H → 1H⁻	Global minima	-0.84	912
	1H global minimum	-1.79	-36
	1H⁻ global minimum	-0.13	1622

The differences between DFT values and the -1.75 V experimental value clearly show that the isomers likely involved in this reduction are the lowest energy **1H** isomer and the corresponding bridging hydride **1H⁻** isomer which results 5.6 kcal/mol higher in energy with respect to **1H⁻** global energy minimum.

We then considered the three reduction pathways considering **1H⁻** isomer as starting point for the modelling of the second reduction process. The idea was to find which was the most accessible reduction

pathway by requiring that the computed potential of the second reduction process is more negative than that of the $1\mathbf{H} \rightarrow 1\mathbf{H}^-$ reduction (-1.79 V). We have thus suggested three different pathways starting from $1\mathbf{H}^-$ isomer with the bridging hydride which are sketched below (Scheme 5).

Scheme 5. $1\mathbf{H}^-$ possible reduction pathways considered for the modelling of the -2.0/-2.1 V reduction potential observed experimentally.



In the $1\mathbf{H}$ minimum pathway the $1\mathbf{H}^- \rightarrow 1\mathbf{H}^{2-}$ reduction brings to the most stable $\mu\mathbf{H}$ $1\mathbf{H}^{2-}$ isomer and $1\mathbf{H}_2 \rightarrow 1\mathbf{H}_2^-$ reduction starts from the $1\mathbf{H}_2$ minimum structure. In the other two pathways, $1\mathbf{H}^-$ before reduction undergoes isomerization: in $1\mathbf{H}$ (2) minimum pathway to the most stable $\mu\mathbf{H}$ - $\mu\mathbf{CO}$ form, in $1\mathbf{H}^-$ minimum pathway to the terminal hydride form. Consequently, the $1\mathbf{H}_2 \rightarrow 1\mathbf{H}_2^-$ reduction process involve in $1\mathbf{H}$ (2) minimum pathway the $1\mathbf{H}_2$ structure obtained from the protonation of the $1\mathbf{H}^-$ minimum form in which one S atom of the TPBP ligand results protonated, while involve the $1\mathbf{H}_2^-$ minimum structure in $1\mathbf{H}^-$ minimum pathway.

In Table 3 are reported the computed reduction potentials.

Table 3. Computed reduction potentials (in V) referred to the Fc/Fc⁺ couple. δ is the difference (in mV) between computed and experimental value of -2.0 V (-2.1 V).

	Geometries	Computed Reduction potential (V)	δ (mV)
1H⁻→1H²⁻	1H minimum path	-1.54	461 (561)
1H₂→1H₂⁻		-1.64	356 (456)
1H⁻→1H²⁻	1H (2) minimum path	-2.64	-640 (-540)
1H₂→1H₂⁻		-1.61	390 (490)
1H⁻→1H²⁻	1H⁻ minimum path	-2.56	-560 (-460)
1H₂→1H₂⁻		-1.93	+70 (+170)

The results obtained suggest that the peak at -2.0/-2.1V might be assigned to the **1H₂→1H₂⁻** reduction along the **1H⁻** minimum path characterized by an isomerization of the **1H⁻** to its most stable isomer. To validate this hypothesis, we investigated the **1H⁻(μ H)→1H⁻(terminal H)** isomerization. Starting from the μ H isomer, the pathway is sketched in Figure 14.

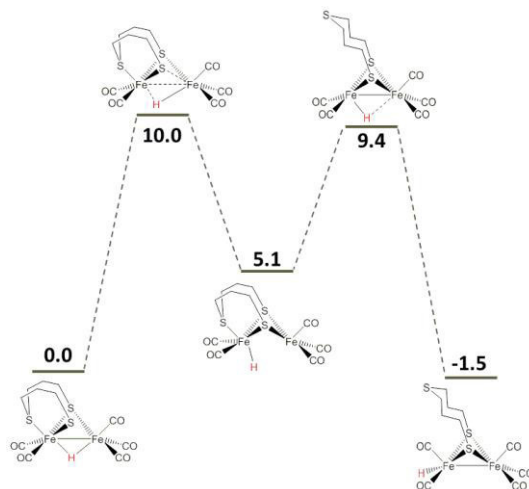


Figure 14. **1H⁻(μ H) → 1H⁻(terminal H)** isomerization pathway starting from the bridging hydride **1H⁻** isomer. Energy differences are computed in kcal·mol⁻¹ with respect to starting point.

Here we have first optimized the structures of intermediates and transition states (TSs) at gas-phase level and then the geometry has been refined considering the CH₂Cl₂ implicit correction. . Starting from the μ H isomer, we found a first intermediate in which the hydride partially loses its bridging coordination

while the dissociated Fe-S bond is restored. The TS between the μH isomer and the last mentioned intermediate is at $10.0 \text{ kcal}\cdot\text{mol}^{-1}$. Then the dissociation of the Fe-S bond (S from the sulfide of the TBPT ligand) yields the final 1H^- terminal hydride form. In this step, the TS corresponds to the 1H^- terminal hydride rotated form obtained from the rotation of the $\text{Fe}(\text{CO})_2\text{H}$ group, and the associated barrier is $4.3 \text{ kcal}\cdot\text{mol}^{-1}$.

In summary, the H_2 formation mechanism proposed on the basis of the DFT speciation on the possible species involved and also on the computed reduction potentials, is shown in Figure 15.

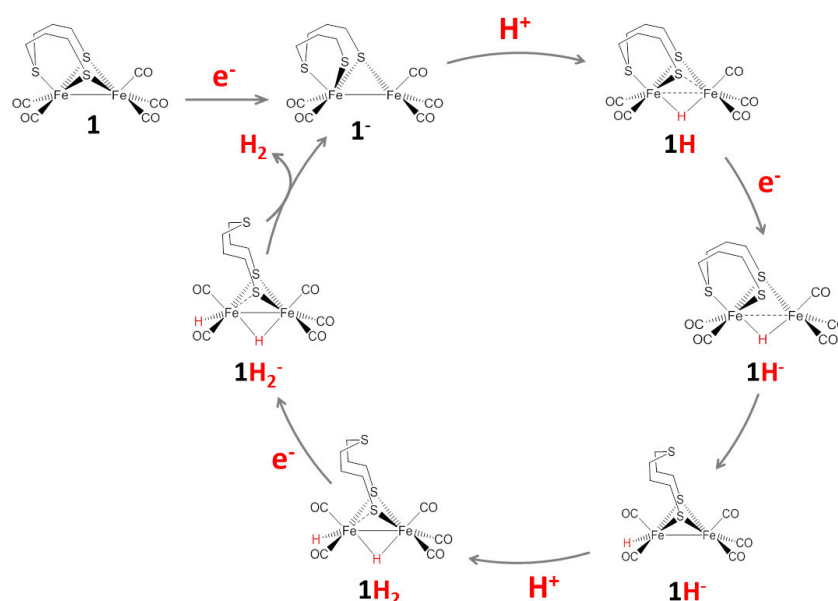


Figure 15. DFT mechanism proposed for the H_2 formation catalyzed by complex **1**.

The $1 \rightarrow 1^-$ reduction yields the formation of the 1^- isomer with one dissociated Fe-S bond; this isomer is the same associated with the $1^- \rightarrow 1^{2-}$ reduction. The first protonation step occurs at the bridging position with the formation of a 1H isomer that retains the 1^- structure with one dissociated Fe-S bond. Similarly, in the successive $1\text{H} \rightarrow 1\text{H}^-$ reduction, 1H^- retains the 1^- structure. This latter undergoes isomerization toward the 1H^- lowest energy isomer characterized by the hydride in equatorial terminal position and by the dissociation of the Fe-S bond. The highest computed energy barrier for this process is 10.0 kcal/mol . The second protonation step yields the 1H_2 isomer with one bridging and one terminal hydride; Fe-S bond is still partially dissociated. Finally, the best match between the possible reduction mechanisms and the -

2.0/-2.1 V second peak in the cyclic voltammetry experiment is assigned to the $\mathbf{1H}_2 \rightarrow \mathbf{1H}_2^-$ reduction with the formation of the $\mathbf{1H}_2^-$ lowest energy form. Moreover, the free energy barrier for the H_2 release from $\mathbf{1H}_2^-$ is $3.4 \text{ kcal}\cdot\text{mol}^{-1}$.

Conclusions

Cyclic voltammetry investigations of the model complexes $[\text{Fe}_2(\text{CO})_5\{\text{TBPT}\}]$ (**1**) and $[\text{Fe}_2(\text{CO})_4(\text{P}(\text{OMe})_3)\{\text{TBPT}\}]$ (**2**) have been investigated in the absence and presence of AcOH. Complex **1** (in MeCN-NBu₄PF₆ or CH₂Cl₂-NBu₄PF₆) is reduced in two successive one-electron steps with the normal ordering of potentials ($E^\circ_1 - E^\circ_2 > 0$). The first one-electron reduction wave of complex **1** ($E_{\text{pc1}} = -1.76 \text{ V}$, CH₂Cl₂, or -1.615 V , MeCN) is observed as a shoulder at the second one-electron reduction wave ($E_{\text{pc2}} = -1.89 \text{ V}$, CH₂Cl₂, or -1.78 V , MeCN). The irreversibility of the reduction of complex **1** arises from fast follow-up reactions that might be mainly after the second electron transfer step. Increasing the scan rate (to more than $1 \text{ V}\cdot\text{s}^{-1}$) leads to slightly reversible reduction of complex **1** in CH₂Cl₂ as well as overlapping of its two cathodic waves. This is not the case for MeCN-NBu₄PF₆ solution. In comparison, cyclic voltammetry of complex **2** in CH₂Cl₂-NBu₄PF₆ solution shows only one irreversible one-electron cathodic wave ($E_{\text{pc}} = -2.11 \text{ V}$) while a second cathodic wave could not be observed within the solvent window reflecting the high electron richness of the iron centers. Moreover, the reduction wave of complex **2** is always irreversible at all scan rates up to $\nu = 10 \text{ V}\cdot\text{s}^{-1}$. The irreversibility of the reduction of complexes **1** and **2** is also observed for other $[\text{Fe}_2\text{S}_3]$ models, which might be due to follow-up reactions initiated most likely by decoordination of the pendent thioether⁴⁰ (for **1**, **2** and $[\text{Fe}_2(\text{CO})_5\{\mu-(\text{SCH}_2)_2\text{CH}_2\text{S}-\mu\text{R}\}]$ ⁴⁰) or dissociation of SR₂ in $[\text{Fe}_2(\text{CO})_5(\text{SR}_2)\{\mu-(\text{SCH}_2)_2\text{CH}_2\}]$ ³⁸. In the presence of AcOH, the monoanionic species of **1** and **2** undergo protonation followed by reduction to give \mathbf{AH}^- (A = **1** or **2**) at the same potential (or less negative) necessary to reduce the neutral complexes. Protonation of \mathbf{AH}^- to \mathbf{AH}_2 gives rise to evolution of H₂ from $\mathbf{2H}_2$, but not from $\mathbf{1H}_2$. For this reason, a catalytic process can be observed at potential less negative than that required for the reduction of the neutral complex **2**, but not **1**. Further

reduction of \mathbf{AH}_2 causes H_2 release from \mathbf{AH}_2^- and regenerating \mathbf{A}^- to close the cycle. Comparing the plots of I_c/I_p vs. equiv. AcOH for complexes **1** and **2** and according to Evan's scale for the catalytic efficiency (*C.E.*) of [FeFe]-hydrogenase models,⁴⁹ *C.E.* for complex **1** is S (descriptor for strong) and for complex **2** is M (descriptor for medium). DFT calculations are performed on the structures of the neutral, monoanionic and dianionic species of complex **1** as well as on all possible intermediates involved in its catalytic cycle. The DFT level of theory adopted in this work nicely reproduces the XRD geometry of **1** and also reduction potentials of the couples $\mathbf{1}/\mathbf{1}^-$ and $\mathbf{1}^-/\mathbf{1}^{2-}$. Calculations show that all the reduced forms (protonated or not) feature the dissociation of one Fe-S bond. The evolution of H_2 from $\mathbf{1H}_2$ is energetically not feasible thus providing support to the possible mechanisms of H_2 release from $\mathbf{1H}_2^-$.

Experimental Section

Materials and Techniques.

Compounds **1** and **2** were synthesized according to the literature procedures.^{17, 39} Chemicals were purchased from Fisher Scientific, Aldrich or Acros and were used without further purification. All solvents were dried and distilled prior to use according to standard methods.

Electrochemistry.

Instrumentation and Procedures. Cyclic voltammetric measurements were conducted in three-electrode technique [glassy carbon disk (diameter = 1.6 mm), the working electrode; reference electrode, Ag/AgCl in CH_3CN ; and a Pt wire, the counter electrode] using a Reference 600 Potentiostat (Gamry Instruments). All experiments were performed in CH_3CN solutions containing 0.1 M $n\text{-Bu}_4\text{NBF}_4$ at room temperature. The solutions were purged with N_2 for 5 minutes and a stream of N_2 was maintained over the solutions during the measurements. All potential values reported in this paper are referenced to the potential of the Fc/Fc⁺ couple.

DFT Calculations.

Computations were performed using pure GGA BP86 functional. The Resolution of Identity (RI) technique was adopted for pure functionals in order to save CPU time. Basis sets of triple- ζ plus

polarization split valence quality (TZVP) were adopted for all atoms in the complex. All the computations presented have been carried out using TURBOMOLE⁵² suite of programs. DFT grid-size was set to standard m3 value. Ground state geometry optimizations were carried out with convergence criteria fixed to 10^{-6} hartree for the energy and 0.001 hartree·bohr⁻¹ for the gradient norm vector. Solvent effect is accounted by using the COSMO (Conductor-like Screening Model) approach⁵³. Atomic charges have been computed within the Natural Bond Orbital (NBO) approach.

The computed reduction potentials are referred to the ferrocenium/ferrocene couple (Fc/Fc⁺), allowing the comparison between experimental and computed values. The absolute reduction potential for the Fc/Fc⁺ couple computed at BP86/TZVP, CH₂Cl₂ COSMO implicit solvent $\epsilon = 8.9$ = it is equal to 5.06 V. The computation of the absolute potentials have been carried out using Nerst equation $\Delta G = -nF \cdot \Delta E$, where n is the number of electrons transferred, F is the Faraday constant (23.061 kcal·mol⁻¹) and ΔE is the total free energy difference between reduced and oxidized forms computed at COSMO level (total DFT energies are computed at the COSMO optimized geometry; enthalpy and entropy contributions to computed free energies have been computed at the gas-phase geometry from the estimated total partition energy at 298.15 K and 1 bar, adopting BP86/DFT scaling factor equal to 0.9914).

Acknowledgments. H. Abul-Futouh, thanks the Deutscher Akademischer Austausch Dienst (DAAD) for scholarship. Thanks to Dr. M. Rudolph for the valuable discussions related to the electrochemistry part.

Supporting Information Available. Figure S1 shows the cyclic voltammetry of 1.0 mM complex **1** in CH₂Cl₂-NBu₄PF₆ solution at $\nu = 0.2$ V·s⁻¹. Cyclic voltammetry of 1.0 mM complex **2** and [Fe₂(CO)₆{ μ -bdt}] (bdt = benzenedithiolate) in CH₂Cl₂-NBu₄PF₆ solutions at $\nu = 0.2$ V·s⁻¹ is shown in Figure S2. Cyclic voltammetry of 2.0 mM AcOH in CH₂Cl₂-NBu₄PF₆ solution at $\nu = 0.2$ V·s⁻¹ is depicted in Figure S3.

References

- [1] Wuebbles, D. J.; Jain, A. K. *Fuel Process. Technol.* **2001**, *71*, 99-119.
- [2] Dunn, S. *Int. J. Hydrogen Energ.* **2002**, *27*, 235-264.
- [3] Momirlan, M.; Veziroglu, T. N. *Int. J. Hydrogen Energ.* **2005**, *30*, 795-802.
- [4] Stephenson, L. H. S. M. *Biochem. J.* **1931**, *25*, 205-214.
- [5] Nicolet, Y.; Piras, C.; Legrand, P.; Hatchikian C. E.; Fontecilla-Camps, J. C. *Structure* **1999**, *7*, 13-23.
- [6] Peters, J. W.; Lanzilotta, W. N.; Lemon B. J.; Seefeldt, L. C. *Science* **1998**, *282*, 1853-1858.
- [7] Apfel, U.-P.; Halpin, Y.; Görls, H.; Vos, J. G.; Schweizer, B.; Linti G.; Weigand, W. *Chem. Biodiversity* **2007**, *4*, 2138-2148.
- [8] Singleton, M. L.; Jenkins, R. M.; Klemashevich C. L.; Darensbourg, M. Y. *C. R. Chim.*, **2008**, *11*, 861-874.
- [9] Apfel, U.-P.; Kowol, C. R.; Halpin, Y.; Kloss, F.; Kübel, J.; Görls, H.; Vos, J. G.; Keppler, B. K.; Morera, E.; Lucente G.; Weigand, W. *J. Inorg. Biochem.* **2009**, *103*, 1236-1244.
- [10] C. M. Thomas, O. Rüdiger, T. Liu, C. E. Carson, M. B. Hall and M. Y. Darensbourg, *Organometallics*, 2007, **26**, 3976-3984.
- [11] R. Trautwein, L. R. Almazahreh, H. Görls and W. Weigand, *Z. Für Anorg. Allg. Chem.*, 2013, **639**, 1512-1519.
- [12] J.-F. Capon, S. Ezzaher, F. Gloaguen, F. Y. Petillon, P. Schollhammer, J. Talarmin, T. J. Davin, J. E. McGrady and K. W. Muir, *New J. Chem.*, 2007, **31**, 2052-2064.
- [13] F. Wang, M. Wang, X. Liu, K. Jin, W. Dong and L. Sun, *Dalton Trans.*, 2007, 3812-3819.
- [14] H.-G. Cui, M. Wang, W.-B. Dong, L.-L. Duan, P. Li and L.-C. Sun, *Polyhedron*, 2007, **26**, 904-910.
- [15] S. Jiang, J. Liu and L. Sun, *Inorg. Chem. Commun.*, 2006, **9**, 290-292.
- [16] L.-C. Song, Z.-Y. Yang, Y.-J. Hua, H.-T. Wang, Y. Liu and Q.-M. Hu, *Organometallics*, 2007, **26**, 2106-2110.

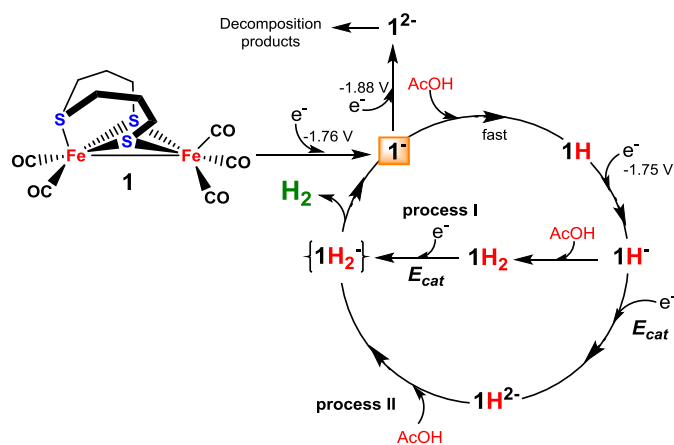
- [17] J. Windhager, M. Rudolph, S. Bräutigam, H. Görls and W. Weigand, *Eur. J. Inorg. Chem.*, 2007, 2748-2760.
- [18] Harb, M. Ph.D. Dissertation, Friedrich-Schiller Universität Jena, Jena, Thüringen, **2009**.
- [19] U.-P. Apfel, D. Troegel, Y. Halpin, S. Tschierlei, U. Uhlemann, H. Görls, M. Schmitt, J. Popp, P. Dunne, M. Venkatesan, M. Coey, M. Rudolph, J. G. Vos, R. Tacke and W. Weigand, *Inorg. Chem.*, 2010, **49**, 10117-10132.
- [20] R. S. Glass, N. E. Gruhn, E. Lorance, M. S. Singh, N. Y. T. Stessman and U. I. Zakai, *Inorg. Chem.*, 2005, **44**, 5728-5737.
- [21] L. R. Almazahreh, U.-P. Apfel, W. Imhof, M. Rudolph, H. Görls, J. Talarmin, P. Schollhammer, M. El-khateeb and W. Weigand, *Organometallics*, 2013, **32**, 4523-4530.
- [22] A. Le Cloirec, S. C. Davies, D. J. Evans, D. L. Hughes, C. J. Pickett, S. P. Best and S. Borg, *Chem. Commun.*, 1999, 2285-2286.
- [23] H. Li and T. B. Rauchfuss, *J. Am. Chem. Soc.*, 2002, **124**, 726-727.
- [24] L.-C. Song, Z.-Y. Yang, H.-Z. Bian, Y. Liu, H.-T. Wang, X.-F. Liu and Q.-M. Hu, *Organometallics*, 2005, **24**, 6126-6135.
- [25] L. R. Almazahreh, W. Imhof, J. Talarmin, P. Schollhammer, H. Görls, M. El-khateeb and W. Weigand, *Dalton Trans.*, 2015, **44**, 7177-7189.
- [26] R. Goy, L. Bertini, C. Elleouet, H. Görls, G. Zampella, J. Talarmin, L. De Gioia, P. Schollhammer, U.-P. Apfel and W. Weigand, *Dalton Trans.*, 2015, **44**, 1690-1699.
- [27] R. Goy, L. Bertini, H. Görls, L. De Gioia, J. Talarmin, G. Zampella, P. Schollhammer and W. Weigand, *Chem. – Eur. J.*, 2015, **21**, 5061-5073.
- [28] M. K. Harb, J. Windhager, A. Daraosheh, H. Görls, L. T. Lockett, N. Okumura, D. H. Evans, R. S. Glass, D. L. Lichtenberger, M. El-khateeb and W. Weigand, *Eur. J. Inorg. Chem.*, 2009, 3414-3420.

- [29] J.-F. Capon, F. Gloaguen, F. Y. Pétilion, P. Schollhammer and J. Talarmin, *Coord. Chem. Rev.*, 2009, **253**, 1476-1494.
- [30] J. W. Tye, J. Lee, H.-W. Wang, R. Mejia-Rodriguez, J. H. Reibenspies, M. B. Hall and M. Y. Darensbourg, *Inorg. Chem.*, 2005, **44**, 5550-5552.
- [31] C. M. Thomas, T. Liu, M. B. Hall and M. Y. Darensbourg, *Inorg. Chem.*, 2008, **47**, 7009-7024.
- [32] J. D. Lawrence, H. Li and T. B. Rauchfuss, *Chem. Commun.*, 2001, 1482-1483.
- [33] L.-C. Song, Z.-Y. Yang, H.-Z. Bian and Q.-M. Hu, *Organometallics*, 2004, **23**, 3082-3084.
- [34] M. Razavet, S. C. Davies, D. L. Hughes, J. E. Barclay, D. J. Evans, S. A. Fairhurst, X. Liu and C. J. Pickett, *Dalton Trans.*, 2003, 586-595.
- [35] M. Razavet, S. C. Davies, D. L. Hughes and C. J. Pickett, *Chem. Commun.*, 2001, 847-848.
- [36] M. Razavet, S. J. Borg, S. J. George, S. P. Best, S. A. Fairhurst and C. J. Pickett, *Chem. Commun.*, 2002, 700-701.
- [37] S. J. George, Z. Cui, M. Razavet and C. J. Pickett, *Chem. – Eur. J.*, 2002, **8**, 4037-4046.
- [38] M.-Q. Hu, C.-B. Ma, Y.-T. Si, C.-N. Chen and Q.-T. Liu, *J. Inorg. Biochem.*, 2007, **101**, 1370-1375.
- [39] A. Q. Daraosheh, M. K. Harb, J. Windhager, H. Görls, M. El-khateeb and W. Weigand, *Organometallics*, 2009, **28**, 6275-6280.
- [40] A. Jablonskytė, J. A. Wright, S. A. Fairhurst, L. R. Webster and C. J. Pickett, *Angew. Chem. Int. Ed.*, 2014, **53**, 10143-10146.
- [41] J.-F. Capon, F. Gloaguen, P. Schollhammer and J. Talarmin, *J. of Electroanal. Chem.*, 2004, **566**, 241-247.
- [42] D. T. Pierce and W. E. Geiger, *J. Am. Chem. Soc.*, 1992, **114**, 6063-6073. And references cited therein.
- [43] A. J. Downard, A. M. Bond, A. J. Clayton, L. R. Hanton and D. A. McMorran, *Inorg. Chem.*, 1996, **35**, 7684-7690.

- [44] S. Stephen Creager, "Solvents and Supporting Electrolytes" in Handbook of Electrochemistry, Ed. Zoski, C. G., Elsevier, Amsterdam, 2007, Chapter 3, Section 3.2, pp 58-60.
- [45] X. Hu, B. S. Brunshwig and J. C. Peters, *J. Am. Chem. Soc.*, 2007, **129**, 8988-8998.
- [46] C. Greco, G. Zampella, L. Bertini, M. Bruschi, P. Fantucci and L. De Gioia, *Inorg. Chem.*, 2007, **46**, 108-116.
- [47] S. J. Borg, T. Behrsing, S. P. Best, M. Razavet, X. Liu and C. J. Pickett, *J. Am. Chem. Soc.*, 2004, **126**, 16988-16999.
- [48] D. H. Pool and D. L. DuBois, *J. Organomet. Chem.*, 2009, **694**, 2858-2865.
- [49] G. A. N. Felton, C. A. Mebi, B. J. Petro, A. K. Vannucci, D. H. Evans, R. S. Glass and D. L. Lichtenberger, *J. Organomet. Chem.*, 2009, **694**, 2681-2699.
- [50] L. Bertini; M. Bruschi; L. De Gioia; P. Fantucci, *J. Phys. Chem. A*, 2007, **111**, 12152-12162.
- [51] C. Greco; G. Zampella; L. Bertini; M. Bruschi; P. Fantucci; L. De Gioia, *Inorg. Chem.*, 2007, **46**, 108-116.
- [52] R. Ahlrichs; M. Bar; M. Haser; H. Horn; C. Kolmel, *Chem. Phys. Lett.*, 1989, **162**, 165-169.
- [53] A. Klamt, *J. Phys. Chem. A*, 1995, **99**, 2224-2235.

Synopsis

The electrochemical and electrocatalytic behaviour of two [FeFe] hydrogenase model complexes containing [Fe₂S₃] moiety has been investigated in the absence and presence of AcOH. The structure of the reduced species as well as the mechanism of the H₂ production was elucidating in detail by Density Functional theory calculations.



Supporting Information

Electrochemical Investigations and Density Functional Calculations on Proton Reduction Cycle Catalyzed by [FeFe]-Hydrogenase Models Featuring [Fe₂S₃] Core

Hassan Abul-futouh,[†] , Laith R. Almazahreh,[†] Ahmad Q. Daraosheh,[‡] Mohammad El-khateeb,[⊥] Luca De Gioia,[§] Giuseppe Zampella^{,§} Wolfgang Weigand^{*,†} and Luca Bertini^{*,§}*

*[†]Institut für Anorganische und Analytische Chemie, Friedrich-Schiller-Universität Jena,
Humboldtstrasse 8, D-07743 Jena, Germany,*

[‡]Faculty of pharmacy, Isra University, P.O. Box 22, 11622 Amman, Jordan.

[§]Department of Biotechnology and Biosciences, University of Milano-Bicocca, 20126 Milan, Italy,

[⊥]Chemistry Department, Jordan University of Science and Technology, 22110 Irbid, Jordan.

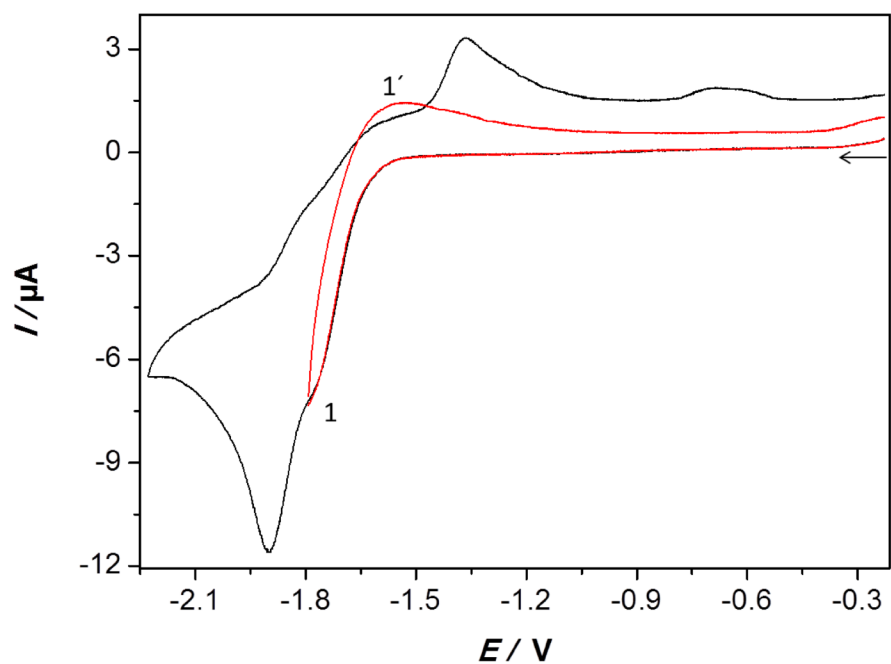


Figure S1. Cyclic voltammetry of 1.0 mM complex **1** in $\text{CH}_2\text{Cl}_2\text{-NBu}_4\text{PF}_6$ solution at $\nu = 0.2 \text{ V}\cdot\text{s}^{-1}$, where the red curve is obtained by reversing the forward scan at $\sim -1.79 \text{ V}$. E is in V against the ferrocenium/ferrocene couple. The arrow indicates the scan direction.

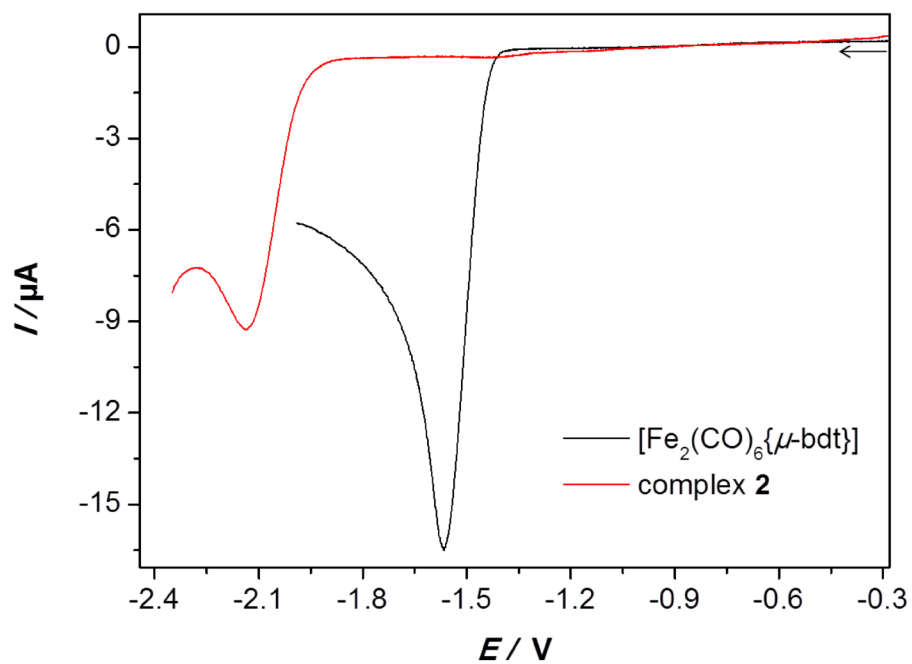


Figure S2. Cyclic voltammetry of 1.0 mM complex **2** and $[\text{Fe}_2(\text{CO})_6\{\mu\text{-bdt}\}]$ (bdt = benzenedithiolate) in $\text{CH}_2\text{Cl}_2\text{-NBu}_4\text{PF}_6$ solutions at $\nu = 0.2 \text{ V}\cdot\text{s}^{-1}$. E is in V against the ferrocenium/ferrocene couple. The arrow indicates the scan direction.

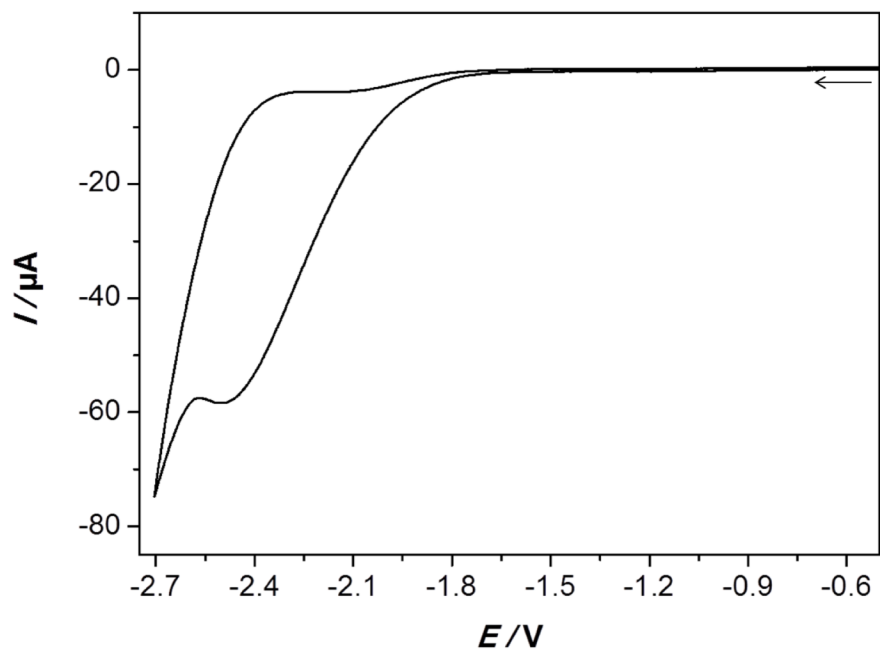


Figure S3. Cyclic voltammetry of 2.0 mM AcOH in $\text{CH}_2\text{Cl}_2\text{-NBu}_4\text{PF}_6$ solution at $\nu = 0.2 \text{ V}\cdot\text{s}^{-1}$. E is in V against the ferrocenium/ferrocene couple. The arrow indicates the scan direction.

Table S1. Fe-Fe and Fe-S experimental (XRD) and DFT optimized bond distances (in Å) for the various isomers considered. Fe-S_{prox} is the Fe-S bond distances between the proximal Fe and the sulfide of the bisthiolatepropylsulfide (BTPS).

	Fe-Fe		Fe-S		Fe-S _{prox}	
1 (XRD)	2.501	2.245	2.257	2.304	2.248	2.245
1	2.524	2.295	2.279	2.350	2.282	2.258
1_{rot}	2.576	2.348	2.323	2.257	2.392	2.304
1⁻	2.731	2.387	2.290	2.389	2.364	2.342
1_{rot}⁻	2.573	2.262	3.430	2.341	2.398	2.303
1⁻Fe-S(1)	2.560	2.352	2.329	2.411	2.287	5.048
1⁻Fe-S(2)	2.591	2.401	3.364	2.306	2.240	2.311
1⁻Fe-S(3)	2.422	2.224	4.547	2.364	2.316	5.798
1_{μCO-Fe-S}	2.561	2.294	2.261	2.347	2.336	5.625
1²⁻_{μCO-Fe-S}	2.437	2.355	2.425	2.380	2.404	5.047
1²⁻_{2Fe-S}	2.432	2.334	4.562	2.318	2.304	5.870
1²⁻_{Fe-S(3)}	2.453	2.294	4.643	2.409	2.356	5.844

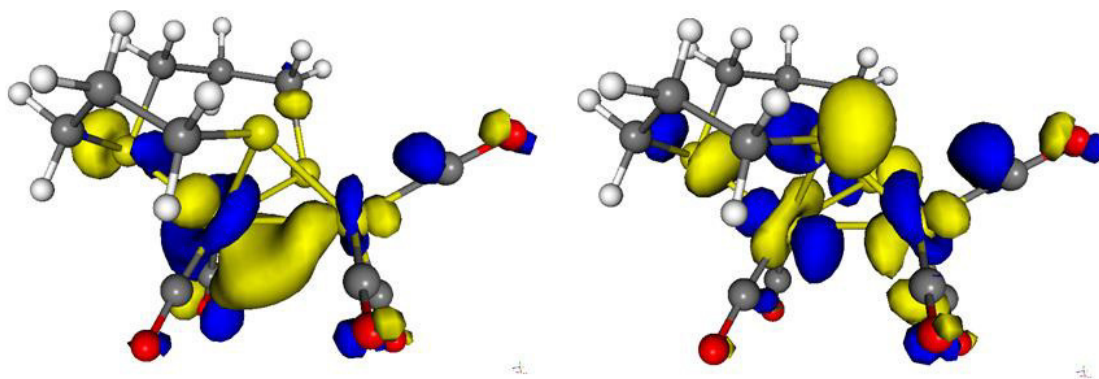


Figure S4. HOMO (left) and LUMO (right) of **1** minimum structure. Isosurface at 0.05 au.

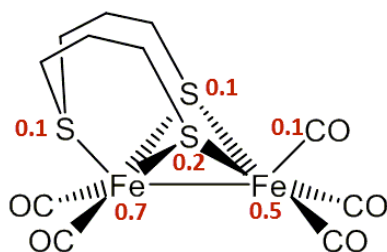


Figure S5. LUMO Mulliken atomic population (in electrons) after one-electron reduction of **1**. Only values equal or higher than 0.1 are reported.

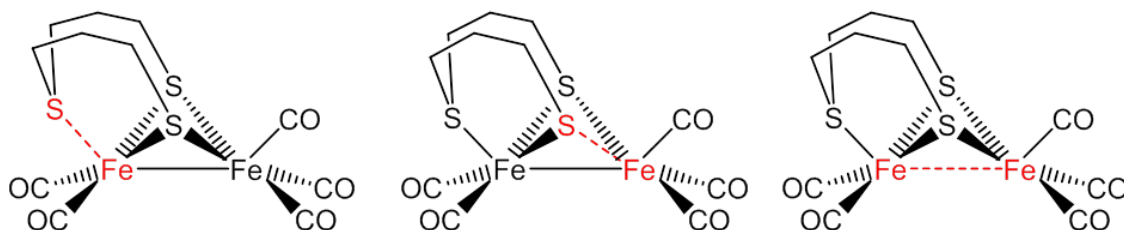


Figure S6. Possible Fe-S bond dissociation upon reduction of **1** according to the analysis of the Frontier MO.

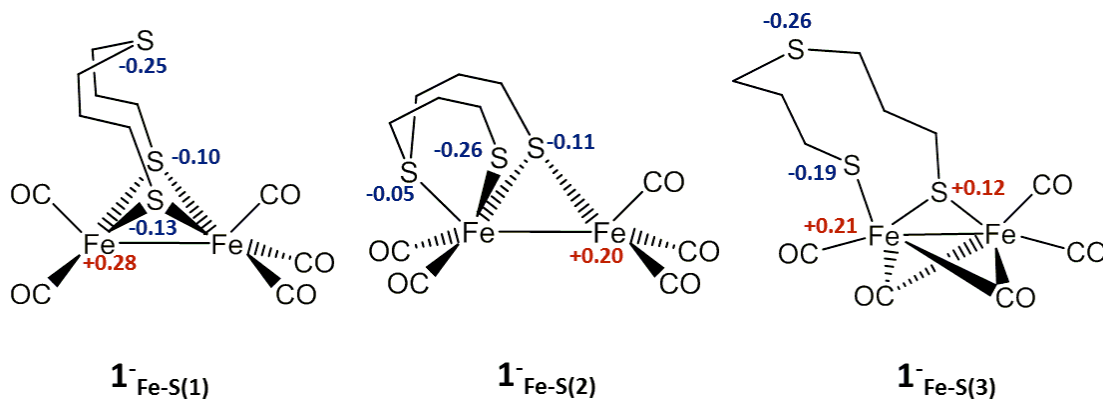


Figure S7. NBO atomic charge differences between $1^-_{\text{Fe-S}(1)}$, $1^-_{\text{Fe-S}(2)}$, $1^-_{\text{Fe-S}(3)}$ and **1**. Positive values and negative values indicate increasing of the positive and negative charges respectively.

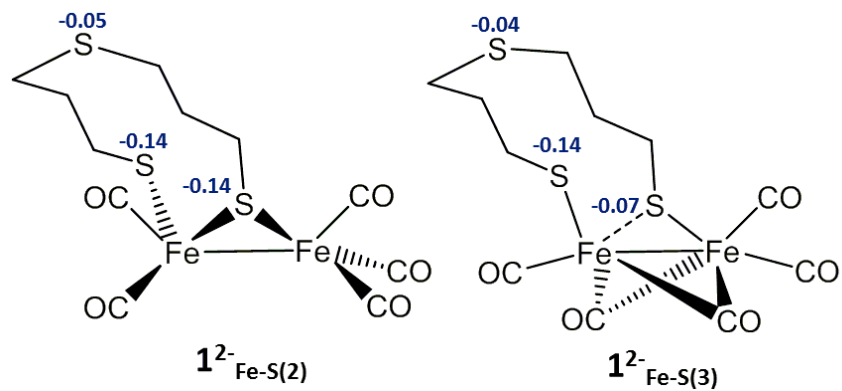


Figure S8. NBO atomic charge differences between $1^{2-}_{\text{Fe-S}(2)}$, $1^{2-}_{\text{Fe-S}(3)}$ and $1^{-}_{\text{Fe-S}(3)}$ computed at the corresponding minimum structures. Negative values indicate increasing of the negative charge.

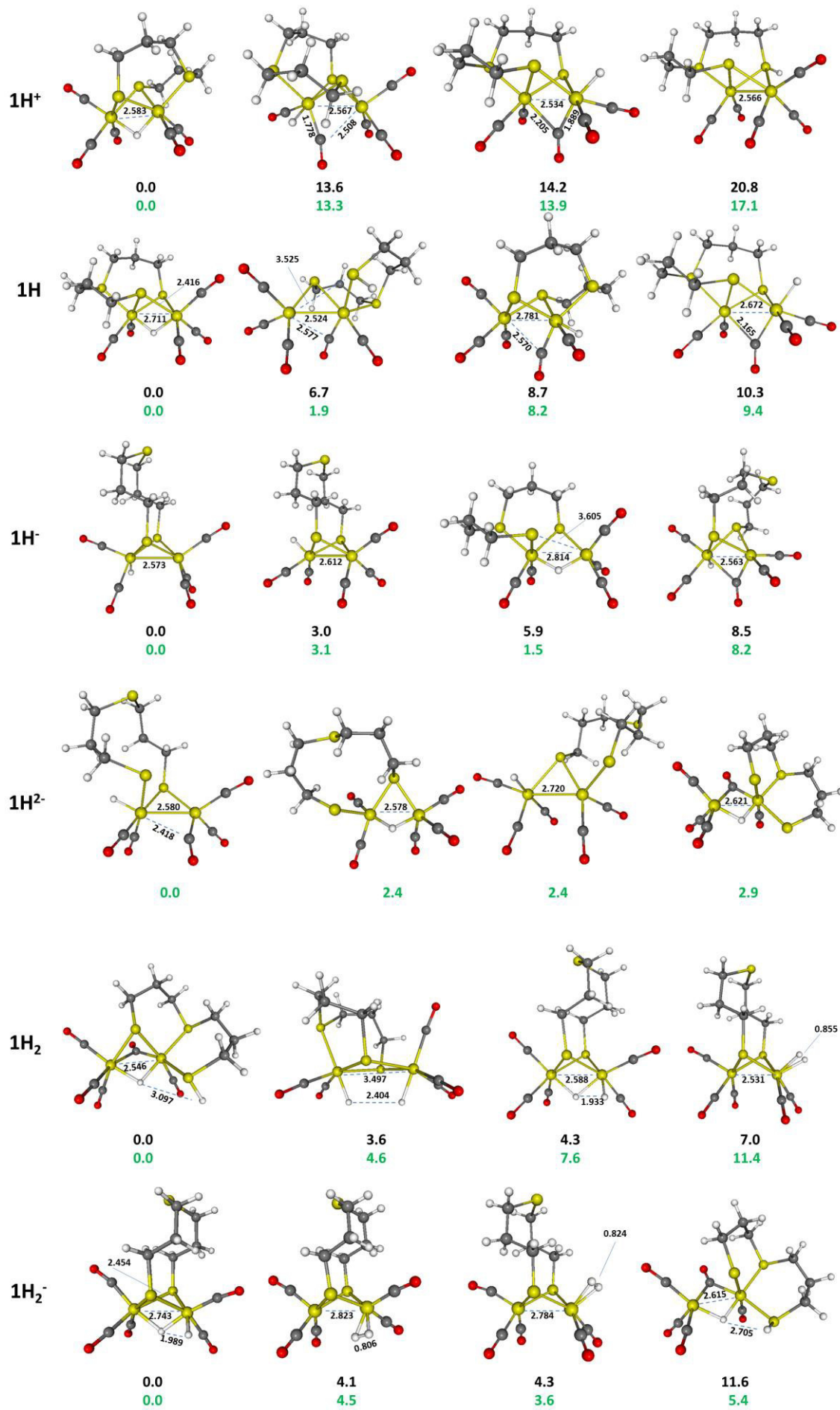


Figure S9. Structure and energetic of the first four most stable isomers of 1H^+ , 1H , 1H^- , 1H^{2-} , 1H_2 , 1H_2^- . Distances are given in Å. Energy differences are computed in $\text{kcal}\cdot\text{mol}^{-1}$ with respect to the lowest energy isomers in gas phase and implicit CH_2Cl_2 (grey).

Protonation of the neutral complex **1** to 1H^+ .

The lowest energy isomer of protonated 1H^+ is the typical bridged hydride form (Figure S10), while terminal hydride both in equatorial or apical position are 13.6 and 14.2 $\text{kcal}\cdot\text{mol}^{-1}$ higher in energy, respectively. The most stable sulfur protonated form is the one protonated at the thiolate (+20.8 $\text{kcal}\cdot\text{mol}^{-1}$). These energy differences do not change significantly when computed from COSMO CH_2Cl_2 optimized forms.

The electronic structure of protonated [FeFe]-hydrogenase models at the $\text{Fe}^{\text{I}}\text{Fe}^{\text{I}}$ redox level has been investigated in many papers.¹ The bond density to form the two new Fe-H bonds in the bridging hydride form comes from the Fe-Fe bond but also from the Fe-ligand bonds. This last aspect is better evidenced by comparison between NBO atomic charges computed for the protonated and unprotonated forms. In our case, NBO charges of **1** and 1H^+ evidenced a significant charge transfer from non-Fe atoms to the hydride (hydride carried a charge of -0.01 units with respect to the initial +1 charge of the incoming proton), in particular from the CO ligand and the S atoms, while Fe atoms are more negative by -0.17 unit in 1H^+ compared to **1** (see Figure S11)

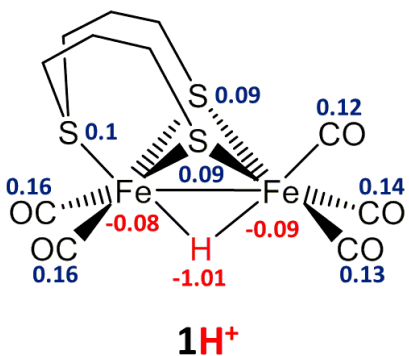


Figure S10. NBO atomic/group charge differences between 1H^+ and **1**.

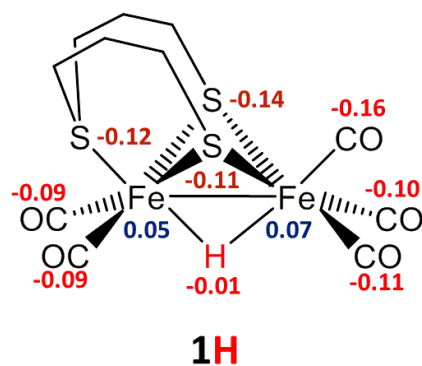


Figure S11. NBO atomic/group charge differences between **1H** and **1H⁺**.

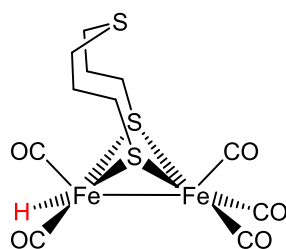


Figure S12. **1H** obtained from protonation at the unsaturated Fe atom of and **1H⁺**.

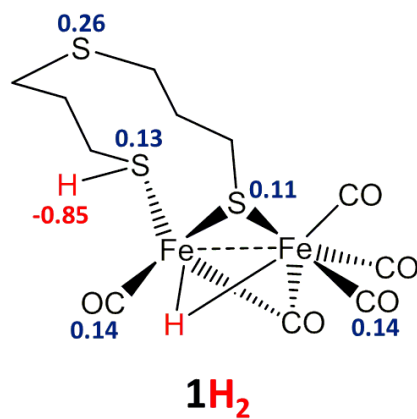


Figure S13. NBO atomic/group charge differences between **1H₂** and **1H⁻**.

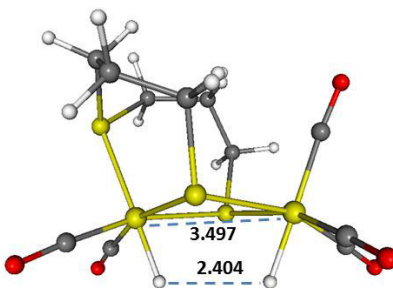


Figure S14. Fe-Fe butterfly structure of **1H₂**. Distances are in Å. This isomer is 3.6 (gas-phase) and 4.3 (implicit CH₂Cl₂) kcal·mol⁻¹ higher in energy with respect to the lowest energy form.

Protonation at the thioether sulfur atom of the TBPT ligand. For all the protonated systems considered in this report, DFT computations show that the protonation at the sulfide of the BTPS ligand is always unfavored and that the sulfide protonated isomers are much higher in energy. In the Figure S15 are reported the energy differences between **1H⁻** and **1H₂** minimum isomers and the corresponding sulfide protonated isomers.

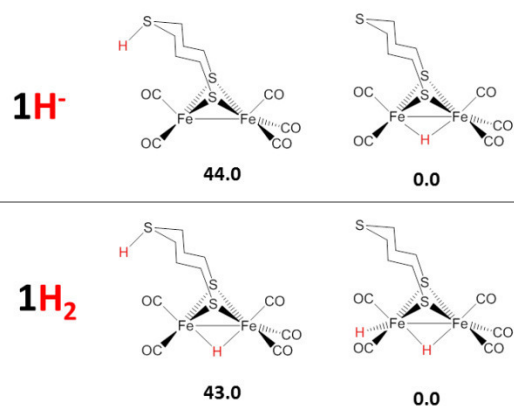


Figure S15. H₂ formation barriers from **1H₂** specie and its reduced form **1H⁻**.

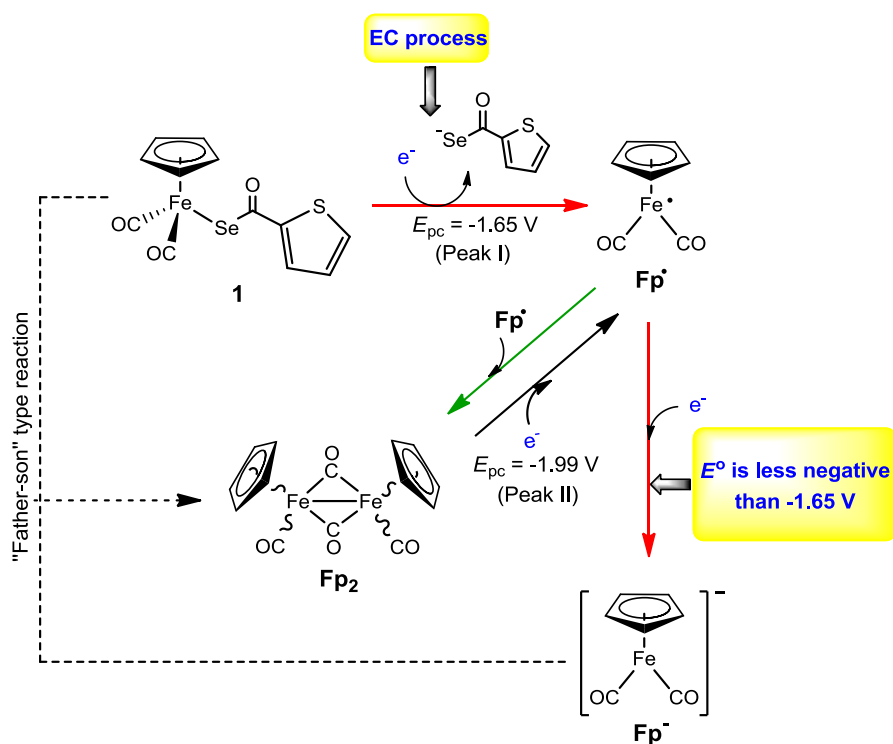
¹ Greco, C.; Zampella, G.; Bertini, L.; Bruschi, M.; Fantucci, P.; De Gioia, L.; *Inorg. Chem.*, **2007**, *46*, 108-116

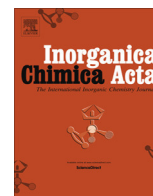
4.7 [HAF-7]

Synthesis, Characterization and Electrochemical Investigations of Heterocyclic-Selenocarboxylate Iron Complexes

Mohammad El-Khateeb, Hassan Abul-Futouh, Helmar Görls, Wolfgang Weigand, Laith R. Almazahreh

Inorganica Chimica Acta, 2016, 449, 14-19.





Synthesis, characterization and electrochemical investigations of heterocyclic-selenocarboxylate iron complexes



Mohammad El-khateeb^{a,*}, Hassan Abul-Futouh^{a,b}, Helmar Görls^b, Wolfgang Weigand^b,
Laith R. Almazahreh^{b,c,*}

^a Chemistry Department, Jordan University of Science and Technology, Irbid 22110, Jordan

^b Institut für Anorganische und Analytische Chemie, Friedrich-Schiller-Universität Jena, Humboldt Straße 8, 07743 Jena, Germany

^c UMR CNRS 6521, Université de Bretagne Occidentale, 6 Avenue Le Gorgeu, C.S. 93837, 29238 Brest-Cedex, France

ARTICLE INFO

Article history:

Received 16 January 2016

Received in revised form 16 April 2016

Accepted 18 April 2016

Available online 23 April 2016

Keywords:

Iron

Selenocarboxylates

Cyclic voltammetry

Characterization

ECE-mechanism

ABSTRACT

Selenocarboxylate complexes of iron containing heterocyclic group of the general formula $\text{CpFe}(\text{CO})_2\text{SeCO-het}$ [het = 2-C₄H₃S (**1**), 2-C₄H₃O (**2**), -CH₂-2-C₄H₃S (**3**)] were prepared from the reaction of iron selenide, $(\mu\text{-Se})[\text{FeCp}(\text{CO})_2]_2$ and the corresponding heterocyclic acid chlorides. These complexes have been characterized by elemental analysis, UV–Vis, IR and ¹H NMR spectroscopic techniques. The X-ray structure of **1** is determined and its electrochemical behavior has been described in details applying cyclic voltammetry.

© 2016 Elsevier B.V. All rights reserved.

1. Introduction

Selenium containing organometallic complexes have witnessed a rapid growth due to their applications in areas such as materials [1–3], catalysis [4–7], electronic industry [8] and biological systems [9]. Recently, some of these complexes have been used as precursors for the synthesis of thin films of metal selenides, which are used in electronic devices [6]. Iron complexes containing selenium are synthesized as models for the [FeFe]-hydrogenase enzymes, which catalyze the proton reduction to produce molecular hydrogen [10–15]. The biological activity of several organoiron selenocarboxylates has been studied [16–18].

The complexes $(\mu\text{-Se}_x)[\text{CpM}(\text{CO})_2]_2$ (M = Fe, x = 1; M = Ru, x = 5) have been synthesized by treatment of the corresponding dimers with selenium element [19,20]. The analogous chromium complexes $(\mu\text{-Se})[\text{Cp}'\text{Cr}(\text{CO})_2]_2$ were also prepared in a similar way (Cp' = C₅H₄Me, C₅H₄COMe, C₅H₄CO₂Me) [21,22]. Tungsten selenides $(\mu\text{-Se}_x)[\text{CpW}(\text{CO})_3]_2$ (x = 2–4) were synthesized via the reaction of the anionic species, $\text{CpW}(\text{CO})_3\text{Li}$, with Se followed by oxidation [23]. The iron selenide $(\mu\text{-Se})[\text{CpFe}(\text{CO})_2]_2$ was found to

be useful in the syntheses of organoiron selenium-complexes. To that end, complexes of the formulae $\text{CpFe}(\text{CO})_2\text{SeCOR}$ [24], $\text{CpFe}(\text{CO})_2\text{SeSO}_2\text{R}$ [25], $\text{CpFe}(\text{CO})_2\text{SeCO}_2\text{R}$ [26], $\text{CpFe}(\text{CO})_2\text{SeCOCO}_2\text{R}$ [27] and $\text{CpFe}(\text{CO})_2\text{SeCSOR}$ [28] have been prepared and fully characterized. In fact, understanding the electrochemistry of the complexes featuring metal–sulfur or metal–selenium bonding would give insights into the catalytic properties of many metalloenzymes. Recently, we have reported the behaviour of the complexes $\text{CpFe}(\text{CO})_2\text{SCO}(2\text{-C}_4\text{H}_3\text{O})$ and $\text{CpFe}(\text{CO})(\text{ER}_3)\text{SCO}(2\text{-C}_4\text{H}_3\text{O})$ (ER₃ = PPh₃, P(OEt)₃, AsPh₃ or SbPh₃) towards oxidation applying cyclic voltammetry [29].

In this report, the synthesis and characterization of iron complexes bearing heterocyclic selenocarboxylate moiety is described. Moreover, we investigate the electrochemical reduction of complex **1** applying cyclic voltammetry. Thus, this work introduces for the first time the electron transfer chemistry of complexes of the type $\text{CpFe}(\text{CO})_2\text{SeCOR}$.

2. Experimental

2.1. Materials and methods

All manipulations were performed using standard Schlenk techniques under a dinitrogen atmosphere. Diethyl ether, hexane, toluene (Na/benzophenone) and CH₂Cl₂ (P₂O₅) were dried

* Corresponding authors at: Institut für Anorganische und Analytische Chemie, Friedrich-Schiller-Universität Jena, Humboldt Straße 8, 07743 Jena, Germany (L.R. Almazahreh).

E-mail address: kateeb@just.edu.jo (M. El-khateeb).

employing standard procedure. The compound $(\mu\text{-Se})[\text{CpFe}(\text{CO})_2]_2$ was prepared by reported procedures [19]. The chemicals: iron dimer $[\text{CpFe}(\text{CO})_2]_2$, 2-furan carbonyl chloride, 2-thiophene carbonyl chloride, 2-thiophene acetyl chloride and elemental selenium were used as received (Acros). For column chromatography, silica gel of particle size 0.063–0.200 mm (70–230 mesh) was employed and the reaction steps were monitored by thin layer chromatography (TLC). Infrared (IR) spectra were recorded on a JASCO FT-IR spectrometer. Electronic spectra were recorded on a Shimadzu 240-UV-Vis spectrophotometer. Nuclear magnetic resonance (NMR) spectra were recorded on a Bruker-Avance 400 MHz spectrometer. Chemical shifts are given in ppm relative to TMS at 0 ppm. Elemental analysis of C, H and S was performed using a vairo EL III CHNS (Elemental analyse GmbH Hanau) as single determination. Melting points were reported on an electrothermal melting point apparatus and are uncorrected.

2.1.1. Electrochemistry

Corrections for the *iR* drop were performed for all experiments. Cyclic voltammetric measurements were conducted in three-electrode technique [glassy carbon disk (diameter $d = 1.6$ mm) as working electrode, Ag/Ag^+ in MeCN as reference electrode, Pt wire as counter electrode] using a Reference 600 Potentiostat (Gamry Instruments). All experiments were performed in MeCN solutions (concentration of the complexes 1.0 mM) containing 0.1 M $[n\text{-Bu}_4\text{N}][\text{BF}_4]$ at room temperature. The solutions were purged with N_2 and a stream of it was maintained over the solutions during the measurements. The vitreous carbon disk was polished on a felt tissue with alumina before each measurement. All potential values reported in this paper are referenced to the potential of the ferrocenium/ferrocene (Fc^+/Fc) couple.

2.2. General procedure for the preparation of $\text{CpFe}(\text{CO})_2\text{SeCO}\text{-het}$, **1–3**

The iron selenide $(\mu\text{-Se})[\text{CpFe}(\text{CO})_2]_2$ (2.83 mmol) and acid chloride (3.40 mmol) were dissolved in 100 mL of diethyl ether. The resulting mixture was stirred overnight at room temperature. The solvent was removed under vacuum and the residue was dissolved in ca. 2 mL of CH_2Cl_2 and was introduced to a silica gel column made up in hexane. Elution with hexane removed any unreacted acid chloride and with a mixture of diethyl ether and hexane (1:1 V:V ratio) gave an orange band which was collected and identified as $\text{CpFe}(\text{CO})_2\text{SeCO}\text{-het}$, followed by a red band which was also collected and identified as $\text{CpFe}(\text{CO})_2\text{Cl}$. The $\text{CpFe}(\text{CO})_2\text{SeCO}\text{-het}$ were recrystallized from $\text{CH}_2\text{Cl}_2/\text{hexane}$ at 0 °C.

2.2.1. $\text{CpFe}(\text{CO})_2\text{SeCO}(2\text{-C}_4\text{H}_3\text{S})$ (**1**)

Brown (82%). m.p.: 144–145 °C. IR (CH_2Cl_2 , cm^{-1}): $\nu_{\text{C}=\text{O}}$ 2040, 1991 (s); $\nu_{\text{SeC}=\text{O}}$ 1610 (m). ^1H NMR (CDCl_3): δ 5.05 (s, 5H, C_5H_5), 7.01 (dd, 1H, $\text{C}_4\text{H}_3\text{S}$), 7.40 (dd, 1H, $\text{C}_4\text{H}_3\text{S}$), 7.74 (d, 1H, $\text{C}_4\text{H}_3\text{S}$). UV-Vis. in Acetonitrile: $\lambda_{\text{max}}(\text{nm})$ (ϵ_{max} , $\text{M}^{-1}\text{cm}^{-1}$): 293 (7.6×10^4), 359 (3.7×10^4). Anal. Calc. for $\text{C}_{12}\text{H}_8\text{FeO}_3\text{SSe}$: C, 39.27; H, 2.20; S, 8.74. Found: C, 39.01; H, 2.19; S, 8.50%.

2.2.2. $\text{CpFe}(\text{CO})_2\text{SeCO}(2\text{-C}_4\text{H}_3\text{O})$ (**2**)

Brown (78%). m.p.: 127–128 °C. IR (CH_2Cl_2 , cm^{-1}): $\nu_{\text{C}=\text{O}}$ 2037, 1990 (s); $\nu_{\text{SeC}=\text{O}}$ 1612 (m). ^1H -NMR (CDCl_3): δ 5.04 (s, 5H, C_5H_5), 6.43 (dd, 1H, $\text{C}_4\text{H}_3\text{O}$), 7.15 (d, 1H, $\text{C}_4\text{H}_3\text{O}$), 7.53 (d, 1H, $\text{C}_4\text{H}_3\text{O}$). UV-Vis. in Acetonitrile: $\lambda_{\text{max}}(\text{nm})$ (ϵ_{max} , $\text{M}^{-1}\text{cm}^{-1}$): 291 (2.1×10^4), 340 (8.20×10^3). Anal. Calc. for $\text{C}_{12}\text{H}_8\text{FeO}_4\text{Se}$: C, 41.06; H, 2.30%. Found: C, 40.89; H, 2.21%.

2.2.3. $\text{CpFe}(\text{CO})_2\text{SeCO}(\text{CH}_2\text{-}2\text{-C}_4\text{H}_3\text{S})$ (**3**)

Orange (68%). m.p.: 111–112 °C. IR (CH_2Cl_2 , cm^{-1}): $\nu_{\text{C}=\text{O}}$ 2035, 1990 (s); $\nu_{\text{SeC}=\text{O}}$ 1617 (m). ^1H NMR (CDCl_3): δ 4.10 (s, 2H, CH_2), 4.95 (s, 5H, C_5H_5), 6.89 (dd, 1H, $\text{C}_4\text{H}_3\text{S}$), 7.26 (d, 2H, $\text{C}_4\text{H}_3\text{S}$). UV-Vis. in

Acetonitrile: $\lambda_{\text{max}}(\text{nm})$ (ϵ_{max} , $\text{M}^{-1}\text{cm}^{-1}$): 291 (1.5×10^4), 335 (8.20×10^3). Anal. Calc. for $\text{C}_{13}\text{H}_{10}\text{FeO}_3\text{SSe}$: C, 40.97; H, 2.64; S, 8.41. Found: C, 40.64; H, 2.54; S, 8.13%.

2.3. Crystal structure determination

The intensity data were collected on a Nonius KappaCCD diffractometer, using graphite-monochromated $\text{Mo K}\alpha$ radiation. Data were corrected for Lorentz and polarization effects; absorption was taken into account on a semi-empirical basis using multiple-scans [30–32]. The structure was solved by direct methods (SHELXS [32]) and refined by full-matrix least squares techniques against Fo^2 (SHELXL-97 [32]). All hydrogen atoms were included at calculated positions with fixed thermal parameters. XP (SIEMENS Analytical X-ray Instruments, Inc.) was used for structure representations.

2.3.1. Crystal data for **1**

$\text{C}_{12}\text{H}_8\text{FeO}_3\text{SSe}$, $\text{Mr} = 367.05$ g mol $^{-1}$, brown prism, size $0.048 \times 0.042 \times 0.038$ mm 3 , monoclinic, space group $P2_1/n$, $a = 9.4600(4)$, $b = 10.7586(4)$, $c = 13.2936(5)$ Å, $\beta = 106.202(2)^\circ$, $V = 1299.24(9)$ Å 3 , $T = -90$ °C, $Z = 4$, $\rho_{\text{calcd.}} = 1.877$ g cm $^{-3}$, μ ($\text{Mo K}\alpha$) = 41.17 cm $^{-1}$, multi-scan, $\text{transmin: } 0.6523$, $\text{transmax: } 0.7456$, $F(000) = 720$, 8588 reflections in $h(-12/11)$, $k(-13/13)$, $l(-16/17)$, measured in the range $2.36^\circ \leq \theta \leq 27.47^\circ$, completeness $\theta_{\text{max}} = 99.5\%$, 2966 independent reflections, $R_{\text{int}} = 0.0525$, 2281 reflections with $F_o > 4\sigma(F_o)$, 163 parameters, 0 restraints, $R1_{\text{obs}} = 0.0382$, $wR2_{\text{obs}} = 0.0807$, $R1_{\text{all}} = 0.0592$, $wR2_{\text{all}} = 0.0881$, $\text{GOF} = 1.045$, largest difference peak and hole: $0.549/-1.066$ e Å $^{-3}$.

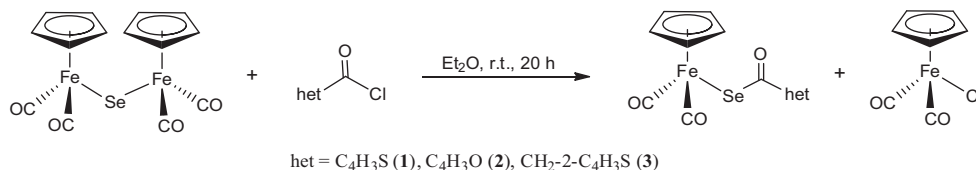
3. Results and discussion

3.1. Synthesis and spectroscopic characterization

Treatment of the selenide complex $(\mu\text{-Se})[\text{CpFe}(\text{CO})_2]_2$ with acid chlorides bearing a heterocyclic group (het) gave the organoiron complexes $\text{CpFe}(\text{CO})_2\text{SeCO}\text{-het}$, **1–3**, and $\text{CpFe}(\text{CO})_2\text{Cl}$ as a side product (Scheme 1).

Complexes **1–3** are air stable as solids and in solutions. Their IR spectra present two strong absorption bands in the ranges of 2035–2040 and 1990–1991 cm^{-1} assigned to the two terminal carbonyl ligand frequencies. These ranges are similar to the analogous aryl selenocarboxylates [19] and lower than those of the thiocarboxylate analogs [29]. The spectra also show a medium band in the range of 1610–1617 cm^{-1} assigned to the C=O of the selenocarboxylate group. This band is higher than that of the corresponding thiocarboxylates due to more double bond character in the C–O bond. The ^1H NMR spectra of **1–3** consist of a singlet in the range of 4.95–5.05 ppm corresponding to the protons of the Cp-ring. This chemical shift range is similar to that observed for the selenocarboxylates and selenocarbonates [19,28]. Three resonances for the heterocyclic protons are shown in the spectra of **1** and **2** while that of **3** showed only two resonances. These behaviors are similar to those observed for the heterocyclic-thiolato ruthenium [33] and heterocyclic-thiocarboxylato complexes [29].

The UV-Vis spectra of **1–3** were measured in acetonitrile to identify the absorption bands expected for these complexes (Fig. 1 as a representative example). Their spectra showed an intense absorption band at $\lambda = 291\text{--}293$ nm. This band is assigned to a ligand–ligand charge transfer (LLCT) type which is comparable to reported systems [34]. Another band is observed in the range of 335–359 nm and is assigned to the Fe–Cp metal to ligand charge transfer (MLCT) transition [23,35,36].



Scheme 1. Synthesis of complexes **1–3** from (μ-Se)[CpFe(CO)₂]₂ and ClCO-het.

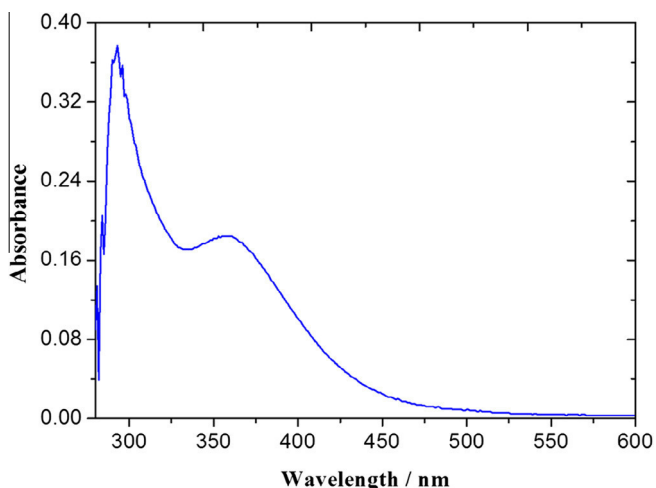


Fig. 1. UV-Vis spectrum for complex **1** in MeCN.

3.2. Molecular structure

Single crystals suitable for X-ray structure determination were obtained by diffusion of dry hexane into a solution of complex **1** in CH₂Cl₂ at 0 °C. Fig. 2 displays the molecular structure of complex **1**.

Complex **1** displays a three legged piano-stool configuration at Fe with η⁵-cyclopentadienyl ligand. The conformation of the SeCO(2-C₄H₃S) ligand observed in the molecular structure of complex **1** places the CO(2-C₄H₃S) group of the ligand in the least sterically congested area between the two CO ligands such that the atom O1 is almost equidistant to the C11 and C12 (O1...C11 = 3.005 Å, O1...C12 = 2.918 Å). This orientation is similar to that reported of the complex CpFe(CO)₂SCO(2-C₄H₃S) [29]. As reported for the complexes CpFe(CO)₂SR (R = Me and ^tBu), the orientation of the ECO(2-C₄H₃S) ligands in the complexes CpFe(CO)₂ECO(2-C₄H₃S) (E = S or Se (**1**)) can allow a filled-filled interaction between the metallic *d* orbitals and the p_π lone pair orbital of the S or the Se atoms [37]. The angle Fe–Se–C1 (104.95(10)°) in complex **1** is smaller than the Fe–S–C1 angle (107.79(8)°) in the S-analogous complex, which can be attributed to the slightly more *s*-character of the valence orbitals of the Se atom than that of the S atom. The Fe–C(Cp) (average = 2.092(3) Å) and Fe–C(O) (1.778(4) Å) bond lengths in complex **1** are similar to those found in other CpFe(CO)₂-containing complexes [23–25,29].

3.3. Electrochemistry

Cyclic voltammetry of complex **1** in MeCN (Fig. 3) at scan rate, *v*, of 0.2 V s⁻¹ shows two reduction waves at *E*_{pc} = –1.65 V (peak I) and –1.99 V (peak II), vs. ferrocenium/ferrocene (Fc⁺/Fc). Reversing the cathodic scan at –1.87 V (red curve in Fig. 3) shows that not only the reduction event II (*E*_{pc} = –1.99 V) is irreversible, but also the reduction of **1** at –1.65 V (peak I). In fact, pure “two-electron” reduction of complex **1** in a single step is particularly unlikely due

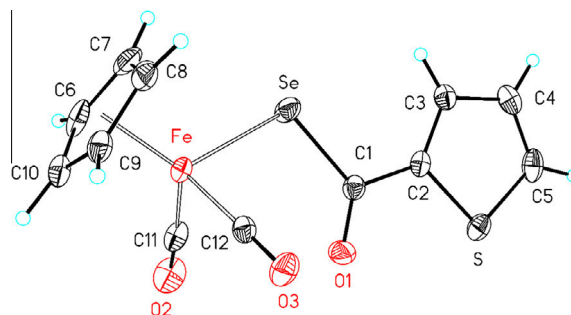


Fig. 2. Molecular structure and numbering scheme of **1**. The ellipsoids represent a probability of 40%, H atoms are shown with arbitrary radii. Selected bond lengths Fe–Se = 2.3854(6), Fe–C11 = 1.778(4), Fe–C12 = 1.778(3), Fe–C6 = 2.088(3), Fe–C8 = 2.095(4), Fe–C9 = 2.091(3), Fe–C7 = 2.094(4), Fe–C10 = 2.091(3), Se–C1 = 1.905(3), C1–O1 = 1.213(4) Å. Selected bond angles C1–Se–Fe = 104.95(10), C12–Fe–Se = 91.67(10), C11–Fe–Se = 92.83(12), C5–Se–C2 = 91.97(17), Se–C1–O1 = 124.1(2)°.

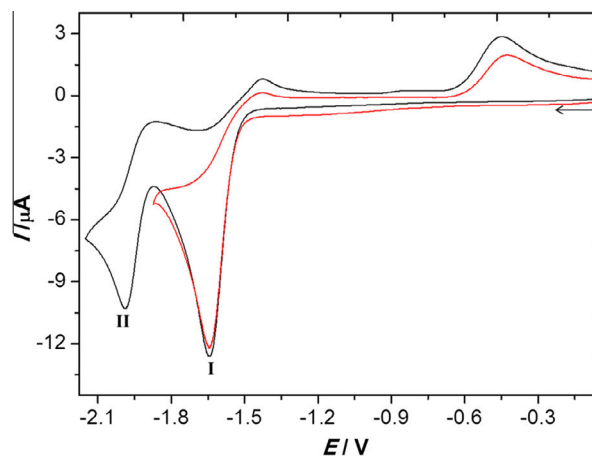


Fig. 3. Cyclic voltammetry of 1.0 mM of **1** in MeCN-[*n*-Bu₄N][BF₄] (0.1 M) at *v* = 0.2 V s⁻¹. Glassy carbon disk (*d* = 1.6 mm). The arrow indicates the scan direction. The potential *E* is given in V and referenced to the Fc⁺/Fc couple.

to the activation barrier. In addition, because of the chemical irreversibility as well as the sharpness of peak I, we exclude a mechanism of two-electron reduction of **1** via two sequential one-electron transfer steps with the normal ordering of potentials¹ [38] such that the dianion **1**²⁻ is obtained from reduction of monoanion **1**⁻ at peak II. We therefore assign the cathodic peak II to a reduction of a product of following chemical reactions on the primary reduced species of **1** (*vide infra*). Figs. 4 and S1 show that

¹ The two-electron reduction with normal ordering of potentials is a case for which the standard potential of the second reduction step (*E*^o2) is more negative than *E*^o1 of the first reduction step (i.e. *E*^o1–*E*^o2 > 0), which is normal because it is thermodynamically more difficult to add an electron to a monoanionic species than to a neutral one. In some cases, a potential inversion (i.e. *E*^o1–*E*^o2 < 0) is observed if a structural change occurred during the electron transfer and led to stabilization of the reduced species. For more details, see reference [38] and the references therein.

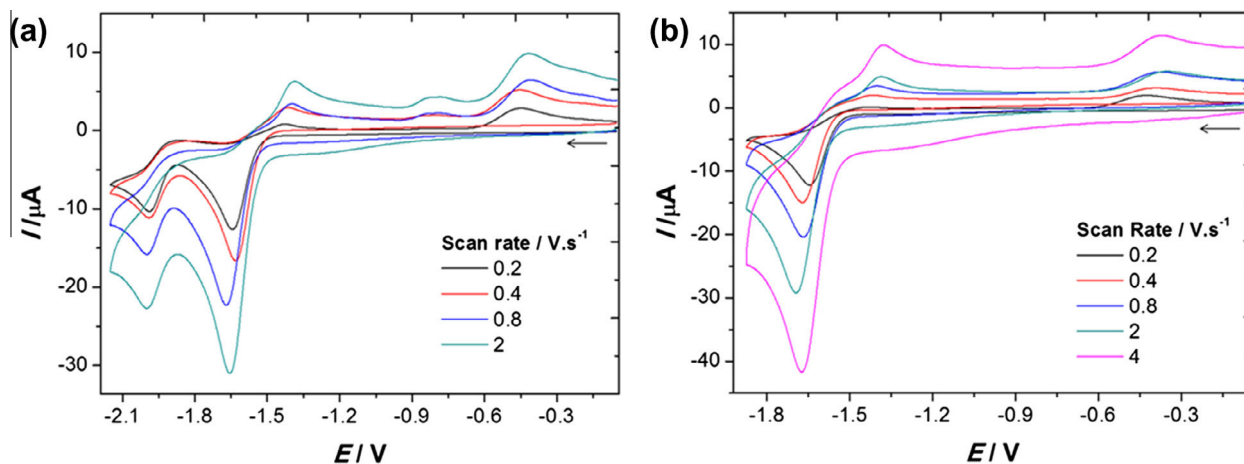


Fig. 4. Cyclic voltammetry of 1.0 mM of **1** in MeCN-[*n*-Bu₄N][BF₄] (0.1 M) at (a) 0.2 V s⁻¹ ≥ *v* ≥ 2 V s⁻¹ (the switching potential is -2.1 V) and (b) 0.2 V s⁻¹ ≥ *v* ≥ 4 V s⁻¹ (the switching potential is -1.87 V). Glassy carbon disk (*d* = 1.6 mm). The arrow indicates the scan direction. The potential *E* is given in V and referenced to the Fc⁺/Fc couple.

the reduction events I and II remain irreversible even at fast scan rates up to 100 V s⁻¹ suggesting fast follow-up reactions. Consequently, the anodic events observed at -1.43 V, -0.83 V and -0.45 V should arise from products of the follow-up reactions.

Studying the current function $I_{pc}/v^{1/2}$ (I_{pc} = cathodic peak current) of the electron transfer process at various scan rates is useful to provide mechanistic information as reported by Nicholson and Shain [39]. The value of $I_{pc}/v^{1/2}$ of peak I significantly decreases as the scan rate increases (Fig. 5). This scan rate dependence of the current function is typical if chemical processes accompany the electron transfer reactions in an ECE mechanism (E = Electron transfer, C = Chemical process) [39]. Almazahreh et al. [39–41] as well as others [42,43] have described the ECE reduction mechanism of several iron-sulfur or iron-selenium systems of the type [Fe₂(CO)₆{μ-(XCH₂)₂E}] (X = RP = O, S, Se, CR₂, X = S or Se), where the intervening chemical step involves cleavage of Fe–S or Fe–Se. We have also shown that the chemical process of the ECE mechanism may involve loss of ligand from the monoanionic species as a result of steric and electronic factors [40].

In the present case, one possible chemical process is the dissociation of the [SeCO(2-C₄H₃S)]⁻ ligand upon reduction of **1** to give the radical intermediate [CpFe(CO)₂][•] (=Fp[•]) accounting for the irreversibility of peak I in Figs. 3 and 4. This 17-electron intermediate (Fp[•]) should then immediately uptake an electron to afford the anionic species Fp⁻, since the standard reduction potential of the redox couple Fp[•]/Fp⁻ ($E^\circ = -1.01$ V [37] or -1.235 V [45]) is less negative than the potential at which **1** is reduced. Thus, the anodic event observed at -1.43 V in the return scan of Fig. 4b should arise from oxidation of Fp⁻. This value is in agreement with that reported by Evans for Fp⁻ obtained from the reduction of the iron dimer [CpFe(CO)₂]₂ (Fp₂) in MeCN [44]. The oxidation process Fp⁻ → Fp[•] + e⁻ is irreversible because of the extremely rapid dimerization of Fp[•] to Fp₂ [44,46]. We also considered the dimerization of the Fp[•] to afford Fp₂ since it is greatly foreseeable process in terms of kinetics and thermodynamics [43]. The peak potential of the second reduction event in Fig. 3 is very similar to that previously reported for the reduction of the iron dimer (Fp₂ + 2e⁻ → 2Fp⁻) [43,46,47]. Therefore, we have additionally performed an independent cyclic voltammetry of Fp₂ and determined its reduction potential to be -1.99 V under our experimental conditions (Fig. S2), which is the same potential of peak II in Figs. 3 and 4a and hence confirming the formation of Fp₂ upon reduction of **1**. The anodic peak observed at -1.43 V in the cyclic voltammetry of Fp₂ (Fig. S2), that is ascribed to the oxidation of Fp⁻ [43], is also present in Fig. 4 and consequently confirms the formation of Fp⁻ from reduction of **1**.

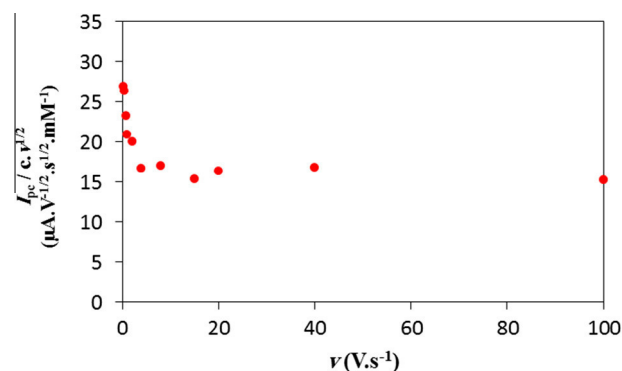
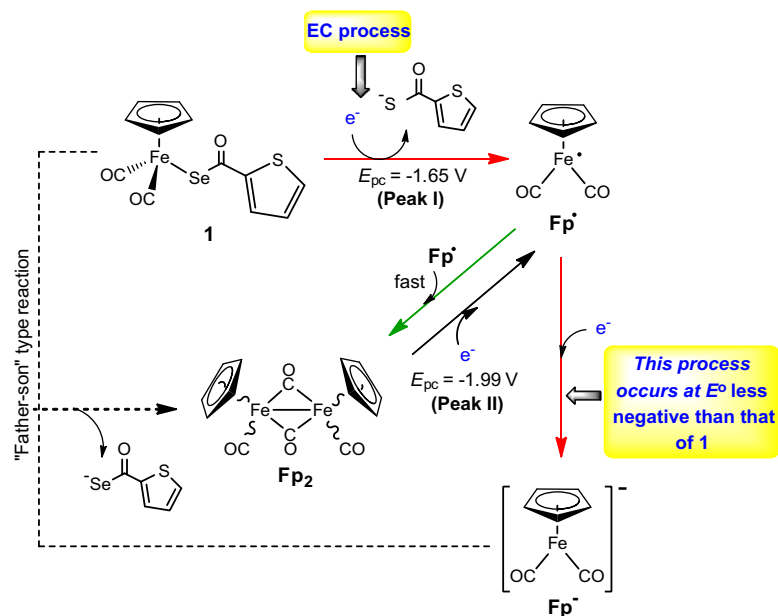


Fig. 5. Scan rate dependence of the current function of the first reduction peak ($E_{pc} = -1.65$ V) of complex **1**.

Although the above results support the proposed formation of Fp₂ and Fp⁻ via ECE mechanism, the decrease of the current function with increasing scan rates is difficult to understand in terms of only these reactions. This is because peak I remains irreversible and the detection of peak II (even at fast scan rates) means that the radical Fp[•] must still be obtained and hence reduced, keeping the same number of transferred electrons ($n = 2$) which is not the case as evident from the plot of the current function against the scan rate (Fig. 5). Thus, another chemical process(es) can also be involved. It is well known that the anion Fp⁻ is one of the strongest nucleophiles within the transition metal anions and it can readily substitute the organohalides and the pseudohalides [48]. Therefore, a reaction between the extraordinary strong nucleophile Fp⁻ and the starting material **1** to produce the iron dimer Fp₂, in a “father-son” type reaction, would contribute to decrease the electron stoichiometry of the overall process (2 electrons for 2 molecules of **1**) as shown in Scheme 2. Indeed, this “father-son” type reaction has been previously proposed for the electrochemical reduction of [Fe(η⁵-C₆H₇)(CO)₃][PF₆] in MeCN [49] as well as for other systems [50,51]. Nevertheless, we are conscious that these chemical steps do not provide a complete picture of the reduction mechanism, which is not presently fully understood.

4. Summary and conclusions

The iron complexes CpFe(CO)₂SeCO-het have been synthesized and characterized. The C=O group of the ligand SeCO(2-C₄H₃S) is



Scheme 2. Summary of the reactions involved in the reduction of complex **1** at glassy carbon electrode. The red arrows indicate the cathodic events responsible for peak I (Fig. 3). The dimerization reaction is shown by the green arrow. The reaction between the anion $Fp^{\bullet-}$ and the starting material **1** (the "father-son" type reaction) is indicated by dashed arrows). (For interpretation of the references to colour in this figure legend, the reader is referred to the web version of this article.)

located between the two $C\equiv O$ ligands in the molecular structure of complex **1** minimizing any steric clash and probably allowing a repulsive filled-filled interaction between the d orbitals of the Fe atom and the p_π lone pair of the Se atom. The electrochemical reduction of **1** by cyclic voltammetry is investigated and a mechanism is proposed as shown in Scheme 2. The reduction of **1** leads to the dissociation of the Fe–Se bond producing the radical Fp^\bullet that dimerizes quickly to Fp_2 or uptakes an electron at the same potential required to reduce **1** affording $Fp^{\bullet-}$ which may react with **1** in a "father-son" type reaction to give Fp_2 . The latter reaction type is possible at fast scan rates at which the diffusion layer is thin.

Acknowledgements

ME thanks Jordan University of Science and Technology, Jordan for financial support. The authors thank Dr. Jean Talarmin (Université de Bretagne Occidentale, France) for the discussions of the electrochemistry. HA-F thanks the DAAD, Germany for scholarship.

Appendix A. Supplementary material

CCDC 1427169 contains the supplementary crystallographic data for **1**. These data can be obtained free of charge from The Cambridge Crystallographic Data Centre via www.ccdc.cam.ac.uk/data_request/cif. Supplementary data associated with this article can be found, in the online version, at <http://dx.doi.org/10.1016/j.ica.2016.04.033>.

References

- [1] S. Kato, O. Niyomura, *Top. Curr. Chem.* 251 (2005) 15.
- [2] S. Dey, V.K. Jain, *Platinum Met. Rev.* 5 (2004) 16.
- [3] J.J. Vittal, D.T. Ng, *Acc. Chem. Res.* 39 (2006) 869.
- [4] M.D. Santana, M. Sáez-Ayala, L. García, J. Pérez, G. García, *Eur. J. Inorg. Chem.* (2007) 4628.
- [5] A. Kumar, G.K. Rao, F. Saleem, A.K. Singh, *J. Chem. Soc., Dalton Trans.* 41 (2012) 11949.
- [6] M.S. Cartese, A.B. Caplan, R.L. Crawford, *BMC Evol. Biol.* 2 (2002) 8.
- [7] J.T. Sampanthar, J.J. Vittal, P.A.W. Dean, *J. Chem. Soc., Dalton Trans.* (1999) 3153.
- [8] E.G. Hope, W. Levason, *Coord. Chem. Rev.* 122 (1993) 109.
- [9] K.R. Chaudhari, A.P. Wadawale, V.G. Jain, N. Yadav, R. Bohra, *Ind. J. Chem.* 49A (2010) 34.
- [10] W. Gao, L.-C. Song, B.-S. Yin, H.-N. Zan, D.-F. Wang, H.-B. Song, *Organometallics* 30 (2011) 4097.
- [11] L.-C. Song, B. Gai, Z.-H. Feng, Z.-Q. Du, Z.-J. Xie, X.-J. Sun, H.-B. Song, *Organometallics* 32 (2013) 3673.
- [12] L.-C. Song, B. Gai, H.-T. Wang, Q.-M. Hu, *J. Inorg. Biochem.* 103 (2009) 805.
- [13] M.K. Harb, T. Niksch, J. Windhager, H. Görls, R. Holze, L.T. Lockett, N. Okumura, D.H. Evans, R.S. Glass, D.L. Lichtenberger, M. El-khateeb, W. Weigand, *Organometallics* 28 (2009) 1039.
- [14] M. El-khateeb, M.K. Harb, Q. Abu-Salem, H. Görls, W. Weigand, *Polyhedron* 61 (2013) 1.
- [15] M.K. Harb, H. Görls, T. Sakamoto, G.A. Felton, D.H. Evans, R.S. Glass, D.L. Lichtenberger, M. El-khateeb, W. Weigand, *Eur. J. Inorg. Chem.* (2010) 3976.
- [16] A.O. Maslat, I. Jibril, M. Abussaud, E.H. Abd-Alhadi, Z. Hamadh, *Appl. Organomet. Chem.* 16 (2001) 44.
- [17] J. Jacob, K. Ahmad, A. Maslat, *J. Carcenog.* 4 (2004) 1.
- [18] A. Maslat, I. Jibril, S. Mized, *Drug Chem. Toxicol.* 33 (2010) 254.
- [19] I. Jibril, O. Abu-Nemrih, *Synth. React. Inorg. Met.-Org. Chem.* 26 (1996) 1409.
- [20] W.A. Herman, J. Rohrmann, H. Hecht, *J. Organomet. Chem.* 290 (1985) 53.
- [21] L.-C. Song, H.-W. Cheng, *Organometallics* 23 (2004) 1072.
- [22] L.-C. Song, H.-W. Cheng, Q.-M. Hu, *J. Organomet. Chem.* 689 (2004) 1849.
- [23] P.G. Jones, C. Thöne, *Inorg. Chem.* 35 (1996) 6625.
- [24] I. Jibril, F.T. Esmadi, H. El-Masri, L. Zsolnai, G. Huttner, *J. Organomet. Chem.* 510 (1996) 109.
- [25] M. El-khateeb, T. Obidate, *Polyhedron* 20 (2001) 2393.
- [26] M. El-khateeb, *Inorg. Chim. Acta* 357 (2004) 4341.
- [27] M. El-khateeb, H. Görls, W. Weigand, *Inorg. Chim. Acta* 360 (2007) 705.
- [28] M. El-khateeb, *Polyhedron* 25 (2006) 1387.
- [29] M. El-khateeb, M. Al-Noaimi, A. Al-Akhras, H. Goerls, W. Weigand, *J. Coord. Chem.* 65 (2012) 2510.
- [30] COLLECT, Data Collection Software; Nonius B.V., Netherlands, 1998.
- [31] Z. Otwinowski, W. Minor, Processing of X-ray diffraction data collected in oscillation mode, in: C.W. Carter, R.M. Sweet (Eds.), *Methods in Enzymology, Macromolecular Crystallography, Part A*, vol. 276, Academic Press, 1997, pp. 307–326.
- [32] G.M. Sheldrick, *Acta Crystallogr. A* 46 (2008) 112.
- [33] M. El-khateeb, M. Al-Noaimi, Z. Al-Amawi, A. Roller, S. Shova, *Inorg. Chim. Acta* 361 (2008) 2957.
- [34] C. Lambert, W. Gaschler, M. Zabel, R. Matschiner, R. Wortmann, *J. Organomet. Chem.* 592 (1999) 109.
- [35] J. Belmont, M. Wrighton, *Organometallics* 5 (1986) 1421.
- [36] T.-H. Wang, C.-H. Hsiao, S.-H. Chen, C.-M. Hsiao, L.Y. Chen, G.-M. Li, B.-C. Hsueh, *J. Organomet. Chem.* 791 (2015) 72.
- [37] M.A. Cranswick, N.E. Gruhn, O. Oorhles-Steele, K.R. Ruddick, N. Burzlaiff, W.A. Schenk, D.L. Lichtenberger, *Inorg. Chim. Acta* 361 (2008) 1122.
- [38] L.R. Almazahreh, R. Trautwein, H. Görls, W. Weigand, *Dalton Trans.* 44 (2015) 18780.

- [39] R.S. Nicholson, I. Shain, *Anal. Chem.* 37 (1965) 178.
- [40] (a) L. Almazahreh, W. Imhof, J. Talarmin, P. Schollhammer, H. Görls, M.Y. El-khateeb, W. Weigand, *Dalton Trans.* 44 (2015) 7177;
(b) L.R. Almazahreh, U.-P. Apfel, W. Imhof, M. Rudolph, H. Görls, J. Talarmin, P. Schollhammer, M. El-khateeb, W. Weigand, *Organometallics* 32 (2013) 4523.
- [41] L.R. Almazahreh Ph.D. thesis, University of Jena, Germany, 2015.
- [42] M.K. Harb, J. Windhager, T. Nicksch, H. Görls, T. Sakamoto, E.R. Smith, R.S. Glass, D.L. Lichtenberger, D.H. Evans, M. El-khateeb, W. Weigand, *Tetrahedron* 68 (2012) 10592.
- [43] G.A.N. Felton, A.K. Vannucci, J. Chen, L.T. Lockett, N. Okumura, B.J. Petro, U.I. Zakai, D.H. Evans, R.S. Glass, D.L. Lichtenberger, *J. Am. Chem. Soc.* 129 (2007) 12521.
- [44] G.A.N. Felton, A.K. Vannucci, N. Okumura, L.T. Lockett, D.H. Evans, R.S. Glass, D.L. Lichtenberger, *Organometallics* 27 (2008) 4671.
- [45] M. Tilset, V.D. Parker, *J. Am. Chem. Soc.* 111 (1989) 6711.
- [46] J.V. Caspar, T.J. Meyer, *J. Am. Chem. Soc.* 102 (1980) 7794.
- [47] E.F. Dalton, S. Ching, R.W. Murray, *Inorg. Chem.* 30 (1991) 2642.
- [48] S. Fukuzumi, K. Ohkubo, M. Fujitsuka, O. Ito, M.C. Teichmann, E. Maisonhaute, C. Amatore, *Inorg. Chem.* 40 (2001) 1213.
- [49] See the following reference and the references therein, R.D. Theys, M.E. Dudley, M.M. Hossain, *Coord. Chem. Rev.* 253 (2009) 180.
- [50] M. Fernanda, N.N. Carvalho, M. Amélia, N.D.A. Lemos, L.F. Veiros, G.R. Stephenson, *J. Organomet. Chem.* 632 (2001) 49.
- [51] (a) S. Lounissi, G. Zampella, J.-F. Capon, L. De Gioia, F. Matoussi, S. Mahfoudhi, F.Y. Pétillon, P. Schollhammer, J. Talarmin, *Chem. Eur. J.* 18 (2012) 11123;
See this reference and the references therein (b) V.G.L. Zchetti, A.M. Granero, S.N. Robledo, M.A. Zon, C.A.D. Rosac, H. Fernández, *J. Braz. Chem. Soc.* 23 (6) (2012) 1131.

Synthesis, Characterization and Electrochemical Investigations of Heterocyclic-Selenocarboxylate Iron Complexes

Mohammad El-khateeb^{a,*}, Hassan Abul-Futouh^{a,b}, Helmar Görls^b, Wolfgang
Weigand^b, Laith R. Almazahreh^{b,c,*}

^a Chemistry Department, Jordan University of Science and Technology, Irbid 22110,
Jordan.

^b Institut für Anorganische und Analytische Chemie, Friedrich-Schiller-Universität
Jena, Humboldt Straße 8, 07743 Jena, Germany.

^c UMR CNRS 6521, Université de Bretagne Occidentale, 6 avenue Le Gorgeu., C.S.
93837, 29238 Brest-Cedex, France

Supporting Information

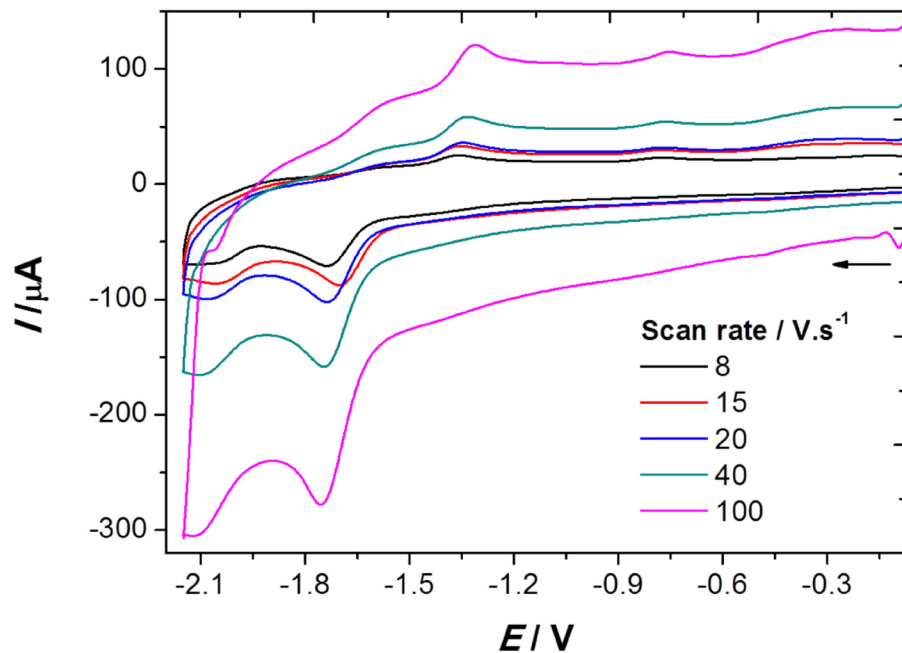


Figure S1. Cyclic voltammetry of 1.0 mM **1** in MeCN- $[n\text{-Bu}_4\text{N}][\text{BF}_4]$ (0.1 M) at $8 \text{ V}\cdot\text{s}^{-1} \leq \nu \leq 100 \text{ V}\cdot\text{s}^{-1}$. Glassy carbon disk ($d = 1.6 \text{ mm}$). The arrow indicates the scan direction. The potential E is given in V and referenced to the Fc^+/Fc couple.

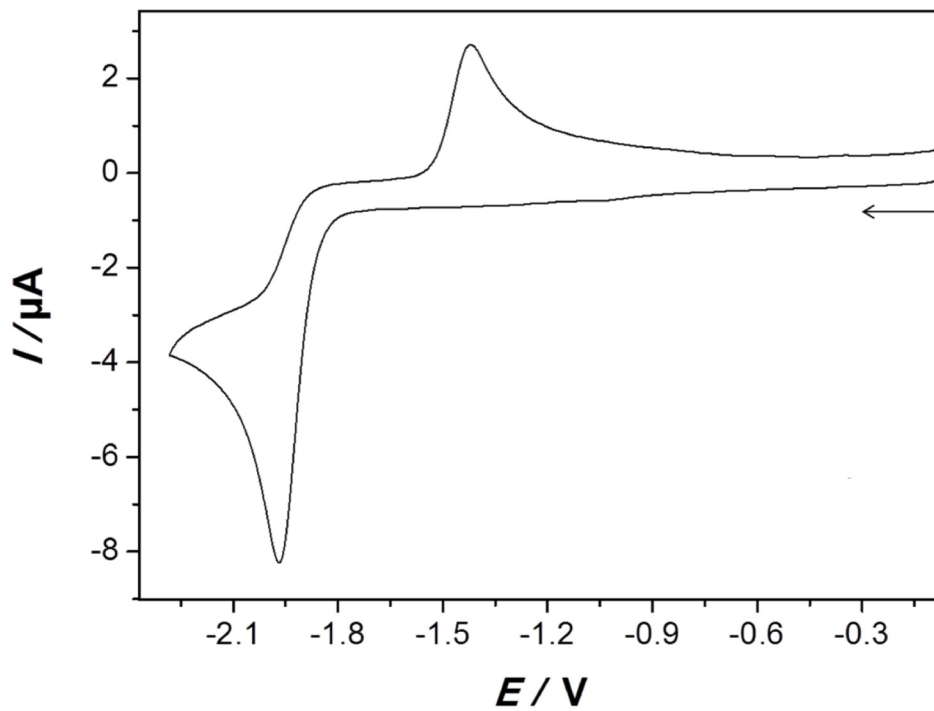
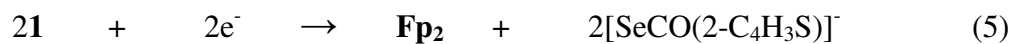
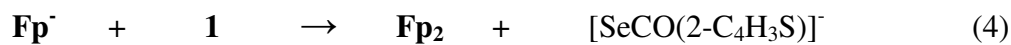
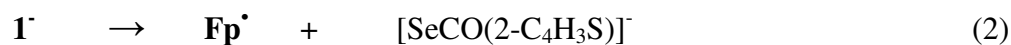


Figure S2. Cyclic voltammetry of $[\text{CpFe}(\text{CO})_2]_2$ (**Fp₂**) in MeCN- $[n\text{-Bu}_4\text{N}][\text{BF}_4]$ (0.1 M) at $\nu = 0.2 \text{ V}\cdot\text{s}^{-1}$. Glassy carbon disk ($d = 1.6 \text{ mm}$). The arrow indicates the scan direction. The potential E is given in V and referenced to the Fc^+/Fc couple.

Cathodic Processes of Complex 1 at -1.65 V (Peak I):

If ‘‘father-son’’ type reaction (equation 4) follows reactions 1-3, the overall reaction 5 would describe a situation in which one mole of electrons is consumed per one mole of complex 1.



5 SUMMARY

The presented works in this dissertation provide a detailed description of the synthesis and characterization of various novel models that mimic the structure of the H-cluster. The redox properties and the catalytic activity of the newly prepared complexes have been studied to evaluate their ability to catalyze electrochemical reduction of protons to give hydrogen molecules. Moreover, the ability of some prepared complexes toward protonation in the presence of Brønsted acids were investigated. In addition, the electronic structure of part of these synthesized models is further analyzed with the aid of DFT computations. The following part will give a brief overview of the published works of this dissertation as well as the unpublished one.

[HAF-1]. The first article in this thesis describes the synthesis of [FeFe]-hydrogenase mimics with μ -(SCH₂)₂ER₂ linkers, where the central atom E is Ge or Sn. In addition, we study in a systematic manner the molecular and electronic structures of the series of complexes depicted in Figure 16.

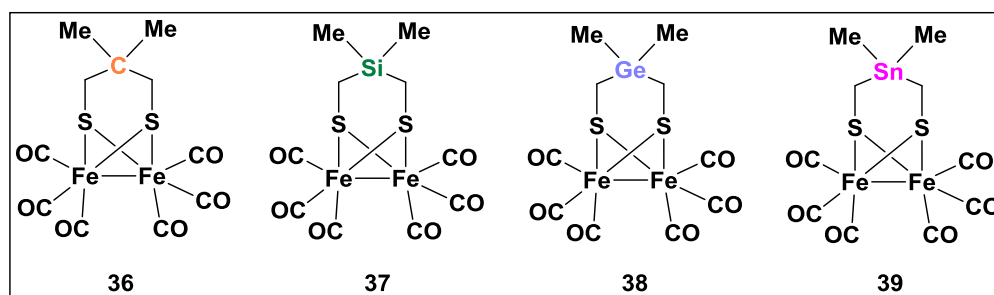
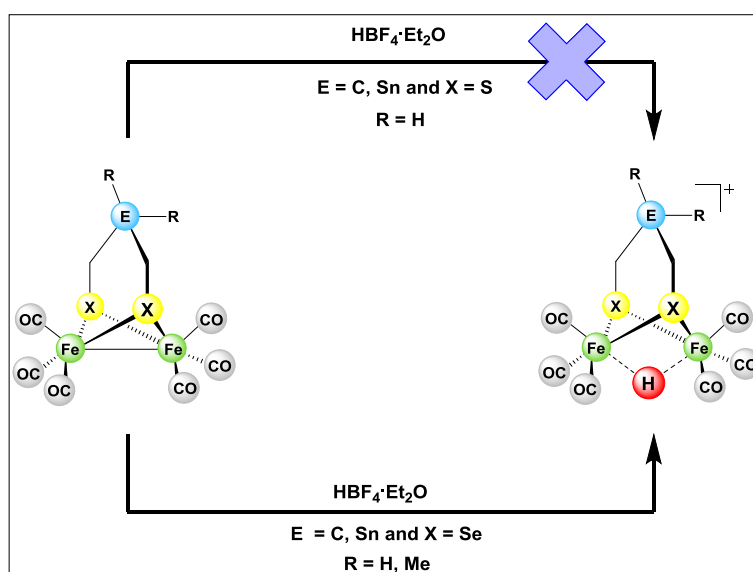


Figure 16. A series of [FeFe]-hydrogenase mimics containing group 14 elements.

As a result of this study, the central six-membered FeSCECS ring preferentially adopts an unusual confirmation with five nearly co-planar atoms (-SCECS-) when E = Ge or Sn in dramatic contrast with the chair/boat conformation when E = C or Si. This could be explained in terms of repulsive steric interaction between the EMe₂ group and the apical carbonyl ligand in [Fe₂(CO)₆{ μ -(SCH₂)₂EMe₂}] complexes. This is also supported with further analysis of these models in the gas phase, which indicates that this near-planarity is the lowest energy conformer. Moreover, the sulfur ionization energies are substantially lowered up on going

from C to Sn in $[\text{Fe}_2(\text{CO})_6\{\mu\text{-(SCH}_2)_2\text{EMe}_2\}]$ ($\text{E} = \text{C, Si, Ge, Sn}$) complexes due to increasing orbital interaction between the σ C-E bond and the sulfur lone pair p orbital. Thus, the sulfur character in the HOMO increases down the series, which makes it more electron-richness going from C to Sn. This is supported by the electrochemical oxidation potentials, where E_{ox} shifts toward less positive values on going from C to Sn. The electrochemical behaviour of complexes **38** and **39** in the absence of a proton source indicates that these complexes follow an ECE mechanism of reduction similar to their analogues **36** and **37**. These complexes catalyze the reduction of protons from moderate and strong acids.

[HAF-2]. In this article, two new complexes $[\text{Fe}_2(\text{CO})_6\{\mu\text{-(SeCH}_2\text{Se)SnMe}_2\}]$ (**40**) and $[\text{Fe}_2(\text{CO})_6\{\mu\text{-(SeCH}_2)_2\text{SnMe}_2\}]$ (**41**) have been synthesized and characterized by variety of spectroscopic methods. The general aim of this study is to investigate the influence of both the central atom in the bridging linker and the bridging chalcogen atoms in determining the basicity properties of the $[\text{Fe}-\text{Fe}]$ -complexes as summarized in Scheme 16.



Scheme 16. Protonation process of complex **41**.

As shown in Scheme 16, the replacement of the $\mu\text{-S}$ atoms in the dithiolato linkers by Se atoms enhances the electron density of the iron cores, which makes it more susceptible to be protonated across the Fe-Fe vector by using a strong acid such as $\text{HBF}_4 \cdot \text{Et}_2\text{O}$. This is supported by a shift $\nu(\text{CO})$ (*ca.* 84 cm^{-1}) to a higher

energy in the IR spectra recorded in solution in the presence of $\text{HBF}_4 \cdot \text{Et}_2\text{O}$. This shift is comparable to those reported in the literature, which implies the formation of a bridging hydride, $\{\text{Fe}(\mu\text{-H})\text{Fe}\}$. Moreover, the appearance of signals in the high-field ^1H NMR spectrum (δ ca. -15.0) together with the shift of the original signals in the $^{77}\text{Se}\{^1\text{H}\}$ NMR spectrum to lower field suggest strong evidence for the formation of the bridging hydride between the two iron atoms, an observation which is reported for the first time, using $\text{HBF}_4 \cdot \text{Et}_2\text{O}$ as a source of protons in hexacarbonyl complexes. Additionally, the replacement of the central carbon atom in the bridging linker by the Sn atom in combination with the $\mu\text{-Se}$ moieties makes it possible for these complexes to be partially protonated employing even a moderate acid such as $\text{CF}_3\text{CO}_2\text{H}$. The electrochemical behaviour of complexes **40** and **41** in the absence of a proton source indicates that these complexes follow an ECE mechanism as well as these complexes catalyze the reduction of protons from AcOH.

[HAF-3]. This article investigates the synthesis and characterization of a macrocyclic complex (Figure 17) by the reaction of $\text{Fe}_3(\text{CO})_{12}$ with 1,2,6,10,11,15-hexathiacyclooctadecane. The resulting 22-membered macrocyclic complex contains two $\text{Fe}_2\text{S}_2(\text{CO})_6$ sub-cluster cores with butterfly structure connected via two identical thioether chain linkers. The molecular structures of the macrocycle complex as well as of 1,2,6,10,11,15-hexathiacyclooctadecane were determined by X-ray crystal structure analysis.

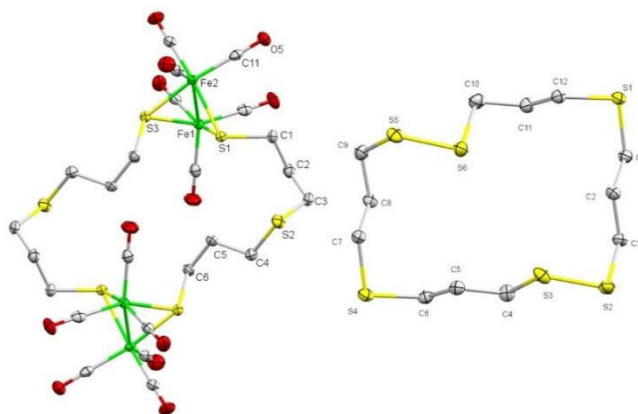


Figure 17. The molecular structures of the macrocycle complex and of 1,2,6,10,11,15-hexathiacyclooctadecane compound.

[HAF-4]. This work report on the preparation of the first naphthalene monoimide (NMI) diselenide derivatives and the synthesis of NMI-disulfide containing two additional halogen atoms in *ortho*- position to the two chalcogens as shown in Figure 18. These compounds were used as pro-ligand to react with $\text{Fe}_3(\text{CO})_{12}$ in boiling THF to afford the [FeFe]-hydrogenase mimics **42-45** (Scheme 17). The resulting complexes **42-45** were characterized by different spectroscopic techniques and investigated their electrochemical and photophysical properties.

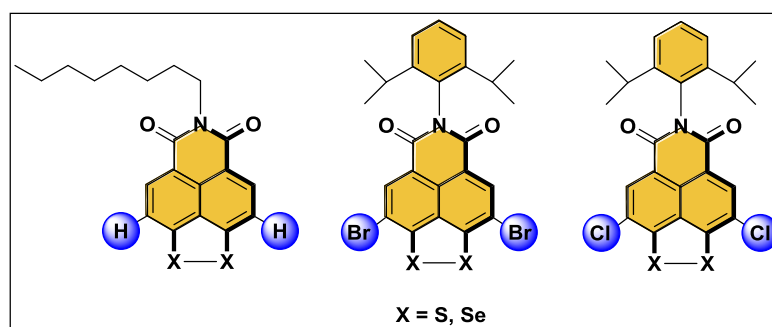
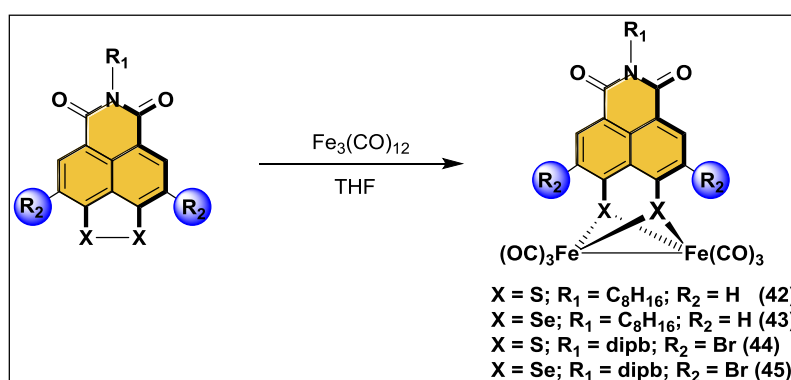


Figure 18. Chemical structures of NMI-dithiol and diselenol compounds.



Scheme 17. Synthetic pathway of complexes **42-45**.

The presence of the imide functionality in the naphthalene skeleton enhanced the chemical stability of the reduced species to proceed via two sequential one-electron processes (EE mechanism) and the introduction of bromine substituents at the 2- and 7-positions of the naphthalene skeleton caused a fine-tuning of the reduction potential. The replacement of the sulfur atoms with selenium atoms in the bridging linker caused a cathodic shift in the oxidation peaks compared with those of the sulfur analogues. The catalytic activity of complexes **42-45** were investigated and reveals their ability to be good catalysts for the reduction of

acetic acid to hydrogen. Detailed investigation of the photophysical properties of the NMI-compounds and complexes **42-45** by means of steady state absorption and emission spectroscopy, revealed drastic quenching of the emission of the diiron complexes with respect to the ligand precursors, which in turn pointed out to efficient transfer of the photo-excited electron to the diiron center. The quantum chemical simulations performed for the complexes indicated their potential to directly transfer a photo-excited electron from the chromophore towards the [FeFe] moiety.

[HAF-5]. The present article provides a detail description of the cyclization of a series of alkyl dithiols having the general formula $[\text{SH}(\text{CH}_2)_n\text{SH}]$ ($n = 4-8$) by following the high dilution technique. The resulting monomeric, dimeric and trimeric disulfides were obtained in better yield compared to that reported in the literature. The molecular structures of the dimeric and trimeric disulfides compounds were determined by X-ray structure analysis. The monomeric and dimeric compounds were used as pro-ligands to react with $\text{Fe}_3(\text{CO})_{12}$ under different conditions to afford complexes with the general formulae $[\text{Fe}_2(\text{CO})_6\{\mu\text{-S}(\text{CH}_2)_n\text{S}\}]$ ($n = 4-8$), $[\text{Fe}_2(\text{CO})_6\{\mu\text{-S}(\text{CH}_2)_n\text{S}\}]_2$ ($n = 6-8$) and $[\text{Fe}_2(\text{CO})_6\{\mu\text{-S}(\text{CH}_2)_n\text{S}\}_2]$ ($n = 6-8$). The goal of this article is to study in a systematic manner how the physical, electrochemical and electrocatalytic features are influenced by increase of n in $[\text{Fe}_2(\text{CO})_6\{\mu\text{-S}(\text{CH}_2)_n\text{S}\}]$ from 2 up to 8 (Figure 19).

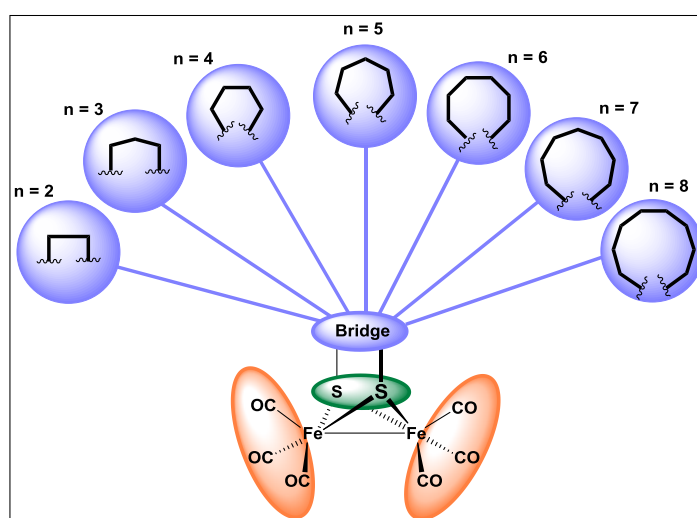


Figure 19. Summary of the complexes with different linker lengths.

Overall, the increase of the length of the chain linker in the dithiolato ligand does not harshly change the electronic properties of the $\text{Fe}(\text{CO})_3$ units. Interestingly, the molecular structures of $[\text{Fe}_2(\text{CO})_6\{\mu\text{-S}(\text{CH}_2)_n\text{S}\}]$ ($n = 4\text{-}7$) complexes showed that SCH_2 -units are constrained to the *aa* conformation, while the molecular structure of the complex $[\text{Fe}_2(\text{CO})_6\{\mu\text{-S}(\text{CH}_2)_8\text{S}\}]$ exhibits an *ae* conformation. Additionally, the redox properties of these complexes were investigated and revealed that the reduction and oxidation potentials of the diiron core in the systematic series from $n = 2$ to 6 are lowered with overall anodic $\Delta E_{1/2}$ and cathodic ΔE_{ox} shifts of 330 and 170 mV, respectively. Moreover, the catalytic activity was also investigated for these complexes in the presence of the weak acid, AcOH. As a result, these complexes reveal their ability to be good catalysts for the reduction of protons with comparable overpotentials (gauged from $E_{\text{cat}/2}$) and their catalytic ability varies in the following order, $n = 7 > 5 > 4 > 6 > 3 > 2$.

[HAF-6]. In this manuscript, the electrochemical behaviour of [FeFe]hydrogenase models featuring [2Fe3S] cores (Figure 20), namely $[\text{Fe}(\text{CO})_5\{\text{TBPT}\}]$ (TBPT = $\mu\text{-}(\text{SC}_3\text{H}_6)_2\text{S}\text{-}\mu$) and $[\text{Fe}(\text{CO})_4(\text{P}(\text{OMe})_3)\{\text{TBPT}\}]$, was investigated in the absence and presence of acetic acid.

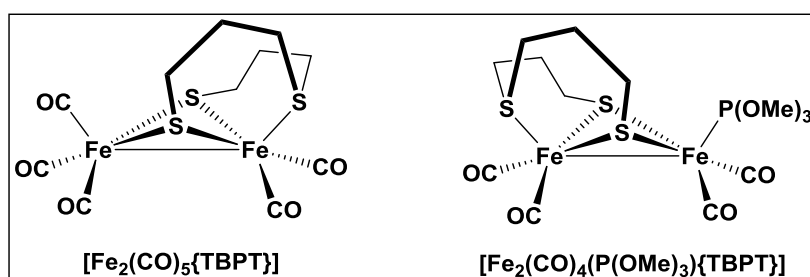
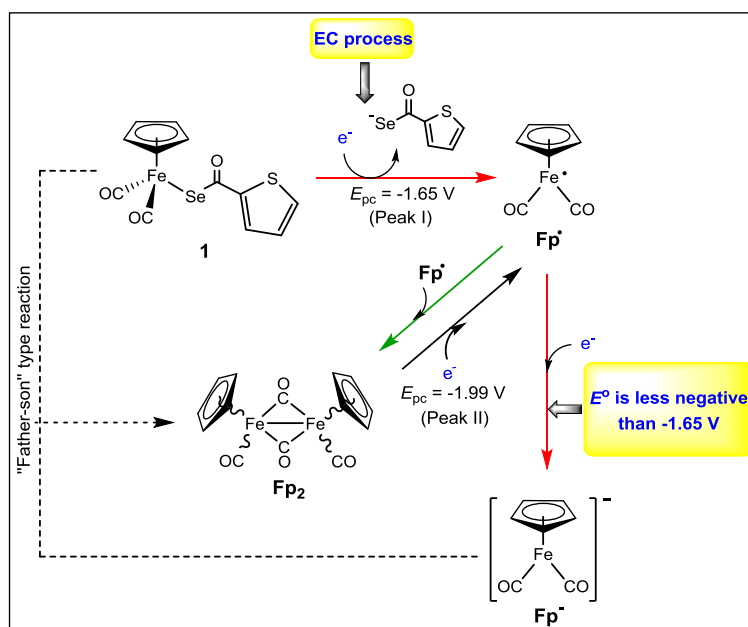


Figure 20. Chemical structures of [2Fe3S] complexes in **[HAF-6]** manuscript.

The complex $[\text{Fe}(\text{CO})_5\{\text{TBPT}\}]$ is reduced in two successive one-electron steps with the normal ordering of potentials ($E^{o_1} - E^{o_2} > 0$), while the complex $[\text{Fe}(\text{CO})_4(\text{P}(\text{OMe})_3)\{\text{TBPT}\}]$ shows only one irreversible one-electron step. DFT calculations are performed on the structures of the neutral, monoanionic and dianionic species of complex $[\text{Fe}(\text{CO})_5\{\text{TBPT}\}]$ as well as on all possible intermediates involved in its catalytic cycle. The DFT level of theory adopted in this work nicely reproduces the molecular structure of $[\text{Fe}(\text{CO})_5\{\text{TBPT}\}]$ and

reduction potentials of the reduced species. Calculations show that all the reduced forms (protonated or not) feature the dissociation of one Fe-S bond. The evolution of H₂ from **AH**₂ (**A** = [Fe(CO)₅{TBPT}]) is energetically not feasible thus providing support to the possible mechanisms of H₂ release from **AH**₂.

[HAF-7]. (The number of compound as illustrated in the article). The iron complexes CpFe(CO)₂SeCO-het have been synthesized and characterized. The C=O group of the ligand SeCO(2-C₄H₃S) is located between the two C≡O ligands in the molecular structure of complex **1** minimizing any steric clash and probably allowing a repulsive filled-filled interaction between the *d* orbitals of the Fe atom and the *p*_π lone pair of the Se atom. The electrochemical reduction of **1** by cyclic voltammetry is investigated and a mechanism is proposed as shown in Scheme 18. The reduction of **1** leads to the dissociation of the Fe-Se bond producing the radical **Fp**[•] that dimerizes quickly to **Fp**₂ or uptakes an electron at the same potential required to reduce **1** affording **Fp**⁻ which may react with **1** in a "father-son" type reaction to give **Fp**₂. The latter reaction type is possible at fast scan rates at which the diffusion layer is thin.



Scheme 18. Summary of the reactions involved in the reduction of complex **1**.

6 ZUSAMMENFASSUNG

Die vorgestellten Arbeiten in dieser Dissertation geben eine detaillierte Beschreibung der Synthese und Charakterisierung verschiedener neuartiger Modelle, die die Struktur des H-Clusters nachahmen. Die Redox Eigenschaften und die katalytische Aktivität der neu hergestellten Komplexe wurden untersucht, um ihre Fähigkeit zur katalytischen elektrochemischen Reduktion von Protonen zu Wasserstoffmolekülen zu bewerten. Darüber hinaus wurde die Fähigkeit einiger synthetisierter Komplexe zur Protonierung in Gegenwart von Brønsted-Säuren untersucht. Darüber hinaus wird die elektronische Struktur eines Teils dieser synthetisierten Modelle mit Hilfe von DFT-Berechnungen weiter analysiert. Der folgende Teil gibt einen kurzen Überblick über die veröffentlichten und unveröffentlichten Arbeiten dieser Dissertation.

[HAF-1]. Der erste Artikel in dieser Arbeit beschreibt die Synthese von Modellen mit μ -(SCH₂)₂ER₂-Linkern, wobei es sich bei dem Zentralatom E um Ge oder Sn handelt. Darüber hinaus untersuchen wir systematisch die molekularen und elektronischen Eigenschaften der in Abbildung 16 dargestellten Komplexreihe.

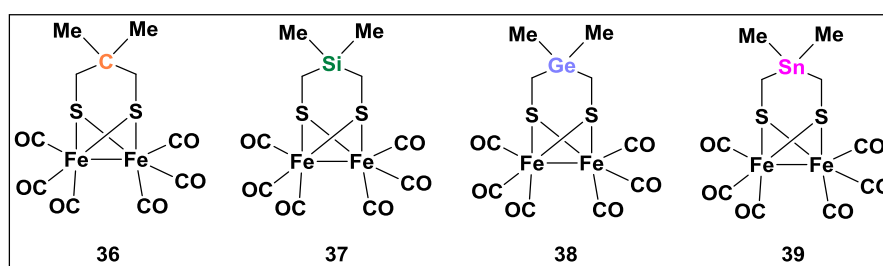
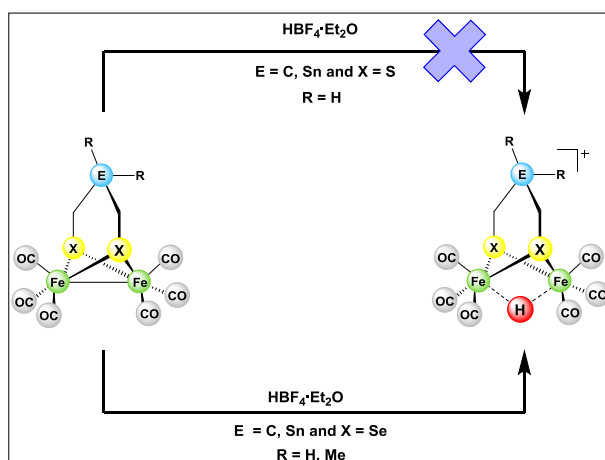


Abbildung 16. Eine Reihe von [FeFe]-Hydrogenasemodellen, die Elemente der Gruppe 14 enthalten.

Als Ergebnis dieser Studie nimmt der zentrale sechsgliedrige FeSCECS-Ring vorzugsweise eine ungewöhnliche Konformation mit fünf nahezu koplanaren Atomen (-SCECS-) ein, wenn E = Ge oder Sn ist, zum deutlichen Unterschied der Stuhl / Boot-Konformation bei E = C oder Si. Dies könnte mit einer sterischen Wechselwirkung zwischen der EMe₂-Gruppe und dem apikalen Carbonylliganden

in $[\text{Fe}_2(\text{CO})_6\{\mu\text{-(SCH}_2)_2\text{EMe}_2\}]$ -Komplexen erklärt werden. Dies wird auch mit einer weiteren Analyse dieser Modelle in der Gasphase unterstützt, was zeigt, dass das quasiplanare Konformer dieses mit der niedrigsten Energie darstellt. Darüber hinaus werden die Schwefel-Ionisationsenergien, bedingt durch die zunehmende Orbital-Wechselwirkung zwischen der σ CE-Bindung und dem mit einem freien Elektronenpaar besetzten p-Orbital des Schwefels, von C bis Sn in $[\text{Fe}_2(\text{CO})_6\{\mu\text{-(SCH}_2)_2\text{EMe}_2\}]$ (E = C, Si, Ge, Sn)-Komplexen deutlich abgesenkt. So steigt der Schwefelcharakter im HOMO in der Serie an, was zu einer Zunahme der Elektronendichte in der Serie von C nach Sn führt. Dies wird durch die elektrochemischen Oxidationspotentiale unterstützt, bei denen E_{ox} zu weniger positiven Werten von C nach Sn verschoben wird. Das elektrochemische Verhalten der Komplexe **38** und **39** in Abwesenheit einer Protonenquelle zeigt an, dass diese Komplexe einem ECE-Mechanismus der Reduktion ähnlich ihren Analoga **36** und **37** folgen. Diese Komplexe katalysieren die Reduktion von Protonen aus mittelstarken und starken Säuren.

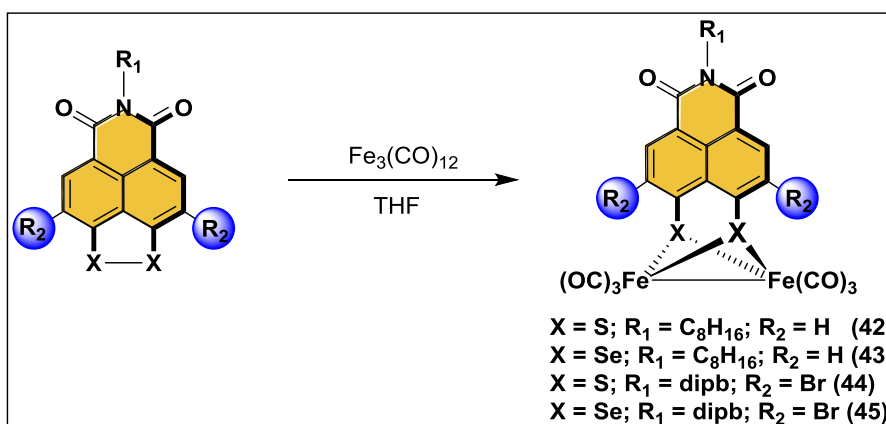
[HAF-2]. In diesem Artikel wurden zwei neueartige Komplexe $[\text{Fe}_2(\text{CO})_6\{\mu\text{-(SeCH}_2\text{Se) SnMe}_2\}]$ (**40**) und $[\text{Fe}_2(\text{CO})_6\{\mu\text{-(SeCH}_2)_2\text{SnMe}_2\}]$ (**41**) synthetisiert und mittels einer Vielzahl spektroskopischer Methoden charakterisiert. Das allgemeine Ziel dieser Studie ist es, den Einfluss sowohl des Brückenkopf-Atoms als auch der überbrückenden Chalkogenatome bei der Bestimmung der Basizitätseigenschaften der $[\text{FeFe}]$ -Komplexe zu untersuchen, wie in Schema 16 zusammengefasst.



Schema 16. Protonierungsreaktionen bei den Komplexen **40** und **41** [HAF-2].

Wie in Schema 16 gezeigt, erhöht der Austausch der μ -S-Atome in den Dithiolato-Linkern durch Se-Atome die Elektronendichte an den Fe Atomen, was sie anfälliger macht, über den Fe-Fe-Vektor unter Verwendung einer starken Säure wie $\text{HBF}_4 \cdot \text{Et}_2\text{O}$ protoniert zu werden. Dies wird durch eine Verschiebung der $\nu(\text{CO})$ -Banden (ca. 84 cm^{-1}) zu höherer Energie in den IR-Spektren der Lösung dieser Komplexe mit $\text{HBF}_4 \cdot \text{Et}_2\text{O}$ unterstützt. Diese Verschiebung ist vergleichbar mit der in der Literatur berichteten, was die Bildung eines verbrückenden Hydrids $\{\text{Fe}(\mu\text{-H})\text{Fe}\}$ impliziert. Darüber hinaus zeigt das Auftreten von Signalen im Hochfeld- ^1H -NMR Spektrum (δ ca. $-15,0$) zusammen mit der Verschiebung der Originalsignale in den $^{77}\text{Se}\{^1\text{H}\}$ NMR-Spektren zu tieferem Feld einen wichtigen Nachweis für die Bildung des verbrückenden Hydrids zwischen den beiden Fe Atome, eine Beobachtung, die, bei Verwendung von $\text{HBF}_4 \cdot \text{Et}_2\text{O}$ als Protonenquelle in Hexacarbonylkomplexen, erstmalig beschrieben wird. Zusätzlich ermöglicht der Austausch eines Kohlenstoffatoms durch das Sn-Atom in Kombination mit den μ -Se-Einheiten, dass diese Komplexe unter Verwendung einer mäßigen Säure wie $\text{CF}_3\text{CO}_2\text{H}$ partiell protoniert werden können. Das elektrochemische Verhalten der Komplexe **40** und **41** in Abwesenheit einer Protonenquelle zeigt, dass diese Komplexe einem ECE-Reduktionsmechanismus folgen. Zusätzlich katalysieren diese Komplexe die Reduktion von Protonen aus AcOH .

[HAF-3]. Dieser Artikel beschreibt die Synthese und Charakterisierung eines makrocyclischen Komplexes (Abbildung 17) durch die Reaktion von $\text{Fe}_3(\text{CO})_{12}$ mit 1,2,6,10,11,15-Hexathiacyclooctadecan. Der resultierende 22-gliedrige makrozyklische Komplex enthält zwei $\text{Fe}_2\text{S}_2(\text{CO})_6$ -Subcluster-Kerne mit Schmetterlingsstruktur, die über zwei identische Thioether-Ketten-Linker verbunden sind. Die Molekülstrukturen des makrozyklischen Komplexes sowie von 1,2,6,10,11,15-Hexathiacyclooctadecan wurden durch Röntgenstrukturanalyse bestimmt.



Schema 17. Synthese der Komplexe **42-45**.

Die Anwesenheit der Imidfunktionalität im Naphthalin-Skelett erhöhte die chemische Stabilität der reduzierten Spezies, die über zwei aufeinanderfolgende Ein-Elektronen-Prozesse (EE-Mechanismus) gebildet werden. Die Einführung von Bromsubstituenten an den 2- und 7-Positionen des Naphthalinskeletts verursachte eine Feinabstimmung des Reduktionspotentials. Der Austausch der verbrückenden Schwefelatome durch Selenatome führte zu einer kathodischen Verschiebung der Oxidationspeaks im Vergleich zu denen der Schwefelanaloga. Die katalytische Aktivität der Komplexe **42-45** wurde untersucht und zeigt ihre Fähigkeit als geeignete Katalysatoren für die Reduktion von Protonen der AcOH zu elementarem Wasserstoff. Eine detaillierte Untersuchung der photophysikalischen Eigenschaften der NMI-Verbindungen und Komplexe **42-45** mittels stationärer Absorptions- und Emissionsspektroskopie zeigte eine drastische Abschwächung der Emissionsintensität der [FeFe]-Komplexe gegenüber den Proliganden, was wiederum auf eine effiziente Übertragung des photoangeregten Elektrons auf das [FeFe]-Zentrum hindeutete. Die für die Komplexe durchgeführten quantenchemischen Simulationen zeigten, dass im Prinzip direkt ein photoangeregtes Elektron aus dem Chromophor in Richtung der [FeFe]-Gruppe übertragen wird.

[HAF-5]. Der vorliegende Artikel liefert eine detaillierte Beschreibung der Cyclisierung einer Reihe von Alkyldithiolen mit der allgemeinen Formel [SH(CH₂)_nSH] (n = 4-8) durch Anwendung des Verdünnungsprinzips. Die resultierenden monomeren, dimeren und trimeren Disulfide wurden in höherer

Ausbeute, als in der Literatur beschrieben, erhalten. Die molekularen Strukturen der dimeren und trimeren Disulfidverbindungen wurden durch Röntgenstrukturanalyse bestimmt. Die monomeren und dimeren Verbindungen wurden als Proliganden verwendet und mit $\text{Fe}_3(\text{CO})_{12}$ unter verschiedenen Bedingungen zur Reaktion gebracht, um Komplexe mit den allgemeinen Formeln $[\text{Fe}_2(\text{CO})_6\{\mu\text{-S}(\text{CH}_2)_n\text{S}\}]$ ($n = 4-8$), $[\text{Fe}_2(\text{CO})_6\{\mu\text{-S}(\text{CH}_2)_n\text{S}\}]_2$ ($n = 6-8$) und $[\text{Fe}_2(\text{CO})_6\{\mu\text{-S}(\text{CH}_2)_n\text{S}\}_2]$ ($n = 6-8$) zu erhalten. Ziel dieses Artikels ist es, systematisch zu untersuchen, wie die physikalischen, elektrochemischen und elektrokatalytischen Merkmale durch die Erhöhung von n in $[\text{Fe}_2(\text{CO})_6\{\mu\text{-S}(\text{CH}_2)_n\text{S}\}]$ von $n = 2 - 8$ beeinflusst werden (Abb 19).

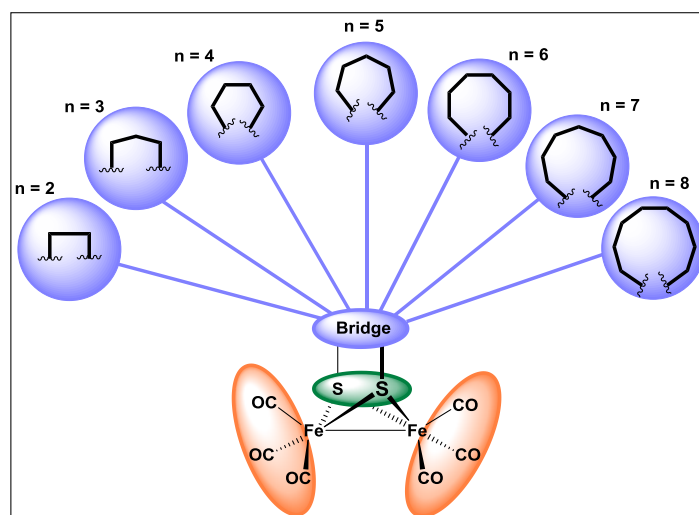


Abbildung 19. Zusammenfassung der Komplexe mit verschiedenen Linkerlängen.

Insgesamt erhöht die Zunahme der Kettenlänge des Dithiolato-Liganden der All-CO-Komplexe die elektronischen Eigenschaften der $\text{Fe}(\text{CO})_3$ -Einheiten nicht deutlich. Interessanterweise zeigten die molekularen Strukturen von $[\text{Fe}_2(\text{CO})_6\{\mu\text{-S}(\text{CH}_2)_n\text{S}\}]$ ($n = 4-7$)-Komplexen, dass die SCH_2 -Einheiten ausschließlich die *aa*-Konformation einnehmen, während die molekulare Struktur des Komplexes $[\text{Fe}_2(\text{CO})_6\{\mu\text{-S}(\text{CH}_2)_8\text{S}\}]$ eine *ae*-Konformation aufweist. Zusätzlich wurden die Redox Eigenschaften dieser Komplexe untersucht. Es wurde gezeigt, dass die Reduktions- und Oxidationspotentiale des $[\text{Fe-Fe}]$ -Kerns in der systematischen Reihe von $n = 2$ bis 6 abgesenkt sind. Die anodischen $\Delta E_{1/2}$ und kathodischen ΔE_{ox} -Verschiebungen betragen 330 und 170 mV. Darüber hinaus wurde die katalytische Aktivität auch für diese Komplexe in Gegenwart der schwachen Säure

Essigsäure untersucht. Als Ergebnis zeigen diese Komplexe ihre Fähigkeit, als Katalysatoren für die Reduktion von Protonen mit vergleichbaren Überpotentialen (aus $E_{cat/2}$) zu fungieren, und ihre katalytische Fähigkeit variiert in der Reihenfolge $n = 7 > 5 > 4 > 6 > 3 > 2$.

[HAF-6]. In diesem Manuskript wurde das elektrochemische Verhalten von [FeFe]-Hydrogenasemodellen mit [2Fe3S]-Einheiten (Abbildung 20), nämlich $[\text{Fe}(\text{CO})_5\{\text{TBPT}\}]$ (TBPT = $\mu\text{-(SC}_3\text{H}_6)_2\text{S-}\mu$) und $[\text{Fe}(\text{CO})_4(\text{P}(\text{OMe})_3)\{\text{TBPT}\}]$ wurde in Abwesenheit und Gegenwart von Essigsäure untersucht.

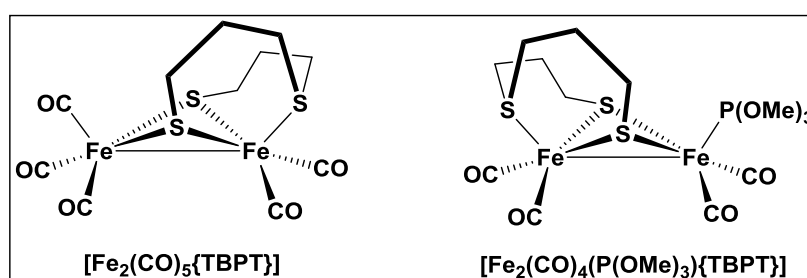
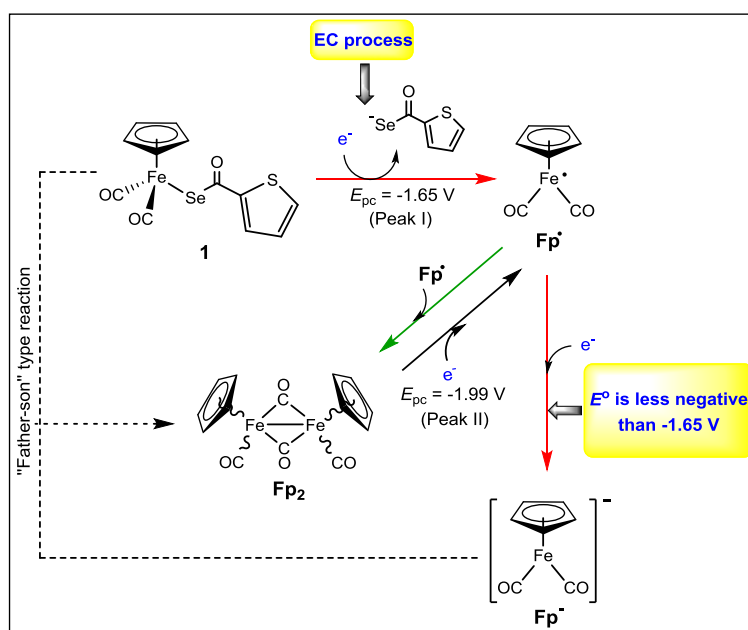


Abbildung 20. Chemische Strukturen von [2Fe3S]-Modellkomplexen in [HAF-6] manuscript.

Der Komplex $[\text{Fe}(\text{CO})_5\{\text{TBPT}\}]$ wird in zwei aufeinanderfolgenden Ein-Elektronen-Schritten mit der normalen Ordnung der Potentiale ($E^{\circ}_1 - E^{\circ}_2 > 0$) reduziert, während der Komplex $[\text{Fe}(\text{CO})_4(\text{P}(\text{OMe})_3)\{\text{TBPT}\}]$ nur einen irreversiblen Ein-Elektronen-Schritt zeigt. DFT-Berechnungen wurden für die Strukturen der neutralen, monoanionischen und dianionischen Spezies des Komplexes $[\text{Fe}(\text{CO})_5\{\text{TBPT}\}]$ sowie an allen möglichen Zwischenprodukten durchgeführt, die an ihrem katalytischen Zyklus beteiligt sind. Die in dieser Arbeit verwendete DFT-Studie reproduziert sowohl die durch Röntgendiffraktometrie bestimmte Struktur von $[\text{Fe}(\text{CO})_5\{\text{TBPT}\}]$, als auch Reduktionspotentiale der reduzierten Spezies. Berechnungen zeigen, dass alle reduzierten Formen (protoniert oder nicht) eine Dissoziation einer Fe-S-Bindung aufweisen. Die Entwicklung von H_2 aus AH_2 ($\text{A} = [\text{Fe}(\text{CO})_5\{\text{TBPT}\}]$) ist energetisch nicht möglich, dafür aber unterstützen die Rechnungen die H_2 -Freisetzung aus AH_2^- .

[HAF-7]. (Die Nummer der hier beschriebenen Verbindung entspricht dieser im Artikel). Die Eisenkomplexe $[\text{CpFe}(\text{CO})_2\text{SeCO-het}]$ wurden synthetisiert und

charakterisiert. Die C=O-Gruppe des Liganden SeCO(2-C₄H₃S) ist zwischen den beiden C≡O-Liganden in der Molekülstruktur des Komplexes **1** orientiert und es wird damit jegliche sterische Wechselwirkung minimiert. Es wird damit vermutlich eine abstoßende Wechselwirkung zwischen den besetzten *d*-Orbitalen des Fe Atoms und dem mit einem nichtbindenden Elektronenpaar besetzten *p* π -Orbitalen des Se-Atoms ermöglicht. Die elektrochemische Reduktion von **1** durch Cyclovoltammetrie wird untersucht und ein Mechanismus wird vorgeschlagen, wie in Schema 18 gezeigt. Die Reduktion von **1** führt zur Dissoziation der Fe-Se-Bindung, die das Radikal **Fp**[•] erzeugt, das entweder schnell zu **Fp**₂ dimerisiert, oder bei gleichem Potential, welches erforderlich ist, um **1** zu reduzieren, ein Elektron aufnimmt, was zu **Fp**⁻ führt, das mit **1** in einer "father-son"-Typ-Reaktion reagieren kann und schliesslich **Fp**₂ ergibt. Der letztere Reaktionstyp ist bei schnellen Verschiebungsgeschwindigkeiten möglich, bei denen die Diffusionsschicht dünn ist.



Scheme 18. Zusammenfassung der Reaktionen bei der Reduktion von Komplex **1**.

7 REFERENCES

1. D. J. Wuebbles and A. K. Jain, *Fuel Process Technol*, 2001, **71**, 99-119.
2. C. Koroneos, A. Dompros, G. Roumbas and N. Moussiopoulos, *International Journal of Hydrogen Energy*, 2004, **29**, 1443-1450.
3. N. Armaroli and V. Balzani, *ChemSusChem*, 2011, **4**, 21-36.
4. M. A. Peña, J. P. Gómez and J. L. G. Fierro, *Applied Catalysis A: General*, 1996, **144**, 7-57.
5. D. L. Trimm and Z. I. Önsan, *Catalysis Reviews*, 2001, **43**, 31-84.
6. R. M. Navarro, M. A. Peña and J. L. G. Fierro, *Chemical Reviews*, 2007, **107**, 3952-3991.
7. J. M. Ogden, *Annu Rev Energ Env*, 1999, **24**, 227-279.
8. F. Mueller-Langer, E. Tzimas, M. Kaltschmitt and S. Peteves, *International Journal of Hydrogen Energy*, 2007, **32**, 3797-3810.
9. P. A. Pilavachi, A. I. Chatzipanagi and A. I. Spyropoulou, *International Journal of Hydrogen Energy*, 2009, **34**, 5294-5303.
10. K. A. Vincent, A. Parkin and F. A. Armstrong, *Chemical Reviews*, 2007, **107**, 4366-4413.
11. C. Tard and C. J. Pickett, *Chemical Reviews*, 2009, **109**, 2245-2274.
12. M. Frey, *ChemBioChem*, 2002, **3**, 153-160.
13. R. Cammack, *Nature*, 1999, **397**, 214-215.
14. P. M. Vignais and B. Billoud, *Chemical Reviews*, 2007, **107**, 4206-4272.
15. J. C. Fontecilla-Camps, A. Volbeda, C. Cavazza and Y. Nicolet, *Chemical Reviews*, 2007, **107**, 4273-4303.
16. A. L. De Lacey, V. M. Fernández, M. Rousset and R. Cammack, *Chemical Reviews*, 2007, **107**, 4304-4330.
17. Y. Nicolet, C. Piras, P. Legrand, C. E. Hatchikian and J. C. Fontecilla-Camps, *Structure*, 1999, **7**, 13-23.
18. S. Roy, S. Shinde, G. A. Hamilton, H. E. Hartnett and A. K. Jones, *European Journal of Inorganic Chemistry*, 2011, **2011**, 1050-1055.
19. D. Das, T. Dutta, K. Nath, S. M. Kotay, A. K. Das and T. N. Veziroglu, *Current Science*, 2006, **90**, 1627-1637.

20. E. Garcin, X. Vernede, E. C. Hatchikian, A. Volbeda, M. Frey and J. C. Fontecilla-Camps, *Structure*, 1999, **7**, 557-566.
21. E. C. Hatchikian, N. Forget, V. M. Fernandez, R. Williams and R. Cammack, *European Journal of Biochemistry*, 1992, **209**, 357-365.
22. M. W. Adams and L. E. Mortenson, *Journal of Biological Chemistry*, 1984, **259**, 7045-7055.
23. R. H. Holm, P. Kennepohl and E. I. Solomon, *Chemical Reviews*, 1996, **96**, 2239-2314.
24. P. M. Vignais, B. Billoud and J. Meyer, *FEMS Microbiology Reviews*, 2001, **25**, 455-501.
25. J. W. Peters, W. N. Lanzilotta, B. J. Lemon and L. C. Seefeldt, *Science*, 1998, **282**, 1853-1858.
26. W. Lubitz, H. Ogata, O. Rüdiger and E. Reijerse, *Chemical Reviews*, 2014, **114**, 4081-4148.
27. A. S. Pandey, T. V. Harris, L. J. Giles, J. W. Peters and R. K. Szilagyi, *Journal of the American Chemical Society*, 2008, **130**, 4533-4540.
28. J. Esselborn, C. Lambertz, A. Adamska-Venkatesh, T. Simmons, G. Berggren, J. Noth, J. Siebel, A. Hemschemeier, V. Artero, E. Reijerse, M. Fontecave, W. Lubitz and T. Happe, *Nat Chem Biol*, 2013, **9**, 607-609.
29. G. Berggren, A. Adamska, C. Lambertz, T. R. Simmons, J. Esselborn, M. Atta, S. Gambarelli, J. M. Mouesca, E. Reijerse, W. Lubitz, T. Happe, V. Artero and M. Fontecave, *Nature*, 2013, **499**, 66-69.
30. C. Sommer, A. Adamska-Venkatesh, K. Pawlak, J. A. Birrell, O. Rüdiger, E. J. Reijerse and W. Lubitz, *Journal of the American Chemical Society*, 2017, **139**, 1440-1443.
31. A. Adamska-Venkatesh, D. Krawietz, J. Siebel, K. Weber, T. Happe, E. Reijerse and W. Lubitz, *Journal of the American Chemical Society*, 2014, **136**, 11339-11346.
32. A. Adamska, A. Silakov, C. Lambertz, O. Rüdiger, T. Happe, E. Reijerse and W. Lubitz, *Angewandte Chemie International Edition*, 2012, **51**, 11458-11462.
33. A. Silakov, E. J. Reijerse, S. P. J. Albracht, E. C. Hatchikian and W. Lubitz, *Journal of the American Chemical Society*, 2007, **129**, 11447-11458.
34. E. J. Reijerse, C. C. Pham, V. Pelmeshnikov, R. Gilbert-Wilson, A. Adamska-Venkatesh, J. F. Siebel, L. B. Gee, Y. Yoda, K. Tamasaku, W. Lubitz, T. B. Rauchfuss and S. P. Cramer, *Journal of the American Chemical Society*, 2017, **139**, 4306-4309.

35. C. Greco, M. Bruschi, L. De Gioia and U. Ryde, *Inorganic Chemistry*, 2007, **46**, 5911-5921.
36. C. V. Popescu and E. Münck, *Journal of the American Chemical Society*, 1999, **121**, 7877-7884.
37. G. Fritz, D. Griesshaber, O. Seth and P. M. H. Kroneck, *Biochemistry*, 2001, **40**, 1317-1324.
38. A. L. De Lacey, C. Stadler, C. Cavazza, E. C. Hatchikian and V. M. Fernandez, *Journal of the American Chemical Society*, 2000, **122**, 11232-11233.
39. W. Lubitz, E. Reijerse and M. van Gastel, *Chemical Reviews*, 2007, **107**, 4331-4365.
40. A. S. Pereira, P. Tavares, I. Moura, J. J. G. Moura and B. H. Huynh, *Journal of the American Chemical Society*, 2001, **123**, 2771-2782.
41. Z. Cao and M. B. Hall, *Journal of the American Chemical Society*, 2001, **123**, 3734-3742.
42. Z.-P. Liu and P. Hu, *Journal of the American Chemical Society*, 2002, **124**, 5175-5182.
43. Y. Nicolet, A. L. de Lacey, X. Vernède, V. M. Fernandez, E. C. Hatchikian and J. C. Fontecilla-Camps, *Journal of the American Chemical Society*, 2001, **123**, 1596-1601.
44. J. Telser, M. J. Benecky, M. W. Adams, L. E. Mortenson and B. M. Hoffman, *Journal of Biological Chemistry*, 1986, **261**, 13536-13541.
45. F. M. Rusnak, M. W. Adams, L. E. Mortenson and E. Münck, *Journal of Biological Chemistry*, 1987, **262**, 38-41.
46. W. Roseboom, A. L. De Lacey, V. M. Fernandez, E. C. Hatchikian and S. P. J. Albracht, *JBIC Journal of Biological Inorganic Chemistry*, 2006, **11**, 102-118.
47. L. Yu, C. Greco, M. Bruschi, U. Ryde, L. De Gioia and M. Reiher, *Inorganic Chemistry*, 2011, **50**, 3888-3900.
48. B. J. Lemon and J. W. Peters, *Biochemistry*, 1999, **38**, 12969-12973.
49. A. J. Pierik, M. Hulstein, W. R. Hagen and S. P. J. Albracht, *European Journal of Biochemistry*, 1998, **258**, 572-578.
50. S. P. J. Albracht, W. Roseboom and E. C. Hatchikian, *JBIC Journal of Biological Inorganic Chemistry*, 2006, **11**, 88-101.
51. H. Reihlen, A. Gruhl and G. v. Hessling, *Justus Liebigs Annalen der Chemie*, 1929, **472**, 268-287.

52. W. Hieber and P. Spacu, *Zeitschrift für anorganische und allgemeine Chemie*, 1937, **233**, 353-364.
53. W. Hieber and J. Gruber, *Zeitschrift für anorganische und allgemeine Chemie*, 1958, **296**, 91-103.
54. W. Hieber and W. Beck, *Zeitschrift für anorganische und allgemeine Chemie*, 1960, **305**, 265-273.
55. R. B. King, *Journal of the American Chemical Society*, 1962, **84**, 2460-2460.
56. L. F. Dahl and C.-H. Wei, *Inorganic Chemistry*, 1963, **2**, 328-333.
57. A. Winter, L. Zsolnai and G. Huttner, *Chemische Berichte*, 1982, **115**, 1286-1304.
58. M. Schmidt, S. M. Contakes and T. B. Rauchfuss, *Journal of the American Chemical Society*, 1999, **121**, 9736-9737.
59. E. J. Lyon, I. P. Georgakaki, J. H. Reibenspies and M. Y. Darensbourg, *Angewandte Chemie International Edition*, 1999, **38**, 3178-3180.
60. A. Le Cloirec, S. C. Davies, D. J. Evans, D. L. Hughes, C. J. Pickett, S. P. Best and S. Borg, *Chemical Communications*, 1999, 2285-2286.
61. H. Li and T. B. Rauchfuss, *Journal of the American Chemical Society*, 2002, **124**, 726-727.
62. L.-C. Song, Z.-Y. Yang, H.-Z. Bian, Y. Liu, H.-T. Wang, X.-F. Liu and Q.-M. Hu, *Organometallics*, 2005, **24**, 6126-6135.
63. T. R. Simmons, G. Berggren, M. Bacchi, M. Fontecave and V. Artero, *Coordination Chemistry Reviews*, 2014, **270-271**, 127-150.
64. Y. Li and T. B. Rauchfuss, *Chemical Reviews*, 2016, **116**, 7043-7077.
65. L.-C. Song, *Accounts of Chemical Research*, 2005, **38**, 21-28.
66. J. D. Lawrence, H. Li, T. B. Rauchfuss, M. Bénard and M.-M. Rohmer, *Angewandte Chemie International Edition*, 2001, **40**, 1768-1771.
67. J.-F. Capon, S. Ezzaher, F. Gloaguen, F. Y. Petillon, P. Schollhammer, J. Talarmin, T. J. Davin, J. E. McGrady and K. W. Muir, *New Journal of Chemistry*, 2007, **31**, 2052-2064.
68. H.-G. Cui, M. Wang, W.-B. Dong, L.-L. Duan, P. Li and L.-C. Sun, *Polyhedron*, 2007, **26**, 904-910.
69. S. Jiang, J. Liu and L. Sun, *Inorganic Chemistry Communications*, 2006, **9**, 290-292.

70. Z. Wang, J.-H. Liu, C.-J. He, S. Jiang, B. Åkermark and L.-C. Sun, *Journal of Organometallic Chemistry*, 2007, **692**, 5501-5507.
71. W.-G. Wang, H.-Y. Wang, G. Si, C.-H. Tung and L.-Z. Wu, *Dalton Transactions*, 2009, 2712-2720.
72. Z. Wang, J. Liu, C. He, S. Jiang, B. Åkermark and L. Sun, *Inorganica Chimica Acta*, 2007, **360**, 2411-2419.
73. Y. Si, C. Ma, M. Hu, H. Chen, C. Chen and Q. Liu, *New Journal of Chemistry*, 2007, **31**, 1448-1454.
74. J. Hou, X. Peng, J. Liu, Y. Gao, X. Zhao, S. Gao and K. Han, *European Journal of Inorganic Chemistry*, 2006, **2006**, 4679-4686.
75. W. Gao, L.-C. Song, B.-S. Yin, H.-N. Zan, D.-F. Wang and H.-B. Song, *Organometallics*, 2011, **30**, 4097-4107.
76. F. Wang, M. Wang, X. Liu, K. Jin, W. Dong and L. Sun, *Dalton Transactions*, 2007, 3812-3819.
77. S. Ott, M. Kritikos, B. Åkermark, L. Sun and R. Lomoth, *Angewandte Chemie International Edition*, 2004, **43**, 1006-1009.
78. M. L. Singleton, R. M. Jenkins, C. L. Klemashevich and M. Y. Darensbourg, *Comptes Rendus Chimie*, 2008, **11**, 861-874.
79. R. Trautwein, L. R. Almazahreh, H. Görls and W. Weigand, *Zeitschrift für anorganische und allgemeine Chemie*, 2013, **639**, 1512-1519.
80. R. Trautwein, L. R. Almazahreh, H. Gorls and W. Weigand, *Dalton Transactions*, 2015, **44**, 18780-18794.
81. U.-P. Apfel, Y. Halpin, H. Görls, J. G. Vos, B. Schweizer, G. Linti and W. Weigand, *Chemistry & Biodiversity*, 2007, **4**, 2138-2148.
82. F. Xu, C. Tard, X. Wang, S. K. Ibrahim, D. L. Hughes, W. Zhong, X. Zeng, Q. Luo, X. Liu and C. J. Pickett, *Chemical Communications*, 2008, 606-608.
83. U.-P. Apfel, C. R. Kowol, Y. Halpin, F. Kloss, J. Kübel, H. Görls, J. G. Vos, B. K. Keppler, E. Morera, G. Lucente and W. Weigand, *Journal of Inorganic Biochemistry*, 2009, **103**, 1236-1244.
84. C. M. Thomas, O. Rüdiger, T. Liu, C. E. Carson, M. B. Hall and M. Y. Darensbourg, *Organometallics*, 2007, **26**, 3976-3984.
85. L.-C. Song, Z.-Y. Yang, Y.-J. Hua, H.-T. Wang, Y. Liu and Q.-M. Hu, *Organometallics*, 2007, **26**, 2106-2110.
86. J. Windhager, M. Rudolph, S. Bräutigam, H. Görls and W. Weigand, *European Journal of Inorganic Chemistry*, 2007, **2007**, 2748-2760.

87. U.-P. Apfel, Y. Halpin, H. Görls, J. G. Vos and W. Weigand, *European Journal of Inorganic Chemistry*, 2011, **2011**, 581-588.
88. U.-P. Apfel, H. Görls, G. A. N. Felton, D. H. Evans, R. S. Glass, D. L. Lichtenberger and W. Weigand, *Helvetica Chimica Acta*, 2012, **95**, 2168-2175.
89. U.-P. Apfel, D. Troegel, Y. Halpin, S. Tschierlei, U. Uhlemann, H. Görls, M. Schmitt, J. Popp, P. Dunne, M. Venkatesan, M. Coey, M. Rudolph, J. G. Vos, R. Tacke and W. Weigand, *Inorganic Chemistry*, 2010, **49**, 10117-10132.
90. R. S. Glass, N. E. Gruhn, E. Lorange, M. S. Singh, N. Y. T. Stessman and U. I. Zakai, *Inorganic Chemistry*, 2005, **44**, 5728-5737.
91. R. S. Glass, N. E. Gruhn, E. Lorange, M. S. Singh, N. Y. T. Stessman and U. I. Zakai, *Inorganic Chemistry*, 2007, **46**, 8098-8098.
92. L. R. Almazahreh, U.-P. Apfel, W. Imhof, M. Rudolph, H. Görls, J. Talarmin, P. Schollhammer, M. El-khateeb and W. Weigand, *Organometallics*, 2013, **32**, 4523-4530.
93. M. K. Harb, J. Windhager, T. Nicksch, H. Görls, T. Sakamoto, E. R. Smith, R. S. Glass, D. L. Lichtenberger, D. H. Evans, M. El-khateeb and W. Weigand, *Tetrahedron*, 2012, **68**, 10592-10599.
94. S. Gao, J. Fan, S. Sun, X. Peng, X. Zhao and J. Hou, *Dalton Transactions*, 2008, 2128-2135.
95. M. K. Harb, U.-P. Apfel, J. Kübel, H. Görls, G. A. N. Felton, T. Sakamoto, D. H. Evans, R. S. Glass, D. L. Lichtenberger, M. El-khateeb and W. Weigand, *Organometallics*, 2009, **28**, 6666-6675.
96. P. Das, J.-F. Capon, F. Gloaguen, F. Y. Pétillon, P. Schollhammer, J. Talarmin and K. W. Muir, *Inorganic Chemistry*, 2004, **43**, 8203-8205.
97. L.-C. Song, Z.-C. Gu, W.-W. Zhang, Q.-L. Li, Y.-X. Wang and H.-F. Wang, *Organometallics*, 2015, **34**, 4147-4157.
98. M. H. Cheah, S. J. Borg and S. P. Best, *Inorganic Chemistry*, 2007, **46**, 1741-1750.
99. R. M. Henry, R. K. Shoemaker, D. L. DuBois and M. R. DuBois, *Journal of the American Chemical Society*, 2006, **128**, 3002-3010.
100. M. Rakowski DuBois and D. L. DuBois, *Chemical Society Reviews*, 2009, **38**, 62-72.
101. G. A. N. Felton, A. K. Vannucci, J. Chen, L. T. Lockett, N. Okumura, B. J. Petro, U. I. Zakai, D. H. Evans, R. S. Glass and D. L. Lichtenberger, *Journal of the American Chemical Society*, 2007, **129**, 12521-12530.

102. L. Maier, *Helvetica Chimica Acta*, 1969, **52**, 845-857.
103. D. Seyferth, R. S. Henderson and L.-C. Song, *Journal of Organometallic Chemistry*, 1980, **192**, C1-C5.
104. H. J. Reich and R. J. Hondal, *ACS Chemical Biology*, 2016, **11**, 821-841.
105. A. Wessjohann Ludger, A. Schneider, M. Abbas and W. Brandt, *Biological Chemistry*, 2007, **388**, 997.
106. U.-P. Apfel, Y. Halpin, M. Gottschaldt, H. Görls, J. G. Vos and W. Weigand, *European Journal of Inorganic Chemistry*, 2008, **2008**, 5112-5118.
107. M. K. Harb, T. Niksch, J. Windhager, H. Görls, R. Holze, L. T. Lockett, N. Okumura, D. H. Evans, R. S. Glass, D. L. Lichtenberger, M. El-khateeb and W. Weigand, *Organometallics*, 2009, **28**, 1039-1048.
108. L.-C. Song, B. Gai, H.-T. Wang and Q.-M. Hu, *Journal of Inorganic Biochemistry*, 2009, **103**, 805-812.
109. M. K. Harb, U.-P. Apfel, T. Sakamoto, M. El-khateeb and W. Weigand, *European Journal of Inorganic Chemistry*, 2011, **2011**, 986-993.
110. J. Noth, J. Esselborn, J. Güldenhaupt, A. Brünje, A. Sawyer, U.-P. Apfel, K. Gerwert, E. Hofmann, M. Winkler and T. Happe, *Angewandte Chemie International Edition*, 2016, **55**, 8396-8400.
111. I. K. Pandey, M. Natarajan and S. Kaur-Ghumaan, *Journal of Inorganic Biochemistry*, 2015, **143**, 88-110.
112. C. Figliola, L. Male, P. N. Horton, M. B. Pitak, S. J. Coles, S. L. Horswell and R. S. Grainger, *Organometallics*, 2014, **33**, 4449-4460.
113. L. Schwartz, P. S. Singh, L. Eriksson, R. Lomoth and S. Ott, *Comptes Rendus Chimie*, 2008, **11**, 875-889.
114. G. Qian, H. Wang, W. Zhong and X. Liu, *Electrochimica Acta*, 2015, **163**, 190-195.
115. C. Topf, U. Monkowius and G. Knör, *Inorganic Chemistry Communications*, 2012, **21**, 147-150.
116. C. Figliola, L. Male, S. L. Horswell and R. S. Grainger, *European Journal of Inorganic Chemistry*, 2015, **2015**, 3146-3156.
117. G. Qian, W. Zhong, Z. Wei, H. Wang, Z. Xiao, L. Long and X. Liu, *New Journal of Chemistry*, 2015, **39**, 9752-9760.
118. P. Li, S. Amirjalayer, F. Hartl, M. Lutz, B. d. Bruin, R. Becker, S. Woutersen and J. N. H. Reek, *Inorganic Chemistry*, 2014, **53**, 5373-5383.

119. R. J. Wright, C. Lim and T. D. Tilley, *Chemistry – A European Journal*, 2009, **15**, 8518-8525.
120. E. S. Donovan, J. J. McCormick, G. S. Nichol and G. A. N. Felton, *Organometallics*, 2012, **31**, 8067-8070.
121. S. Pullen, H. Fei, A. Orthaber, S. M. Cohen and S. Ott, *Journal of the American Chemical Society*, 2013, **135**, 16997-17003.
122. J.-F. Capon, F. Gloaguen, F. Y. Pétilion, P. Schollhammer and J. Talarmin, *Coordination Chemistry Reviews*, 2009, **253**, 1476-1494.
123. F. Gloaguen and T. B. Rauchfuss, *Chemical Society Reviews*, 2009, **38**, 100-108.
124. X. Zeng, Z. Li, Z. Xiao, Y. Wang and X. Liu, *Electrochemistry Communications*, 2010, **12**, 342-345.
125. J. Zhao, Z. Wei, X. Zeng and X. Liu, *Dalton Transactions*, 2012, **41**, 11125-11133.
126. F. Gloaguen, D. Morvan, J.-F. Capon, P. Schollhammer and J. Talarmin, *Journal of Electroanalytical Chemistry*, 2007, **603**, 15-20.
127. J.-F. Capon, F. Gloaguen, P. Schollhammer and J. Talarmin, *Journal of Electroanalytical Chemistry*, 2004, **566**, 241-247.
128. J. Chen, A. K. Vannucci, C. A. Mebi, N. Okumura, S. C. Borowski, M. Swenson, L. T. Lockett, D. H. Evans, R. S. Glass and D. L. Lichtenberger, *Organometallics*, 2010, **29**, 5330-5340.
129. G. A. N. Felton, C. A. Mebi, B. J. Petro, A. K. Vannucci, D. H. Evans, R. S. Glass and D. L. Lichtenberger, *Journal of Organometallic Chemistry*, 2009, **694**, 2681-2699.
130. A. P. S. Samuel, D. T. Co, C. L. Stern and M. R. Wasielewski, *Journal of the American Chemical Society*, 2010, **132**, 8813-8815.
131. L.-C. Song, D.-S. Guo, Q.-M. Hu and X.-Y. Huang, *Organometallics*, 2000, **19**, 960-962.
132. F. C. J. M. van Veggel, W. Verboom and D. N. Reinhoudt, *Chemical Reviews*, 1994, **94**, 279-299.
133. H. Plenio and D. Burth, *Organometallics*, 1996, **15**, 1151-1156.
134. Y.-C. Liu, L.-K. Tu, T.-H. Yen, G.-H. Lee, S.-T. Yang and M.-H. Chiang, *Inorganic Chemistry*, 2010, **49**, 6409-6420.
135. L.-C. Song, H.-T. Fan and Q.-M. Hu, *Journal of the American Chemical Society*, 2002, **124**, 4566-4567.

136. M.-H. Chiang, Y.-C. Liu, S.-T. Yang and G.-H. Lee, *Inorganic Chemistry*, 2009, **48**, 7604-7612.
137. L.-C. Song, J. Gao, H.-T. Wang, Y.-J. Hua, H.-T. Fan, X.-G. Zhang and Q.-M. Hu, *Organometallics*, 2006, **25**, 5724-5729.
138. Y. Zhang, Y.-T. Si, M.-Q. Hu, C.-N. Chen and Q.-T. Liu, *Acta Crystallographica Section C*, 2007, **63**, m499-m500.
139. Y.-C. Liu, L.-K. Tu, T.-H. Yen, G.-H. Lee and M.-H. Chiang, *Dalton Transactions*, 2011, **40**, 2528-2541.
140. W. Gao, J. Liu, B. Åkermark and L. Sun, *Inorganic Chemistry*, 2006, **45**, 9169-9171.
141. L.-C. Song, F.-H. Gong, T. Meng, J.-H. Ge, L.-N. Cui and Q.-M. Hu, *Organometallics*, 2004, **23**, 823-831.
142. M. K. Harb, A. Daraosheh, H. Görls, E. R. Smith, G. J. Meyer, M. T. Swenson, T. Sakamoto, R. S. Glass, D. L. Lichtenberger, D. H. Evans, M. El-khateeb and W. Weigand, *Heteroatom Chemistry*, 2014, **25**, 592-606.
143. M. Razavet, S. C. Davies, D. L. Hughes and C. J. Pickett, *Chemical Communications*, 2001, 847-848.
144. M. Razavet, S. J. Borg, S. J. George, S. P. Best, S. A. Fairhurst and C. J. Pickett, *Chemical Communications*, 2002, 700-701.
145. S. J. George, Z. Cui, M. Razavet and C. J. Pickett, *Chemistry – A European Journal*, 2002, **8**, 4037-4046.
146. M. Razavet, S. C. Davies, D. L. Hughes, J. E. Barclay, D. J. Evans, S. A. Fairhurst, X. Liu and C. J. Pickett, *Dalton Transactions*, 2003, 586-595.
147. J. D. Lawrence, H. Li and T. B. Rauchfuss, *Chemical Communications*, 2001, 1482-1483.
148. L.-C. Song, Z.-Y. Yang, H.-Z. Bian and Q.-M. Hu, *Organometallics*, 2004, **23**, 3082-3084.
149. M.-Q. Hu, C.-B. Ma, Y.-T. Si, C.-N. Chen and Q.-T. Liu, *Journal of Inorganic Biochemistry*, 2007, **101**, 1370-1375.
150. A. Q. Daraosheh, M. K. Harb, J. Windhager, H. Görls, M. El-khateeb and W. Weigand, *Organometallics*, 2009, **28**, 6275-6280.
151. M. G. I. Galinato, C. M. Whaley, D. Roberts, P. Wang and N. Lehnert, *European Journal of Inorganic Chemistry*, 2011, **2011**, 1147-1154.
152. C. Liu, J. N. T. Peck, J. A. Wright, C. J. Pickett and M. B. Hall, *European Journal of Inorganic Chemistry*, 2011, **2011**, 1080-1093.

153. T. Zhou, Y. Mo, A. Liu, Z. Zhou and K. R. Tsai, *Inorganic Chemistry*, 2004, **43**, 923-930.
154. G. Zampella, C. Greco, P. Fantucci and L. De Gioia, *Inorganic Chemistry*, 2006, **45**, 4109-4118.
155. S. Ott, M. Kritikos, B. Åkermark, L. Sun and R. Lomoth, *Angewandte Chemie*, 2004, **116**, 1024-1027.
156. W. Gao, J. Sun, T. Åkermark, M. Li, L. Eriksson, L. Sun and B. Åkermark, *Chemistry – A European Journal*, 2010, **16**, 2537-2546.
157. S. Jiang, J. Liu, Y. Shi, Z. Wang, B. Åkermark and L. Sun, *Dalton Transactions*, 2007, 896-902.
158. K. Fauvel, R. Mathieu and R. Poilblanc, *Inorganic Chemistry*, 1976, **15**, 976-978.
159. M. Bruschi, P. Fantucci and L. De Gioia, *Inorganic Chemistry*, 2002, **41**, 1421-1429.
160. S. Tschierlei, S. Ott and R. Lomoth, *Energy & Environmental Science*, 2011, **4**, 2340-2352.
161. N. Wang, M. Wang, L. Chen and L. Sun, *Dalton Transactions*, 2013, **42**, 12059-12071.
162. S. Ezzaher, A. Gogoll, C. Bruhn and S. Ott, *Chemical Communications*, 2010, **46**, 5775-5777.
163. W. Dong, M. Wang, X. Liu, K. Jin, G. Li, F. Wang and L. Sun, *Chemical Communications*, 2006, 305-307.
164. R. Zaffaroni, T. B. Rauchfuss, D. L. Gray, L. De Gioia and G. Zampella, *Journal of the American Chemical Society*, 2012, **134**, 19260-19269.
165. D. Schilter, J. M. Camara, M. T. Huynh, S. Hammes-Schiffer and T. B. Rauchfuss, *Chemical Reviews*, 2016, **116**, 8693-8749.
166. S. L. Matthews and D. M. Heinekey, *Inorganic Chemistry*, 2010, **49**, 9746-9748.
167. Y.-C. Liu, K.-T. Chu, Y.-L. Huang, C.-H. Hsu, G.-H. Lee, M.-C. Tseng and M.-H. Chiang, *ACS Catalysis*, 2016, **6**, 2559-2576.
168. J. A. Cabeza, M. A. Martínez-García, V. Riera, D. Ardura and S. García-Granda, *Organometallics*, 1998, **17**, 1471-1477.
169. M. C. Ortega-Alfaro, N. Hernández, I. Cerna, J. G. López-Cortés, E. Gómez, R. A. Toscano and C. Alvarez-Toledano, *Journal of Organometallic Chemistry*, 2004, **689**, 885-893.

170. D. Morvan, J.-F. Capon, F. Gloaguen, A. Le Goff, M. Marchivie, F. Michaud, P. Schollhammer, J. Talarmin, J.-J. Yaouanc, R. Pichon and N. Kervarec, *Organometallics*, 2007, **26**, 2042-2052.
171. X. Zhao, I. P. Georgakaki, M. L. Miller, J. C. Yarbrough and M. Y. Darensbourg, *Journal of the American Chemical Society*, 2001, **123**, 9710-9711.
172. X. Zhao, C.-Y. Chiang, M. L. Miller, M. V. Rampersad and M. Y. Darensbourg, *Journal of the American Chemical Society*, 2003, **125**, 518-524.
173. J.-F. Capon, F. Gloaguen, P. Schollhammer and J. Talarmin, *Journal of Electroanalytical Chemistry*, 2006, **595**, 47-52.
174. F. Quentel, G. Passard and F. Gloaguen, *Energy & Environmental Science*, 2012, **5**, 7757-7761.
175. R. J. Wright, W. Zhang, X. Yang, M. Fasulo and T. D. Tilley, *Dalton Transactions*, 2012, **41**, 73-82.

8 ACKNOWLEDGEMENTS

First, I would like to thank my supervisor, prof. Dr. Wolfgang Weigand, for his enthusiastic and friendly supervision during my Ph.D study and research, and I am indebted to him for the work we have carried out and the successes we have achieved. He always gave me the possibility to follow my own research strategies and supported me in my way.

I also wish to thank my co-advisor, prof. Dr. Mohammad El-khteb, for supporting me during my research work and for proofreading my manuscripts as well as my thesis.

I would also like to acknowledge prof. Dr. Grzegorz Mlostoń from the university of Łódź, Poland for providing me the opportunity to work in his laboratory in the course of my studies.

My sincere acknowledgment to prof. Dr. Kalina Peneva for her support and excellent collaboration with her group. Also, I thank prof. Dr. Benjamin Dietzek and his group for the photophysical measurements of some of my complexes.

Many thanks to Dr. Luca Bertini from the university of Milano-Bicocca, Italy for his collaboration and theoretical calculations of my complexes. I also thank prof. Dr. Richard S. Glass and his group from the university of Arizona, Tucson for the nice collaboration.

Furthermore, I would like to thank Dr. Manfred Rudolph for his lab skills in electrochemistry and scientific discussions. I thank Dr. Helmar Görls for the X-ray structural determination of my complexes in this thesis and thanks to individuals (technicians, co-workers, craftsmen and electricians) of the IAAC institute, especially everyone who measured NMR and Ms spectra, and performed elemental analysis of my complexes.

I have to thank the Deutscher Akademischer Austausch Dienst (DAAD) for their financial support of my Ph.D studies during my stay in Germany. Finally, I would like to thank my family and friends for their support in my life.

9 CURRICULUM VITAE

Hassan Abul Futouh

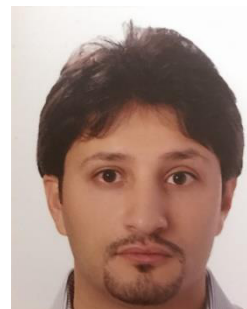
Address: Charlotten Str. 23
07749 Jena, Germany

Phone: 004917676264453

E-mail: habulfutouh@yahoo.com, habulfutouh@gmail.com

Date of Birth: 07. May. 1986

Nationality: Jordanian



Education

(Since Oct. 2013-2017) Friedrich-Schiller-Universität Jen Jena / Germany
Ph.D. student in inorganic chemistry

- Architectural Mimics of [FeFe]-Hydrogenase H-Cluster: Synthesis, Characterization and Electrochemical Studies.
- The financial support for the Ph.D. studies is through a fellowship from "Deutscher Akademischer Austausch Dienst, DAAD".

(Sep. 2008-Jan. 2011) Jordan University of Science and Technology Irbid / Jordan
M.Sc. in applied chemistry

- Synthesis of molybdenum and tungsten complexes containing O-alkyl thiooxalato ligands.
- The financial support for the M.Sc. project was from Alexander von Humboldt Foundation.

(Sep. 2004-Jul. 2008) Jordan University of Science and Technology Irbid / Jordan
B.Sc. in applied chemistry

Experiences

(Sep. 2012-2013) UMM AL-QURA University Al-Qunfudah / Saudi Arabia
Lecturer.

- Teaching Organic, Analytical, Inorganic and General Chemistry Labs.

(Feb. 2011-2012) Jordan University of Science and Technology Irbid / Jordan
Lecturer.

- Teaching Organic, Analytical, Inorganic and General Chemistry Labs.

(Sep. 2011-2012) Jordan Academy for Maritime Studies Amman / Jordan
Lecturer.

- Teaching General Chemistry Courses 101, 102.

(Jan. 2011-2012) Jordan University of Science and Technology Irbid / Jordan
Researcher.

- Synthesis, Characterization and Photolytic Reactions of Heterocyclic-selenocarboxylate Organoiron.
- Mild and Convenient Synthesis of 1,2,3-triodobenzene and its Derivatives for their Applications in one pot Tandem Reaction.

Training Courses at Royal Scientific Society: This training was for two months during the B.Sc. studies in the QC labs and stability department.

Conferences

- Poster: **1st Ulm Symposium on Solar-Driven Chemistry**, Ulm/Germany (8th – 10th Oct. 2017): [FeFe]-Hydrogenase H-cluster Mimics Mediated by Naphthalene Monoimide Derivatives of Peri-Substituted Dichalcogenides.
- Talk: **Xth International Mini-Symposium: Selenium Containing Compounds on the Borderline of Chemistry, Biology and Medicine**, Lodz / Poland (25th May 2017): Selenium Makes the Difference: Protonation of [FeFe]-Hydrogenase Mimics with Diselenolato Ligands.
- Talk: **27th International Symposium on Organic Chemistry of Sulfur**, Jena / Germany (24-29. Jul. 2016): Tuning the Effect of the Dithiolate Linker “[μ -S(CH₂)_nS] (n = 6-8) on the Stabilization or Destabilization of the Rotated Structure in [FeFe]-Hydrogenase Models.
- Participant: **International Conference on Advanced Materials**, Irbid / Jordan (27-29. Apr. 2015).
- Talk: **MANS-12**, Freiberg / Germany (11. Sep. 2014): Electrochemical and Electrocatalytical Features of [Fe₂S₃]-Hydrogenases Model Complexes.
- Participant: **DAAD Stipendiatentreffen**, Jena / Germany (27-29. Mar. 2015).
- Participant: **DAAD Stipendiatentreffen**, Würzburg / Germany (11-13. Apr. 2014).
- Member of the organizing committees: **10th Jordanian Chemical Conference**, Irbid / Jordan (May, 2010).
- Participant: **Eurasia Conference on Chemical Sciences-11**, Dead Sea / Jordan (6-10. Oct. 2010).

Activities

- Participant in the workshop at Service Center Research and Transfer: How to apply for research funding in Germany, Jena, Germany.
- Guest researcher at University of Lodz in Poland: Synthesis of germanium-containing compounds as starting materials for [FeFe]-hydrogenase models.
- Trainee at Tatweer (Business and export development project for Jordanian enterprises): Training sessions on customer relationship management, Amman / Jordan.
- Participant at Chemical Security Engagement Program (CSP): Chemical safety and security workshop, Amman / Jordan.

Publications

1. Kinetics and Mechanism of Ligand Substitution Reactions in [*cis*-M(CO)₄(amine)(EPh₃)] Complexes (M = Mo, W; amine = pyridine, piperidine; E=

- As, Sb): K. J. Asali, M. El-khateeb, Y. Foudeh, **H. Abul-Futouh**, *J. Coord. Chem.*, **2017**, *Accepted manuscript*.
2. Synthesis and Electrochemical Investigation of Mono- and Di-phosphite substituted [FeFe]-Hydrogenase H-Cluster Mimics: **H. Abul-Futouh**, H. Görls, W. Weigand, *Zeitschrift für anorganische und allgemeine Chemie*, **2017**, *Accepted Manuscript*, DOI: 1002/zaac.201700308.
 3. [FeFe]-Hydrogenase H-Cluster Mimics with Various -S(CH₂)_nS- Linker Lengths (n = 2-8): A Systematic Study: **H. Abul-Futouh**, L. R. Almazahreh, M. K. Harb, H. Görls, M. El-khateeb, W. Weigand, *Inorg. Chem.* **2017**, *56*, 10437-10451.
 4. [FeFe]-Hydrogenase H-Cluster Mimics Mediated by Naphthalene Monoimide Derivatives of Peri-Substituted Dichalcogenides: **H. Abul-Futouh**, Y. Zagranyski, C. Müller, M. Schulz, S. Kupfer, H. Görls, M. El-khateeb, S. Gräfe, B. Dietzek, K. Peneva, W. Weigand, *Dalton Trans.* **2017**, *46*, 11180-11191.
 5. A new macrocyclic [FeFe]-hydrogenase H cluster model: **H. Abul-Futouh**, H. Görls, W. Weigand, *Phosphorus, Sulfur Silicon Relat. Elem.*, **2017**, *192*, 634-637.
 6. Selenium makes the difference: protonation of [FeFe]-hydrogenase mimics with diselenolato ligands: **H. Abul-Futouh**, M. El-khateeb, H. Görls, K. J. Asali, W. Weigand, *Dalton Trans.*, **2017**, *46*, 2937-2947.
 7. [FeFe]-Hydrogenase H-cluster mimics with unique planar μ -(SCH₂)₂ER₂ linkers (E= Ge and Sn): **H. Abul-Futouh**, L. R. Almazahreh, T. Sakamoto, N. Y. T. Stessman, D. L. Lichtenberger, R. S. Glass, H. Görls, M. El-khateeb, P. Schollhammer, G. Mloston, W. Weigand, *Chem. Eur. J.*, **2017**, *23*, 346-359.
 8. Synthesis, characterization and electrochemical investigations of heterocyclic-selenocarboxylate iron complexes: M. El-khateeb, **H. Abul-Futouh**, H. Görls, W. Weigand, L. R. Almazahreh, *Inorg. Chim. Acta*, **2016**, *449*, 14-19.
 9. A Mild and Convenient Synthesis of 1,2,3-Triiodoarenes via Consecutive Iodination/Diazotization/Iodination Strategy: R. M. Al-Zoubi, **H. Abul Futouh**, R. McDonald, *Aust. J. Chem.*, **2014**, *66*, 1570-1575.
 10. Mono-and bi-iron chalcogenocarboxylate complexes: M. El-khateeb, M. Al-Noaimi, N. Al-Rejjal, **H. Abul Fetouh**, H. Görls, W. Weigand, *Trans. Met. Chem.*, **2013**, *38*, 529-534.
 11. O-Alkylthiooxalato and dithiocarboxylato complexes of molybdenum and tungsten: M. El-khateeb, **H. Abul Futouh**, K. Asali, W. Weigand, *Polyhedron*, **2012**, *38*, 185-189.

Language Proficiency

- English: full professional proficiency
- German: elementary proficiency
- Arabic: native proficiency

Technical Skills and Expertise

- MS office, Origin
- Synthetic chemistry of metal compounds
- Electrochemistry of metal compounds

- Spectroscopic techniques (e.g. IR, NMR)

Personal Skills

- Meet deadlines with good follow up.
- High level of professionalism.
- Initiation and planning.
- Communication and presentation skills.

Hassan Abul-Futouh

10 DECLARATION OF AUTHORSHIP

I declare that this thesis and the work presented herewith are my own and have been generated by me as the result of my own original research.

11 SELBSTSTÄNDIGKEITSERKLÄRUNG

Ich erkläre, dass ich die vorliegende Arbeit selbstständig und unter Verwendung der angegebenen Hilfsmittel, persönlichen Mitteilungen und Quellen angefertigt habe.

Jena,

Hassan Abul-Futouh